2021

Microstructural and Microchemical Studies of Fluid–Chondrule Interactions in a Pristine CR Carbonaceous Chondrite and Apatite in Martian Nakhlites

Marina Martínez

Marina Martínez Jiménez

Candidate

Earth and Planetary Sciences

Department

This dissertation is approved, and it is acceptable in quality and form for publication:

Approved by the Dissertation Committee:

Dr. Adrian J. Brearley, Chairperson

Dr. Charles K. Shearer

Dr. Steven B. Simon

Dr. Jin S. Zhang

Dr. Hope A. Ishii

MICROSTRUCTURAL AND MICROCHEMICAL STUDIES OF FLUID–CHONDRULE INTERACTIONS IN A PRISTINE CR CARBONACEOUS CHONDRITE
AND
APATITE IN MARTIAN NAKHLITES

by

MARINA MARTÍNEZ JIMÉNEZ

B.S., Geology, Autonomous University of Barcelona, 2013
M.S., Astrophysics, Particle Physics, and Cosmology, University of Barcelona, 2015

DISSERTATION

Submitted in Partial Fulfillment of the
Requirements for the Degree of

Doctor of Philosophy
Earth and Planetary Sciences

The University of New Mexico
Albuquerque, New Mexico

December, 2021

DEDICATION

This thesis is dedicated to my father, Rafael Martínez. He was a physics teacher who introduced me to the world of science with his enthusiasm, curiosity, and hard-working ethic. His beautiful values and enormous heart were an inspiration, and his example of honesty, bravery, and strength will always be in me. I don't have the words to express how much I love him, how much he meant to me, and how grateful I am for having had him as a father.

These were some things he used to say:

- Time does not exist,
- Everything depends on the reference system,
- Each thing happens in its exact, right moment.

Això és per a tu, papa.

ACKNOWLEDGEMENTS

It impossible to express with words how much this Ph.D. has meant to me. As an international student (and an adventurer), I put myself completely out of my comfort zone, thus I lived experiences with a lot more intensity. I went through many internal changes and dark places, but today I only feel gratitude for them, because I learnt so much about life, and they brought me to the discovery of becoming myself.

First and foremost, I thank my advisor, Adrian. He has been incredibly supportive and provided me with excellent guidance and help with anything I needed. He has had unlimited patience going over long discussions and answering my million questions. I've learnt more than I would have ever imagined. I am also indebted to Chip for his helpful comments and for sharing his profound knowledge in my second project. Special thanks to my committee: Hope, for thought-provoking exchanged emails and comments, Jin, for accepting being in my committee with very short notice, and Steve.

I am thankful for the NASA Grants to Adrian for funding these projects, and for the numerous scholarships I received by the Department of Earth and Planetary Sciences during these years. I am thankful for the incredible staff at the Department: Paula, Cindy, Cecilia, Faith, and Mabel, who provided huge help in all matters. I can't thank Cecilia enough for taking care of me like a guardian angel. I thank Ying-Bing Jiang and Elena Dobrica for their guidance on the TEM, Mike Spilde for his assistance on the Probe, and Jess Johnson for her help on the Mineralogy lab.

I am extremely thankful for the encouragement, mentoring, guidance, advises, and friendship of Viorel Atudorei, without whom I would never have made it this far. He has been my main support in Albuquerque and the nexus to many of my friends.

I thank the Land of Enchantment and the southwest: the desert, the sunsets, the solitude, the clouds, the birds… This is really one of the most special and magic places on Earth.

I deeply thank all the amazing long-life friends I made in Albuquerque. They have been critical in keeping me sane, making me move forward, and gifted me with unforgettable memories. Special thanks to Collin for his pure love, help, and incredible support – I will never forget. Andressa, Clarissa, Laura, Oana, Elena, Elisabeth, Jennifer, John, Manel, Jon, Fran, Maxi, thank you for so much.

I thank all the people across the ocean who were always with me despite the physical distance. My beautiful family, my mom Marina and my sister Sabina, for all their unconditional love and support, their partners, and not least, my grandfather. And obviously, I thank all my Catalan friends for… you know, everything.

I am also indebted to Josep Trigo, who introduced me to the fascinating world of meteorites eight years ago and helped me to find a way to keep going. Finally, I thank COVID for adding extra challenges the week of my submission and making this last year and a half a whole mess. Life has become more exciting (and valuable).

MICROSTRUCTURAL AND MICROCHEMICAL STUDIES OF FLUID–CHONDRULE INTERACTIONS IN A PRISTINE CR CARBONACEOUS CHONDRITE AND APATITE IN MARTIAN NAKHLITES

by

MARINA MARTÍNEZ JIMÉNEZ

B.S., Geology, Autonomous University of Barcelona, 2013
M.S., Astrophysics, Particle Physics, and Cosmology, University of Barcelona, 2015
Ph.D., Earth and Planetary Sciences, University of New Mexico, 2021

ABSTRACT

PROJECT 1: Chondrites are the most primitive objects in the solar system, aggregates of the material that formed in the solar protoplanetary disk during the first 1-5 million years of its formation. However, petrographic observations indicate that most chondrites have been modified by secondary processes, including aqueous alteration, thermal metamorphism, and shock. Fortunately, a few chondrites largely escaped these processes and are considered pristine, such as the CR carbonaceous chondrite Queen Alexandra Range (QUE) 99177. QUE 99177 is an excellent sample for deciphering information about the reactions that took place between unaltered anhydrous solar nebular components and water under highly disequilibrium conditions, as well as primary processes in the solar nebula. The goal of this work is to constrain the earliest interactions between anhydrous chondrules in QUE 99177 with their associated fine-grained, hydrated matrix material.

Models to characterize the aqueous alteration degree of a given chondrite are contentious. Therefore, Chapter 1 proposes a new proxy for assessing the degree of

aqueous alteration in weakly altered CR chondrites based on the presence and characteristics of a recently discovered type of rim around chondrules called *smooth rims*. Smooth rims have been observed surrounding type I chondrules in a few weakly altered CR chondrites, but their nature and formation mechanisms remained unknown. We unravel the origin of these rims and their importance to understanding the earliest fluid-chondrule interactions. Chapter 2 focuses on characterizing the different occurrences of phosphates present in and around type II (mainly) and type I chondrules in QUE 99177. Calcium phosphates are generally considered secondary products, but work has been limited. This study provides evidence of both solar nebular and parent body processes in the formation of Ca phosphates and acquires new insights into the behavior of P during the earliest stages of aqueous alteration in the CR chondrite parent body.

PROJECT 2: The Martian meteorites (Shergottites-Nakhlites-Chassignites and several unique lithologies) represent a direct sampling of igneous processes on Mars, covering a range of different Martian mantle sources and emplacement environments. Although models account for many of their observations, the detailed magmatic processes have not been fully elucidated yet. In Chapter 3, we examine the micro- and nano- structures of apatites using transmission electron microscopy in the two nakhlites NWA 998 and Nakhla. Such microstructural data are currently essentially lacking for samples of planetary or even terrestrial apatite, yet apatite is widely used as an important tracer for reconstructing petrogenetic processes in different planetary environments. In particular, Martian apatite is used for constraining potential volatile reservoirs (the mantle and/or the crust), therefore, understanding apatite microstructures is of fundamental importance for providing robust interpretations of the geochemical data obtained from

apatite. In Chapter 3, we show evidence of late igneous and subsolidus reactions that support a model based on crustal assimilation and is inconsistent with the presence of fluids. We discuss the limitations of using apatite to constrain volatile abundances and their sources.

PROJECT 3: High-pressure phases resulting from impacts between asteroids provide excellent opportunities to study phase transitions of the constituent minerals of the Earth's mantle as well as the dynamics of shock-induced solid-state processes. In Chapter 4, we examine the high-pressure phases enclosed in an exceptionally large shock-induced melt vein in the L6 ordinary chondrite Villalbeto de la Peña. The high-pressure phases identified include: ringwoodite, Ca-rich majorite, Ca-poor majorite, maskelynite, lingunite, pyroxene glass, magnesiowüstite, and ferropericlase. We focus on the behavior of Ca-rich pyroxene because there are only a few occurrences of its high-pressure transformations reported in the literature. Several of our observations represent the first time specific phenomena have been described, such as diopside undergoing direct melting without transforming into its high-pressure polymorph (majorite) and fine-scale zonation in majorite-pyrope grains in the matrix. We discuss implications for the thermal histories and cooling rates in the shock event.

TABLE OF CONTENTS

LIST OF FIGURES

LIST OF TABLES

PREFACE

This thesis consists of four chapters and two appendices. Each chapter is written as a separate, independent manuscript with its own introduction, methods, discussion, conclusions, and references. The thesis is composed of three different research topics. Two of them resulted from the development of the Ph.D. proposals presented during my comprehensive examination in April 2018, which comprise chapters 1 to 3. Chapter 4 belongs to a project that I started at the Institute of Space Sciences (IEEC-CSIC) in Barcelona, before my arrival to Albuquerque. The vast majority of the analytical work was done by myself, I wrote all the drafts of each chapter, and I will be the first author on the resulting publications. Adrian Brearley contributed significantly to interpretation of the data and editing of all the manuscripts.

The first project (Chapters 1 and 2) follows the line of research of Adrian Brearley, focused on understanding aqueous alteration processes in CR carbonaceous chondrites to provide insights into the origin and history of the early solar system. I have studied the least altered CR chondrite known to date, Queen Alexandra Range 99177, to unravel some of the earliest effects that melting of primordial water ice had on anhydrous materials that accreted into the CR parent body. Both chapters utilize the same thin sections. While previous work has focused on the matrix (e.g., Le Guillou et al., 2015), because water ice accreted within the fine-grained matrix and this is the material that is expected to alter first, little work has been done to understand if chondrules were also affected by early fluids. Chapters 1 and 2 provide a detailed examination of the interfaces between chondrules and the hydrated matrix. As such, some repetition between these two chapters was unavoidable.

Chapter 1 investigates the occurrence and characteristics of a recently discovered type of rim, called *smooth rims*, surrounding type I chondrules. Smooth rims have been typically associated with aqueous alteration, but data that characterize which phases constitute them were lacking. Our acquired knowledge from smooth rims has contributed to our understanding of the earliest effects of aqueous alteration in the CR parent body, provided insights into the conditions of the first altering fluid, and assessed the relevance that chondrules had in these first stages of alteration. Some of the data were presented at the 2019 Annual Meteoritical Society Meeting (Martínez and Brearley, 2019), from which I received the Wiley-Blackwell Award for an outstanding oral presentation. This chapter will be submitted for publication in Geochimica et Cosmochimica Acta.

Chapter 2 presents a detailed characterization of the different Ca phosphates occurrences found in QUE 99177, some of them representing the first descriptions in the literature. It extends work on Ca- and P-bearing layers around chondrules in weakly altered chondrites by Burger and Brearley (2004, 2005), Brearley and Burger (2009), and Brearley (2011). Chapter 2 discerns between solar nebula and parent body origins for the different Ca phosphates found in QUE 99177 and provides further insights into the earliest fluid-chondrule interactions. This chapter will be submitted for publication in Geochimica et Cosmochimica Acta.

Chapter 3 focuses on understanding volatile sources on Mars. Guidance and interpretation of my results were mentored by Charles Shearer and Adrian Brearley. Chapter 3 uses apatite microstructures in two nakhlites, NWA 998 and Nakhla, to unravel further insights into the petrogenetic model for the origin of the chassignites-nakhlites. This study represents the first attempt to use the microstructures of apatite to constrain

petrogenetic models, and the acquired knowledge can also be related to other planetary bodies, including the Moon, achondrites, chondrites, and the Earth. Preliminary work was presented at the 2020 Lunar and Planetary Science Conference as Martínez et al. (2020).

Chapter 4 is a separate, independent project that I started in Barcelona in 2015 under the supervision of Josep Maria Trigo at the Institute of Space Sciences (ICE-CSIC). I finished the manuscript at UNM with the mentoring of Adrian Brearley, who contributed greatly to interpretations and editing. The project changed completely, and all the TEM work was performed at the University of New Mexico; therefore, I have included this study as a chapter. The project investigates a shock melt vein in the highly shocked Villalbeto de la Peña L6 chondrite at the micron and submicron scales. Preliminary results were presented at the 2017 Annual Meeting of the Meteoritical Society (Martínez-Jiménez and Brearley, 2017) and the study was published in 2019 in *Meteoritics &Planetary Science* as Martínez et al. (2019).

Appendix 1 consists of the individual EPMA analyses for data acquired in Chapters 1 and 2, and Appendix 2 provides supporting data for Chapter 3, which includes additional BSE images of apatites in the nakhlites NWA 998 and Nakhla, and mineral compositions of accessory phases in the studied Nakhla intercumulus region.

All the chapters have used transmission electron microscopy as the main technique and emphasize the significant extent of valuable information that resides at the micron- and nanoscales.

References:

Brearley, A. J. and Burger, P. V. 2009. Mechanisms of aqueous alteration of type IIA chondrule glass in the CR chondrite EET 92105: Insights from FIB/TEM analysis. *Meteoritics and Planetary Science Supplement* 72:5148.

Brearley, A. J. 2011. Formation of Ca-Phosphates During Aqueous Alteration of Type IIA Chondrules in the Y-791198 CM2 Carbonaceous Chondrite. *74th Annual Meeting of the Meteoritical Society.* Abstract #5364.

Burger, P. V. and Brearley, A. J. 2004. Chondrule glass alteration in type IIA chondrules in the CR2 chondrites EET 87770 and EET 92105: Insights into elemental exchange between chondrules and matrices. *35th Lunar and Planetary Science Conference*. Abstract #1966.

Burger, P. V. and Brearley, A. J. 2005. Localized chemical redistribution during aqueous alteration in CR2 carbonaceous chondrites EET 87770 and EET 92105. *36th Lunar and Planetary Science Conference.* Abstract #2288.

Le Guillou, C., Changela, H. G., and Brearley, A. J. 2015. Widespread oxidized and hydrated amorphous silicates in CR chondrites matrices: Implications for alteration conditions and H2 degassing of asteroids. *Earth and Planetary Science Letters* 420:162–173.

Martínez-Jiménez, M. and Brearley, A. J. 2017. Phase Transformation Mechanisms of Ca-Majorite in the Shocked Villalbeto de la Peña Ordinary Chondrite: Clues to Cooling Paths in Shocked Meteorites. *80th Annual Meeting of the Meteoritical Society*. Abstract# 6160.

Martínez, M. and Brearley, A. J. 2019. Smooth rims in Queen Alexandra Range (QUE) 99177: The earliest stages of fluid-rock interactions in the most pristine CR chondrite. *82nd Annual Meeting of The Meteoritical Society*. Abstract# 6097.

Martínez, M., Brearley, A. J., Trigo-Rodríguez, J. M., and Llorca, J. (2019) New observations on high-pressure phases in a shock melt vein in the Villalbeto de la Peña meteorite: Insights into the shock behavior of diopside. *Meteoritics & Planetary Science* 54:2845–2863.

Martínez, M., Brearley, A. J., and Shearer, C. K. 2020. Reading the microstructure of apatite in the Moon and Mars to constrain the petrogenetic evolution of Chassignites and Nakhlites and assess their volatile sources. *51st Lunar and Planetary Science Conference*. Abstract# 1878.

CHAPTER 1

Smooth rims in Queen Alexandra Range 99177: Fluid–chondrule interactions and clues on the geochemical conditions of the primordial fluid that altered the CR carbonaceous chondrites

In collaboration with:
Adrian J. Brearley

To be submitted for publication to:
Geochimica et Cosmochimica Acta

Abstract

QUE 99177 is the least altered CR carbonaceous chondrite that exists in our collections, with mineralogical and isotopic characteristics that indicate a high level of pristinity. In this study, we aim to understand if and how chondrules in QUE 99177 interacted with the hydrated matrix during the earliest stages of alteration in the parent body. We propose a method based on the occurrence of the so-called *smooth rims* as best recorders of the earliest fluid–chondrule interactions. Although their nature and origin remained unknown, they have been related to aqueous alteration. Several analytical techniques (SEM, EPMA, and FIB-TEM) were used to study numerous smooth rims to characterize their constituent phases, unravel their precursor material(s), assess their formation mechanisms, and constrain the conditions of the altering fluid. Smooth rims are the most common type of rims around type I chondrules and exclusively occur around chondrules with Silica-rich Igneous Rims (SIRs). Smooth rims consist of an Fe-rich, hydrous silicate material that gives low analytical totals and contains Si and Fe in roughly equal proportions, minor Mg, Al, Ca, and Mn, and trace S, Ni, Na, Cr, K, P, and Ti. TEM observations reveal they consist of an amorphous Fe-rich silicate gel that contains

unaltered crystalline phases and igneous glass. The amorphous gel preserves previous crystal outlines with morphologies consistent with silica (cristobalite) grains in SIRs and has a composition identical to pseudomorphic silica replacements in SIRs. Crystalline phases consist of igneous, unaltered, zoned pyroxenes with compositions consistent with pyroxenes in SIRs (rich in moderately volatile elements), albite, and chromite. This study concludes that smooth rims derive from low-temperature aqueous alteration of silica in SIRs by an Fe-rich fluid. Evidence argues strongly that the source of Fe derived from leaching of soluble elements from amorphous silicates in the matrix, which quickly reacted with melted water ice. The amorphous silicate gel in smooth rims and the amorphous silicates in the matrix underwent progressive oxidation due to the extensive hydration. Silica dissolved whereas feldspar and glass remained unaltered because (1) the fluid was slightly alkaline, (2) cristobalite has a reaction rate much higher than quartz and feldspar, and (3) the alteration was very limited and fast, indicating that it was due solely to melting of accreted ice and there was no introduction of an external fluid.

1. Introduction

The CR carbonaceous chondrites are among the most primitive objects in the solar system, preserving a diverse range of solid materials that formed by different processes in the solar nebula. A number of studies have documented the pristine characteristics of CR chondrites, including: refractory lithophile/Mg abundances relative to CI chondrites of ~1.0 (Kallemeyn and Wasson, 1981), a solar Co/Ni ratio in Fe,Ni metal, inherited from primary condensation in the nebula (Weisberg et al., 1995; Connolly et al., 2001), positive $\delta^{15}N$ anomalies (Weisberg et al., 1995; Krot et al., 2002), and a fine-grained matrix that contains the most pristine insoluble organic matter of any

chondrite group, with the highest D/H ratio (Martins et al., 2007; Pizzarello and Holmes, 2009; Alexander et al., 2012; Le Guillou et al., 2015). They also have among the highest presolar silicate grain abundances of any of the chondrite groups (Floss and Stadermann, 2009), with exception of the CO3 chondrite DOM 08006 (Nittler et al., 2018).

The CR carbonaceous chondrites, typified by Renazzo (van Schmus and Wood, 1967), are characterized by abundant Mg-rich (type I) chondrules (Weisberg et al., 1993; Krot et al., 2004), abundant Fe,Ni metal mainly in chondrules and rare in the matrix, Fe,Ni metal mantles on chondrules, rare FeO-rich (type II) chondrules, abundant dark inclusions (DI), low abundances of Calcium-Aluminum-rich Inclusions (CAIs), and varying abundances of Ameboid Olivine Aggregates (AOAs) (Weisberg et al., 1993, 1995, 2004). Chondrules and matrix in the CR chondrites make up ~70 and ~30% by volume, respectively (Schrader et al., 2011). The CR chondrites have escaped thermal metamorphism but show a range of aqueous alteration, from petrologic type 2 to type 1 (Weisberg et al., 1993, 1995; Abreu and Brearley, 2010; Harju et al., 2014; Howard et al., 2015; Weisberg and Huber, 2010). Most CR chondrites are type 2, consisting of nearly intact nebular materials, but one type 1 CR chondrite exists, GRO 95577, a sample that lacks anhydrous silicates and exhibits complete replacement of all the primary components by secondary alteration products (Weisberg and Huber, 2007). The range of aqueous alteration is reflected in the bulk O-isotopic compositions of the CR chondrites, which define a linear array with a slope of 0.71 ± 0.06 that is distinct from any other group (Schrader et al., 2011).

The widespread aqueous alteration effects observed in the CRs and other chondrite groups have broad implications regarding the role of water in the early solar

system. For example, understanding the earliest stages of aqueous alteration in chondrites is of fundamental importance to unravel how, when, and how much water was incorporated into asteroidal parent bodies, how many different reservoirs of water existed, and how water modified the diverse nebular materials that accreted from the protoplanetary disk. However, the earliest stages of aqueous alteration are rarely preserved in carbonaceous chondrites. Most of the CR chondrites, like Renazzo, exhibit a comparatively advanced degree of aqueous alteration, with the exception of a few CR chondrites, such as QUE 99177 and MET 00426.

Queen Alexandra Range 99177 is considered the least-altered CR chondrite currently known and was originally suggested to be of petrologic type 3.0 by Abreu and Brearley (2010), based on its petrographic and mineralogical characteristics. These include highly unequilibrated chondrule phenocryst compositions (Weisberg et al., 1993; Connolly et al., 2007; Berlin, 2009; Schrader et al., 2010), chondrules with glassy mesostasis, high presolar grain abundances (Floss and Stadermann, 2009), dominance of amorphous silicates in the matrix (Abreu and Brearley, 2010; Le Guillou et al., 2015), high sulfur content in the matrix, present as nanophases of Fe,Ni sulfides, pristine insoluble organic matter with the highest D/H ratio (e.g., Alexander et al., 2012), and minimal evidence of carbonates and magnetite framboids (Weisberg, 1993; Brearley, 2006; Abreu and Brearley, 2010; Le Guillou et al., 2015; Howard et al., 2015; Changela et al., 2018). Amorphous silicates in CR chondrite matrices are considered to be the primary products of disequilibrium condensation processes in the solar nebula (Chizmadia and Brearley, 2008; Abreu and Brearley, 2010; Leroux et al., 2015; Brearley

and Le Guillou, 2015; Brearley, 2016). All the above features indicate that QUE 99177 is essentially completely unmetamorphosed.

The effects of the primordial water on chondrites are well characterized and extensive work has been done, but mainly in the matrices of CM and CR chondrites (e.g., Barber, 1981; Zolensky et al., 1993; Lauretta et al., 2000; Chizmadia and Brearley, 2008; Le Guillou and Brearley, 2014; Le Guillou et al., 2015; Leroux et al., 2015; Vollmer et al., 2020), because fine-grained materials are expected to alter much earlier and faster than chondrules. Refractory inclusions have also been investigated to gain insights into the earliest effects of aqueous alteration on chondrites. For example, recent work on CO3 chondrites (e.g., Simon et al., 2019) have shown evidence of exchange between initially ^{16}O-rich grossite ($CaAl_4O_7$) and a ^{16}O-poor fluid during hydrothermal alteration in the CO parent body. Only a few studies have been done on chondrules, mainly focusing on CM chondrites (Bunch and Chang, 1980; Richardson, 1981; Hanowski and Brearley, 2001), but the interaction between chondrules and matrix in this group of chondrites during the earliest stages of aqueous alteration is obscured because of the advanced degree of alteration they experienced. In ordinary chondrites and CO and CV carbonaceous chondrites, fayalite has provided insights into the isotopic composition of the initial fluid (Doyle et al., 2015). Alternatively, the CR chondrites offer excellent possibilities to study the primordial interaction between chondrules and matrix, because the relationship between them is better preserved, and most of the CR2 chondrites are much less altered than any CM2 chondrite. However, they are largely unexplored, with the exception of the work by Burger and Brearley (2004), who found elemental exchange between type IIA chondrule glass and matrix during aqueous alteration. To investigate

the interaction of these components is fundamental to understanding elemental mass transfer between chondrules and matrix during aqueous alteration and decipher information about the reactions that took place between unaltered anhydrous solar nebular components and water under highly disequilibrium conditions.

Unfortunately, the alteration degree of a given CR chondrite is challenging to determine, especially because there are different approaches used in the literature – e.g., O-isotopic compositions (Schrader et al., 2011), mineralogy (Harju et al., 2014; Howard et al., 2015), and water content (Alexander et al., 2012, 2013), which have led to disagreements and inconsistencies when assigning a petrologic subtype that reflects the degree of aqueous alteration. In the present study, we have explored alteration processes in the least altered CR chondrite known, QUE 99177, focusing specifically on petrologic characteristics that may be most sensitive to the earliest stages of aqueous alteration, which are not fully understood in any meteorite group. The overall goal is to provide new constraints on if and how chondrules were affected by liquid water in the earliest stages of aqueous alteration in the CR carbonaceous chondrite parent body and propose a simple method for tracking the degree of alteration in the weakly altered CR chondrites beneficial to defining the relative degrees of alteration. Hence, we propose a method based on the occurrence and characteristics of the so-called *smooth rims*.

Smooth rims are a type of rims that have been noted in several recent studies of CR carbonaceous chondrites (Harju et al., 2014; Jones et al., 2015; Abreu, 2016; Komatsu et al., 2019), but their nature and origin remain unknown. In the limited number of studies, some authors have suggested that smooth rims are comprised of phyllosilicates (e.g., Harju et al., 2014; Jones et al., 2015). Jones et al. (2015) and Brearley and Jones

(2016) used TEM to study the replacement product of silica in silica-bearing rims in EET 92042, which shares compositional characteristics to the material in smooth rims, and suggested that it consists of phyllosilicates or an amorphous gel-like phase. However, none of these studies explicitly focused on smooth rims, yielding unclear evidence of a link between the replacement product of silica and the formation of smooth rims. Also, EET 92042, although relatively minimally altered, appears to show a higher degree of alteration than QUE 99177, based on its oxygen isotopic composition (Schrader et al., 2011). To summarize, we have carefully examined the potential interaction between chondrules and matrix in QUE 99177 focusing on smooth rims with the objectives of (i) characterize their constituent phases, (ii) unravel the nature of their precursor materials, and (iii) assess the alteration conditions of the fluid that formed smooth rims, which may have broader implications regarding the role of water in the early solar system.

2. Samples and analytical methods

We have examined two 1-inch round, polished thin sections, numbers 18 and 19, of the least-altered CR chondrite known, QUE 99177 (Fig. 1.1) from the Antarctic Meteorite Collection at Johnson Space Center. The two thin sections were carbon coated prior to SEM analyses that were performed under high-vacuum conditions. Complete thin section mosaics of QUE 99177 were obtained using backscattered electron (BSE) imaging (Fig. 1.1) and energy dispersive spectroscopy (EDS) X-ray spectral mapping on a FEI Quanta 3D Dualbeam® field emission gun scanning electron microscope-focused ion beam instrument (FEGSEM-FIB) equipped with an EDAX Genesis EDS system, using an Apollo 40 SDD 40 mm^2 EDS detector. Combined elemental RGB maps were acquired at 30 kV and between 16 – 22 nA, created to enable identification and location

of silica-rich igneous rims, smooth rims, and other features of interest. Numbers were assigned to each chondrule in both thin sections for consistent identification during the analyses (Fig. 1.1). High-resolution X-ray spectral mapping of multiple areas of interest in eleven smooth rims were performed using different combinations of elemental RGB X-ray maps to investigate their textural and compositional characteristics in detail. RGB X-ray maps were also used to select spots for point analyses by electron microprobe.

Seven chondrules with smooth rims and adjacent matrices were analyzed by quantitative wavelength-dispersive spectroscopy (WDS) analysis, which were conducted on a JEOL 8200 electron probe microanalyzer (EPMA) equipped with five WDS spectrometers. Analytical conditions were a 15 kV accelerating voltage, a 20 nA beam current, and a 1, 3 or 5 μm spot size, depending on the phase. Between 5 and 11 areas were selected in each smooth rim with associated matrix, and 10 to 25 analytical points were measured on each area. The analyzed phases include smooth rims, matrix, pyroxenes, silica, and mesostasis regions. Individual values are found in Tables A1.1 – A1.18 in Appendix 1. The following calibration standards from the Taylor Company Standard block were used: olivine (Si, Mg, Fe), diopside (Si, Mg, Ca), spessartine (Mn), albite (Na), orthoclase (K, Al), sphene (Ti), Wilberforce F-apatite (P), chromite (Cr), nickel metal (Ni), and pyrite (S). Almandine was used as an additional standard for oxygen calibration. In addition, cathodoluminescence (CL) images were acquired at the University of New Mexico with optical stage operated at 15kV and 300-400 μA, using a VEGA3 TESCAN.

An important analytical issue is that EPMA analyses on silica have been performed using pyroxene and olivine as standards instead of quartz, the only appropriate

standard for a pure silica phase. Consequently, the analytical totals for silica are low (Table 1.1). Nonetheless, all the other phases analyzed here by EPMA (smooth rims, pyroxenes, and mesostasis regions) are correct because they have silica contents similar to the standards. Terrestrial weathering veins and dark inclusions were avoided while selecting points so that analyses only represent smooth rims and corresponding adjacent fine-grained matrices, although alteration can be hidden below the foil surface.

Four FIB sections were extracted from four different smooth rims around different chondrules to examine their microstructures in detail using TEM: two in section 18 (Ch13 and Ch14, Fig. 1.1a) and two in section 19 (Ch3 and Ch22, Fig. 1.1b), designated FIB1 (Ch3), FIB2 (Ch22), FIB3 (Ch14), and FIB4 (Ch13), covering a representation of the range of textures observed in smooth rims. An additional FIB section, designated FIB5, was extracted on a silica grain from a Silica-rich Igneous Rim (SIR) that shows alteration (Ch9, Fig. 1.1b). We exercised caution when selecting the locations to extract FIB sections because QUE 99177 is an Antarctic find. We chose smooth rims with minimal evidence of terrestrial weathering, trying to avoid Fe oxyhydroxide veins crosscutting throughout, within the limited possibilities. In addition, the FIB sections were selected in areas of the smooth rims where the interface with the matrix lacks evidence of dark inclusions. The targeted adjacent matrix material for FIB-TEM analysis thus represents the textural diversity observed in the matrix. The five FIB sections were prepared using the FEI Quanta 3D Dualbeam® FEG-SEM/FIB instrument. Platinum strips, ~2 μm-wide, ~2.5 μm-thick, and up to 20 μm in length, were first deposited across each area of interest to protect the FIB sections from ion beam damage during sample preparation. The FIB sections were extracted from the thin sections by the *in-situ* lift-out technique

using an Omniprobe 200 micromanipulator and were attached to copper (Cu) Omniprobe TEM half grids. Ion milling to electron transparency was carried out at an accelerating voltage of 30 kV, gradually decreasing the beam current from 0.5 nA to 50 pA during the final stages of thinning. Final millings were carried out at 5 kV to reduce the ion-damage layers from the surfaces of the FIB sections.

The mineralogy, composition, and texture of the different components that define the smooth rim at the micron and submicron scales were studied using JEOL 2010F FASTEM FEG scanning transmission electron microscope (STEM), operated at 200 kV. A variety of electron techniques were used, including bright-field TEM (BF-TEM), high-resolution TEM (HR-TEM), high-angle annular dark-field (HAADF) scanning TEM (STEM), and selected area electron diffraction (SAED). Digital bright-field (BF) and dark-field (DF) TEM images were first acquired and processed using GATAN Microscopy Suite® (GMS) imaging software. Semi-quantitative and quantitative X-ray analysis data were obtained using an Oxford Aztec X-ray analysis system with a X-Max 80N 80 mm^2 SDD energy dispersive X-ray spectrometer (EDS) system. Full spectral X-ray maps from selected regions of interest were collected in STEM mode, and quantitative analyses were obtained from them. Individual TEM-EDS and STEM-EDS analyses were also performed on each of the phases in the FIB sections with live count times of 300 sec (TEM) and 500 sec (STEM) and a nominal beam diameter ranging from 10 to 500 nm. Quantification of EDS spectra was carried out using the Cliff-Lorimer thin film approximation using theoretical k-factors. Errors were all <5%. The analyses assume oxygen present according to oxide stoichiometry and normalized to 100 wt%.

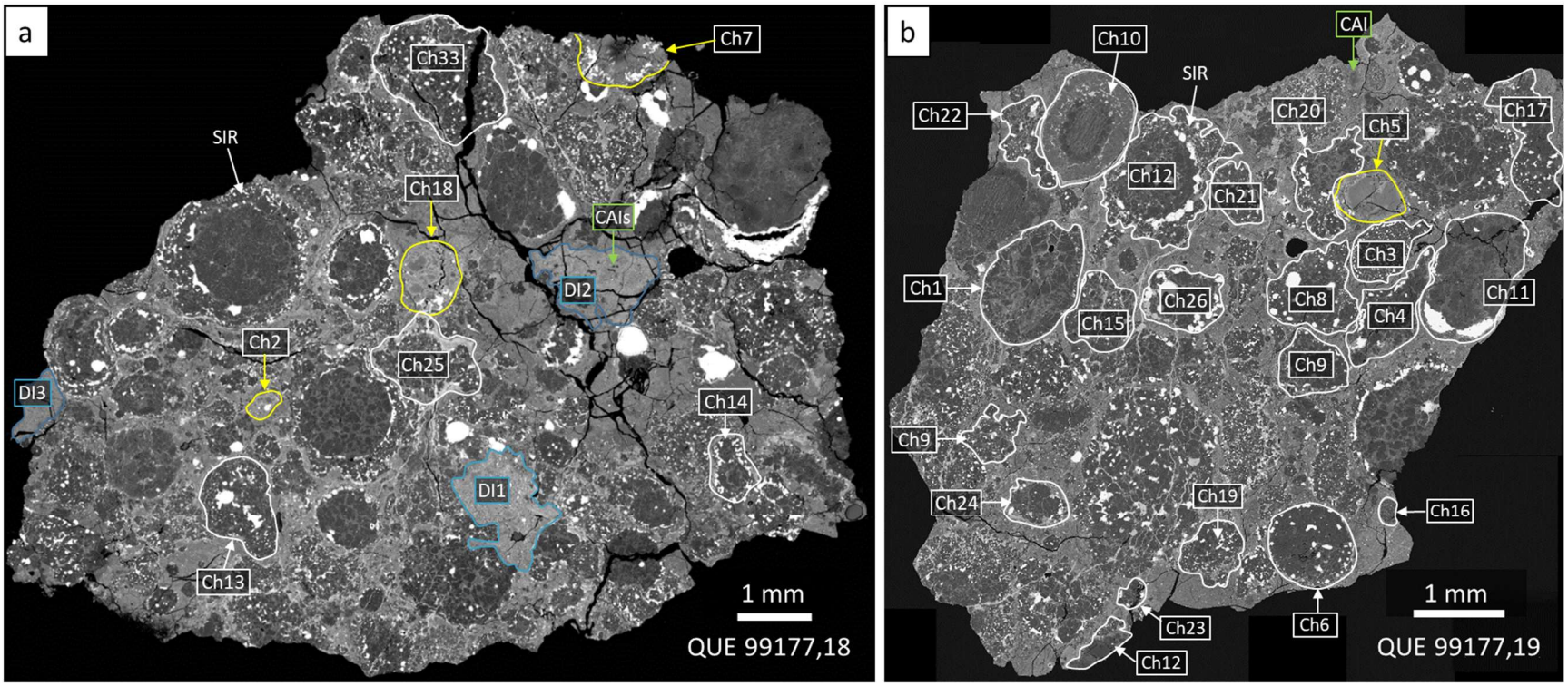

Figure 1.1. Backscattered electron mosaics of the two thin sections of QUE 99177 studied, numbers 18 (a) and 19 (b). Chondrules are remarkably well distinguished, as well as their relationship with the matrix. The vast majority of chondrules are type I and exhibit a diversity of textures: barred olivine (BO, e.g., Ch10), porphyritic olivine (PO, e.g., Ch16), porphyritic olivine and pyroxene (POP, e.g., Ch4, Ch6, Ch8, Ch22), porphyritic pyroxene (PP, e.g., Ch3), and composite chondrules (e.g., Ch1, Ch14), among others. Rare type IIA chondrules are also distinguished (outlined in yellow), which are investigated in Chapter 2. Many chondrules are metal-rich with igneous rims or have metal-rich mantles. The matrix of section 18 contains a higher abundance of dark inclusions (DI, in blue) compared to section 19. Calcium-Aluminum-rich Inclusions (CAI) shown in Fig. 1.3 are marked in green here. Chondrules outlined in white are the selected type I chondrules surrounded by rims (mostly smooth rims) examined in this work.

3. Results

3.1. General petrologic characteristics of QUE 99177

The petrology and mineralogy of QUE 99177 has been previously described by Abreu and Brearley (2010). QUE 99177 is an Antarctic find classified as a CR chondrite with terrestrial weathering grade B (Russell et al., 2002). Terrestrial Fe-hydroxides veins are heterogeneously distributed through the meteorite, varying from highly abundant (e.g., Fig. 1.2a) to rarer or absent (e.g., Fig. 1.2b). They have a distinct electron albedo (the albedo corresponds to the average Z) that is also consistent with weathered Fe,Ni metal grains in rims around chondrules adjacent to the matrix where terrestrial veins are present. Generally, the development of veins throughout the thin section and the extent of the alteration is extremely localized and high-magnification SEM imaging suggests that terrestrial weathering does not appear to have affected the material on either side of the veins. This is consistent with work by Abreu and Brearley (2010) and Le Guillou and Brearley (2014) on QUE 99177, who argued that matrix was not affected to any significant degree by terrestrial alteration veins.

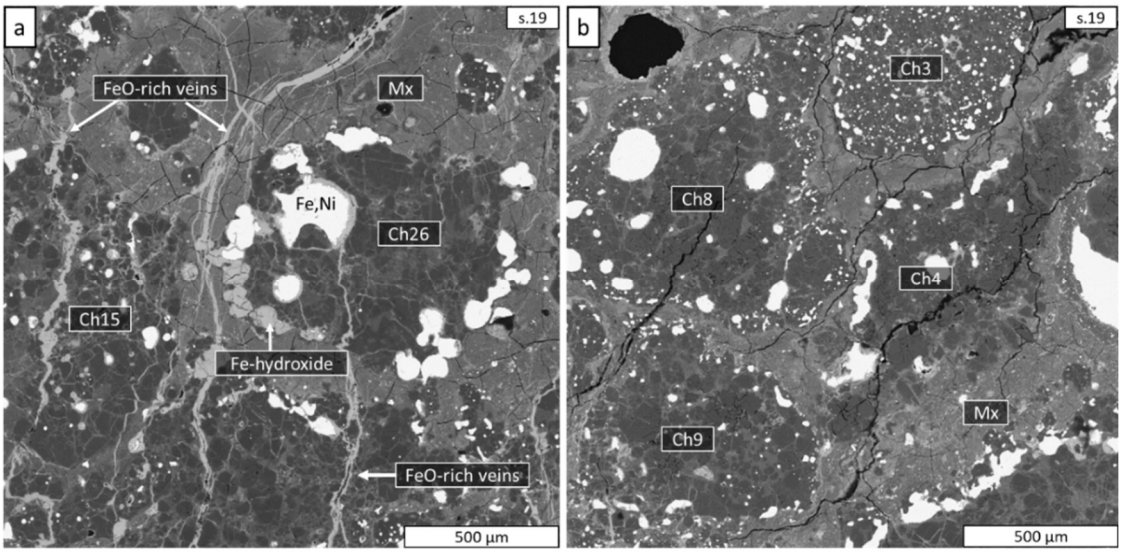

Figure 1.2. (*On previous page*). BSE images showing terrestrial weathering in QUE 99177,19 chondrules (Ch) and matrix (Mx). Weathering effects are heterogeneously distributed. a) General region with a set of N-S oriented FeO-rich terrestrial veins crosscutting and surrounding several chondrules containing Fe,Ni metal, some of them altered to Fe-hydroxides. b) Different region of the thin section showing lack of terrestrial veins.

Chondrules in QUE 99177 are generally large but range from a few tens of microns to ~2 mm in apparent diameter. Most are MgO-rich (type I), metal rich or surrounded by continuous or discontinuous Fe,Ni-bearing mantles, and often surrounded by igneous rims (SIRs) that contain silica (SiO_2), as well as pyroxene-rich igneous rims (PIR) (Weisberg et al., 1993, 2006; Kallemeyn et al., 1994; Krot et al., 2004). Rare type IIA chondrules are also present, which have been described by Schrader et al. (2015). Although calcite is present in very low abundances in the CR chondrites (<1%; Howard et al., 2015), we have observed that calcite is more common in some areas of QUE 99177 than previously recognized by Harju et al. (2014), who also reported ≤1 vol.%, and by Abreu (2016), who only reported Ca carbonates in the most altered CR chondrites. Calcite in QUE 99177 is present as small (from a few microns up to 30 μm in size) clusters of grains or isolated micron-sized grains, heterogeneously distributed throughout the matrix, quite abundant in some regions (e.g., Fig. 1.3b, in blue). Magnetite framboids are also observed in the matrix of QUE 99177, although they are mostly associated with dark inclusions in thin section #18, being much rarer in thin section #19. Several small (<200 μm) CAIs are identified within the matrix of thin section #19 (e.g., Fig. 1.3c) and in a large (mm-size) dark inclusion in thin section #18 (Fig. 1.3d).

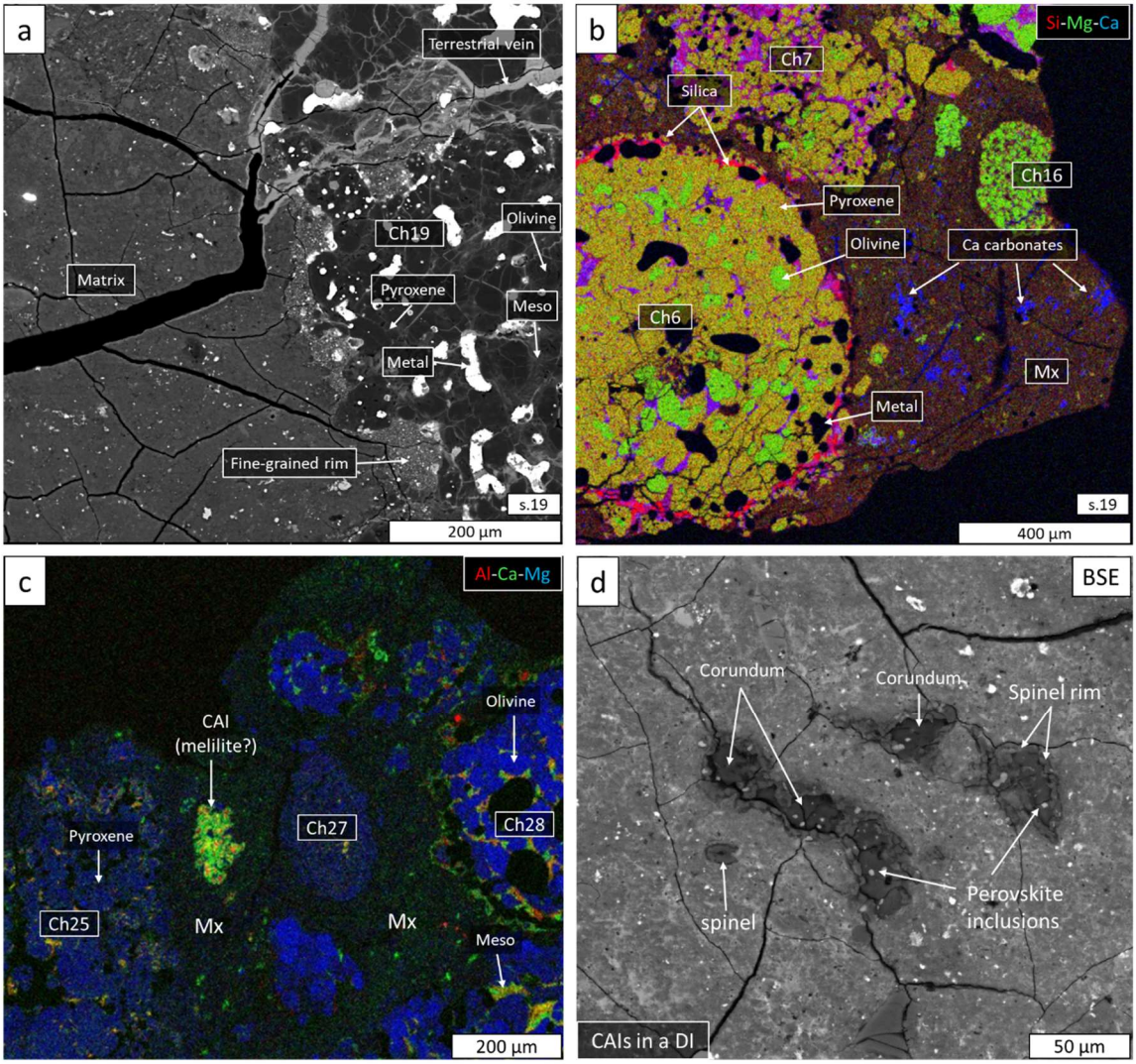

Figure 1.3. BSE images of QUE 99177 showing petrographic characteristics of the matrix. a) BSE image of the edge of chondrule 19 (Ch19) showing a large portion of the adjacent fine-grained matrix material. Note that the matrix is very fine-grained, crosscut by several fractures, and contains sulfides that range from submicron to several microns in size, heterogeneously distributed throughout. b) Combined RGB elemental X-ray map for Si-Mg-Ca map of a region showing a high abundance of Ca-carbonate grains in the matrix (in blue), and a POP chondrule (Ch6) containing pyroxene (in orange), olivine (in green), silica (in red), and metal grains. c) Combined elemental RGB X-ray map for Al-Ca-Mg showing a ~120 µm-size Calcium-Aluminum-rich Inclusion (CAI in Fig. 1.1b), likely consisting of melilite, and exhibiting the characteristic irregular morphology. Chondrules contain magnesian silicates (olivine and/or pyroxene) and mesostasis regions (meso). d) BSE image of a dark inclusion (CAIs in DI2 in Fig. 1.1a) in QUE 99177,18 showing several CAIs within. The dark inclusion contains a total of 6 CAIs that consist of corundum cores (darker gray), surrounded by spinel rims, with abundant perovskite inclusions (micron to submicron in size).

Figure 1.4 illustrates different examples of the types of rims other than smooth rims found around chondrules in QUE 99177. These are coarse-grained rims (Fig. 1.4a,b), rare fine-grained rims (Fig. 1.4c,d) (Abreu and Brearley, 2010), very-fine-grained Fe-rich rims (Fig. 1.4d,e), and rare rims similar to those described in CM chondrites by Metzler et al. (1992). Smooth rims, the focus of this work, represent about 70% of the total rims in QUE 99177 (many chondrules lack rims), and are described in detail in section 3.2. The abundance of smooth rims has been calculated by counting and numbering each chondrule that is surrounded by a smooth rim (identified with BSE full-thin section maps along with X-ray maps) divided by the total number of type I chondrules in each thin section. Our results indicate that about 40% and 30% of the type I chondrules in QUE 99177,19 and QUE 99177,18, respectively, contain smooth rims.

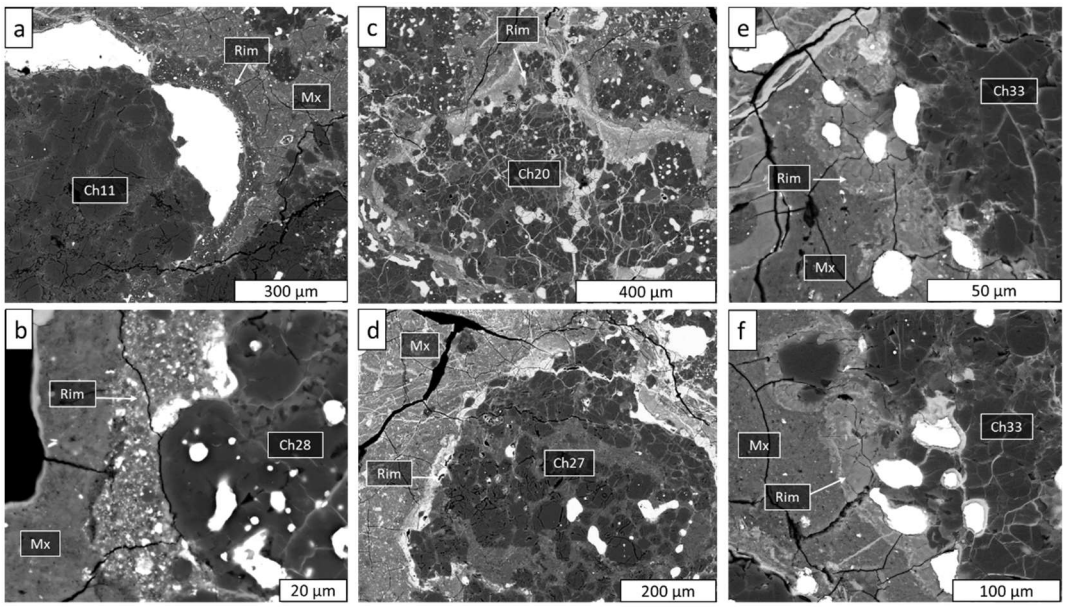

Figure 1.4. BSE images of different types of rims around chondrules in QUE 99177 other than smooth rims (read in columns). (a) Coarse-grained igneous rim around a type IAB chondrule that is contains large metal grains at its periphery. (b) Coarse-grained rim around a metal-rich type I chondrule. (c) Fine-grained rim surrounding a metal-rich chondrule affected by pervasive weathering. (d) Fine-grained rim around a metal-bearing POP type I chondrule. (e) and (f) very fine-grained rim around a metal-bearing type IA chondrule. Fine-grained rims have higher electron albedo in the BSE images than the surrounding matrix due to an enrichment in Fe.

3.2. Petrography of silica-rich igneous rims and smooth rims

Chondrules with smooth rims were identified and numbered in each BSE-SEM full thin section mosaic using full thin section RGB elemental X-ray maps for Si-Mg-Fe to determine their occurrences and assess their relationship with chondrules. Chondrules that contain smooth rims are exclusively type I (Mg-rich) and exhibit porphyritic olivine (PO), porphyritic olivine and pyroxene (POP), and porphyritic pyroxene (PP) textures. Because all chondrules that exhibit smooth rims also contain Silica-rich Igneous Rims (SIRs) (the opposite is not established), we infer that these two components are closely associated. Their general petrographic characteristics are described in this section.

Silica-rich Igneous Rims

Silica-rich igneous rims have been documented in detail in CR chondrites by Krot et al. (2004). They are a type of layered, coarse-grained, igneous rim around type I chondrules characterized by being sulfide-free, enriched in moderately volatile elements, and containing high-Ca and low-Ca pyroxenes, Fe,Ni nodules, and a nearly pure SiO_2 phase (Krot et al., 2004). In QUE 99177, SIRs are continuous or discontinuous around chondrules (e.g., some chondrules are broken or fragmented) and can reach widths up to ~200 μm. Pyroxene compositions obtained by EPMA from seven SIRs that contain smooth rims, along with pyroxene compositions from the interior of the same chondrules, are illustrated in the quadrilateral plot in Figure 1.5 (individual values are tabulated in Table A1.1 in Appendix 1). The SIRs contain a high abundance of silica grains, distributed continuously or discontinuously around the rims (Fig. 1.6a, in red), ranging from ~5 to ~25 μm in size, with rounded to elongated or lath-shaped morphologies (Fig. 1.6b-d). They have a mean composition (n = 4) of 83.54 wt% SiO_2, 0.68 wt% FeO, 0.3

wt% Al_2O_3, <0.18 wt% the sum of alkali oxides, and 0.1 wt% the sum of MgO, TiO_2, P_2O_5, MnO, and SO_3, in decreasing order (Table 1.1). However, we interpret that silica is not hydrated and that errors are attributed to not having used quartz as a standard for silica (see section 2). Some silica grains in the SIRs appear to have been replaced to varying degrees by a pseudomorphic phase with higher electron albedo (preserving the original silica morphology, e.g., Fig. 1.6b), sometimes embayed or corroded by this phase. The replacement phase is described in more detail in section 3.5. In most cases, the altered silica product coexists with relict silica grains in the SIR (Fig. 1.6b) and in some cases, the alteration phase appears to have been crystallographically controlled along a specific direction (e.g., orientation of the silica grain, Fig. 1.6c). A general observation is that SIRs that exhibit replacement of silica near the smooth rims can also contain unaltered silica further inside the SIR (Fig. 1.6b), but the opposite trend is not observed. Where silica is completely pseudomorphically replaced in a given SIR, caution was needed to avoid bias using solely silica in combined RGB elemental X-ray maps to identify SIRs.

Unaltered mesostasis regions in SIRs occur with irregular morphologies, ranging from ~10 to ~50 μm in size, filling interstitial spaces between Ca-rich pyroxenes and silica. They are largely clear and glassy (Fig. 1.6d-f) but can also be replaced by a phase with a higher electron albedo throughout the SIR. Glassy mesostasis can contain micron to submicron-sized quench crystallites of acicular albite or anorthite towards the interior of chondrules. Cathodoluminescence (CL) images show that mesostasis regions luminesce in pink while silica luminesces in bright blue (e.g., Fig. 1.6g). Mesostasis regions within SIRs and inside chondrules were analyzed in five chondrules using EPMA

(Tables 1.1 and A1.2-A1.6 in Appendix 1), revealing heterogeneous alkali distributions between chondrules and within chondrules (Fig. 1.6h). Mesostasis regions located in the interior of chondrules are more Ca- and Al-rich, whereas interstitial glass at the outer parts of chondrules and within SIRs are more Si-, Fe-, Mn-, and K-rich, with a much lower Ca content (Table 1.1), and a variable Na content, which can be very high (e.g., Ch8, inset in Fig. 1.6h). These observations are consistent with zoned mesostasis regions observed in type I chondrules in Semarkona (Matsunami et al., 1993; Alexander and Grossman, 2005; Libourel et al., 2006; Nagahara et al., 2008) and other CR chondrites (Libourel et al., 2006; Berlin, 2009). The EPMA totals for glass in SIRs are much lower (average of 88.9 wt%) compared to mesostasis in the interior of chondrules (average of 98.2 wt%), suggesting that glass is hydrated or that alkalis were lost during microprobe analyses, given that Na (which is abundant at the chondrule peripheries) is highly beam sensitive; or a combination of both processes. Sometimes, Mn enrichments are observed by X-ray maps (e.g., Fig. 1.6f) at the interface between SIRs and adjacent matrix material, forming a nearly continuous layer.

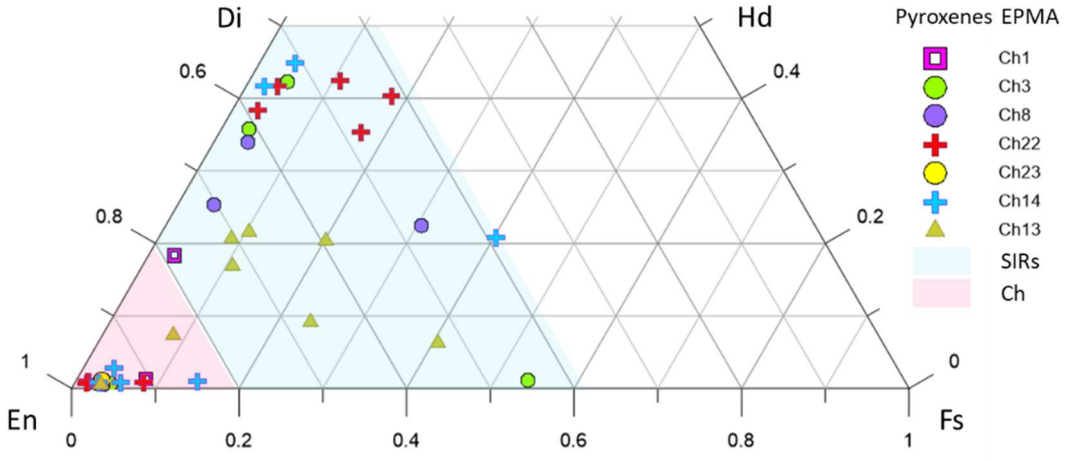

Figure 1.5. *(On previous page).* Pyroxene En-Fs-Wo quadrilateral plot (mol%) showing the compositions of pyroxenes in seven chondrules and adjacent SIRs (Chondrules 1, 3, 8, 22, and 23 in section 19, and chondrules 13 and 14 in section 18) obtained by EPMA (Table A1.1 in Appendix 1). Symbols represent individual analyses. Analyses in the enstatite (En) apex-range (area shaded in pink) sample chondrule pyroxene compositions while analyses expanding towards the Ca-rich (Di) and Fe-rich (Fs) (area shaded in blue) represent pyroxenes compositions obtained in chondrule SIRs. There is no overlap between pyroxenes compositions in SIRs and pyroxenes in the chondrule interior.

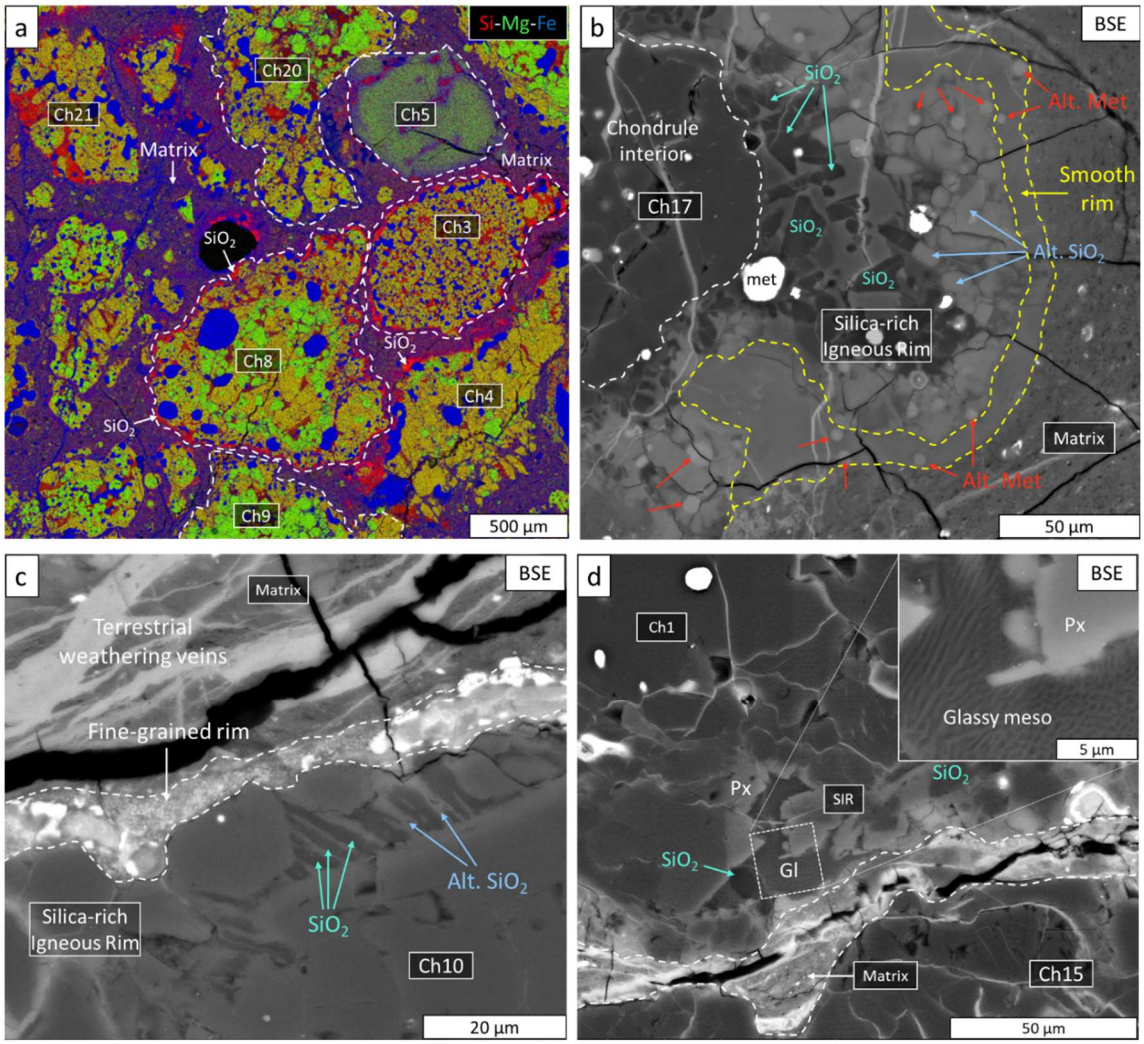

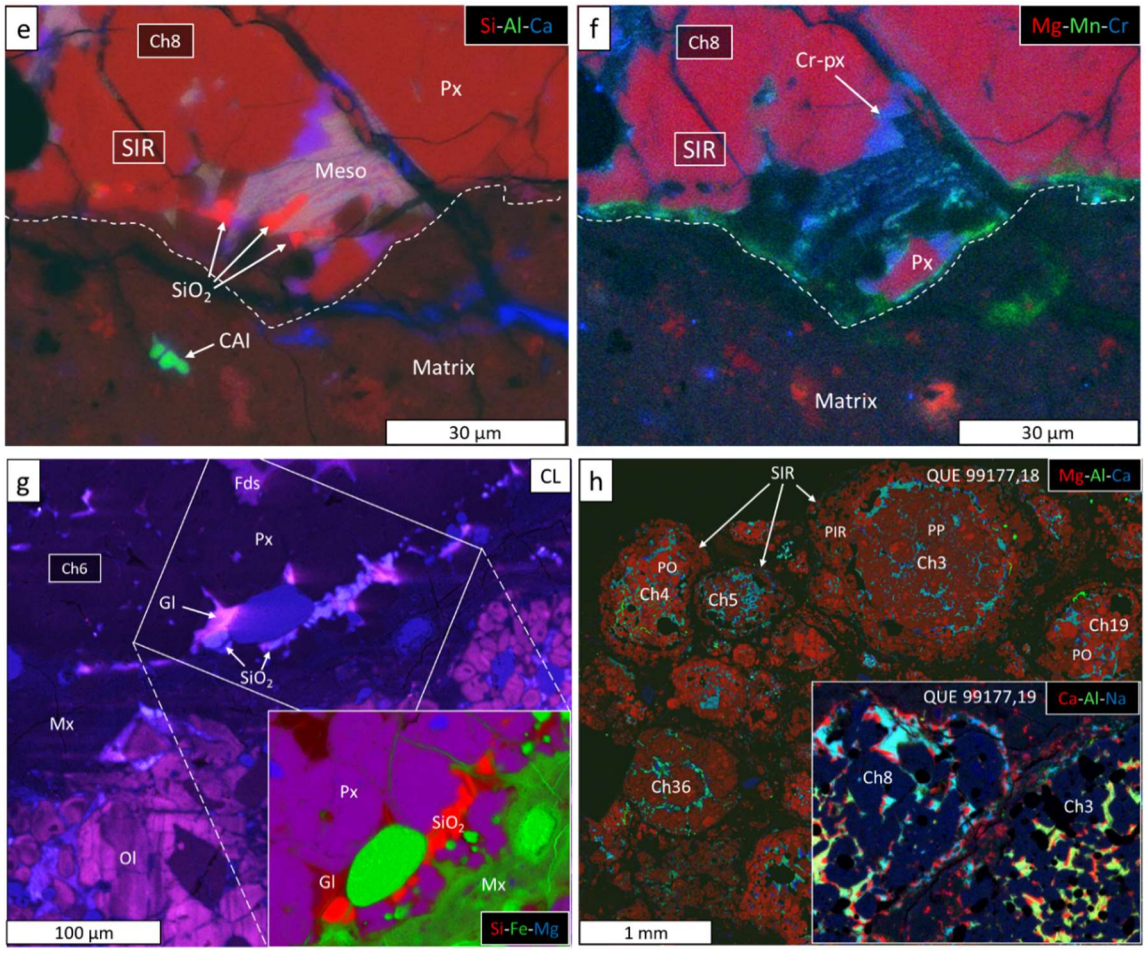

Figure 1.6. *(On previous and present pages).* SEM images of silica, silica alteration, and mesostasis regions in the SIRs of chondrules in QUE 99177. a) Combined RGB (Si-Mg-Fe) elemental X-ray map of several chondrules with associated matrix. Some chondrules are outlined for reference. Chondrule 8 is a type I POP metal-bearing chondrule with a large, continuous PIR and SIR, Ch3 is a type I, PP metal-rich chondrule with a continuous SIR, and Ch4 is a non-spherical type I POP metal-bearing chondrule with a discontinuous SIR. Note that matrix around chondrules 3, 4, and 8, with smooth rims around them, contains a higher concentration of Si (redder) compared to other regions of the matrix (bluer). b) BSE image of the smooth rim around Ch17 (outlined in yellow dashed lines) showing silica grains (indicated in turquoise) in contact with the smooth rim. Silica grains are lath-shaped, randomly orientated, and completely altered close to the smooth rim (indicated in blue) but partially altered towards the interior of the SIR, to unaltered further inside the chondrule. Fe,Ni metal blebs are also altered in the smooth rim and the SIR (Alt. Met, indicated with red arrows). Note that the smooth rim (~10-50 µm thick) is well developed around this chondrule. c) BSE image of a region of Ch10 showing that silica in the SIR is partially altered along the direction of the orientation of the silica grain. d) BSE image of a region in the edge of chondrule 1 (Ch1) showing the SIR mesostasis with glassy mesostasis (zoomed in), silica, and Ca-rich pyroxene. The dashed lines mark the limit between the chondrules and the matrix. *(Caption continues on the following page).*

Figure 1.6. *(Caption continued from the previous page).* e) and f) Combined RGB elemental X-ray maps for Si-Al-Ca and Mg-Mn-Cr of the same region in chondrule 8 (Ch8) showing the interface between the chondrule and the matrix where silica grains, glass, and a Mn-rich rim are apparent. g) CL image of chondrule 6 (Ch6), a type I PP chondrule in which silica (Si) luminesces blue and the glass (Gl) luminesces pink. Inset shows a combined RGB elemental X-ray map for Si-Fe-Mg of the square region. h) Combined RGB elemental X-ray map for Mg-Al-Ca showing heterogeneity of mesostasis regions within several chondrules and their rims. Inset with Ca-Al-Na map of a different region showing that section 19 displays a larger heterogeneity of Na in mesostasis regions, which is mainly located at the chondrule peripheries. SIR = Silica-rich Igneous Rim, PIR = pyroxene-rich igneous rim, PP = porphyritic pyroxene, PO = porphyritic olivine, Alt. Si = altered silica, Px = pyroxene, Ol = olivine, Mx = matrix, Fds = feldspar, Meso = mesostasis, Gl = glass.

Table 1.1. Representative EPMA analyses of mesostasis regions and silica in seven chondrules with SIRs in QUE 99177, measured with a focused 3 µm spot size. See analytical concerns for silica in section 2. M_{SIR} = mesostasis (glass and/or feldspar) in the SIR, M_i = mesostasis in the interior of the chondrule. Individual analyses are found in Tables A1.2 – A1.6 in Appendix 1.

	Ch13,14	Ch22		Ch1	Ch3		Ch8		Ch14	Mean	Mean
Oxides wt%	Silica n=4	M_{SIR} n=5	M_i n=3	M_{SIR} n=11	M_{SIR} n=14	M_i n=9	M_{SIR} n=22	M_i n=7	M_{SIR} n=5	M_{SIR} n=60	M_i n=19
SiO_2	83.54	55.69	53.43	55.90	71.21	69.60	69.06	56.18	68.52	66.10	62.10
P_2O_5	0.01	0.04	0.09	0.06	0.02	0.03	0.01	0.01	0.02	0.03	0.03
TiO_2	0.04	0.12	0.06	0.24	0.17	0.62	0.29	0.38	0.08	0.21	0.44
Al_2O_3	0.30	13.22	26.92	13.41	8.39	14.39	14.80	21.97	9.89	12.17	19.16
Cr_2O_3	n.d.	0.35	0.10	0.11	0.23	0.13	0.23	0.25	0.02	0.20	0.17
SO_3	0.01	0.31	0.01	n.d.	0.14	0.01	0.03	n.d.	0.01	0.08	0.00
FeO	0.68	12.12	0.98	12.45	4.81	2.58	2.96	1.66	2.02	6.17	1.99
MnO	0.01	0.75	0.18	0.17	0.62	0.66	0.66	0.30	0.06	0.52	0.45
MgO	0.06	3.02	2.98	2.18	3.45	1.43	1.59	2.75	0.54	2.16	2.16
CaO	0.09	5.04	11.35	6.88	1.69	6.07	2.19	11.48	5.49	3.40	8.90
Na_2O	0.07	3.40	3.71	0.99	1.41	1.28	2.38	2.76	0.63	1.84	2.21
K_2O	0.01	0.20	0.06	0.02	0.93	0.74	1.05	0.22	0.04	0.66	0.44
NiO	0.02	0.18	0.10	0.16	0.39	0.09	0.09	0.12	0.08	0.19	0.10
Total	84.85	94.43	99.96	92.57	93.44	97.64	95.35	98.06	87.40	88.89	98.16

n.d. = not detected

Smooth rims

Smooth rims have thicknesses up to ~50 μm (average of ~20 μm) and appear to be very distinct from the matrix, because they are texturally very homogeneous (e.g., Fig. 1.6b, 1.7a-e), but the boundary between the smooth rim and the SIR is sometimes diffuse (e.g., Fig. 1.6c). The interfaces between smooth rims and matrices are sharp, vary from regular (e.g., Fig. 1.7a) to highly irregular (Fig. 1.7d), and they generally have a slightly higher BSE contrast compared to the matrix (Fig. 1.7). Backscattered images show that in some cases, the matrix becomes slightly more homogeneous in texture close to the smooth rim, up to 20-40 μm from the chondrule edge. In addition, the matrix material is enriched in Si around a chondrule that is surrounded by a smooth rim, seen in the RGB elemental X-ray map for Si-Mg-Fe (e.g., Fig. 1.6a), between ~50 and ~300 μm around a given chondrule with a SIR, relative to chondrules that lack smooth rims.

Individual smooth rims are often continuous around the entire periphery of an individual chondrule, although the thickness of a smooth rim around a particular chondrule can vary significantly. Smooth rims also appear discontinuous, but partly because some chondrules are fragmented or broken, likely due to brecciation. Unlike the matrix, individual mineral grains cannot be resolved in smooth rims by FEG-SEM. However, high-magnification BSE images show that sometimes, smooth rims exhibit compositional heterogeneities, seen as dark and light regions of low- and high-Z contrasts under the SEM (Fig. 1.7c,d). In these cases, the darker areas are irregular in shape (~5 to 30 μm in size), randomly distributed, and edges are either diffusive or sharp, while the lighter areas generally comprise the interstitial regions or a groundmass that occupy larger areas. Sometimes, the interface between a smooth rim and the adjacent matrix is

decorated with a higher concentration of micron-sized sulfide grains, as previously noticed by Jones et al. (2015). Less commonly, the interface exhibits an accumulation of Ca phosphate grains, ~1-10 μm in size, and occasionally, these occur within the smooth rim itself (Fig. 2.6a-d in Chapter 2). Calcium phosphates around type IA chondrules are less obvious than Ca phosphates around type IIA chondrules (e.g., Martinez-Jimenez and Brearley, 2018), but probably they are more common than previously recognized.

The boundary between a smooth rim and the adjacent matrix appears sharp in BSE imaging (Fig. 1.7). RGB elemental X-ray maps for Fe-Ni-S show that these three elements combined act as best tracers for distinguishing the boundary between smooth rims and matrices, because the abundances of S and Ni change dramatically from extremely minimal within smooth rims, although not completely absent, to highly abundant in the matrix (Fig. 1.7f). Iron is present in both smooth rims and matrices, but smooth rims are Fe-enriched compared to the matrix, which gives the observed higher electron albedo in BSE imaging.

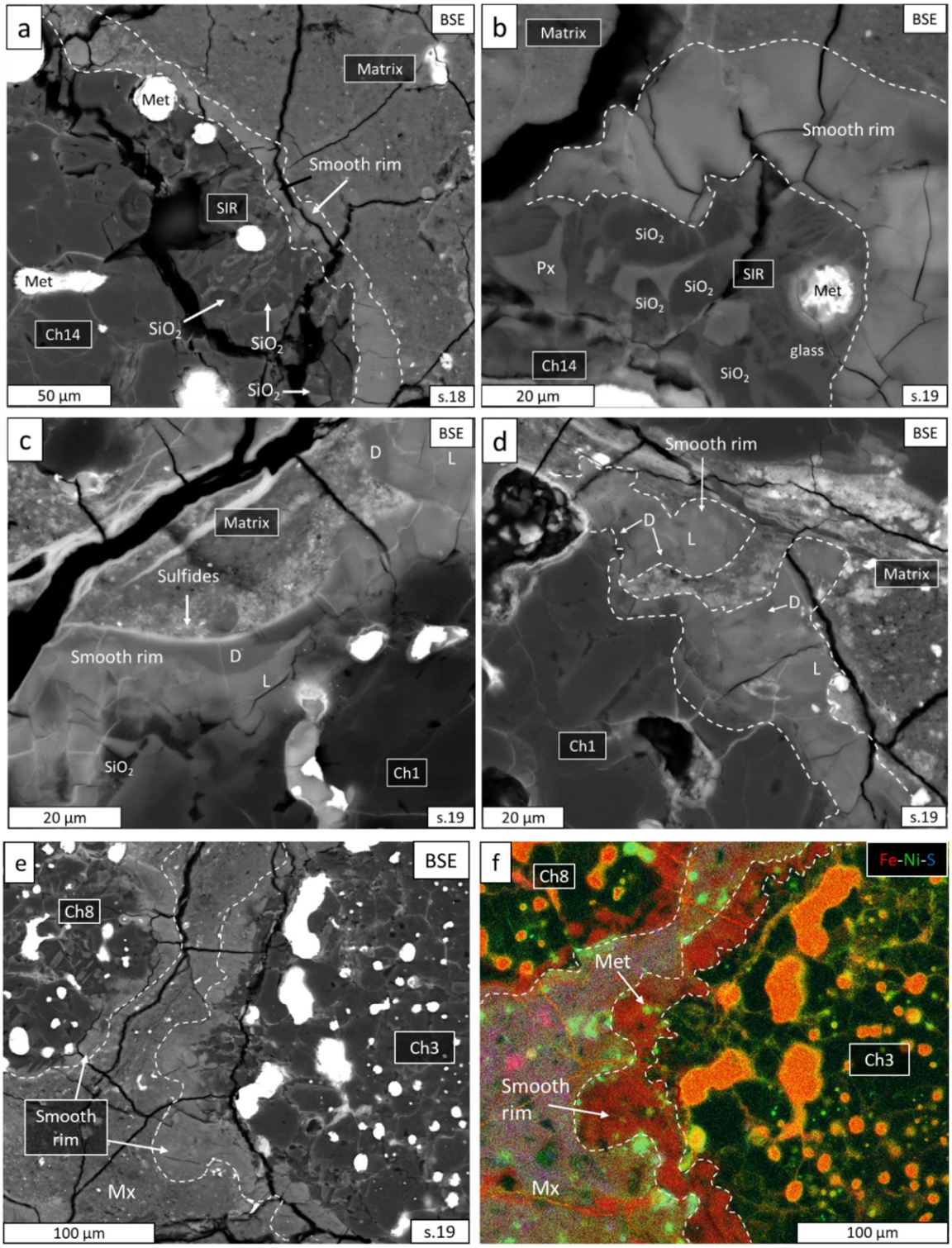

Figure 1.7. SEM images of smooth rims around chondrules in QUE 99177. a) General view of a smooth rim around a chondrule (Ch14) showing that smooth rims are texturally homogeneous, well-distinguished, associated with silica from the SIR, and have a higher electron albedo compared to the adjacent matrix. *(Caption continues on the following page).*

Figure 1.7. *(Caption continued from the previous page).* b) BSE image of a region showing the homogeneous appearance of the smooth rim with irregular width, and its associated rounded and lath-shaped silica grains in the SIR. c) and d) BSE images of two different regions of the smooth rim around chondrule 1 (Ch1) where light (L) and dark (D) areas are distinguished due to differences in electron albedo within the smooth rim. The region in (c) is affected by a network of localized terrestrial weathering veins, but the adjacent material appears unaffected. The boundary between the smooth rim and the adjacent matrix is sharp and highly irregular. e) BSE image showing regions of Ch3 and Ch8 surrounded by smooth rims and matrix between them. The RGB elemental X-ray map for Fe-Ni-S of the same region shown in (f) illustrates that the smooth rims are best distinguished using these elements, because Ni and S are depleted in smooth rims compared to the matrix. The white dashed lines mark the boundary between the smooth rim and the matrix and the smooth rim and the chondrule SIR. Note that the smooth rim contains a few altered Fe,Ni metal blebs in it (Met), not distinguished in the BSE image in (e).

3.3. Smooth rim and corresponding adjacent matrix chemistry

Backscattered electron images and SEM-EDS analyses indicate that smooth rims essentially consist of an Fe- and Si-rich phase, but the presence of other minor and trace elements suggests they may also contain a variety of other phases. We selected representative chondrules with smooth rims and their adjacent fine-grained matrix material for compositional analysis using focused beam (3 or 5 μm diameter) electron probe microanalysis (Tables A1.7-A1.19 in Appendix 1). Five chondrules in QUE 99177,19 (Chondrules 1, 3, 8, 22, and 23, Fig. 1.1b) and two in QUE 99177,18 (Chondrules 13 and 14, Fig. 1.1a) were analyzed. A total of 134 analyses were obtained in smooth rims and 83 in their adjacent matrix material; representative analyses are tabulated in Table 1.2. The averaged analytical total for smooth rims is 83.21 wt%, which is about 4 wt% less than the average totals for adjacent matrices (87.29 wt%), suggesting that smooth rims are more hydrated than the matrix (Table 1.2). Although not evident in Table 1.2, we also observe that analytical totals are slightly different between dark and light regions, which is discussed in more detail below.

Smooth rims contain roughly equal amounts of SiO_2 and FeO (~37 wt% each), with some MgO (~4 wt%), Al_2O_3 (~2 wt%), CaO (~1 wt%), MnO (~0.5 wt%), and trace NiO, Na_2O, Cr_2O_3, SO_3, P_2O_5, K_2O, and TiO_2 (<1 wt%, in decreasing order) (Table 1.2a). Our results show that smooth rim compositions are slightly enriched in Fe, Mn, Al, and Ca relative to their adjacent matrices (Table 1.2b), whereas the matrix is enriched in Mg, S, Ni, Na, and P, in decreasing order, although there is some overlap for Na and Cr contents between the two datasets. Ternary Fe-Si-Mg and Ca-Mg-Mn (normalized element wt%) diagrams showing the compositions of smooth rims and matrices are reported in Figure 1.8. Smooth rims data lie very close to the Fe-Si join of the ternary diagram (Fig. 1.8a) and Mg and Fe show a negative correlation with one another (Fig. 1.9). Generally, smooth rim compositions, from individual microprobe analyses, range from >40 to <75% for Fe (Fig. 1.8a), and the data for the matrix are distinct (Fig. 1.8b), i.e., there is minimal overlap between the two datasets, smooth rims and matrix. Matrix data define a linear array with a larger range of Mg/Si ratios compared to smooth rims. Both smooth rims and matrix show some variations in Fe, ranging from 23 to 62% in smooth rims and from >30 to <70% in the matrix. Matrix data for Fe are in agreement with Abreu and Brearley (2010), although their analyses reach higher Fe contents (80% Fe). Magnesium in the matrix is more variable than in smooth rims, ranging from 2 to 28% Mg (Fig. 1.8b), while smooth rims range from 0 to 15% (Fig. 1.8a). Ternary Ca-Mg-Mn (element wt%) diagrams in Figure 1.8c,d show a much larger variability for smooth rims than matrix. Smooth rims data extend from the Mg apex towards <40% Mn and <45% Ca (Fig. 1.8c), whereas the data for matrix lie on a linear array close to the Ca-Mg join, with the majority of the data concentrated in the Mg apex (Fig. 1.8d).

Table 1.2. Average compositions (oxide wt%) and standard deviations (σ) for individual smooth rims (1.2a) and adjacent matrix material (1.2b) obtained by EPMA on seven chondrules in QUE 99177 (Chondrules 1, 3, 8, 22, 23 in QUE 99177,19, and chondrules 13, and 14 in QUE 99177,18). The last four columns on Table 2A refer to data from Harju et al. (2014) in QUE 99177 smooth rims, where 'dark' and 'light' refers to regions with different BSE contrast, and Krot et al. (2004) data on phyllosilicates resulting from silica alteration in GRA 95229 and PCA 91082 (oxide wt%).

Table 1.2a – Smooth rims

	This work													Harju et al. 2014		Krot et al. 2004	
	Ch1		Ch3		Ch8		Ch22		Ch23		Ch14		**SR Mean**	SR Norm	QUE 99177		GRA 95229[1]	PCA 91082[2]
Oxides wt%	*23*	*σ*	*22*	*σ*	*26*	*σ*	*30*	*σ*	*17*	*σ*	*16*	*σ*	*n=134*	*n=134*	*Light (15)*	*Dark (4)*	n=2	n=3
SiO_2	34.20	*3.69*	39.46	*2.57*	33.89	*4.37*	39.82	*2.93*	40.40	*2.81*	33.15	*1.04*	36.92	44,37	37	39.2	39.86	42.05
P_2O_5	0.38	*0.60*	0.25	*0.32*	0.04	*0.06*	0.09	*0.06*	0.07	*0.05*	0.02	*0.02*	0.14	0,17	n.d.	n.d.	n.d.	n.d.
TiO_2	0.07	*0.07*	0.05	*0.04*	0.05	*0.04*	0.04	*0.03*	0.06	*0.05*	0.05	*0.02*	0.05	0,06	n.d.	n.d.	0.04	0.04
Al_2O_3	2.45	*1.94*	1.59	*0.72*	2.17	*1.54*	1.38	*0.96*	1.74	*1.19*	0.62	*0.33*	1.71	2,05	2.7	3.8	0.35	0.55
Cr_2O_3	0.42	*0.81*	0.26	*0.43*	0.17	*0.26*	0.19	*0.20*	0.39	*0.55*	0.06	*0.10*	0.25	0,29	0.09	0.24	0.06	0.06
FeO	37.08	*4.13*	34.95	*4.52*	38.68	*4.69*	37.16	*3.75*	36.31	*5.09*	41.16	*3.00*	37.45	45,01	39.4	29.9	37.93	39.98
MgO	5.76	*2.19*	5.05	*2.53*	3.27	*1.72*	2.73	*1.60*	4.48	*2.27*	3.57	*2.77*	4.06	4,87	0.25	0.29	0.42	0.39
CaO	0.90	*1.30*	1.37	*1.90*	1.86	*2.56*	0.94	*1.46*	1.14	*1.23*	0.39	*0.31*	1.14	1,37	3.7	11.1	4.13	1.98
MnO	0.37	*0.21*	0.72	*0.29*	0.50	*0.39*	0.56	*0.57*	0.82	*0.53*	0.13	*0.13*	0.52	0,63	0.49	0.93	0.19	0.18
Na_2O	0.26	*0.42*	0.21	*0.22*	0.34	*0.32*	0.30	*0.23*	0.22	*0.17*	0.18	*0.05*	0.26	0,31	0.1	0.16	0.26	0.57
K_2O	0.04	*0.03*	0.14	*0.05*	0.18	*0.09*	0.06	*0.02*	0.12	*0.05*	0.30	*0.10*	0.13	0,15	0.18	0.12	0.13	0.31
NiO	0.70	*0.20*	0.24	*0.06*	0.05	*0.11*	0.42	*0.25*	0.51	*0.32*	0.02	*0.05*	0.32	0,39	0.19	0.25	n.d.	n.d.
SO_3	0.14	*0.16*	0.13	*0.12*	0.52	*1.28*	0.16	*0.13*	0.19	*0.14*	0.35	*0.50*	0.25	0,30	n.d.	n.d.	n.d.	n.d.
Total	**82.75**	***3.57***	**84.42**	***3.24***	**81.70**	***2.91***	**83.84**	***2.50***	**86.43**	***2.36***	**80.01**	***1.75***	**83.21**	**100**	**84.1**	**86.00**	**83.37**	**83.05**

[1]average composition of two smooth rim analyses around one chondrule.

[2]average composition of four smooth rim analyses around two chondrules (two analyses each).

n = number of analyses

n.d. = not detected

Norm = normalized to 100 for comparison purposes with TEM analyses

Table 1.2. (*Continued*). Average compositions and standard deviations of fine-grained matrix material adjacent to smooth rims in QUE 99177.

Table 1.2b – Matrix

Oxides wt%	Ch1		Ch3		Ch8		Ch22		Ch23		Ch13		Ch14		**Matrix mean**	
	n=11	*σ*	*n=8*	*σ*	*n=14*	*σ*	*n=27*	*σ*	*n=9*	*σ*	n=4	*σ*	*n=10*	*σ*	***n=83***	*σ*
SiO_2	31.45	*2.73*	37.27	*3.68*	31.42	*3.03*	37.88	*3.44*	36.38	*3.50*	27.20	*1.42*	33.55	*2.84*	**34.68**	*4.46*
P_2O_5	0.32	*0.12*	0.34	*0.38*	0.05	*0.05*	0.30	*0.16*	0.28	*0.20*	0.03	*0.02*	0.02	*0.02*	**0.22**	*0.21*
TiO_2	0.05	*0.02*	0.06	*0.02*	0.06	*0.02*	0.06	*0.03*	0.06	*0.03*	0.05	*0.00*	0.06	*0.03*	**0.06**	*0.02*
Al_2O_3	1.19	*0.36*	1.09	*0.41*	1.32	*0.41*	1.38	*0.41*	1.35	*0.69*	1.47	*0.27*	1.29	*0.46*	**1.31**	*0.44*
Cr_2O_3	0.38	*0.18*	0.49	*0.45*	0.31	*0.10*	0.33	*0.09*	0.74	*0.72*	0.27	*0.03*	0.31	*0.06*	**0.39**	*0.31*
FeO	38.18	*4.28*	28.64	*3.65*	33.28	*3.52*	30.48	*3.37*	31.53	*3.02*	33.96	*2.72*	32.06	*3.55*	**32.27**	*4.35*
MgO	9.58	*4.35*	12.92	*4.61*	12.74	*4.35*	13.49	*3.92*	10.58	*4.31*	14.79	*1.63*	12.70	*3.04*	**12.44**	*4.13*
CaO	0.64	*0.53*	1.54	*1.48*	0.96	*0.50*	0.90	*0.41*	1.69	*1.61*	0.57	*0.35*	0.83	*0.51*	**1.00**	*0.85*
MnO	0.25	*0.10*	0.47	*0.27*	0.29	*0.07*	0.29	*0.17*	0.56	*0.39*	0.24	*0.06*	0.22	*0.13*	**0.32**	*0.21*
Na_2O	0.19	*0.08*	0.60	*0.13*	0.68	*0.21*	0.22	*0.12*	0.38	*0.19*	0.37	*0.09*	0.24	*0.07*	**0.36**	*0.23*
K_2O	0.02	*0.02*	0.11	*0.02*	0.15	*0.04*	0.04	*0.04*	0.09	*0.02*	0.07	*0.03*	0.18	*0.04*	**0.09**	*0.06*
SO_3	4.47	*2.70*	4.03	*2.74*	0.38	*0.22*	3.29	*1.18*	3.85	*2.47*	0.73	*0.15*	0.23	*0.15*	**2.60**	*2.29*
NiO	1.23	*0.47*	1.21	*0.43*	1.80	*0.88*	1.52	*0.63*	1.79	*1.13*	1.84	*0.53*	1.80	*0.43*	**1.58**	*0.71*
Total	87.94	*3.91*	88.76	*4.97*	83.43	*2.87*	90.19	*4.26*	89.28	*3.03*	81.61	*3.13*	83.49	*2.93*	**87.29**	*4.75*

n = number of analyses
σ = standard deviation

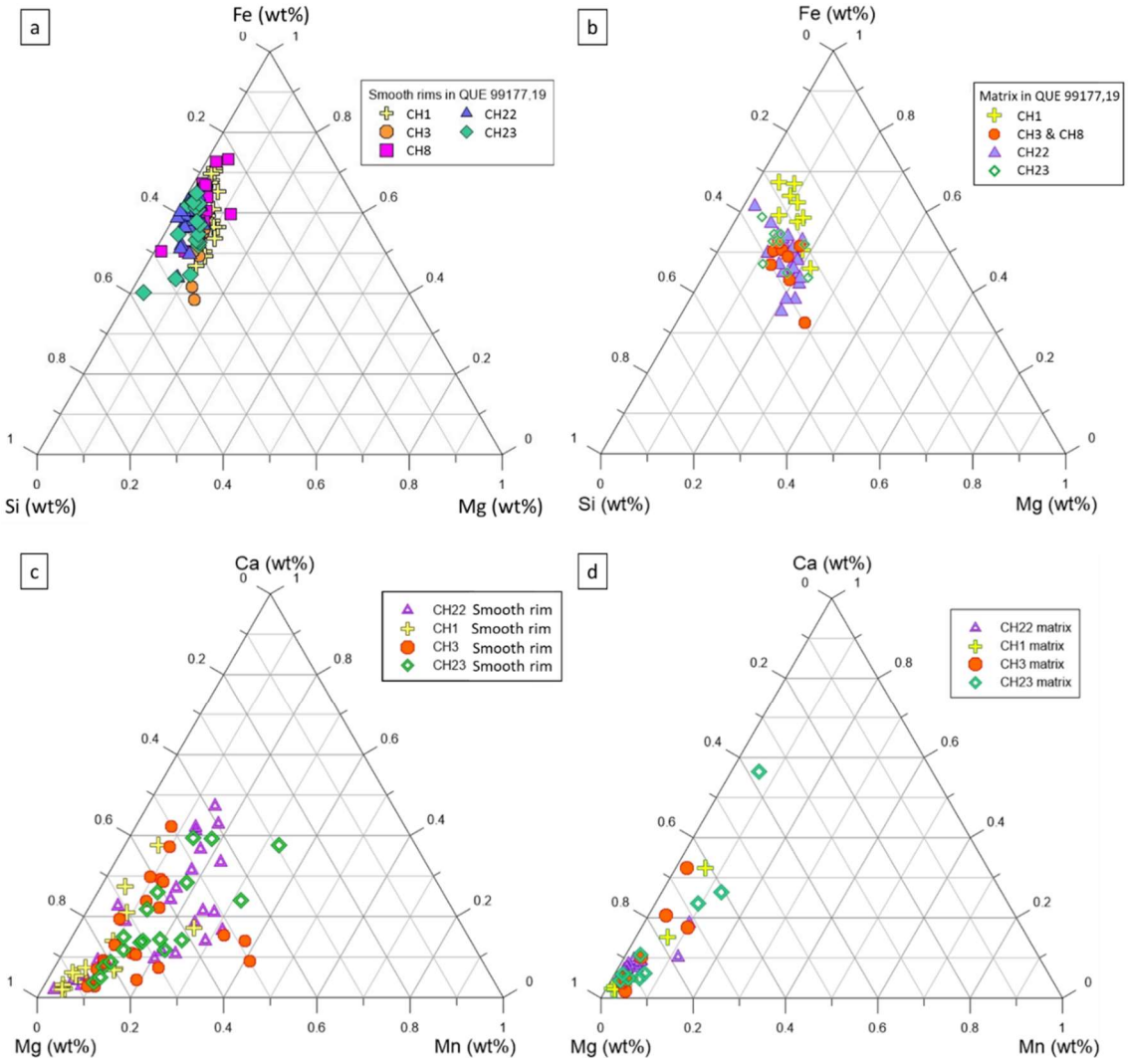

Figure 1.8. Ternary diagrams (normalized element wt%) for Si-Mg-Fe (a and b) and Mg-Mn-Ca (c and d) showing probe data for smooth rims (left) and matrix (right) around chondrules in QUE 99177. Points are individual analysis. Note that chondrules 3 and 8 are adjacent to one another (e.g., Fig. 1.5a) and therefore, they share analyses for the matrix. Data in smooth rims show a much larger variability in Ca and Mn (up to ~50 wt%) compared to the matrix.

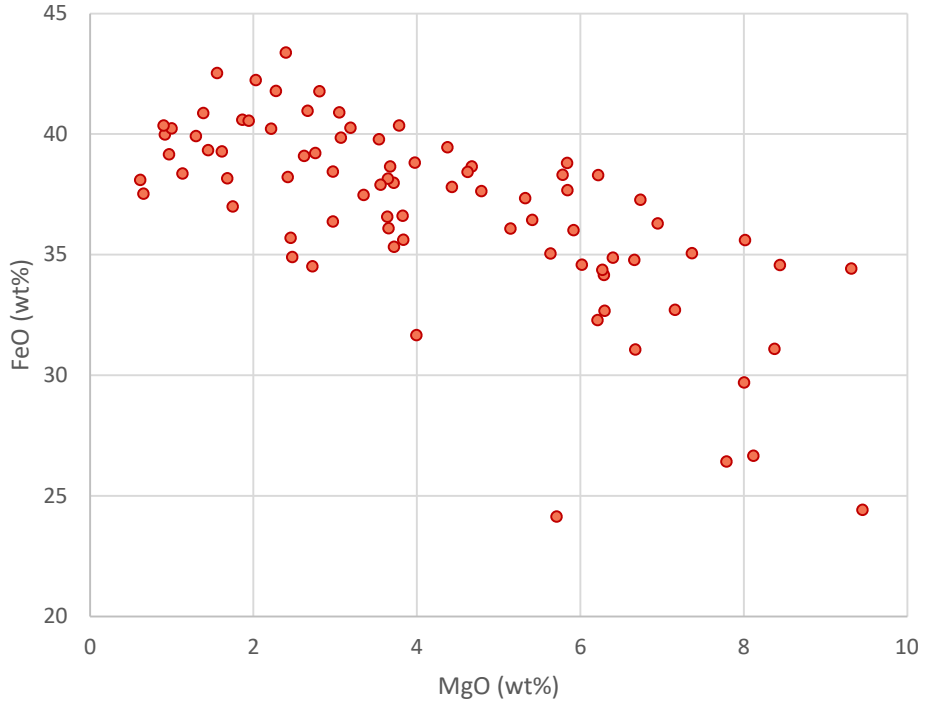

Figure 1.9. FeO versus MgO (oxides wt%) plot showing individual EPMA analysis in smooth rims around four chondrules in QUE 99177,19 demonstrating an inverse correlation between Fe and Mg and that the Mg concentration is much lower than Fe.

Chemical compositions of selected BSE light and dark areas (20 dark and 23 light) of smooth rims around two chondrules (Ch1 and Ch3) were measured using quantitative EPMA analyses (1-3 µm-diameter beam) in an attempt to understand the observed compositional heterogeneity in smooth rims (Fig. 1.10; Tables 1.3 and A1.20-A1.21 in Appendix 1). Chondrules 1 and 3 were selected because they show the clearest distinctions between dark and light areas (lower and higher BSE contrasts, e.g., Figs. 1,7c,d, 1.12a). The data show a clear trend of increasing Ca (up to 4.5 wt% CaO), Cr (up to 3.5 wt% Cr_2O_3), and MgO/FeO ratios in the darker areas (Fig. 1.10). The darker areas are also enriched in Al, Ti, P, and Na relative to the lighter areas (Table 1.3). In addition, the darker areas exhibit somewhat higher analytical totals (83.9 wt% average) compared

to the lighter areas (81.6 wt%), suggesting that the lighter material is more hydrated than the darker material. Based on the textural information obtained by SEM and compositional analyses obtained by EPMA, we cannot constrain which phases are contributing to the compositional heterogeneity in smooth rims. Consequently, we have further investigated the dark and light areas using TEM (section 3.4).

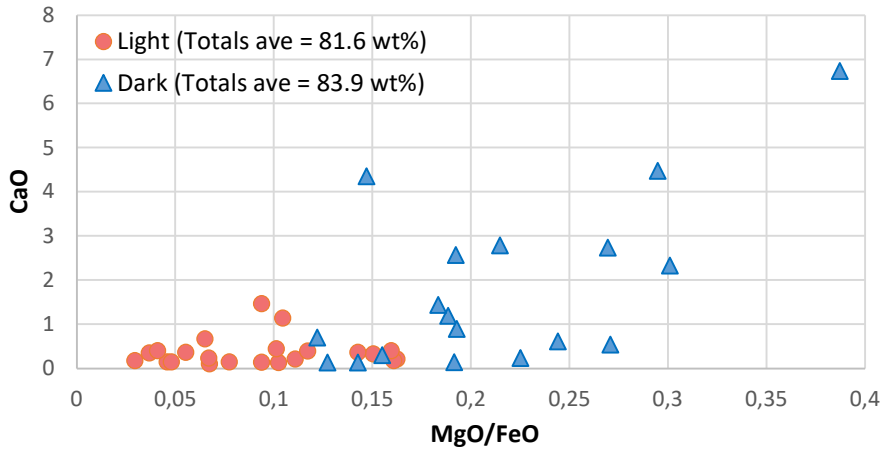

Figure 1.10. CaO (oxides wt%) against MgO/FeO ratio plot of BSE-light (red circles) and BSE-dark smooth rim areas (blue triangles). Average oxide compositions from EPMA analysis of smooth rims around two chondrules (Ch1 and Ch3) in QUE 99177,19. Points are individual analysis.

Table 1.3. Average smooth rim compositions of BSE- light and dark regions obtained by EPMA (oxides wt%) in two chondrules (Ch1 and Ch3) in QUE 99177,19. *n* = number of analyses. Individual analyses are found in Tables A1.20 and A1.21 in Appendix 1.

Oxides wt%	Light *n*=23	Dark *n*=20
SiO_2	35.40	32.77
P_2O_5	0.17	1.07
TiO_2	0.05	0.23
Al_2O_3	1.75	5.67
Cr_2O_3	0.10	0.57
SO_3	0.43	0.69
FeO	38.68	30.35
MnO	0.50	0.51
MgO	3.76	6.22
CaO	0.36	4.80
Na_2O	0.13	0.34
K_2O	0.11	0.08
NiO	0.11	0.16
Total	81.61	83.87

Finally, elemental abundance patterns for average matrix and smooth rims (normalized to CI chondrites and Mg) are represented in Figure 1.11. Refractory lithophile elements in the matrix are unfractionated relative to CI abundances. Sodium and S show depletions, but Si, Cr, Mn, P, Ni, and Fe, show slight enrichments up to 2 x CI chondrite. The abundance patterns for smooth rims are quite different from the matrix with significant enrichment for all elements (including refractory lithophile elements), with the exception of Ni and S, both showing strong depletions consistent with the distinctly different concentrations of these two elements seen in elemental X-ray maps of smooth rims in contact with matrix (e.g., Fig. 1.7f). Overall, Figure 1.11 shows that smooth rims have notable enrichments in the moderately volatile elements Cr, Mn, and P, and in the alkalis Na and K, up to 10 x CI chondrite values.

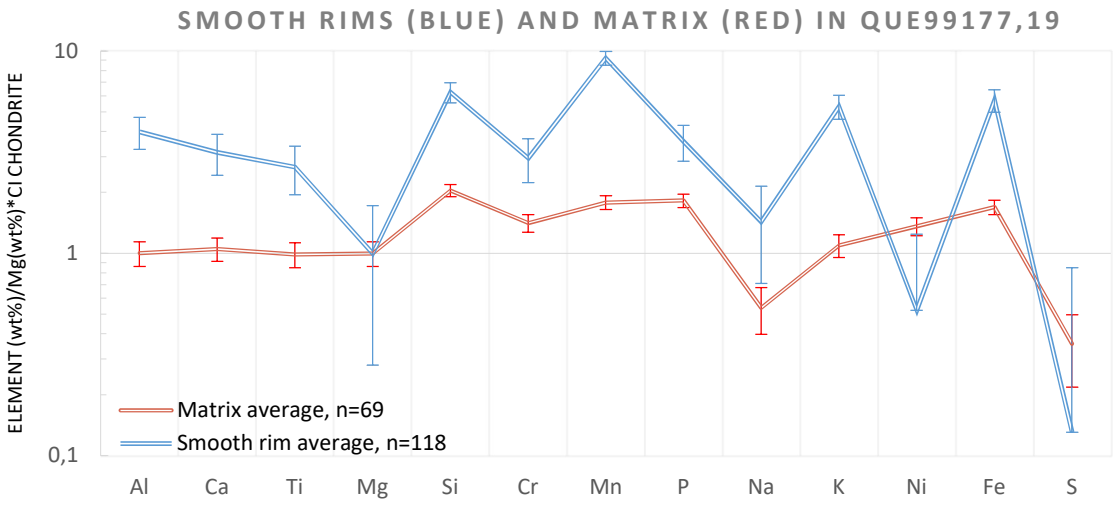

Figure 1.11. Average elemental abundance patterns for matrix (n = 69) and smooth rims (n = 118) in QUE 99177,19 (element wt% normalized to Mg and to CI chondrite average values – Lodders, 2003). Lithophile, siderophile, and chalcophile elements are individually arranged in order of decreasing condensation temperature. Error bars represented as vertical lines correspond to the standard deviations (1σ).

3.4. TEM observations of smooth rims

A total of four FIB sections were extracted, one each from four different smooth rims around chondrules in QUE 99177, to examine their microstructures in detail using TEM: two in section 19 and two in section 18 (Fig. 1.12), designated FIB1 (Fig. 1.12b), FIB2 (Fig. 1.12d), FIB3 (Fig. 1.12g), and FIB4 (Fig. 1.12i), representing the range of textures observed in smooth rims. An additional FIB section (FIB5) was extracted in a silica grain that is partially altered to identify the nature of the unaltered polymorph and further investigate the replacement of silica and its role in the formation of smooth rims.

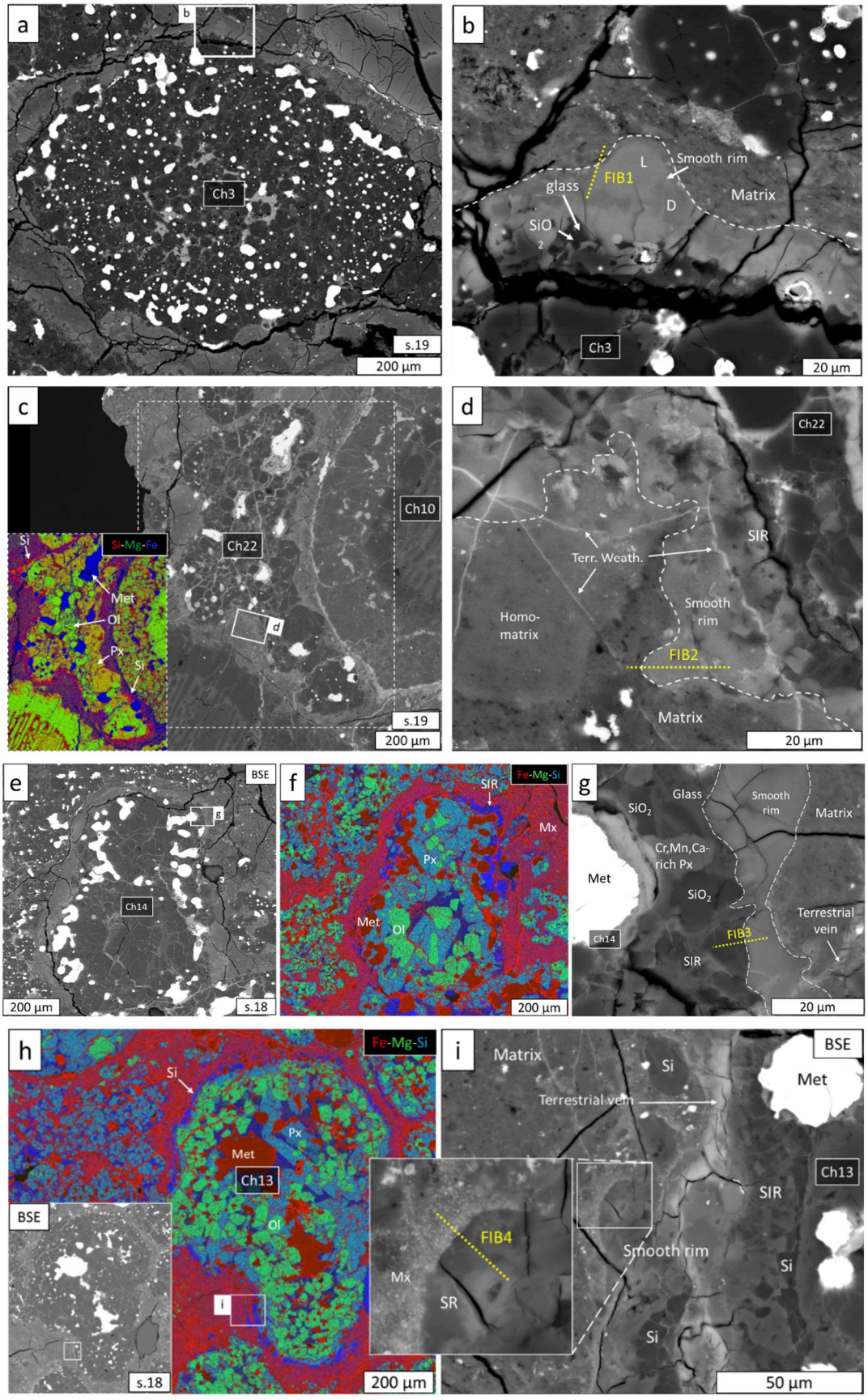
a
b
Ch3
s.19
200 µm
b
L
Smooth rim
FIB1
glass
Matrix
D
SiO2
Ch3
20 µm
c
Ch10
Si
Si-Mg-Fe
Ch22
Met
Ol
Px
Si
d
s.19
200 µm
d
Ch22
SIR
Terr. Weath.
Homo-matrix
Smooth rim
FIB2
Matrix
20 µm
e
BSE
g
Ch14
200 µm
s.18
f
Fe-Mg-Si
SIR
Mx
Px
Met
Ol
200 µm
g
Glass
SiO2
Smooth rim
Matrix
Cr,Mn,Ca-rich Px
Met
SiO2
Terrestrial vein
Ch14
FIB3
SIR
20 µm
h
Fe-Mg-Si
Si
Px
Met
Ch13
Ol
BSE
i
s.18
200 µm
i
Matrix
Si
BSE
Met
Terrestrial vein
Ch13
SIR
FIB4
Smooth rim
Mx
SR
Si
Si
50 µm

Figure 1.12. *(On previous page).* BSE images and RGB element maps of the smooth rim regions from which four FIB sections were extracted. a) BSE image of Ch3, a rounded, type IB, metal-rich PP chondrule, showing the location (white square) of the smooth rim area where FIB1 was extracted. b) Close-up BSE image (white box in (a)) showing the exact location of FIB1, which extends from the two-tone smooth rim into the matrix. c) BSE image of Ch22, a type IA, metal-rich POP chondrule, with inset RGB EDS X-ray map (R = Si, G = Mg, B = Fe) showing olivine (green), pyroxene (orange), metal (blue), and silica (red) around the chondrule rim. Matrix appears in purple. The boxed region indicates the smooth rim location where the FIB section was extracted. d) Close-up BSE image (white box in (c)) showing the exact location of FIB2, cut across the smooth rim to the matrix. Some regions of the matrix adjacent to the smooth rim appear more homogeneous in texture (Homo-matrix). e) BSE image of Ch14, a composite type IA POP chondrule with a metal-bearing mantle that contains a SIR and is surrounded by a smooth rim. The white square shows the location of the cut. f) Elemental X-ray RGB map for Fe-Mg-Si showing olivine (green), pyroxene (light blue), metal (red), and silica (bright blue) around the chondrule rim. Matrix appears in pink. g) Close-up BSE image (white box in (e)), showing the location of FIB3, which extends from the silica to the smooth rim. h) Elemental X-ray RGB map of Ch13 for Fe-Mg-Si showing olivine (green), pyroxene (lighter blue), mesostasis (darker blue), and metallic grains (red). The silica-rich rim from the SIR appears in bright blue. Inset of BSE image of Ch13, a type IA, metal-rich, POP chondrule. The white square indicates the location where the FIB section was extracted. i) Close-up BSE image (white box in (h)) showing inset of the exact location of FIB4. Note that the matrix at the interface with the smooth rims contains a higher concentration of sulfides.

3.4.1 TEM study of the smooth rim around chondrule 3 (FIB1)

The first FIB section (FIB1) was extracted across the boundary between the smooth rim around chondrule 3 (Ch3) and the matrix in QUE 99177,19 (Fig. 1.1b, 1.12a,b). Chondrule 3 is a rounded, type IB, porphyritic pyroxene (PP), metal-rich chondrule, ~700 μm in size, containing a SIR. Silica and glass within the SIR were detected by EPMA, closely associated with the smooth rim (Fig. 1.12b). The interface between the smooth rim and the matrix is decorated with Ca-phosphate grains, detected by EPMA (Chapter 2). The smooth rim shows clear compositional heterogeneities at the 10-μm scale and thus, the FIB section was oriented to target material from the two different Z-contrast regions. A HAADF STEM mosaic of the FIB section and selected X-ray maps of the smooth rim and matrix are shown in Figure 1.13.

The most noteworthy discovery is that ~70% of the smooth rim area in the FIB section is composed of an amorphous Fe- and Si-rich phase, based on electron diffraction patterns and STEM-EDS analyses of this phase (Fig. 1.13a). The amorphous material is completely featureless, with no differences in Z contrast, and contains a few fractures and terrestrial weathering (Fe-oxide or oxyhydroxide) veins, ~30 nm in width, that crosscut one another. The amorphous silicate compositions in different locations of the FIB section were measured using STEM-EDS analyses and are given in Table 1.4. Note that oxygen is assumed by stoichiometry and the obtained wt% oxides are normalized to 100. The amorphous material contains, on average, Si and Fe (50.64 wt% SiO_2 and 33.77 wt% FeO), some Mg (8.27 wt% MgO), Al (3.32 wt% Al_2O_3), Na (2.06 wt% Na_2O), and <2 wt% other elements, which include S (0.45 wt% SO_3) (Table 1.4). Sodium content is highly variable, ranging from 1.7 to 4 wt% Na_2O, but ubiquitous throughout the amorphous silicate material (Table 1.4). Observed at this scale, we infer that the amorphous material corresponds to the lighter regions observed with SEM imaging.

The second most important discovery is the presence of crystalline phases heterogeneously distributed within the amorphous material, ranging from a few nm to ~3 μm in size (Fig. 1.13a-d). High abundances of these phases correspond to the darker regions observed by SEM. They consist of anhedral to subhedral, equant to elongated crystals of Ca-, Mg-rich pyroxenes, based on STEM-EDS analyses and diffraction patterns (Fig. 1.13b-d, Table 1.5). Figure 1.13b shows a diopside grain consisting of a nanocrystalline aggregate of randomly oriented grains (~40-300 nm) with compositions ranging from diopside to augite (Table 1.5). Individual pyroxene compositions are presented in a quadrilateral pyroxene plot in Figure 1.14.

All pyroxenes have a composition ranging from diopside to augite, except one grain identified as clinoferrosilite (Table 1.5), and they show zonation and exsolution lamellae. Pyroxenes are Mn- and Cr-rich in roughly equal proportions and inversely correlated, ranging from 1.7 to 12.0 wt% Cr_2O_3, with an average of 4.5 wt% Cr_2O_3, and from 2.1 to 8.9 wt% MnO with an average of 4.4 wt% MnO (Table 1.5). The Mn and Cr contents vary highly between and within grains (Fig. 1.13d). Sodium is also detected in all pyroxenes, ranging from 0.6 to 5.8 wt% Na_2O, with an average of 2.2 Na_2O, obeying the coupled substitution $Ca^{2+} + Mg^{2+} = Na^{+} + Cr^{3+}$ (Table 1.5). Z-contrast dark-field STEM imaging of the Ca-rich pyroxenes shows that they exhibit twinning, and STEM-EDS analyses and X-ray compositional maps reveal that zonation is due to variations in the Ca, Cr, and Mn contents, ranging from $En_{67}Wo_{29}Fs_4$ to En_{54} $Wo_{42}Fs_4$ (Table 1.5). RGB elemental X-ray maps show that Ca and Mn are inversely correlated (Fig. 1.13c,d). In the quadrilateral pyroxene plot in Figure 1.14, we show that pyroxene compositions in this smooth rim are consistent with pyroxene microprobe compositions from the chondrule SIR (except for the clinoferrosilite, which is not sampled by EPMA).

The interface between the smooth rim and the matrix is extremely sharp at the nanometer scale (Fig. 1.13a,e). Figure 1.13b-d shows a dark-field STEM image of a region of the smooth rim (white dashed square in Fig. 1.13a) at the interface with the matrix, along with combined RGB X-ray elemental maps for Fe-Mg-Si and Si-Ca-P of this area. The map in (c) shows the presence of an elongated (300 nm long) Ca-sulfate grain at the interface with the matrix. The interface also contains a relatively large (~500 nm) Fe-Ni-Cu-Na-Zn-sulfide grain that exhibits zonation, ranging from Na-, S-, Zn-, Cu-rich sulfide in the core to Fe-Ni-metal at the rim (Fig. 1.13d,f). The adjacent matrix

exhibits significant textural and mineralogical complexity (Fig. 1.13e) that has not been reported previously in QUE 99177 (Abreu and Brearley, 2010; Le Guillou et al., 2015). It is dominated by a groundmass of amorphous silicates, organic matter, a few Mg-rich silicates (enstatite and/or forsterite grains, 100-500 nm in size, Fig. 1.13h), Ca phosphates (Fig. 1.13c,e), and nanosulfides (pyrrhotite and pentlandite; Fig. 1.13i); porosity being low. Differences with previous studies of matrix in QUE 99177 include a lower abundance of nanosulfides, a fairly uniform high P and Na abundance in STEM X-ray maps within the regions of amorphous silicates, and large (μm-sized), highly irregularly-shaped Ca phosphate regions intermixed with regions of the matrix, identified with STEM elemental X-ray maps (Fig. 1.13h). Calcium phosphates show a smooth appearance, interstitial to patches or regions of matrix relicts with rare nano-inclusions of sulfides (Fig. 1.13e), which are described and discussed in detail in Chapter 2.

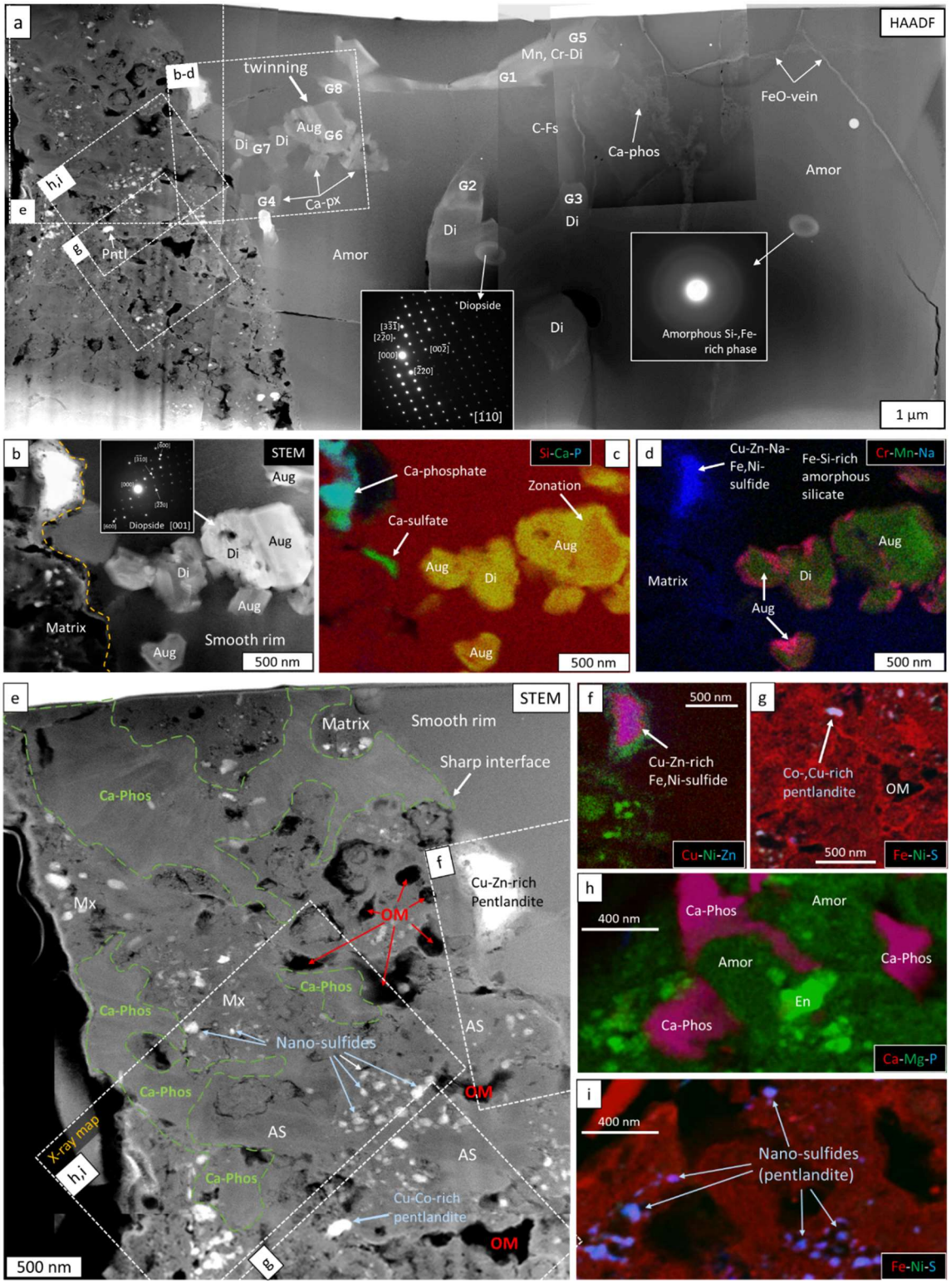

Figure 1.13. TEM images of FIB1 extracted in the smooth rim around chondrule 3 (Fig. 1.12a,b). a) Dark-field STEM mosaic of FIB1 showing the smooth rim and adjacent matrix. *(Caption continues on the following page).*

Figure 1.13. *(Caption continued from the previous page).* The smooth rim largely consists of an amorphous silicate phase that shows no diffraction contrast, characteristic of an amorphous material, with inset of a corresponding diffraction pattern. Crystalline Ca-, Mg-rich pyroxene, which are Cr- and Mn-rich, are embedded in the amorphous phase (inset of a diffraction pattern consistent with the [110] zone axis of diopside – EDS beam contamination mark is appreciated in the FIB section mosaic). b) DF STEM image of pyroxenes (augite and diopside) near the matrix with inset [001] zone axis diffraction pattern from diopside. c) Si-Ca-P map from (b) showing Ca variations in pyroxenes, Ca phosphate in the matrix, and Ca sulfate at the interface. d) Cr-Mn-Na map from (b) showing variations in the Cr and Mn content within pyroxene grains. Chromium is concentrated at the rims and Mn is inversely correlated with Ca. The sulfide grain at the interface contains Na in the core. e) Dark-field STEM mosaic of a region in the matrix adjacent to the smooth rim. The interface between the smooth rim and the matrix is extremely sharp. The matrix consists of amorphous silicates, pyroxenes, Ca phosphates (Ca-phos), organic matter (OM), nanosulfides, and Cu-, Co-rich sulfide grains. f) Cu-Ni-Zn map showing the enrichment of Cu and Zn in a sulfide grain and a zone of Ni-rich rim surrounding the core of the grain. g) Fe-Ni-S map of a region in the matrix marked in (e) showing a Co-Cu-rich pentlandite nanograin. h) Ca-Mg-P map of a region marked in (e) showing irregular regions of Ca phosphates in the matrix, some submicron-sized grains of enstatite (En), and regions of amorphous silicates (AS). i) Fe-Ni-S map of the same region as (h) showing nanosulfide grains heterogeneously distributed in the matrix.

Table 1.4. Individual STEM-EDS analyses (oxides wt%) of the amorphous Fe-rich silicate phase in the smooth rim around chondrule 3 (FIB1).

Oxides wt%	Sp1	Sp2	Sp3	Sp4	Sp5	Sp6	**Mean**	Vein +amor
SiO_2	50.44	50.52	49.76	49.41	52.06	51.65	**50.64**	27.86
P_2O_5	0.20	0.23	0.41	0.09	0.13	0.11	**0.20**	0.56
TiO_2	0.12	0.13	0.01	0.03	0.16	0.08	**0.09**	n.d.
Al_2O_3	3.76	3.61	3.03	3.62	2.64	3.23	**3.32**	1.85
Cr_2O_3	0.06	0.07	0.05	0.13	0.06	0.24	**0.10**	0.04
SO_3	0.52	0.31	0.36	0.51	0.44	0.54	**0.45**	3.56
FeO	33.96	33.42	36.13	35.65	30.81	32.64	**33.77**	56.56
MnO	0.42	0.52	0.37	0.61	0.49	0.59	**0.50**	0.61
MgO	8.03	8.75	7.35	7.52	8.74	9.22	**8.27**	3.18
CaO	0.31	0.31	0.51	0.28	0.20	0.44	**0.34**	0.73
Na_2O	1.71	1.75	1.83	1.96	4.05	1.06	**2.06**	2.35
K_2O	0.12	0.21	0.07	0.17	0.18	0.12	**0.15**	0.19
NiO	0.24	0.18	0.08	0.03	0.01	0.08	**0.10**	2.52
ZnO	0.12	n.d.	0.03	n.d.	0.04	n.d.	**0.03**	n.d.
Total	100	100	100	100	100	100	**100**	100

n.d. = not detected

Sp = spectrum#

Table 1.5. Individual STEM-EDS analyses of pyroxene grains (eight diopside-augite grains and one clinoferrosilite grain) embedded in the amorphous material of the smooth rim around chondrule 3 (FIB1). Grains numbered in Fig. 1.13a. n.d. = not detected

Oxides wt%	G1	G1	G1	G2	G3	G4	G5	G6	G6	G6	G7	G8	**Mean**	C-Fs
SiO_2	51.1	54.23	54.72	55.31	52.68	57.98	52.55	57.25	57.07	56.78	56.90	55.15	**55.14**	48.60
P_2O_5	0.05	n.d.	0.05	n.d.	n.d.	n.d.	0.07	0.28	0.22	0.11	0.24	n.d.	**0.08**	0.04
TiO_2	0.51	0.02	0.17	0.36	0.69	0.35	0.50	0.28	0.14	0.16	0.13	0.17	**0.29**	n.d.
Al_2O_3	4.81	2.17	2.31	3.50	5.94	0.33	5.09	0.30	0.51	0.78	0.53	1.13	**2.28**	3.59
Cr_2O_3	3.67	5.67	12.04	3.64	2.95	10.65	2.70	1.70	2.00	2.11	3.20	3.62	**4.50**	0.24
SO_3	0.21	n.d.	n.d.	n.d.	0.08	0.13	0.10	n.d.	n.d.	0.18	0.16	0.22	**0.09**	0.17
FeO	2.23	4.46	4.29	1.89	1.21	2.67	7.15	1.91	2.38	4.61	3.44	11.47	**3.98**	37.94
MnO	4.43	3.72	2.07	3.95	4.64	2.29	3.96	8.94	6.39	4.56	4.76	3.26	**4.42**	0.48
MgO	15.16	12.41	8.22	15.37	16.32	9.95	13.22	17.64	15.68	14.58	13.07	9.60	**13.44**	6.95
CaO	17.21	14.25	10.35	14.78	14.85	9.96	13.98	10.46	14.00	14.32	15.69	12.79	**13.55**	0.48
Na_2O	0.62	3.07	5.78	1.20	0.63	5.69	0.69	1.23	1.60	1.81	1.87	2.58	**2.23**	1.50
Total	100	100	100	100	100	100	100	100	100	100	100	100	**100**	100
En	53	49	46	57	59	53	48	67	58	53	50	38	**53**	24
Fs	4	10	13	4	2	8	15	4	5	9	7	26	**9**	75
Wo	43	41	41	39	39	38	37	29	37	37	43	36	**38**	1
formulae based on 6 oxygens														
Si	1.87	2.00	2.02	1.99	1.90	2.11	1.94	2.07	2.07	2.07	2.07	2.06	**2.02**	1.96
Ti	0.01	n.d.	n.d.	0.01	0.02	0.01	0.01	0.01	n.d.	n.d.	n.d.	n.d.	**0.01**	n.d.
Al	0.21	0.09	0.1	0.15	0.25	0.01	0.22	0.01	0.02	0.03	0.02	0.05	**0.10**	0.17
Cr	0.11	0.17	0.35	0.10	0.08	0.31	0.08	0.05	0.06	0.06	0.09	0.11	**0.13**	0.01
Fe	0.07	0.14	0.13	0.06	0.04	0.08	0.22	0.06	0.07	0.14	0.10	0.36	**0.12**	1.28
Mn	0.14	0.12	0.06	0.12	0.14	0.07	0.12	0.27	0.20	0.14	0.15	0.10	**0.14**	0.02
Mg	0.83	0.68	0.45	0.82	0.88	0.54	0.73	0.95	0.85	0.79	0.71	0.54	**0.73**	0.42
Ca	0.68	0.56	0.41	0.57	0.57	0.39	0.55	0.41	0.54	0.56	0.61	0.51	**0.53**	0.02
Na	0.04	0.22	0.41	0.08	0.04	0.40	0.05	0.09	0.11	0.13	0.13	0.19	**0.16**	0.12
Total cat.	3.97	3.98	3.96	3.92	3.93	3.92	3.93	3.92	3.93	3.93	3.91	3.93	**3.94**	4.00

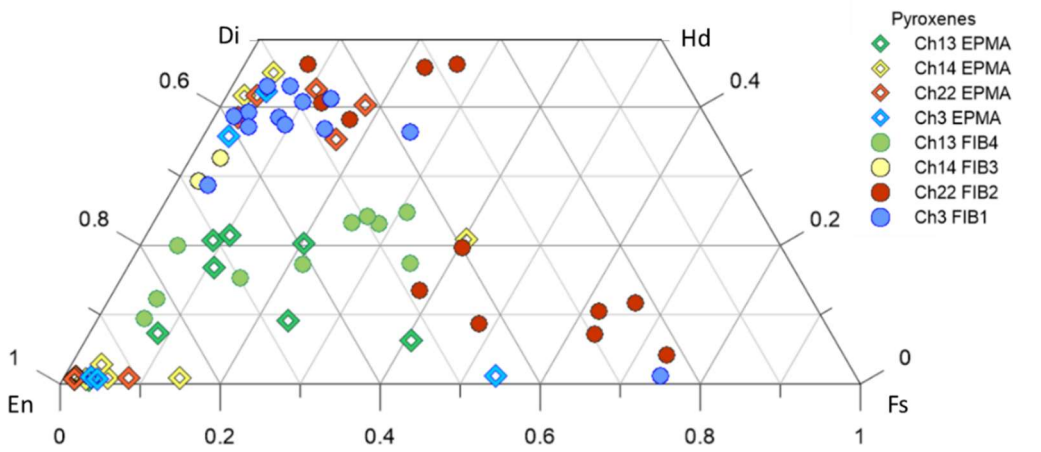

Figure. 1.14. Pyroxene En-Fs-Wo quadrilateral plot (mol%) showing the compositions of pyroxenes in the different FIB sections (smooth rims around chondrules 3 and 22 in QUE 99177,19, and 13 and 14 in QUE 99177,18), analyzed by STEM-EDS (Tables 1.5, 1.7, 1.8, and 1.10 – note that some grains contain more than one analysis), along with EPMA analyses of pyroxenes in SIRs of the same chondrules (individual analyses in Table A1.1 in Appendix 1). Each point represents an individual analysis. Scanning TEM-EDS data from pyroxenes embedded in the amorphous silicate of FIB1 (Ch3), FIB2 (Ch22), FIB3 (Ch14), and FIB4 (Ch13) are represented with blue, brown, yellow, and green dots, respectively. Probe analyses from pyroxenes in SIRs and interior of chondrules 3, 22, 14, and 13 are represented with blue, brown, yellow, and green hollow diamonds, respectively.

3.4.2. TEM study of the smooth rim around chondrule 22 (FIB2)

The second FIB section (FIB2) was extracted across the boundary between the smooth rim and the matrix around Chondrule 22, an irregularly-shaped, elongated (with long and short dimensions of ~200 µm x ~1 mm, respectively) type IAB, metal-rich, POP chondrule (Fig. 1.1b, 1.12c). Metal grains in the chondrule occur in a bimodal distribution of large (50-150 µm) and small (a few µm) sizes. Chondrule 22 has a SIR and is surrounded by a notable, irregular but continuous smooth rim that ranges from ~10 to ~45 µm in width. A HAADF STEM mosaic of the FIB section is shown in Figure 1.15a, revealing that the smooth rim is similar to FIB1 in overall appearance. An amorphous Fe- and Si-rich phase composes about 70% of the FIB section area, with a composition that is largely consistent with the amorphous silicate phase in FIB1. STEM-

EDS compositions for the amorphous silicate material in different areas of the FIB section are presented in Table 1.6. The average composition is slightly richer in Si and Fe (53.1 wt% SiO_2 and 37.3 wt% FeO), and slightly poorer in Mg, Al, Mn, and Ca compared to FIB1 (4.6 wt% MgO, 2.3 wt% Al_2O_3, 0.3 wt% MnO, and 0.1 wt% CaO). Unlike in FIB1, Na in the amorphous material is heterogeneously distributed and only detectable close to crystalline phases (Fig. 1.15a), ranging from 0 to 6.76 wt% Na_2O (Table 1.6). The higher Na values are not correlated with the Al content; therefore, we cannot rule out that the observed Na enrichment is caused by elemental mobilization from the interstitial phases (Fig. 1.15a) and/or the electron beam during the analyses, rather than inherent to the amorphous silicate phase. Dark-field STEM imaging shows that the amorphous silicate material preserves distinct previous crystal outlines throughout the FIB section with lath-shaped morphologies (indicated with green arrows in Fig. 1.15a). The interface between the smooth rim and the matrix is also extremely sharp (Fig. 1.15a).

Dark-field STEM imaging shows that different phases are present within the smooth rim. These phases form elongated arrays and are identified as pyroxenes, feldspar, and igneous glass, based on quantitative STEM-EDS analyses and electron diffraction patterns (Fig. 1.15e-h, Table 1.7). Pyroxenes in FIB2 are smaller (~20 nm to ~1 μm in size), exhibit euhedral to anhedral morphologies, and display a wider range of compositions compared to FIB1, from $En_{14}Wo_4Fs_{82}$ to $En_{23}Wo_{47}Fs_{30}$ (Table 1.7). Pyroxenes are grouped in a bimodal distribution of low-Ca pyroxenes, dominated by ferrosilite and pigeonite, and high-Ca pyroxenes, dominated by diopside-hedenbergite (Fig. 1.14). Individual Ca-rich pyroxenes show twinning and zonation in Ca, Fe, and Mg, which decrease from core to rim. In addition, Mn is strongly zoned, increasing from core

to rim, as illustrated in the EDS X-ray map shown in Figure 1.15d. In fact, all pyroxenes are extremely Mn-rich, ranging from 4.4 to 11.6 wt% MnO, with an average of 7.8 wt% MnO (Table 1.7), whereas Cr contents are low (average 0.3 wt% Cr_2O_3, Table 1.7).

Albitic feldspar and interstitial glass also occur in FIB2 (Fig. 1.15c,i), two phases that are not present in FIB1. Glass and feldspar analyses are tabulated in Table 1.7. Alkali loss from both phases is attributed to electron beam volatilization during analyses. Besides, albite undergoes rapid electron beam-induced amorphization, as shown in Figure 1.15i.2, but several SAEDs (inset in Fig. 1.15i.1) were acquired before amorphization occurred by minimizing the electron dose. Albite occurs interstitial to the regions of the amorphous silicate (dashed lines in Fig. 1.15i.1), in areas ranging from 100 nm up to 3 μm in size, as well as polysynthetically twinned, subhedral to euhedral grains about 0.5 μm in size (Figure 1.15c). Transmission electron microscopy shows that the interface between albite and the amorphous Fe-rich silicate phase is sharp on a nanoscale, with well-defined, curvilinear grain boundaries (Fig. 1.15i.1). Pyroxene and albite are present in roughly equal proportions and closely intergrown (Fig. 1.15c). The glass has a composition typical of a late-stage quenched, residual, igneous melt (~81 wt% SiO_2, 15 wt% Al_2O_3, 2 wt% FeO, 1 wt% Na_2O, and 0.6 wt% MgO; Table 1.7) and occurs interstitial to albite and pyroxene grains (indicated with yellow arrows in Fig. 1.15a,b), characterized by lack of diffraction or structure.

The matrix consists of highly abundant, homogeneously distributed amorphous silicates, which serve as a groundmass for organic matter (OM) nanoglobules, silicates such as ferromagnesian olivines (~200 nm), nanosulfides, and nanoparticles of Fe,Ni metal. Organic matter particles, up to ~1 μm in size, contain some Fe, S, and Si and

exhibit the typical globular textures (Fig. 1.15j) (e.g., De Gregorio et al., 2013). Based on DF and BF imaging, the porosity is very low, similar to observations on FIB1. Overall, the texture appears similar to matrices in the pristine CR chondrites MET 00426 (Le Guillou and Brearley, 2014), GRA 95229, MIL 07525, and EET 92161 (Vollmer et al., 2020).

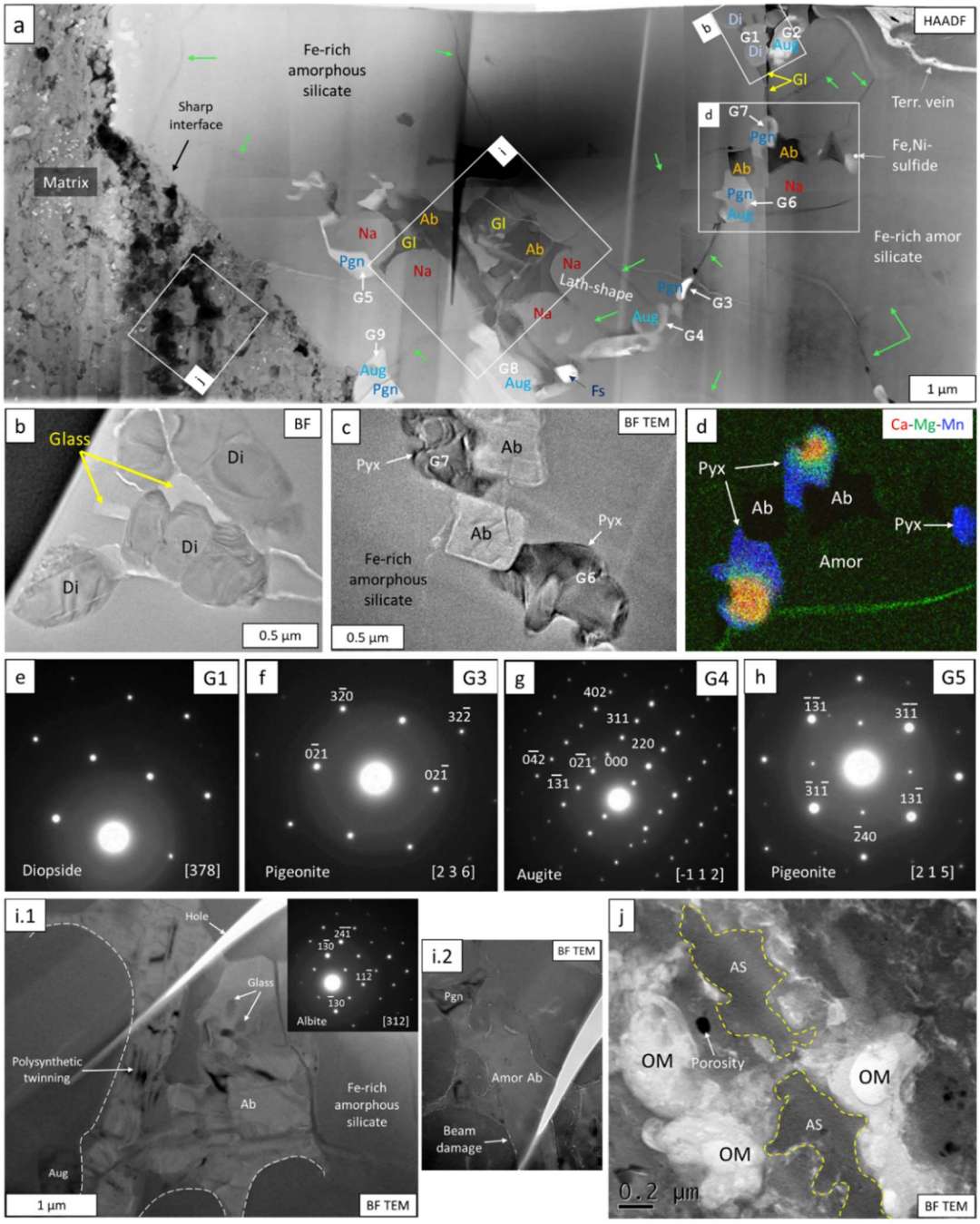

Figure 1.15. *(On previous page).* TEM images of FIB2 extracted in the smooth rim around chondrule 22 in QUE 99177,19. SEM images of the chondrule are shown in Fig. 1.12c-d. SEM and TEM images of the smooth rim around chondrule 22 (Ch22) in QUE 99177,19. a) HAADF STEM mosaic of FIB2 in the smooth in contact with matrix (on the left portion). The smooth rim is dominated by an amorphous Si- and Fe-rich phase. 'Na' in red indicates that the amorphous silicate contains Na. The crystals interstitial to the amorphous phase are pyroxenes with different compositions, albite, and glass. The amorphous material appears to preserve outlines of preexisting crystals, with lath-shaped morphologies (indicated with green arrows) that have undergone replacement. The interface between the smooth rim and the matrix is extremely sharp. b) Bright-field TEM image of euhedral to subhedral pyroxene grains with interstitial igneous glass. c) Bright-field TEM image of a region of the smooth rim showing two euhedral albite grains and two anhedral pyroxene grains that are intergrown, embedded in the amorphous silicate. d) Ca-Mg-Mn from a region in (a) showing the strong zonation of these elements in pyroxenes. e-h) SAED patterns of four pyroxene grains in the smooth rim (diopside, pigeonite, augite, and pigeonite). i) Bright-field TEM images of albite (same region in i.1 and i.2, before and after) showing polysynthetic twinning (i.1) and electron beam damage features (i.2). The outlines of albite crystals (shown by white, dashed curves) indicate that albite is interstitial to preexisting mineral phases. j) Bright-field TEM image of a region in the matrix showing globular organic matter particles embedded in an amorphous silicates (AS) groundmass and some nanoporosity. Legend: Amor = amorphous, AS = amorphous silicates in the matrix Px = pyroxene, Di = diopside, Aug = augite, Pgn = pigeonite, Ab = albite, Gl = glass, OM = organic matter.

Table 1.6. Individual STEM-EDS analyses (oxides wt%) of the amorphous Fe-rich silicate phase and glass in the smooth rim around chondrule 22 (FIB2).

Oxides wt%	Sp1	Sp2	Sp3	Sp4	Sp5	Sp6	Sp7	Sp8	**Mean**
SiO_2	54.76	51.12	50.32	52.56	52.52	52.71	55.16	55.75	**53.11**
TiO_2	0.01	n.d.	n.d.	n.d.	0.22	n.d.	n.d.	0.05	**0.04**
Al_2O_3	3.28	2.85	2.93	2.33	2.48	2.45	1.32	0.96	**2.33**
Cr_2O_3	n.d.	0.01	n.d.	0.30	n.d.	0.03	n.d.	0.05	**n.d.**
SO_3	0.15	0.63	0.35	0.49	0.30	0.22	0.12	0.23	**0.31**
FeO	34.22	37.23	33.22	40.20	40.40	37.78	37.84	37.68	**37.32**
MnO	0.44	0.14	0.43	0.38	n.d.	0.42	0.21	0.26	**0.29**
MgO	4.58	4.53	5.73	3.74	3.80	5.88	4.70	3.89	**4.61**
CaO	0.15	0.04	0.20	n.d.	0.17	0.04	0.06	0.07	**0.09**
Na_2O	2.41	3.42	6.76	n.d.	n.d.	0.30	0.59	1.03	**1.81**
K_2O	n.d.	0.02	0.06	n.d.	0.10	0.17	n.d.	0.03	**0.05**
Total	100	100	100	100	100	100	100	100	**100**

n.d. = not detected

Sp = spectrum#

Table 1.7. Individual STEM-EDS analyses (oxides wt%) of pyroxenes, feldspar, and glass in the smooth rim around Ch22 (FIB2). n.d. = not detected.

Oxides wt%	Px G1	G3	G4	G5	G6	G6	G7	G7	G8	G9	G9	Albite	Glass	Glass	Glass	Mean glass
SiO_2	54.49	52.84	55.45	52.66	56.06	57.30	58.00	59.83	54.46	55.68	51.63	70.94	81.46	80.96	79.86	80.76
P_2O_5	0.65	0.52	0.14	0.45	0.50	0.27	0.23	0.43	n.d.	0.26	n.d.	0.27	0.31	0.03	n.d.	0.11
TiO_2	0.27	n.d.	0.11	0.11	0.22	0.11	0.10	0.22	0.18	0.06	0.13	0.17	0.18	n.d.	n.d.	0.06
Al_2O_3	2.10	1.62	2.06	1.76	0.52	0.50	0.24	0.65	1.35	1.33	2.65	14.02	13.46	15.08	15.98	14.84
Cr_2O_3	1.89	n.d.	0.07	n.d.	0.10	0.12	0.02	0.10	0.62	0.77	n.d.	n.d.	n.d.	n.d.	n.d.	n.d.
SO_3	0.16	0.26	0.46	n.d.	0.09	0.10	0.02	0.01	n.d.	n.d.	0.54	0.50	0.09	0.08	n.d.	0.06
FeO	11.42	27.13	8.64	24.55	4.23	16.74	18.73	5.91	10.20	10.27	29.22	9.45	1.83	1.79	2.13	1.92
MnO	4.93	11.58	5.09	10.64	4.51	8.74	10.17	4.40	6.97	7.15	4.86	0.32	0.24	0.21	n.d.	0.15
MgO	6.62	4.55	12.61	6.07	13.66	9.29	9.48	12.62	6.99	7.99	7.69	1.46	0.54	0.58	0.68	0.60
CaO	15.53	1.21	14.99	3.22	19.11	6.39	2.66	15.14	18.39	16.15	2.57	0.22	0.01	0.15	0.26	0.14
Na_2O	1.92	n.d.	0.37	0.51	0.99	0.43	0.33	0.66	0.80	0.26	0.54	2.65	1.52	1.07	1.08	1.22
K_2O	0.02	n.d.	n.d.	0.03	0.01	0.02	0.01	0.02	0.04	0.08	0.17	n.d.	n.d.	0.05	n.d.	0.02
ZnO	n.d.	0.29	n.d.	0.10	n.d.	n.d.	n.d.	n.d.	0.02	n.d.	0.08	n.d.	0.35	n.d.	n.d.	0.12
Total	100	100	100	100	100	100	100	100	100	100	100	100	100	100	100	100
En	20	14	35	18	37	29	31	37	20	23	19	An 8				
Wo	46	4	41	10	52	20	9	45	52	47	7	Ab 92				
Fs	34	82	24	73	11	52	61	18	29	30	74	Or 0				
formulae based on 6 oxygens [6O]												*[8O]*				
Si	2.05	2.10	2.04	2.07	2.05	2.16	2.19	2.16	2.07	2.10	2.02	3.15				
P	0.02	0.02	n.d.	0.02	0.02	0.01	0.01	0.01	n.d.	0.01	n.d.	n.d.				
Ti	0.01	n.d.	n.d.	n.d.	0.01	n.d.	n.d.	0.01	0.01	n.d.	n.d.	0.01				
Al	0.09	0.08	0.09	0.08	0.02	0.02	0.01	0.03	0.06	0.06	0.12	0.73				
Cr	0.06	n.d.	n.d.	n.d.	n.d.	n.d.	n.d.	n.d.	0.02	0.02	n.d.	n.d.				
Fe	0.36	0.90	0.27	0.81	0.13	0.53	0.59	0.18	0.32	0.32	0.96	0.35				
Mn	0.16	0.39	0.16	0.35	0.14	0.28	0.33	0.13	0.22	0.23	0.16	0.01				
Mg	0.37	0.27	0.69	0.36	0.75	0.52	0.53	0.68	0.40	0.45	0.45	0.10				
Ca	0.63	0.05	0.59	0.14	0.75	0.26	0.11	0.58	0.75	0.65	0.11	0.01				
Na	0.14	n.d.	0.03	0.04	0.07	0.03	0.02	0.05	0.06	0.02	0.04	0.23				
Sum Cat	3.89	3.82	3.89	3.88	3.94	3.82	3.80	3.83	3.91	3.86	3.90	4.59				

3.4.3. TEM study of the smooth rim around chondrule 14 (FIB3)

The third FIB section (FIB3) was extracted in the smooth rim around chondrule 14 in QUE 99177,18 (Fig. 1.1a, 1.12e-g). Chondrule 14 is a composite, rounded, type IAB, POP, metal-rich chondrule, ~950 μm in its longest dimension (Fig. 1.12e,f). Metal grains form a mantle (~100 μm wide) rimming the outermost part of the composite chondrule. Chondrule 14 is penetrated by an extensive network of terrestrial Fe-oxyhydroxide weathering veins. The SIR is relatively thick (~50 μm) and exhibits abundant, rounded, lath-shaped, and randomly oriented silica grains, 15 – 20 μm in size, Cr-, Mn-, Ca- rich pyroxene, and Ca-rich glass that can contain nano-crystallites. Electron microprobe analyses of glass has very low totals (84.8 wt%, Table 1.1) and the mesostasis is enriched in Ca and Na (Table 1.1). The smooth rim is continuous around the SIR, varying in width from ~10 to ~25 μm, and some regions contain fine-scale Z-contrast heterogeneities (Fig. 1.7a). High-magnification BSE imaging shows evidence of crystal outlines at the micron-scale that appear to have been replaced pseudomorphically, with tiny (~10 microns) high-Ca pyroxene grains embedded in it, detected by SEM-EDS. Altered metallic grains are common at the periphery of the smooth rim, but the alteration is more likely attributed to terrestrial weathering. The adjacent matrix exhibits a more homogeneous texture compared to other areas of the matrix in the thin section. The FIB section was cut across the smooth rim to the interior of the SIR, including silica (Fig. 1.16c).

A HAADF STEM mosaic of the FIB section reveals the presence of a large, altered metal grain that was hidden below the surface of the FIB section, occupying about 35% of the FIB section area, as well as several terrestrial weathering veins a few

nanometers in width (Fig. 1.16a). The featureless amorphous material in FIB3 only represents about 20% of the FIB section area and its composition is presented in Table 1.8. It differs from other FIB sections in that it contains higher Fe (44.5 wt% FeO), slightly higher K (0.5 wt% K_2O), lower Mg (1.7 wt% MgO), and Na is below detection limits. The higher FeO content (up to 11 wt% more FeO) is attributed to terrestrial weathering. Silica (Table 1.8) occupies about 30% of the FIB section area and contains the characteristic wormy features resulting from ion beam redeposition during FIB preparation. The presence of artifacts from redeposition may indicate that elemental chemistry might be contaminated. Although a [581] zone axis SAED pattern from silica was obtained (Fig. 1.16b), the grain was rapidly amorphized by the electron beam and the obtained pattern was not sufficient to unambiguously identify the silica polymorph as tridymite or cristobalite, because both have a very similar structure. However, cristobalite has been identified in one smooth rim in A-881828 CR chondrite (Komatsu et al., 2019) using Raman spectroscopy, in Brearley and Jones (2016) by electron diffraction patterns, and in the ungrouped carbonaceous chondrite Y-82094 by Kimura et al. (2013) (technique not specified). Thus, it is more likely that silica in this FIB section also corresponds to cristobalite. The interface between the amorphous phase and silica is extremely sharp and curved, and there is no evidence of any intergrowth between the two phases.

Pyroxene has also been identified in this FIB section, although in a much smaller proportion compared to the other FIB sections. Pyroxene is present as a thin (~0,5 μm in width), elongated, anhedral array that crosscuts the FIB section. Pyroxene exhibits exsolution lamellae and porosity (20-100 nm pore size, Fig. 1.16c,d), and is extensively

affected by interconnected terrestrial weathering veins that surround and penetrate the grains. Clean analyses of the pyroxene were difficult to obtain due to the presence of the veins, but two analyses are shown in Table 1.8, which reveal that pyroxene is augitic (average composition $En_{66}Wo_{31}$) and contains Cr and Mn in roughly equal proportions (~3.0 wt% Cr_2O_3 and 2.5 wt% MnO). In addition, a single, anhedral chromite grain (1.8 x 0.6 µm in size) is found on an edge of the FIB section (Fig. 1.16a,e, Table 1.8).

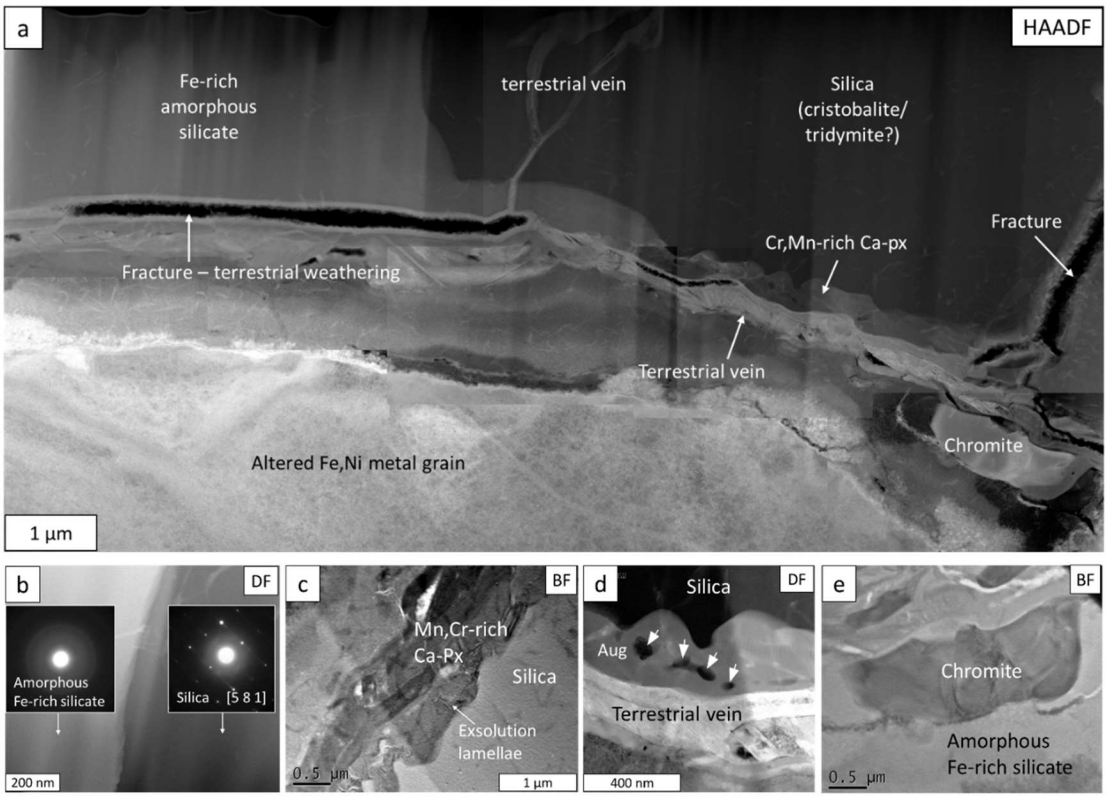

Figure 1.16. TEM images of FIB3 extracted in the smooth rim around chondrule 14 (Ch14) in QUE 99177,18. a) HAADF STEM mosaic of FIB3 showing that the interface between the smooth rim and silica is extremely sharp but curved. The FIB section contains a large, altered metal grain in the lower portion and several fractures. An elongate array of Ca-rich pyroxenes and a chromite grain are also identified along the boundary between the smooth rim and the terrestrial alteration products. b) Boundary between the amorphous silicate material and silica with their corresponding SAED patterns. c) Bright-field TEM image of the pyroxene linear array showing the irregular texture. Fine-grained exsolution lamellae in the pyroxene are also identified. Wormy-like features in silica are attributed to ion redeposition during FIB preparation. d) Dark-field STEM image of the pyroxene showing the presence of nanoporosity (white arrows) and interconnected terrestrial weathered veins. e) Bright-field TEM image of the chromite grain embedded in the amorphous Fe-rich silicate phase.

Table 1.8. Individual STEM- and TEM-EDS analyses (oxides wt%) of the phases that appear in the smooth rim around chondrule 14 (FIB3) in QUE 99177,18: amorphous Fe-rich silicate phase (Amor), pyroxene (Px), and chromite (Chr).

Oxides wt%	Sp1	Sp2	Sp3	Sp4	Sp5	Sp6	**Amor Mean**	Silica n=5		Px	Px	Chr
SiO_2	53.38	53.99	52.74	50.13	50.69	51.92	**52.14**	99.22	**SiO_2**	54.53	53.37	0.86
Al_2O_3	0.92	1.12	1.35	1.25	1.22	0.89	**1.13**	0.60	**Al_2O_3**	4.47	4.69	3.20
SO3	n.d.	n.d.	n.d.	0.19	0.15	n.d.	**0.06**	n.d.	**TiO_2**	1.30	1.47	0.47
FeO	43.53	42.86	43.10	46.27	45.86	45.21	**44.47**	0.17	**Cr_2O_3**	2.76	3.11	65.43
MgO	1.59	1.55	2.45	1.53	1.41	1.35	**1.65**	n.d.	**FeO**	1.42	2.01	13.91
CaO	n.d.	n.d.	n.d.	0.11	0.10	n.d.	**0.04**	n.d.	**MgO**	20.69	19.14	8.51
K_2O	0.58	0.48	0.37	0.52	0.57	0.63	**0.53**	n.d.	**CaO**	12.41	13.63	0.17
									MnO	2.43	2.58	7.44
Total	100	100	100	100	100	100	**100**	100		100	100	100
									En	68	64	
									Fs	3	4	
									Wo	29	33	

n.d. = not detected
Sp = spectrum#

3.4.4. TEM study of the smooth rim around chondrule 13 (FIB4)

FIB section 4 (FIB4) was extracted across the smooth rim around chondrule 13 (Fig 1.1b, 1.12h) to the matrix, targeting a region of the matrix that has a higher concentration of micron-sized sulfide grains at the interface with the smooth rim (Fig. 1.12i), detected by SEM-EDS. Chondrule 13 is a rounded, type IAB, POP chondrule, ~800 μm in its longest dimension, with large (~200 μm) and small (~10 - 20 μm) metallic grains homogeneously distributed. The chondrule has a SIR, ~70 μm in width, that contains a continuous layer of silica grains (Fig. 1.12h). The smooth rim locally exhibits a globular texture but is continuous around the chondrule, ranging from ~10 to 35 μm in width, and is closely associated with silica and/or glass from the SIR. The characteristic higher and lower electron albedo regions in BSE imaging (inset in Fig. 1.12i) are also distinguished in this smooth rim. The chondrule and the smooth rim are extensively

affected by terrestrial weathering veins, which crosscut and penetrate the chondrule, especially the outermost ~200 microns.

A HAADF STEM mosaic of the FIB section is presented in Figure 1.17a. The foil contains several curved, terrestrial weathering veins that crosscut one another at different orientations. In FIB4, the amorphous Fe-rich silicate material composes about 55% of the FIB section area. Like the other FIB sections, the amorphous phase consists of an Fe-rich silicate phase (49.1 wt% SiO_2, 36.3 wt% FeO), with some Mg (9.0 wt% MgO), Al (4.6 wt% Al_2O_3), and trace K (~0.25 wt% K_2O) (Table 1.9), but differs in that S is slightly higher (~1 wt% SO_3) and homogeneously distributed throughout the amorphous phase. The amorphous silicate material preserves previous curved crystal outlines (in green in Fig. 1.17a).

Pyroxenes are the only crystalline phase identified in this FIB section (outlined in yellow dashed lines in Fig. 1.17a), occupying 18% of the FIB section area. They occur as clusters of grains or isolated grains in random orientations embedded in the amorphous material, ranging from ~150 nm to ~3 μm in size. They exhibit rounded, anhedral to subhedral textures with common exsolution lamellae (Fig. 1.17a,b), an observation that is consistent with pyroxenes in other FIB sections. Pyroxene compositions are consistent with pigeonite, identified with SAED patterns and STEM-EDS (Figs. 1.14, 1.17d,e, Table 1.10). Iron and Mg contents in pyroxenes are highly variable, ranging from $En_{85}Wo_9Fs_6$ to $En_{44}Wo_{35}Fs_{31}$, while the Ca content roughly consistent, ranging from ~6 to 10 wt% CaO. All pyroxenes contain Cr and Mn (2.04 wt% Cr_2O_3 and 1.54 wt% MnO averages) and some grains contain Na (~1.1 wt% Na_2O), obeying the coupled substitution $Ca^{2+} + Mg^{2+} = Na^{+} + Cr^{3+}$, as well as trace Ti (0.35 wt% TiO_2).

The fine-grained matrix material composes the remaining 27% of the FIB section area and exhibits a rather different texture compared to matrix material in FIB1 and FIB2. However, its texture is generally consistent with matrix in QUE 99177 reported elsewhere (Brunner, 2012), with the exception that amorphous silicates are essentially lacking (Fig. 1.18a). The matrix also lacks porosity and contains a few terrestrial weathered veins, but they do not appear to have affected the material surrounding them. Scanning TEM dark-field imaging shows that the first ~500 nm width of matrix from the interface with the smooth rim is enriched in Fe and the interface with the smooth rim is partially fractured (Fig. 1.17a). Elemental STEM X-ray maps of the interface show that in this case, the matrix is enriched in Fe compared to the smooth rim (Fig. 1.17f-h). The matrix mainly consists of sulfides and crystalline ferromagnesian silicates. Sulfides (100-500 nm in size) are of two kinds: anhedral, subrounded pyrrhotite grains (in purple in Fig. 1.17h) and euhedral to subhedral pentlandite grains (in green in Fig. 1.17h). Crystalline ferromagnesian silicates are found as aggregates of grains that can show annealing (note the triple junctions in Fig. 1.18c) and are associated with pyrrhotite. They can be up to 2 μm in size (Fig. 1.18b,c) and are identified as low-Ca, Mg-rich pyroxene, with a mean composition of $En_{75}Wo_4Fs_{21}$, and Fe-rich olivine (Fa_{60}), identified with TEM-EDS. Individual and aggregated nanoglobules of organic grains are also distinguished (Fig. 1.18a) but are much less abundant and smaller in size (200-500 nm in size) than in the other FIB sections studied here.

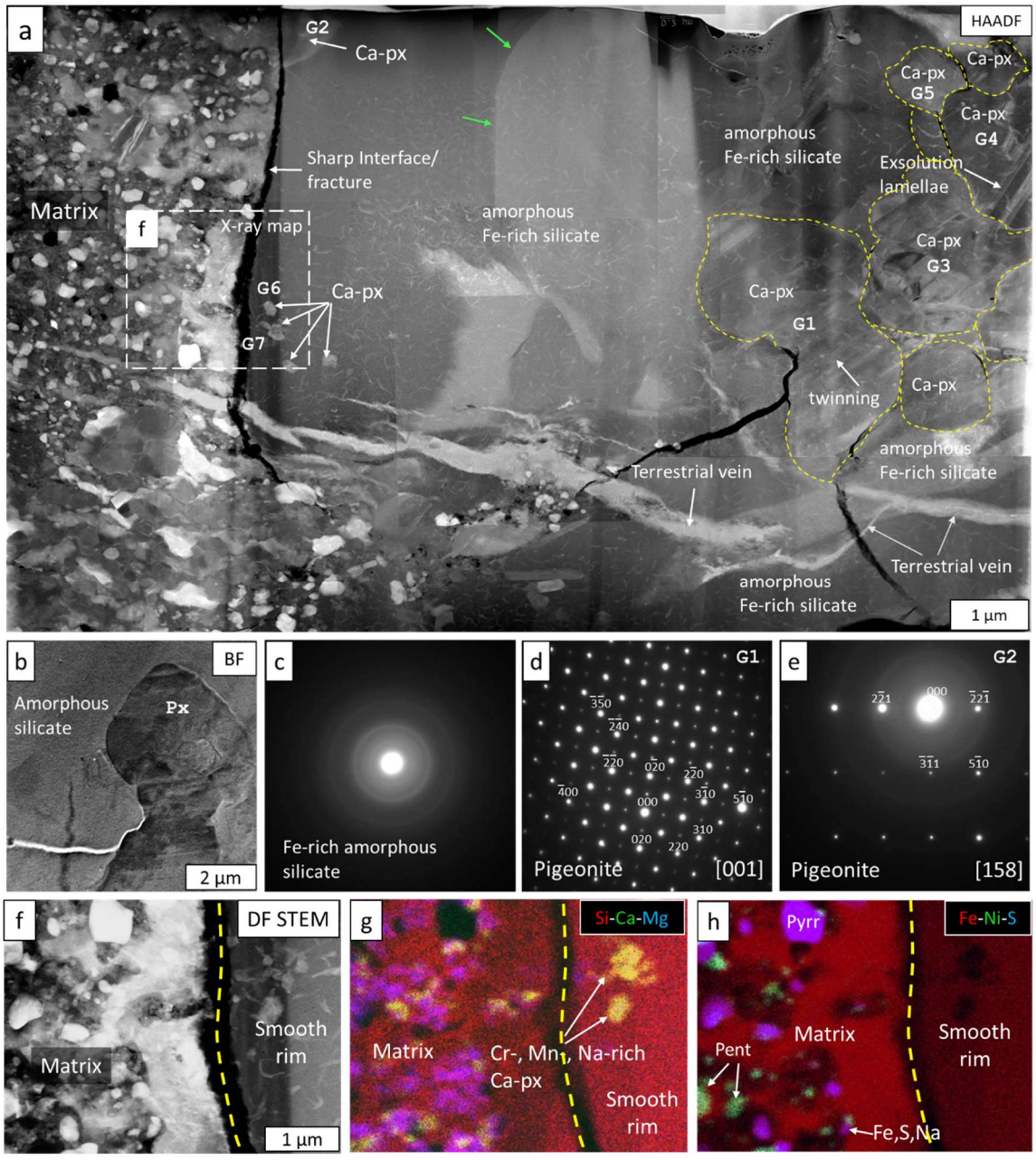

Figure 1.17. TEM images of FIB4 extracted in the smooth rim around chondrule 13 (Ch13) in QUE 99177,18 (Fig. 1.12h,i). a) Dark-field STEM mosaic of the extracted FIB section (FIB4) showing that the smooth rim consists of an amorphous Fe-rich silicate phase, Ca-rich pyroxenes (outlined in yellow dashed-lines), and terrestrial weathering veins. The FIB section contains abundant wormy features (~1 µm long), homogeneously distributed throughout the FIB section, which are re-deposited C-rich products caused by the ion beam during FIB preparation. In the matrix, the darker areas are low-Z phases such as organic matter, silicates (enstatite, olivine), and very fine-grained material, and the high-Z phases are sulfides (pyrrhotite and pentlandite). b) Bright-field TEM image of a pyroxene grain (G1) showing twinning. *(Caption continues on the following page).*

Figure 1.17. *(Caption continued from the previous page).* TEM images of the smooth rim around chondrule 13 (Ch13). c) SAED pattern of the amorphous material. d) and e) SAED patterns of two pyroxene grains (G1 and G2) obtained with the same FIB-orientation to show that pyroxenes are in different crystallographic orientations, the [001] and [158] zone axes, respectively. f) Dark-field STEM image along with elemental RGB X-ray maps (g) and (h) showing the interface between the smooth rim and the matrix. The matrix is enriched in Fe relative to the smooth rim, perhaps due to terrestrial weathering. g) Si-Ca-Mg map showing the enrichment of Si in the smooth rim compared to the matrix, the presence of Mg- and Ca-rich silicates in the matrix, and submicron-sized Ca-rich pyroxenes embedded in the smooth rim, which are also enriched in Cr, Mn, and Na. h) Fe-Ni-S map showing the enrichment of Fe in the matrix and the presence of nanophases pyrrhotites (in purple) and pentlandites (in green).

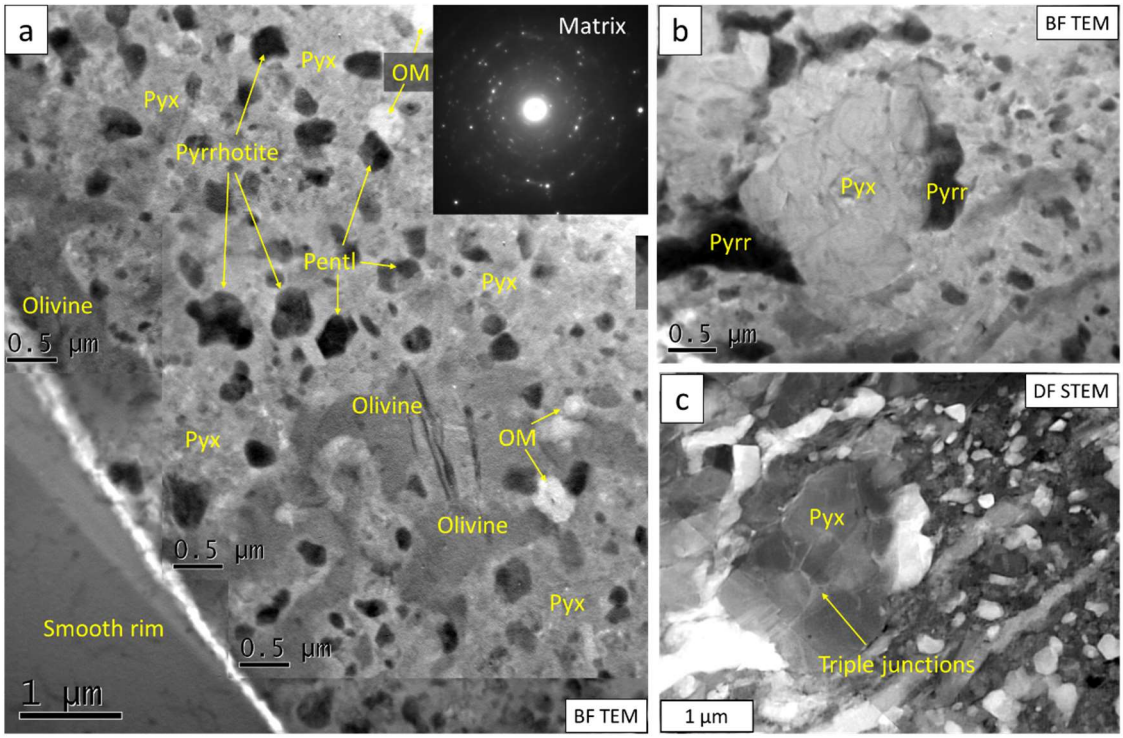

Figure 1.18. Bright-field TEM and dark-field STEM images of a matrix region in FIB4 showing examples of silicates and sulfides. a) Bright-field TEM mosaic of the examined region in the matrix showing that it mostly consists of nanosulfides (pyrrhotite and pentlandite) and aggregates of silicates (Mg-rich pyroxene and Fe-rich olivine). Only a few organic grains are distinguished. Inset (top right) is an electron diffraction pattern of this region, showing that crystalline nanograins are randomly oriented. b) Bright-field TEM image showing pyroxenes associated with troilite. c) Dark-field STEM image of (b) showing that pyroxene consists of an aggregate of crystals that show annealing (triple junctions).

Table 1.9. Individual STEM-EDS analyses (oxides wt%) of the amorphous Fe-rich silicate phase in the smooth rim around chondrule 13 in QUE 99177,18 (FIB4).

Oxides wt%	Sp1	Sp2	Sp3	Sp4	Sp5	Sp6	Sp7	Sp8	**Mean**
SiO_2	51.24	49.97	48.86	49.15	49.85	44.48	49.43	49.73	**49.09**
Al_2O_3	4.83	3.8	3.55	3.74	3.99	7.67	3.82	5.39	**4.60**
SO_3	0.97	0.92	1.05	0.97	0.79	0.99	0.87	1.28	**0.98**
FeO	27.67	37.95	39.17	39.25	37.88	38.49	38.9	31.05	**36.30**
MgO	15.29	7.09	7.14	6.69	7.49	8.37	6.98	12.54	**8.95**
K_2O	n.d.	0.27	0.22	0.2	n.d.	n.d.	n.d.	n.d.	**0.09**
Total	100	100	100	100	100	100	100	100	**100**

n.d.= not detected

Table 1.10. Individual TEM-EDS analyses (oxides wt%) of pyroxenes in the smooth rim around Ch13 (FIB4). G# = grain number (referred to Fig. 1.17a)

Oxides wt%	**G1**	**G2**	**G2**	**G3**	**G4**	**G4**	**G5**	**G6**	**G7**	**G7**	**Mean**
SiO_2	54.91	53.07	54.11	51.6	56.5	56.46	52.39	53.47	53.25	54.01	**53.98**
TiO_2	n.d.	0.49	n.d.	0.2	n.d.	n.d.	0.41	n.d.	0.31	n.d.	**0.14**
Al_2O_3	2.38	2.96	3.20	2.13	1.48	1.22	3.79	3.44	2.43	2.37	**2.54**
Cr_2O_3	2.04	2.54	1.99	1.68	1.69	1.81	1.15	1.94	2.67	2.84	**2.04**
SO_3	n.d.	n.d.	n.d.	0.87	n.d.	n.d.	n.d.	n.d.	0.52	n.d.	**0.14**
FeO	2.85	16.25	18.07	9.34	3.67	3.67	12.72	13.94	14.92	14.02	**10.95**
MnO	2.32	1.52	0.74	2.01	2.61	2.36	1.56	0.63	0.82	0.83	**1.54**
MgO	25.93	13.03	13.76	24.64	28.18	29.89	20.06	16.35	14.41	14.75	**20.10**
CaO	9.57	10.14	6.99	7.53	5.87	4.59	7.92	10.23	9.54	10.06	**8.24**
Na_2O	n.d.	n.d.	1.14	n.d.	n.d.	n.d.	n.d.	n.d.	1.10	1.12	**0.34**
Total	100	100	100	100	100	100	100	100	100	100	**100**
En	44	48	75	70	82	85	61	52	49	49	**61**
Wo	25	17	20	15	12	9	17	23	23	24	**19**
Fs	31	35	5	15	6	6	22	25	28	26	**20**
formulae based on 6 oxygens											
Si	1.99	2.02	1.94	1.87	1.98	1.97	1.92	1.97	1.98	2.00	**1.96**
Ti	0.01	n.d.	n.d.	0.01	n.d.	n.d.	0.01	n.d.	0.01	n.d.	**n.d.**
Al	0.13	0.14	0.10	0.09	0.06	0.05	0.16	0.15	0.11	0.10	**0.11**
Cr	0.08	0.06	0.06	0.05	0.05	0.05	0.03	0.06	0.08	0.08	**0.06**
Fe	0.51	0.56	0.08	0.28	0.11	0.11	0.39	0.43	0.46	0.43	**0.34**
Mn	0.05	0.02	0.07	0.06	0.08	0.07	0.05	0.02	0.03	0.03	**0.05**
Mg	0.73	0.76	1.37	1.33	1.47	1.56	1.10	0.90	0.80	0.81	**1.08**
Ca	0.41	0.28	0.36	0.29	0.22	0.17	0.31	0.40	0.38	0.40	**0.32**
Na	n.d.	0.08	n.d.	n.d.	n.d.	n.d.	n.d.	n.d.	0.08	0.08	**0.02**
Total cat.	3.90	3.93	3.98	4.01	3.97	3.98	3.97	3.93	3.93	3.94	**3.95**

n.d. = not detected

3.5. TEM study of a partially altered silica grain (FIB5)

An additional FIB section (FIB5) was cut in an elongated silica grain, 15 μm in size, in the SIR of chondrule 19 (Fig. 1.1b) in QUE 99177,19, an irregularly shaped, type IB, metal-rich, PP chondrule, 400 μm in size, that contains a high abundance of silica grains in the rim. The selected silica grain is partially altered by a phase with a higher electron albedo that was also targeted in the FIB. A dark-field STEM mosaic with inset diffraction patterns is shown in Figure 1.19. Silica has been identified as cristobalite, based on electron diffraction patterns and TEM-EDS analyses (Table 1.11, phase #3). The alteration product is an amorphous Fe-rich silicate phase that consists of two distinct Z-contrast layers, designated phase #1 and phase #2 (Table 1.11). Phase #2 is slightly Fe-richer, MgO-poorer, and contains Ca (0.45 CaO), alkalis (0.31 Na_2O and 0.39 K_2O), and P (0.24 P_2O_5) relative to phase #1 (Table 1.11). The mean compositions of these phases have essentially the same composition as the amorphous silicate material in the smooth rims (Tables 1.4, 1.6, 1.8, and 1.9). Several terrestrial weathering veins crosscut the silica, but higher-magnification images (inset in Fig. 1.19) show that alteration veins do not visibly affect the material adjacent to the veins.

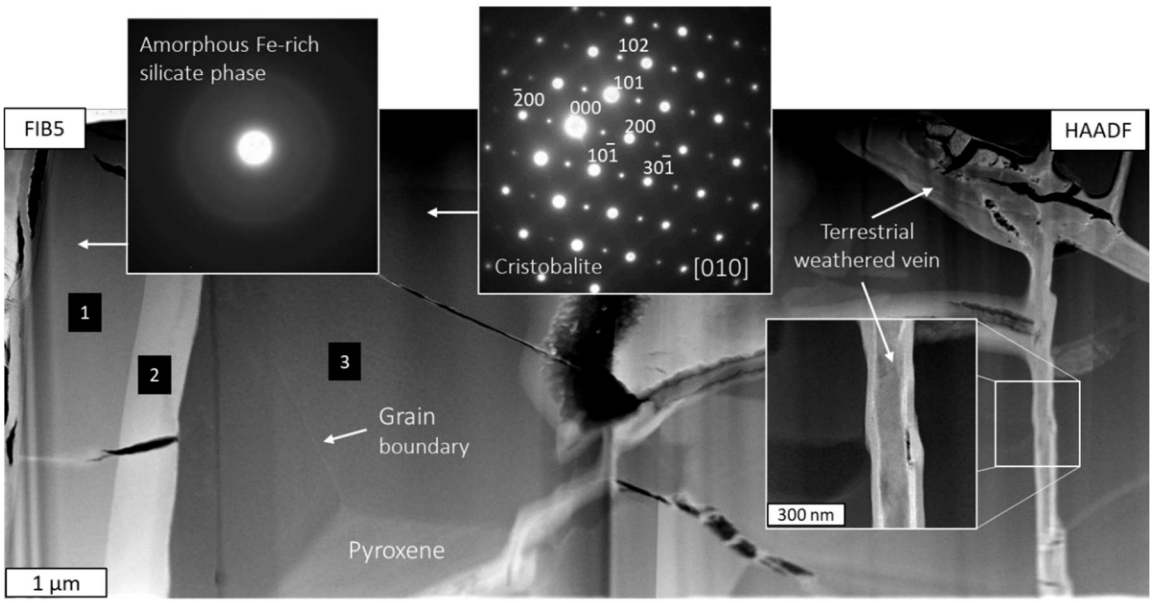

Figure 1.19. HAADF STEM mosaic of a FIB section (FIB5) extracted from a partially altered silica grain in the SIR of Chondrule 9 (QUE 99177,19) that has undergone pseudomorphic replacement. Insets show electron diffraction patterns of silica, identified as cristobalite with [010] zone axis, and the pseudomorphic replacement phase, seen as amorphous. Additional inset of a terrestrial weathering vein shows that margins are sharp, and that the alteration does not affect the silica. Grain boundaries in silica are also distinguished, and pyroxene is identified at the lower-center part of the FIB section. Phase numbers (1, 2, and 3) referred to Table 1.11.

Table 1.11. Individual STEM-EDS analyses (oxides wt%) of the amorphous Fe-rich silicate (phases #1 and #2) and silica (phase #3) extracted in FIB5, the partially altered silica grain in the SIR of chondrule 9 in QUE 99177,19.

Oxides wt%	phase #1					**Mean**	Phase #2						**Mean**	Phase #3			**Mean**
SiO_2	52.41	49.83	51.17	53.97	49.49	**51.38**	53.27	51.52	49.71	54.40	54.33	56.15	**53.23**	98.02	98.95	99.39	**98.79**
P_2O_5	n.d.	n.d.	n.d.	0.09	0.21	**0.06**	0.39	n.d.	1.00	n.d.	0.06	n.d.	**0.24**	n.d.	n.d.	n.d.	**n.d.**
TiO_2	n.d.	n.d.	0.25	0.11	0.26	**0.12**	n.d.	n.d.	n.d.	n.d.	0.11	0.91	**0.17**	0.23	n.d.	n.d.	**0.08**
Al_2O_3	0.12	1.27	1.64	0.73	n.d.	**0.75**	0.51	n.d.	n.d.	0.01	1.95	0.84	**0.55**	0.90	0.42	0.14	**0.49**
Cr_2O_3	0.23	0.09	0.37	0.19	0.82	**0.34**	0.29	0.15	0.91	0.35	0.05	0.78	**0.42**	0.12	0.05	0.10	**0.09**
SO_3	1.03	0.60	0.55	n.d.	0.73	**0.58**	0.31	0.18	1.04	0.93	n.d.	1.08	**0.59**	0.13	n.d.	0.11	**0.08**
FeO	34.72	37.59	36.08	33.06	45.84	**37.46**	42.32	44.78	44.87	41.96	40.79	35.78	**41.75**	n.d.	n.d.	n.d.	**n.d.**
MnO	n.d.	n.d.	n.d.	0.02	n.d.	**n.d.**	n.d.	n.d.	n.d.	n.d.	n.d.	n.d.	**n.d.**	n.d.	0.05	n.d.	**0.02**
MgO	11.26	10.47	9.92	11.72	1.96	**9.06**	1.89	1.85	1.30	1.86	1.30	3.15	**1.89**	0.28	0.41	0.09	**0.26**
CaO	0.18	n.d.	0.02	n.d.	0.20	**0.08**	0.45	n.d.	0.66	n.d.	1.13	0.43	**0.45**	n.d.	n.d.	0.06	**0.02**
Na_2O	n.d.	n.d.	n.d.	n.d.	0.46	**0.09**	0.57	0.94	n.d.	0.21	0.14	n.d.	**0.31**	0.32	n.d.	n.d.	**0.11**
K_2O	0.05	0.15	n.d.	0.11	0.02	**0.07**	n.d.	0.57	0.50	0.28	0.13	0.88	**0.39**	n.d.	0.12	0.11	**0.08**
Total	100	100	100	100	100	**100**	100	100	100	100	100	100	**100**	100	100	100	**100**

n.d = not detected

4. Discussion

The least-altered CR carbonaceous chondrites contain important information about the earliest interactions between primordial water and the solid materials that formed by condensation or melting in the solar nebula. Understanding the first stages of aqueous alteration in chondrites is important for unraveling several fundamental questions, such as how many different water reservoirs existed in the solar nebula, how many alteration events took place between primordial water and solid nebular materials, the effects that the alteration events had on primary phases, and the elemental mass transport that resulted from such fluid-rock interactions, among others, which influenced the overall petrological evolution of small asteroidal bodies. However, understanding the earliest stages of aqueous alteration is extremely challenging, because fine-grained matrix materials are very reactive and hence, they may have been modified significantly during these early stages of alteration (e.g., Bunch and Chang, 1980; Zolensky et al., 1993). In addition, the earliest stages of aqueous alteration are rarely preserved in carbonaceous chondrites, with the exception of a few CR chondrites, such as QUE 99177.

None of the previous studies on smooth rims has attempted to understand the origin and formation mechanisms of smooth rims in detail. Because the presence of smooth rims is thus far limited to the least-altered CR chondrites, characterizing them is essential for a complete understanding of the earliest stages of aqueous alteration. In the following discussion, we expose the evidence that demonstrates that smooth rims are dominated by a hydrated Fe-rich silicate gel that resulted from the interaction between fluids circulating through the fine-grained matrix and cristobalite in Silica-rich Igneous Rims (SIRs) on chondrules (section 4.1). Then, we discuss the conditions of the fluid

required to form smooth rims given the extremely high susceptibility of cristobalite to aqueous alteration (section 4.2). Finally, we assess the overall elemental exchange between chondrules and matrix, evaluating the importance of smooth rims for understanding and interpreting the earliest stages of aqueous alteration in the CR parent body (section 4.3).

4.1. Relationship between smooth rims and silica-rich igneous rims (SIRs)

Smooth rims have been largely overlooked in previous studies of CR chondrites with low degrees of alteration due to their smaller scales (from a few microns up to ~50 μm width, with an average of ~20 μm width) compared to fine- and coarse-grained rims, which are seen at the millimeter scale. However, our detailed examination of QUE 99177 using higher-magnification BSE and elemental RGB X-ray maps (e.g., Fig. 1.6b, 1.7) indicates that smooth rims are the most common type of rims in QUE 99177 and smooth rims only occur around chondrules with SIRs, consistent with previous observations by Jones et al. (2015) in EET 92042 CR chondrite. Krot et al. (2004) considered the following possibilities on the formation of SIRs: (i) the chondrule core, the pyroxene-rich rim (PIR) and the SIR crystallized as independent, near-equilibrium quasi-closed systems by progressive addition of material with higher SiO_2, MnO, and Na_2O and lower Al_2O_3, CaO, and TiO_2 than the starting material; (ii) SIRs crystallized on surfaces of solidified or partially solidified chondrules by addition of silica-normative materials followed by subsequent melting and/or direct condensation of $SiO_{(gas)}$ into the chondrule melt; (iii) SIRs formed from a highly fractionated nebular gas (Si/Mg > 1), and (iv) CR chondrules (with PIRs and SIRs) are best explained by a model of condensation with partial

isolation, in which preferential isolation of olivine into chondrules increased volatile lithophile elements (Mn, Na, and K) in late condensates.

In the present study, we have made the following series of observations that evaluate the origin of smooth rims and constrain their precursor materials: (1) smooth rims only occur around chondrules that contain SIRs; (2) smooth rims are associated with silica from the SIR; (3) silica in the SIR is commonly replaced by a pseudomorphic phase; (4) when altered and unaltered silica grains coexist in the same SIR, altered grains are only present at the outermost parts of the SIR (closer to the matrix or smooth rim); (5) the amorphous silicate phase in smooth rims is hydrated, (6) smooth rims are enriched in the moderately volatile elements Mn, Cr, Na, and K, and depleted in S and Ni; (7) smooth rims contain igneous phases (pyroxene, albite, glass, and/or chromite); (8) the amorphous Fe-rich silicate gel in smooth rims preserves outlines of precursor crystalline phases, and (9) the amorphous Fe-rich silicate phase has a composition that matches pseudomorphic replacements of cristobalite in SIRs (and phyllosilicates that resulted from silica dissolution in literature). All these lines of evidence support a strong genetic relationship of smooth rims with SIRs. They are discussed in more detail below to conclude that smooth rims are the product of the earliest stages of aqueous alteration of SIRs, specifically, the pseudomorphic replacement of cristobalite by an amorphous, hydrated silicate gel.

4.1.1. Comparison of smooth rims compositional data from this study and the literature

Smooth rims have been recently documented in QUE 99177, MET 00426, and LAP 02342 by Harju et al. (2014), in EET 92042 by Jones et al. (2015), and in LAP

02342 by Abreu (2016), suggesting that they consist of phyllosilicates (or a possible gel-like phase, Jones et al., 2015), products of aqueous alteration. However, the detailed petrography, possible formation mechanisms, relationship to aqueous alteration, and the potential precursor materials of smooth rims were not studied in detail in any of these studies.

Our results obtained by EPMA in six smooth rims (Tables 1.2a, A1.7-A1.12 in Appendix 1) show that they contain mainly Si and Fe in roughly equal proportions, and that the Cr, Mn, Mg, and Ca contents vary greatly (large standard deviations) from smooth rim to smooth rim, and even within a particular smooth rim. As noted in Table 1.2, smooth rims have very low analytical totals (83.21 wt% average), which are even lower than the totals of their adjacent matrix materials (87.29 wt% average), indicative of an extensive hydration. Smooth rim compositions reported here are in agreement with compositional data reported by Harju et al. (2014), who reported EPMA compositions for smooth rims ("phyllosilicates") in QUE 99177 (shown in Table 1.2a), MET 00426, and LAP 02342, the three least altered CR chondrites that exist in our collections. The data were presented in two separated BSE contrast categories: the BSE-light areas and the BSE-dark areas. Our EPMA results, correlated with TEM observations, show that the 'BSE-dark material', which exhibits higher totals, contains higher abundance of igneous silicates embedded in the amorphous gel (higher MgO, Cr_2O_3, and CaO mostly from pyroxenes), whereas the 'BSE-light material', which exhibits lower totals, solely corresponds to the hydrated amorphous gel. Our compositional data for smooth rims are also remarkably similar to Krot et al. (2004) data for Fe-rich phyllosilicates replacing silica in chondrule SIRs (including the low totals) in the CR chondrites El Djouf, PCA

91082, and GRA 95229, although the authors did not describe these occurrences as smooth rims. Therefore, chemical compositions are not a clear diagnosis for distinguishing between phyllosilicates and smooth rims, because a mixture of an amorphous FeO-rich silicate gel, pyroxenes, felspar, glass, and/or chromite, results in a very similar (or identical) composition to phyllosilicates. In addition, the data from Harju et al. (2014) and Krot et al. (2004), with only three and four analyses in GRA 95229 and PCA 91082, respectively, were made on a limited number of samples and are not representative of these alteration phases, given the observed compositional heterogeneity of these rims.

4.1.2. Smooth rims are dominated by an amorphous Fe-rich silicate gel

The most relevant observation presented here is that all the studied FIB sections reveal that the major alteration phase that constitutes smooth rims is an amorphous Fe-rich silicate material that is hydrated. Evidence for hydration is supported by the low EPMA totals plus the lack of porosity or organic grains at the micron to submicron scales that could otherwise explain the low compositional totals. Additional evidence for alteration includes the presence of Ca phosphates in and nearby smooth rims in FIB1 (described in Chapter 2) that indicates that aqueous alteration took place (Fig. 1.13), and the more homogenized texture of some regions of the matrix close to smooth rims, which may also be indicative of aqueous alteration (e.g., Fig. 1.12d). None of the studied FIB sections has evidence of phyllosilicates. The amorphous silicate gel has a normalized TEM-EDS composition of about 50 wt% SiO_2 and 37 wt% FeO, being the remaining 8.4 wt% minor Mg and Al, and 2 wt% trace elements (Na, S, K, Mn, P, Ca, Cr, Ti, Ni, in decreasing order). For comparison purposes (EPMA and S/TEM-EDS), we have

calculated the normalized probe data in smooth rims (Table 1.2a), which gives a composition of 44.4 wt% SiO_2, 44.9 wt% FeO, 8.3 wt% the sum of the minor elements Mg, Al, and Ca, and 2.3 wt% the sum of trace elements (Mn, Ni, S, Na, Cr, K, P, and Ti, in decreasing order). Hence, the main difference between normalized electron microprobe analyses in smooth rims and S/TEM-EDS data in the amorphous silicate gel mainly recalls in the Ca content, which is in minor abundance by EPMA analyses (normalized average of 1.37 wt% CaO), and only trace (normalized average of 0.1 wt% CaO) by S/TEM-EDS analyses. Sodium also shows significant differences, being higher in the amorphous silicate by S/TEM (0.90 wt% Na_2O average) than in the normalized EPMA analyses of smooth rims (0.31 wt% Na_2O average). Such compositional differences are attributed to the fact that smooth rims contain igneous phases embedded in the amorphous gel, discussed below.

4.1.3. Presence of igneous phases in smooth rims

The compositional differences between normalized electron microprobe data in smooth rims and S/TEM-EDS data in the amorphous silicate material mentioned above are expected, because electron microprobe data include the amorphous silicate plus crystalline phases and glass within the excitation volume of the electron beam, whereas TEM data only reflect the (normalized) amorphous silicate gel composition. Indeed, our observations from multiple FIB sections of smooth rims show that they contain unaltered crystalline silicates (pyroxene, feldspar, and chromite) and tiny portions of interstitial glass, and that these phases are in a relatively similar abundance in each FIB section, occupying about 15 - 25% of a given smooth rim area. Their sizes are also similar in each

FIB section, ranging from submicron to ~3 μm in size. These phases are too small to be characterized by SEM and hence, this is the first study that has observed them.

Among the igneous material, pyroxene is the only phase that is ubiquitous in all the FIB sections, sharing many similarities in composition and texture. The strong Ca-rich nature of pyroxenes (Tables 1.5, 1.7, 1.8, and 1.10) gives the observed Ca-enrichment of smooth rims by EPMA mentioned above (Table 1.2a). Pyroxenes also have an enrichment in moderately volatile elements (up to 12 wt% Cr_2O_3, 12.6 wt% MnO, and 5.77 wt% Na_2O) that is unusual. They have typical characteristics of pyroxene compositions reported by Krot et al. (2004), although our data extend to significantly higher Mn-, Cr-, and Na-rich compositions, presumably due to their very small sizes combined with the fact that they are compositionally zoned (Fig. 1.13d). Thus, microprobe analyses, with a higher excitation volume than the sizes of pyroxenes, are not able to sample their entire range of compositions. Such enrichment in moderately volatile elements is discussed by Krot et al. (2004), who suggested that it was inherited from a fractionated nebular gas enriched in Si, Mn, Cr, Na, and K relative to Mg. Therefore, pyroxenes in smooth rims are primary (igneous) in origin and reflect the moderately volatile elements of the SIRs.

The relationship between pyroxenes in smooth rims and pyroxenes in SIRs is shown in Figure 1.14, where the dataset of pyroxenes embedded in the amorphous silicate material of smooth rims obtained by TEM-EDS correlates with compositions of pyroxenes in SIRs from the same chondrules, obtained by EPMA. The relationship appears more pronounced in FIB4 (green symbols in Fig. 1.14) and in the Ca-, Mg-rich subgroup in FIB2 (brown symbols in Fig. 1.14), although pyroxenes in FIB1 and FIB3

also show this relationship. Therefore, although some scatter occurs, pyroxenes in each FIB section are clustered in a particular composition, except for pyroxenes in FIB2, which show two different trends. Figure 1.14 illustrates that some of the pyroxene compositions in SIRs are not reflected by EPMA analyses (especially the Fe-rich group). This is due to the larger spatial resolution of electron microprobe analyses in smooth rims compared to the sizes of pyroxenes.

To link the presence of Ca, Mg, and Mn detected by EPMA to pyroxenes within smooth rims, Figure 1.20a plots normalized Ca-Mg-Mn (wt% element) data obtained by EPMA of four different smooth rims, along with individual STEM-EDS analyses of pyroxenes in FIB2, because pyroxenes in FIB2 show the greatest compositional variations. In addition, Figure 1.20b shows the normalized CaO versus MnO values extracted from the ternary plot in Figure 1.20a to show that pyroxene analyses span from diopside-augitic (orange line) to pigeonitic (blue line) compositions, and that analyses in between the two groups likely represent core-to-rim gradations (zoning) of individual grains. This is expected because, as mentioned above, the spatial resolution of the microprobe analyses in smooth rims can be bigger than the size of the pyroxene grains (and their zonation). The plot demonstrates that the compositional trends for Mn in the smooth rims obtained by EPMA are directly linked to the occurrence of these elements in pyroxenes (Fig. 1.20a) within the excitation volume of EPMA.

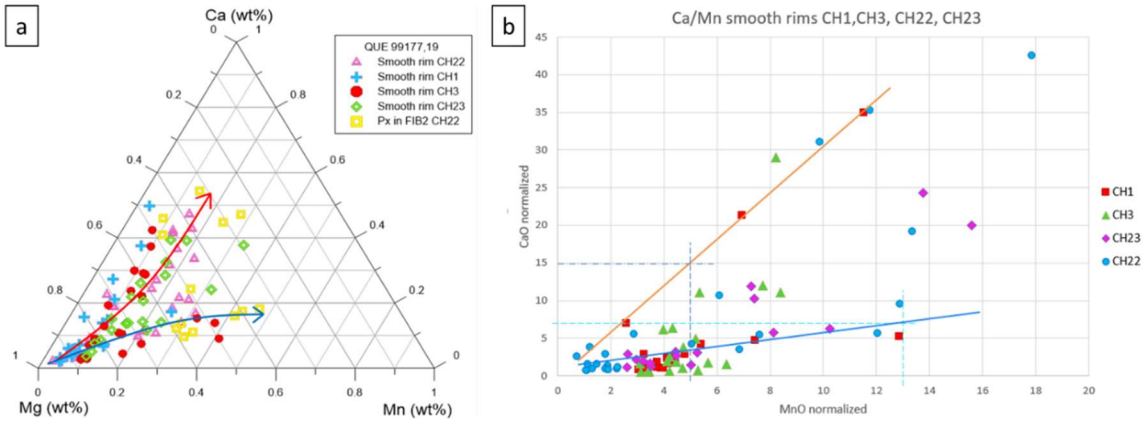

Figure 1.20. Normalized Ca-Mg-Mn content (element wt%) in smooth rims around four chondrules (Ch1, Ch3, Ch22, and Ch23) obtained by EPMA along with STEM-EDS analyses of pyroxenes embedded in the smooth rim of Ch22. Plot (a) shows that the Ca-Mg-Mn variability in smooth rims by EPMA is attributed to crystalline pyroxenes embedded in the amorphous silicate gel. Two trends are apparent on the ternary plot, resulting from fine-grained pyroxenes within the smooth rims, thus, they represent two different compositions (red and blue arrows). One trend (red arrow) represents the Mn-rich diopside/augite trend, and the second trend (blue arrow) is the result of Mn-rich pigeonite. b) Normalized CaO-MnO plot extracted from the triangular plot in (a) again showing the two trends (orange line corresponds to diopside/augite group, and blue line corresponds to pigeonite group). Values in the middle likely represent EPMA analyses that sample both pyroxenes, possibly as a result of the very fine-scale gradations from augitic to pigeonitic observed in many grains by TEM.

Finally, Figure 1.21 illustrates a pyroxene quadrilateral plot (mol%) comparing EPMA pyroxene compositions in SIRs around five chondrules that also contain smooth rims from this work (blue crosses; Table A1.1 in Appendix 1), individual pyroxene STEM-EDS analyses in smooth rims from this work (green diamonds; Tables 1.5, 1.7, 1.8, 1.10), and pyroxene compositions in SIRs from CR chondrites by Krot et al. (2004) (red circles). Pyroxene compositions in smooth rims are consistent with pyroxene compositions in SIRs from this work and in SIRs from Krot et al. (2004) work, with the exception of the FeO-rich pyroxenes, which are not sampled by Krot et al. (2004). This might be due to the much coarser grains studied by Krot et al. (2004). In addition, although Krot et al. (2004) found that high Mn and Cr contents only occur in high-Ca

pyroxenes in the SIRs (latest condensates), this study shows that elevated concentration of these elements can also be present in low-Ca (pigeonitic) pyroxenes (Table 1.7).

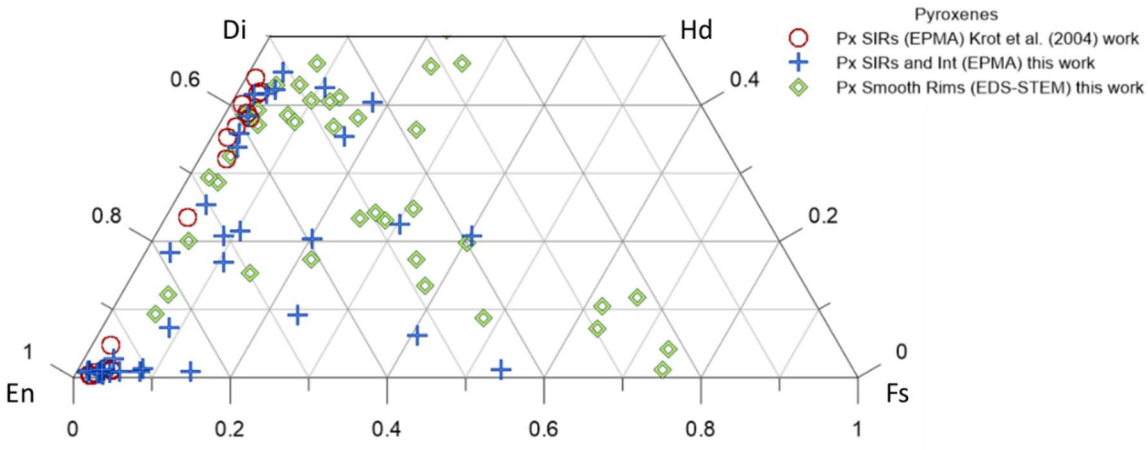

Figure 1.21. Pyroxene En-Fs-Wo quadrilateral plot (mol%) comparing pyroxene compositions in SIRs between this work and Krot et al. (2004). Low-Ca and high-Ca pyroxene compositions in SIRs obtained by EPMA from Krot et al. (2004) are represented by red circles. Pyroxene compositions obtained by EPMA (this work) from seven chondrule SIRs that contain smooth rims (Ch1, Ch3, Ch8, Ch22, Ch23, Ch13, and Ch14) are represented by blue crosses. Pyroxene compositions obtained by STEM-EDS analyses from four smooth rims (around Ch3, Ch22, 13, and 14) from this work are represented by hollow green diamonds.

The overall variations in pyroxene compositions between different rims are explained by a combination of variations in composition of the precursor materials for different SIRs and variations in composition of the different trapped melt pockets that crystallized at different times, as a result of distinct heating and cooling histories. Krot et al. (2004) observed that the Ca content varies as a function of the distance from the rim, with low-Ca pyroxenes closer to the chondrule host boundary and high-Ca pyroxenes closer to the matrix. However, this study shows a more complex relationship, because the small pyroxene grains in the smooth rims contain core-to-rim Ca variations. Such Ca variations (zonation) reflect and support a primary, igneous crystallization under conditions of disequilibrium at high temperature (Lindsley, 1983) in the solar nebula.

An igneous origin is also supported by the interstitial texture of albite in FIB2 (Fig. 1.15), in which the curved interfaces suggest it consists of a mesostasis region that crystallized in the interstitial spaces between previously crystallized grains, and by the survival of interstitial mesostasis glass, which is also detected in FIB2, between pyroxene and albite crystals (Fig. 1.15b, i.1, Table 1.7). The fact that pyroxenes, feldspar, and interstitial glass are unaltered is a further indicator that these phases are primary and that they survived the alteration process that formed smooth rims.

4.1.4. The precursor of the amorphous phase is cristobalite in SIRs

We have observed previous crystal outlines (green arrows in Figs. 1.15a and 1.17a) by Z-contrast dark-field STEM imaging in the amorphous silicate phase that are indicative of pseudomorphic replacements. These outlines have rounded and elongated lath-shaped morphologies that are consistent with petrographic observations of silica grains in the SIRs, which exhibit the same morphologies (e.g., Figs. 1.6b, 1.7b). The textural relationship between pseudomorphic replacements observed by TEM and silica replacement observed by SEM is also consistent with other lines of evidence, such as the complete absence of unaltered silica at the outer parts of the smooth rims in contact with the matrix. Indeed, we report direct evidence of replacement of silica (cristobalite) by an amorphous silicate phase (Fig. 1.19) with the exact same composition (normalized to 100) of the amorphous silicate gel in the smooth rims (Table 1.11), confirming that the amorphous silicate gel resulted from silica dissolution.

Therefore, we conclude that cristobalite in the SIRs was replaced entirely or partially during a very early stage of alteration by reaction with an aqueous Fe-rich fluid, resulting in a hydrated, amorphous Fe-rich silicate gel. Preservation of silica only

occurred (if at all) at the inner parts of the SIRs, close to chondrule interiors. Based on observations by Le Guillou and Brearley (2014), at least some of the water in CR chondrites may have been accreted into the matrix as composite water/ice grains. Therefore, melting of primary water ice grains was the most likely source of the aqueous fluid that altered SIRs, and the geochemical conditions of alteration were favorable to rapid dissolution of cristobalite compared to other silicates, such as crystalline olivines, pyroxenes, and sulfides in the matrix, which do not show any apparent evidence of replacement (e.g., Figs. 1.13e, 1.15j, 1.18), consistent with other studies in literature (e.g., Brunner, 2012). As discussed above, the low totals detected by EPMA from unaltered silica grains from SIRs are attributed to errors for not having used quartz as a standard for silica compositions in the electron microprobe, and we interpret silica to be anhydrous. The fact that the alteration product of cristobalite is an amorphous silicate phase is indicative of a very low temperature alteration process (e.g., Jones and Brearley, 2006).

4.1.5. Matrix observations adjacent to smooth rims

The presence of primary, nebular material, such as submicron to micron-sized amorphous silicates, crystalline Mg-rich silicates, sulfides with fine-scale heterogeneous distributions, and organic material found in the matrix of QUE 99177 adjacent to smooth rims, indicates that QUE 99177 is a highly primitive meteorite with a very low petrographic type and metamorphic grade, because there is no recrystallization nor chemical homogenization of the major (Fe, Mg) and minor elements that would indicate an equilibration process (Grossman and Brearley, 2005).

SEM and TEM observations on smooth rims made here, such as the sharp contact between smooth rims and matrix and the presence of submicron-sized sulfides sometimes

decorating these interfaces, agree reasonably well with the work of Jones et al. (2015). The sharp interface suggests that the matrix material is not (or minimally) involved in the formation of smooth rims (Figs. 1.13, 1.15, 1.17). The presence of organic material and amorphous silicates, the high abundance of sulfide grains, and the lack of phyllosilicates in the matrix adjacent to smooth rims indicate that temperature remained very low (probably about 25 ºC, e.g., Grossman and Brearley, 2005; Abreu and Brearley, 2010; Le Guillou and Brearley, 2014; Changela et al., 2018). Matrix adjacent to smooth rims appear similar to other regions of the matrix in QUE 99177, also consistent with the conclusion that the process that formed smooth rims did not affect the matrix material to a large extent. Among the FIB sections studied here, matrix in FIB2 appears the least altered, because of the high abundance of amorphous silicates, organic matter, and heterogeneous distribution of sulfides (Fig. 1.15j), whereas matrix in FIB1 (Fig. 1.13e) appears more affected by aqueous alteration, seen by the groundmass of Ca phosphates consistent with apatite composition (see Chapter 2), although amorphous silicates, organic matter, and sulfides are also present throughout.

4.2. Unraveling the conditions of the altering fluid

The extent of silica (cristobalite) dissolution that formed smooth rims seems surprising, given that much finer-grained albitic feldspar and interstitial glass, which are also susceptible to alteration by aqueous fluids, appear unaffected (Fig. 1.15). The discovery of unaltered primary albite grains and very small regions of interstitial glass surrounded by a hydrated amorphous silicate gel is unexpected and demonstrates that cristobalite was highly sensitive to aqueous alteration, even at very low degrees of alteration. Previous studies of, for example, CM chondrites, have indicated that

mesostasis glass in chondrules and feldspar in CAIs are among the first silicates to be affected by aqueous alteration (e.g., Grossman et al., 2000; Burger and Brearley, 2004). However, our observations suggest that cristobalite in the SIRs was significantly more susceptible to alteration than these phases under the conditions of alteration experienced by QUE 99177.

Despite the number of studies dedicated to understanding the dissolution of silica (e.g., Alexander et al., 1954; Iler, 1955; Knauss and Wolery, 1988; Fletcher and Sposito, 1989; Bennett, 1991; House and Orr, 1992; Dove, 1995; Sjöberg, 1996, Strandh et al., 1997; Jolivet et al., 2000; Icopini et al., 2005; Dove et al., 2005, 2008; Bickmore, 2008; Wallace et al., 2010; Skorina and Tikhomirova, 2012; Crundwell, 2017; Zhu et al., 2018) and feldspar (e.g., Garrels and Howard, 1957; Amrhein and Suarez, 1988; Casey et al., 1989, 1991; Murphy and Helgeson, 1989; Blum and Lasaga, 1988, 1991; Schott, 1990; Casey and Bunker 1990; Hellman et al. 1990; Wollast and Chou, 1992; Oelkers et al. 1994; Oelkers and Schott, 1995; Brantley and Stillings, 1996; Chen and Brantley, 1997; Strandh et al., 1997; Stefánsson and Arnórsson, 2000; Tromas and Meech, 2001; Ohlin et al. 2010; Hellmann et al., 2012; Skorina and Allanore, 2015), to unravel the fluid conditions at which the SIRs were altered is challenging, because some caveats still exist to reconcile experimental observations with theoretical models. This is partly because the dissolution process of a given mineral in aqueous solutions occurs at the dynamic fluid-solid interface operating at nano- to subnano-meter scales. In the following discussion, we consider the geochemical properties of aqueous fluids that are most likely to increase the rates of dissolution of silica (and more specifically, cristobalite) over feldspar in order to estimate the conditions in the fluid during the earliest stages of alteration in the CR

chondrite parent body. A primary goal of this study is to determine the conditions that resulted in such a significant dissolution of cristobalite, yet preserved albite and glass (e.g., understand why silica in smooth rims reacted much more rapidly than albite or glass). To this end, we commence discussing the parameter that has the most influence on the dissolution of silica and feldspar, the pH, and the importance of the silica polymorph (cristobalite instead of quartz). We follow the discussion by assessing the overall conditions required to form smooth rims (e.g., water source, fluid conditions, and time constraints), and we evaluate other parameters that may have played a minor role in the alteration process of silica.

4.2.1. Conditions required to dissolve cristobalite faster than albite

The geochemical parameter that has the strongest effect on the dissolution of silica is the pH. The dissolution rate diagram for the main silicate minerals as a function of pH illustrated by Brantley (2008) shows that silica (quartz) dissolves much slower than any other mineral (except kaolinite) under acidic conditions. Although silica in the SIRs is cristobalite rather than quartz, the diagram shows that the difference in dissolution rates between quartz and albite under acidic conditions is too large (albite dissolving almost two orders of magnitude faster) to account for additional factors (other than pH) that would dramatically reverse the two curves. Therefore, dissolution of silica without complete eradication of mesostasis is extremely difficult to reconcile under acidic conditions. Rather, the solubility curves for quartz and albite shown in Brantley (2008) diagram become comparable at basic pH, albite being slightly less soluble. Therefore, an alkaline pH can account for silica dissolving faster than albite in QUE 99177, which is

consistent with the alkaline conditions required to precipitate Ca carbonates (e.g., Fig. 1.3b) and Ca phosphates (Fig. 1.13e) observed in the matrix of QUE 99177.

In basic solutions, the predominant surface sites in silica are negative, deprotonated silanols (SiO^-), with a high affinity to react with cations (Zhu et al., 2018). Based on the model by Crundwell et al. (2017), at high pH, the independent removal of Si^{4+} and O^{2-} ions (cations removed in excess) from the silica surface go into solution and leave charged vacancies on the surface (proportional to the difference in the concentration of anionic and cationic vacancies) that increase the potential difference across the Stern layer. The increase of field strength enhances the dissolution of silica. Based on other models (e.g., Zhu et al., 2018), the dissolution of silica is mainly caused by the attack of OH^- molecules against the surface structure Si-O-Si, promoting hydrolysis. For feldspar, it is still unclear which functional groups form at the fluid–mineral interface at different stages of the dissolution process and how their interactions with water molecules modify the surface chemistry in various pH ranges (see Skorina and Allanore, 2015). Feldspar dissolves in both strong acids and strong bases, and the solubility increases exponentially with pH below 4 and above 8 (e.g., Amrhein and Suarez, 1988). The dissolution rate for feldspar is minimal when pH is neutral, because repolymerization of hydrated feldspar surfaces is faster, slowing the overall release of feldspar components in solution (Wild et al., 2016). Therefore, it is unlikely that the pH of the altering fluid in QUE 99177 had a strong alkalinity.

Quartz is the only silica polymorph represented in the diagram from Brandley (2008), and the difference in solubility rates between quartz and albite are very small. The fact that our observations on smooth rims reflect a much larger solubility rate of

silica (cristobalite) compared to albite suggests that cristobalite must dissolve at much higher rates than quartz (and albite) under alkaline conditions. Indeed, experimental studies show that there are major differences in solubility among silica polymorphs. Solubility increases with changes in the crystal structure to less ordered structures as follows: quartz < cristobalite < tridymite < coesite < amorphous silica (Iler, 1955, 1979; Stöber, 1967). Therefore, both high-temperature silica polymorphs are more susceptible to dissolve than quartz (e.g., Fornier and Rowe, 1962). Cristobalite and tridymite form at high temperatures and low pressures, and are very similar in structure, although there are some differences. With respect to structural bonding, tridymite is much less stable than cristobalite and undergoes a cascade of displacive phase transitions to form alpha, beta, and gamma polymorphs (Gutzow et al., 2011). In addition, cristobalite has a higher density than tridymite due to differences in orientation of the stacking of its tetrahedral sheets.

Experiments by Zhu et al. (2018) on the dissolution of α-quartz and α-cristobalite with different compounds demonstrate that α-cristobalite is far more susceptible to dissolution with NaOH solution than quartz, and that the amount of silicon released is about 30 times higher than that in acid and electrolyte solutions. The authors attribute this difference to a much higher abundance of oxygen vacancy defects in quartz compared with cristobalite, such that OH^- get trapped into the defects with positive charges and the reduction of available OH^- slows down the process of hydrolyzing the Si-O bonds. Therefore, in addition to an alkaline fluid, silica in SIRs dissolved because it was present as cristobalite rather than quartz.

Of additional importance, the preservation of feldspar and dissolution of silica at a slightly basic pH required that alteration occurred in a very short period of time, almost instantaneously, otherwise feldspar would also have dissolved. Therefore, the amount of fluid was very limited, because once all the water was consumed by rapid dissolution of cristobalite, the alteration process effectively ceased, preventing feldspar dissolution. This is consistent with alkaline fluids dominating at low water/rock (W/R) ratios (≤10) (Hanowski and Brearley, 2001). Consequently, we infer that the water reservoir contributing to smooth rim formation was solely the original water ice grains that accreted with other components in the matrix, and there was absence of any additional water from an external source.

4.2.2. Presence of inorganic ions in the altering fluid

An additional parameter that could have enhanced the solubility of silica without affecting that of albite is the presence of inorganic ions (e.g., Shmulovich et al., 2001). When the pH is higher than the point of zero charge (PZC) of the silica polymorph, the effect of inorganic ions, such as Fe^{3+}, Al^{3+}, Na^{+}, K^{+}, Li^{+}, Fe^{3+}, Ca^{2+}, Mg^{2+}, Mn^{3+}, and other more complex species, play a critical role in dissolving silica by weakening the Si-O bonds and promoting hydrolysis (Berger et al., 1994, Dove, 1990, 1999; Jolivet et al., 2000; Rimstidt, 2015). For example, at the circum-neutral pH range of most natural waters, several studies show that the dissolution rate of quartz is increased 50–100 times when alkaline or alkaline earth cations are introduced into otherwise ion-free water (Van Cappellen and Qiu, 1997a,b; Dove et al., 2005). The negatively-charged oxide silica surface causes preferential concentration of cations into the interfacial layer (Berger et al., 1994; Dove, 1990), disrupting the surface structure and allowing water to have more

direct access to Si-O-Si linkages (Zhu et al., 2018). This behavior is unique for silica and not observed in other silicate minerals (Stillings and Brantley, 1995). For feldspar, the presence of inorganic cations such as Na^{+}, K^{+}, Li^{+}, Ca^{2+}, Mg^{2+}, Al^{3+}, Mn^{3+}, Fe^{3+} act in the opposite way, because they decrease the formation of leached layers in the surface.

Although ferric iron is the most important ion that affects the dissolution of silica (e.g., Krauskopf, 1956), we cannot construct a coherent model where Fe^{3+} enhanced the solubility of silica relative to feldspar. Studies dedicated to understanding the interaction between aqueous silicic acid and Fe^{3+} are limited (e.g., Porter and Weber, 1971; Olson and O'Melia, 1973; Reardon, 1979), but they show that (i) the solubility of amorphous silica is enhanced with Fe^{3+} concentration for acidic pH (Reardon, 1979), (ii) relatively stable ferric ion complexes with dissolved silica with Fe concentration lower than 5×10^{-5} M (Porter and Weber, 1971); (iii) when Fe^{3+} complexes with silica, the acidity of the solution increases (Porter and Weber, 1971); and (iv) ferric silicate complexing ($FeH_3SiO_4^{2+}$) appears maximized near a pH of 2 (Reardon, 1979; Olson and O'Melia, 1973). Therefore, based on the evidence that QUE 99177 experienced fluid alteration at an alkaline pH, we infer that the solubility of Fe^{3+} was very low compared to Fe^{2+}. This is consistent with TEM observations in the matrix adjacent to smooth rims showing that sulfides are unaltered and heterogeneously distributed at fine-scales. Our results also show that S, which is a common element in the matrix, typically has a detection limit of less than 0.5 wt% SO_3 in smooth rims by EPMA (average 0.25 wt% SO_3, Table 1.2a), thus, S was not in a soluble form that could be transported. Therefore, the lack of sulfur in smooth rims suggests that oxidation of sulfides to form soluble sulfate did not occur; if it had, it would have mobilized Fe from sulfides and lowered the pH. Even during the

earliest stages of alteration in the CR chondrites, when there is evidence that the pH was at its lowest, there is no evidence that indicates that sulfides underwent oxidation in the matrix (Zolotov, 2012).

4.2.3. Sensitivity of dissolution rates to changes in temperature

While at pH < 8.5, the rate of dissolution of silica (quartz) increases in a roughly linear relation, mainly governed by the concentration of Na^+ and OH^- ions (Fleming and Crerar, 1982; Crundwell, 2017) and is independent of pH, in alkaline regions, the rate of silica dissolution is dependent on the concentrations of ions such as Na^+ and OH^- (independently, not as NaOH) and on the temperature (Crundwell, 2017). The dissolution rate of feldspar also increases with temperature, but the change is much slower. For example, an increase of 45ºC (from 25 to 70ºC) increases the dissolution rate of quartz by about 2 orders of magnitude (Knaus and Wolery, 1988; Brady and Walther, 1990; Bennet, 1991; House and Orr, 1992), while for feldspar, the same increase in the net dissolution rate (about two orders of magnitude) requires an increase in temperature of 100ºC (in the range of 25-300ºC at constant pH, e.g., Hellmann, 1994). Although it is unlikely that smooth rims experienced a temperature variation of more than 50 ºC, the fact that the dissolution rate of silica increases more rapidly with temperature could have been an additional factor favoring silica dissolution relative to feldspar.

4.2.4. Additional minor constraints on the alteration

Catalytic Na+

Because the amorphous Fe-rich silicate gel contains some Al and Na (3 wt% Al_2O_3, 1 wt% Na_2O, average of 30 analyses in the amorphous hydrated gel in four different smooth rims) and a relationship between Na and relict feldspar is observed

(section 4.1.1), it is possible that minor, incipient dissolution of feldspar took place during the earliest stages of aqueous alteration. In fact, Na content has been detected up to 4 wt% Na_2O in FIB1 (Table 1.4) and up to 6.76 wt% Na_2O in FIB2 (Table 1.6). The dissolution of feldspar involves the release of large cations (Na^+, K^+, Ca^{2+}) and Al^{3+} via ion exchange (Garrels and Howard, 1957; Casey et al., 1989; Murphy and Helgeson, 1989; Chou and Wollast, 1989; Wollast and Chou, 1992). Protonation of surface hydroxyl sites at albite surface exposed to the fluid (Blum and Lasaga 1988, 1991; Schott 1990) left a leached, hydrated surface layers that affected the tetrahedron-octahedron-tetrahedron structure of the feldspar by hydrolysis and eventually released hydrated silica and alumina species from the crystal structure (Casey et al., 1989, 1991; Casey and Bunker, 1990, Hellman et al., 1990; Oelkers et al., 1994). Thus, the presence of large cations released during incipient dissolution of feldspar could have reacted with the negative silica surfaces, enhancing silica dissolution rates and decreasing feldspar dissolution rates (Rimstidt, 2015). Among the inorganic ions detected in the amorphous silicate gel by EPMA and STEM-EDS (Na^+, Mg^{2+}, Al^{3+}, and Fe^{3+}), large Na^+ cations have the highest influence on silica dissolution for being catalytic (Zhu et al., 2018), because they accelerate the removal of anions from the surface of silica and promote dissolution (e.g., Wallace et al., 2010). However, although this process could have enhanced silica dissolution, it played a minor role on the formation of smooth rims, given the insufficient amount of feldspar to promote the extent of silica dissolution. In addition, the lack of Al-rich pseudomorphs of altered albite (Al being highly immobile) embedded within the smooth rims indicates that feldspar did not experience much dissolution.

Light and heavy isotopes in water ions

Light or heavy isotopic water ions do not influence the rate of dissolution of silica in alkaline solutions (Casey et al., 1990), but it is worth noticing that at a basic pH, the rate of dissolution of quartz is the same for both isotopically heavy and light water, whereas at acidic pH, the rate of dissolution of quartz in isotopically heavy water ions is lower than in isotopically light water ions (Casey, 1990). These observations are explained by the Crundwell (2017) equations, which show that in acidic solutions, the rate of dissolution of silica is dependent on the dissociation constant of water, which is lower in D_2O, whereas the rate of dissolution in alkaline solutions is not. Calculations for dissolution of silica by Crundwell (2017) have concluded that the rate in heavy water ions should be 37% of the rate in light water ions. This suggests that water ions in the altering fluid could have been heavy or light.

Fluid saturated state

At pH above 7 and at high saturation states, the speciation of alumina and silica is very sensitive to the time-temperature history, fluid composition, and the presence of a mineral surface (Ohlin et al., 2010). The dissolution rates for feldspars are very slow when the fluid is oversaturated, since feldspars require a far from equilibrium state (low fluid saturation) to dissolve (Warfvinge and Sverdrup, 1992; Stillings and Brantley, 1995; Stefánsson and Arnórsson, 2000; White and Brantley, 2003; Beig and Lüttge, 2006). Therefore, the altering fluid was at a state of high saturation, which is consistent with the lack of porosity associated with dissolution of any of the phases, and supports that silica underwent immediate dissolution and precipitation.

Crystal defects and surface properties

Crystal defects also affect mineral dissolution kinetics. Surface inhomogeneity at the submicron to atomic scales affect the mineral surface charge, and hence, the pH dependence of the dissolution rate. The specific planes of the crystals that were in contact with the fluid, and the amount of crystal defects could have been two other factors in controlling the rate of dissolution of feldspar, since there is preferential dissolution along specific crystallographic planes (Fenter et al., 2003; Daval et al. 2013; Yang et al., 2014) and crystal defects enhance the rate of dissolution (Nangia and Garrison, 2003; Morrow et al., 2009; Yang et al., 2013). Therefore, although this parameter is unlikely to have inhibited the dissolution of albite by an order of magnitude compared with silica, it is likely that feldspar in smooth rims have low density of defects.

4.3. Elemental mobilization during the earliest stages of fluid-chondrule interactions: The source of Fe in smooth rims and redistribution of silica in the matrix

The formation of an amorphous Fe-rich silicate gel in smooth rims requires the interaction of the altering silica with an Fe^{2+}-rich fluid. Because the amorphous Fe-rich silicate gel in smooth rims appears compositionally similar for the major elements Si and Fe among the different rims studied (Tables 1.4, 1.6, 1.8, 1.9), it is more likely that the source of Fe^{2+} was external from the chondrule SIRs rather than internal. We thus argue that Fe, a highly mobile element, was derived from the matrix and introduced during the dissolution process of cristobalite (e.g., Fe^{2+} moved through a static fluid by diffusion). The small-scale compositional variations of smooth rims among and within FIB sections, on the contrary, are attributed to small-scale elemental mobility during alteration. For

example, Na varies greatly in the amorphous silicate gel (from 0 to ~7 wt% Na_2O, Table 1.6), and such variations might be related to local elemental mobilization from the feldspar, given that the amount of Na in the amorphous material in FIB2 (Fig. 1.15) is related to its spatial association with feldspar, although Na mobilized by the electron beam during analyses cannot be ruled out. It is likely that a high amount of Si, proportional to the introduced amount of Fe in the amorphous silicate gel in smooth rims, was released from cristobalite dissolution into the matrix, seen by the Si-enrichment in the matrix close to smooth rims relative to the matrix surrounding chondrules that lack smooth rims (e.g., Fig. 1.6a, Fig. 1.22).

A potential source of Fe^{2+} from the matrix is amorphous silicates (AS) in the matrix. Evidence that supports a primary origin for the AS is well documented in literature (Chizmadia and Brearley, 2008; Le Guillou and Brearley, 2014; Le Guillou et al., 2015; Leroux et al., 2015; Brearley, 2016), which includes: (i) they only occur in the least altered chondrites known (Brearley, 1993; Greshake, 1997; Scott and Krot, 2005; Chizmadia and Brearley, 2008; Abreu and Brearley, 2010; Davidson et al., 2014; Le Guillou and Brearley, 2014; Leroux et al., 2015), (ii) meteorites that contain a high abundance of AS, also have the highest abundance of presolar silicates (Nguyen et al., 2010), and (iii) AS show a heterogeneous relationship with Ni-bearing sulfides (e.g., some areas are sulfide-rich and some areas are sulfide-poor). All these characteristics are consistent with matrix observations made here (Fig. 1.13e-i, 1.15j), except for matrix in FIB4, which compositional (lack of AS, presence of ferroan olivine) and textural (triple junctions in pyroxene) observations (Fig. 1.18) suggest a different formation mechanism (e.g., dust accreted hot onto the chondrule). Given that it is not possible to condense Fe

into olivine by a condensation process in the solar nebula, it is inferred that AS formed as nebular or interstellar disequilibrium condensates that could not crystallize due to rapid cooling and/or low pressure conditions (Krot et al., 2005). An additional argument for this hypothesis is that it is extremely difficult to envision a parent body process where some mineral phase in the matrix altered to form AS, especially if most of them are surrounded by unaltered fine-grained Ni-bearing sulfides.

Experimental data show that amorphous silicates in the matrix are highly reactive with the presence of water (e.g., Chizmadia, 2007; Takigawa et al., 2019). Thus, we argue that AS were hydrated very rapidly, releasing soluble elements (mainly Fe^{2+} and perhaps small amounts of other soluble elements such as Na^{+} and Ca^{2+}) into the fluid. The Fe-rich fluid altered silica grains in the SIRs, but the fluid was very limited and further reactions were inhibited. After that, the AS in the matrix, and probably the amorphous silicate gel in smooth rims, underwent progressive oxidation due to the extensive hydration they experienced (Le Guillou et al., 2015). An additional, unexplored, potential source of Fe is from early alteration of Fe,Ni metal nodules in SIRs (e.g., Hanowski and Brearley, 2000). Backscatter electron images of smooth rims show that some metal blebs in SIRs appear altered to a phase with a higher electron albedo (preserving Ni content and their original morphologies) without the presence of terrestrial weathered veins crosscutting them (e.g., Fig. 1.5b). Because the third dimension is not visible in BSE images, and because QUE 99177 is significantly terrestrially altered, further TEM work is needed to constrain the origin of the alteration of these grains and assess whether metal grains could serve as another potential source of Fe in smooth rims.

Nonetheless, it is unlikely that alteration Fe,Ni metal grains alone could account for the large amount of amorphous Fe-rich material formed.

Finally, the excess of Si released from the dissolution of cristobalite was transferred into the matrix as a Si-rich fluid and modified the composition of the AS over a scale of 10s to ~100s of microns (Fig. 1.22). An important implication of these results is that even during the earliest stages of alteration, the composition of the AS in the matrix may have been modified to different degrees due to alteration of the most reactive components of chondrules, such as SIRs, as discovered in this study, which were not previously recognized. This modification appears, however, to be localized and restricted by relatively short scale mass transport of elements. Nevertheless, careful attention is needed when choosing regions of the matrix to investigate particular processes in the least-altered CR chondrites – e.g., regions between chondrules that are not surrounded by smooth rims (indicated as Si-poor in Fig. 1.22) are best for understanding solar nebular characteristics.

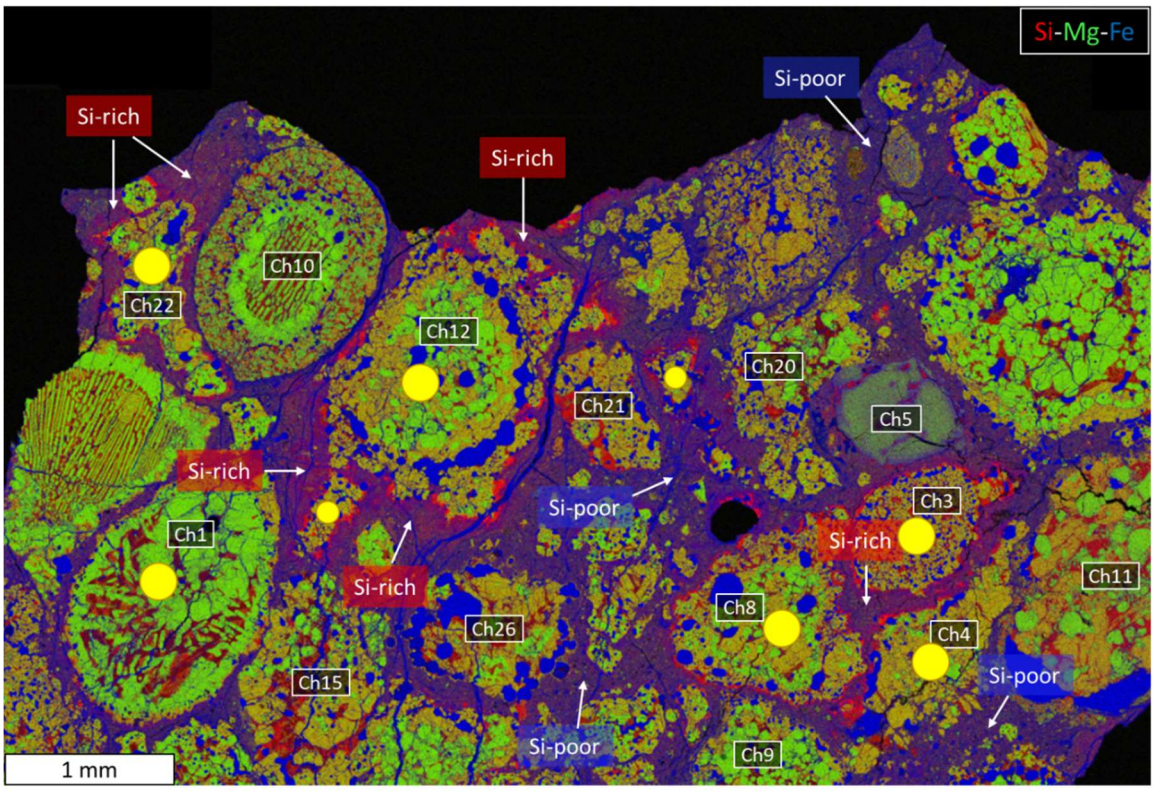

Fig. 1.22. Combined RGB (Si-Mg-Fe) elemental X-ray map of chondrules with associated fine-grained matrix material showing the Si-enrichment of the early fluid in the matrix due to alteration of cristobalite in SIRs. Ch# with a yellow mark indicates chondrules surrounded by smooth rims. Note that matrix around chondrules with smooth rims around them contain a higher concentration of Si (Si-rich) compared to other regions of the matrix surrounding chondrules that lack smooth rims (Si-poor).

5. Conclusions

The overall characteristics of QUE 99177 (matrix and chondrules) indicate that QUE 99177 is a highly pristine meteorite (e.g., highest presolar grains than any other meteorite known). In fact, QUE 99177 is considered the least altered CR chondrite, and it is essentially unmetamorphosed. We show that the so-called *smooth rims* can be used as a proxy for assessing the degree of alteration of weakly altered CR chondrites. Smooth rims surround type I chondrules and are the product of the earliest fluid-chondrule interactions in the CR parent body. In particular, cristobalite in silica-rich igneous rims (SIRs) underwent alteration by fluids that resulted from melting of the first water ice

grains that accreted within amorphous silicates in the matrix. We show that the alteration product of cristobalite, which constitutes the major phase in smooth rims, is an amorphous Fe-rich silicate gel, indicative of a low alteration process. TEM work reveals that the amorphous silica gel contains unaltered crystalline, igneous silicates (pyroxene, albite, chromite, and/or glass) from SIRs that survived the alteration process. Pyroxenes within smooth rims can be significantly more Mn- and Cr-rich than previously reported pyroxenes in SIRs by Krot et al. (2004), and the observed enrichments are attributed to small scale zonation of fine-grained crystals that are within the excitation volume of EPMA. We have established a clear relationship between the carriers of Mn, Mg, and Ca, in smooth rims by EPMA with igneous pyroxenes, thus EPMA analyses can be used to demonstrate an origin of smooth rims by alteration of SIRs in other smooth rims on other chondrites.

During alteration, the amorphous silicates in the matrix (primary nebular components) hydrated rapidly and leached mobile elements (mainly Fe^{2+}) that went into solution and were transported into chondrule-matrix interfaces. The Fe^{2+}-rich fluid reacted with cristobalite grains in the SIRs, but the alteration was very limited, because once the fluid reacted with silica, the alteration ceased, preventing feldspar to dissolve. The altering fluid was slightly alkaline (pH ~ 9), demonstrating that cristobalite must dissolve at much higher rates than quartz (and albite) under alkaline conditions, and the alteration was very fast due to a very limited reservoir (absence of an additional fluid source). It is likely that the Si-rich fluid resulted from this interaction modified the composition of primary amorphous silicates in the matrix in a very localized scale. The identification and characterization of smooth rims in other weakly altered CR chondrites

(e.g., number of chondrules surrounded by smooth rims, degree of silica alteration in SIRs, survival or alteration of igneous phases in smooth rims) can serve as powerful tools for assigning a degree of alteration of a given CR chondrite and overall, re-evaluate our current understanding of the earliest stages of aqueous alteration in chondrites.

Acknowledgements

We would like to acknowledge Mike Spilde from the Electron Microbeam Analyses Facility for his excellent assistance to the electron microprobe. US Antarctic meteorite samples were recovered by the Antarctic Search for Meteorites (ANSMET) program, which has been funded by NSF and NASA, and characterized and curated by the Department of Mineral Sciences of the Smithsonian Institution and Astromaterials Curation Office at NASA Johnson Space Center. This work was supported and funded by NASA Cosmochemistry Grant NNX15AD28G to A. J. Brearley.

References

Abreu, N. M. 2016. Why is it so difficult to classify Renazzo-type (CR) carbonaceous chondrites? – Implications from TEM observations of matrices for the sequences of aqueous alteration. *Geochimica et Cosmochimica Acta* 194:91–122.

Abreu, N. M. and Brearley, A. J. 2010. Early solar system processes recorded in the matrices of two highly pristine CR3 carbonaceous chondrites, MET 00426 and QUE 99177. *Geochimica et Cosmochimica Acta* 74:1146–1171.

Alexander C. M. O'D. and Grossman J. N. 2005. Alkali elemental and potassium isotopic compositions of Semarkona chondrules. *Meteoritics and Planetary Science* 40:541–556.

Alexander, C. M. O'D., Bowden, R., Fogel, M. L., Howard, K. T., and Greenwood, R. C. 2012. The classification of CM and CR chondrites using bulk H abundances and isotopes. *43rd Lunar and Planetary Science Conference.* Abstract #2799.

Alexander, C. M. O'D., Howard, K. T., Bowden, R., and Fogel, M. L. 2013. The classification of CM and CR chondrites using bulk H, C and N abundances and isotopic compositions. *Geochimica et Cosmochimica Acta* 123:244–260.

Alexander, G. B., Heston, W. M., and Iler, R. K. 1954. The solubility of amorphous silica in water. *The Journal of Physical Chemistry* 58:453–455.

Amrhein, C. and Suarez, D. L. 1988. The use of a surface complexation model to describe the kinetics of ligand-promoted dissolution of anorthite. *Geochimica et Cosmochimica Acta* 52:2785–2793.

Barber, D. J. 1981. Matrix phyllosilicates and associated minerals in C2M carbonaceous chondrites. *Geochimica et Cosmochimica Acta* 45:945–970.

Beig, M. S. and Lüttge, A. 2006. Albite dissolution kinetics as a function of distance from equilibrium: Implications for natural feldspar weathering. *Geochimica et Cosmochimica Acta* 70:1402–1420.

Bennett, P. C. 1991. Quartz dissolution in organic-rich aqueous systems. *Geochimica et Cosmochimica Acta* 55:1781–1797.

Berger, G., Cadore, E., Schott, J., and Dove, P. M. 1994. Dissolution rate of quartz in lead and sodium electrolyte solutions between 25 and 300 C: Effect of the nature of surface complexes and reaction affinity. *Geochimica et Cosmochimica Acta* 58:541–551.

Berlin, J. 2009. Mineralogy and bulk chemistry of chondrules and matrix in petrologic type 3 chondrites: Implications for early solar system processes. PhD Thesis. The University of New Mexico.

Bickmore, B. R., Wheeler, J. C., Bates, B., Nagy, K. L., and Eggett, D. L. 2008. Reaction pathways for quartz dissolution determined by statistical and graphical analysis of macroscopic experimental data. *Geochimica et Cosmochimica Acta* 72:4521–4536.

Blum, A. and Lasaga, A. 1988. Role of surface speciation in the low-temperature dissolution of minerals. *Nature* 331:431–433.

Blum, A. E. and Lasaga, A. C. 1991. The role of surface speciation in the dissolution of albite. *Geochimica et Cosmochimica Acta* 55*:*2193–2201.

Brady, P. V. and Walther, J. V. 1990. Kinetics of quartz dissolution at low temperatures. *Chemical geology* 82:253–264.

Brantley, S. L. 2008. Kinetics of mineral dissolution. In *Kinetics of water-rock interaction.* Springer, New York, NY. Pp. 151–210.

Brantley, S. L. and Stillings, L. 1996. Feldspar dissolution at 25 C and low pH. *American Journal of Science* 296:101–127.

Brearley, A. J. 1993. Matrix and fine-grained rims in the unequilibrated CO3 chondrite, ALHA77307: Origins and evidence for diverse, primitive nebular dust components. *Geochimica et Cosmochimica Acta 57*:1521–1550.

Brearley A. J. 2006. The Action of Water. In *Meteorites and the Early Solar System II* (eds. D.S. Lauretta D. S. and H. Y. McSween). The University of Arizona Press, Tucson, AZ. Pp. 584–624.

Brearley, A. J. 2016. Diverse anhydrous silicates in a fine-grained rim in the weakly altered CM2 chondrite Queen Elizabeth Range 97990: Evidence for the localized preservation of pristine nebular dust in CM chondrites. *79th Annual Meeting of the Meteoritical Society.* Abstract #6190.

Brearley, A. J. and Le Guillou, C. 2015. More Evidence of the importance of amorphous silicates in CM carbonaceous chondrites: new observations from a fine-grained rim in the CM2 chondrite, TIL 91722. *78th Annual Meeting of the Meteoritical Society*. Abstract #5192.

Brearley, A.J. and Jones, R.H. 2016. Dissolution and replacement of cristobalite by amorphous Fe-rich silicate gel in silica-bearing Type I chondrules in the Elephant Moraine (EET) 92042 CR2 carbonaceous chondrite. *47th Lunar and Planetary Science Conference*. Abstract# 1897.

Bunch, T. E. and Chang, S. 1980. Carbonaceous chondrites—II. Carbonaceous chondrite phyllosilicates and light element geochemistry as indicators of parent body processes and surface conditions. *Geochimica et Cosmochimica Acta* 44:1543–1577.

Burger, P. V. and Brearley, A. J. 2004. Chondrule glass alteration in type IIA chondrules in the CR2 chondrites EET 87770 and EET 92105: Insights into elemental exchange between chondrules and matrices. *35th Lunar and Planetary Science*. Abstract #1966.

Casey, W. H. and Bunker, B. 1990. Leaching of mineral and glass surface geochemistry. *Mineralogical Society of America* 23:397–426.

Casey, W. H., Westrich, H. R., and Arnold, G. W. 1989. The surface chemistry of dissolving labradorite feldspar. *Geochimica et Cosmochimica Acta* 53:821–832.

Casey, W. H., Lasaga, A. C., and Gibbs, G. V. 1990. Mechanisms of silica dissolution as inferred from the kinetic isotope effect. *Geochimica et Cosmochimica Acta* 54:3369–3378.

Casey, W. H., Westrich, H. R., and Holdren, G. R. 1991. Dissolution rates of plagioclase at pH= 2 and 3. *American Mineralogist* 76:211–217.

Changela, H. G., Le Guillou, C., Bernard, S., and Brearley, A. J. 2018. Hydrothermal evolution of the morphology, molecular composition, and distribution of organic matter in CR (Renazzo-type) chondrites. *Meteoritics & Planetary Science* 53:1006–1029.

Chen, Y. and Brantley, S. L. 1997. Temperature-and pH-dependence of albite dissolution rate at acid pH. *Chemical Geology* 135:275–290.

Chizmadia, L. J. 2007. Reproduction of phyllosilicate textures in CM2 chondrites during experimental hydration of amorphous silicate smokes. *38th Lunar and Planetary Science Conference*. Abstract# 1005.

Chizmadia, L. J., and Brearley, A. J. 2008. Mineralogy, aqueous alteration, and primitive textural characteristics of fine-grained rims in the Y-791198 CM2 carbonaceous chondrite: TEM observations and comparison to ALHA81002. *Geochimica et Cosmochimica Acta* 72:602–625.

Connolly Jr, H. C., Huss, G. R., and Wasserburg, G. J. 2001. On the formation of Fe-Ni metal in Renazzo-like carbonaceous chondrites. *Geochimica et Cosmochimica Acta* 65:4567–4588.

Connolly, H. C., Smith, C., Benedix, G., Folco, L., Righter, K., Zipfel, J., Yamaguchi, A., and Aoudjehane, H. C. 2007. The Meteoritical Bulletin, No. 92, 2007 September. *Meteoritics & Planetary Science* 42:1647–1694.

Crundwell, F. K. 2017. On the mechanism of the dissolution of quartz and silica in aqueous solutions. *ACS omega* 2:1116–1127.

Daval, D., Hellmann, R., Saldi, G. D., Wirth, R., and Knauss, K. G. 2013. Linking nm-scale measurements of silicate surfaces to macroscopic dissolution rate laws: New insights based on diopside. *Geochimica et Cosmochimica Acta* 107:121–134.

Davidson, J., Busemann, H., Nittler, L. R., Alexander, C. M. D., Orthous-Daunay, F. R., Franchi, I. A., and Hoppe, P. 2014. Abundances of presolar silicon carbide grains in primitive meteorites determined by NanoSIMS. *Geochimica et Cosmochimica Acta* 139:248–266.

De Gregorio, B. T., Stroud, R. M., Nittler, L. R., and Alexander, C. M. O., Bassim N. D., Cody G. D., Kilcoyne A. L. D., Sandford S. A., Milam S. N., Nuevo M., and Zega T. J. 2013. Isotopic and chemical variation of organic nanoglobules in primitive meteorites. *Meteoritics & Planetary Science* 48:904–928.

Dove, P. M. 1995. Kinetic and thermodynamic controls on silica reactivity in weathering environments. In: *Chemical weathering rates of silicate minerals*, vol 31, pp 235-290. Eds: A.F. White and S.L. Brantley, Mineralogical Society of America.

Dove, P. M. 1999. The dissolution kinetics of quartz in aqueous mixed cation solutions. *Geochimica et Cosmochimica Acta* 63:3715-3727.

Dove, P. M. and Crerar, D. A. 1990. Kinetics of quartz dissolution in electrolyte solutions using a hydrothermal mixed flow reactor. *Geochimica et Cosmochimica Acta* 54:955–969.

Dove P. M., Han N., and De Yoreo J. J. 2005. Mechanisms of classical crystal growth theory explain quartz and silicate dissolution behavior. *Proc Natl Acad Sci USA* 102:15357–15362.

Dove, P. M., Han, N., Wallace, A. F., and De Yoreo, J. J. 2008. Kinetics of amorphous silica dissolution and the paradox of the silica polymorphs. *Proceedings of the National Academy of Sciences* 105:9903–9908.

Doyle, P. M., Jogo, K., Nagashima, K., Krot, A. N., Wakita, S., Ciesla, F. J., and Hutcheon, I. D. 2015. Early aqueous activity on the ordinary and carbonaceous chondrite parent bodies recorded by fayalite. *Nature Communications* 6:1–10.

Fenter, P., Park, C., Cheng, L., Zhang, Z., Krekeler, M. P. S., and Sturchio, N. C. 2003. Orthoclase dissolution kinetics probed by in situ X-ray reflectivity: effects of temperature, pH, and crystal orientation. *Geochimica et Cosmochimica Acta* 67:197–211.

Fleming, B. A. and Crerar, D. A. 1982. Silicic acid ionization and calculation of silica solubility at elevated temperature and pH application to geothermal fluid processing and reinjection. *Geothermics* 11:15–29.

Fletcher, P. and Sposito, G. 1989. The chemical modelling of clay/electrolyte interactions for montmorillonite. *Clay Minerals* 24:375–391.

Floss, C. and Stadermann, F. 2009. Auger Nanoprobe analysis of presolar ferromagnesian silicate grains from primitive CR chondrites QUE 99177 and MET 00426. *Geochimica et Cosmochimica Acta* 73:2415–2440.

Fournier, R. O. and Rowe, J. J. 1962. The solubility of cristobalite along the three-phase curve, gas plus liquid plus cristobalite. *American Mineralogist: Journal of Earth and Planetary Materials* 47: 897–902.

Garrels, R. M. and Howard, P. 1957. Reactions of feldspar and mica with water at low temperature and pressure. *Clays and clay minerals* 6:68–88.

Greshake, A. 1997. The primitive matrix components of the unique carbonaceous chondrite Acfer 094: A TEM study. *Geochimica et Cosmochimica Acta* 61: 437–452.

Grossman, J. N., and Brearley, A. J. 2005. The onset of metamorphism in ordinary and carbonaceous chondrites. *Meteoritics & Planetary Science* 40:87–122.

Grossman, J. N., Alexander, C. M. O. D., Wang, J., and Brearley, A. J. 2000. Bleached chondrules: Evidence for widespread aqueous processes on the parent asteroids of ordinary chondrites. *Meteoritics & Planetary Science* 35:467–486.

Gutzow, I, Pascova, R, Jordanov, N., Gutzov, S., Penkov, I., Markovska, I., Schmelzer, J.W.P., and Ludwig, F-P. (2011). Structure, Thermodynamic Properties, Solubility and Synthesis of the Different Modifications of Silica. In: *Nuclear Theory and Applications* (eds, J.W.P Schmelzer, G. Ropke, and V.B. Priezzhev). Pp 137–196.

Hanowski, N. P., and Brearley, A. J. 2001. Aqueous alteration of chondrules in the CM carbonaceous chondrite, Allan Hills 81002: Implications for parent body alteration. *Geochimica et Cosmochimica Acta* 65:495–518.

Harju E. R., Rubin A. E., Ahn I., Choi B.-G., Ziegler K., and Wasson J. 2014. Progressive aqueous alteration of CR carbonaceous chondrites. *Geochimica et Cosmochimica Acta* 139:267–292.

Hellmann, R. 1994. The albite-water system: Part I. The kinetics of dissolution as a function of pH at 100, 200 and 300 C. *Geochimica et Cosmochimica Acta* 58:595–611.

Hellmann, R., Eggleston, C. M., Hochella Jr, M. F., and Crerar, D. A. 1990. The formation of leached layers on albite surfaces during dissolution under hydrothermal conditions. *Geochimica et Cosmochimica Acta* 54:1267–1281.

Hellmann, R., Wirth, R., Daval, D., Barnes, J. P., Penisson, J. M., Tisserand, D., Epicier, T., Florin, B., and Hervig, R. L. 2012. Unifying natural and laboratory chemical weathering with interfacial dissolution–reprecipitation: a study based on the

nanometer-scale chemistry of fluid–silicate interfaces. *Chemical Geology* 294:203–216.

House, W. A. and Orr, D. R. 1992. Investigation of the pH dependence of the kinetics of quartz dissolution at 25 C. *Journal of the Chemical Society, Faraday Transactions* 88:233–241.

Howard, K. T., Alexander, C. O. D., Schrader, D. L., and Dyl, K. A. 2015. Classification of hydrous meteorites (CR, CM and C2 ungrouped) by phyllosilicate fraction: PSD-XRD modal mineralogy and planetesimal environments. *Geochimica et Cosmochimica Acta* 149:206–222.

Icopini, G. A., Brantley, S. L., and Heaney, P. J. 2005. Kinetics of silica oligomerization and nanocolloid formation as a function of pH and ionic strength at 25 C. *Geochimica et Cosmochimica Acta* 69:293–303.

Iler, R. K. 1955. The Colloid Chemistry of Silica and Silicates. Cornell University Press, New York, NY. Vol 80. Pp 86.

Iler, K. R. 1979. The chemistry of silica. Solubility, polymerization, colloid and surface properties and biochemistry of silica. John Wiley & Sons, New York, NY.

Jones, C. L. and Brearley, A. J. 2006. Experimental aqueous alteration of the Allende meteorite under oxidizing conditions: constraints on asteroidal alteration. *Geochimica et Cosmochimica Acta* 70:1040–1058.

Jones, R. H., Brearley, A. J., Henkel, T., and Lyon, I. 2015. Assessing the degree of secondary alteration in chondrules from one of the least altered CR chondrites, EET 92042. *78th Annual Meeting of the Meteoritical Society*. Abstract #5190.

Jolivet, J. P., Henry, M., and Livage, J. 2000. Metal oxide chemistry and synthesis: from solution to solid state. Wiley-Blackwell.

Kallemeyn, G. W. and Wasson, J. T. 1981. The compositional classification of chondrites—I. The carbonaceous chondrite groups. *Geochimica et Cosmochimica Acta* 45:1217–1230.

Kallemeyn G. W., Rubin A. E., and Wasson J. T. 1994. The compositional classification of chondrites: VI. The CR carbonaceous chondrite group. *Geochimica et Cosmochimica Acta* 58:2873–2888.

Kimura, M., Yamaguchi, A., Imae, N., Mikouchi, T., and Weisberg, M. K. 2013. Abundant anomolous chondrules in an ungrouped carbonaceous chondrite, Y-82094. *Meteoritics and Planetary Science Supplement* 76:5079.

Knauss, K. G. and Wolery, T. J. 1988. The dissolution kinetics of quartz as a function of pH and time at 70 C. *Geochimica et Cosmochimica Acta* 52:43–53.

Komatsu, M., Fagan, T. J., Kimura, M., Yamaguchi, A., Yasutake, M., Mikouchi, T., and Zolensky, M. 2019. Examination of silica polymorphs in the CR Chondrites. *50th Lunar and Planetary Science*. Abstract #1750.

Krauskopf, K. B. 1956. Dissolution and precipitation of silica at low temperatures. *Geochimica et Cosmochimica Acta* 10:1–26.

Krot, A. N., Meibom, A., Weisberg, M. K., and Keil, K. 2002. The CR chondrite clan: Implications for early solar system processes. *Meteoritics & Planetary Science* 37:1451–1490.

Krot, A. N., Libourel, G., Goodrich, C. A., and Petaev, M. I. 2004. Silica-rich igneous rims around magnesian chondrules in CR carbonaceous chondrites: Evidence for condensation origin from fractionated nebular gas. *Meteoritics & Planetary Science* 39:1931–1955.

Lauretta, D. S., Hua, X., and Buseck, P. R. 2000. Mineralogy of fine-grained rims in the ALH 81002 CM chondrite. *Geochimica et Cosmochimica Acta* 64:3263–3273.

Le Guillou, C. and Brearley, A. 2014. Relationships between organics, water and early stages of aqueous alteration in the pristine CR3.0 chondrite MET 00426. *Geochimica et Cosmochimica Acta* 131:344–367.

Le Guillou, C., Changela, H. G., and Brearley, A. J. 2015. Widespread oxidized and hydrated amorphous silicates in CR chondrites matrices: Implications for alteration conditions and H2 degassing of asteroids. *Earth and Planetary Science Letters* 420:162–173.

Leroux, H., Cuvillier, P., Zanda, B., and Hewins, R. H. 2015. GEMS-like material in the matrix of the Paris meteorite and the early stages of alteration of CM chondrites. *Geochimica et Cosmochimica Acta* 170:247–265.

Libourel G., Krot A. N., and Tissandier L. 2006. Role of gas-melt interaction during chondrule formation. *Earth and Planetary Science Letters* 251:232–240.

Lindsley, D. H. 1983. Pyroxene thermometry. *American Mineralogist* 68:477–493.

Lodders, K. 2003. Solar system abundances and condensation temperatures of the elements. *The Astrophysical Journal* 591:1220.

Martins, Z., Hofmann, B. A., Gnos, E., Greenwood, R. C., Verchovsky, A., Franchi, I. A., Jull, J. A., Botta, O., Glavin, P., Dworkin, J. P., and Ehrenfreund, P. 2007. Amino acid composition, petrology, geochemistry, ^{14}C terrestrial age and oxygen isotopes of the Shişr 033 CR chondrite. *Meteoritics & Planetary Science* 42:1581–1595.

Martínez-Jiménez, M. and Brearley, A. J. 2018. Aqueous alteration effects in chondrules in the most pristine CR2 chondrite, Queen Alexandra Range (QUE) 99177: Further insights into the earliest stages of fluid-rock interaction. *49th Lunar and Planetary Science Conference*. Abstract #2274.

Matsunami S., Ninagawa K., Nishimura S., Kubono N., Yamamoto I., Kohata M., Wada T., Yamashita Y., Lu J., Sears D. W. G., and Nishimura H. 1993. Thermoluminescence and compositional zoning in the mesostasis of a Semarkona group A1 chondrule and new insights into the chondrule-forming process. *Geochimica et Cosmochimica Acta* 57:2101–2110.

Metzler, K., Bischoff, A., and Stöffler, D. 1992. Accretionary dust mantles in CM chondrites: Evidence for solar nebula processes. *Geochimica et Cosmochimica Acta* 56:2873–2897.

Murphy, W. M. and Helgeson, H. C. 1989. Thermodynamic and kinetic constraints on reaction rates among minerals and aqueous solutions; IV, Retrieval of rate constants and activation parameters for the hydrolysis of pyroxene, wollastonite, olivine, andalusite, quartz, and nepheline. *American Journal of Science* 289:17–101.

Nagahara H., Kita N. T., Ozawa K., and Morishita Y. 2008. Condensation of major elements during chondrule formation and its implication to the origin of chondrules. *Geochimica et Cosmochimica Acta* 72:1442–1465.

Nguyen, A. N., Nittler, L. R., Stadermann, F. J., Stroud, R. M., and Alexander, C. M. D. O'D. 2010. Coordinated analyses of presolar grains in the Allan Hills 77307 and Queen Elizabeth Range 99177 meteorites. *The Astrophysical Journal* 719:166–189.

Nittler, L. R., Alexander, C. M. D. O'D., Davidson, J., Riebe, M. E., Stroud, R. M., and Wang, J. 2018. High abundances of presolar grains and ^{15}N-rich organic matter in CO3. 0 chondrite dominion range 08006. *Geochimica et cosmochimica acta* 226:107–131.

Oelkers, E. H. and Schott, J. 1995. Experimental study of anorthite dissolution and the relative mechanism of feldspar hydrolysis. *Geochimica et Cosmochimica Acta* 59:5039–5053.

Oelkers, E. H., Schott, J., and Devidal, J. L. 1994. The effect of aluminum, pH, and chemical affinity on the rates of aluminosilicate dissolution reactions. *Geochimica et Cosmochimica Acta* 58:2011–2024.

Ohlin, C. A., Villa, E. M., Rustad, J. R., and Casey, W. H. 2010. Dissolution of insulating oxide materials at the molecular scale. *Nature materials* 9:11–19.

Olson, L. L. and O'Melia, C. R. 1973. The interactions of Fe (III) with $Si(OH)_4$. *Journal of Inorganic and Nuclear Chemistry* 35:1977–1985.

Pizzarello, S. and Holmes, W. 2009. Nitrogen-containing compounds in two CR2 meteorites: ^{15}N composition, molecular distribution and precursor molecules. *Geochimica et Cosmochimica Acta* 73:2150–2162.

Porter, R. A. and Weber Jr, W. J. 1971. The interaction of silicic acid with iron (III) and uranyl ions in dilute aqueous solution. *Journal of Inorganic and Nuclear Chemistry* 33:2443–2449.

Reardon, E. J., Allison, G. B., and Fritz, P. 1979. Seasonal chemical and isotopic variations of soil CO2 at Trout Creek, Ontario. In *Developments in Water Science* (Vol. 12, pp. 355-371). Elsevier.

Richardson, S. M. 1981. Alteration of mesostasis in chondrules and aggregates from three C2 carbonaceous chondrites. *Earth and Planetary Science Letters* 52:67-75.

Rimstidt, J. D. 2015. Rate equations for sodium catalyzed quartz dissolution. *Geochimica et Cosmochimica Acta* 167:195–204.

Russell S. S., Zipfel J., Grossman Jeffrey N., and Grady M. M. 2002. The meteoritical bulletin, No. 86, 2002 July. *Meteoritics and Planetary Science* 37:A157–A184.

Schott, J. 1990. Modeling of the dissolution of strained and unstrained multiple oxides: The surface speciation approach. *Aquatic chemical kinetics* 337–366.

Schrader, D. L., Connolly, H. C., and Lauretta, D. S. 2010. On the nebular and aqueous signatures in the CR chondrites. *41st Lunar and Planetary Science Conference*. Abstract #1262.

Schrader D. L., Franchi I. A., Connolly H. C., Greenwood R. C., Lauretta D. S., and Gibson J. M. 2011. The formation and alteration of the Renazzo-like

carbonaceous chondrites I: Implications of bulk-oxygen isotopic composition. *Geochimica et Cosmochimica Acta* 75:308–325.

Scott, E. R. and Krot, A. N. 2005. Thermal processing of silicate dust in the solar nebula: clues from primitive chondrite matrices. *The Astrophysical Journal* 623:571–578.

Simon, S. B., Krot, A. N., & Nagashima, K. (2019). Oxygen and Al-Mg isotopic compositions of grossite-bearing refractory inclusions from CO3 chondrites. *Meteoritics & Planetary Science*, *54*(6), 1362-1378.

Skorina, T. and Tikhomirova, I. 2012. Alkali silicate binders: effect of SiO_2/Na_2O ratio and alkali metal ion type on the structure and mechanical properties. *Journal of Materials Science* 47:5050–5059.

Skorina, T. and Allanore, A. 2015. Aqueous alteration of potassium-bearing aluminosilicate minerals: from mechanism to processing. *Green Chemistry* 17:2123–2136.

Shmulovich, K., Graham, C., and Yardley, B. 2001. Quartz, albite and diopside solubilities in H_2O–NaCl and H_2O –CO_2 fluids at 0.5–0.9 GPa. *Contributions to Mineralogy and Petrology* 141:95–108.

Sjöberg, S. 1996. Silica in aqueous environments. *Journal of Non-Crystalline Solids* 196:51–57.

Stefánsson, A. and Arnórsson, S. 2000. Feldspar saturation state in natural waters. *Geochimica et Cosmochimica Acta* 64:2567–2584.

Stillings, L. L. and Brantley, S. L. 1995. Feldspar dissolution at 25°C and pH 3: Reaction stoichiometry and the effect of cations. *Geochimica et Cosmochimica Acta* 59:1483–1496.

Strandh, H., Pettersson, L. G., Sjöberg, L., and Wahlgren, U. 1997. Quantum chemical studies of the effects on silicate mineral dissolution rates by adsorption of alkali metals. *Geochimica et Cosmochimica Acta* 61:2577–2587.

Stoeber, W. 1967. Formation of silicic acid in aqueous suspensions of different silica modifications. In *Advances in Chemistry* (Vol. 67). Equilibrium concepts in Natural Water Systems, Chapter 7, pp. 161–182.

Takigawa, A., Furukawa, Y., Kimura, Y., Davidsson, B., and Nakamura, T. 2019. Exposure experiments of amorphous silicates and organics to cometary ice and vapor analogs. *The Astrophysical Journal* 881:27–35.

Tromans, D. and Meech, J. A. 2001. Enhanced dissolution of minerals: stored energy, amorphism and mechanical activation. *Minerals Engineering* 14:1359–1377.

Van Cappellen P, Qiu L. 1997a. Biogenic silica dissolution in sediments of the Southern Ocean. II. Kinetics. *Deep-Sea Res II* 44:1129–1149.

Van Cappellen P, Qiu L. 1997b. Biogenic silica dissolution in sediments of the Southern Ocean. I. Solubility. *Deep-Sea Res II* 44:1109–1128.

Van Schmus, W. R. and Wood, J. A. 1967. A chemical-petrologic classification for the chondritic meteorites. *Geochimica et Cosmochimica Acta* 31:747–765.

Vollmer, C., Pelka, M., Leitner, J., and Janssen, A. 2020. Amorphous silicates as a record of solar nebular and parent body processes—A transmission electron microscope study of fine-grained rims and matrix in three Antarctic CR chondrites. *Meteoritics & Planetary Science 55*:1491–1508.

Wallace, A. F., Gibbs, G. V., and Dove, P. M. 2010. Influence of ion-associated water on the hydrolysis of Si− O bonded interactions. *The Journal of Physical Chemistry A* 114:2534–2542.

Warfvinge, P. and Sverdrup, H. 1992. Calculating critical loads of acid deposition with PROFILE—a steady-state soil chemistry model. *Water, Air, and Soil Pollution* 63:119–143.

Weisberg M. K., Prinz M., Clayton R. N., and Mayeda T. K. 1993. The CR (Renazzo-type) carbonaceous chondrite group and its implications. *Geochimica et Cosmochimica Acta* 57:1567–1586.

Weisberg, M. K., Prinz, M., Clayton, R. N., Mayeda, T. K., Grady, M. M., and Pillinger, C. T. 1995. The CR chondrite clan. *Antarctic Meteorite Research* 8:11.

Weisberg, M. K., Connolly, H. C., and Ebel, D. S. 2004. Petrology and origin of amoeboid olivine aggregates in CR chondrites. *Meteoritics & Planetary Science* 39:1741–1753.

Weisberg M. K., McCoy T. J., and Krot A. N. 2006. Systematic and evaluation of meteorite classification. In *Meteorites and the Early Solar System II* (eds. D. S. Lauretta and H. Y. McSween). Pp. 19–52.

Weisberg, M. K. and Huber, H. 2007. The GRO 95577 CR1 chondrite and hydration of the CR parent body. *Meteoritics & Planetary Science* 42:1495–1503.

White, A. F. and Brantley, S. L. 2003. The effect of time on the weathering of silicate minerals: why do weathering rates differ in the laboratory and field? *Chemical Geology* 202:479–506.

Wild, B., Daval, D., Guyot, F., Knauss, K. G., Pollet-Villard, M., and Imfeld, G. 2016. pH-dependent control of feldspar dissolution rate by altered surface layers. *Chemical Geology* 442:148–159.

Wollast, R. and Chou, L. 1992. Surface reactions during the early stages of weathering of albite. *Geochimica et Cosmochimica Acta* 56:3113–3121.

Yang, Y., Min, Y., Lococo, J., and Jun, Y. S. 2014. Effects of Al/Si ordering on feldspar dissolution: Part I. Crystallographic control on the stoichiometry of dissolution reaction. *Geochimica et Cosmochimica Acta* 126:574–594.

Zhu, J., Tang, C., Wei, J., Li, Z., Laipan, M., He, H., Liang, X., Tao, Q., and Cai, L. 2018. Structural effects on dissolution of silica polymorphs in various solutions. *Inorganica Chimica Acta* 471:57–65.

Zolensky, M., Barrett, R., and Browning, L. 1993. Mineralogy and composition of matrix and chondrule rims in carbonaceous chondrites. *Geochimica et Cosmochimica Acta* 57: 3123–3148.

Zolotov, M. Y. 2012. Aqueous fluid composition in CI chondritic materials: Chemical equilibrium assessments in closed systems. *Icarus* 220:713–729.

CHAPTER 2

Phosphates associated with chondrules in the CR carbonaceous chondrite Queen Alexandra Range 99177: Evidence for solar nebular and parent body processes

In collaboration with:
Adrian J. Brearley

To be submitted for publication to:
Geochimica et Cosmochimica Acta

Abstract

Phosphorus-bearing minerals in carbonaceous chondrites are of primary importance because they record early aqueous alteration effects in the parent asteroid, and they potentially provide clues on solar nebular processes. However, P-bearing minerals in primitive carbonaceous chondrites have not been studied extensively and thus, their origins are not well understood. Recent work on Ca phosphates around the edges of type IIA chondrules in primitive CR and CM chondrites has shown that Ca phosphates are generally associated with aqueous alteration in the parent body. In the present study, we have characterized the different occurrences of Ca phosphates found in the least altered CR chondrite known, QUE 99177, to better understand their origins (solar nebular versus parent body) and their behavior during the earliest stages of aqueous alteration using SEM, EPMA, and TEM techniques. The following occurrences of Ca phosphates have been identified: (a) discrete layers at the periphery of mesostasis regions in type IIA chondrules at the interface with the matrix, consisting of elongate, submicron-sized rods of merrillite, (b) nanometer-sized grains of apatite or whitlockite distributed in a fine-grained rim around a type IIA chondrule, (c) abundant, micron-sized grains of apatite or

whitlockite homogeneously distributed in the matrix around a type IIA chondrule, (d) nanometer- to micron-sized grains in discrete regions at the interface between smooth rims around type I chondrules (whitlockite) and adjacent matrix (apatite), and (e) isolated grains of apatite (several microns in size) in the matrix. Our new data and a reappraisal of old data indicate they record a variety of formation processes. Primary (solar nebula) origins include (a) and (b), formed by quenching of Ca- and P-bearing melts in chondrules at the final stages of crystallization and by oxidation of schreibersite, respectively. Secondary (parent body) processes during aqueous alteration are inferred for the rest by (c) leaching of Ca, P, and alkalis from chondrule mesostasis during aqueous alteration and (d, e) oxidation of Fe,Ni metal grains in chondrule Silica-rich Igneous Rims (SIRs). Overall, our observations show that there is significant diversity in Ca phosphate occurrences within QUE 99177 and demonstrate, for the first time, that they formed by both primary solar nebular and secondary parent body processes. These results provide additional clues on the conditions within the protoplanetary disk in which type IIA chondrules formed and constrain the earliest stages of aqueous alteration in the CR chondrite parent body.

1. Introduction

Chondrites are the fossil record of the origin of our solar system, representing cosmic sediments and/or breccias composed of aggregates of material that formed in the solar protoplanetary disk during the first 1-5 million years (Ma) of its formation, which began 4,567 Ma ago (Amelin et al., 2002; Bouvier and Wadhwa, 2010). Almost all chondritic components formed by thermal processing of interstellar dust in the protoplanetary nebula before they accreted into asteroidal parent bodies (e.g., Scott and

Krot, 2005). Once the material was hosted in their parent asteroids, metamorphism and aqueous alteration were the two major secondary processes that affected asteroidal components (e.g., Zolensky and McSween, 1988; Brearley, 2006). Consequently, secondary processes have changed the primary nebular material to some degree. Among the chondrite groups, the CR carbonaceous chondrites are the most primitive chondrites known (see Chapter 1), which make them excellent candidates to study early solar system processes, especially the role of water. The CR chondrites escaped thermal metamorphism and exhibit a complete aqueous alteration progression, from nearly intact nebular materials to full replacement by secondary products (Abreu and Brearley, 2010; Harju et al., 2014; Howard et al., 2015). In addition, the relationships between chondrules and matrix appears best preserved in the CR chondrites, which means that chondrules have preserved an original textural relationship with the matrix, with no metamorphic overprint.

Studies aimed at deciphering aqueous alteration in chondrules have focused on type II chondrules because these chondrules contain glass that is among the most sensitive phase to aqueous alteration and the main source of P. Evidence of alteration of chondrule glass in the CR chondrites has previously been observed only in moderately to highly altered CR chondrites, such as Renazzo. However, more recent work on Ca- and P-bearing layers around the edges of type IIA chondrules in the two weakly altered CR chondrites, EET 92105 and EET 87770 (Burger and Brearley, 2004, 2005; Brearley and Burger, 2009), suggested that during the earliest stages of aqueous alteration in the parent body, Ca and P were leached from P-bearing chondrule glass in type IIA chondrules by aqueous fluids. These studies concluded that (i) Ca phosphates around type II chondrules

consist of whitlockite or apatite, secondary phases resulting from mass transfer of Ca and P from the chondrule glass into altered zones on chondrule edges and/or adjacent fine-grained matrices of CM and CR chondrites, (ii) Ca and P mobilization began very early during the aqueous alteration process, and (iii) a change in pH stabilized the precipitation of apatite at geochemical fronts at the edges of chondrules (Brearley, 2011).

Although EET 92105 and EET 87770, the two CR chondrites used in these studies, show a very limited degree of alteration, they are more altered than QUE 99177 and thus, they represent a more advanced stage of alteration. In the present study, we aim to determine if there is evidence that glass in type II chondrules in the least altered CR chondrite known, QUE 99177, also show signs of alteration.

Despite the low abundance of phosphorus in the solar nebula (Anders and Grevesse, 1989), P is an extremely important element for planetary evolution. For example, phosphides (schreibersite) are important in biology as they are minerals that corrode in water to form a variety of reactive P compounds (Pasek and Lauretta, 2005; Bryant and Kee, 2006), which are thought to be important for the biogeochemistry of prebiotic life on early Earth delivered during early meteorite bombardment (e.g., Oro, 1961; Anders, 1989; Pasek, 2017). Phosphides are commonly found in enstatite chondrites (e.g., see Weeks and Sears, 1985), because P is siderophile at low oxygen fugacities. Calcium phosphates (apatite, whitlockite, and merrillite) are also important as they can incorporate the volatile elements, Cl and F, as well as water (e.g., Boyce et al., 2010), and are also important hosts of Rare-Earth Elements (REEs) (e.g., Hughes et al., 1991). Therefore, the goals of the present study are to (i) identify the different occurrences of fine-grained Ca phosphates associated with type IIA (mainly) and type I

chondrules and their associated fine-grained matrix material, (ii) understand their formation mechanisms to discern between asteroidal and preaccretionary processes, and (iii) estimate the overall extent to which chondrules in QUE 99177 have been affected by hydrous fluids (e.g., elemental mass transport between chondrules and matrix).

2. Experimental techniques

Two 1-inch round, polished thin sections, numbers 18 and 19, of the least-altered CR chondrite known, QUE 99177 (Fig. 1.1 in Chapter 1), from the Antarctic Meteorite Collection at Johnson Space Center were examined. Complete thin section mosaics of QUE 99177 were obtained using backscattered electron (BSE) imaging and energy dispersive spectroscopy (EDS) X-ray mapping on a FEI Quanta 3D Dualbeam® Field Emission Gun Scanning Electron Microscope-Focused Ion Beam instrument (FEGSEM-FIB) equipped with an EDAX Genesis EDS system with an Apollo 40 SDD 40 mm^2 EDS detector at the University of New Mexico. Combined elemental RGB maps were created from spectral EDS X-ray maps to enable identification and location of Ca phosphates in QUE 99177. High-resolution X-ray spectral maps of selected areas of interest of type IIA chondrules and other regions of interest (e.g., the interfaces between type I chondrules and adjacent fine-grained matrix) were also acquired.

Quantitative analyses of chondrule mesostasis and Ca phosphates were obtained by wavelength-dispersive spectrometry (WDS) on a JEOL 8200 electron probe microanalyzer (EPMA) at the University of New Mexico operating at 15 kV with a 10 nA beam current and a 3 to 5 μm spot size. We used the following standards from the Taylor Company Standard block: olivine (Si, Mg, Fe), diopside (Si, Mg, Ca), spessartine (Mn),

albite (Na), orthoclase (K, Al), sphene (Ti), Wilberforce F-apatite (P), chromite (Cr), nickel metal (Ni), and pyrite (S).

Two focused ion beam (FIB) sections were prepared at the University of New Mexico for TEM analysis, one from a type IIA chondrule (Ch18, Fig. 1.1a in Chapter 1) and one from a type IB chondrule (Ch3, Fig. 1.1b in Chapter 1), using standard FIB sample preparation techniques (e.g., Mayer et al., 2007) on the FEI Quanta 3D Dualbeam FEG-SEM/FIB instrument with a final polish conducted at 5 kV to reduce surface amorphization. QUE 99177 is a breccia (Weisberg et al., 1993) and therefore, careful investigation at the planned FIB locations was required to establish that the interface between the selected mesostasis regions and matrices were original contacts and not modified by brecciation. The two FIB sections were extracted from selected locations, which exhibit different textures and contain Ca and P, detected by SEM-EDS elemental X-ray maps. The sections were imaged at the University of New Mexico using a JEOL 2010F Scanning Transmission Electron Microscope (STEM) operating at 200 kV in TEM and STEM modes using bright-field (BF) imaging and high-angle annular dark-field (HAADF) imaging, respectively. STEM-EDS maps in the two FIB sections were obtained over a ~2.3 μm x 1.8 μm regions using an Oxford Instrument AZtec EDS system equipped with an Oxford Instruments X-Max 80T 80 mm^2 SDD EDS detector. Quantitative analyses were obtained from the maps. Errors were all <5%. The analyses assume oxygen present according to oxide stoichiometry and normalized to 100 wt%.

3. Results

Figure 1.1 in Chapter 1 shows two BSE maps of the two thin sections of QUE 99177 in which type II chondrules are outlined in yellow and type I chondrules, in white.

Chondrules referred to in the text, figures, and tables are labeled in this figure by chondrule number. The abbreviation "Ch" followed by the number identifies the chondrule. The investigated type II chondrules are Ch18, Ch7, Ch5, and Ch2 (Fig. 1.1 in Chapter 1). The only type I chondrule studied in this chapter is Ch3 (Fig. 1.1b in Chapter 1).

3.1 Petrography of Ca phosphates

3.1.1. Calcium phosphates associated with type IIA chondrules

There are four type II chondrules (Ch18, Ch5, Ch7, Ch2, Fig. 2.1) in the two studied thin sections of QUE 99177, out a total of ~140 chondrules. Therefore, type II chondrules only represent about 3% of the total chondrules in QUE 99177. The four chondrules exhibit a porphyritic olivine (PO) texture and have roughly rounded to oval morphologies with sizes ranging from 400 μm to 1 mm (longest dimensions). Olivine phenocrysts exhibit normal zoning (Jones, 1990; Noguchi, 1995), seen by the higher contrast (bright regions at the edges of the crystals) indicating FeO enrichments towards the rim (e.g., Fig. 2.1). Mesostasis in these four type IIA chondrules is feldspathic in composition and preserves clear glass with Ca-bearing microcrystallites (Table 1.1 in Chapter 1). Mesostasis regions appear minimally altered, if at all, based on SEM imaging (e.g., pristine chondrule glass is preserved). Opaque minerals in the type IIA chondrules are mainly sulfides (pyrrhotite, and pentlandite) and chromite (Singerling and Brearley, 2015, 2018, 2020; Schrader et al., 2016; Singerling et al., 2016), and are present either as micron-sized grains or as larger grains or grain assemblages (~100-150 μm-size). Full thin section elemental X-ray map mosaics show that P and Ca are consistently present

surrounding type II chondrules, although their occurrences and abundances vary among them. The general characteristics of Ch18, Ch2, and Ch7 are briefly described below.

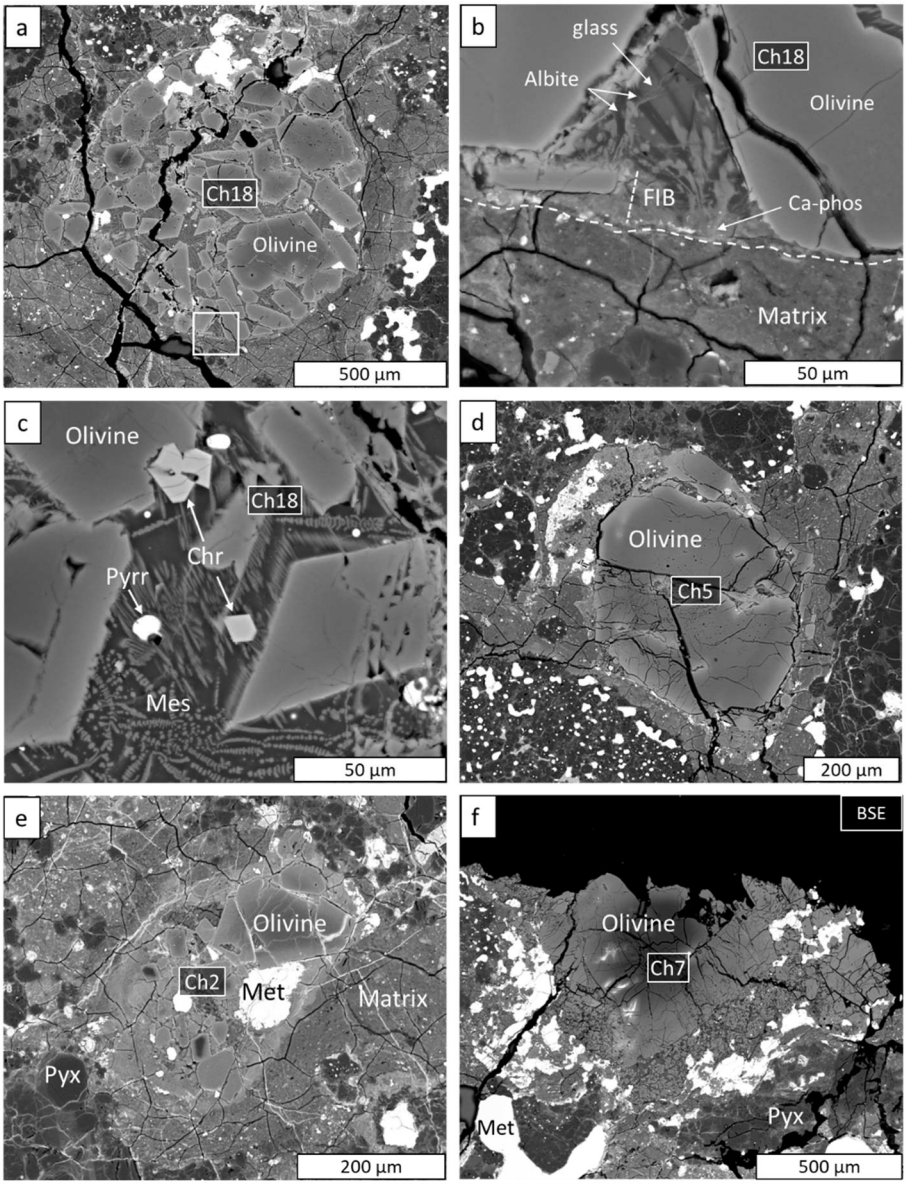

Figure 2.1. BSE images of type IIA chondrules in QUE 99177. a) Chondrule 18 is a rounded, 1 mm-sized PO type IIA chondrule exhibiting Ca and P enrichments around its periphery, which have been examined by TEM (square region in (b)) and elemental X-ray maps (Fig. 2.2). b) Close-up image of the square region in (a) showing the complex mesostasis region where the FIB section was extracted. The mesostasis contains clear glass, acicular albite crystallites, and Ca phosphates. c) Close-up image of chondrule 18 showing that the mesostasis regions between olivine phenocrysts contain glass with quenched crystallites, 10-20 µm-sized pyrrhotites, and chromites. *(Caption continues on the following page).*

Figure 2.1. *(Caption continued from the previous page).* d) Chondrule 5 is a PO type IIA chondrule that contains a lower portion of mesostasis regions and larger porphyritic olivines. It is surrounded by a fine-grained rim. e) Chondrule 2 is an oval PO type IIA sulfide-bearing chondrule, 400 μm in its longest dimension, and is surrounded by a fine-grained rim with abundant Ca phosphates (Fig. 2.3). (f) Chondrule 7 is a type IIA chondrule consisting of a single, large olivine grain surrounded by fine-grained FeO-rich olivine, Na, K-rich mesostasis regions, Ca phosphates, chromites, and sulfides (Figs. 2.4 and 2.5).

3.1.1.1 Chondrule 18

Chondrule 18 (Ch18) is a large (~1 mm in diameter), rounded, sulfide-bearing PO chondrule that is crosscut by a fracture (Fig. 2.1a). Quantitative compositions of mesostasis regions in this chondrule were measured by EPMA (Table 2.1). Chondrule mesostasis consists of clear Na-, Ca-, K-rich glass, isotropic under crossed polarized light, that contains randomly oriented, acicular, quench crystallites of feldspar (Figs. 2.1b.c, 2.2c,d). EPMA results show widespread heterogeneity in Na, varying from 1.22 to 12.14 wt% Na_2O, with an average of 8.15 wt% Na_2O, and in Ca, ranging from 0.91 to 6.26 wt% CaO, with an average of 2 wt% CaO. Potassium content is roughly constant (1.2 wt% K_2O average), and P varies from 0.59 up to 4.27 wt% P_2O_5, with an average of 1.11 wt% P_2O_5 (Table 2.1). The BSE-Ca-P and Al-Ca-P X-ray maps (Fig. 2.2a,d) clearly illustrate that Ca and P form a continuous, thin (5-20 μm in width) layer around the chondrule perimeter. The Ca-phosphate layer is included inside the mesostasis region. The interface between the chondrule and the matrix is sharp, and the nearby fine-grained matrix material adjacent to the chondrule does not show evidence of Ca and P enrichments, but shows Fe and S depletions across a distance of 25-40 μm from the chondrule edge (Fig. 2.2e,f).

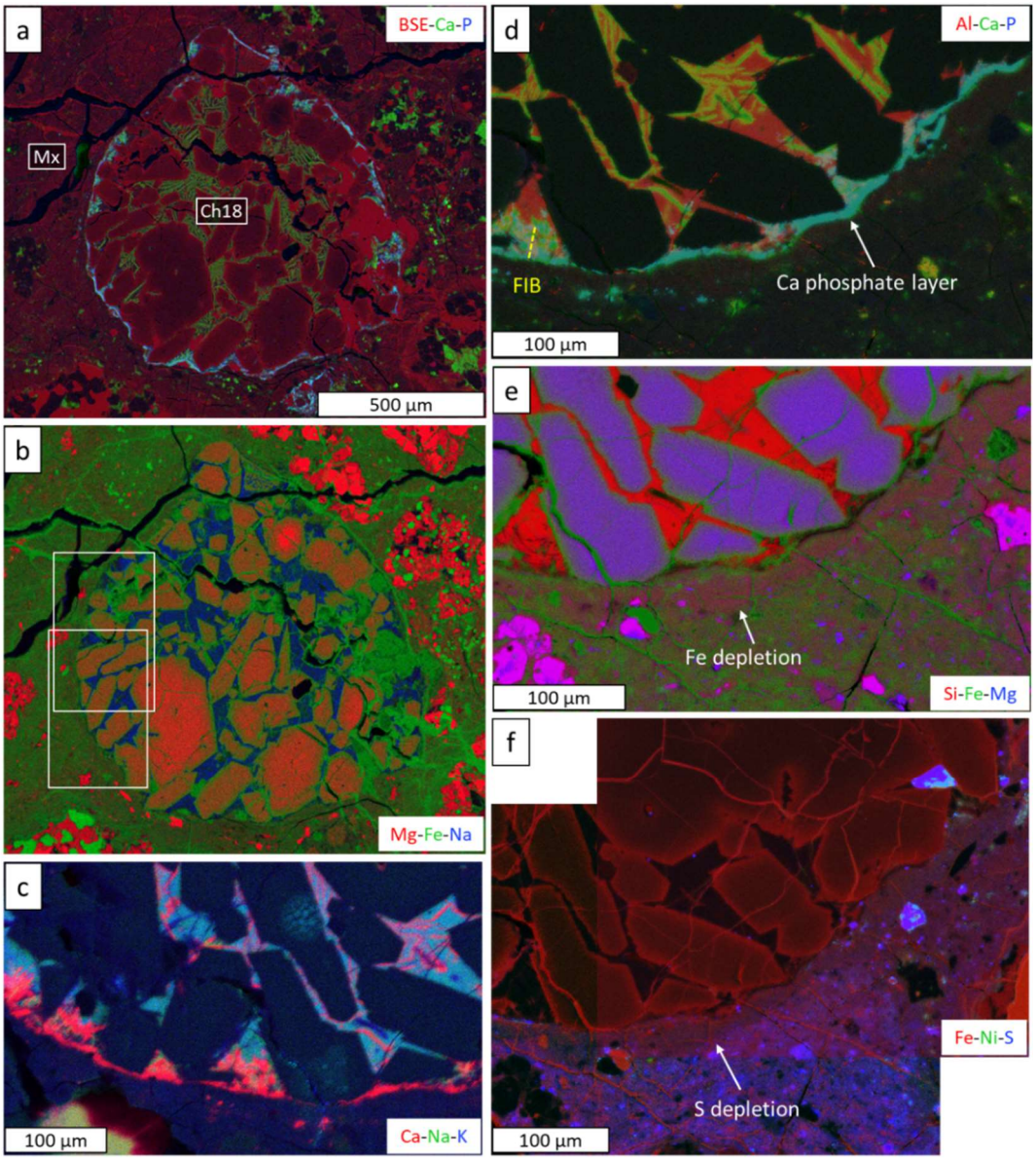

Figure 2.2. SEM-EDS elemental RGB X-ray maps of the type IIA chondrule 18 (Ch18). (a) BSE-Ca-P map of the chondrule showing the Ca- and P-enrichment in the mesostasis regions around the periphery of the chondrule. The Mg-Fe-Na map in (b) shows normal, concentric zoning in olivine phenocrysts, which are Mg-rich in the cores (in red) and Fe-richer at the rims (in green), and the chondrule mesostasis is highly enriched in Na. The two white squares outline the location of close-up maps shown in (c-f). Alkali content (Na-Ca-K) map in (c) of the region marked in (b) shows that mesostasis glass is also enriched in K and contains Ca-rich crystallites. d) Al-Ca-P map of the region marked in (b) shows that the Ca- and P-rich phase (in aquamarine) is located inside the chondrule mesostasis, exactly at the edge of the chondrule, and the interface with the matrix is sharp. The location of the FIB section is shown in a dashed yellow line. The Si-Fe-Mg map in (e) shows that the matrix adjacent to the chondrule is depleted in Fe across a 20-25 µm zone from the chondrule edge. Finally, the Fe-Ni-S map in (f) illustrates S depletions in the matrix correlated with depletions in Fe in (e).

Table 2.1. Individual analyses of chondrule mesostasis glass compositions obtained by EPMA (oxides wt%), using a 3-5 µm-sized beam, in the type IIA Ch18 containing a narrow Ca-P-enrichment at its periphery. Analysis #3 (FIB) corresponds to the location later studied by TEM.

Oxides wt%	1	2	3 FIB	4	5	6	7	8	9	10	13	**Mean**
SiO_2	57.72	59.16	60.15	58.49	58.74	56.36	57.79	51.11	59.95	55.82	56.82	**57.47**
P_2O_5	1.44	0.99	0.68	0.97	0.59	0.58	0.66	0.79	0.62	4.27	0.61	**1.11**
TiO_2	0.37	0.45	0.37	0.49	0.53	0.33	0.39	0.33	0.44	0.21	0.40	**0.39**
Al_2O_3	14.23	13.98	15.63	13.07	13.26	14.56	14.87	13.75	15.58	16.20	16.64	**14.71**
Cr_2O_3	n.d.	n.d.	0.03	0.01	0.04	0.04	n.d.	0.02	n.d.	0.02	0.01	**0.02**
FeO	14.11	13.01	8.51	13.32	12.39	13.51	14.53	18.79	13.03	5.06	11.87	**12.56**
MnO	0.29	0.30	0.20	0.31	0.25	0.22	0.19	0.24	0.23	0.09	0.22	**0.23**
MgO	0.51	0.59	0.53	0.91	0.75	0.32	0.48	0.41	0.36	0.83	0.44	**0.56**
CaO	2.09	1.36	2.73	1.66	1.90	1.11	1.38	0.91	1.35	6.26	1.01	**1.98**
Na_2O	4.38	6.23	9.82	7.40	11.96	11.20	7.31	8.79	1.22	9.22	12.14	**8.15**
K_2O	1.22	1.30	0.64	1.34	1.37	1.34	1.34	1.25	1.32	0.44	1.39	**1.18**
NiO	n.d.	0.03	n.d.	n.d.	n.d.	0.37	0.08	0.12	n.d.	0.01	0.02	**0.06**
Total	96.37	97.41	99.31	97.97	101.78	99.93	99.00	96.51	94.11	98.43	101.57	**98.40**

n.d. = not detected

3.1.1.2. Chondrule 2

Chondrule 2 (Ch2) is a type IIA PO chondrule that shows pervasive terrestrial alteration and is surrounded by a fine-grained rim (Fig. 2.1e). Olivine grains are Mg-rich, normally zoned, and X-ray maps show significant depletions in the alkalis Na and K, but locally, some regions with elevated Na and K are still present (Fig. 2.3b-d). Silica is also lower in the alkali-free regions of the mesostasis (Fig. 2.3e, regions of mesostasis in green), whereas Fe is higher (Fig. 2.3g). The observations suggest that most of the mesostasis glass in this chondrule has undergone aqueous alteration. There are two types of Ca phosphates associated with Ch2. Inside the chondrule, Ca-bearing phosphates are present further into the interior of the chondrule compared to Ch18, within microcrystalline mesostasis regions rather than at the mesostasis chondrule periphery. These Ca phosphates exhibit fine-grained dendritic morphologies (dendrites are ~5-10 µm in length), are in very low abundance, and contain Na, consistent with merrillite

composition (Fig. 2.3f). Outside the chondrule, abundant Ca phosphates occur as nanometer- to micron-sized grains, homogeneously distributed in the fine-grained rim, across a wide (~25-100 µm in width) region around the chondrule (Fig. 2.3a). In addition, abundant hot spots of Ca are present in the mesostasis, mostly concentrated at the outer parts of the chondrule and around the large sulfide grain inside the chondrule (Fig. 2.3b,d), consistent with Ca-rich pyroxenes of quench origin, based on their textures. The large (~180 µm) sulfide grain consists of a complex pyrrhotite-pentlandite intergrowth (Fig. 2.3g). A few micron-sized chromites are also present within the chondrule (Fig. 2.3f in green).

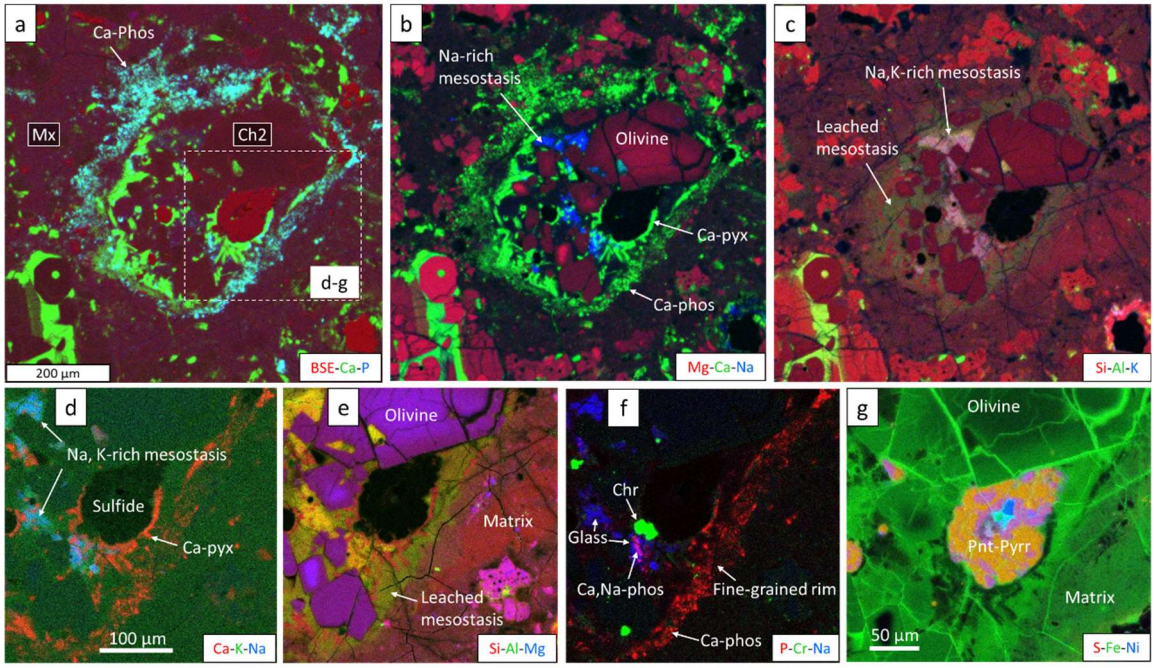

Figure 2.3. SEM-EDS elemental RGB X-ray maps of type IIA chondrule 2 (Ch2) in QUE 99177,18. a) BSE-Ca-P map showing the Ca-phosphate grain distribution in the fine-grained rim around Ch2. b) Mg-Ca-Na map showing that olivine is normally zoned, and that some regions of the mesostasis are highly enriched in Na (blue), while Ca is concentrated in hot spots near the edges of the chondrule and around the sulfide grain. c) Si-Al-K map of the full chondrule showing that K correlates with Na in (b) and that some regions of the mesostasis are depleted in K and Na, suggesting that they have been leached due to aqueous alteration. *(Caption continues on the following page).*

Figure 2.3. *(Caption continued from the previous page).* d) Close-up Ca-K-Na map of the dashed square region marked in (a) showing that the glass is Na- and K-rich and that the Ca-rich pyroxene (Ca-pyx) has quenched textures around the sulfide grain. e) Close-up Si-Al-Mg map showing altered mesostasis in green (alkali-free, Si-poor, and Fe-rich), Ca-rich pyroxene with quench textures in red, alkali-rich mesostasis in yellow, and strongly zoned olivine grains in purple. f) Close-up P-Cr-Na map showing that P (in red) is found within the fine-grained rim, probably corresponding to apatite or whitlockite, and a different, Ca-, Na-rich phosphate, probably corresponding to merrillite, is found inside the chondrule mesostasis at the outer parts of the chondrule. Micron-sized grains of chromite (Chr) are also shown in green. g) Close-up S-Fe-Ni map showing the complex chemical distribution of the sulfide grain assemblage, the Fe-enrichment within the leached mesostasis region, and terrestrial alteration veins.

3.1.1.3. Chondrule 7

Chondrule 7 (Ch7) is a type IIA chondrule, ~1 mm in its longest dimension, that appears minimally terrestrially altered (Fig. 2.1f). It is dominated by a single, large (~800 μm), normally zoned olivine phenocryst in addition to smaller grains of olivine (up to ~100 μm size), interstitial mesostasis, Ca-rich pyroxene grains (~20 μm size), Ca phosphates, sulfides, and micron-sized chromite grains. The elemental distribution of these phases is shown in Figure 2.4. Figure 2.5 shows RGB elemental X-ray maps of three selected regions in Ch7 (see Fig. 2.4a for locations) illustrating the distribution of different mineral phases and Ca phosphates around Ch7. Chondrule 7 shares similarities with other type IIA chondrules studied here. It contains a mesostasis that is highly enriched in alkalis (Na and K), Ca is mainly present within abundant Ca-rich pyroxenes that are evenly distributed around the outer parts of the chondrule (Figs. 2.4d, 2.5c,h), and Ca phosphates are present along the chondrule periphery as well-defined layers (Figs. 2.4f, 2.5a,b,e,h). The opaque phases consist of sulfides (pyrrhotite-pentlandite intergrowths) and chromite (Figs. 2.4c, 2.5i). Nickel-bearing sulfides (~120 μm in size) are anhedral and highly abundant at the outer regions of the chondrule (Fig. 2.4c), and chromite grains are micron-sized and randomly distributed throughout (Fig. 2.4d).

Calcium phosphates in Ch7 occur in two different textural occurrences: as narrow, discontinuous, curved layers within the mesostasis regions around the perimeter of the chondrule (Ca-phos (1) in Fig. 2.5), and as nanometer-sized grains ubiquitously distributed in the fine-grained matrix (10-60 μm-size) around the chondrule exterior (Ca-phos (2) in Fig. 2.5). It is possible that the matrix is part of a fine-grained rim that was disrupted by brecciation. The first occurrence is similar to Ca phosphates described in Ch18 (Fig. 2.2), but unlike Ch18, instead of a single, continuous layer outlining the periphery of the chondrule, several Ca phosphates occur as shorter bands (100-150 μm-long) (Fig. 2.4f, 2.5a,e) within the mesostasis regions around the irregularly-shaped chondrule periphery. Elemental X-ray maps show that layers of Ca phosphates in Ch7 contain Na (Fig. 2.5b,e,i), consistent with merrillite compositions and similar to Ch18 and the phosphate within a mesostasis region in Ch2. The second occurrence of Ca phosphates is located outside the chondrule, in the fine-grained rim. Calcium phosphate grains outside the chondrule lack Na and halogens, but more accurate compositions are difficult to resolve with SEM-EDS due to their small grain sizes.

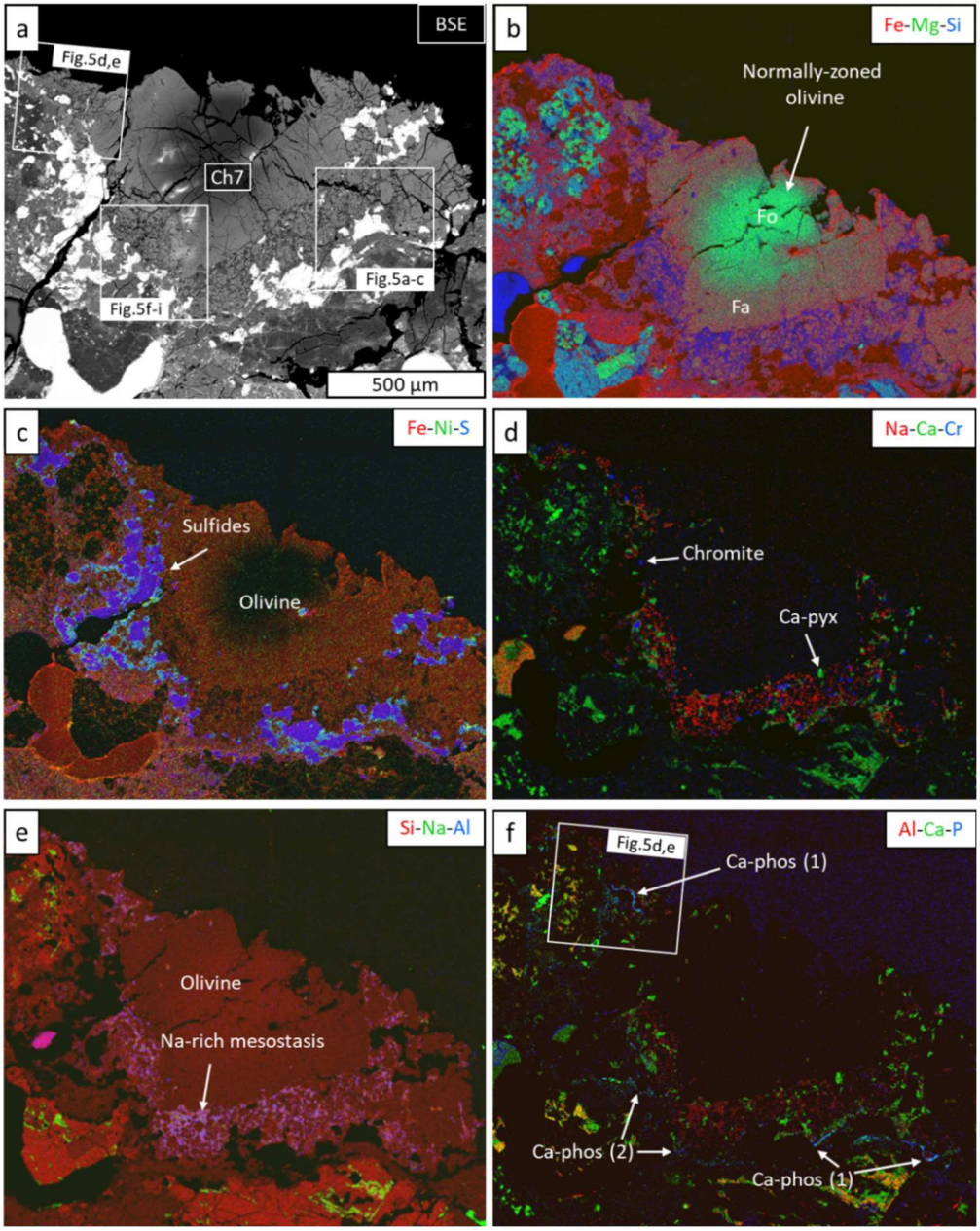

Figure 2.4. BSE image and corresponding elemental RGB X-ray maps of type IIA chondrule 7 (Ch7) in QUE 99177,18. Chondrule 7 is largely dominated by a single olivine phenocryst, 1 mm in its maximum dimension. The olivine is strongly zoned (b) and is surrounded by a thick (~150-300 µm-wide) layer that contains small (~20 µm-size average), FeO-rich olivines (b), Ni-rich sulfides (c), interstitial Na-rich glass (d,e), and micron-sized chromites, homogeneously distributed throughout the layer of fine-grained olivine (d). Small, Ca-rich pyroxene (Ca-pyx) grains are also randomly distributed in the rim (d). f) Al-Ca-P map showing Ca-phosphate layers in blue, designated Ca-phos (1), which are discontinuously distributed within mesostasis regions around the chondrule periphery, exactly at the interface with the matrix, as thin (a few microns), elongated bands (up to 150 µm-long). Nanometer-sized grains of Ca phosphates, designated Ca-phos (2), are also distributed in diffuse regions outside the chondrule, shown in Fig. 2.5.

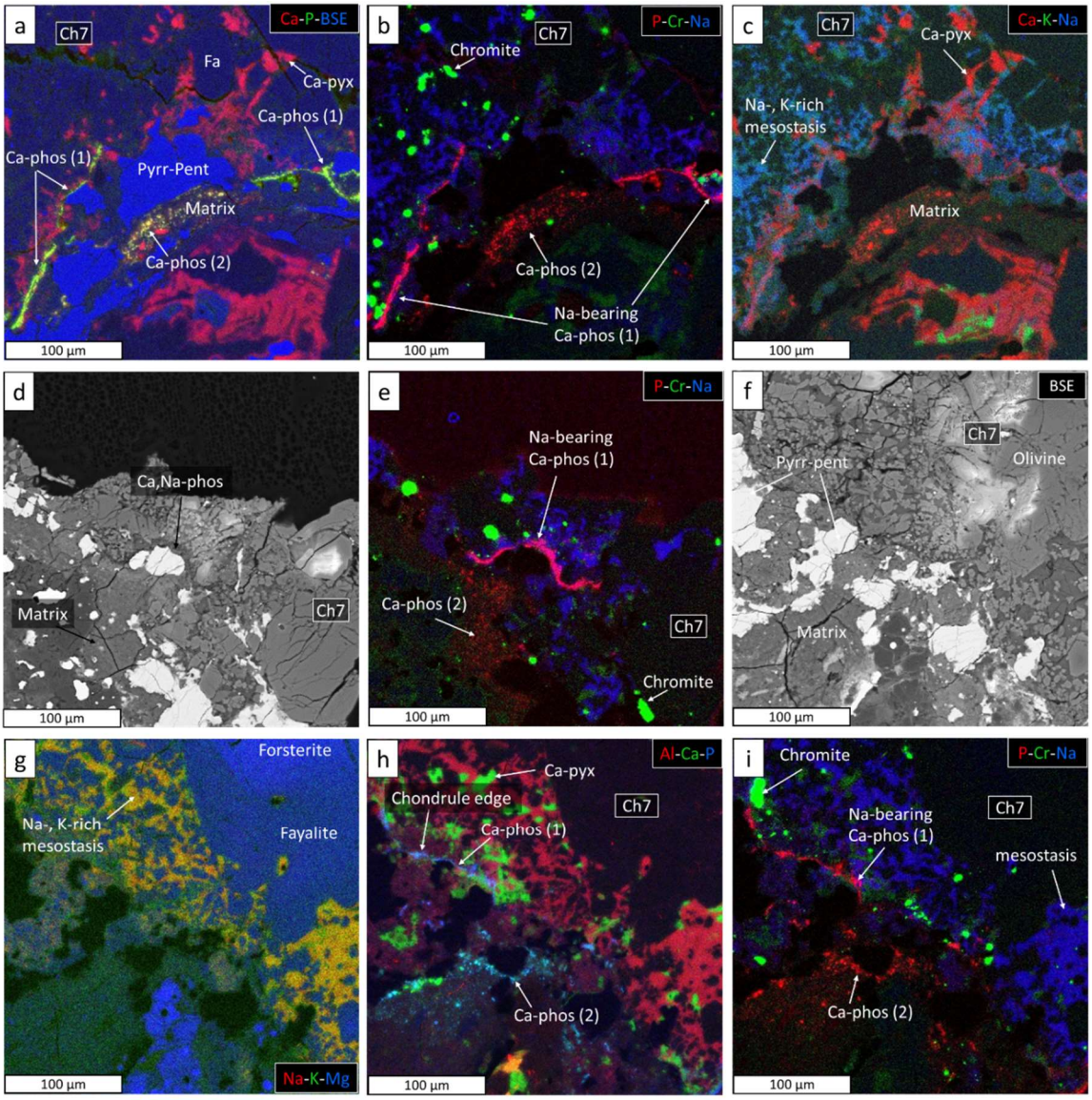

Figure 2.5. High magnification BSE and corresponding elemental RGB X-ray maps of three regions in type IIA Ch7 (white squares in Fig. 2.4) showing the detailed, fine-scale occurrences of Ca phosphates. a) Ca-P-BSE image showing the distribution of Ca phosphates in yellow in this part of the chondrule. b) P-Cr-Na map of the same region in (a) showing that Ca phosphates are of two different types: Na-bearing Ca phosphates (Ca-phos (1)) are distributed in discontinuous layers inside the mesostasis regions around the perimeter of the chondrule, and nanometer-sized Ca phosphates (Ca-phos (2)) occur outside the chondrule, in the fine-grained rim. Chromite grains are shown in green. c) Ca-K-Na map of the same region in (a) showing that mesostasis regions around the large olivine grain are Na- and K-rich, with associated Ca-rich pyroxenes (Ca-pyx). d) BSE image of a region showing the interface between the olivine-rich chondrule and the fine-grained matrix. *(Caption continues on the following page).*

Figure 2.5. *(Caption continued from the previous page).* e) P-Cr-Na map of (d) showing the two different occurrences of P-bearing phases in this region: a Na-bearing Ca phosphate (in pink) that is in a curved layer within a mesostasis region outlining the periphery of the chondrule (Ca-phos (1)), and a Ca-rich phosphate (in red), occurring as abundant nanometer-sized grains in the adjacent matrix (Ca-phos (2)). Chromite grains are shown in green. f) BSE image of a different region showing the large olivine grain that dominates the chondrule, the mesostasis regions, the sulfide-rich outer region, and the fine-grained rim material. g) Na-K-Mg map showing that the mesostasis is enriched in the alkalis, K and Na and a rather abrupt change in olivine composition (zoning) in the large clast. h) Al-Ca-P map of region in (f) showing the occurrence of Ca phosphates around Ch7 in light blue. Ca-rich pyroxenes are shown in green and mesostasis in red. i) P-Cr-Na map of the region in (f) showing the same two occurrences of Ca phosphates as shown earlier in (b) and (e). Chromite grains are shown in green and Na-rich mesostasis in blue.

3.1.2. Calcium phosphates around type I chondrules

Calcium phosphates have also been identified around type I chondrules in QUE 99177, associated with smooth rims, a type of rim (~25 μm-width) that formed by aqueous alteration of the chondrule SIR (see Chapter 1). Unlike phosphates around type IIA chondrules, phosphates associated with type I chondrules are present only around a few chondrules (type A or B) as single, rounded grains (~2-5 μm-size), decorating small, discrete regions (≤5 μm) at the interface between smooth rims and matrix (Fig. 2.6a,b) or inside smooth rims (Fig. 2.6c,d). Calcium carbonates are commonly associated with this type of phosphate (Fig. 2,6b,d).

Although terrestrial alteration in the sample is pervasive (Russell et al., 2002), some (P-bearing) Fe,Ni metal grains (~3 - 10 μm in size) in smooth rims and SIRs are partially or fully altered to a lower Z-contrast phase, but crosscutting terrestrial veins are absent, suggesting that alteration could be pre-terrestrial. The altered metal grains within the SIRs that lack visible terrestrial weathering veins are altered close to or within the smooth rims but unaltered towards the interior of the chondrules. The altered metal grains preserve their original bleb morphologies (red arrows in Fig. 2.6e,f).

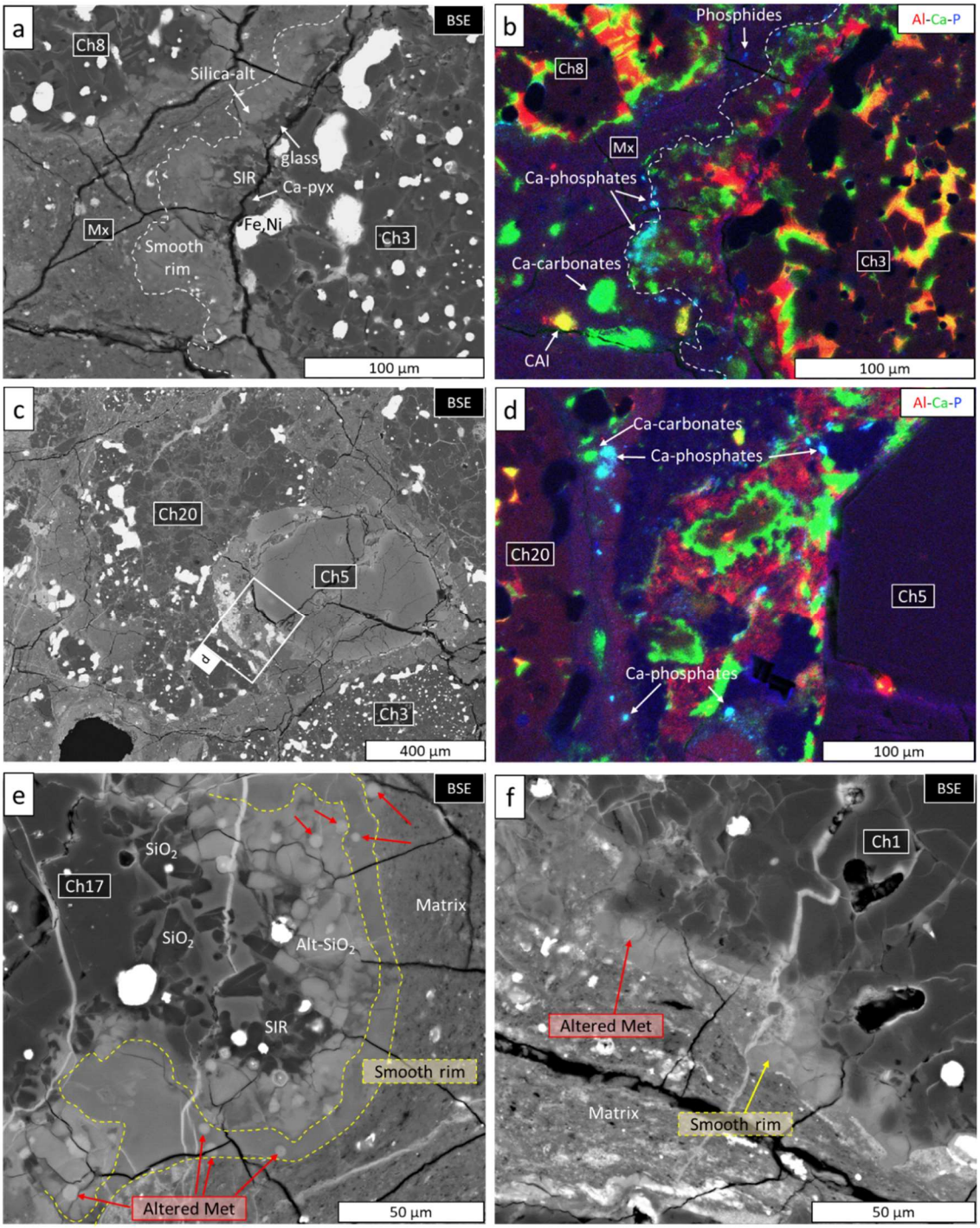

Figure 2.6. SEM images of Ca phosphates around type IA chondrules in QUE 99177. a) BSE image and corresponding RGB elemental X-ray map for Al-Ca-P in (b) showing the smooth rim around chondrule 3 where Ca phosphates have been identified at the interface between the smooth rim and the matrix. Nanometer-sized grains of Ni-bearing phosphides are also present in the matrix. *(Caption continues on the following page).*

Figure 2.6. *(Caption continued from the previous page).* c) BSE image showing a typical region affected by brecciation in which a type IA chondrule (Ch20) is molded around a type IIA chondrule (Ch5). The region marked with a white square is shown in (d). d) Al-Ca-P map showing Ca phosphates associated with Ca carbonates that are randomly distributed in the fine-grained rims of Ch5 and Ch20, indicating that they formed after brecciation. e) and f) BSE images of smooth rims around Ch17 and Ch1, respectively, showing that Fe,Ni metal blebs within the smooth rim are fully altered to a lower Z-contrast phase (red arrows). Altered metal blebs preserve their original morphologies and no terrestrial alteration veins crosscut them.

3.1.3 Isolated Ca phosphates and Ni phosphides in the matrix

Calcium phosphate grains of similar sizes to those found in smooth rims or at their interfaces with their adjacent matrices are also observed in discrete regions within the matrix, at distances up to ~150 μm from chondrule edges (e.g., Fig. 2.7a,b). These Ca-phosphate grains typically form aggregates with Ca carbonates (Fig. 2.7b) and nanometer-sized grains of Ni-bearing sulfides (pentlandite?) (Fig. 2.7c,d). As shown in Figure 2.7b, the abundance of Ca carbonates in some regions of the matrix is higher than average (Abreu and Brearley, 2010; Le Guillou et al., 2015; Abreu, 2016; Howard et al. 2015; Changela et al., 2018). With respect to Z-contrast in BSE imaging, Ca phosphates are not very different from Ca carbonates, and these phases are not very different from the groundmass of fine-grained matrix materials (e.g., amorphous silicates) thus, elemental X-ray maps are required to discriminate them. SEM-EDS X-ray elemental maps show that Ca and P in isolated phosphates in the matrix are not correlated with Na. Quantitative EPMA analyses of Ca-phosphate grains adjacent to Ch11 (Fig. 2.7a,b) are given in Table 2.2. However, these grains are small (< 10 microns), and the electron beam excitation volume is similar to the sizes of the grains, resulting in X-ray contributions from adjacent phases in the matrix within the analyses. Although the Na content is rather high (up to 2.13 wt% Na_2O), the CaO/P_2O_5 ratio (1.43 for the best

analysis) suggests these phases are consistent with apatite compositions (CaO/P_2O_5 ~ 1.32), rather than merrillite or whitlockite (CaO/P_2O_5 ~ 1.02).

Elemental RGB X-ray maps and SEM-EDS analyses of selected regions in QUE 99177 also show the presence of nanometer to micron-sized Ni-bearing phosphides in the matrix (Fig. 2.7c). Nickel-bearing phosphides, ~1-7 μm in size, are randomly distributed throughout the fine-grained matrix (Fig. 27e,f). However, it was not possible to determine accurate chemical compositions for these grains by EPMA due to their small grain sizes.

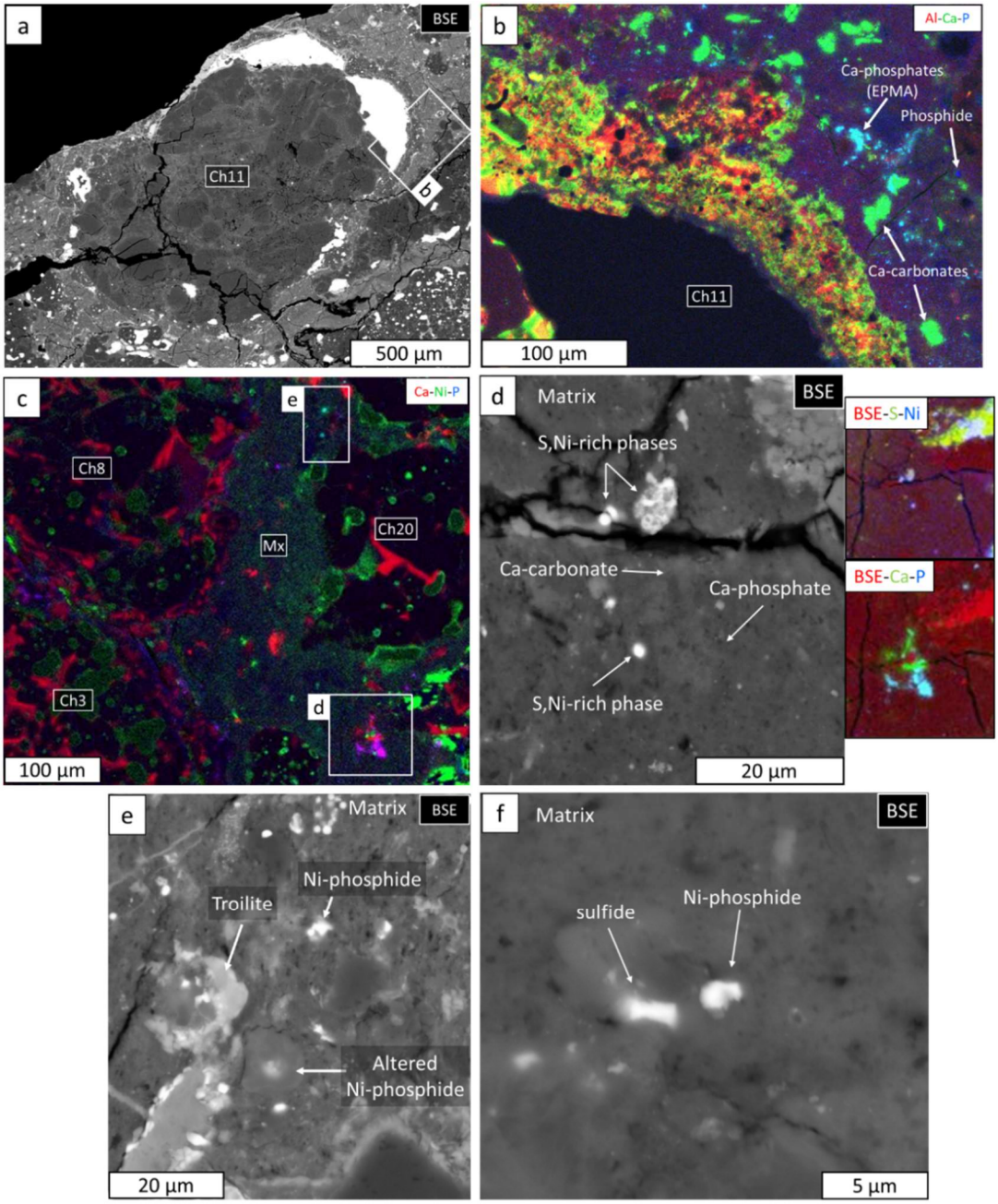

Figure 2.7. BSE images and elemental RGB X-ray maps of Ca phosphates and Ni phosphides identified in the matrix of QUE 99177. a) BSE image of chondrule 11 (Ch11), a type IA POP chondrule with an Fe,Ni-bearing mantle showing the region of the Al-Ca-P map in (b) (white square). b) Al-Ca-P map showing the fine-grained rim around Ch11, Ca phosphates, and Ca carbonates in the matrix. c) Ca-Ni-P map of a large region in QUE 99177 showing the locations of Ca phosphates associated with Ca carbonates (d) and two Ni phosphide grains (e) located in the matrix. d) High magnification BSE image of the square region marked in (d) along with BSE-Ca-P and BSE-S-Ni maps showing the Ca phosphate associated with Ca carbonate and sulfides. e) BSE image of the two Ni-phosphide grains, one of them showing incipient alteration. f) BSE image of a Ni phosphide and a sulfide grain, 2-3 µm in size, in the matrix.

Table 2.2. Individual EPMA analyses (oxides wt%) of isolated Ca phosphates in the matrix close to Ch11 (Fig. 2.7b), mixed with matrix material.

Oxides wt%	G1	G2	G3
SiO_2	18.99	20.53	15.44
P_2O_5	8.70	6.60	12.15
TiO_2	0.03	0.07	0.05
Al_2O_3	1.29	1.21	1.28
Cr_2O_3	0.20	0.34	0.22
FeO	23.41	27.48	25.34
MnO	10.29	11.96	7.67
MgO	0.19	0.22	0.21
CaO	15.14	9.58	17.37
Na_2O	1.70	1.53	2.13
K_2O	0.10	0.11	0.11
SO_3	4.45	7.34	6.14
NiO	0.72	1.02	0.79
Total	85.22	87.99	88.90
CaO/P_2O_5	1.74	1.45	1.43

3.2. TEM work

3.2.1. TEM observations on Ca phosphates in the type IIA Ch18

The detailed microstructures and mineralogy of the phosphate minerals detected with EDS-SEM elemental X-ray maps in Ch18 (Fig. 2.2d) were investigated in detail using TEM. Calcium phosphates occur at the outer edges of the mesostasis regions in contact with the fine-grained matrix material, forming a nearly continuous layer around the perimeter of the chondrule (Figs. 2.2a). The FIB section was extracted from a region of the chondrule that consists of clear glass, acicular crystallites of Na-rich plagioclase, and Ca phosphates within the chondrule at the interface with the matrix, based on SEM-EDS analyses (Fig. 2.1b).

A HAADF STEM mosaic of the extracted FIB section and selected STEM X-ray map areas are presented in Figure 2.8. There is no evidence of terrestrial weathering in the FIB section. Transmission electron microscopy analyses (EDS-STEM analyses,

STEM elemental X-ray maps, and SAED patterns) indicate that the Ca- and P-bearing phase is the anhydrous Ca-phosphate mineral, merrillite rather than apatite or whitlockite (Fig. 2.8a, Table 2.3). Phosphates are abundant in the FIB section, well-crystallized, and exhibit elongated, rounded, rod morphologies, 0.3-0.5 μm in width by 1-2 μm in length. They preserve crystallographic continuity in two different orientations, approximately perpendicular and parallel to the FIB cut (Fig. 2.8a). The rods that are cut perpendicular to the elongation direction appear circular in shape and are more abundant in the upper and center regions of the FIB section, while grains at the right-hand side and on the lower-left hand side of the FIB section exhibit more elongated morphologies (Fig. 2.8a). Dark-field STEM images show that merrillite rods contain abundant nanopores (< 100 nm) and approximately 90% of them have alteration rims (~50 nm width) around them (Fig. 2.8d). The altered rims have a lower-Z contrast in DF-STEM images and STEM X-ray maps show that they contain Fe and S (Fig. 2.8f,g). In addition, a merrillite grain appears fully altered ('Alt. grain' in Fig. 2.8d). It contains Fe (45.8 wt% FeO), Al (17.5 wt% Al_2O_3), Si (12.5 wt% SiO_2), Na (11.3 wt% Na_2O), S (5.4 wt% SO_3), P (4.3 wt% P_2O_5), Mg (1.6 MgO), and trace Ca, Ni, K, Cr, and Ti (Table 2.3B). Merrillite rods can also occur intergrown with diopside, identified based on SAED patterns and EDS analyses (Fig. 2.8a, Table 2.3B). Merrillite compositions in this intergrowth are given in Table 2.3 for comparison with isolated merrillite grains that crystallized outside. Iron-rich olivine (Fa_{63}) (Table 2.3B) occupies about 50% of the FIB section area and some merrillite grains form long arrays completely embedded in the olivine. About 50% of the interstitial regions between merrillite rods consist of a featureless, lower Z-contrast phase in DF-STEM images (Fig. 2.8b), identified as albite, based on electron diffraction

patterns (Fig. 2.8a), EDS-STEM analyses (Table 2.3B), and elemental X-ray maps (Fig. 2.8f,g). The albite has a composition of $Ab_{70-92}An_{7-9}Or_{2-3}$ (Table 2.3B), but the measured Na contents in albite are low, ranging between 5.6 and 8.6 wt% Na_2O, due to Na volatilization by the electron beam. About 40% of the interstitial regions consist of a fine-grained, fibrous (50-100 nm in size), high Z-contrast phase identified as cronstedtite, based on d-spacings measurements from diffraction ring patterns (Fig. 2.8b,c). Cronstedtite fibers have variable orientations (Fig. 2.8e), indicated by ring-diffraction patterns (Fig. 2.8c) and the interface between this phase and albite is sharp, but irregular (Fig. 2.8g). STEM-EDS analyses of cronstedtite are given in Table 2.3B. Finally, some interstitial regions are filled with a featureless, intermediate Z-contrast phase (Fig. 2.8d) with a composition consistent with Fe-rich phyllosilicate, possibly saponite ('Sap', Table 2.3B). An iron sulfide grain (0.5 μm in size) also occurs associated with regions of cronstedtite and merrillite (Fig. 2.8g). No evidence of chondrule glass was found in this FIB section.

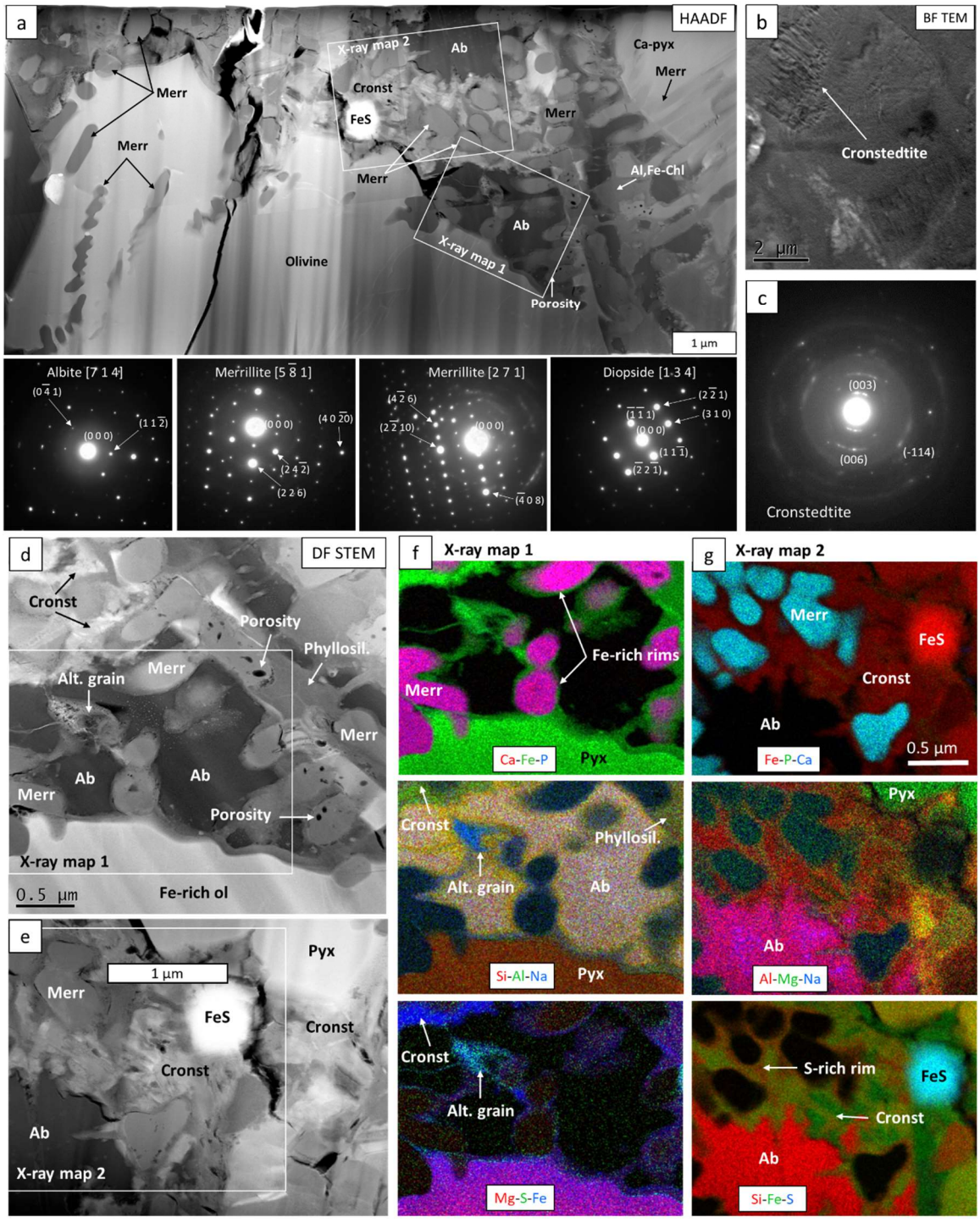

Figure 2.8. TEM images from the FIB section extracted in the Ca-phosphate layer around the type IIA Ch18 (location shown in Fig. 2.1b). a) HAADF mosaic of the FIB section showing a high abundance of Ca phosphates identified as merrillite (Merr), some of them intergrown with Fe-rich olivine and Ca-rich pyroxene. Albite and cronstedtite are found interstitial to Ca phosphates. An iron sulfide grain is located in the upper part of the FIB section. Electron diffraction patterns of albite, merrillite, and diopside are also shown. *(Figure caption continues on the following page).*

Figure 2.8. *(Caption continued from previous page).* b) Bright-field TEM image of cronstedtite along with (c), its SAED ring pattern. d) Dark-field STEM image of a higher magnification region in (a) showing that merrillite contains porosity and alteration rims. One phosphate grain is fully altered (Alt. grain). Cronstedtite (higher-Z contrast phase) occurs between merrillite grains and exhibits a fibrous texture. Albite (lower-Z contrast phase) appears smooth (lacks structure) and is interstitial to the other phases. White square marks the location of the STEM X-ray elemental maps in (f). e) Higher magnification DF-STEM image of a region in (a) showing the complex relationship between merrillite rods, cronstedtite (fibrous), and albite (homogeneous-looking). The white square marks the region where X-ray maps were extracted in (g). f) (read as a column) Three RGB X-ray maps (Ca-Fe-P, Si-Al-Na, and Mg-S-Fe) showing that merrillite has Fe-, S-, and Al-rich rims, olivine is Fe-rich, and the altered merrillite grain is Na- and S-rich. Cronstedtite is shown in the top-left corner. g) (read as a column) Three RGB X-ray maps (Fe-P-Ca, Al-Mg-Na, and Si-Fe-S) showing that the interface between albite and cronstedtite is sharp and irregular, and the merrillite rims also contain Si and Mg. Legend: Ab = albite, Merr = merrillite, Pyr = pyroxene, Cronst = cronstedtite, Phyllosil = phyllosilicate, Alt. grain = altered grain.

Table 2.3. STEM-EDS analyses (oxides wt%) of the different phases identified in the FIB section extracted from a mesostasis region in direct contact with matrix material in the type IIA Ch18. A) Merrillite and merrillite embedded in Ca-rich pyroxene (Ca-px). B) Albite, pyroxene, olivine, cronstedtite (Cronst.), phyllosilicate (saponite?), and altered merrillite rims. Each individual analysis was extracted in a different grain from the STEM spectral EDS maps. n.d. = not detected.

Table 2.3A

Oxides wt%	Merrillite										Merrillite in Ca-px			
SiO_2	1.77	1.80	2.60	2.63	4.14	4.41	5.18	3.21	4.01	4.34	12.85	8.40	3.14	8.66
TiO_2	n.d.	n.d.	0.09	0.03	0.07	0.20	n.d.	0.04	0.23	0.05	0.25	n.d.	0.16	0.08
Al_2O_3	0.31	0.27	0.51	0.52	4.65	4.99	4.71	4.78	4.80	5.01	0.48	2.42	0.32	0.31
Cr_2O_3	0.03	0.08	0.19	0.03	n.d.	n.d.	n.d.	0.15	0.11	0.10	0.07	n.d.	0.06	0.06
FeO	1.73	2.22	3.06	2.87	2.29	3.48	2.83	2.18	3.89	2.80	3.99	9.56	1.83	3.19
MnO	0.06	0.09	0.06	0.19	n.d.	0.17	0.16	0.26	0.17	0.25	0.23	0.05	0.12	0.07
MgO	3.10	3.37	3.29	3.43	2.28	1.29	2.92	2.65	1.29	2.84	4.72	3.62	3.40	4.38
CaO	43.68	41.62	42.26	41.67	40.11	39.52	38.53	42.09	39.00	41.28	37.48	34.57	41.62	39.84
Na_2O	2.26	2.06	1.91	2.26	2.09	1.42	2.29	2.02	1.64	1.62	1.92	1.86	2.44	2.15
K_2O	n.d.	0.01	0.08	n.d.	0.08	0.01	n.d.	n.d.	n.d.	n.d.	0.05	0.15	0.08	0.08
P_2O_5	46.85	48.47	45.73	46.36	44.09	44.14	43.17	42.61	44.80	41.45	37.96	38.75	46.83	41.17
SO_3	0.21	n.d.	0.21	0.01	0.18	0.38	0.21	n.d.	0.05	0.24	n.d.	0.61	n.d.	n.d.
Total	100	100	100	100	100	100	100	100	100	100	100	100	100	100
Mineral formulae based on 56 oxygens														
Si	0.62	0.63	0.92	0.93	1.45	1.54	1.80	1.14	1.40	1.53	4.50	3.01	1.10	3.04
Ti	n.d.	n.d.	0.02	0.01	0.02	0.05	n.d.	0.01	0.06	0.01	0.07	n.d.	0.04	0.02
Al	0.13	0.11	0.21	0.22	1.91	2.05	1.94	1.99	1.97	2.09	0.20	1.02	0.13	0.13
Cr	0.01	0.02	0.05	0.01	n.d.	n.d.	n.d.	0.04	0.03	0.03	0.02	n.d.	0.02	0.02
Fe	0.51	0.65	0.91	0.85	0.67	1.01	0.82	0.64	1.13	0.83	1.17	2.86	0.54	0.94
Mn	0.02	0.03	0.02	0.06	n.d.	0.05	0.05	0.08	0.05	0.08	0.07	0.02	0.04	0.02
Mg	1.63	1.76	1.74	1.80	1.19	0.67	1.52	1.40	0.67	1.50	2.46	1.93	1.77	2.30
Ca	16.51	15.57	16.02	15.73	14.98	14.76	14.38	15.95	14.57	15.63	14.06	13.26	15.61	15.01
Na	1.55	1.40	1.31	1.54	1.41	0.96	1.54	1.39	1.11	1.11	1.30	1.29	1.66	1.47
K	n.d.	n.d.	0.04	n.d.	0.04	n.d.	n.d.	n.d.	n.d.	n.d.	0.02	0.07	0.04	0.04
P	13.99	14.33	13.69	13.83	13.01	13.02	12.73	12.76	13.23	12.40	11.25	11.74	13.88	12.25
S	0.06	n.d.	0.06	n.d.	0.05	0.10	0.06	n.d.	0.01	0.06	n.d.	0.16	n.d.	n.d.
Total	35.02	34.50	34.99	34.98	34.73	34.22	34.84	35.39	34.24	35.27	35.11	35.36	34.81	35.23

Table 2.3B—Continued

Oxides wt%	Albite					Pyroxene		Olivine	Cronst.	Sap	Alt. rim
SiO_2	65.90	68.97	61.32	66.35	67.72	55.22	54.24	36.32	29.81	38.49	12.48
P_2O_5	0.31	0.67	2.44	0.22	n.d.	0.33	0.93	0.34	0.76	0.57	4.29
TiO_2	0.01	0.09	0.16	n.d.	n.d.	1.14	1.04	n.d.	0.10	0.06	0.12
Al_2O_3	19.86	21.26	18.73	23.57	23.53	2.06	1.47	5.52	18.58	16.96	17.53
Cr_2O_3	0.06	0.10	0.07	n.d.	0.02	0.32	0.40	0.07	0.04	n.d.	0.16
SO_3	0.03	n.d.	0.07	0.17	0.11	n.d.	n.d.	n.d.	0.37	0.55	5.36
FeO	3.70	1.11	6.33	0.78	0.62	11.21	12.28	41.86	46.78	33.46	45.84
MnO	0.01	n.d.	0.07	0.11	0.06	0.46	0.41	1.24	0.25	0.45	0.03
MgO	0.74	0.21	1.62	n.d.	0.13	10.88	9.88	13.80	1.31	7.23	1.63
CaO	0.55	0.77	3.14	0.59	0.62	17.44	19.09	0.80	0.53	0.28	0.47
Na_2O	8.56	6.53	5.60	7.78	6.80	0.94	0.23	n.d.	1.40	1.80	11.30
K_2O	0.26	0.29	0.46	0.42	0.37	n.d.	0.02	0.05	0.07	0.11	0.34
NiO	n.d.	n.d.	n.d.	n.d.	n.d.	n.d.	n.d.	n.d.	n.d.	0.04	0.43
Total	100	100	100	100	100	100	100	100	100	100	100
	Mineral formulae										
Si	2.91	2.97	2.75	2.88	2.92	2.04	2.02	1.03	4.74	5.62	
P	0.01	0.02	0.09	0.01	n.d.	0.01	0.03	0.01	0.10	0.07	
Ti	n.d.	n.d.	0.01	n.d.	n.d.	0.03	0.03	n.d.	0.01	0.01	
Al	1.03	1.08	0.99	1.21	1.20	0.09	0.06	0.18	3.48	2.92	
Cr	n.d.	n.d.	n.d.	n.d.	n.d.	0.01	0.01	n.d.	0.01	n.d.	
S	n.d.	n.d.	n.d.	0.01	0.01	n.d.	n.d.	n.d.	0.09	0.12	
Fe^{+2}	0.14	0.04	0.24	0.03	0.02	0.35	0.38	1.00	6.22	4.08	
Mn	n.d.	n.d.	n.d.	n.d.	n.d.	0.01	0.01	0.03	0.03	0.06	
Mg	0.05	0.01	0.11	n.d.	0.01	0.60	0.55	0.58	0.31	1.57	
Ca	0.03	0.04	0.15	0.03	0.03	0.69	0.76	0.02	0.09	0.04	
Na	0.73	0.55	0.49	0.65	0.57	0.07	0.02	n.d.	0.43	0.51	
K	0.01	0.02	0.03	0.02	0.02	n.d.	n.d.	n.d.	0.01	0.02	
Ni	n.d.	n.d.	n.d.	n.d.	n.d.	n.d.	n.d.	n.d.	n.d.	0.01	
O	8	8	8	8	8	6	6	4	22	22	
Total cat	4.92	4.73	4.86	4.84	4.77	3.90	3.88	2.86	15.53	15.02	
	Ab 92	Ab 86	Ab 60	Ab 89	Ab 88	En 37	En 32	Fa 63			
	An 7	An 11	An 37	An 7	An 9	Fs 21	Fs 23	Fo 37			
	Or 2	Or 3	Or 3	Or 3	Or 3	Wo 42	Wo 45				

3.2.2. TEM observations on Ca phosphates at the interface between the smooth rim and the matrix around the type I Ch3

Calcium phosphates around type IA chondrules have not been reported previously in the literature. We have investigated the mineralogy and texture of the Ca phosphate grains detected by elemental X-ray maps and EPMA across the interface between the smooth rim and the matrix around Ch3 using TEM (Figs. 1.12b and 1.13 in Chapter 1). The petrologic characteristics of Ch3 are described in Chapter 1 (section 3.4.1).

Transmission electron microscopy reveals two different occurrences of Ca phosphates in the FIB section. The first (designated Ca-phos #1 in Fig. 2.9) is completely embedded in the hydrated, amorphous Fe-rich silicate gel that constitutes the smooth rim, a type of rim that formed by alteration of silica in the SIR and is described in Chapter 1. Dark-field STEM imaging and elemental X-ray maps reveal that Ca phosphate #1 is extremely fine-grained (40-60 nm), forming irregular, diffusive, porous regions (ranging from a few nanometers to ~500 nm in size) consisting of aggregates of nanometer-sized grains (Fig. 2.9a). Nanometer-sized grains of magnesioferrite and pentlandite (~5-20 nm in size) are also associated with Ca phosphates based on STEM-EDS elemental X-ray maps (Fig. 2.9c,d). The second occurrence of Ca phosphate (designated Ca-phos #2 in Fig. 2.9) is found in the matrix and has a Z-contrast and texture in DF-STEM imaging that is similar to the amorphous silicates in the matrix (Figs. 2.9e-h and 1.13e in Chapter 1). Calcium phosphate #2 forms highly irregular, smooth regions (up to ~2 μm-size) occupying about 35% of the upper-half area of the matrix in the FIB section (Fig. 1.13e in Chapter 1). These regions lack porosity and have radiating textures of somewhat acicular crystals in some areas (Fig. 2.9g), enclosing regions of relict matrix (fine-grained

silicates, organic matter, Mg-silicates, and nanosulfides). Figure 2.9e,f also shows an irregular grain of Ca sulfate (~250 nm-size) close to the interface with the matrix, associated with Ca phosphate, that appears filling an elongated, curved region or fracture (~300 nm-long) at the interface with the smooth rim. Scanning TEM-EDS analyses of the two Ca phosphate grains (#1 and #2) are reported in Table 2.4. Analyses in Ca phosphate #1 (in the smooth rim) show the presence of variable amounts of Si (7.4 – 20 wt% SiO_2), Fe (5 – 14.3 wt% FeO), Mg (1.2 – 4.1 wt% MgO), Na (2.8 – 4.1 wt% Na_2O), and Al (0.7 – 1.4 wt% Al_2O_3), and minor (less than 1 wt%) Mn and S (Table 2.4). Calcium phosphate #1 has a mean atomic Ca/P consistent with whitlockite (1.52, c.f. ideal whitlockite 1.50) (Fig. 2.10). Because Ca phosphate #1 is closely intergrown with the amorphous silicate material, the analyses were subject to contamination from the amorphous silicate, which explains the high Si and Fe contents detected by STEM-EDS. This is shown in a FeO versus SiO_2 plot (Fig. 2.11), where individual analyses of Ca phosphates #1 and #2 define a linear array, positively correlated, indicating that these two elements occur in the same phase, distinct from the Ca phosphates. The Si-Fe content of the amorphous silicate gel in the smooth rim analyzed in this FIB section (Fig. 2.11) lies on the extrapolated trendline for the Ca phosphate. Therefore, we interpret the Si and Fe contents in Ca phosphate #1 as being due to beam overlap with the amorphous Fe-rich silicate gel (Fig. 2.9b). Calcium phosphate #2 (in the matrix) shows less compositional variability. It contains approximately 10 wt% SiO_2, 6.5 wt% FeO, 4.4 wt% Na_2O, and 1.2 wt% MgO in average. It has a mean atomic Ca/P ratio of 1.62, which is higher than the Ca phosphate in the smooth rim and closer to the ideal apatite value (1.67) (Fig. 2.10). In a Na versus Ca plot, these two elements show no correlation (Fig. 2.11B), indicating that there is no

substitution for one another. Therefore, Na is not present in the phosphate structure in these two occurrences of Ca phosphates (Table 2.4, Fig. 2.9d).

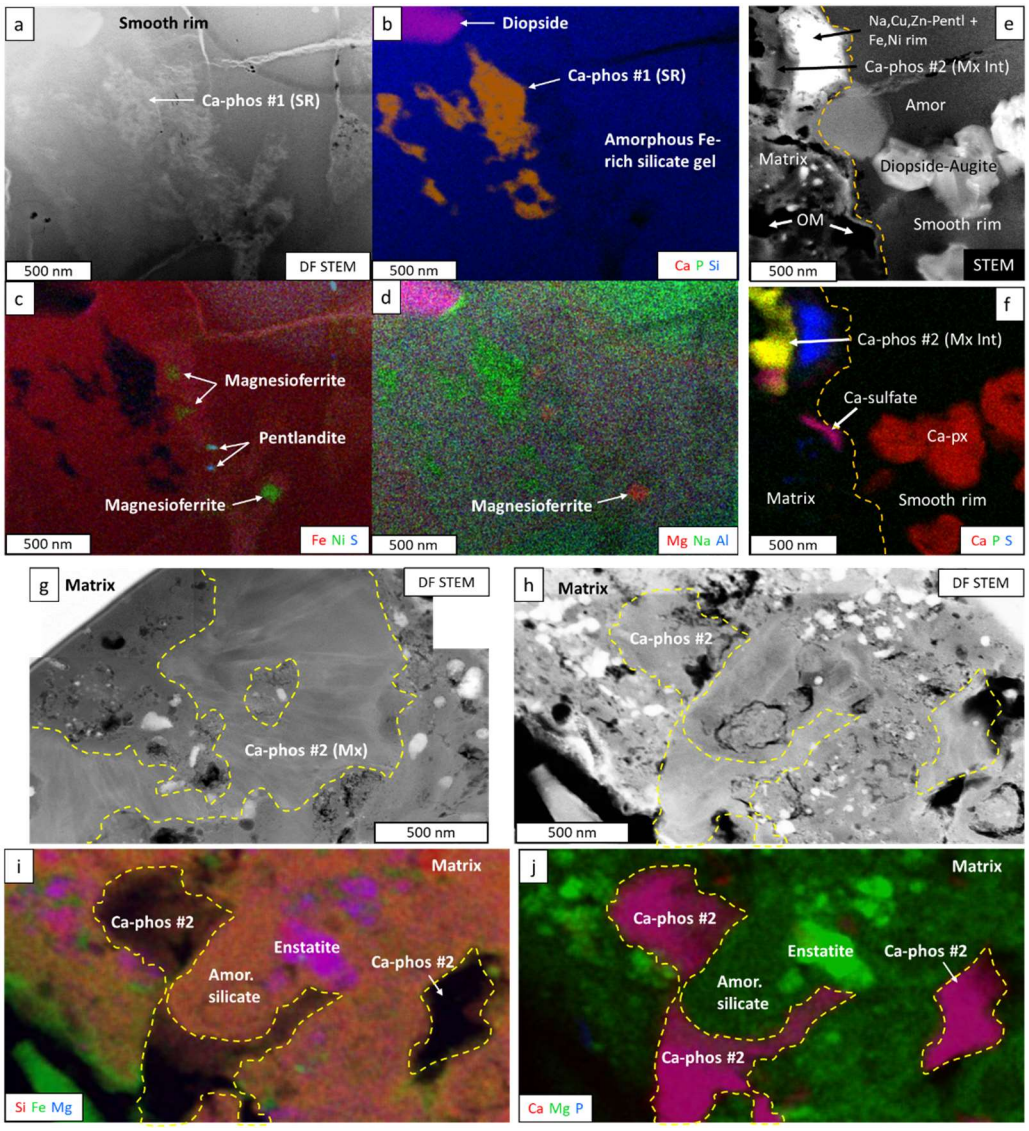

Figure 2.9. STEM images of the two different occurrences of Ca phosphates found in a FIB section (FIB1 in Chapter 1) extracted at the interface between the smooth rim around chondrule 3 (Ch3) and the matrix. Calcium phosphates are designated Ca phosphates #1 and #2, referring to their occurrence in the smooth rim and the matrix, respectively. a) Dark-field STEM image of Ca phosphate #1 found in the smooth rim showing that Ca phosphates have a granular, heterogeneous appearance and define irregular regions. b) STEM-EDS elemental X-ray map of Ca-P-Si for the area marked in (a) showing that Ca-phosphate regions are porous and highly irregular. c) Fe-Ni-S map of the region in (a) showing the presence of magnesioferrite and pentlandite grains associated with Ca phosphates. *(Figure caption continues on the following page).*

Figure 2.9. *(Caption continued from previous page).* d) Mg-Na-Al map showing that Na is present in the Ca-phosphate areas (but not exclusively). e) Dark-field STEM image of a region at the interface between the matrix and the smooth rim (interface outlined in dashed yellow line) along with a Ca-P-S map in (f) of the same region showing a grain of Ca phosphate and a grain of Ca sulfate at the interface. g) Dark-field STEM image of Ca-phosphate #2 in the matrix showing that it has a smooth appearance and a radiating to fibrous texture. h) Dark-field STEM image along with two elemental X-ray maps (i) Si-Fe-Mg and (j) Ca-Mg-P of the same region in the matrix showing the occurrence of Ca phosphate #2, defining irregular regions and exhibiting a texture and a Z-contrast that is similar to amorphous silicates in the matrix. Amor = amorphous.

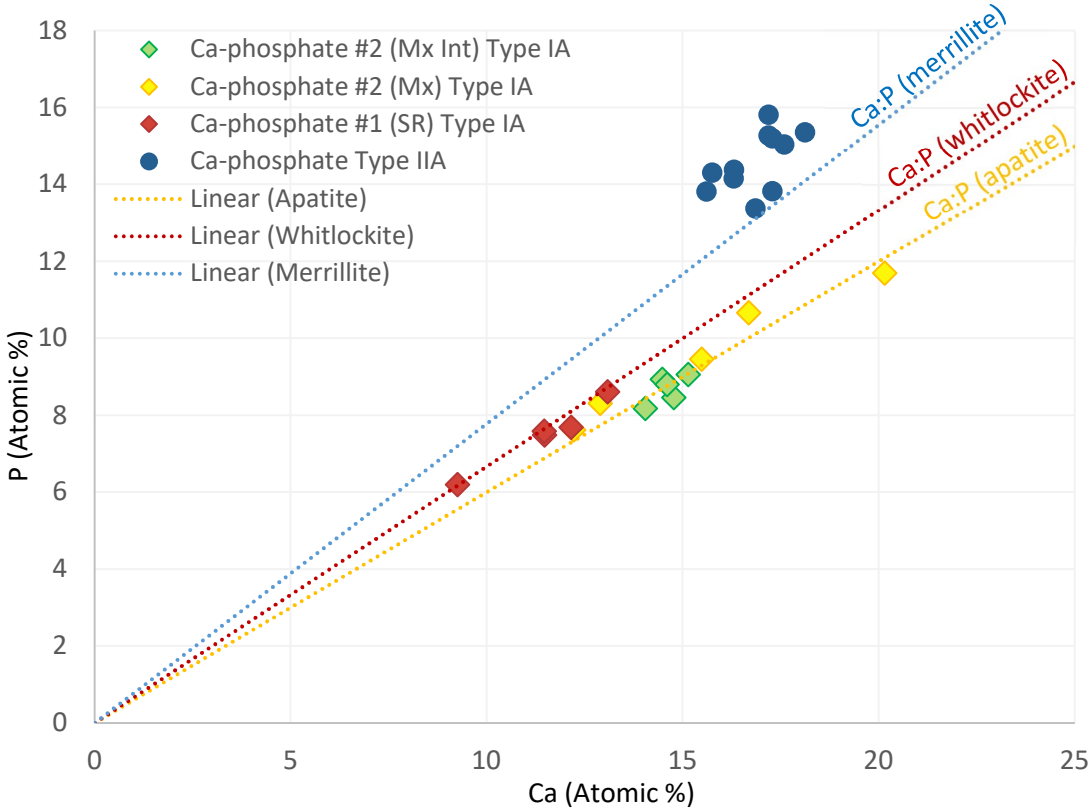

Figure 2.10. Phosphorus versus Ca (atomic wt%) plot of the different Ca phosphate occurrences around the type IB Ch3 and the type IIA Ch18. The different trend lines correspond to the Ca/P ratios for the different Ca phosphate minerals (ideal compositions), yellow, red, and blue for apatite, whitlockite, and merrillite, respectively, to allow differentiation between the different Ca phosphates present in the FIB section. There are two occurrences of Ca phosphates around type IB Ch3, designated Ca-phosphate #1 and #2. Ca-phosphate #1, in red, refers to nanometer-sized grains aggregated inside the smooth rim, embedded in the amorphous Fe-rich silicate gel, identified as whitlockite. Ca-phosphate #2, in green and yellow, refers to Ca phosphates in the matrix, which correspond to apatite. Green squares (Mx Int) refer to grains exactly at the interface with the smooth rim, whereas yellow squares (Mx) refer to grains occupying irregular, smooth areas in the matrix, shown in Figure 2.9h-j. Finally, Ca phosphates in the type IIA chondrule Ch18 are plotted in blue, for reference, corresponding to merrillite compositions.

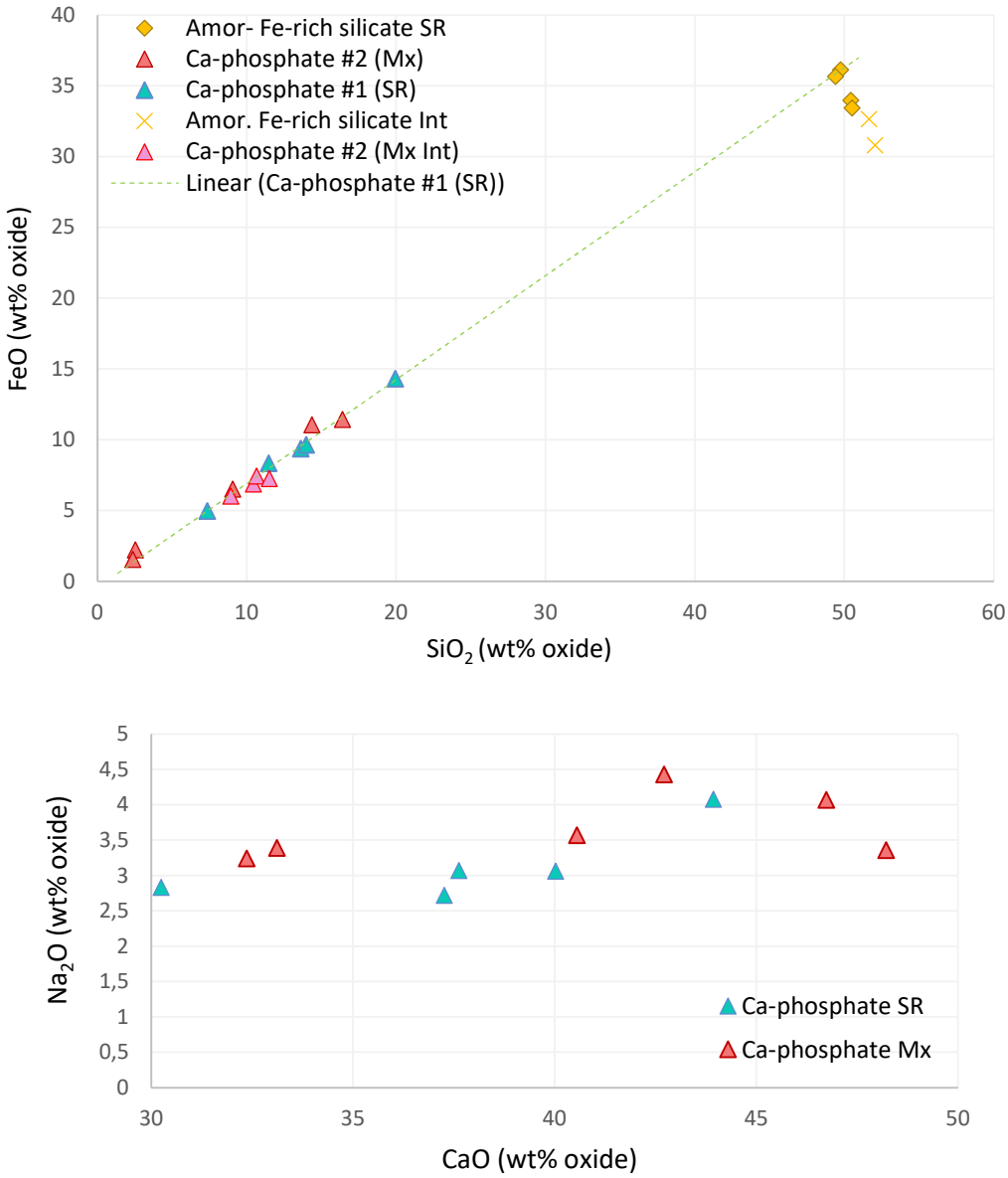

Figure 2.11. Two plots showing the relationship between Ca phosphates and the amorphous silicate gel in the smooth rim around Ch3. A) FeO versus SiO_2 (wt% oxide) plot of the amorphous Fe-rich silicate gel STEM-EDS (in yellow) from Table 1.4 in Chapter 1, and Ca-phosphates #1 (smooth rim, in blue) and #2 (matrix, in red) STEM-EDS analyses at the interface between the smooth rim and the matrix around Ch3. Int = interface. Dashed green line is the best-fit linear array based on Ca-phosphates #1. B) Na_2O versus CaO (wt% oxide) plot from Ca phosphates #1 (smooth rim, SR) and #2 (matrix, Mx) around Ch3 (FIB1), showing that there is no correlation between the two elements, indicating that Na is not substituting into the phosphate for Ca, and thus, Ca phosphates in the smooth rim do not contain Na.

Table 2.4. STEM-EDS analyses of Ca phosphates in FIB1 (Ch3) described in Chapter 1. Calcium phosphates in FIB1 have two different occurrences with two different textures: #1 refers to Ca phosphates found inside the smooth rim (nanometer aggregates) and #2 refers to Ca phosphates found in the adjacent fine-grained matrix material (homogeneous, radiating groundmass). Each individual analysis represents a different area, except the last value in #2, which is the mean of 11 analyses in #2 from a grain close to the interface with the smooth rim. Standard deviations (σ) are included to show the heterogeneity of phosphates #1 compared to phosphates #2.

Oxides wt%	#1	#1	#1	#1	#1	**Mean #1** *(σ)*	#2	#2	#2	#2	#2	#2	**Mean #2** *(σ)*
P_2O_5	31.08	36.61	32.08	31.13	25.68	**31.32** *(3.89)*	33.13	33.82	33.62	33.23	32.45	32.77	**33.17** *(0.51)*
SiO_2	13.63	7.39	11.47	13.93	19.95	**13.27** *(4.56)*	10.54	8.95	9.70	9.46	10.79	10.46	**9.98** *(0.72)*
TiO_2	0.01	n.d.	n.d.	n.d.	n.d.	**n.d.**	0.04	0.10	n.d.	0.16	0.06	0.07	**0.07** *(0.05)*
Al_2O_3	1.00	0.98	0.73	0.97	1.35	**1.01** *(0.22)*	0.60	0.78	0.42	0.72	0.70	0.69	**0.65** *(0.13)*
Cr_2O_3	0.05	n.d.	0.02	0.03	0.07	**0.03** *(0.03)*	0.12	0.15	0.07	0.07	0.10	0.09	**0.10** *(0.03)*
SO_3	0.35	0.07	0.06	0.29	0.71	**0.30** *(0.27)*	0.04	n.d.	n.d.	0.37	0.13	0.18	**0.12** *(0.14)*
FeO	9.37	4.96	8.34	9.61	14.32	**9.32** *(3.35)*	6.90	6.02	6.15	6.12	6.88	6.87	**6.49** *(0.43)*
MnO	0.63	0.50	0.54	0.71	0.63	**0.60** *(0.08)*	0.16	0.26	0.22	0.36	0.28	0.29	**0.26** *(0.07)*
MgO	3.10	1.20	3.60	3.05	4.11	**3.01** *(1.10)*	1.21	1.14	1.31	1.10	1.26	1.39	**1.24** *(0.11)*
CaO	37.63	44.03	40.02	37.13	30.25	**37.81** *(5.03)*	43.02	44.26	44.39	43.57	42.87	42.71	**43.47** *(0.72)*
Na_2O	3.07	4.09	3.06	3.05	2.83	**3.22** *(0.50)*	4.18	4.53	4.06	4.83	4.44	4.43	**4.41** *(0.27)*
K_2O	0.07	0.16	0.08	0.12	0.10	**0.11** *(0.04)*	0.06	n.d.	0.07	n.d.	0.03	0.05	**0.03** *(0.03)*
Total	100	100	100	100	100	**100**	100	100	100	100	100	100	**100**
Ca/P (at.%)	1.53	1.52	1.58	1.50	1.49	**1.52**	1.64	1.60	1.55	1.72	1.56	1.66	**1.62**

n.d. = not detected

4. Discussion

Chondrules are the principal component of the most common meteorites, chondrites; therefore, knowledge of how they formed is of fundamental importance to understanding our early solar system and perhaps the evolution of other protoplanetary disks and planetary systems. However, despite the number of studies dedicated to understanding how chondrules formed, many significant questions remain about the origin of these enigmatic objects (e.g., Friend et al., 2016; Pape et al., 2019). The main handicap is that all chondrites have experienced some degree of parent-body processing that has modified their original constituents. However, whereas the fine-grained matrix material is most compromised by aqueous alteration and thermal metamorphism, the primary characteristics of chondrules are not affected to the same degree. There are a few meteorites that preserve a remarkably pristine record of early solar system processes, such as Acfer 094 (ungrouped chondrite), ALH A77307 (CO chondrite), DOM 08006 (CO chondrite), DOM 08004 (CO chondrite), QUE 99177 (CR chondrite), MET 00426 (CR chondrite) and other CR chondrites, as well as some parts of Semarkona (LL ordinary chondrite). Pristine chondrites preserve a mixture of primary components that formed at different temperatures, pressures, fO_2, etc., that are far from chemical, isotopic, and textural equilibrium. Their study allows identification of critical information about physical and chemical conditions present in the solar nebula during chondrule formation, evidence of early solar system processes in matrices, and how fluids may have modified their original characteristics.

Phosphate minerals in primitive chondrites are of particular importance because they potentially record their conditions of formation in the solar nebula as well as the

earliest stages of aqueous alteration in the parent body. Iron metal alloy (Fe, Ni, Co, and/or Pd) and schreibersite (Fe_3P) start condensing out of the solar nebula at elevated temperatures (1357 K and 1248 K, respectively; Lodders, 2003). Chondritic evidence and theoretical calculations show that at 1225 K, P reacts with Fe as a refractory alloy (Fegley and Lewis, 1980; Pirim et al., 2014; Pasek et al., 2019), but phosphorus never reacts (dissolves) into metal to an amount higher than a fraction of the total P (20%) or about 1 mol% of the metal alloy (Pasek et al., 2019). Upon cooling, schreibersite ($(Fe,Ni)_3P$) exsolves from P-bearing metal grains at 1053 K (Grossman and Olsen, 1974; Wai and Wasson, 1977; Fegley and Lewis, 1980) and becomes Ni-enriched until it oxidizes to phosphates, at 850 K (Pasek et al., 2019). Apatite first forms but as temperature decreases, it competes with anhydrous $Ca_3(PO_4)_2$ (analogous to merrillite), which dominates until 400 K, when apatite dominates again (Pasek et al., 2019). Therefore, in chondritic meteorites, P in type I chondrules is siderophile, present in metal grains, because type I chondrules formed under more reducing conditions at higher temperatures (e.g., Scott and Krot, 2005). On the contrary, P in type II chondrules is a typical lithophile element incompatible during magmatic fractionation, because type II chondrules formed under more oxidizing conditions. However, both types of chondrules formed under more oxidizing conditions than the canonical solar nebula (e.g., Prieto et al., 2002). Thus, type II chondrules contain mesostases that are significantly more enriched in P (e.g., up to 4.27 wt% P_2O_5, Table 1) relative to type I chondrule mesostases (e.g., 0.03 wt% P_2O_5 in QUE 99177, Table 1.1 in Chapter 1). Surprisingly, phosphides in chondritic matrices are rare, estimated to represent <1% of the total P accreted in carbonaceous chondrites (Pasek et al., 2004).

The behavior of phosphates in pristine chondrites has not been explored in extensive detail, but a few studies in the literature argue that they are the result of oxidation of P released from metal grains during very minimal thermal metamorphism and subsequent interaction with Ca silicates (e.g., Murrell and Burnett, 1983; Goreva and Burnett, 2001; Goreva and Lauretta, 2004). Studies describing the different occurrences of P-bearing phases in pristine chondrites include Rubin and Grossman (1985) and Goreva and Lauretta (2004). On the one hand, Rubin and Grossman (1985) studied phosphate-sulfide assemblages in type 3 carbonaceous and ordinary chondrites and argued that once schreibersite crystallized at metal grain boundaries during cooling, metal-schreibersite and sulfide-schreibersite assemblages accreted rims of fine-grained silicates that reacted with schreibersite to form merrillite and chlorapatite. On the other hand, Goreva and Lauretta (2004) identified three occurrences in the Semarkona LL3.0 ordinary chondrite that are similar to some of the occurrences described here: (1) merrillite rims around chondrules, (2) merrillite in the mesostasis of type II chondrules, and (3) P-rich phases associated with Fe-rich rims around type I chondrules and as Fe-rich assemblages in the matrix. Although Semarkona shows minimal evidence of thermal metamorphism, the authors interpreted these phases as being the result of parent body metamorphism, but also suggested that an immiscible P-rich component from residual feldspathic melts within chondrules could produce Ca phosphates in occurrence (2).

While studying the interaction of anhydrous chondrules and hydrated matrix in the pristine CR carbonaceous chondrite QUE 99177, we have observed a number of different occurrences of Ca phosphates that provide information about the origin and behavior of P in minimally altered chondrite samples. Here, we aim to constrain their

formation mechanisms to acquire new insights into the behavior of Ca and P during the earliest stages of aqueous alteration in the CR parent body. In the following sections, we discuss the observations that support a solar nebular (primary) origin for Ca-phosphate layers within mesostasis regions at the outer edges of type IIA chondrules and assess a possible formation mechanism for them (section 4.1); we discuss possible origins (solar nebula or parent body) for a different occurrences of Ca phosphates associated with type II chondrules (section 4.2); we build on observations that support a secondary origin for the Ca phosphates associated with smooth rims and matrix around type IA chondrules, indicative of mass-transfer reactions during the earliest stages of aqueous alteration in the parent body (section 4.3); and finally, we discuss the formation mechanisms of isolated P-bearing phases in the matrix (section 4.4).

4.1. Igneous Ca phosphates within mesostasis regions of type IIA chondrules formed in the solar nebula

Previous work on phosphates in weakly altered chondrites (Semarkona LL3 ordinary chondrite, EET 92105 CR chondrite, and Y-791198 CM chondrite) have described merrillite forming layers around type II chondrule peripheries and within microcrystalline mesostasis and mesostasis glass (Goreva and Lauretta, 2004; Burger and Brearley, 2004, 2005; Brearley and Burger, 2009; Brearley, 2011). These studies show that leaching of alkalis and P from P-bearing chondrule glass during the earliest stages of aqueous alteration precipitated (secondary) Ca-phosphate layers in the adjacent matrix at the interface with chondrules, caused by a change in pH in the altering aqueous solutions.

Our TEM work on Ca phosphates at the edge of a type IIA chondrule (Ch18) (Figs. 2.2, 2.8) in QUE 99177 is remarkably similar to Ca phosphates reported within the

mesostasis glass close to the periphery of type IIA chondrules in the weakly altered CR chondrite EET 92105 (Brearley and Burger, 2009) and the CM chondrite Y-791198 (Brearley, 2011). These phosphates share the following characteristics: (i) they form a well-crystallized network of elongated, curved rods with widths between 0.1 to 0.8 μm, (ii) they preserve crystallographic continuity, (iii) they exhibit nanoporosity, (iv) most rods are surrounded by alteration rims, and (v) they are found inside altered or partially altered chondrule glass. Although previous studies suggested that the composition of these phosphates was consistent with whitlockite, our results indicate that Ca phosphates in the type IIA Ch18 consist of merrillite (Table 2.3, Fig. 2.10). However, because merrillite and whitlockite form a solid solution (Hughes et al., 2008), the presence of whitlockite in other studies by substitution of hydrogen by calcium ($H \leftrightarrow Ca_{0.5})_2$ in merrillite inside the mesostasis regions cannot be ruled out. In addition to Ch18, Ca phosphates containing Na have been identified at the periphery of Ch7 (Fig. 2.4f, 2.5) forming very similar layer-like morphologies, and in a minor proportion, inside the mesostasis regions of Ch2 (Fig. 2.3f), both also consistent with merrillite compositions. Based on the above characteristics (texture and composition), we conclude that this type of Ca phosphate in type II chondrules is primary in origin, formed by quenching at the final stages of crystallization of P-rich chondrule melts, consistent with an igneous crystallization in the solar nebula. Consequently, within a thin section and even within the same type II chondrule, both primary and secondary Ca phosphates can coexist.

The mesostasis region that contains primary phosphates in Ch18 has been minimally affected by aqueous fluids in the parent body (Fig. 2.2 and 2.8). Chondrule glass has been replaced by cronstedtite in a region ~15-20 μm-wide across the edge of the

chondrule to the interface with the matrix, while clear glass is still preserved in the interior of the chondrule mesostasis (Fig. 2.1b), and albitic plagioclase appears unaltered. Albite is found in the chondrule mesostasis as acicular crystals seen by SEM, consistent with a primary, igneous origin, because plagioclase produced through devitrification of chondrule mesostasis glass is extremely fine-grained and does not display a lath-shaped morphology under SEM (Huss et al., 2006). Under the TEM, albite also occurs filling irregular regions between merrillite rods, in direct contact with cronstedtite. The presence of a phyllosilicate phase replacing chondrule glass surrounded by primary albite indicates that chondrule glass is extremely susceptible to aqueous alteration and/or albite is more resistant to alteration than previously recognized.

Transmission electron microscopy also reveals incipient aqueous alteration of the Ca-phosphate rods, such as the presence of nanopores, thin (0.1 μm) alteration rims, and a Na- and S-rich grain that seems to have formed by alteration of a merrillite grain (Fig. 2.8d,f). The alteration rims around Ca phosphates are enriched in Fe and S, consistent with those reported around phosphates in the CM Y-791198 by Brearley (2011). Based on these observations and on X-ray maps showing Fe and S depletions in the matrix in a region 20-40 μm from the chondrule edge (Fig. 2.2e,f), we infer that elemental exchange between the chondrule and the matrix was minimal, dominated by mobilization of Fe and S by aqueous fluids from the adjacent matrix into the chondrule mesostasis during aqueous alteration. These fluids partially altered chondrule glass, lowered the pH of the fluid (Brearley, 2011), and introduced Fe and S into the altered region of the mesostasis. This is supported by the fact that the spatial area of the matrix that is depleted in Fe and S is remarkably similar to the region of alteration in the chondrule mesostasis in contact

with the matrix (Fig. 2.2). The very fine-grained nature of cronstedtite (nanocrystals) indicates that the degree of alteration was very limited, and occurred at low temperatures, for a short period of time, otherwise phyllosilicates would undergone grain growth with time and become coarser-grained (Jones and Brearley, 2006; Brearley and Burger, 2007). The absence of thermally-driven growth of phyllosilicates is consistent with observations on the CM chondrite Y-791198 (Chizmadia and Brearley, 2008). However, Mg-rich phyllosilicates replacing chondrule glass observed in CM chondrites are absent here, consistent with QUE 99177 representing a lower degree of alteration than other weakly altered samples studied in the literature. At more advanced degrees of alteration, a higher availability of Mg ions from the matrix penetrate the chondrule mesostasis and crystallize as Mg-rich phyllosilicates.

To summarize, Ca- and P-bearing layers exclusively observed in mesostasis regions at the periphery of type IIA chondrules in contact with the matrix (not outside chondrules) are igneous in origin, formed by quenching at the final stages of crystallization of a P-enriched mesostasis melt in the solar nebula. Relict, unaltered Ca-rich pyroxenes with quenched textures are also common in type IIA chondrules in QUE 99177 (e.g., Fig. 2.3b,c) and in the CM chondrite Y-791198 (Brearley and Chizmadia, 2005), also supporting a primary origin in which the residual melt became enriched in incompatible elements (e.g., P, Ca, REEs) and supersaturated in the species to stabilize Ca-rich pyroxene and Ca phosphates.

4.1.1. Exploring a formation mechanism for merrillite in mesostasis regions of type IIA chondrules

Type IIA chondrules formed in highly oxidizing environments relative to the solar value due to enrichments in either dust (e.g., Ebel and Grossman, 2000; Hewins et al., 2005; Jones et al., 2005; Grossman et al., 2008; Alexander et al., 2008; Grossman, 2010) or ice (Ciesla and Cuzzi, 2006; Grossman, 2010; Grossman et al., 2012; Fedkin et al., 2012). Previous studies have shown that under oxidizing conditions, the concentration of P_2O_5 rises rapidly in silicate melts as metal is oxidized due to rapid dephosphorization of Fe-P alloys by reaction with molten silicate at 1550 ºC (Gaye and Ribound, 1977). Therefore, it is likely that high P enrichments in type II chondrule melts were sufficient to allow crystallization of merrillite. This is consistent with work on the Y-791198 CM chondrite (Brearley and Chizmadia, 2005), which supports the hypothesis that residual melts in type IIA chondrules became enriched in incompatible elements (e.g., P, Ca, REEs) and supersaturated in the species to stabilize Ca-rich pyroxene and Ca phosphate.

The forsteritic cores in FeO-rich olivine phenocrysts in type II chondrules (Jones, 1990; Wasson and Rubin, 2003; Jones et al., 2005; Lauretta et al., 2006) have been interpreted as relicts of reduced solid precursors that underwent oxidation during the melting event(s) that formed type II chondrules. This evidence suggests that at least partial oxidation of metallic iron occurred on the timescale of chondrule formation. The fact that relict forsteritic grains are compositionally and isotopically identical to magnesian olivines in type I chondrules (Connolly and Huss, 2010) and the discovery of rare Fe,Ni metal grains in type II chondrules (Jones, 1994; Schrader et al., 2008) led to the idea that type II chondrules formed by oxidation of type I chondrule precursors.

Villeneuve et al. (2015), for example, proposed a model that reproduces the whole range of textures and chemical diversity in type A chondrules, where type IIA chondrules record the most oxidizing conditions, derived from reduced type IA chondrule precursors that were partially melted and recrystallized in a relatively oxidizing environment, a vapor plume. Further evidence for this kind of oxidation events comes from the presence of P-rich boundary layers (0.3-0.4 wt% P_2O_5) coating relict forsteritic cores that correlate with the major siderophile elements Fe, Cr, Co, and Ni, and the occurrence of whitlockite in the P-rich zones (Hewins, 2009; Villeneuve et al., 2015). Forsterite relicts were found to be enriched in Ca and Al, and depleted in P, as well as siderophile elements, whereas the fayalitic overgrowths were found to be enriched in Fe, Mn, Cr, P, Ni, and Co. Hewins (2009) concluded that P-rich zones represent periods of rapid growth and Villeneuve et al. (2015) argued that the sudden oxidation of Fe,Ni metal blebs in type I chondrules released siderophile elements into the melt.

The formation of Ca-phosphate layers (merrillite) inside mesostasis regions at the periphery of type II chondrules could thus fit into this model, because they crystallized from a mesostasis melt that was enriched in P. The model, however, has some problems. For example, the oxidation of Fe from Fe,Ni metal would have diluted MnO and would not have created the positive correlation observed between FeO and MnO (Hewins and Zanda, 2012). Secondly, this model does not explain Ni depletions in type II chondrules relative to type I chondrules (Jones, 1990), which should have remained constant given that Ni is a siderophile element and cannot leave the chondrule melt. Finally, the model does not explain the variability in igneous histories that type II chondrules record (e.g.,

different precursor compositions, redox conditions, and cooling rates; Schrader et al., 2015).

4.2. Calcium phosphates in fine-grained rims around type IIA chondrules: Solar nebular and parent body processes

Elemental X-ray maps of the type IIA chondrules Ch2 and Ch7 show the presence of Ca phosphates in their adjacent matrix material. However, the Ca phosphate occurrences around these two chondrules differ from one another (Figs. 2.3-2.5). Calcium phosphates in fine-grained rims of Ch2 and Ch7 show variations in grain size (several microns in Ch2 versus nanometer-sized in Ch7), abundance (highly abundant in Ch2 versus lower abundance in Ch7), and distances from chondrules edges (up to ~100 μm for Ch2 versus ~20-50 μm for Ch7). Elemental X-ray maps show that these Ca phosphates lack Na, suggesting that they have compositions consistent with apatite or whitlockite, but EPMA analyses were not performed in these phases due to their small grain sizes. The differences in textures between these two chondrules appear to correlate with differences in the composition of their associated chondrule mesostasis; only Ch2 shows evidence of alteration of mesostasis glass and leaching of elements. Therefore, the above variations may indicate different formation mechanisms and/or origins for the Ca phosphates in the two chondrules. We suggest a primary origin for Ca phosphates associated with Ch7 (section 4.2.1), which records oxidation of schreibersite in the solar nebula, and a secondary origin for Ch2, which records transfer of material between chondrule and matrix during aqueous alteration in the parent body (leaching of P and Ca from chondrule mesostasis) (Burger and Brearley, 2004; Burger and Brearley, 2005; Brearley and Burger 2009; Brearley, 2011) (section 4.2.2).

4.2.1. Primary Ca phosphates around Ch7 formed by oxidation of schreibersite

In this part of the discussion, we focus on a type of Ca phosphate that has not been previously described in the literature: nanometer-sized grains of Ca phosphates in the fine-grained rim around Ch7 (Figs. 2.4 and 2.5). Fine-grained rims are widely regarded as having formed by accretion of dust onto the surfaces of chondrules (Huss et al., 2005). The fine-grained outer region of Ch7 contains ferroan olivine, Na,K-rich mesostasis glass, Ca-rich pyroxene, chromite, and merrillite (primary phosphate), suggesting that the rim could have formed by melting of a volatile-rich dust layer that accreted onto the chondrule surface and mixed with the preexisting chondrule melt (e.g., a similar formation mechanism as coarse-grained igneous rims on chondrules). Nano-grains of Ca phosphates outside the chondrule are evenly distributed within the rim, with a composition consistent with apatite or whitlockite (e.g., Fig. 2.5b,e,h). They are in contact with primary merrillite layers in the alkali-rich mesostasis periphery of the chondrule and with pyrrhotite-pentlandite grains, phases that are found at the interface between the chondrule and the adjacent fine-grained rim (Fig. 2.5). The large pyrrhotite-pentlandite veneer around the chondrule (Fig. 2.4c) marks the boundary with the matrix. Pyrrhotite-pentlandite intergrowths in CR chondrites are primary in origin, formed from S-, and Ni-rich liquids at 988-1350ºC that cooled to form a monosulfide solid solution (mss) that crystallized Fe,Ni metal and then unmixed into pentlandite-pyrrhotite assemblages at 597 ºC (Kitakaze et al., 2011; Schrader et al., 2015). During chondrule melting, immiscible silicate and Fe-Ni-S melts formed (e.g., Zanda et al., 1995; Lauretta et al., 1995; McCoy et al., 1999); silicate phases crystallized at 1147-1247ºC, whereas the mss crystallized at slightly lower T, about 1097 K, and thus, formed interstitially to the

silicate phases (e.g., Singerling and Brearley, 2018), consistent with morphologies observed in Ch7 (Fig. 2.4).

Therefore, the characteristics of Ca phosphates found in the fine-grained rim around Ch7 clearly do not fit the model proposed by Villeneuve et al. (2015) that we have used to explain primary merrillite rods in mesostasis regions, because the grains are located in the fine-grained rim outside the chondrule. An origin by leaching of Ca and P from mesostasis glass is also difficult to reconcile, given that the mesostasis regions appear highly enriched in Na and K, indicative of pristine chondrule glass that has not experienced any parent body aqueous alteration. Given that a parent body formation process seems unlikely, we explore a primary origin. In a solar nebular setting, we consider two possible mechanisms: (1) evaporation–recondensation during melting of chondrules (e.g., Kong et al., 1999) and (2) oxidation of schreibersite.

Evaporation of volatile and moderately volatile elements in Ch7 is difficult to reconcile because type II chondrules are approximately chondritic in composition (McSween, 1977; Hewins, 1991) and contain no evidence that Na and S were lost by evaporation. Sodium and S retention in type II chondrules is explained by rapid heating and non-linear cooling rates in a much more oxidizing conditions than the canonical solar nebula (Yu et al., 1996; Yu and Hewins, 1998). The high ambient Na pressure required to retain Na in chondrule melts prevents any evaporation (Yu and Hewins, 1998; Hewins and Zanda, 2012) and is also implausible because of the extreme dust and/or ice enrichments that it requires (Hewins, 1997; Yu and Hewins, 1998; Fedkin et al., 2012). The oxygen fugacities required to prevent volatile loss and control olivine compositions may have been obtained by internal buffering rather than by moderate levels of dust

evaporation (Hewins, 1997). Sulfur, which has a 50% condensation temperature of 664 K (Lodders, 2003), was retained in the chondrule melt because the period of time the chondrule spent above the liquidus was short or, alternatively, gas-melt interaction reached an equilibrium between S-rich gas and the chondrule melt where no loss (no evaporation) occurred. The second scenario implies high nebular pressures with dust enrichments, which increase the condensation temperature of S (Ebel and Grossman, 2000). Isotopic data (e.g., ^{41}K) also argue in favor of limited evaporation from chondrule melts (e.g., Alexander et al., 2000), because the heavy isotope enrichments that would be the expected mass fractionation signature of evaporation of moderately elements are absent in chondrules (Fedkin et al., 2012). Therefore, it is unlikely that Ca phosphates present around the fine-grained rim in Ch7 recondensed from evaporated chondrule volatiles. This is consistent with recent calculations based on thermodynamic equilibrium models and metal phosphidation kinetics coupled to a gas diffusion model conducted by Pasek (2019) that concludes P was highly unlikely to have been present as a volatile element throughout much of the solar nebula.

To this end, we propose a different primary formation mechanism for these type of Ca phosphates, which is by oxidation of schreibersite. As mentioned earlier, at temperatures in the 1100 – 1200 K range (Lodders, 2003; Pasek et al., 2019) in the in the early solar nebula, small quantities of P were incorporated into Fe,Ni metal alloy grains, which became one of the precursors of type I chondrules. The highly oxidation conditions that type II chondrules experienced allowed the formation of Ca phosphates by oxidation of phosphides (schreibersite, Fe_3P). Apatite is the first Ca phosphate that forms at 850 K (Pasek et al., 2019), but as temperature decreased, schreibersite was oxidized to the

anhydrous phase $Ca_3(PO_4)_2$ (analogous to merrillite), which dominated until 400 K, when apatite became dominant again (Pasek et al., 2019). The anhydrous phase is consistent with the lack of halogens in the nano-phosphates around Ch7. Thus, if Ca phosphates around Ch7 formed by oxidation of solid schreibersite, they record temperatures in the solar nebula between 700 and 400 K assuming equilibrium conditions. The small sizes of these grains are also consistent with phosphide grains heterogeneously distributed in the matrix of QUE 99177 (Fig. 2.6b, 2.7b,e,f), overall providing compelling evidence that Ca phosphates around Ch7 formed from an anhydrous precursor.

4.2.2. Secondary Ca phosphates in fine-grained rims around type IIA chondrules

Observations of chondrule mesostasis in ordinary chondrites, CM, and CR chondrites show that mesostasis glass is one of the most susceptible phases to alteration. Prior to aqueous alteration of type IIA chondrules, chondrule mesostases are generally enriched in P, Ca, Na, and K (e.g., Jones, 1990). During the early stages of parent body processing, water ice in the chondrite matrix began to melt, penetrating regions of chondrule mesostasis that were in contact with the matrix (Burger and Brearley, 2004, 2005; Brearley and Burger, 2009; Brearley, 2011). The high reactivity of chondrule glass with fluids is widely apparent in CM chondrites, where typically, chondrule glass has been completely replaced by phyllosilicates (Rubin et al., 2007; Chizmadia and Brearley, 2008). However, in CR chondrites (and very rarely in CM chondrites), pristine, clear chondrule glass is still preserved in some type IIA chondrules, such as QUE 99177.

Recent studies have examined detailed alteration reactions during the early stages of aqueous alteration involving mass transfer between type IIA chondrule mesostasis and matrix (Burger and Brearley, 2004, 2005; Brearley and Chizmadia, 2005; Brearley and

Burger, 2009; Brearley, 2011). TEM work on leached, yet texturally unaltered glass in EET 92105 showed that the glass contains abundant nanopores with no evidence of phyllosilicates (Brearley and Burger, 2009). This observation suggests that the initial stage of aqueous alteration involved hydration of glass without the formation of phyllosilicates. The next step was inferred to involve elemental exchange between chondrules and matrix. Type IIA chondrule mesostases in QUE 99177 are enriched in alkalis, although their alkali content is highly variable among the different chondrules. Burger and Brearley (2004) found that during the aqueous alteration process, (i) Na and K were leached from chondrule glass and redistributed into the matrix, without forming any apparent Na- or K rich phase around the chondrule, (ii) Si from the chondrule mesostasis was lost from the zone of altered chondrule glass, and (iii) Mg and Fe were mobilized from the matrix into mesostasis regions, contributing to the precipitation of Mg- and Fe-bearing phyllosilicates. For Ca, Burger and Brearley (2004) noticed differences between the two CR chondrites studied. In EET92105, Ca was found inside the altered glass, whereas in EET87770, Ca was highly depleted in the mesostasis regions and Ca phosphate was found in the adjacent matrix material. Therefore, they inferred that EET87770 was more altered compared to EET92105. Brearley and Chizmadia (2005) suggested that the hydrolysis of Si-rich mesostasis glass (and formation of phyllosilicates) generated a fluid in the interior of chondrules that was more acidic (Drever, 1997). Therefore, Brearley (2011), on the investigation of Ca phosphates on a type IIA chondrule in the CM chondrite Y-791198, concluded that Ca and P that was leached from chondrule mesostases during aqueous alteration encountered a fluid in the matrix that was more alkaline, precipitating apatite at geochemical fronts on the edges of

chondrules. Although this mechanism is valid for many type II chondrules, such as Ch2, the present study demonstrates that phosphates described in Brearley (2011) are most likely primary in origin, probably consisting of merrillite rather than apatite, similar to Ch18 (section 4.1).

Calcium phosphates resulting from alteration of P-rich mesostasis glass are present in EET 92105 and EET 87770 (Burger and Brearley 2004, 2005), as well as around Ch2 in QUE 99177 (Fig. 2.3). Similarly, observations on Ch2 provide evidence of elemental exchange between the chondrule and the matrix, which is apparent by the partial leaching of P, Ca, Si, Na, and K from the chondrule glass in a large portion of the observed chondrule mesostasis (Fig. 2.3c,e) and the introduction of Fe (and water) into the chondrule (Fig. 2.3g). Sodium and K did not precipitate locally in any solid phase, consistent with ions travelling in solution further distances, because of their higher solubility (Burger and Brearley, 2005), but Ca and P precipitated as Ca phosphates in the fine-grained rim at a geochemical reaction front in the adjacent matrix. Further evidence for a parent body process is the positive correlation between the size of the leached chondrule mesostasis area and the abundance of Ca phosphates around type II chondrules. Chondrule 2, with the largest area of leached mesostasis, is the chondrule surrounded by a higher abundance of Ca phosphates (Fig. 2.3). Likewise, Ch5, with the lowest proportion of mesostasis regions, is surrounded by only a very few Ca phosphate grains (Fig. 2.6d). Further TEM work on this type of Ca phosphates around type IIA chondrules will reveal mineral phases and textures that will allow a more detailed petrologic understanding of their formation mechanisms.

4.3. Other secondary (parent body) Ca phosphates in QUE 99177

We have identified petrographic occurrences of Ca phosphates different from those formed in fine-grained rims around type IIA chondrules, but they also appear to have formed after chondrule formation. These distinct Ca phosphates are much less abundant and occur distributed around type IA chondrules (Fig. 2.6) and in the matrix (Fig. 2.7) as nanometer- to micron-sized grains. Primary P in type I chondrules and in matrix is mainly contained in Fe,Ni metal grains and in phosphides, respectively. Therefore, the alteration reactions that formed these Ca phosphates must be different from those that formed Ca phosphates around type IIA chondrules. In the sections that follow, we explore possible formation mechanisms of Ca phosphates around type I chondrules at the interface between their smooth rims and matrix, which have not been recognized before (section 4.3.1), and isolated Ca phosphate grains aggregated in small (1-2 μm) regions in the matrix (section 4.3.2), by aqueous alteration of Fe,Ni metal grains in chondrules.

4.3.1. Secondary Ca phosphates around type IA chondrules

Calcium phosphates around type IA chondrules are rare and exclusively associated with smooth rims, a type of rim that formed by aqueous alteration of the chondrule Silica-rich Igneous Rim (SIR) (see Chapter 1). In Chapter 1, we show that smooth rims (~20 μm-wide) essentially consist of an Fe-rich amorphous silicate gel (hydrated), Ca pyroxenes rich in Mn and Cr, and minor feldspar, glass, and/or chromite. Although many of the Fe,Ni metal blebs contained in type IA chondrule have been affected by terrestrial alteration (see Fig. 1.2 in Chapter 1), some smooth rims contain altered Fe,Ni metal blebs (e.g., Fig. 2.6e,f) that lack terrestrial veins crosscutting them, which suggests that at least some of the alteration could be pre-terrestrial.

Calcium phosphates around type IA chondrules are of two types: (1) located in the matrix exactly at the interface with the smooth rim (apatite) and (2) within the smooth rim (whitlockite) (Figs. 2.9, 2.10), with textures that also differ one another and from primary phosphates in type IIA chondrules. In addition, a submicron Ca-sulfate grain associated with Ca phosphates was found exactly at the interface between the smooth rim and the matrix around the studied chondrule (Fig. 2.9f). It is the only Ca sulfate found within the FIB section, but the abundance of this phase in other regions of the smooth rim that contain Ca phosphates has not been explored. The presence of Ca phosphates, possible pre-terrestrially altered Fe,Ni metal blebs, and one Ca sulfate suggests that the oxidizing fluid responsible for the dissolution of silica in the chondrule SIR during the earliest stages of aqueous alteration was also responsible for alteration of Fe,Ni metal blebs that released P in solution and precipitation of Ca phosphates. In addition, these observations indicate that the interface between the smooth rim and the matrix records an important geochemical front.

Evidence thus suggests that during alteration, P from altered Fe,Ni blebs in SIRs and Ca from the SIR mesostasis (feldspar) migrated outwards through an aqueous pore fluid and precipitated as apatite and/or whitlockite. In fact, Burger and Brearley (2004) noticed an increase in Ca peripheral to Fe,Ni metal grains in the matrix adjacent to the altered chondrule and argued that during the initial stages of the aqueous alteration process, the pH was acidic (high availability of H^+) to oxidize metal grains and to mobilize Ca, which generated a local chemical microenvironment. Therefore, Ca phosphates around type IA chondrules meet all the petrological criteria (e.g., they are hydrated and associated with smooth rims and altered Fe,Ni metal grains) of secondary

products formed between the interaction of the hydrated matrix and the anhydrous chondrule during the earliest stages of aqueous alteration in the parent body. Additional evidence for a secondary origin is found in Figure 2.6d, which illustrates an example of a type IIA chondrule (Ch5) molded against a neighboring type IA chondrule surrounded by a smooth rim (Ch20). The fact that Ca phosphates are distributed evenly within the smooth rim of Ch20 and in the fine-grained rim around Ch5 indicates that Ca phosphates formed during or after the formation of smooth rims, but not before.

Leaching of P from chondrule mesostases is ruled out because the P content of type I chondrule mesostases is extremely low (Table 1.1 in Chapter 1). Instead, P is easily released from alteration of Fe,Ni metal grains in the SIRs around type IA chondrules during the earliest stages of aqueous alteration. Phosphides (e.g., schreibersite) in the matrix as a possible source for P is also ruled out, because Ca phosphates decorate discrete regions at the interface between the smooth rim and the matrix. Furthermore, despite the low P content contained in Fe,Ni metal grains in CR carbonaceous chondrites (from 0.01 up to 1.10, Weisberg et al., 1993) compared to phosphides in the matrix, the abundance and sizes of Fe,Ni metal grains in type IA chondrules is much higher compared to nanometer-sized phosphides. Thus, Ca and P are more likely derived from the chondrule or the chondrule rim rather than the matrix.

4.3.2. Formation of Ca phosphates in the matrix

Isolated grains and grain assemblages of Ca phosphates in the matrix of QUE 99177 are remarkably similar in texture and size to phosphate grains identified at the interface between smooth rims and fine-grained matrices around type IA chondrules. Often, Ca phosphates are associated with Ca carbonates (Fig. 2.7d), a phase that is known

to have formed in the parent body from alkaline aqueous fluids, but Ca carbonates are more abundant in the matrix than Ca carbonates. Less frequently, Ca phosphates are closely associated with pentlandite (Fig. 2.7e).

Isolated P-bearing phases in the matrix of pristine chondrites have been previously noted in the literature (Goreva and Lauretta, 2004), but many questions remain about their nature and origins. Calcium phosphates in the matrix of QUE 99177 are different in texture and composition to those reported by Goreva and Lauretta (2004), who reported P-rich assemblages in the matrix of Semarkona. In Goreva and Lauretta (2004), P-bearing assemblages consist of merrillite, Fe,Ni metal, Fe-rich sulfides, and Fe-rich silicate (e.g., olivine), as well as P dissolved in the olivine. The authors could not discern between a solar nebula (Taylor et al., 1981) or a parent body origin similar to that proposed for carbide-magnetite assemblages in unequilibrated ordinary chondrites (Krot et al., 1997). In QUE 99177, Ca phosphates could have formed by the same oxidizing fluid that altered chondrule SIRs, but it is not clear whether they formed by aqueous alteration of Fe,Ni grains in type I chondrule SIRs, as mentioned above, or by a different process, such as parent body oxidation of phosphides in the matrix. The precipitation of Ca phosphates not only depends on the pH but also on the geochemistry of the altering fluid (e.g., activity of Ca ions in solution), but evidence indicates that the fluid was circum-neutral to mildly alkaline (see Chapter 1) in order to account for the preservation of Ca phosphates in the matrix (Faure, 1988). Therefore, the textural and mineralogical characteristics of isolated Ca phosphates (hydrated) in the matrix suggest that they are most likely derived from oxidation of Fe,Ni metal grains in chondrule SIRs (e.g., Fig. 2.6e,f) similar to phosphates discussed in section 4.3.1.

5. Conclusions

In the present study, we have described the different occurrences of Ca- and P-bearing phases found in the least altered CR chondrite known, QUE 99177, some of them for the first time. Most of the phosphates are found associated with (in and/or around) type II chondrules, but a few occurrences are associated with type I chondrules. The main discovery is that these phases record both primary processes in the solar nebula and secondary processes occurred during the earliest stages of aqueous alteration in the parent body. Therefore, P-bearing phases are extremely important for understanding early processes in the nebula that influenced planetary history and evolution, as well as the earliest interactions between primordial water in the solar system and anhydrous chondrules.

Primary phases identified in QUE 99177 are of two types, both associated with type IIA chondrules. The first occurrence consists of submicron merrillite rods forming narrow layers within mesostasis regions around the periphery of type II chondrules, previously reported in literature. We conclude that P_2O_5 enrichments in type IIA chondrule melts were sufficient to crystallize primary igneous phosphates in mesostasis regions by quenching at the final stages of crystallization. Here, we also report the first cronstedtite replacing chondrule glass in a CR chondrite. The second occurrence of primary Ca phosphate consists of tiny (nanometer-sized) grains of possibly an anhydrous merrillite analogue, evenly distributed in the fine-grained rim around a type IIA chondrule, which have not been previously reported in the literature. We infer that this type of nanometer Ca phosphates formed by oxidation of schreibersite in the solar nebula at temperatures between 664 and 400 K.

Secondary phases include abundant micron-sized apatite grains around type II chondrules that record elemental exchange between anhydrous chondrules and hydrated matrix during the earliest stages of aqueous alteration in the parent body. Following previous work by Burger and Brearley (2004, 2005), Brearley and Burger (2009), and Brearley (2011), we conclude that leaching of Ca and P from type II chondrule mesostasis glass by a mildly alkaline fluid precipitated Ca phosphate around chondrules. Alkalis and Si were also leached whereas Fe and Mg were introduced into the altered chondrule mesostasis. Finally, Ca phosphates are also related to parent body aqueous alteration by oxidation of P-bearing Fe,Ni metal blebs in type I chondrules, which released P in solution into the matrix. Calcium phosphates precipitated at geochemical fronts located at the interface between smooth rims and matrices, but also at further distances as isolated Ca phosphates in the matrix.

Acknowledgements

US Antarctic meteorite samples are recovered by the Antarctic Search for Meteorites (ANSMET) program, which has been funded by NSF and NASA, and characterized and curated by the Department of Mineral Sciences of the Smithsonian Institution and Astromaterials Curation Office at NASA Johnson Space Center. This work was supported and funded by NASA Cosmochemistry Grant NNX15AD28G to A. J. Brearley.

References

Abreu, N. M. and Brearley, A. J. 2010. Early solar system processes recorded in the matrices of two highly pristine CR3 carbonaceous chondrites, MET 00426 and QUE 99177. *Geochimica et Cosmochimica Acta* 74:1146–1171.

Alexander, C. M. O'D., Grossman, J. N., Wang, J., Zanda, B., Bourot-Denise, M., and Hewins, R. H. 2000. The lack of potassium-isotopic fractionation in Bishunpur chondrules. *Meteoritics & Planetary Science* 35:859–868.

Alexander, C. O. D., Grossman, J. N., Ebel, D. S., and Ciesla, F. J. 2008. The formation conditions of chondrules and chondrites. *Science* 320:1617–1619.

Amelin, Y., Krot, A. N., Hutcheon, I. D., and Ulyanov, A. A. 2002. Lead isotopic ages of chondrules and calcium-aluminum-rich inclusions. *Science* 297:1678–1683.

Anders, E. 1989. Pre-biotic organic matter from comets and asteroids. *Nature* 342:255–257.

Anders, E. and Grevesse, N. 1989. Abundances of the elements: Meteoritic and solar. *Geochimica et Cosmochimica Acta* 53:197–214.

Berlin, J., Jones, R. H., and Brearley, A. J. 2011. Fe-Mn systematics of type IIA chondrules in unequilibrated CO, CR, and ordinary chondrites. *Meteoritics & Planetary Science* 46:513–533.

Bouvier, A. and Wadhwa, M. 2010. The age of the Solar System redefined by the oldest Pb–Pb age of a meteoritic inclusion. *Nature geoscience* 3:637–641.

Boyce, J. W., Liu, Y., Rossman, G. R., Guan, Y., Eiler, J. M., Stolper, E. M., and Taylor, L. A. 2010. Lunar apatite with terrestrial volatile abundances. *Nature* 466:466–469.

Brearley A. J. 2006. The action of water. In *Meteorites and the Early Solar System II*, edited by Lauretta D. S. and McSween H. Y. University of Arizona, Tucson, AZ. Pp. 584–624.

Brearley, A. J. 2011. Formation of Ca-phosphates during aqueous alteration of type IIA chondrules in the Y-791198 CM2 carbonaceous chondrite. *74th Annual Meeting of the Meteoritical Society.* Abstract #5364.

Brearley, A.J. and Chizmadia, L.J. 2005. On the behavior of phosphorus during the aqueous alteration of CM2 chondrites. *36th Lunar and Planetary Science Conference.* Abstract #2176.

Brearley A. J. and Burger P. V. 2007. Hydrothermal alteration behavior of Kainsaz (CO3) at low temperatures under reducing conditions: insights into incipient aqueous alteration of carbonaceous chondrites. *37th Lunar and Planetary Science Conference*. Abstract #1687.

Brearley, A. J. and Burger, P. V. 2009. Mechanisms of aqueous alteration of type IIA chondrule glass in the CR chondrite EET 92105: Insights from FIB/TEM analysis. *Meteoritics and Planetary Science Supplement* 72:5148.

Bryant, D. E. and Kee, T. P. 2006. Direct evidence for the availability of reactive, water soluble phosphorus on the early Earth. H-Phosphinic acid from the Nantan meteorite. *Chemical communications* 22:2344–2346.

Burger, P. V. and Brearley, A. J. 2004. Chondrule glass alteration in type IIA chondrules in the CR2 chondrites EET 87770 and EET 92105: Insights into elemental exchange between chondrules and matrices. *35th Lunar and Planetary Science Conference*. Abstract #1966.

Burger, P. V. and Brearley, A. J. 2005. Localized chemical redistribution during aqueous alteration in CR2 carbonaceous chondrites EET 87770 and EET 92105. *36th Lunar and Planetary Science Conference.* Abstract #2288.

Changela, H. G., Le Guillou, C., Bernard, S., and Brearley, A. J. 2018. Hydrothermal evolution of the morphology, molecular composition, and distribution of organic matter in CR (Renazzo-type) chondrites. *Meteoritics & Planetary Science* 53:1006–1029.

Chizmadia, L. J. and Brearley, A. J. 2008. Mineralogy, aqueous alteration, and primitive textural characteristics of fine-grained rims in the Y-791198 CM2 carbonaceous chondrite: TEM observations and comparison to ALHA81002. *Geochimica et Cosmochimica Acta* 72:602–625.

Ciesla, F. J. and Cuzzi, J. N. 2006. The evolution of the water distribution in a viscous protoplanetary disk. *Icarus* 181:178–204.

Connolly Jr, H. C. and Huss, G. R. 2010. Compositional evolution of the protoplanetary disk: Oxygen isotopes of type-II chondrules from CR2 chondrites. *Geochimica et Cosmochimica Acta* 74:2473–2483.

Connolly, H. C. and Jones, R. H. 2016. Chondrules: The canonical and noncanonical views. *Journal of Geophysical Research: Planets* 121:1885–1899.

Connolly, H. C., Huss, G. R., Nagashima, K., Weisberg, M. K., Ash, R. D., Ebel, D. S., Schrader, D. L., and Lauretta, D. S. 2008. Oxygen isotopes and the nature and origins of type-II chondrules in CR2 chondrites. *39th Lunar and Planetary Science Conference*. Abstract #1675.

Drever, J. I. 1997. The geochemistry of natural waters: Surface and groundwater environments. 3rd edition, Prentice Hall (Upper Saddle River, N.J.). Pp. 436.

Ebel, D. S. and Grossman, L. 2000. Condensation in dust-enriched systems. *Geochimica et Cosmochimica Acta* 64:339–366.

Faure, G. 1997. *Principles and applications of geochemistry.* Vol. 625. 2nd Edition, Prentice Hall (Upper Saddle River, N.J.).

Fedkin, A. V., Grossman, L., Ciesla, F. J., and Simon, S. B. 2012. Mineralogical and isotopic constraints on chondrule formation from shock wave thermal histories. *Geochimica et Cosmochimica Acta* 87:81–116.

Fegley Jr, B. and Lewis, J. S. 1980. Volatile element chemistry in the solar nebula: Na, K, F, Cl, Br, and P. *Icarus* 41:439–455.

Friend, P., Hezel, D. C., and Mucerschi, D. 2016. The conditions of chondrule formation, Part II: Open system. *Geochimica et Cosmochimica Acta* 173:198–209.

Gaye, H. and Riboud, P. V. 1977. Oxidation kinetics of iron alloy drops in oxidizing slags. *Metallurgical transactions B* 8:409–415.

Goreva, J. S. and Burnett, D. S. 2001. Phosphate control on the thorium/uranium variations in ordinary chondrites: improving solar system abundances. *Meteoritics & Planetary Science* 36:63–74.

Goreva, J. S. and Lauretta, D. S. 2004. Phosphate Minerals in Semarkona (LL3. 0). *35th Lunar and Planetary Science Conference*. Abstract #2065.

Grossman, L. 2010. Vapor-condensed phase processes in the early solar system. *Meteoritics & Planetary Science* 45:7–20.

Grossman, L. and Olsen, E. 1974. Origin of the high-temperature fraction of C2 chondrites. *Geochimica et Cosmochimica Acta* 38:173–187.

Grossman, L., Beckett, J. R., Fedkin, A. V., Simon, S. B., and Ciesla, F. J. 2008. Redox conditions in the solar nebula: Observational, experimental, and theoretical constraints. *Reviews in Mineralogy and Geochemistry* 68:93–140.

Grossman, L., Fedkin, A. V., and Simon, S. B. 2012. Formation of the first oxidized iron in the solar system. *Meteoritics & Planetary Science* 47:2160–2169.

Harju E. R., Rubin A. E., Ahn I., Choi B.-G., Ziegler K., and Wasson J. 2014. Progressive aqueous alteration of CR carbonaceous chondrites. *Geochimica et Cosmochimica Acta* 139:267–292.

Hewins, R. H. 1991. Retention of sodium during chondrule melting. *Geochimica et Cosmochimica Acta* 55:935–942.

Hewins, R. H. 1997. Chondrules. *Annual Review of Earth and Planetary Sciences* 25:61–83.

Hewins R. H., Connolly H. C. Lofgren, G. E., Jr., and Libourel G. 2005. Experimental constraints on chondrule formation. In *Chondrites and the Protoplanetary Disk* (eds. A. N. Krot, E. R. D. Scott, and B. Reipurth). Astronomical Society of the Pacific Conference Series. Pp. 286–316.

Hewins, R. H., Ganguly, J., and Mariani, E. 2009. Diffusion modeling of cooling rates of relict olivine in Semarkona chondrules. *40th Lunar and Planetary Science Conference*. Abstract #1513.

Hewins, R. H. and Zanda, B. 2012. Chondrules: Precursors and interactions with the nebular gas. *Meteoritics & Planetary Science* 47:1120–1138.

Howard, K. T., Alexander, C. M. O'D., Schrader, D. L., and Dyl, K. A. 2015. Classification of hydrous meteorites (CR, CM and C2 ungrouped) by phyllosilicate fraction: PSD-XRD modal mineralogy and planetesimal environments. *Geochimica et Cosmochimica Acta* 149:206–222.

Hughes, J. M., Jolliff, B. L., and Rakovan, J. 2008. The crystal chemistry of whitlockite and merrillite and the dehydrogenation of whitlockite to merrillite. *American Mineralogist* 93:1300–1305.

Huss, G. R., Alexander, C.M. O'D., Palme H., Bland P.A., and Wasson J.T. 2005. Genetic relationships between chondrules, fine-grained rims, and interchondrule matrix. In *Chondrites and the protoplanetary disk* (eds. A. N. Krot, E. R. D. Scott, and B. Reipurth). Astronomical Society of the Pacific Conference Series. Pp. 701.

Huss, G. R., Rubin A. E., and Grossman J. N. 2006. Thermal metamorphism in chondrites. In *Meteorites and the Early Solar System II*, edited by Lauretta D. S., and McSween Jr. H. Y. The University of Arizona Press. Tucson, AZ. Pp. 567–586.

Jones, R. H. 1990. Petrology and mineralogy of type II, FeO-rich chondrules in Semarkona (LL3. 0): Origin by closed-system fractional crystallization, with evidence for supercooling. *Geochimica et Cosmochimica Acta* 54:1785–1802.

Jones, R. H. 1994. Petrology of FeO-poor, porphyritic pyroxene chondrules in the Semarkona chondrite. *Geochimica et Cosmochimica Acta* 58:5325-5340.

Jones, R. H., Grossman, J. N., and Rubin, A. E. 2005. Chemical, mineralogical and isotopic properties of chondrules: Clues to their origin. In *Chondrites and the protoplanetary disk* (eds. A. N. Krot, E. R. D. Scott, and B. Reipurth). Astronomical Society of the Pacific Conference Series. Pp. 251.

Jones C. L. and Brearley A. J. 2006. Experimental aqueous alteration of the Allende CV3 carbonaceous chondrites: insights into asteroidal aqueous alteration. *Geochimica et Cosmochimica Acta* 70:1040–1058.

Kitakaze, A., Sugaki, A., Itoh, H., and Komatsu, R. 2011. A revision of phase relations in the system Fe–Ni–S from 650 to 450 C. *The Canadian Mineralogist* 49:1687–1710.

Kong, P., Ebihara, M., and Palme, H. 1999. Distribution of siderophile elements in CR chondrites: Evidence for evaporation and recondensation during chondrule formation. *Geochimica et Cosmochimica Acta* 63:2637–2652.

Krot, A. N., Zolensky, M. E., Wasson, J. T., Scott, E. R., Keil, K., and Ohsumi, K. 1997. Carbide-magnetite assemblages in type-3 ordinary chondrites. *Geochimica et Cosmochimica Acta* 61:219–237.

Lauretta, D. S., Kremser, D. T., and Fegley Jr, B. 1995. Nickel fractionation during troilite formation in the solar nebula. *26th Lunar and Planetary Science Conference* 831-832 (Abstract).

Lauretta, D. S., Nagahara, H., and Alexander, C. M. O. D. 2006. Petrology and origin of ferromagnesian silicate chondrules. In *Meteorites and the early solar system II* (eds. Lauretta D. S. and McSween Jr. H. Y.). The University of Arizona Press. Tucson, AZ. Pp. 431–459.

Le Guillou, C., Changela, H. G., and Brearley, A. J. 2015. Widespread oxidized and hydrated amorphous silicates in CR chondrites matrices: Implications for alteration conditions and H2 degassing of asteroids. *Earth and Planetary Science Letters* 420:162–173.

Lodders, K. 2003. Solar system abundances and condensation temperatures of the elements. *The Astrophysical Journal* 591:1220.

Mayer, J., Giannuzzi, L. A., Kamino, T., and Michael, J. 2007. TEM sample preparation and FIB-induced damage. *Material Research Society Bulletin* 32:400–407.

McCoy, T. J., Dickinson, T. L., and Lofgren, G. E. 1999. Partial melting of the Indarch (EH4) meteorite: A textural, chemical, and phase relations view of melting and melt migration. *Meteoritics & Planetary Science* 34:735–746.

McSween Jr, H. Y. 1977. Chemical and petrographic constraints on the origin of chondrules and inclusions in carbonaceous chondrites. *Geochimica et Cosmochimica Acta* 41:1843–1860.

Murrell, M. T. and Burnett, D. S. 1983. The behavior of actinides, phosphorus, and rare earth elements during chondrite metamorphism. *Geochimica et Cosmochimica Acta* 47:1999–2014.

Noguchi T. 1995. Petrology and mineralogy of the PCA 91082 chondrite and its comparison with the Yamato-793495 (CR) chondrite. *Proceedings of the NIPR Symposium on Antarctic Meteorites* 8:33–62.

Oró, J. 1961. Comets and the formation of biochemical compounds on the primitive Earth. *Nature* 190:389–390.

Pape, J., Mezger, K., Bouvier, A. S., and Baumgartner, L. P. 2019. Time and duration of chondrule formation: Constraints from ^{26}Al-^{26}Mg ages of individual chondrules. *Geochimica et Cosmochimica Acta* 244:416–436.

Pasek, M. A. 2017. Schreibersite on the early Earth: scenarios for prebiotic phosphorylation. *Geoscience Frontiers* 8:329–335.

Pasek, M. A. 2019. Phosphorus volatility in the early solar nebula. *Icarus* 317:59–65.

Pasek, M. A., Smith, V. D., and Lauretta, D. S. 2004. A quantitative NMR analysis of phosphorus in carbonaceous and ordinary chondrites. *35th Lunar and Planetary Science Conference*. Abstract #1703.

Pasek, M. A. and Lauretta, D. S. 2005. Aqueous corrosion of phosphide minerals from iron meteorites: a highly reactive source of prebiotic phosphorus on the surface of the early Earth. *Astrobiology* 5:515–535.

Pirim, C., Pasek, M. A., Sokolov, D. A., Sidorov, A. N., Gann, R. D., and Orlando, T. M. 2014. Investigation of schreibersite and intrinsic oxidation products from Sikhote-Alin, Seymchan, and Odessa meteorites and Fe_3P and Fe_2NiP synthetic surrogates. *Geochimica et Cosmochimica Acta* 140:259–274.

Prieto, C. A., Lambert, D. L., and Asplund, M. 2002. A reappraisal of the solar photospheric C/O ratio. *The Astrophysical Journal Letters* 573:L137–L140.

Rubin, A. E. and Grossman, J. N. 1985. Phosphate-sulfide assemblages and Al/Ca ratios in type-3 chondrites. *Meteoritics* 20:479–489.

Rubin, A. E., Trigo-Rodríguez, J. M., Huber, H., and Wasson, J. T. 2007. Progressive aqueous alteration of CM carbonaceous chondrites. *Geochimica et Cosmochimica Acta* 71:2361–2382.

Schrader, D. L., Connolly Jr, H. C., and Lauretta, D. S. 2008. Opaque phases in type-II chondrules from CR2 chondrites: Implications for CR parent body formation. *Geochimica et Cosmochimica Acta*, 72:6124–6140.

Schrader, D. L., Connolly Jr, H. C., Lauretta, D. S., Nagashima, K., Huss, G. R., Davidson, J., and Domanik, K. J. 2013. The formation and alteration of the Renazzo-like carbonaceous chondrites II: Linking O-isotope composition and oxidation state of chondrule olivine. *Geochimica et Cosmochimica Acta* 101:302–327.

Schrader, D. L., Connolly Jr, H. C., Lauretta, D. S., Zega, T. J., Davidson, J., and Domanik, K. J. 2015. The formation and alteration of the Renazzo-like carbonaceous chondrites III: Toward understanding the genesis of ferromagnesian chondrules. *Meteoritics & Planetary Science* 50:15–50.

Schrader, D. L., Davidson, J., and McCoy, T. J. 2016. Widespread evidence for high-temperature formation of pentlandite in chondrites. *Geochimica et Cosmochimica Acta* 189:359–376.

Scott, E. R. and Krot, A. N. 2005. Chondritic meteorites and the high-temperature nebular origins of their components. In *Chondrites and the protoplanetary disk* (eds. A. N. Krot, E. R. D. Scott, and B. Reipurth). Astronomical Society of the Pacific Conference Series. Pp. 15−53.

Singerling, S. A. and Brearley, A. J. 2015. The Effects of Aqueous Alteration on Primary Iron Sulfides in CR and CM Chondrites. *78th Annual Meeting of the Meteoritical Society.* Abstract #5271.

Singerling, S. A. and Brearley, A. J. 2018. Primary iron sulfides in CM and CR carbonaceous chondrites: Insights into nebular processes. *Meteoritics & Planetary Science* 53:2078–2106.

Singerling, S. A. and Brearley, A. J. 2020. Altered primary iron sulfides in CM2 and CR2 carbonaceous chondrites: Insights into parent body processes. *Meteoritics & Planetary Science* 55:496–523.

Singerling, S. A., Sutton, S. R., Lanzirotti, A., Newville, M., and Brearley, A. J. 2016. Synchrotron X-Ray fluorescence analysis of trace elements in focused ion beam prepared sections of carbonaceous chondrite iron sulfides (CM and CR) and associated metal (CR). *79th Annual Meeting of the Meteoritical Society.* Abstract #6239.

Taylor, G. J., Okada, A., Scott, E. R. D., Rubin, A. E., Huss, G. R., and Keil, K. 1981. The occurrence and implications of carbide-magnetite assemblages in unequilibrated ordinary chondrites. In *Lunar and Planetary Science Conference* 12:1076–1078.

Villeneuve, J., Libourel, G., & Soulié, C. 2015. Relationships between type I and type II chondrules: Implications on chondrule formation processes. *Geochimica et Cosmochimica Acta* 160:277–305.

Wai, C. M., and Wasson, J. T. 1977. Nebular condensation of moderately volatile elements and their abundances in ordinary chondrites. *Earth and Planetary Science Letters* 36:1–13.

Wasson, J. T., and Rubin, A. E. 2003. Ubiquitous low-FeO relict grains in type II chondrules and limited overgrowths on phenocrysts following the final melting event. *Geochimica et Cosmochimica Acta* 67: 2239–2250.

Wasson, J. T. and Rubin, A. E. 2010. Metal in CR chondrites. *Geochimica et Cosmochimica Acta* 74:2212–2230.

Weeks, K. S. and Sears, D. W. 1985. Chemical and physical studies of type 3 chondrites—V: The enstatite chondrites. *Geochimica et Cosmochimica Acta 49*:1525–1536.

Weisberg, M. K., Prinz, M., Clayton, R. N., and Mayeda, T. K. 1993. The CR (Renazzo-type) carbonaceous chondrite group and its implications. *Geochimica et Cosmochimica Acta* 57:1567–1586.

Yu Y., Hewins, R. H., and Zanda B. 1996. Sodium and sulfur in chondrules: heating time and cooling curves. In *Chondrules and the protoplanetary disk* (eds. R. H. Hewins, R. Jones, and E. Scott). Cambridge University Press. Pp. 213.

Yu, Y. and Hewins, R. H. 1998. Transient heating and chondrule formation: Evidence from sodium loss in flash heating simulation experiments. *Geochimica et Cosmochimica Acta* 62:159–172.

Zanda, B., Bourot-Denise, M., and Hewins, R. H. 1995. Condensate sulfide and its metamorphic transformations in primitive chondrites. *Meteoritics* 30: 605–606.

Zanda B. 2004. Chondrules. *Earth and Planetary Science Letters* 224:1–17.

Zolensky, M. and McSween Jr, H. Y. 1988. Aqueous alteration. In *Meteorites and the early solar system* (eds. J. F. Kerridge and M. S. Matthews). The University of Arizona Press, Tucson, AZ. Pp. 114–143.

CHAPTER 3

A detailed TEM investigation of Martian apatite: Thermal evolution and volatile sources in the nakhlites NWA 998 and Nakhla

In collaboration with:
Charles K. Shearer
Adrian J. Brearley

To be submitted for publication to:
Geochimica et Cosmochimica Acta

Abstract

Apatite grains from the Martian nakhlites NWA 998 and Nakhla were investigated using transmission electron microscopy to examine their micro- and nanostructures and provide new insights into petrogenetic models for the origin of the chassignites and nakhlites. This is the most detailed TEM investigation of apatite in the nakhlites to date. The microstructures of selected F-, Cl-, OH-bearing apatites in NWA 998 and Nakhla are characterized by a domain structure at the 5-10 nm-scale defined by undulous lattice fringes and slight differences in contrast, indicative of localized elastic strain within the lattices and misorientations in the crystal. The domain structure records a primary post-magmatic signature formed during initial subsolidus cooling (~600 ºC), in which halogens clustered by phase separation (exsolution), but overall preserved continuity in the crystalline structure. Vacancies likely played a key role stabilizing these ternary apatites that otherwise would be immiscible. Apatites in Nakhla show large variations in halogens and REEs within and between grains that are only a few microns

apart, consistent with growth under disequilibrium conditions. Nakhla apatites preserve chemical zonation that is incompatible with the presence of an aqueous fluid, but consistent with crystallization from a late-stage melt that became Cl-enriched. There is no evidence of subsolidus ionic diffusion or post-magmatic fluid interactions that affected bulk apatite compositions in NWA 998 and Nakhla. A melt inclusion has been discovered in a cumulus apatite in NWA 998 with daughter chlorapatite (4.72 wt% Cl, 0.45 wt% F) and chloro-amphibole (4.75 wt% Cl) identified as chloro-ferro-ferri-barroisite, the first amphibole reported in NWA 998. The melt inclusion remained as a closed system although post-entrapment processes modified the chemical composition of the original trapped melt, resulting in an overestimation of Cl abundance. The chemistry of the melt inclusion and the amphiboles support mixing of Cl-rich sediments rather than K-metasomatism. Martian amphiboles likely stabilized at lower pressures (and temperatures) than terrestrial amphiboles due to their higher Cl contents, which constrains their formation temperature lower than 400 ºC, the current estimate. Finally, we report a late-stage, metasomatic fluorapatite in NWA 998 that grew on opened cleavage planes in the host apatite, forming apatite that is enriched more than 2x above the F concentration in the host apatite. The formation of this epitaxial fluorapatite represents a coupled dissolution-reprecipitation process caused by a low-temperature (~300ºC), slightly acidic, aqueous fluid that acted as a closed system. The late hydrothermal event only affected apatite on an extremely localized scale, without affecting the primary magmatic signatures of apatite. Thus, our results indicate that NWA 998 and Nakhla apatites experienced varying degrees of late igneous and subsolidus reactions and support a model based on crustal assimilation.

1. Introduction

The calcium phosphate apatite occurs in a wide range of terrestrial and extraterrestrial samples and has been used to estimate the activities (fugacities) of volatiles, such as F, Cl, and OH, both in melts and fluids. These studies provide important insights into the role of volatiles in magmatic and hydrothermal planetary processes, the identification of planetary volatile reservoirs, and provide glimpses into primordial volatile behavior during the early Solar System (e.g., accretion and differentiation; Sharp et al., 2016). Most recently, the volatile contents and their isotopic compositions (D/H, $\delta^{37}Cl$, $^{18}O/^{16}O$) in apatite have been used to better understand many of these processes related to the origin and evolution of Mars (e.g., Greenwood et al., 2003, 2008; Williams et al. 2016; Bellucci et al., 2017; Shearer et al., 2018).

Mars is a volatile-rich planet (Dreibus and Wänke, 1985; Wänke and Dreibus, 1988; Wänke, 1991; Halliday et al., 2001) and its mantle is one of the major geochemical reservoirs for volatiles (Chen and Wasserburg, 1986; Jagoutz, 1991; Dreibus and Jagoutz, 2002). Mantle-derived magmas, represented by Martian meteorites (e.g., shergottites, nakhlites, chassignites), provide a fundamental starting point to explore Martian volatile reservoirs (mantle, crust, and atmosphere) and their interactions. Investigations of Martian meteorites, combined with experimental studies, have suggested that Martian parental magmas are somewhat unique in that they appear to contain little water, but abundant chlorine (enriched 2.5x compared to the Earth) (Dreibus and Wanke, 1987; Filiberto and Treiman, 2009; Taylor, 2013). The contribution of crustal and atmospheric volatiles to mantle-derived magmas and their crystallization products may partially disguise the character of the mantle volatile reservoirs. Sulfur (e.g., Franz et al., 2014),

chlorine (e.g., Williams et al., 2016; Sharp et al., 2016; Shearer et al., 2018), oxygen (e.g., Agee et al., 2013), and noble gas (Ott, 1988; Swindle, 2002; Cartwright et al., 2013) isotopic systematics of Martian meteorites illustrate these contributions.

The texture and major element (Cl, F, and the molecule OH) and isotopic (Cl, H) compositions of apatite in nakhlites and chassignites have also revealed potential mixing of mantle and crustal volatile reservoirs at both magmatic and hydrothermal conditions (e.g., Leshin et al., 1996; McCubbin et al., 2013; McCubbin and Nekvasil, 2008; Hu et al., 2014; Shearer et al., 2018). Despite the wealth of data from compositional and isotopic studies of apatite, there has only been a limited number of studies of the microstructural characteristics of extraterrestrial apatite (i.e., Słaby et al., 2017; Barnes et al., 2017; Birski et al., 2019). These studies demonstrate that micro- and nanostructural examination of apatite have the potential to provide constraints on conditions of crystallization, precipitation, and fluid interaction on Mars. In particular, the microstructures of apatite may provide additional insights into the contributions of distinct volatile reservoirs to the geochemical evolution of Martian basalts and the timing of the interactions of fluids from these different reservoirs. Such studies may also provide important context for understanding the chemical and isotopic compositions of apatite, notably the possible modification of the primary compositions by late-stage fluid interactions.

One of the main caveats in using apatite as a petrogenetic indicator is that the extreme variability of F:Cl ratios in Nakhla apatite cannot be explained by a typical igneous process (e.g., Meurer and Boudreau, 1996). Therefore, different hypotheses have been proposed to account for this variability, including secondary processes involving

aqueous fluids (McCubbin and Nekvasil, 2008; McCubbin et al., 2013) and crystallization from a magma that underwent crustal assimilation (e.g., Usui et al., 2012; Lin et al., 2013; Shearer et al., 2017). In these different scenarios, the mechanism of formation of apatite grains with variable F:Cl ratios is different. For scenarios where fluids are involved, different sources for the fluid have been suggested, for example aqueous alkali-ferrous chloride fluids that exsolved from the parental melt as it crystallized (Giesting and Filiberto, 2016), or alternatively, crustal fluids (brines) that infiltrated from the surface (McCubbin et al., 2013; Cartwright et al., 2013). Another possibility that has been proposed for the Shergottites is Cl-rich aqueous brines that formed through degassing of the magma chamber or sills when magmas crystallized at depth (Howarth et al., 2015). In all cases of fluid involvement, a Cl-, LREE-rich fluid migrated upward to the cumulate pile and enriched the residual liquid in Cl during the ascension, resulting in equilibration of interstitial phases with the brine and forming Cl-rich apatites (McCubbin and Nekvasil, 2008; McCubbin et al., 2013). Chlorine partitioned into the fluid phase whereas F was retained in the melt (Holland, 1972; Kilinc and Burnham, 1972; Aiuppa et al., 2009; Ustunisik et al., 2011). Crustal assimilation for the source of Cl has also been suggested, supported by the existence of two Cl-isotopic reservoirs recorded in apatites from the Chassigny meteorite: intercumulus apatites are enriched in heavy Cl, corresponding to the values from the crust, whereas apatite inside melt inclusions in olivine are enriched in light Cl, corresponding to the mantle signature, as well as to the primordial solar system composition from which Mars accreted (Shearer et al., 2017). Such discovery led to the conclusion that the crust (heavy reservoir) likely played a role during Chassigny crystallization.

To this end, in the present study we have focused on the microstructural characterization of apatite from two Martian basalts, NWA 998 and Nakhla, using Transmission Electron Microscopy. The objectives of this study are: (1) determine if apatites in these meteorites record additional information at the micron to nanometer scales that can provide new insights into the magmatic and subsolidus evolution of volatiles in the Martian volcanic system, (2) determine the potential role that hydrothermal systems played in the volatile evolution of nakhlites, and (3) evaluate how the post-magmatic history affects the utilization of apatite to reconstruct the magmatic and volatile behavior of the Martian mantle. The current lack of microstructural information for apatite in the nakhlites represents a major gap in interpreting the volatile record preserved in this complex mineral.

2. Samples and analytical methods

We studied apatite grains in the two nakhlite meteorites, Northwest Africa 998 (,002) and Nakhla. Northwest Africa 998 is a find with a terrestrial residence age of 6000 ± 1000 years (Nishiizumi et al., 2004) and Nakhla is an observed fall (Egypt, 1911). Estimated depths for NWA 998 and Nakhla in the cumulus pile are >>30 m and ~10 m, respectively (Mikouchi et al., 2003, 2006, 2012). The studied samples are polished 1-inch round petrographic thin sections from the Institute of Meteoritics Collection at the University of New Mexico. After being coated with a 10 nm layer of carbon, each thin section was studied to identify and locate apatite grains using backscattered electron (BSE) imaging and energy dispersive spectroscopy (EDS) X-ray analysis on a FEI Quanta 3D Dualbeam© field emission gun (FEG) SEM/FIB. The analytical conditions used were 30 kV accelerating voltage and a beam current of 4 nA. The instrument is

equipped with an EDAX Genesis EDS system and an Apollo 40 SDD 40 mm^2 EDS detector for qualitative X-ray analysis. Complete BSE mosaics of the entire thin section of each meteorite were obtained using SEM in order to assess the general spatial distribution of apatite grains and aid location of apatite grains within the samples. We did not perform quantitative analyses of the complete distribution or modal abundance of the apatite grains. BSE imaging at very low kV (5-10 kV) and high contrast were performed to examine apatite grains at high magnifications and determine their possible microstructures and petrographic occurrences, such as veins.

Focused ion beam (FIB) samples for transmission electron microscopy (TEM) of selected apatite grains were prepared with the FIB technique using the FEI Quanta 3D FEGSEM/FIB instrument. The region of interest was protected from sputtering by the Ga^+ beam by depositing a 2 μm-thick Pt strip across the area prior to sample extraction. TEM samples were removed from the thin sections by the *in situ* lift-out technique using an Omniprobe 200 micromanipulator and transferred onto Cu half grids. These samples were then ion milled to a thickness of approximately 50 nm for optimal high-resolution imaging with ion beam currents decreasing from 1 nA down to 53 pA for the final stage of ion milling, at 30 kV operating voltage. Redeposition of sputtered material occurred on some FIB sections, which was removed using a low-angle final polishing step with a 2 kV and 50 pA ion beam. Bright-field (BF) TEM imaging, high-resolution TEM (HRTEM), TEM-EDS, STEM-EDS, selected area electron diffraction (SAED), high-angle annular dark field (HAADF) imaging, and STEM-EDS mapping were performed on the FIB samples using a JEOL 2010F FEG TEM/scanning TEM (STEM) operating at 200 kV using GATAN Microscopy Suite® (GMS) imaging software. Quantitative EDS

analyses were obtained using an Oxford AZTec X-ray analysis system with a X-Max 80N 80 mm^2 SDD energy dispersive X-ray spectrometer (EDS) detector system. Each spectrum was collected for 300 and 500 seconds in regular TEM mode and Scanning TEM mode, respectively, using a spot size of 5 and a defocused beam of ~100 nm in TEM mode to reduce beam damage. Quantification of EDS data was conducted using the Cliff-Lorimer thin film approximation with theoretical k-factors. Errors were all <5% (relative error). The analyses assume oxygen present according to oxide stoichiometry and normalized to 100 wt%. Energy Filtered TEM combined with HRTEM were used to characterize the local distribution of Cl in the apatite nanostructure. EFTEM images were acquired using a 3 mm GIF entrance with a collection time of 10 seconds. All SEM and TEM studies were performed at the Department of Earth and Planetary Science at the University of New Mexico.

The measured X-ray flux from apatite is affected by crystal orientation (Stormer et al., 1993). As a result, apparent F concentrations can change by as much as 100% when the electron beam is parallel to the *c* axis (Stormer et al., 1993), which is the case for FIB sections 2 (NWA 998) and 3 (Nakhla). Therefore, there might be errors with the apparent F concentration reported here (less for Cl, Ca, and P; Webster and Piccoli, 2015). To correct that, we have used a relatively large TEM electron beam diameter (~1-2 μm), as far as it was possible, to reduce the electron beam densities. FIB1 (NWA 998), cut parallel to the *c* axis, gives more accurate analyses for F and Cl, as the electron beam is incident perpendicular to the *c* axis (Goldoff et al., 2012). However, because FIBs 1 and 2 (NWA 998) give similar results, we consider this effect to be minimal. Furthermore, the missing component is represented by Z content in the tables (1 = F + Cl + Z), which

includes OH and vacancies; thus, the halogen site is assumed not fully occupied (Piccoli and Candela, 2002) (see section 4.1).

3. Results

3.1. Apatite petrography of NWA 998 and Nakhla

3.1.1. Northwest Africa 998

The studied thin section (,002) contains a single piece (~9 mm in its maximum length) of the Martian augite-rich cumulate basalt NWA 998 (Fig. 3.1), which represents the most equilibrated nakhlite currently known (McCubbin et al., 2013). The predicted crystallization sequence starts with subhedral olivine, followed by orthopyroxene, titanomagnetite, zoned augite, pigeonite, which represents the framework of the rock with a modal abundance of ~75 vol% (Treiman and Irving, 2008), plagioclase, and interstitial mesostasis regions (Irving et al., 2002; Russell et al., 2003; Treiman, 2005; Treiman and Irving, 2008). Late-stage intercumulus regions consist of potassium feldspar, chlorapatite, pyrrhotite, chalcopyrite, titanomagnetite, and alkali-rich glass. Apatite is the only reported phosphate present in the nakhlites, merrillite being absent (Treiman and Irving, 2008; McCubbin et al., 2013).

Apatites are coarse grained, ranging from ~5 to ~200 μm in size (relatively large in comparison to other samples), randomly distributed, fractured, and mainly subhedral, but several euhedral grains were also identified. SEM images of NWA 998 apatites are presented in Fig. 3.2a-k and A2.1 in Appendix 2. They mainly occur with pigeonite, alkali feldspar, K-, Na-rich glass (maskelynite), titanomagnetite, ilmenite, and troilite, typically associated with large fractures between cumulus pyroxene grains. All apatite grains lack observable zonation at the SEM scale. The relatively large sizes of the

apatites, which reach similar sizes to other crystals in the paragenetic sequence (e.g., 3.2a-c,f,h,k), and their occurrence as mineral inclusions within titanomagnetite (e.g., apatites 12.1, 12.2, 5.2, 5.4 in Fig. 3.2d,g,) have been interpreted as indicating a relatively early crystallization inside melt pockets during growth of the cumulus minerals (McCubbin et al., 2013). Petrographic observations made here (e.g., Fig. 3.2g,h) indicate that cumulus apatite crystallized before titanomagnetite. Apatite is not a cumulus phase in any other nakhlite, being NWA 998 the most evolved nakhlite (McCubbin et al., 2013). Here, we will refer to cumulus apatites as those that are totally or partially included in pigeonite (e.g., at the interface between cumulus Fe-rich pigeonite grains, Fig. 3.1) or augite (e.g., Fig. 3.2a-c,e,h,k), which are generally larger and equant. Intercumulus apatites are those that are included in K-rich interstitial melt pockets, which are generally smaller and acicular (e.g., Fig. 3.2d,i,j). Cumulus apatites may have crystallized at the very end of the pyroxene crystallization, near their surface between cumulus pigeonite grains, regions where incompatible elements accumulated. Compositionally, apatites in NWA 998 show little variation along the F-Cl join (~1:1 ratio) in the ternary plot of the Z-site occupancy ($F_{0.84}Cl_{0.76}OH_{0.40}$ Atoms Per Formula Unit (apfu); McCubbin et al., 2013), with a typical OH content >20% of the Z-site occupancy, calculated based on stoichiometry (Bunch and Reid, 1975; Treiman and Irving, 2008; McCubbin et al., 2013). Nonetheless, Channon et al. (2011) only measured 0.07-0.11 wt% H_2O in NWA 998 apatite using secondary ion mass spectrometry (SIMS). A ternary F-Cl-Z plot, where Z = missing component, of NWA 998 and Nakhla apatite compositions reported in the literature by EPMA and SIMS, along with results obtained in the present study by TEM-EDS, is presented in Figure 3.3.

3.1.2. Nakhla

A mosaic of the studied thin section is shown in Figure 3.1b. Unlike NWA 998, Nakhla does not contain coarse-grained apatite, and apatite is only found as acicular to platy needles included in mesostasis glass and feldspar (Figs. 3.2l-r and A2.1 in Appendix 2). Thus, apatite in Nakhla only crystallized in the interstitial regions between cumulus grains under conditions far from equilibrium and rapid cooling. Apatite has also been identified within melt inclusions in olivine crystals (McCubbin et al., 2013, and references therein). The mesostasis regions are randomly distributed throughout the thin section, ranging from ~50 μm to ~370 μm in size, and contain diverse minerals such as alkali feldspar, chlorapatite, chromite, kaersutite (hydrous amphibole), pigeonite, augite, titanomagnetite with ilmenite exsolution lamellae, silica, and sulfides (pyrite, troilite, and chalcopyrite), among others (Harvey and McSween, 1992; Bridges and Grady, 1999, 2000; Treiman, 2005). Since apatites in Nakhla belong to a less evolved stage in the paragenetic sequence of the parental liquid compared to NWA 998 (Wadhwa and Crozaz, 1995; Treiman and Irving, 2008; McCubbin et al., 2013), cumulus orthopyroxene does not occur in this sample, the abundance of augite is higher, and the intercumulus mesostasis is more vitrophyric. Apatite grains in Nakhla have highly variable F:Cl ratios from very Cl-rich to very F-rich, with a missing component abundance ranging from 0 to 14 mol% (McCubbin et al., 2013) (Fig. 3.3). Although apatite only has a modal abundance of ~0.5%, it accounts for 85% of the La, 30% of the Eu, and 50% of the HREE present in Nakhla (Wadhwa and Crozaz, 1992, 1995, 2003).

Apatites range from moderately to highly elongated, most likely due to different orientations of elongate crystals within the section, and have subhedral to anhedral habits.

Nakhla apatites are significantly smaller (~1-5 μm thick and up to 50 μm long, with a mean length of ~20 μm) compared to NWA 998 apatites. The myriad of apatites occur in groups of crystals that range from randomly oriented (most cases, e.g., Fig. 3.2l,n) to parallel or subparallel (rarer, e.g., Fig. 3.2m). They are found in almost all intercumulus residual mesostasis pockets, closely intergrown with K-rich glass, associated with plagioclase (~50 μm in size) that is compositional zoned in An content, titanomagnetite (~ 20-50 μm size), troilite (ranging from sub-μm to ~20 μm in size), and silica (ranging from a few microns to ~20 μm in size, Figs. 3.2r and A2.1i in Appendix 2). Typically, each intercumulus region contains more than one individual apatite grain. Fractures are present in all apatite grains. Sometimes micron-sized apatites can occur in trails at the interface between feldspathic glass and crystalline feldspar (e.g., Fig. 3.2q). In contrast to NWA 998, apatites in Nakhla show zonation, where the cores of the apatite needles present lower Z contrast in BSE imaging (e.g., apatite 2.2. in Fig. 3.2n). We have identified some grains that also show deformation (Figs. 3.2r and A2.1k in Appendix 2).

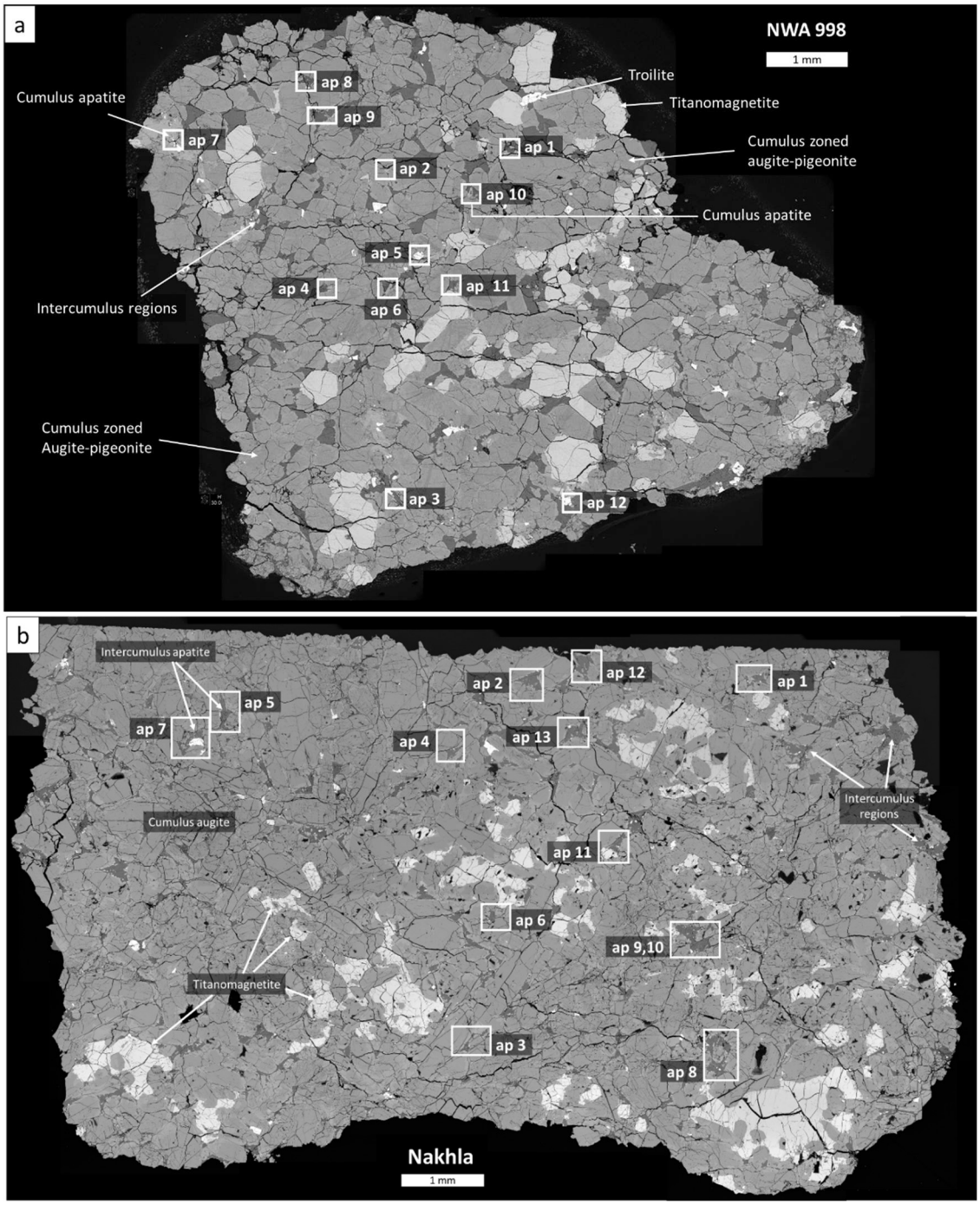

Figure 3.1. BSE mosaics of the two thin sections of the Martian basalts used in this study. (a) NWA 998 thin section showing cumulus pyroxenes (in medium grey), titanomagnetite (in lighter grey), and troilite (in white). Intercumulus regions are shown in darker grey, which are randomly distributed and range from ~100 µm to ~500 µm, and some contain intercumulus apatite. Apatite grains (up to ~200 µm in size) are commonly found embedded in cumulus pigeonite or augite. b) Nakhla thin section showing cumulus pyroxenes, which comprise most of the area, titanomagnetite, which varies greatly in size (in light grey), and intercumulus regions (in dark grey), ranging from ~50 to ~370 µm in size. *(Caption continues on the following page).*

Figure 3.1. *(Caption continues from previous page).* Apatites in Nakhla are exclusively found inside intercumulus melt pockets. White squares indicate the locations of the apatite grains that were selected for this study, which represent a large subpopulation of all apatites in the samples. Individual apatite grains are shown and described in Figures 3.2 and A2.1 in Appendix 2.

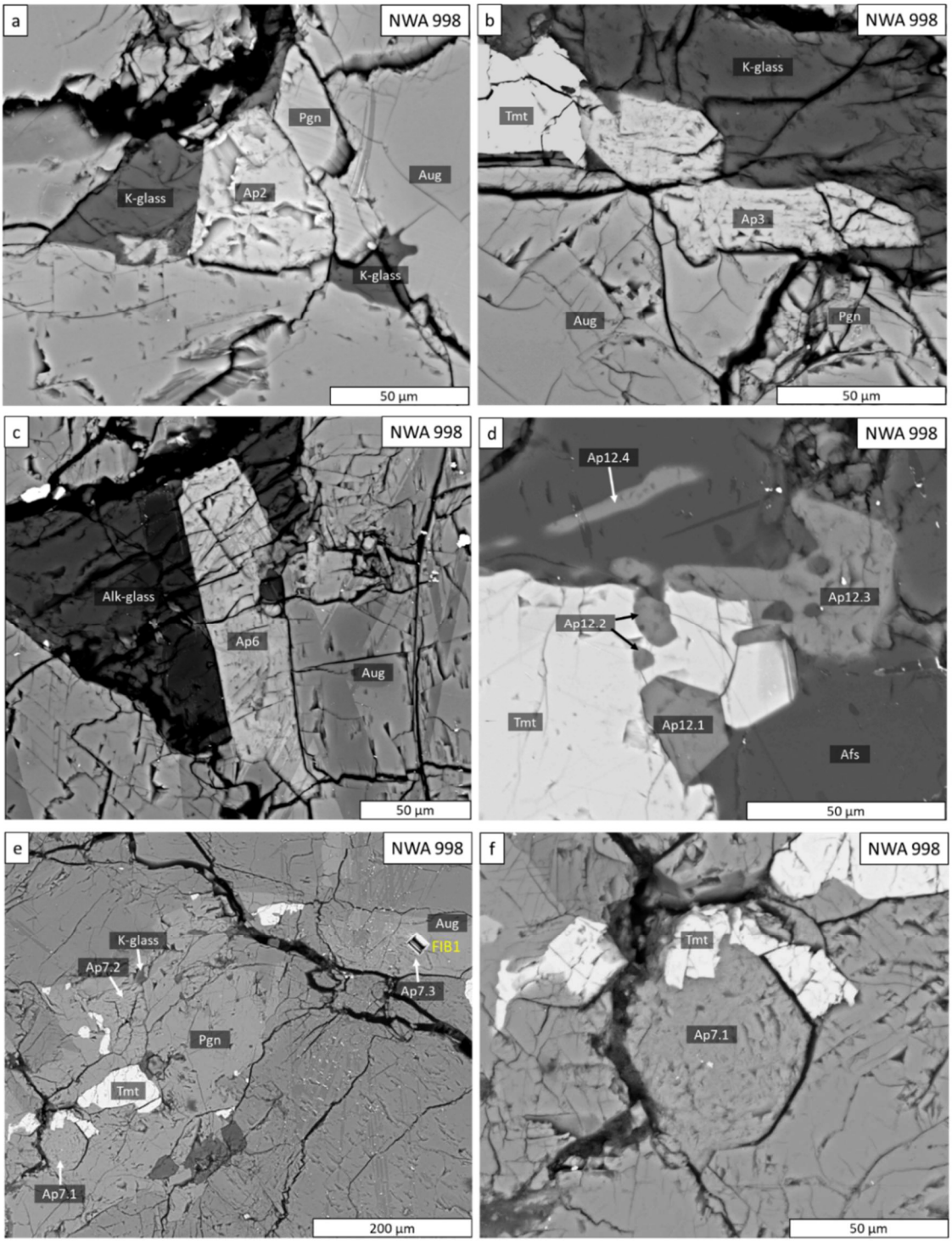

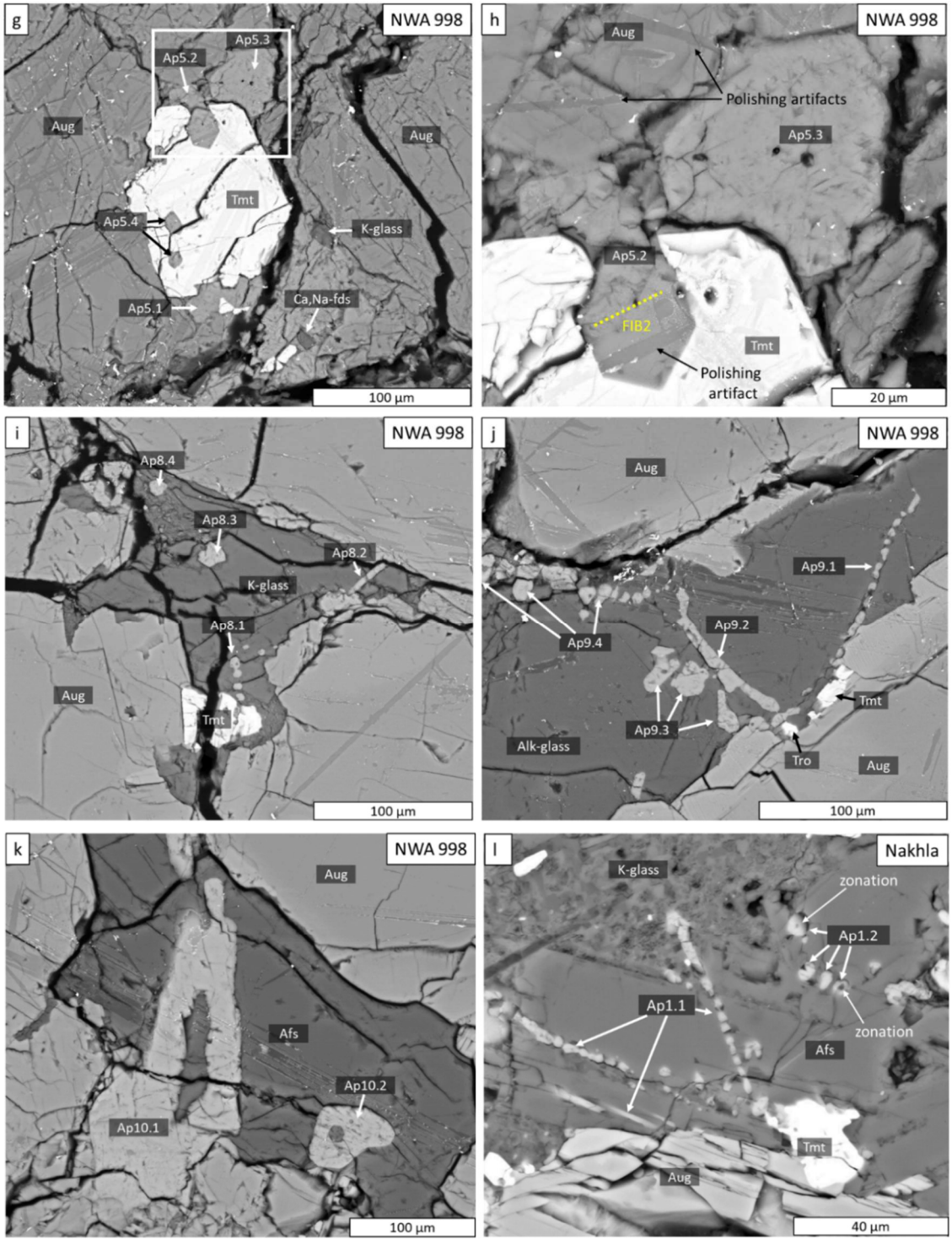
g
NWA 998
Ap5.2
Ap5.3
Aug
Aug
Tmt
Ap5.4
K-glass
Ap5.1
Ca,Na-fds
100 µm
h
NWA 998
Aug
Polishing artifacts
Ap5.3
Ap5.2
FIB2
Tmt
Polishing artifact
20 µm
i
NWA 998
Ap8.4
Ap8.3
Ap8.2
K-glass
Ap8.1
Aug
Tmt
100 µm
j
NWA 998
Aug
Ap9.1
Ap9.4
Ap9.2
Tmt
Ap9.3
Alk-glass
Tro
Aug
100 µm
k
NWA 998
Aug
Afs
Ap10.2
Ap10.1
100 µm
l
Nakhla
K-glass
zonation
Ap1.2
Ap1.1
zonation
Afs
Tmt
Aug
40 µm

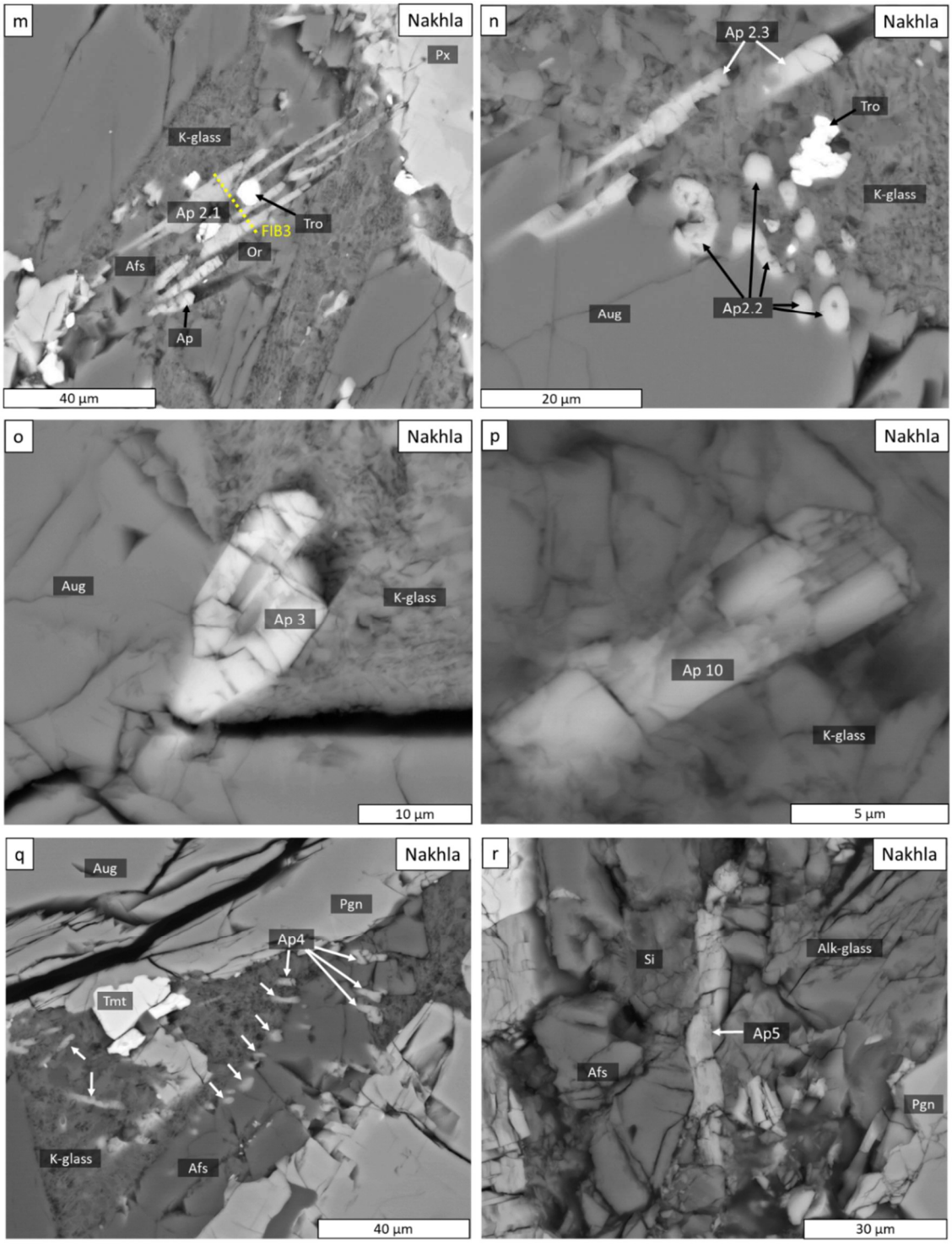

Figure 3.2. *(On present and previous pages).* Backscattered electron SEM images of apatite grains in NWA 998 (a-k) and Nakhla (l-r). Apatite numbers referred in Fig. 3.1. NWA 998: **a)** Apatite 2 (Ap2): Anhedral intercumulus chlorapatite, ~50 µm size, associated with K-rich glass, zoned pyroxene, and a fracture. *(Caption continues on the following page).*

Figure 3.2. *(Caption continues from previous page).* **b)** Apatite 3 (Ap3): Anhedral intercumulus chlorapatite, ~100 µm in size, associated with titanomagnetite, K-rich glass, and zoned pyroxene. **c)** Apatite 6 (Ap6): Anhedral intercumulus chlorapatite, ~120 µm long, associated with alkali-rich glass and augite. **d)** Apatites 12 (Ap12): Anhedral intercumulus chlorapatite grains, ~25–35 µm size, included in alkali feldspar and intergrown with titanomagnetite. **e)** Apatites 7 (Ap7): Anhedral to euhedral cumulus apatite grains, included in pigeonite (Ap7.1 and 7.2) and augite (Ap7.3). FIB section 1 was extracted in Ap7.3, which is a subhedral, ~75 µm long, and fully included in augite. **f)** Close up of Apatite 7.1, a euhedral (basal section) cumulus apatite, 55 µm in size, intergrown with titanomagnetite and fully included in pigeonite. **g)** Apatites 5 (Ap5): Euhedral cumulus chlorapatites with sizes ranging from ~10 to 50 µm, partially intergrown (Ap5.1, 5.2, and 5.3) or totally included (Ap5.4) in titanomagnetite. **h)** Close up of the euhedral cumulus Ap5.2, ~40 µm long, where FIB section 2 was extracted, and subhedral chlorapatite 5.3 (~50 µm size). The observed straight, linear features are artifacts caused by thin section polishing. **i)** Apatites 8 (Ap8): Euhedral to subhedral intercumulus apatite grains, ~5 µm in size, cut perpendicular to the *c* axis embedded in a melt pocket of K-rich glass (with minor Na), ~120 µm in size. Close-up images are found in Fig. A2.1c-e in Appendix 2. **j)** Apatites 9 (Ap9): Anhedral to subhedral intercumulus apatites, ranging from ~5 to 80 µm-size, embedded in Na, K-rich maskelynite in a large (up to ~580 µm-size) melt pocket. Some apatites contain minor Si and are associated with Cr-rich titanomagnetite and troilite. **k)** Apatites 10 (Ap10): Large (up to 200 µm in size) anhedral intercumulus apatites partially included in alkali feldspar and augite. Nakhla: **l)** Apatites 1 (Ap1): Acicular intercumulus apatites, ~5 µm in size, randomly oriented, embedded in alkali feldspar and K-rich glass, and associated with titanomagnetite. Apatites cut close to either parallel (Ap1.1) or perpendicular (Ap.1.2) to the *c* direction showing zonation. **m)** and **n)** Intercumulus apatites number 2 (Ap2): **m)** parallel to subparallel acicular chlorapatites included in K-rich glass and alkali feldspar, associated with troilite. FIB3 was cut perpendicular to the elongation direction. **n)** Micron-sized group of intercumulus apatites cut perpendicular and subparallel to the *c* axis, partially included between a K-rich glass in a melt pocket and the host pyroxene. Apatites 2.2 are compositionally zoned. **o)** Apatite 3 (Ap3): Euhedral, zoned intercumulus apatite, ~15 µm-size, in the interstice between a K-rich maskelynite melt pocket and augite. **q)** Apatites 4 (Ap4): Micron-sized intercumulus apatites decorating the margins of a mesostasis melt pocket. **r)** Apatite 5 (Ap5): Possible shocked intercumulus chlorapatite containing minor Si included in a mesostasis pocket between augite crystals. Titanomagnetite, silica, and fragmented augite crystals are included within the melt pocket. The interstitial melt pocket is alkali-rich glass. Abbreviations are indicated as follows: Ap = apatite, Afs = alkali feldspar, Alk-glass = alkali-rich glass, K-glass = K-rich glass, Pgn = pigeonite, Aug = augite, Tmt = titanomagnetite, Tro = troilite, and Si = silica.

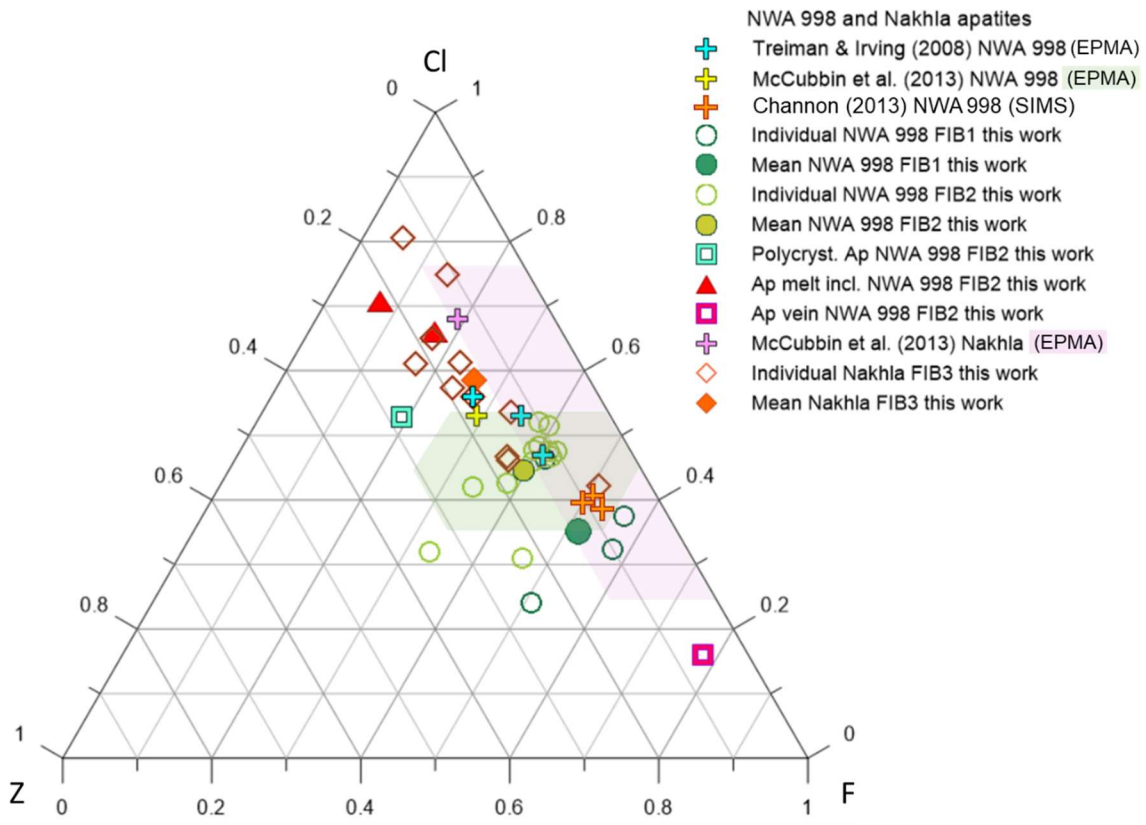

Figure 3.3. Ternary plot of apatite X-site occupancy (mol%) for NWA 998 and Nakhla. Unless otherwise indicated, individual symbols represent single analyses. Aquamarine and yellow crosses represent multiple analyses of NWA 998 apatites from Treiman and Irving (2008) and McCubbin et al. (2013), respectively, obtained by EPMA (the shadowed green area comprise the full range of apatite values obtained by McCubbin et al., 2013). Orange crosses represent SIMS analyses of NWA 998 apatite from Channon (2013). Individual NWA 998 apatite values from this work are represented by dark (FIB1) and light (FIB2) green open circles, with their respective averaged compositions represented by filled dark and light green circles. The composition of the polycrystalline apatite in NWA 998 is represented by turquoise hollow square represents, apatite in the melt inclusion of NWA 998 apatite, by filled red triangles, and the composition of the epitaxial vein in NWA 998 apatite, by a hollow pink square. The averaged composition of Nakhla apatites by McCubbin et al. (2013) is represented by a pink square (the shadowed pink area comprise the full range of compositions). The composition of Nakhla apatites obtained by TEM EDS analyses is represented by hollow (individual analyses) and filled (averaged) orange diamonds. All analyses of this work were obtained by semiquantitative analyses TEM-EDS. Data from this work are tabulated in Tables 3.1-3.4. Z = missing component (OH + vacancies).

3.2. TEM observations

3.2.1. Cumulus apatite in NWA 998

Apatites in NWA 998 are among the largest found in the Martian meteorites (e.g., McCubbin et al., 2013) and textural interpretations suggest both cumulus and intercumulus origins. In NWA 998, two foils from two different cumulus apatite grains were cut for microstructural analysis using TEM, numbered FIB1 (apatite 7.3 in Fig. 3.2e) and FIB2 (apatite 5.2 in Fig. 3.2g,h).

FIB1 was cut parallel to the elongated direction of a euhedral to subhedral apatite grain, ~25 x 80 μm size, entirely included in Fe-rich pigeonite (Fig. 3.4a). A dark-field STEM mosaic of the FIB section shows nm-scale worm-like features (Fig. 3.4d) that are present on all the phases in the section including epoxy-filling fractures, thus these are not original features, but artifacts caused by re-deposition during FIB preparation. The FIB section was subsequently cleaned using low kV, low angle FIB milling as explained in section 2, prior to doing TEM-EDS analyses. Transmission electron microscopy shows that apatite is present in the upper part of the FIB section, comprising about 65% of the FIB section area, and consists of a single crystal with a few slightly misoriented subgrains, a few parallel, straight fractures (~0.2-0.5 μm-size) that crosscut the FIB section, which were filled with epoxy during thin section preparation, and some dislocations. The parallel nature of the fractures (parallel to the (111) plane, Fig. 3.4c) suggests that apatite develops preferential planes of fracture during shock within a particular crystallographic direction, a feature that has been described in other minerals (e.g., Pittarello et al., 2020). The dislocations occur as elongate arrays (Fig. 3.4b,c), heterogeneously distributed, subparallel to the fractures. Energy dispersive X-ray

analyses and diffraction patterns reveal that the lower part of the FIB section consists of Fe-rich, Ca-poor pyroxene, consistent with pigeonite composition (Table 3.1). In addition, the pigeonite is associated with a pore ~1.5-2 μm in size (Fig. 3.4b,d). Despite the fractures and dislocations, the apatite within the FIB section looks homogeneous at the micron scale (Fig. 3.4b,c). Based on quantitative TEM-EDS analyses, apatite has slightly more chlorine (2.40 wt% average) than F (1.90 wt% average) (Cl/F = 1.26, Table 3.1), and with REE concentrations that are below detection levels for EDS analysis.

Electron diffraction patterns show a diffuse streaking parallel to the [111] direction (Fig. 3.4d, inset). We have further investigated the possible origin of this streaking using dark-field STEM imaging, which reveals compositional heterogeneities in the form of mottled Z-contrast regions at the 5-10 nm scale (Fig. 3.5a). These regions consist of irregularly shaped domains with lower Z contrast, surrounded by continuous higher-Z regions. Although the proportions of these two different domains are approximately equal throughout the FIB section, we cannot rule out the possibility that these features were produced by beam damage.

High-resolution TEM images taken parallel to the [1-21] zone axis also reveal a domain structure at the 5-10 nm scale (Fig. 3.5b,c) that could be attributable to the same domains seen with dark-field STEM. In the HRTEM images, domains are apparent from differences in the contrast in the lattice fringes and each domain region has a slight misorientation relative to one another (Fig. 3.5b,c). These misorientations between domains are apparent when viewing the HRTEM images at a low angle to the page along the lattice fringes. Lattice planes are continuous, but show distinct, slight curvature around the edges of the domains, and narrow diffuse boundaries appear to distinguish one

domain from another, which might be attributed to the presence of vacancies, all indicative of highly localized strain within the structure. We attribute the streaking (Fig. 3.4d, inset) to the presence of these domains (Fig. 3.5b,c).

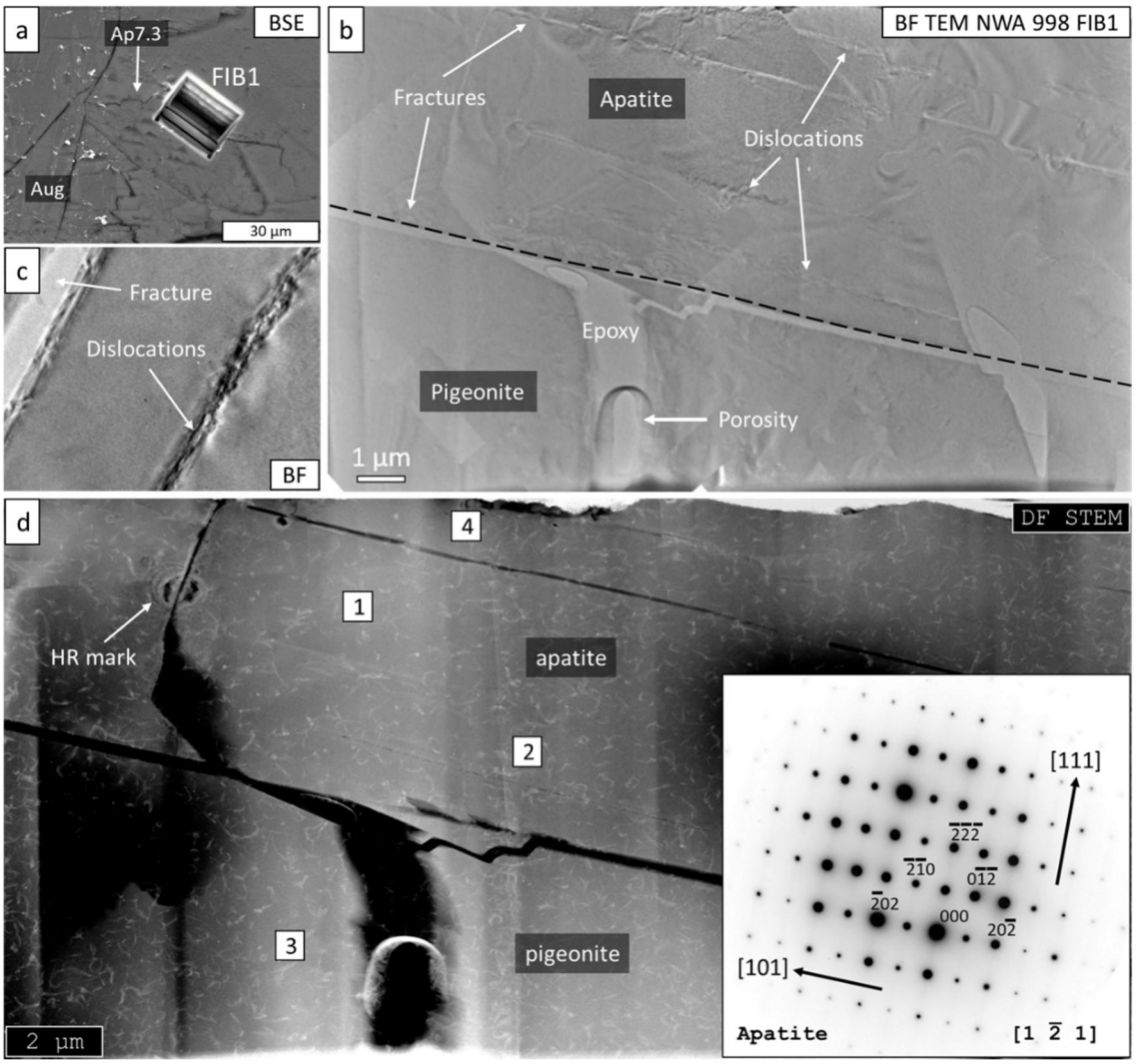

Figure 3.4. SEM and TEM images of FIB1 extracted in apatite 7 in NWA 998. a) BSE image of the location of the FIB section extracted from apatite grain 7.3, cut parallel to the *c* direction. b) Bright-field TEM mosaic of NWA 998 cumulus apatite FIB1. Pigeonite is identified at the lower part of the FIB section based on SEM-EDS analyses. The grain boundary between apatite and pigeonite is marked with a dashed black line. c) BF-TEM image showing the distribution of fractures and dislocations, which are parallel and subparallel to each other. d) Dark-field STEM mosaic showing the location of EDS analyses (Table 1). The observed nanometer-scale, worm-like features throughout the FIB section are caused by re-deposition during FIB sample preparation. Inset in (d) shows a [1-21] zone axis diffraction pattern of apatite showing diffuse streaking parallel to the [111] direction.

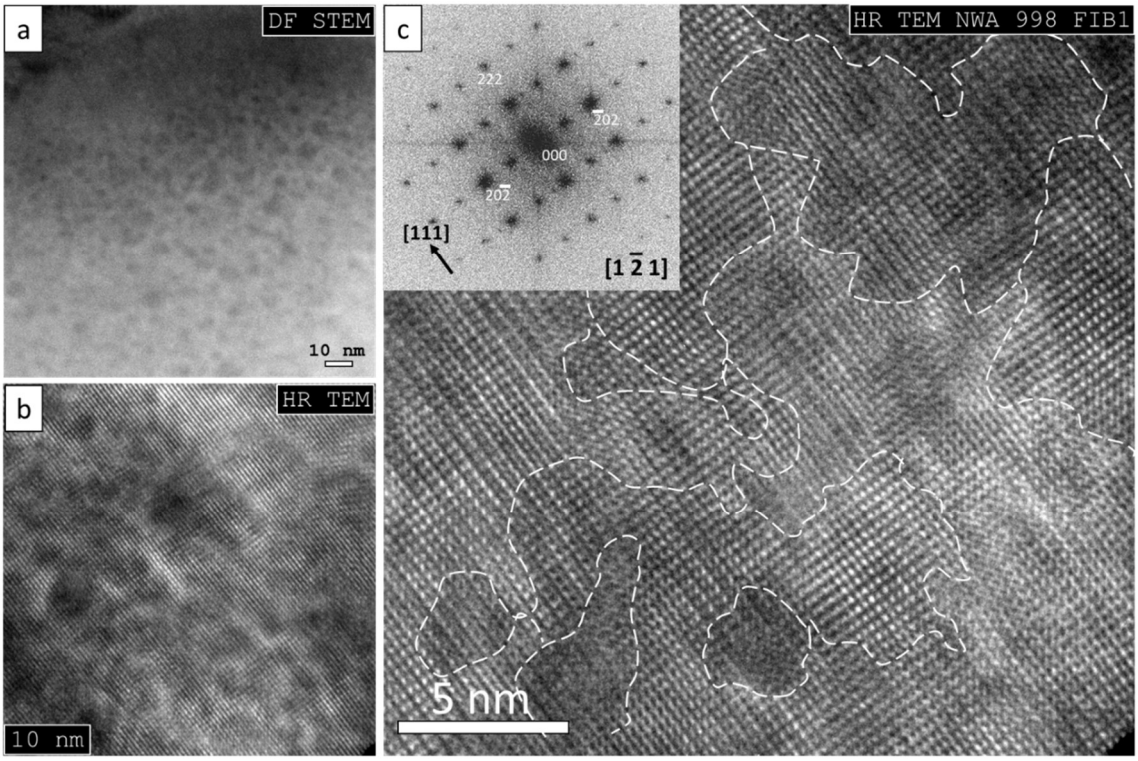

Figure 3.5. TEM images showing mottled nanotextures in NWA 998 apatite. a) Dark-Field STEM Z-contrast image showing 5-10 nm-size domains with different Z-contrast indicative of compositional differences between them. b) HRTEM image showing the mottled texture with different domains 5-10 nm in size, apparent by mismatches and differences in the contrast in the lattice fringes. c) Close-up HRTEM image with inset Fast Fourier Transform (FFT) indicating the direction of the streaking parallel to the [111] direction. Different domains are marked in dashed white lines, showing that some domains are very close to exactly down the zone axis, while others show a slight misorientation. The differences in contrast in the lattice fringes is indicative of slight differences in orientation of the different domains and strain in the lattice.

Table 3.1. TEM-EDS analyses (oxide wt%) on apatite 7.3 (Fig. 3.2e) and pigeonite in NWA 998 FIB1.

Oxides wt%	Apatite				**Mean**		Pigeonite
P_2O_5	37.70	39.90	40.15	38.52	**39.60**	SiO_2	56.47
SiO_2	2.44	1.63	1.22	2.57	**1.99**	Al_2O_3	0.51
CaO	56.08	53.86	53.60	53.87	**55.09**	FeO	23.39
FeO	0.30	0.27	0.32	0.42	**0.33**	MnO	0.67
F	1.86	2.13	1.53	2.07	**1.92**	MgO	17.29
Cl	1.64	2.22	3.18	2.56	**2.43**	CaO	1.68
Total	100	100	100	100	**100**		100
Cl/F (wt%)	0.88	1.04	2.08	1.24	**1.26**		
Structural formulae based on 13 oxygens						*Based on 6 [O]*	
P	2.75	2.90	2.93	2.81	**2.85**	Si	2.1
Si	0.21	0.14	0.10	0.22	**0.17**	Al	0.02
Ca	5.18	4.96	4.95	4.99	**5.02**	Fe	0.73
Fe	0.02	0.02	0.02	0.03	**0.02**	Mg	0.96
F	0.51	0.58	0.42	0.57	**0.52**	Mn	0.02
Cl	0.24	0.32	0.46	0.37	**0.35**	Ca	0.07
Z	0.25	0.10	0.12	0.06	**0.13**		
Total cat	8.17	8.01	8.01	8.06	**8.06**		
Ca/P atomic	1.89	1.71	1.69	1.77	**1.76**		

n.d. = not detected
Z = missing component (OH + vacancies)

FIB2 samples a different euhedral to subhedral cumulus apatite grain in NWA 998, closely intergrown with titanomagnetite and Ca-rich pyroxene (apatite 5.2 in Fig. 3.2g,h). The foil was cut perpendicular to the elongation direction of the crystal to further investigate the cause of the streaking parallel to the [111] zone axis observed in electron diffraction patterns from apatite 7.3 in FIB1. Bright-field and dark-field TEM images, combined with diffraction patterns, reveal that apatite in FIB2 is a single crystal with a few subgrains in slightly different orientations (Fig. 3.6). Apatite compositions are quite constant throughout the FIB section, ranging from 1.26 to 1.74 wt% F and 2.17 to 3.59 wt% Cl (Table 3.2), with an average halogen content Cl/F of 2.11, slightly Cl-enriched compared to FIB1 (values plotted in Fig. 3.3). Silica content in the different areas is variable, ranging from 0.79 to 3.12 wt% SiO_2 (Table 3.2). In a Si versus Ca/P (atomic %)

plot, the positive correlation indicates that silica is bonded in the apatite structure by the common substitution $PO_4^{3} + O^{2+} = SiO_4^{4+} + OH^{-}$ (Figure 3.7a). Rare-earth elements have not been detected in any analysis. A fragmented vein, ~100-200 nm wide, crosscuts the FIB section and surrounds a melt inclusion that is located at the center-right, which is described below. Apatite appears mostly homogeneous with a few dislocations (Fig. 3.6a) and diffraction patterns indicate that the FIB section is oriented close to the *c* axis (the [001] zone axis). The SAEDs from apatite on the left side of the FIB section reveal streaking in the [313] and [543] directions (Fig. 3.6a, inset) and apatite on the right side of the FIB exhibits a few dislocations, a few subgrain boundaries, and curved cleavage in the (100) planes at 120° angles that show slight curvature. Diffraction patterns reveal that in general, the apatite subgrains are slightly misoriented relative to one another. An exception is a small region (green dashed square in Fig. 3.6a) consisting of polycrystalline apatite (0.5 μm-size) with a composition Cl/F of 5.14 (Table 3.2) that differs from the single crystal apatite. High-resolution TEM imaging of the homogeneous-looking single crystal apatite shows the presence of domains, similar to the nanostructure observed in FIB1, but the domains in FIB2 are more variable (Fig. 3.8). Lattice planes in some areas show notably more curvature than in FIB1, indicative of strong localized strain in the structure (Fig. 3.8a). High-resolution TEM imaging in the polycrystalline apatite (Fig. 3.8b) shows that some grains have lattice fringes that are less well-defined than others to somewhat amorphous material.

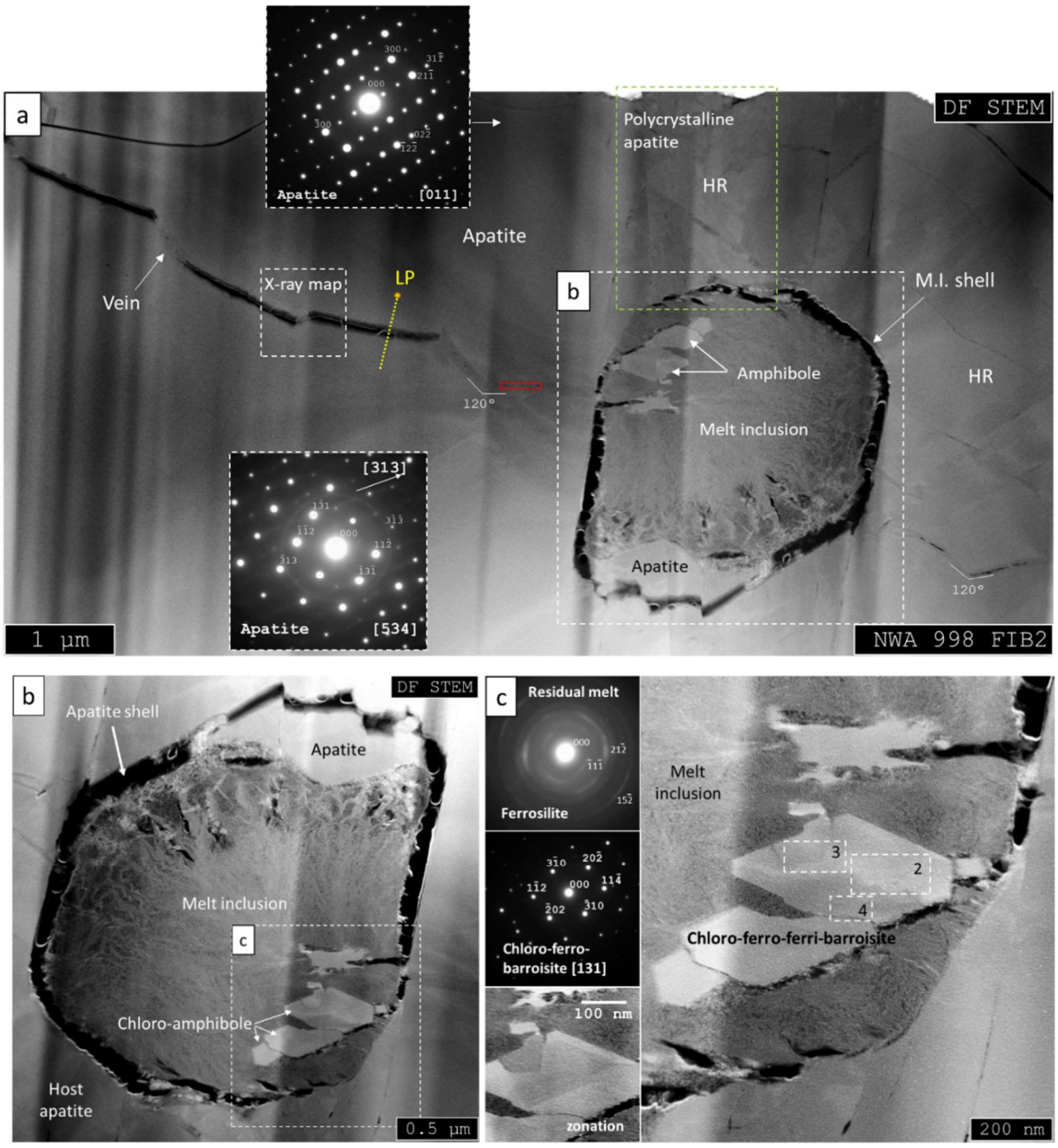

Figure 3.6. TEM images of FIB2 extracted in Apatite 5 in NWA 998. a) Dark-field STEM mosaic of FIB2 in NWA 998 apatite oriented parallel to the [011] zone axis showing that it is mostly homogeneous in texture, except for a small region where apatite is polycrystalline (green dashed square). Cleavage planes show curvature and opening (fracturing). Red dashed rectangle represent location of EDS-TEM analysis in the vein. The inset of the [534] zone axis diffraction pattern shows streaking in the [313] direction. A melt inclusion (M.I.) is outlined by a dashed white square and shown in detail in b) and c). b) Melt inclusion in apatite with a radial texture and daughter crystals of chloro-ferrobarroisite. Numbers in white dashed squares indicate STEM-EDS analysis locations. *(Caption continues on the following page).*

Figure 3.6. *(Caption continued from the previous page).* c) Higher magnification image of the euhedral daughter crystals of chloro-ferro-ferri-barroisite in the melt inclusion (dashed squares represent STEM-EDS analyses locations), along with its diffraction pattern in the [131] zone axis, higher magnification image of the zonation, and a diffraction pattern of the interior of the melt inclusion showing diffuse diffraction rings consistent with ferrosilite. EDS-STEM analyses found in Tables 3.2 and 3.3. HR = high-resolution TEM (Fig. 3.7), LP = line profile (see Fig. 3.9).

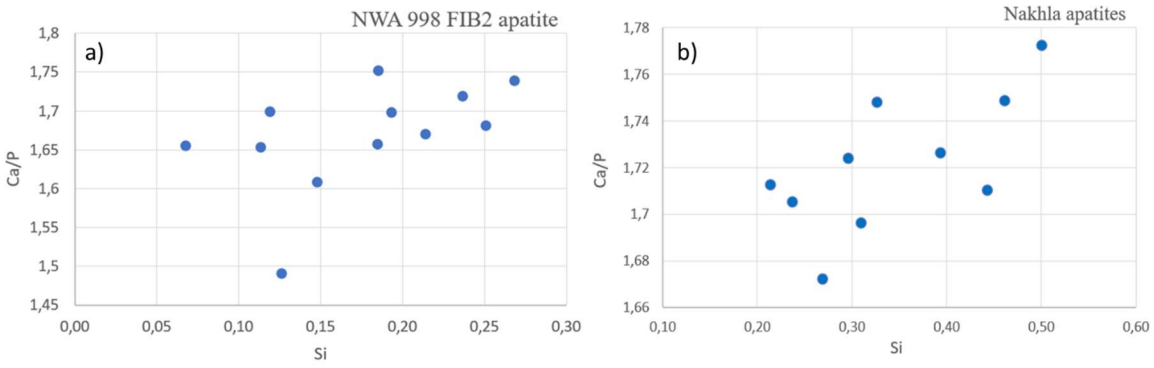

Figure 3.7. Ca/P versus Si (atomic %) from a) NWA 998 cumulus apatite (FIB2) and b) Nakhla intercumulus apatites (FIB3), obtained by TEM-EDS.

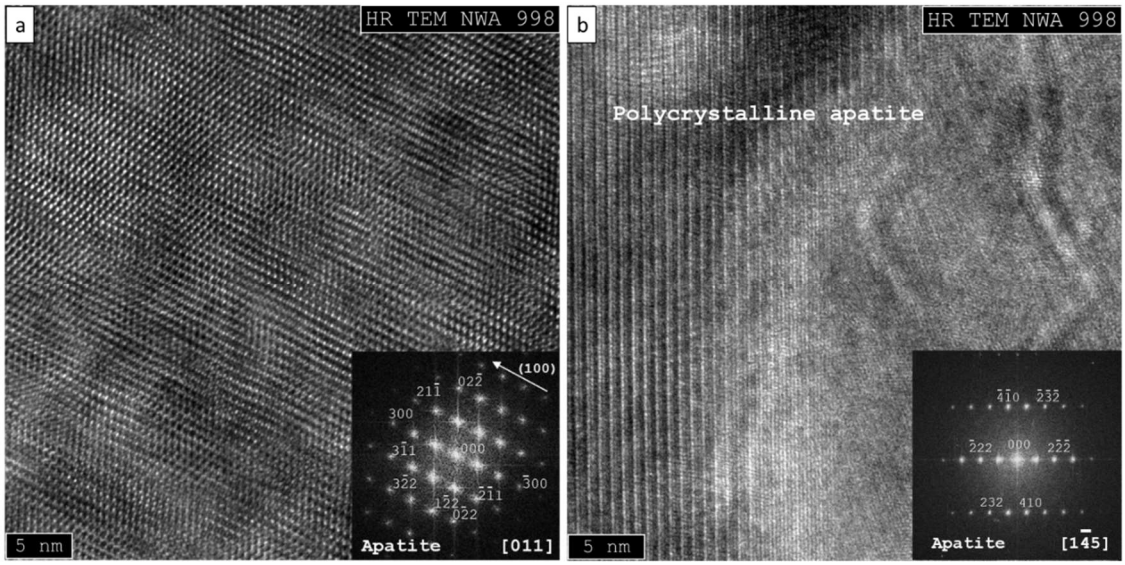

Figure 3.8. High-resolution TEM images of two different regions in NWA 998 apatite (FIB2). a) Single crystal apatite in the right-hand side of the FIB section, with 3 wt% Cl and 1.5 wt% F. The HRTEM image shows that (100) lattice fringes exhibit evidence of curvature (undulosity), indicative of strain in the lattice. b) Polycrystalline apatite (region marked with a green dashed square in Figure 3.6a), with 3.65 wt% Cl and 0.71 wt% F. Note the grain boundary (different orientations of the lattice fringes). Selected area electron diffraction patterns of the crystal on the left show that the crystal is orientated parallel to the [011] zone axis. Apatite in this area does not show curvature of the lattice fringes nor significant diffraction contrast.

Table 3.2. TEM-EDS analyses (oxide wt%) of the host apatite, the vein, and the polycrystalline (Polycr) apatites in NWA 998 FIB2 after cleaning the FIB section at 5 kV to remove redeposited material.

Oxides wt%	Host apatite												**Mean**	vein	Polycr
P_2O_5	40.42	42.90	40.84	40.01	39.46	39.28	38.93	39.76	40.10	38.66	39.44	38.64	**39.87**	35.39	40.06
SiO_2	0.79	1.52	1.75	1.33	1.39	2.25	2.76	2.50	2.16	2.14	2.93	3.12	**2.05**	10.40	2.82
Al_2O_3	1.34	1.21	1.28	1.30	1.47	0.53	0.42	0.40	0.19	0.30	0.23	0.11	**0.73**	0.12	0.13
SO_3	n.d.	n.d.	n.d.	n.d.	n.d.	n.d.	n.d.	n.d.	n.d.	n.d.	n.d.	n.d.	**n.d.**	0.50	n.d.
CaO	52.81	50.44	51.83	52.19	52.90	52.64	52.82	52.39	52.43	53.45	52.30	53.02	**52.43**	49.25	52.46
FeO	0.46	0.41	0.40	0.42	0.42	0.33	0.31	0.30	0.32	0.51	0.27	0.33	**0.38**	0.24	0.18
F	1.26	1.27	1.74	1.45	1.42	1.40	1.56	1.49	1.47	1.44	1.57	1.53	**1.47**	2.96	0.71
Cl	2.91	2.27	2.17	3.28	2.93	3.59	3.22	3.18	3.33	3.50	3.27	3.26	**3.08**	1.14	3.65
Total	100	100	100	100	100	100	100	100	100	100	100	100	**100**	100	100
Cl/F (wt%)	2.31	1.79	1.25	2.26	2.06	2.56	2.06	2.13	2.27	2.43	2.08	2.13	**2.11**	0.39	5.14
P	2.92	3.02	2.92	2.90	2.86	2.86	2.83	2.88	2.91	2.83	2.86	2.81	**2.88**	2.50	2.88
Si	0.07	0.13	0.15	0.11	0.12	0.19	0.24	0.21	0.18	0.19	0.25	0.27	**0.18**	0.87	0.24
Al	0.13	0.12	0.13	0.13	0.15	0.05	0.04	0.04	0.02	0.03	0.02	0.01	**0.07**	0.01	0.01
S	n.d.	n.d.	n.d.	n.d.	n.d.	n.d.	n.d.	n.d.	n.d.	n.d.	n.d.	n.d.	**n.d.**	0.09	n.d.
Ca	4.83	4.50	4.69	4.79	4.86	4.86	4.87	4.80	4.81	4.96	4.80	4.89	**4.81**	4.40	4.78
Fe	0.03	0.03	0.03	0.03	0.03	0.02	0.02	0.02	0.02	0.04	0.02	0.02	**0.03**	0.02	0.01
F	0.34	0.33	0.46	0.39	0.38	0.38	0.42	0.40	0.40	0.39	0.42	0.42	**0.40**	0.78	0.19
Cl	0.42	0.32	0.31	0.48	0.42	0.52	0.47	0.46	0.48	0.51	0.47	0.47	**0.45**	0.16	0.53
Z	0.24	0.35	0.23	0.13	0.19	0.10	0.11	0.14	0.12	0.09	0.10	0.11	**0.16**	0.06	0.28
Total cat	7.99	7.79	7.91	7.97	8.02	7.99	8.00	7.95	7.95	8.05	7.95	8.01	**7.30**	7.88	7.93
Ca/P atomic	1.66	1.49	1.61	1.65	1.70	1.70	1.72	1.67	1.66	1.75	1.68	1.74	**1.67**	1.76	1.66

n.d. = not detected

Z = missing component (OH + vacancies)

3.2.1.1. Mineralogy and morphology of the veins in NWA 998 apatite

The fractures observed in FIB2 are fragmented and curved, very different from the straight and parallel fractures in FIB1 (Fig. 3.4). However, the different crystallographic orientation of FIB2 with respect to FIB1 (90º) probably accounts for the difference in the characteristics of the fractures. Based on electron diffraction patterns, the fractures are parallel to (100), one of the known cleavage planes, albeit imperfect, in apatite. The fractures are partially filled with a porous, nanocrystalline phase (100-200 nm wide, Fig. 3.9) that diffraction patterns show consists of apatite. In addition to the nanocrystalline apatite, distinct zones of apatite are present on either side of the fracture (100-200 nm wide) that are characterized by strain contrast compared to the host apatite (Fig. 3.9a,b). The strained apatite is in crystallographic continuity with the adjacent Cl-rich fluorapatite host with parallel [011] zone axes (Fig. 3.9a,b). These features were completely filled veins before sample preparation, but holes developed preferentially during FIB preparation. Scanning TEM-EDS analyses reveal that apatite in the vein consists of fluorapatite (~3 wt% F and ~ 1 wt% Cl) and a Si-rich phase (10.4 wt% SiO_2, Table 3.2). Nonetheless, since the X-ray intensity decreases in the vein due to preferential thinning, the increase of F and Si must be higher than is apparent. Bright-field and dark-field STEM images show that the interface between Cl-rich fluorapatite and epitaxial fluorapatite in the vein is sharp (Fig. 3.9c). Details of the compositional changes in the apatite across the vein-host interface (yellow dashed lines in Fig. 3.10) were obtained by STEM-EDS X-ray intensity line profiles. We have plotted different X-ray intensity ratios to illustrate this trend more clearly as the line profiles show significant noise. The F/Cl ratio within the vein is variable with an overall increase of F over Cl with respect to the

host Cl-rich fluorapatite (Fig. 3.10). The Si/P and the Ca/P ratios also increase significantly in the vein (Fig. 3.10). Based on the substitution $PO_4^{3-} + O^{2-} = SiO_4^{4-} + OH^-$, we infer that silica is not bonded in the apatite structure, because the Ca/P ratio does not increase with increasing Si content (Fig. 3.10). The line profile also reveals a slight increase in Si concentration at one end of the X-ray intensity profile that is not accompanied by an increase of the Ca/P ratio.

Porosity in the vein also shows some complexity. Pores are smaller (~1 nm), rounded, and occur in a trail at the outermost edges of the vein, close to the interface with the host apatite, but are larger (~3-5 nm), more elliptical, and less abundant in the center of the vein (Fig. 3.9c). High-resolution TEM imaging of apatite in the vein shows that lattice planes are continuous and straight, with no evidence of domains. However, the nanostructure exhibits complex contrast differences (Fig. 3.9d). Randomly distributed, irregular regions of amorphous material intermixed with crystalline apatite are also apparent in HRTEM images, likely the source of silica in the vein (Fig. 3.9e). Based on the appearance of the vein, the crystallographic continuity between host and vein apatites, the compositional zoning, the presence of nanoporosity, and the occurrence of nanometer regions of amorphous material in the vein, we suggest that fluorapatite is an epitaxial overgrowth caused by fluid-mediated processes (dissolution-reprecipitation), which is discussed in more detail in section 4.3.

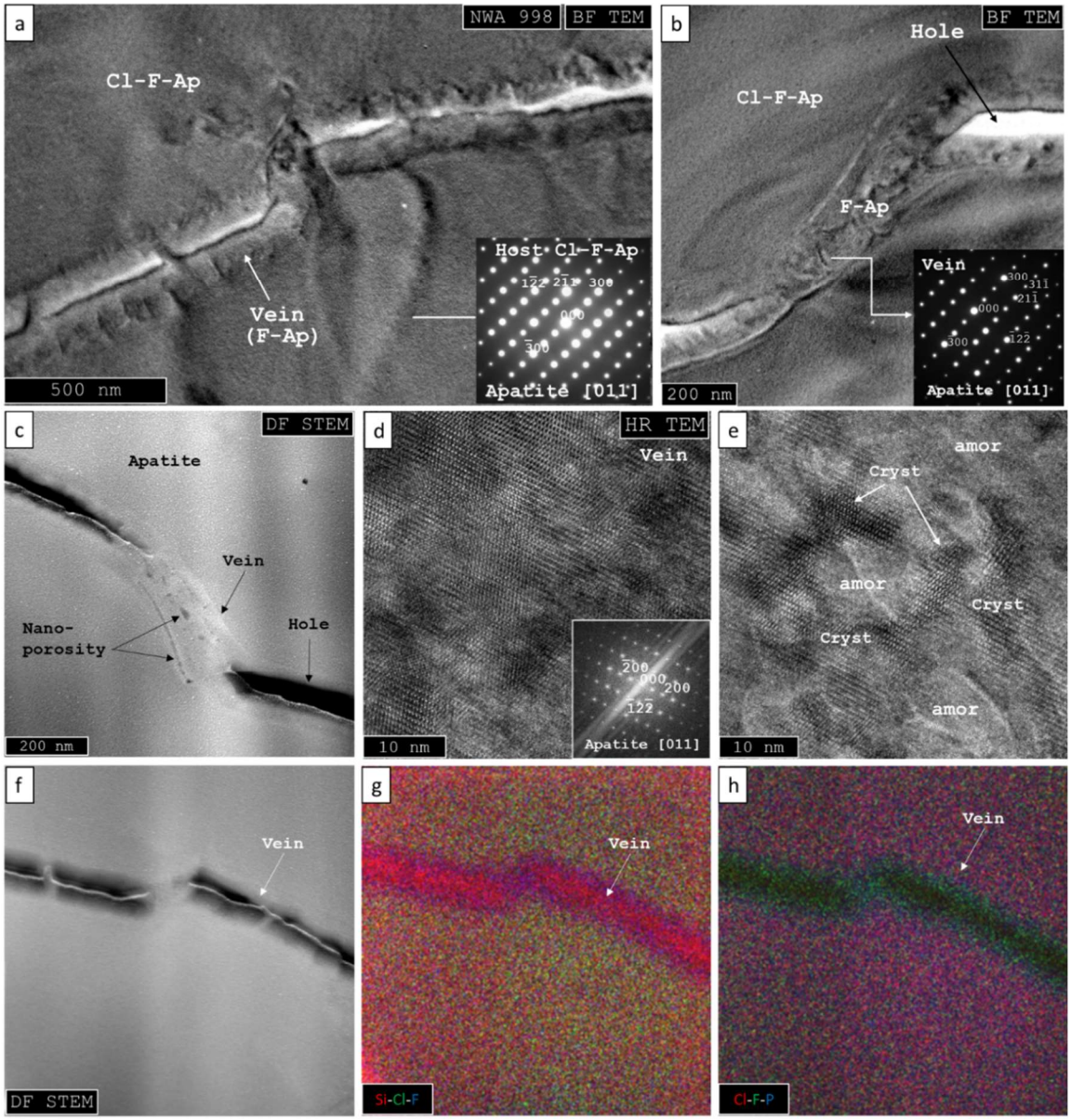

Figure 3.9. TEM and STEM images of the thin vein, 150 nm in width, crosscutting apatite in NWA 998 FIB2. a) Bright-field TEM image of a region of the vein showing localized strain contrast and overgrowth of a phase around the fracture. a) Bright-field TEM image of a region of the vein that is completely filled with fluorapatite (F-ap) in crystallographic continuity. The vein shows high strain contrast with respect to host apatite (Cl-F-apatite). b) Bright-field TEM image with inset SAED of [011] zone axis shows that apatite is filling the vein. c) Dark-field STEM image of (b) shows compositional heterogeneity and nanoporosity in the filled parts of the vein. d) and e) High-resolution TEM images in the vein showing crystalline regions with 5-10 nm domains mingled with regions of amorphous material. f-h) Dark-field STEM image along with RGB compositional X-ray maps in Si-Cl-F (g) and Cl-F-P (h) showing that the vein is enriched in F on the sides and Si in the center. Abbreviations: amor = amorphous material, Cryst = crystalline apatite.

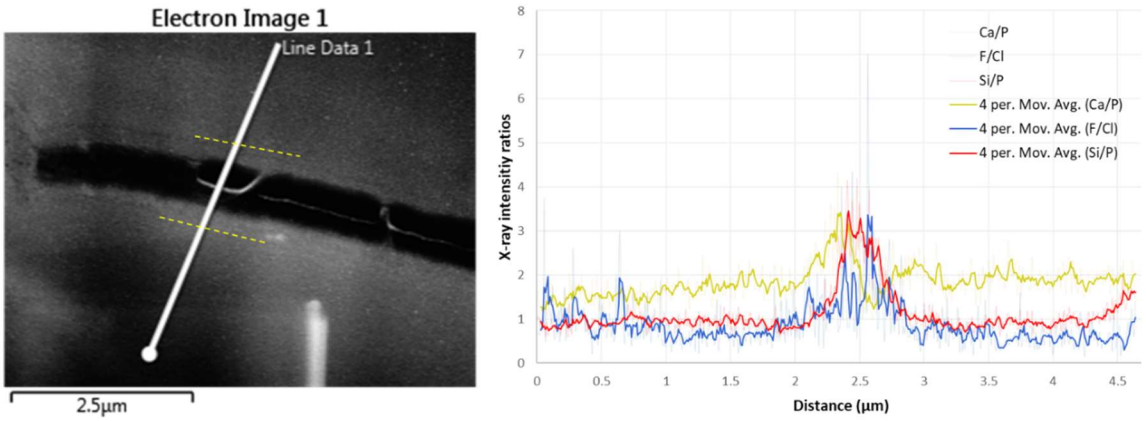

Figure 3.10. Scanning TEM-EDS X-ray intensity line profiles of Ca/P, F/Cl, and Si/P ratios plotted against distance in apatite NWA 998 vein. The dashed yellow lines mark the sharp contact between the vein and the host apatite. The vein in this area is about 1 µm in width. The plot shows that the F/Cl ratio (blue line) is variable across the vein but overall, F in the vein significantly increases with respect to host apatite. The Si/P ratio (red line) increases consistently through the vein, and Ca/P ratio although variable, also increases (yellow line). Note the lack of correlation between Si/P and Ca/P at the far-right end of the profile.

3.2.1.2. Melt inclusion with chloro-amphibole in NWA 998 apatite

A melt inclusion (right-center of the FIB) was discovered below the surface of the FIB2 foil that was not apparent in SEM images of the sample. This is the first melt inclusion found in apatite in a nakhlite, formed from the trapping of a tiny parcel of magma during the growth of apatite. It is rounded, ~3 µm in diameter, and the periphery is surrounded by a ~100 nm thick rim of epoxy with holes (Fig. 3.6a,b). The rim around the periphery appears to have formed either as a result of a change in volume of the melt, presumably due to crystallization of the melt inclusion, or by preferential thinning of another phase during FIB ion milling. Because the holes around the rim resemble those seen along apatite cleavage planes (veins) described above, it is likely that ion milling eroded the first phase that crystallized around the edge of the inclusion, and the fluid that infiltrated through the cleavage planes described above affected the inclusion-host interface (apatite shell).

The interior of the melt inclusion is multiphase, texturally heterogeneous, and exhibits a radial, nanocrystalline structure (Fig. 3.6a,b) consisting of pyroxene and interstitial K-rich glass with chlorapatite and daughter minerals of amphibole, detected with STEM-EDS analyses. Nucleation of daughter minerals on the walls of melt inclusions, forming complete or partial rinds, is a common feature of crystallization of small closed systems (Guzmies et al., 2008; Goodrich et al., 2013). The bulk composition of the melt is presented in Table 3.3. TEM-EDS analyses of an area of the melt inclusion that mainly consists of nanocrystalline grains and very little glass is consistent with Ca- and Fe-rich pyroxene with a composition $(Ca_{0,08}Fe_{0,89})_{0,97}(Mg_{0,58}Fe_{0,12}Ti_{0,02}Al_{0,28})_1(Si_{1,7}Al_{0,3})_2O_6$ (first spectrum in Table 3.3). The inclusion shows significant variations in SiO_2 (43 to 66 wt%) and Al_2O_3 (5.1 to 12.5 wt%) (Table 3.3), which are attributed to the variations in the amount of glass within the analytical volume. Electron diffraction patterns from the residual crystallized melt (pyroxene and glass intergrowth) consist of somewhat diffuse rings indicative of nanocrystalline phases consistent with ferrosilite in random crystallographic orientations (Fig. 3.6c).

Chlorapatite is present in one part of the melt inclusion (Fig. 3.6a,b) and the interface between the enclosed chlorapatite and the crystallized melt is sharp. Quantitative STEM-EDS data from the apatite inside the melt inclusion show it is highly enriched in Cl and F-poor (~4.7 wt% Cl and ~0.5 wt% F, Table 3.3, Fig. 3.3) compared to the host apatite (Table 3.2).

The inclusion also contains three euhedral, rhombic to pseudo-polygonal daughter crystals of an amphibole, ~200-500 nm in size, rimming one side of the inclusion wall

(Fig. 3.6). We cannot determine if they are partially rimming more regions of the wall of the inclusion because we are only seeing a 2D slice of the sphere. Chloro-amphibole crystals exhibit sharp, compositional zoning (Fig. 3.6c), but the differences in composition between the rim and the core are difficult to determine with STEM-EDS, because their sizes are too small to obtain clean, single phase analyses. However, EDS-STEM spectra collected in the core show the presence of K while the rim contains Na; Ca being present in both. Electron diffraction data are consistent with a monoclinic amphibole that is best fit with barroisite, indexed with a zone axis of [131] (Fig. 3.6c). The chloro-amphibole in NWA 998 melt inclusion (Cl =1.2 apfu) contains higher Si and Na contents (48.43 wt% SiO_2 and ~2.23 wt% Na_2O), lower K and Ca contents (~1.12 wt% K_2O or K = 0.224 apfu, and 5.41 wt% CaO), and slightly less Cl (4.75 wt% Cl or 1.2 apfu, Table 2) than amphiboles reported in other nakhlites in literature (Sautter et al., 2006; Giesting and Filiberto, 2016). The low Ti content in the amphibole (~0-0.5 wt% TiO_2, Table 3.3) has been explained in other melt inclusions in the MIL nakhlites by the close intergrowth between the host mineral and titanomagnetite (Sautter et al, 2006; Giesting and Filiberto, 2016), which is consistent with apatite crystallizing partially or totally included in titanomagnetite (Fig. 3.2g,h). The calculated formula was obtained with STEM-EDS analysis and has a composition consistent with chloro-ferro-ferri-barroisite, a sodium-calcium amphibole with a composition of $(K_{0,224}Na_{0,587}\square_{0,189})(Na_{0,091}Ca_{0,909})(Fe^{3+}_{0,508}Fe^{2+}_{3}Mn_{0,174}Al_{1,441})(Si_{7,593}Al_{0,407})O_{22}(Cl_{1,2}OH_{0,8})$ (Table 3.3). The amphibole formula units were calculated on the basis of the amphibole classification scheme of Hawthorne et al. (2012). The sum of cations in the octahedral and tetrahedral sites is 13.00, with most of the A site occupied by Na and K, OH^{-} was

calculated by difference assuming $Cl^{-} + F^{-} + OH^{-} = 2$ apfu. On a Cl (wt%) versus $A]_{(Na+K)}$ (apfu) plot, the new amphibole is in agreement with other nakhlites in the literature, as compiled by Giesting and Filiberto (2016) (Fig. 3.11). This is the first amphibole found in NWA 998, and the first barroisite discovered in a Martian meteorite.

Table 3.3. STEM-EDS analyses (oxide wt%) of the different phases in the melt inclusion in NWA 998 apatite. A) Individual analyses for residual melt (pyroxene + glass), amphibole, and apatite inside the melt inclusion. Specific locations presented in Fig 3.6. Amphibole based on 22 oxygens; apatite based on 13 oxygens.

3.3A	**Melt inclusion in NWA 998 apatite**								
	Residual silicate melt (Px + glass)					Amphibole		Apatite melt inclusion	
SiO_2	43.39	57.54	66.37	46.14	SiO_2	48.43	P_2O_5	38.38	36.73
Al_2O_3	12.45	8.93	5.14	9.00	TiO_2	n.d.	SiO_2	3.08	6.85
TiO_2	0.52	n.d.	n.d.	n.d.	Al_2O_3	10.00	Al_2O_3	1.53	0.36
P_2O_5	n.d.	n.d.	n.d.	0.52	FeO	26.75	CaO	51.45	49.81
FeO	30.67	23.35	19.67	30.97	MnO	1.31	FeO	0.40	1.06
MnO	n.d.	n.d.	n.d.	0.41	CaO	5.41	F	0.62	0.27
MgO	9.86	7.6	6.16	8.94	Na_2O	2.23	Cl	4.53	4.91
CaO	1.99	1.63	1.45	2.34	K_2O	1.12	Total	100	100
K_2O	1.12	0.95	1.21	1.57	Cl	4.75	Cl/F	7.31	18.19
SO_3	n.d.	n.d.	n.d.	0.05	Total	100			
Cl	n.d.	n.d.	n.d.	0.08					
Total	100	100	100	100					
	Structural Formulae								
Si	1.7				Si	7.593	P	2.79	2.66
Al	0.58				Al	1.848	Si	0,26	0.58
Ti	0.02				Ti	n.d.	Al	0,15	0.04
Fe	1.01				Fe	3.508	Ca	4.74	4.56
Mn	n.d.				Mn	0.174	Fe	0.03	0.08
Mg	0.58				Ca	0.909	F	0.17	0.07
Ca	0.08				Na	0.678	Cl	0.66	0.71
O	6				K	0.224	Z	0.17	0.22
					Cl	1.20	Total cat	7.97	7.91
					O	23	Ca/P atomic	1.70	1.71

n.d. = not detected
Z = missing component (OH + vacancies)

Table 3.3. *(Continuation)*. STEM-EDS analyses (oxide wt%) of the different phases in the melt inclusion in NWA 998 apatite. Bulk composition calculated by combining modal abundance (vol%) and chemistry (wt%). Abundances in areal%. Px+Gl = pyroxene + glass, Ap = apatite, Amph = amphibole, Ap MI = apatite inside the melt inclusion.

3.3B	Residual silicate melt (Px + Gl)	Amph	Ap MI	**Bulk Composition**
	N=5	N=1	N=2	(78% Px+Gl, 17% Ap, 5% Amph)
SiO_2	53.36	48.43	4.96	**44.89**
Al_2O_3	8.88	10.00	0.94	**7.59**
TiO_2	0.13	n.d.	n.d.	**0.10**
P_2O_5	0.13	n.d.	37.56	**6.49**
FeO	26.16	26.75	0.73	**21.87**
MnO	0.10	1.31	n.d.	**0.15**
MgO	8.14	n.d.	n.d.	**6.35**
CaO	1.85	5.41	50.63	**10.32**
Na_2O	n.d.	2.23	n.d.	**0.11**
K_2O	1.21	1.12	n.d.	**1.00**
SO3	0.01	n.d.	n.d.	**0.01**
Cl	0.02	4.75	4.72	**1.06**
F	n.d.	n.d.	0.45	**0.08**
Total	100	100	100	**100**

n.d. = not detected

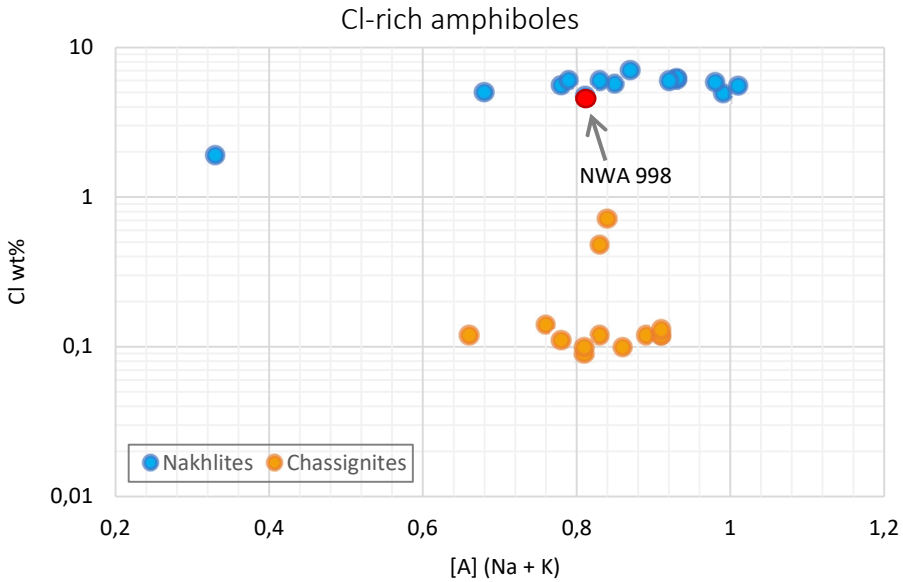

Figure 3.11. Variation in proportion of Cl (wt%) in Cl-rich amphibole as a function of $[A]_{(Na+K)}$ (apfu) from this work (NWA 998, red dot) compared to Nakhlites and Chassignites from literature, as compiled by Giesting and Filiberto (2016).

3.2.2. Intercumulus apatite in Nakhla

Apatites in Nakhla are more challenging to study than apatites in NWA 998, because they occur as acicular crystals that rarely exceed a few microns in width. A FIB section (designated FIB3) was removed perpendicular to the elongation direction of a cluster of similarly oriented acicular apatite grains identified with SEM-EDS within a mesostasis melt pocket (Fig. 3.2m) to further investigate their microstructures in detail. Transmission electron microscopy reveals a complex structure with four subhedral to euhedral apatite grains (3-5 μm size), numbered from 1 to 4 in Figure 3.12. The compositions of these grains have been determined with STEM-EDS (Table 3.4). The four apatite grains exhibit similar shapes and sizes, their interior is fracture free except for apatite 4, which contains some fractures that crosscut the crystal, and the cleavage is well distinguished in apatites 1 and 3 (Fig. 3.12c). Apatite 3 has a rounded shape and is surrounded by radial nanoporosity and/or fractures. Selected area electron diffraction patterns show that the four grains are oriented perpendicular to the *c* axis, the [001] zone axis (Fig. 3.12c,d), and bright-field TEM images show that they have strong contrast, indicative of significant strain. Apatites 1 and 4 are embedded in crystalline phases, which STEM-EDS and diffraction patterns reveal are tridymite (SiO_2) and K-, Na-feldspar ($Or_{61.3}Ab_{38.6}$, Table A2.1 in Appendix 2) (Fig. 3.12f). Potassium feldspar has an atomic Si/Al ratio of 3.8, which is slightly higher for an alkali feldspar, but small regions of K-rich glass (maskelynite) have been also identified in this FIB section. We attribute the low alkali content in feldspar (5 wt% K_2O, 2 wt% Na_2O) to volatile loss caused by electron beam irradiation. Apatites 2 and 3 are mostly embedded in an amorphous material, based on electron diffraction patterns of this phase (Fig. 3.12b). The amorphous

material is completely featureless, with no differences in Z contrast at any magnification, and it is crosscut by a few veins (Fig. 3.12a). Qualitative TEM-EDS analyses of the amorphous material indicate it is almost pure SiO_2 with trace concentrations of Al_2O_3 (up to 0.9 wt%). Amorphous silica and crystalline K-,Na-feldspar constitute the groundmass between grains (Fig. 3.12a,f). In addition, small (~1 μm-size) crystals, with textures that suggest they were the last phases that crystallized, are included in the K-,Na-rich feldspar (Fig. 3.12f). Scanning TEM-EDS and diffraction patterns reveal that this phase is also tridymite. Tridymite is enclosed in shells of a low Z-contrast material that is too fine-grained to resolve.

Z-contrast STEM imaging on apatite 3 shows that it nucleated on a region on the left-hand side of the grain, with subsequent layers of growth (~20-50 μm wide each) distinguished around it (Fig. 3.12d,e). TEM-EDS analyses show zonation of halogens (Table 3.4), where Cl content is lower in the core (4.47 wt%) and higher at the rim (5.50 wt%), whereas F behaves in the opposite way (0.62 wt% in the core and 0.20 wt% at the rim). Rare-earth elements are also higher in the core (0.55 wt% Ce_2O_3 and 0.33 wt% Nd_2O_3) than the rim (0.13 wt% Ce_2O_3 and 0.05 wt% Nd_2O_3). Iron shows zonation with the same trend, ranging from 0.44 wt% FeO in the core to 0.14 wt% FeO at the rim. Similarly, the SiO_2 content is higher in the core (5.16 wt%) than at the rim (3.42 wt%) in this grain, ruling out contamination from adjacent feldspar. In fact, silica is variable between and within grains, and on a plot of Ca/P versus Si (Fig. 3.7b), the positive correlation indicates that silica is bonded in the apatite structure, based on the substitution $PO_4^{3} + O^{2+} = SiO_4^{4+} + OH^{-}$. In general, SiO_2 contents from the four apatite grains are higher than in NWA 998, ranging from ~2.48 to 5.93 wt% (Table 3.4). All apatites

contain trace, variable amounts of REEs (up to 0.59 wt% Ce_2O_3 and 0.33 wt% Nd_2O_3). Overall, the F and Cl contents vary significantly from grain to grain and even within grains and have higher wt% Cl/F ratios (1.55 - 27.50) than NWA 998 apatites (1.26 for FIB1 and 2.35 for FIB2). Halogens range from 0.2 to 1.9 wt% for F, with a mean of 0.95 wt% F, and from 2.9 to 5.5 wt% Cl, with a mean of 4.02 wt% Cl (Table 3.4). This is broadly consistent with previous reports of apatite compositions in Nakhla (e.g., McCubbin et al. 2013; Fig. 3.3).

High-resolution TEM images were obtained viewed down the [001] zone axis on apatite 1 (Fig. 3.2m). Curvature of lattice fringes is much less apparent but also distinguishable perpendicular to the (001) direction (Fig. 3.13a,b). Some regions appear to be amorphous (Fig. 3.13c), and some areas exhibit the characteristic mottled Z-contrast (Fig. 3.13c), also seen in NWA 998 apatites (FIB1 and FIB2). Energy-Filtered TEM was performed to characterize the Cl distribution in a feature that followed the apatite cleavage, because it exhibits a higher Z contrast. The EFTEM map shows very slight differences in Cl content in this feature (Fig. 3.13d).

Finally, the FIB section also contains a fibrous phase that is closely associated with all the phases. Scanning TEM-EDS analyses show that it consists of K-, Fe-rich phyllosilicates with minor Cl (0.7-1.26 wt% Cl), consistent with a composition close to glauconite or illite (Table A2.1 in Appendix 2). The higher silica content (63.5 wt% SiO_2) is due to obtaining normalized (anhydrous) values by TEM. Clay minerals occur throughout the FIB section as veins (Fig. 3.12a), filling porosity (e.g., Fig. 3.12a,b), filling interstitial regions between grains (~40 - 600 nm in size) (Fig. 3.12a,b,f), and surrounding other phases such as silica (Fig. 3.12a,f). The phyllosilicates have a sheet

texture with nanocrystalline flakes arranged in clusters. Phyllosilicates (saponite, serpentine, hydrous minerals from the iddingsite group, and berthierine) have been previously reported in Nakhla and other nakhlites as alteration products interpreted to form due to interaction with hydrothermal aqueous fluids at the surface and near subsurface of Mars (McCubbin et al., 2013; Muttik et al., 2014; Lee et al., 2015; Lee and Chatzitheodoridis, 2016) or as products of terrestrial alteration (Hicks et al., 2014).

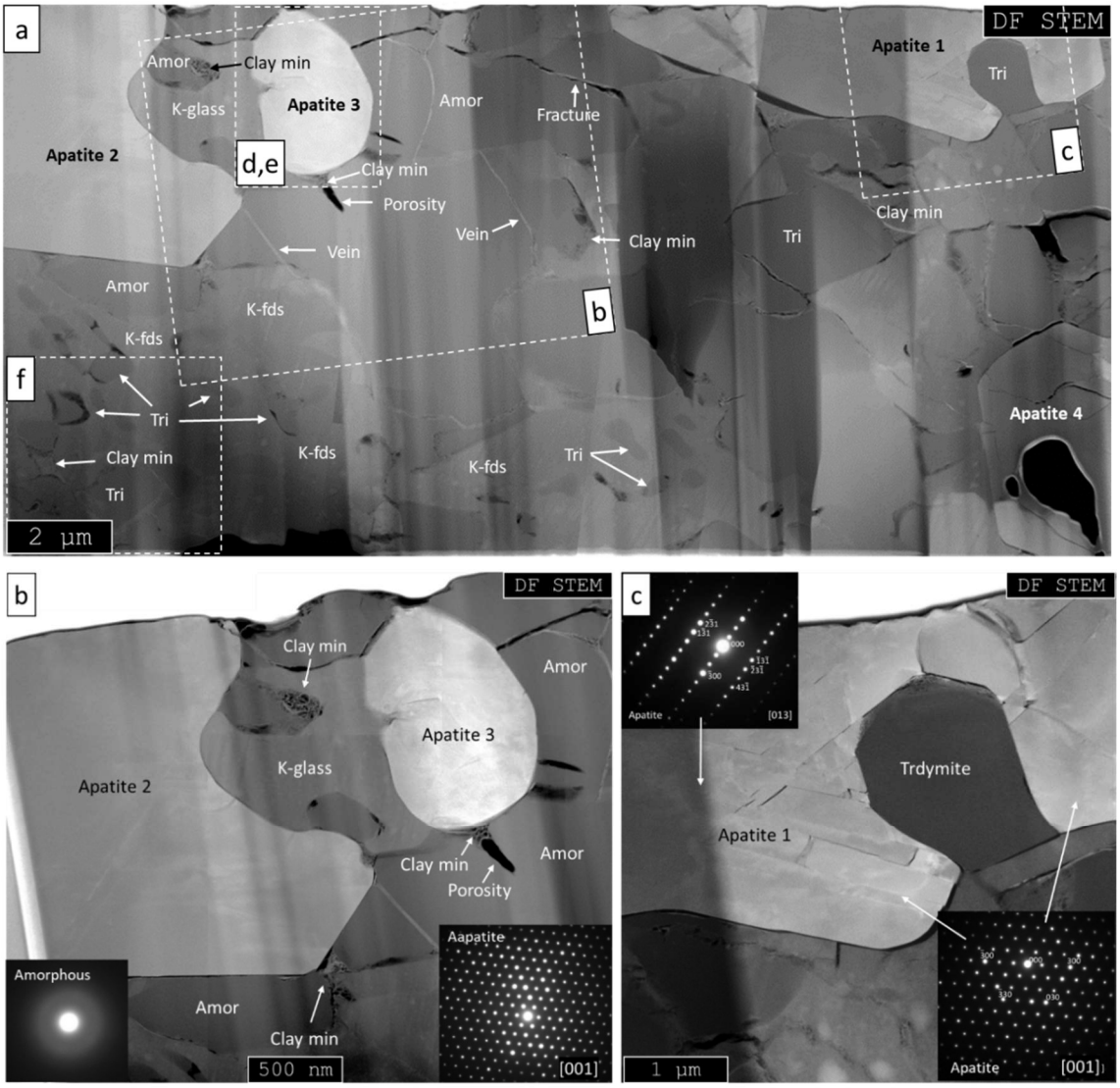

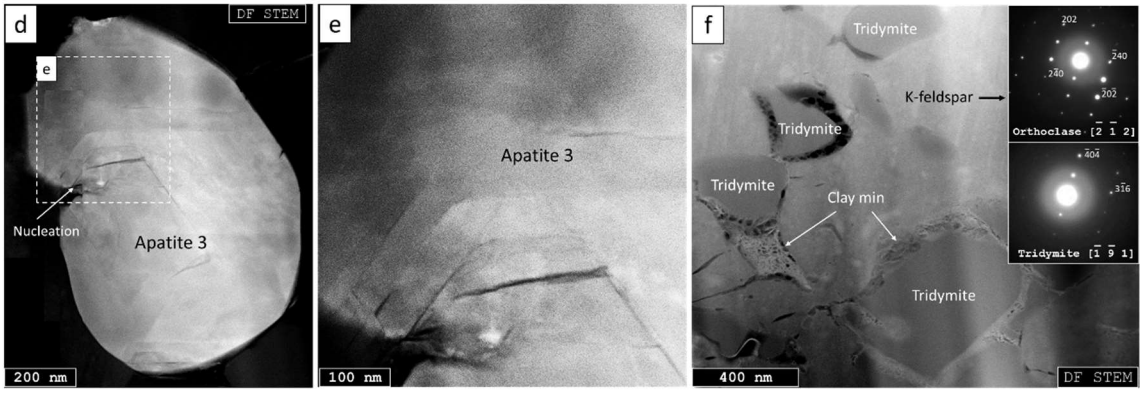

Figure 3.12. *(On previous and present page).* STEM images of Nakhla intercumulus apatites (FIB3). a) Dark-field STEM mosaic of the FIB section showing apatite grains numbered from 1 to 4. Other phases include silica (tridymite), amorphous silica, K-,Na-rich feldspar, and clay minerals (phyllosilicates). b) Close-up dark-field STEM image of a region in (a) showing apatites 2 and 3 with corresponding diffraction patterns, both viewed down the *c* axis. Fractures and/or porosity occur in a general radial pattern around apatite 3 and are filled with clay minerals. Apatites are embedded in an amorphous silica phase and K-rich glass. c) Close-up dark-field STEM image of apatite 1 with corresponding diffraction patterns showing that the grain is cut perpendicular to the *c* axis. d) Dark-field STEM image of apatite grain 3 shows a texture that suggests apatite nucleated at a region on the left-hand side of the grain. e) Close-up of the region in (d) shows the corresponding layers of growth (~50-100 μm in width). f) Dark-field STEM image of a region marked in (a) showing clay minerals surrounding grains of crystalline silica (tridymite) and filling interstitial regions. The mesostasis also contains K-, Na-rich feldspar with characteristic polysynthetic twinning. Inset of the diffraction patterns for tridymite and orthoclase are also shown. Legend: Amor = amorphous SiO_2, Tri = tridymite, K-fds = K, Na-rich feldspar, K-glass = K-rich feldspathic glass (maskelynite), clay min = clay minerals.

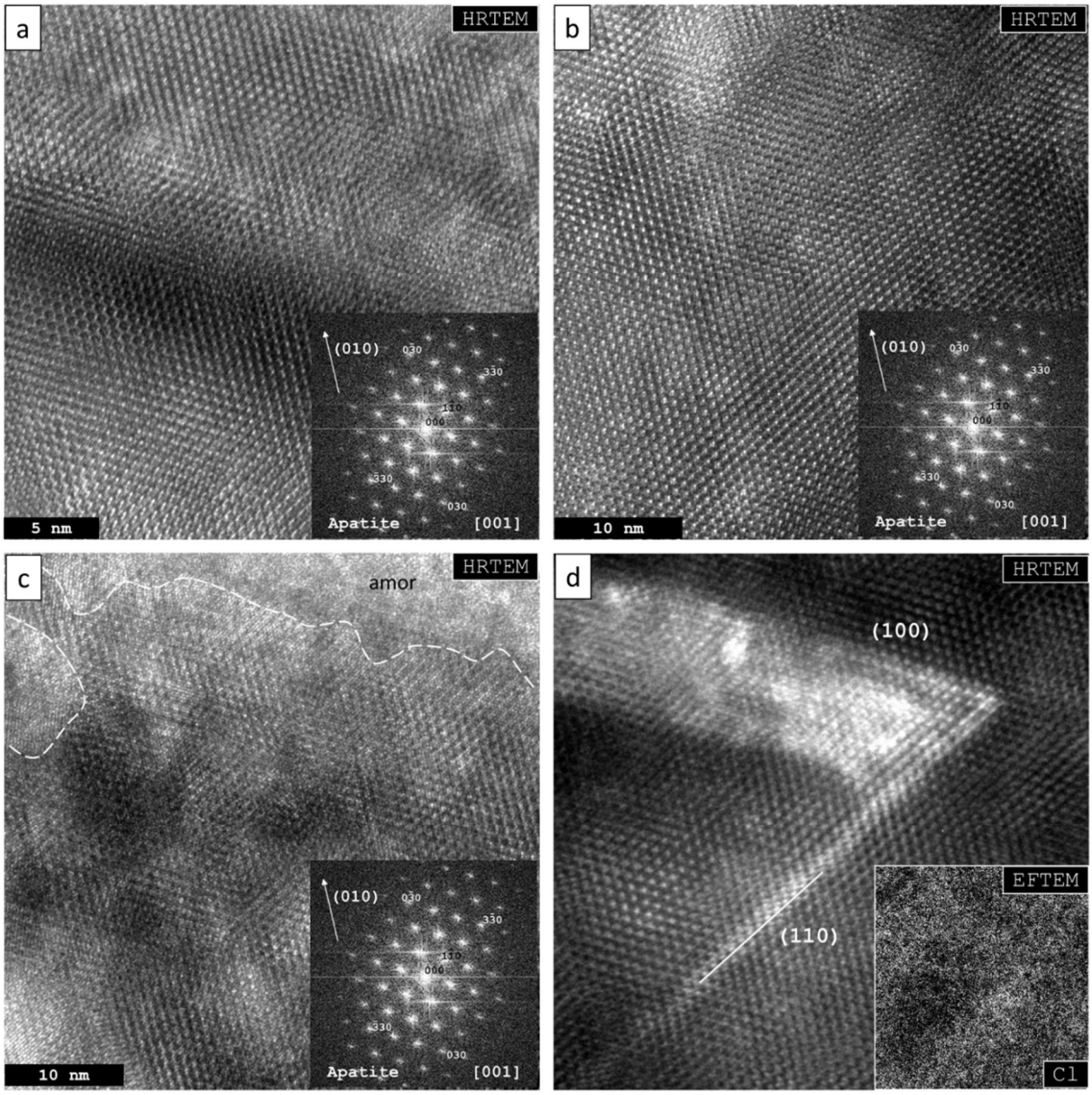

Figure 3.13. High-resolution TEM images of Nakhla apatites in FIB3 showing a) and b) the hexagonal crystal structure viewed down the [001] zone axis, and slight curvature of the (010) lattice fringes in (a) but not in (b). The region in (c) shows changes in the contrast of the lattice fringes due to slight changes of orientation of the different domains and slight curvature of (010) planes (same direction as in (a) and (b)). d) High-resolution TEM image of planar features in apatite, showing brighter regions in the (110) and the (100) planes. Inset of Cl map (lower right) performed with EFTEM shows that very slight differences in Cl concentration are apparent. However, the heterogeneity does not appear to correspond to the brighter regions observed with HTEM.

Table 3.4. TEM and STEM-EDS analyses (oxides wt%) of the four apatite grains in Nakhla (FIB3).

Oxides wt%	Ap1	Ap1	Ap2	Ap2	Ap2	Ap3C	Ap3C	Ap3R	Ap3R	Ap4	Ap4	Mean
P_2O_5	38.82	38.96	38.36	37.61	39.19	37.61	37.42	38.20	38.48	36.90	35.43	37.91
SiO_2	2.48	2.76	3.81	5.41	3.14	4.58	5.16	3.42	3.59	5.93	3.91	4.02
Al_2O_3	0.30	0.08	n.d.	0.13	0.36	0.42	0.43	0.30	0.36	0.94	0.32	0.33
Ce_2O_3	0.45	0.59	n.d.	n.d.	0.09	0.53	0.55	0.14	0.13	0.30	n.d.	0.25
Nd_2O_3	0.19	0.23	n.d.	n.d.	0.09	0.33	0.31	0.06	0.05	0.21	n.d.	0.13
MnO	0.06	n.d.	n.d.	n.d.	0.09	0.08	0.06	0.05	0.05	0.18	n.d.	0.05
CaO	52.46	52.41	52.90	51.88	51.70	51.22	50.50	51.97	51.49	51.61	55.48	52.15
FeO	0.32	0.37	0.08	0.15	0.24	0.41	0.44	0.21	0.14	0.56	0.27	0.29
SO3	n.d.	n.d.	n.d.	n.d.	n.d.	n.d.	n.d.	n.d.	n.d.	n.d.	0.15	0.01
F	1.22	1.34	1.00	0.87	0.84	0.62	0.63	0.52	0.20	1.90	1.33	0.95
Cl	3.66	3.21	3.86	3.96	4.24	4.18	4.47	5.12	5.50	2.93	3.11	4.02
Total	100	100	100	100	100	100	100	100	100	100	100	100
Cl/F	3.00	2.40	3.86	4.55	5.05	6.74	7.10	9.85	27.50	1.55	2.34	4.23
Structural formulae based on 13 [O]												
P	2.84	2.84	2.79	2.72	2.85	2.74	2.72	2.80	2.81	2.64	2.62	2.76
Si	0.21	0.24	0.33	0.46	0.27	0.39	0.44	0.30	0.31	0.50	0.34	0.35
Al	0.03	0.01	n.d.	0.01	0.04	0.04	0.04	0.03	0.04	0.09	0.03	0.03
Ce	0.01	0.02	n.d.	n.d.	n.d.	0.02	0.02	n.d.	n.d.	0.01	n.d.	0.01
Nd	0.01	0.01	n.d.	n.d.	n.d.	0.01	0.01	n.d.	n.d.	0.01	n.d.	n.d.
Mn	n.d.	n.d.	n.d.	n.d.	0.01	0.01	n.d.	n.d.	n.d.	0.01	n.d.	n.d.
Ca	4.86	4.84	4.87	4.75	4.76	4.73	4.66	4.83	4.77	4.68	5.19	4.81
Fe	0.02	0.03	0.01	0.01	0.02	0.03	0.03	0.01	0.01	0.04	0.02	0.02
S	n.d.	n.d.	n.d.	n.d.	n.d.	n.d.	n.d.	n.d.	n.d.	n.d.	0.02	n.d.
F	0.33	0.37	0.27	0.23	0.23	0.17	0.17	0.14	0.05	0.51	0.37	0.26
Cl	0.54	0.47	0.56	0.57	0.62	0.61	0.65	0.75	0.80	0.42	0.46	0.59
Z	0.13	0.17	0.17	0.19	0.16	0.22	0.18	0.11	0.14	0.07	0.17	0.16
Total cat	8.00	7.98	7.99	7.96	7.94	7.96	7.93	7.98	7.95	7.98	8.23	7.99
Ca/P atomic	1.71	1.71	1.75	1.75	1.67	1.73	1.71	1.72	1.70	1.77	1.98	1.74

Ap# = apatite number (in Fig. 3.12a)
C = core, R = rim
Z = calculated missing component (OH + vacancies)
n.d. = not detected

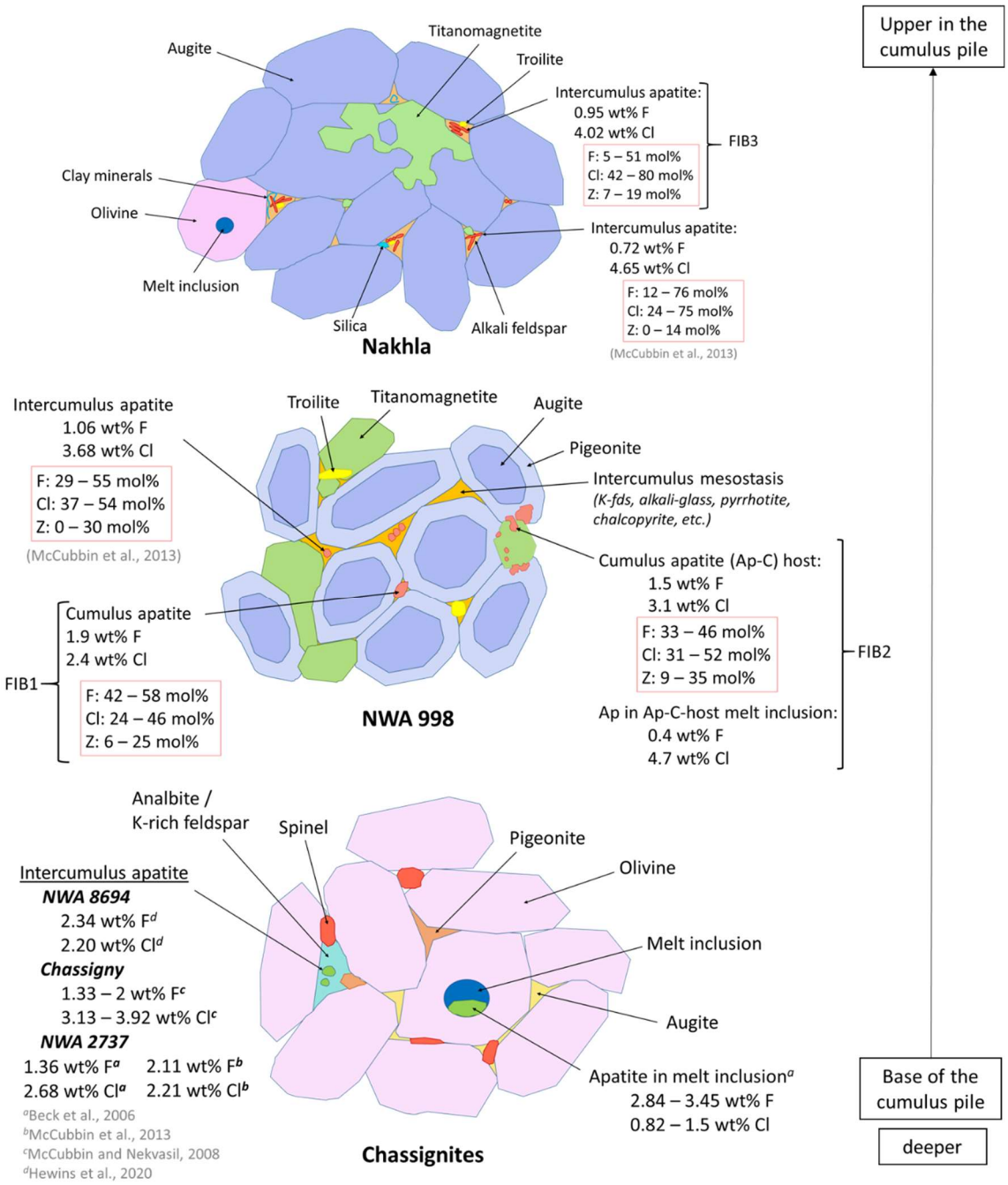

Figure 3.14. Schematic representation (not to scale) of the chassignites NWA 2737, Chassigny, and NWA 8694 (data from Beck et al., 2006; McCubbin and Nekvasil, 2008; McCubbin et al., 2013; and Hewins et al., 2020), and the nakhlites NWA 998 (data from McCubbin et al., 2013 and this work) and Nakhla (data from McCubbin et al., 2013 and this work) with their different apatite occurrences and halogen evolution. Differences in orientation of the crystal relative to the incident beam in apatite grains might result in variations in the F and Cl contents (Stormer et al., 1993).

4. Discussion

The nakhlites are cumulate rocks from Mars derived from a shallow level magma body or a thick lava flow (e.g., Lentz et al., 1999; Mikouchi et al., 2003, 2012; Treiman, 2005, Day et al., 2006; Treiman and Irving, 2008), although recent studies support multiple flows or hypabyssal intrusions (Hewins et al., 2020). These magmas are products of melting from the Martian interior (Floran et al., 1978; Harvey and McSween, 1992; Lentz et al., 1999; Treiman, 2005; Beck et al., 2006; Mikouchi et al., 2006, 2012). Chassignites and nakhlites have been petrologically linked to the same magmatic system (Jagoutz, 1996; Shih et al., 1998; Nyquist et al., 2001; Eugster et al., 2002; Eugster, 2003; Marti and Mathew, 2004; Bogard and Garrison, 2008; Park et al., 2009; Korochantseva et al., 2011; Carlson and Boyet, 2009), and several nakhlites (NWA 817, MIL 03346/ 090039/ 090032/ 090136, and NWA 5790) may record the eruptive event (e.g., Day et al., 2006). Superimposed on this magmatic record are potential subsolidus processes. There has been reported evidence that the nakhlite magma body experienced at least two interactions with hydrothermal fluids (Gooding et al., 1991). One was a magmatic hydrothermal fluid exsolved from the nakhlite magma during cooling (McCubbin et al., 2013), and the other was a later, shallower, aqueous brine resulting from an impact adjacent to the nakhlite parent rocks that formed secondary, low-temperature minerals (Ashworth and Hutchison, 1975; Newsom, 1980; Gooding et al., 1991; Abramov and Kring, 2005; Changela and Bridges, 2010; Bridges and Schwenzer, 2012; Hicks et al., 2014; Lee et al., 2015). Therefore, one of the major questions that need to be resolved is whether the source of Cl present in the nakhlites came from a shallow source, such as a fluid or assimilation of the country rock, or from a deeper, magmatic fluid. This debate

arises from the fact that apatites in the chassignites and nakhlites exhibit large variations in Cl content and isotope composition between grains and smaller variations within grains.

Apatite textures and compositions in the nakhlites have been used to reconstruct their magmatic and subsolidus histories and to better understand volatile reservoirs, their interactions, and their behavior in the martian crust and mantle. However, it is clear from our observations that apatite associated with nakhlites reflect a complex record of both magmatic and subsolidus processes and that extracting petrogenetic and volatile records are difficult and fraught with interpretive issues. For these reasons, examining apatite at the nanometer scale provides valuable insights into this complex thermal, geochemical, and volatile history, and can help resolve the important question of whether basalts can be used as reliable windows into the volatile geochemistry of the Martian mantle.

In the sections below, we discuss a complex range of microstructures observed in NWA 998 and Nakhla apatites that have not been described before: domain structures at the nanoscale, Z-contrast differences at the nanoscale, veins filling opened cleavage planes, zonation of halogens and REEs, and regions of an amorphous phase in Nakhla apatite. All these observations indicate that apatite records a variety of different processes that occurred at different times in the evolutionary history of the host rock. We therefore attempt to interpret the origin of these micro- and nanostructures and their timing in the following order: (4.1) presence of a domain structure in solid-solution apatite in the 5-10 nanometer scale that record a subsolidus cooling history and their importance in discerning between OH and vacancies in apatite for the missing component; (4.2) differences in apatite textures and compositions at the microscale between NWA 998 and

Nakhla; and (4.3) evidence of multiple fluid-mediated signatures in NWA 998 apatite. In addition, we also discuss (4.4) the discovery of a melt inclusion with chloro-amphibole and chloroapatite in NWA 998 and its importance in discerning between the contribution of a fluid or sediment. All these observations provide new insights into the complex interactions that the nakhlite magma body experienced and can help discern between the four proposed models to explain the geochemical signatures of the chassignites-nakhlites: (1) mantle-derived magmas with no crustal component (e.g., Jones, 1989; Longhi, 1991), (2) assimilation of crust by mantle-derived magmas (e.g., Sautter et al., 2006; Usui et al., 2012; Shearer et al., 2017), (3) addition of a fluid-phase during crystallization (e.g., McCubbin and Nekvasil, 2008; McCubbin et al,, 2013), and (4) near solidus or subsolidus metasomatism (e,g,, Treiman et al., 2007).

4.1. Nanostructures in solid-solution apatites from NWA 998 and Nakhla using HRTEM: Primary subsolidus signatures and possible vacancies in the missing component

There are very few micro- or nano-structural studies of natural terrestrial or extraterrestrial apatite (Ferraris et al., 2005; Słaby et al., 2017; Barnes et al., 2017; Birski et al., 2019) thus, this is essentially an unexplored area of research. In the present study, two domain structures are found at the nanoscale, one seen with high-resolution TEM and another one seen with dark-field TEM (Figs. 3.5, 3.7, and 3.13). Each technique reveals different characteristics of the domain structure – the first is the presence of localized strain and the second is differences in composition. The domain structure seen with HRTEM is defined by slight differences in contrast, related to changes in orientations of the crystal relative to the incident beam. It is associated with undulose lattice fringes,

indicative of localized strain within the structure (Fig. 3.8a). NWA 998 apatite displays a much higher degree of undulosity of the lattice fringes compared to Nakhla apatite. The boundaries between the domains in HRTEM images appear to be narrow and diffuse but continuous, causing differences in contrast, because these are the regions where the strain in the lattice is greatest, i.e., there is the largest misorientation relative to the crystal structure as a whole. The mismatch between the different domains is apparently accommodated by elastic strain in the structure, inferred by the lack of dislocations. The domain texture seen with dark-field STEM in NWA 998 apatite indicates compositional differences between the domains and might be due to the differences in the concentration of the two halogens, F and Cl. However, EFTEM imaging and EELS spectra were not sufficient to determine that Cl and F segregation are responsible for the domains. Nonetheless, the fact that the nanostructural domains observed with STEM are at the same scale (5-10 nm) as and HRTEM domains may suggest that differences in orientations of the crystal and localized strain within the structure (nanotextures seen with HRTEM) are related to differences in compositions (nanotexture seen with dark-field STEM).

A possible explanation for these phenomena can be understood by a consideration of the crystal structure of apatite, particularly, the location of the halogens. The apatite crystal structure ($P6_3/m$) consists of three cation polyhedra: the rigid PO_4 polyhedra, which remain invariant with the different halogens, the $Ca(1)O_9$ tricapped trigonal prism, which has little response to variations in F, Cl, and OH concentrations, and the $Ca(2)O_5X(O)$ polyhedron (X=F, Cl, OH), which experiences the major structural response, because it is bonded to the anion column (Hughes et al., 1989; Hughes and

Rakovan, 2002). Fluorine, Cl, and OH ions are located inside the channels that create the arrangement of planar triangles of Ca(2) atoms at z=1/4 and z=3/4 by the hexagonal screw 6_3, perpendicular to the c axis. In NWA 998 and Nakhla apatites, F and Cl are in solid solution among the anion column, thus the coordinated cation Ca(2) creates two different sites, one for F and unshifted Cl (and OH if present), and one for shifted Cl, enabling the optimum Ca-Cl bond distance to be maintained (Bauer and Klee, 1993). In pure chlorapatite and hydroxyapatite, the mirror plane symmetry disappears because Cl or OH arrange above or below the mirror plane, forcing the structure to order and becoming monoclinic ($P2_1/b$). However, in most natural samples, the hexagonal $P6_3/m$ symmetry is preserved because each mirror-related plane is half-occupied, or there are enough vacancies (in chlorapatite) or impurities (F ions in hydroxyapatite) in the anion column to destroy the ordering (Sudarsanan and Young, 1969; Elliott et al., 1973; Hughes and Rakovan, 2002). In fact, it is likely that some apatites in Nakhla, extremely Cl-rich and F-poor (Cl/F ratio up to 27.5, Table 3.4, Figs. 3.3, 3.14), preserve the hexagonal structure (Fig. 3.13a) due to the presence of vacancies in the structure (besides OH), which are discussed below. Ordering in the Ca and P sites when other elements substitute (e.g., Si in the P site or REEs in Ca sites), and ordering caused by the variety of anion substitutions in the halogen column result in a variety of different structural responses that is not well characterized yet (e.g., McConnell, 1973; Hughes et al., 1991; Hughes and Rakovan, 2002; Kelly et al., 2017).

We therefore suggest that the domain structures observed in NWA 998 and Nakhla are the result of a nanoscale segregation (exsolution) of the halogens into distinct F- and Cl-rich domains, which have different unit cell parameters (a=9.598Å; vol. 543Å^3

Cl-apatite, c.f. 9.3973Å; vol. 523Å^3 F-apatite, Hughes et al., 1989). Although the volume difference between the endmembers is only ~1%, it may be sufficient to cause lattice strain between F- and Cl-rich domains. This assumption seems reasonable given that Cl is 36% larger than F, resulting in disordering of Cl in the halogen column, due to its displacement 1.2 Å above and below the mirror plane (Hounslow and Chao, 1968; Hughes et al., 1989). This conclusion is further supported by the fact that the domain structures observed in NWA 998 and Nakhla are not observed in apatite from lunar basalts (Martínez et al., 2020), which is predominantly fluorapatite and displays a uniform nanostructure. We rule out that these domains are caused by REEs given that the abundance of REEs in much higher in Nakhla apatite but NWA 998 apatite shows a higher number of domains and more strain (undulosity of the lattice fringes) within the structure compared to Nakhla (Figs. 3.7a, 3.12a,b).

The highly undulose lattice fringes in NWA 998 apatite observed with HRTEM (larger lattice strain) compared to Nakhla is ascribed to the distinct Cl/F ratios (1.63 average of NWA 998 apatites, versus 4.23 average of Nakhla apatites, Tables 3.1, 3.2, 3.4, Fig. 3.3). More similar F and Cl contents may result in a higher abundance of domains with different Cl/F ratios caused by the mixing process of the two halogens. When Cl dominates the apatite structure, as seen in Nakhla, the domain abundance diminishes (Fig. 3.13). The *a* and *b* directions are the most affected by changes in the halogen column, since the twist angle of the CaO_6 metaprisms (which are connected with the PO_4 tetrahedron) is highly sensitive to composition and expands or contract to satisfy the CaO_6X polyhedra bonding requirements (White et al., 2005). Thus, the halogen channel expands or shrinks perpendicular to the basal plane, consistent with the direction

of undulosity obtained from HRTEM, the (100) direction (Fig. 3.8a). FIB3 (Nakhla) and FIB2 (NWA 998), sliced perpendicular (or close to perpendicular) to the crystallographic *c* axis, exhibit the most favorable crystallographic orientation for lattice mismatches (but the least favorable direction for compositional analyses; Stormer et al., 1993). In addition, diffraction patterns from NWA 998 apatite show diffuse streaking along the [111] and [313] directions (Figs. 3.4d, 3.6a), ascribed to inter-channel disorder between Cl and F ions (Ferraris et al., 2005). The optimal phase boundaries for different compositional domains form between lattice planes in F- and Cl-apatite domains with the lowest lattice mismatch, (111) and (313) being two of them.

A domain structure caused by phase separation at the nanometer scale has previously been observed in apatite (Ferraris et al., 2005). This study found a complex nanostructure in the (001) direction (apatite sliced perpendicular to the *c* axis) defined by differences in contrast and beam sensitivity in HRTEM at two different scales one order of magnitude apart. At a larger order of magnitude, guest apatite was observed as irregularly-shaped regions of a darker contrast in BF-TEM images amidst host-apatite, consistent with Cl- and F-rich apatites, respectively (Ferraris et al., 2005). At a smaller order of magnitude, bright areas 5-10 nm in diameter with poorly defined hexagonal facets were identified as ellestadite, a monoclinic apatite variety with formula $Ca_5(SiO_4,PO_4,SO_4)_3(F,Cl,OH)$. Both host and guest apatites have similar *c* but distinct *a* parameters and their interfaces are coherent with possible lattice mismatch to preserve coherency at domains of about 15 nm extent. Ferraris et al. (2005) concluded that F- and Cl-bearing apatite as a single phase is thermodynamically unstable and that spinodal decomposition produced continuous growth of two phases instantly. The authors also

distinguished two geothermometric events: a first, long, kinetically-driven phase separation close to the coherent spinodal decomposition temperature, which produced F- and Cl-rich apatites; and a second, short, diffusion-dependent period at a slightly higher temperature (contact metamorphism) that generated ellestadite domains.

The nanoscale exsolution domains observed in the present work have not been reported previously in any F-Cl-OH apatite. However, crystallographic studies by Hughes et al. (1989) on three near endmember apatites clearly demonstrate that the structural configurations of the column anions (F, Cl, OH) are not miscible. For example, for a binary apatite with composition $Ca_5(PO_4)_3(OH_{0.5}Cl_{0.5})$, each of the OH or F sites would be one-fourth occupied by its respective occupant, OH or Cl, and same would happen with ternary apatites. Hence, anion-anion distances calculated by Hughes et al. (1989) for column anions using end-member data precludes such a disordered $P6_3/m$ arrangement. Although complete disordering of OH and Cl is not feasible, there are possible ways that ternary solid solution can be accommodated. For example, vacancies play an essential role in stabilizing these apatite structures, because ordering can occur within single columns but not among different anion columns (Hughes et al., 1989). Based on the fact that NWA 998 apatites have the highest missing component abundances, commonly higher than 30 mol% (Fig. 3.3), but only 0.07 to 0.11 wt% water has been measured in NWA 998 apatite by SIMS (Channon et al., 2011), suggests that vacancies are likely present in the missing component. Hughes et al. (1989) predicted that although the overall near-endmember chlorapatite preserves the $P6_3/m$ symmetry, the structure may contain regions with Cl clusters ordered above or below the plane in a given column (local ordering). Hughes et al. (1989) also suggested that binary and ternary apatites

respond to solid solution in at least two ways: by large (0.4 Å) shifts of anion positions relative to the endmembers, and by reduction of symmetry to monoclinic. Our results show that the hexagonal symmetry is maintained, indicating that large displacements of anion positions likely occur, and/or that vacancies are present, which may be located at the boundary between domains, seen as blurry but coherent interfaces, separating clusters of Cl, F, and/or OH anions (Figs. 3.5b,c, 3.8a, 3.13b).

An important implication is thus that when OH is derived by stoichiometry when using EPMA analyses in Martian nakhlites, the result is likely overestimated. The coherent interfaces between the different domains are consistent with Ferraris et al. (2005) results, indicating that strain between the domains was small enough to be accommodated by elastic strain, and the lattice remains continuous across the boundary between the domains. The fact that the domain sizes are very small (5-10 nm) and coherent indicate that either the domains formed at low temperature (~600 ºC) or that the cooling rate was fast, preventing coarsening and formation of interfacial dislocations and/or semicoherent interfaces between the domains. This is consistent with cooling rates calculated by Mikouchi and Miyamoto (2002) for the nakhlites, indicative of subsolidus atomic diffusion, based on chemical zooning profiles (Fe-Mg and Ca) in olivine cores and assuming that olivine started cooling at 1100ºC. The authors also noted that Nakhla exhibits irregular Ca-zoning profiles in olivines, suggesting a more complex crystallization history than other nakhlites (Mikouchi and Miyamoto, 2002). Finally, recent work by Li and Costa (2020) showed that there is a stronger non-ideality mixing along the F-Cl join compared to F-OH or Cl-OH joins, and showed that at magmatic temperatures higher than 800-1250 ºC, the calculated W^G values are not high enough to

produce a miscibility gap in ternary apatite (Li and Costa, 2020). If the microstructures seen in NWA 998 and Nakhla indeed record miscibility gaps between F and Cl, then the apatite in NWA 998 had to form at lower temperatures (less than 800 ºC), consistent with the discussion above, or alternatively, if apatite formed above 800 ºC (above the miscibility gap), the exsolution had to form at a temperature lower than 800 ºC. In addition, vacancies were essential in stabilizing ternary apatites and eliminating a miscibility gap at high temperatures.

To summarize, our observations indicate that the fine-scale micro- and nanostructures observed in NWA 998 and Nakhla are a primary, post-magmatic signature formed during the initial subsolidus cooling (i.e., small size of the domains). The process formed at low temperatures (~600 ºC) and vacancies in the halogen column stabilized ternary apatites at higher temperatures (but less than 800ºC). There is no evidence of post-magmatic fluid interaction in the bulk apatite, such as pores, fractures, and/or significant dislocations. We observe a few dislocations parallel to the *c* axis, but they are not effective enough for fluid-transfer pathways into the bulk apatite. Any post-magmatic fluid interaction would have promoted coarsening of the domains or complete eradication of the microstructures.

4.2. Microstructural work on Nakhla apatite: Evidence for crustal assimilation

Apatite plays a critical role in understanding the magmatic system on Mars and can provide additional insights into the sources of volatiles. Apatite is widely used as a petrogenetic indicator because the F-Cl-OH ratio in apatite varies proportionally with the F-Cl-OH ratio of the melt from which it crystallizes, reflecting the role of volatiles in different episodes. However, the halogen and hydroxyl contents of apatite do not

represent the F-Cl-OH ratio of its parental fluid or melt (Piccoli and Candela, 2002; Boyce et al., 2014). Experimental studies on apatite melt-partitioning reveal that apatite prefers F over Cl, and Cl over OH (Stormer and Carmichael, 1971; Mathez and Webster, 2005; Boyce et al., 2014; McCubbin et al., 2015). Similarly, because individual minerals in cumulate samples do not modally represent the larger parent magma from which the cumulates formed, the study of apatite provides little indication about the REE concentration of the system in which they formed. In the following section, we discuss the microstructures and compositions of the four intercumulus apatite grains analyzed in Nakhla by TEM to evaluate which of the four petrogenetic models the observations support best.

TEM-EDS analyses show that the four apatite grains exhibit large variations in Cl and F contents (Cl ranging from 2.82 to 4.83 wt%, F ranging from 0.09 to 1.43 wt%, Table 3.4), consistent within the range obtained by EPMA by McCubbin et al. (2013) (Figs. 3.3, 3.14). Ascribing these variations, which are also apparent within individual grains, simply by fractional crystallization is not sufficient, given the range over these variations occur, and they might be explained by (1) outgassing of the residual melt (Sautter et al., 2006) or (2) degassing of a Cl-rich fluid after the melt reached chloride saturation (McCubbin et al., 2013). The recently discovered ferroan chassignite NWA 8694 also requires a more complex process to reproduce olivine as ferroan as in NWA 8694 (Fo_{54}), and magma mixing is suggested (Hewins et al., 2020). In addition, apatite δD values are much lower than some of the clay-like alteration assemblage δD values, indicating that the majority of OH in Nakhla apatites is not derived from Martian atmospheric water (Hallis et al., 2012). Instead, the wide compositional variable might be

attributable to either assimilation of crust (Sautter et al., 2006) or interaction with Martian groundwater during crystallization (McCubbin et al., 2013). Based on the following arguments, we support a model based on crustal assimilation in a Cl-rich melt:

1) The small scale at which compositional variations occur in Nakhla apatites indicates that the mineral assemblages in late-stage residual melt pockets did not grow in local equilibrium but were connected to the larger cumulus pile, sensitive to changes in composition of the overall system. Therefore, this is consistent with an open system.
2) The textural occurrence of apatite 3, cut perpendicular to the *c* axis and exhibiting a nucleation region with subsequent layers of growth, provides an opportunity to learn about the evolution of the melt during apatite crystallization (Fig. 3.12d). Although X-ray STEM maps of Cl *Kα* for apatite 3 (not shown) do not show compositional heterogeneities within the grain, TEM-EDS analyses of this grain show zonation of elements, where F, REEs, Si, and Fe are higher in the core, while Cl content increases towards the rim. The observed increase of Cl/F ratio with progressive crystallization is consistent with sequential crystallization from a melt that was becoming Cl-enriched through time due to preferential F incorporated into the apatite structure mentioned above. Rare-Earth Elements decrease from core to rim, also characteristic of apatite crystallizing from a late-stage melt (Jolliff et al., 1993). The zonation is thus inconsistent with crystallization from an aqueous fluid because Cl would have preferentially stayed in solution (the fluid) and apatite would not have become Cl-enriched in the outer

layers. The fluid would have been lost from the system because interstitial regions were open systems.

3) There is no evidence of subsolidus equilibration which would have erased the zonation, indicating that the apatite grew and cooled rapidly. The fact that apatite also shows zonation in Fe also supports that there is no indication of subsolidus equilibration, given that Fe and Mg equilibrates more readily in phosphates than REEs (Hess et al., 1990).

4) High-resolution TEM imaging shows that the crystal structure of apatite is highly heterogeneous. Some images show low contrast indicative of low strain and hexagonal configuration of apatite structure with straight lattice fringes (Fig. 3.13a), while other areas show higher contrast differences and slightly curvature of the lattice fringes in the (010) plane (Fig. 3.13b). We infer that these heterogeneities are caused by the large compositional variations (e.g., F/Cl differences and/or REEs, Table 3.4), and areas that show more complexity in the structure due to slight amorphization might be indicative of post-magmatic fluid interaction (Fig. 3.13b). Signatures of post-magmatic fluid interaction in the FIB section are evident, such as the presence of clay minerals filling porosity or veins outlining other mineral phases (Fig. 3.12), but they do not seem to have affected the primary apatite. Clay-like vein assemblages, or 'iddingsite' veins are well documented in literature and formed as a result of Martian surficial aqueous alteration of the nakhlite basalt (e.g., Ashworth and Hutchison, 1975; Reid and Bunch, 1975; Gooding et al., 1991; Bridges et al., 2001; Gillet et al., 2002; Trieman, 2005). Therefore, although the intercumulus melt in which

apatites are found has evidence of post-magmatic fluid interaction, they affected apatites minimally on a very localized scale and did not change their original primary magmatic compositional and microtextural characteristics.

To summarize, given that (i) different apatites that are only a few microns apart in the same melt pocket show large variability of Cl/F (wt%) ratios (Table 3.4, Figs. 3.3, 3.14), (ii) the zonation in apatite 3 is consistent with late-stage crystallization from a melt, (iii) the heterogeneities in the nanostructure of apatite are variable, and (iv) there is no evidence of a fluid phase interaction during apatite crystallization, we conclude that Nakhla apatites crystallized from a melt that experienced mechanical mixing of crustal sediments (Sautter et al., 2006). Post-magmatic aqueous alteration by a superficial Martian fluid is evident (e.g., presence of clay minerals), but did not affect the primary characteristics of apatite.

4.3. Metasomatic replacement in cleavage planes of NWA 998 apatite

Apatite grains in the NWA 998 nakhlite occur as single crystals with subgrain microstructures (Figs. 3.3, 3.6a). Here, we report the first epitaxial fluorapatite (~3 wt% F, ~1 wt% Cl, Table 3.2) growing on the walls of a vein that is parallel to the (100) imperfect cleavage planes of F-bearing chlorapatite (1.47 wt% F, 3.08 wt% Cl, Table 3.2) in NWA 998 (Fig. 3.9a). Replacement reactions have been observed to occur not only along grain boundaries but also inside crystals (e.g., Engvik et al., 2009). The present discovery represents a subsolidus process that only appears to have affected apatite at extremely localized scales. The elevated SiO_2 content in the vein compared to the host apatite suggests the presence of an additional Si-rich phase within the vein. Chlorine is not completely absent in the vein apatite (0.8-1.1 wt% Cl, compared to 3.1 in host

apatite), but previous experiments have demonstrated that a small amount of Cl can remain in the crystals after ion exchange under hydrothermal conditions (Yanagisawa et al., 1999).

We have observed the following characteristics in the veins of NWA 998 apatite: presence of porosity, compositional zonation, nanometer regions of amorphous material, and a sharp boundary interface between the vein and the parent F-bearing chlorapatite (Fig. 3.9). All these characteristics are indicative of a coupled dissolution-reprecipitation process caused by a fluid (Yanagisawa et al., 1999; Putnis and Putnis, 2007; Engvik et al., 2009). Therefore, these veins record the presence of fluids after crystallization of NWA 998 apatite and serve as an example of fluid-mediated apatite replacement that generates apatite of different composition. The composition of new apatite that precipitates from the fluid is thermodynamically more stable (Pollok et al., 2011; Raufaste et al., 2011) and is mainly governed by the characteristics of the fluid phase from which it is precipitating, such as the composition of the fluid, the pH, the fluid to mineral ratio (F/M), and the temperature and pressure (Kusebauch et al., 2015). Previous experiments that focused on ion exchange of Cl^- by OH^- and by F^- have shown that in general, higher concentrations of the alkaline solution and higher fluid to mineral ratio (higher F/M), favor more extensive replacement. Thus, the fluid that percolated in the opened cleavage planes of NWA 998 apatite was likely fairly acidic. These experiments have demonstrated that a F-containing solution will be depleted during interaction with Cl-apatite, and that F concentration in the new apatite is strongly dependent on overall F^- concentration in the fluid, but not on Cl^- concentration (Kusebauch et al., 2015), because F is highly compatible and strongly partitions into apatite compared to Cl (Zhu and

Sverjensky, 1991). Therefore, a fluid that circulates through Cl-rich apatite will end up Cl-enriched and F-depleted through the reaction:

$Cl\text{-}F\text{-}OH\text{-}Ap + Cl(?)\text{-}(F)\text{-}OH^{-}(aq) \rightarrow F\text{-}OH(?)\text{-}Ap + Cl^{-}(aq)$

We propose that a fluid initially out of equilibrium with the apatite infiltrated through the cleavage pathways and promoted dissolution of the parent F-bearing chlorapatite. The discovery of amorphous material (10 nm-scale) intermixed with crystalline fluorapatite (Fig. 3.9d) provides evidence for dissolution and low temperature reprecipitation. Consequently, chemical components were redistributed (ion exchange) between both the parent apatite and the fluid. New apatite grew first epitaxially on the walls of the vein, from the surfaces of the crystals that were in contact with the reaction media (Yanagisawa et al., 1999), and in local equilibrium with the fluid from which it was crystallizing (e.g., Kusebauch et al., 2015). The observed zonation shows that the fluid evolved towards Cl-enriched and F-, OH-depleted (lower OH^- activities), and indicates that the fluid was a very limited reservoir. Since water dissociates to H^+ and OH^-, for a NaCl-bearing fluid, as OH^- is incorporated into the apatite structure, HCl forms and the pH drops. In this case, the decrease in OH^- concentration in the fluid could be the major factor in the development of the zonation in the vein (see Kusebauch et al., 2015). Therefore, apatite that formed last (center of the vein) incorporated less F and OH as it formed in equilibrium with a fluid that was already depleted, because most F and OH were already consumed (Kusebauch et al., 2015) (Fig. 3.9). The zonation in the vein is thus caused by the evolving composition of the limited fluid reservoir that is effectively acting like a closed system.

The presence of nanometer-scale porosity observed in the vein (Fig. 3.9c) provides further evidence of a replacement reaction in apatite and is consistent with dissolution under hydrothermal conditions. Two kinds of porosity occur in the vein: smaller and more abundant pores at the outermost parts and larger and less abundant at the center (Fig. 3.9c). It is plausible that the smaller pores might be nanometer tunnels in three dimensions, parallel to the *c* axis of apatite (e.g., Young, 1980; Brenan, 1993; Yanagisawa et al., 1999). First, the introduction of an aqueous brine that was out of equilibrium with apatite triggered the dissolution of chlorapatite, where Ca and P dissolved into the fluid in a very localized scale and changed its composition. The smaller pores at the vein interface are evidence of dissolution of parent apatite, produced before fluorapatite began to crystallize. Pores were cavities filled with fluid that formed a continuous network that allowed fast exchange of ions between the host apatite and the fluid (e.g., Engvik et al., 2009). Calcium and P went into solution and were then used to form new fluorapatite, F being mainly externally derived. The presence of an amorphous material in the vein, likely silica-rich, suggests that some mass loss on the local scale must have occurred in order to allow growth of the new apatite phase. The larger porosity at the center of the vein formed last, being the last fluid-filled pore spaces that were left over from the crystallization of zoned apatite, because of the mass loss produced by dissolution of host chlorapatite.

Kusebauch et al. (2015) reacted synthetic endmember chlorapatite with various solutions containing NaCl, KOH, and NaF at temperatures ranging from 400 to 700 ºC to investigate the replacement products and understand the behavior of halogens during metamorphism. Epitaxial apatite is observed in all of the products to different degrees.

Apatite reacting with the NaF solution was the only experiment that produced fluorapatite with the three-endmember solid solution, hence F was completely derived from the external fluid. Experiments demonstrated that temperature has a major effect on the composition of epitaxial apatite, X_{OH} increasing with temperature (Zhu and Sverjensky, 1991; Yanagisawa et al., 1999). Replacement with intermediate and low concentrated NaF solutions produced F-rich apatite with variable compositions, whereas replacement with highly concentrated (1.5-3 wt%) NaF solutions lead to the formation of almost pure fluorapatite with a temperature dependent portion of the Cl component as follows: at 400 and 500ºC, X_{Cl} was 0.5 and at 600-700ºC, the product was almost pure fluorapatite and only traces of Cl were measured. Based on these data, we infer that the epitaxial vein in NWA 998 apatite formed at less than 400ºC (see Fig. 8 in Kasubauch et al., 2015) and the solution that infiltrated into the opened cleavage planes contained F. The observed low porosity in the vein (Fig. 3.8a,b,c) also indicates that little material was dissolved and that the reaction was roughly isovolumetric. Therefore, to account for the increase in the F/Cl ratio observed in the vein (there are > 2x more F in the vein compared to the host apatite, Table 3.2, Fig 3.3) and in order to maintain the same volume, we argue that some Cl from the chlorapatite structure was dissolved into solution and additional F from the fluid was added into the epitaxial apatite. Nonetheless, it is likely that some of the F was also derived from the precursor F-rich chlorapatite. Another possibility would be that there was simply anionic exchange between the existing F-rich chlorapatite and the F-bearing solution and hence, no dissolution occurred, but this is inconsistent with the amorphous regions observed with HRTEM (Fig. 3.9e).

Although OH is more readily incorporated into replaced or epitaxial apatite at higher temperature (Yanagisawa et al., 1999; Kusebauch et al., 2015), the zonation in the apatite vein indicates that there could have been a dependency on the amount of OH in the solution despite the low temperature. For experiments using NaCl, as the fluid becomes more acidic, OH^- enters the apatite structure. Therefore, in Kasubauch et al. (2015) experiments, the constant change of pH (as HCl is produced during replacement) also affected the composition of replaced apatite and produced zonation. On the contrary, experiments using KOH are buffered and OH activity is fixed, resulting in a constant composition of replaced apatite (Kasubauch et al., 2015). Therefore, the zonation in the epitaxial apatite in NWA 998 apatite is consistent with the fluid being fairly acidic. Furthermore, Cl diffusion is slower in OH-bearing apatite than in OH-poor crystals (Brenan, 1994), likely because the flux of Cl is affected by that of OH (Li et al., 2020).

The duration of Kusebauch et al. (2015) experiments was between 7 to 17 days and experiments were terminated by quenching at cooling rates of 100ºC/min, because the study was focused on long-duration fluid mineral interactions (Kusebauch et al., 2015). This suggests that the veins in NWA 998 apatite could have been formed in only a few days to a few weeks of duration. Nevertheless, caution should be exercised when comparing natural samples with experiments because there are some constraints. For example, quenching might have helped preserve the sharp interface if formed, while NWA 998 cooled more slowly. The fact that the veins in NWA 998 apatite are zoned and preserve a sharp interface with the host apatite (Fig. 3.8a,b,c) indicate that they formed at low temperatures (lower than 400 ºC) in order to prevent diffusional equilibration and eradication of the microstructures (i.e., coarsening of the porosity), especially taking into

account that the veins are less than a micron in width. To better estimate the temperature of formation of the veins, we have used the equation that calculates diffusion coefficients (D*) of Cl from Li et al. (2020) work as a function of the temperature (equation 1). The equation was obtained from experiments performed on natural Durango apatite between 800 and 1100 ºC, 1 atm, and oxygen fugacity at the wüstite-magnetite buffer, using a multicomponent diffusion model.

$$D^*_{Cl} = 7\binom{+12}{-4} \times 10^{-5} \times \left[exp^{\left(\frac{-294(\pm 12)KJ/mol}{RT}\right)}\right] m^2/s \quad (1)$$

Diffusion coefficients from Li et al. (2020) work using equation (1) have been extrapolated for temperatures below 800 ºC. Applying a diffusion distance of Cl in the vein of 100 nm (Figs. 3.9, 3.10), we have calculated different times of Cl diffusion as a function of temperature using the Fick's second law of diffusion (equation 2):

$$t = \frac{1}{2 \times D^*_{Cl}}\, x^2 \quad (2)$$

Where *x* is the diffusion distance and *t* is time.

The results are shown in Figure 3.15. In order to extract the temperature of formation of the veins in NWA 998 from Figure 3.15, we have considered that the veins formed at the same time as other secondary minerals in the nakhlites. However, the age(s) of formation of secondary minerals in the Nakhlites are challenging to obtain, because the minerals are fine-grained, difficult to separate from the host, and it is possible that contamination of Martian atmospheric gases (e.g., ^{40}Ar) were implanted after the formation of the phyllosilicates (e.g., during shock). Despite the challenges, some studies have successfully dated noble gases of 'iddingsite' in the nakhlites and obtained an age of ~650 Ma (Swindle et al., 2000, in the Lafayette meteorite).

Therefore, if the vein in NWA 998 has a similar age as Lafayette 'iddingsite', formed during a shock event that triggered a hydrothermal system in the Nakhlites (e.g., Changela and Bridges, 2010) (discussed below), we infer that the vein quenched at about 300 ºC (blue star in Fig. 3.15). Nonetheless, this temperature must be taken as an estimate, because it is possible that the diffusivity coefficients of Cl obtained from Li et al. (2020) at high temperatures (equation 1) are different at lower temperatures.

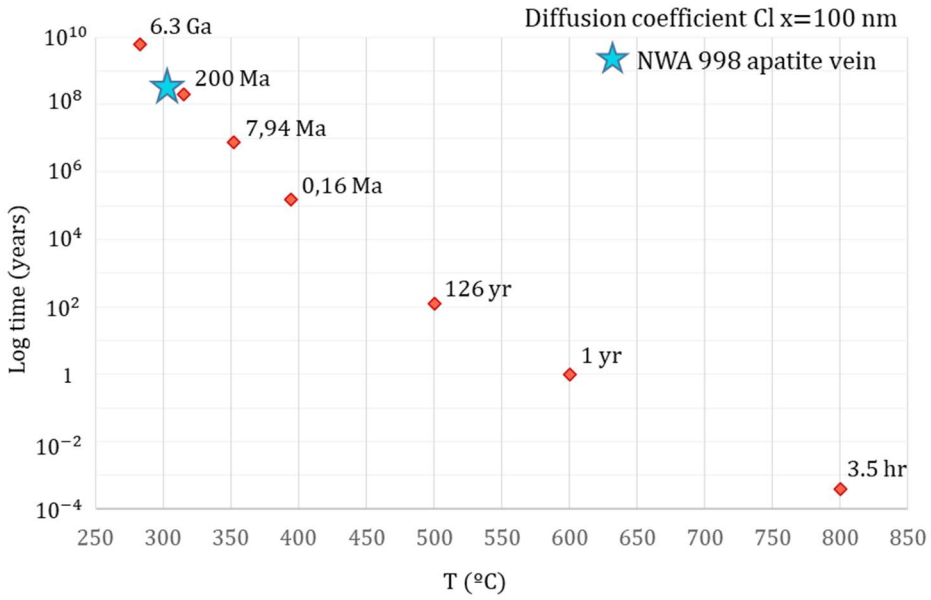

Fig. 3.15. Logarithm of time (years) versus temperature (ºC) using different diffusion coefficients of Cl as a function of temperature extracted from Li et al. (2020) (equation 1) and applied to equation 2. The only diffusion coefficient that has been directly extracted from Li et al. (2020) is at 800 ºC (3.5 hours). Below 800 ºC, diffusion coefficients have been extrapolated.

A potential sequence of events to explain the formation of the veins is illustrated in Figure 3.16. Cleavage planes of apatite were fractured and opened either by an impact or simply by settling in the magma chamber (Fig. 3.6a). Infiltration of the fluid through the opened cleavage planes occurred but the fluid was not circulating. The observed zonation and fractionation between F and Cl require a closed system within the vein and not a continuous reservoir of fluid, because that would have constantly changed the Cl

concentration in the fluid (i.e., lower concentration of Cl in the fluid). It is plausible that the veins formed very quickly (e.g., hydrothermal fluid 'quenched' into the cold host apatite) and acted as a closed system (e.g., fluid injected during an impact), with insufficient time for interaction between the larger fluid reservoir in the host rock.

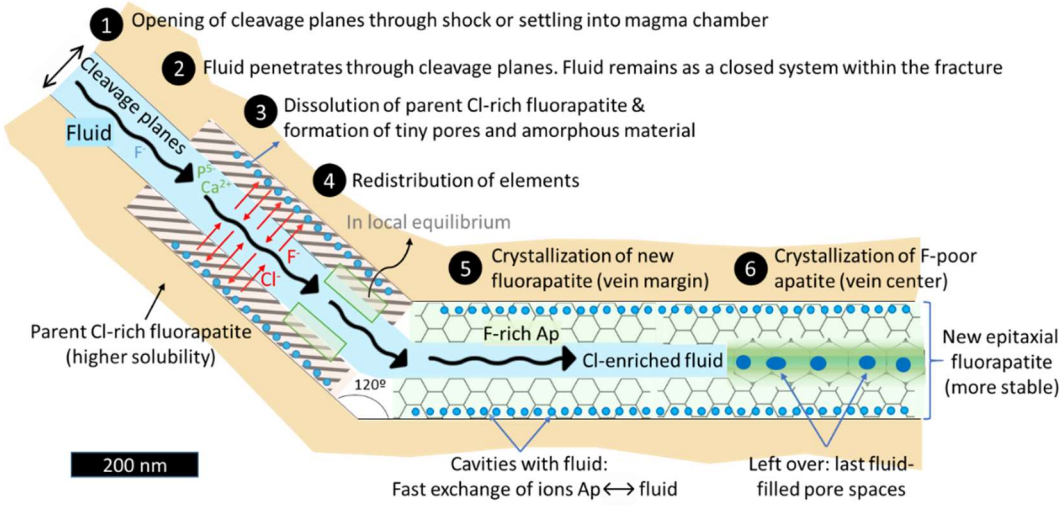

Figure 3.16. Illustration showing the interface-coupled dissolution-reprecipitation process in the formation of the veins within the cleavage planes of F-bearing chlorapatite in NWA 998. The fluid penetrated the opened cleavage planes producing new epitaxial, compositionally zoned, fluorapatite as a vein filling from dissolution of host F-bearing chlorapatite. Steps represented with numbers: (1) Opening of cleavage planes, (2) penetration of a F-rich fluid, (3) dissolution of host F-bearing chlorapatite and formation of tiny pores at the reaction interface, (4) Ca and P go into solution and reprecipitate to form new apatite, (5) F and Si are externally introduced from the fluid, F is preferentially used to form new apatite while the fluid gets enriched in Cl, and (6) crystallization of F-poor apatite in the vein center.

Several studies have confirmed that the nakhlites were subjected to shock, although it was relatively mild compared to other groups of Martian meteorites (e.g., Lambert 1987; Malavergne et al., 2001; Fritz et al., 2005; Murty et al., 2005). One of the hypotheses that has gained popularity is that an impact-induced hydrothermal system adjacent to the nakhlite parent rocks fractured the nakhlites and formed secondary alteration minerals (Changela and Bridges, 2010). Whether the veins observed in NWA

998 apatite occurred during this impact event or the two events occurred independently (first, the impact and later, a fluid percolated through the fractures) is not clear from this study, but the following observations can be made: (i) there is no evidence of microscale veining in BSE imaging, thus the amount of fluid in this specific event was relatively limited or localized in scale; (ii) the small scale of the vein and the zoning indicate that the vein could not have formed when the rock was at relatively high temperature and/or undergoing slow cooling, otherwise the zoning would have equilibrated due to volume diffusion; and (iii) limited fracturing in apatite and the relatively low dislocation density and subgrain structure indicate that these features could have been caused by a process other than shock, such as crystal settling in the magma chamber or post solidification movement within the magma chamber, given the cumulus nature of apatite 5. Alternatively, the vein could have formed by rapid injection of a hotter hydrothermal fluid into a cold rock, where the surrounding rock 'quenched' the fluid, resulting in rapid growth of the vein apatite and the development of zoning as fractionation between the fluid and apatite occurred. The last case might be compatible with an impact origin of the vein, although not pervasive (see iii), but we cannot differentiate between primary subsolidus cooling and a mild impact.

To summarize, the veins in NWA 998 apatite record a low temperature (~300 ºC) fluid-interaction process that occurred at some time after the magmatic crystallization of NWA 998 apatite. Parent F-bearing chlorapatite was epitaxially converted to fluorapatite (>2x enriched in F) by an interface-coupled dissolution-reprecipitation process that was extremely localized and acted as a closed system. The fluid was F-rich and fairly acidic,

and infiltration could have been caused by a mild impact that triggered a hydrothermal system or alternatively, fractures occurred simply by settling in the magma chamber.

4.4. Mineralogical insights into the magmatic nakhlite system from the study of a melt inclusion

4.4.1. Melt inclusion in NWA 998 apatite

Melt inclusions in nakhlites have been reported in silicate phases such as olivine and pyroxene (Sautter et al., 2006; Giesting and Filiberto, 2014, 2016) but none in apatite, because apatite grains are typically the size of regular inclusions in olivine and pyroxene (20-100 μm in size). Melt inclusions in cumulus apatites in NWA 998 may be more common than previously recognized given that one of the two FIB sections extracted here contains a melt inclusion. However, the extremely small sizes of apatite melt inclusions compared to melt inclusions in olivine or pyroxene are challenging and only accessible by transmission electron microscopy. Therefore, here we report the first melt inclusion discovered in extraterrestrial apatite (Fig. 3.6). The textural occurrence of the apatite that contains the melt inclusion (Apatite 5, Figs. 3.1a, 3.2g) corresponds to cumulus apatite based on its size and adjacent phases (McCubbin et al., 2013). The melt inclusion is extremely small (~3 μm-size) and multiphase, containing ~78% residual melt, ~17% chlorapatite, and ~5% chloro-amphibole.

The melt inclusion records the composition of the residual evolved melt at the time of apatite crystallization. However, it is very rare that melt inclusions preserve the exact composition of the trapped melt, because different processes result in chemical modification of the melt inclusion after or even during trapping (e.g., Danyushevsky et al., 2000; Kent, 2008). Post-entrapment processes are related to the particular pressure

and temperature the melt inclusion experienced, which are typically different from the surrounding melt. Several studies have also shown that more rapid re-equilibration (diffusive exchange between the inclusion and the host-mineral and/or external melt) is expected in inclusions that are smaller and have larger ratios of inclusion to host mineral radius (Danyushevsky et al., 2000, 2002; Gaetani and Warson, 2000, 2002; Cottrell et al., 2002; Spandler et al., 2007). Although the size of the melt inclusion is extremely small, the host apatite grain is also small, and the fact that apatite inside the melt inclusion contains higher Cl content (4.72 wt% Cl, 0.45 wt% F) than host chlorapatite (2.96 wt% Cl and 1.14 wt% F, Table 3.3, Figs. 3.3, 3.14), indicates that post re-equilibration processes between the melt inclusion and the host apatite or external melt were minimal, if at all. Volatile elements were likely preserved because the temperature remained close to the surrounding host mineral and pressure change was extremely small. Although the observed shell of apatite around the inclusion (Fig. 3.6) could suggest that change in volume did occur, it is more likely that the shell records dissolution processes during the post-magmatic hydrothermal system explained above (section 4.3), because the melt inclusion–host mineral interface is a susceptible pathway for fluid infiltration. The small size of the inclusion also prevented decrepitation, since several studies have shown that the larger the melt inclusion, the more likely it will crack (Tait, 1992; Schiano and Bourdon, 1999). Fracturing would have led to changes in pressure within the inclusion and loss of volatile elements and infiltration of fluids that caused alteration or weathering (e.g., Nielsen et al., 1998), which we do not observe. Therefore, we assume that the melt inclusion system remained closed and resulted in fractional crystallization of new minerals.

The observed shell around the melt inclusion could represent the first apatite crystallizing on the inclusion wall (serving as nucleation sites), once the melt was trapped and temperature dropped (Sobolev and Kostyuk, 1975; Roedder, 1984; Sovolev, 1996; Kress and Ghiorso, 2004), and this first apatite was F-rich following established F/Cl partitioning in apatite (e.g., Mathez and Webster, 2005; McCubbin et al., 2014). Consequently, the formation of F-rich apatite around the inclusion progressively depleted the trapped melt in F relative to Cl and other compatible elements in apatite, such as REEs (e.g., see Kent, 2008 and references therein). This process is likely partly responsible for the high enrichment in Cl and depletion in F of apatite inside the melt inclusion compared to host apatite and to apatite in the olivine-hosted melt inclusion reported in McCubbin and Nekvasil (2008) (Fig. 3.14). Numerical and experimental corrections applied to melt inclusions in olivine (see Kent, 2008 and references therein) have demonstrated that there is little effect on partitioning of incompatible elements into olivine beyond the uncertainties associated with measurements. In addition, the greater the pressure- and temperature-dependence of the partition coefficients, the more difficult it is to apply the corrections of this effect (Kent, 2008). Because apatite can incorporate common silicate incompatible elements into its structure, the calculated bulk composition in the apatite melt inclusion could contain higher apatite incompatible elements (e.g., Cl) than the original trapped melt.

Therefore, the calculated bulk composition of the melt inclusion presented in Table 3.3B must be considered approximate and caution must be exercised, because they can provide misleading insights into the host magma composition. Different approaches have been used to correct these effects in Martian melt inclusions in the literature (e.g.,

Varela et al., 2001; Stockstill et al., 2005), but none have been applied here. Instead, we have calculated the bulk composition using a simple modal recombination method by averaging different spot analyses in the different phases: five in the pyroxene + glass phase, one in the amphibole, and two in apatite, and the melt inclusion composition has been calculated based on the modal abundance of each phase (Table 3.3B). We have treated the intergrown pyroxene + glass as a single phase, because the regions of glass were too small to analyze separately. An additional caveat in the calculated bulk composition is that the mineral proportions on the exposed 2D surface may not necessarily represent the actual modal abundance in the entire volume of the melt inclusion.

The calculated bulk composition of the melt inclusion has a pyroxenitic composition corresponding to a basalt (Table 3.3B), based on the total alkali-silica diagram, consistent with the other nakhlites (e.g., Treiman, 2005, Table 3.5). The inferred Cl content in the melt is about 1 wt% Cl, which is within typical basaltic liquids and below chloride saturation values (Webster and De Vivo, 2002; McCubbin et al., 2013). The approximate bulk composition of the NWA 998 apatite melt inclusion is FeO-, MgO-, CaO-, P_2O_5-enriched, and Na_2O-, K_2O-, and Al_2O_3-poorer compared to intercumulus melt from Treiman and Irving (2018) (Table 3.5), but these differences are explained by the fact that the melt inclusion in NWA 998 was a closed system while mesostasis pockets were open systems that underwent dilution effects, possible volatilization, and equilibration. The melt inclusion in NWA 998 apatite has a composition that overall is consistent with the inferred composition that closely represents the original parental melt from Nakhla in the literature (Varela et al., 2001; Stockstill et al., 2005; Sautter et al.,

2012; Treiman and Goodrich, 2001). It contains similar CaO, Al_2O_3, and FeO contents but lower SiO_2 and Na_2O and higher P_2O_5, MgO, and K_2O (Table 3.5). The lower silica content probably reflects the uncertainties in the bulk composition and the 3D effect discussed earlier. However, as explained above, the bulk composition changed when new F-apatite formed rimming the inclusion and when additional daughter apatite crystallized on the edge of the melt inclusion, which would have increased the SiO_2 content in the residual melt. In general, augite-hosted melt inclusions are potassium-poor (0.4 wt% K_2O, Stockstill et al., 2005), while olivine-hosted melt inclusions are potassium-rich (~2.4 K_2O, Treiman and Goodrich, 2001; Sautter et al., 2012), and the potassium difference is suggested to be due to differences in growth rates of host minerals. The melt inclusions trapped in a fast-growing host mineral, such as olivine, is not considered to be representative of the parental melt composition (Goodrich et al., 2010). The composition of the apatite-hosted melt inclusion in NWA 998 contains intermediate potassium content (1 wt% K_2O), consistent with cumulus apatite crystallizing before apatite in intercumulus melts. Surprisingly, the FeO/MgO ratio of the bulk composition is lower (3.44) than the values in other melt inclusion compositions, except for the data of Varela et al. (2001) (Table 3.5), which is not expected for a late crystallization product. This value could suggest that the apatite was crystallizing at a similar time to the inclusions in the other silicate phases (i.e., augite in other nakhlites).

Overall, based on the calculated melt inclusion bulk composition and the discovery of daughter chloro-apatite and chloro-amphibole in the apatite-host melt inclusion of NWA 998, we infer that the magma from which NWA 998 crystallized was Cl-rich (although probably Cl is overestimated as explained above) during the nakhlite

cumulus pile crystallization. We do not find any evidence of fluid involved in the crystallization of apatite in the post-magmatic stages, either within the apatite host or the melt inclusion that modified the original apatite or melt inclusion compositions. The post-magmatic hydrothermal fluid that infiltrated through opened cleavage planes and through the melt-host interface had extremely localized effects, only ~100 nm in width. Because amphiboles in melt inclusions in the chassignites belong to the kaersutite group minerals (e.g., Beck et al., 2006), being Cl-poor, we provide further evidence that the chassignites and nakhlites might record a separation between mantle-derived melts and crustal-mantle-derived melts, consistent with isotopic data from Shearer et al. (2017). This study has not found evidence that a brine-like surface fluid percolated into the cumulate pile during crystallization (McCubbin and Nekvasil, 2008; McCubbin et al., 2013; and Cartwright et al., 2013), and supports crustal assimilation.

To summarize, apatite-host melt inclusions are considered rare in literature (Webster and Piccoli, 2015), but it is likely that they have been overlooked because they require TEM work given their smaller sizes. Our observations indicate that the melt inclusion in cumulus NWA 998 apatite remained as a closed system during fractional crystallization and that re-equilibration and/or chemical modification after entrapment was minimal. However, several effects must be taken into account that modified the original trapped melt composition. The outer shell in the melt inclusion might represent crystallization of the first fluorapatite at the melt-crystal interface, which enriched the melt inclusion in incompatible elements, such as Cl. Therefore, the fact that cumulus apatite inside the melt inclusion is significantly enriched in Cl than host-apatite might be partially due to this effect. However, chloro-apatite and chloro-amphibole crystallizing in

the melt inclusion indicate that the melt was Cl-rich. We infer that the hydrothermal post-magmatic fluid that penetrated through cleavage planes of host apatite explained above, reacted with the F-apatite rim around the inclusion, but the interaction was extremely localized and did not penetrate the inclusion or host apatite beyond the rim. Petrologic observations and compositional analyses of apatite in apatite-host melt inclusion in NWA 998 support crustal assimilation in the nakhlites pile rather than a surface brine that percolated in the cumulus pile during crystallization.

Table 3.5. Comparison between the calculated bulk composition (BC) of the melt inclusion in NWA 998 apatite with previous analytical studies of melt inclusions in augite (Varela et al., 2001; Stockstill et al., 2005; Sautter et al, 2012) and olivine (Treiman and Goodrich, 2001) in Nakhla. Treiman and Irving (2008) data represent the average composition of mesostasis regions analyzed in NWA 998 by EPMA. Compositions in wt% oxides.

	BC this work	Varela et al. 2001	Stockstill et al. 2005	Stockstill et al. 2005	Sautter et al. 2006	Treiman and Goodrich	Treiman and Irving 2008
Oxides wt%		GH(6)	NA03	S04	NPM05	NK01	Meso
SiO_2	44.89	55.4	47.2	51.2	49.1	49.8	58.98
P_2O_5	6.49	n.d.	0.09	0.97	0.36	0.6	n.d.
TiO_2	0.10	1.07	0.88	0.84	1.10	0.8	0.27
Al_2O_3	7.59	9.4	5.90	7.10	6.20	7.5	14.07
FeO	21.87	13.4	26.9	19.6	22.6	22.3	5.07
MnO	0.15	0.24	0.71	0.53	0.55	0.5	0.1
MgO	6.35	4.9	4.60	4.6	5.30	4.6	0.8
CaO	10.32	10.2	10.10	11.2	12.1	10.4	0.62
Na_2O	0.11	3.2	2.30	2.10	1.80	1.1	3.47
K_2O	1.00	0.6	0.39	0.7	0.32	2.4	5.63
F	0.08	n.d.	n.d.	n.d.	n.d.	n.d.	n.d.
Cl	1.06	n.d.	n.d.	n.d.	n.d.	n.d.	n.d.
Total	100	98.41	99.07	98.84	99.43	100	89.01
FeO/MgO	3.44	2.73	5.85	4.26	4.26	4.85	6.34

n.d. = not detected

4.4.2. Chloro-amphibole in NWA 998 melt inclusion

Amphiboles in Martian meteorites have been found in melt inclusions inside pigeonite (shergottites), olivine (chassignites), augite (MIL 03346, Sautter et al., 2006; NWA 5790, McCubbin et al., 2013), as well as in large (~100 μm) melt patches in intercumulus regions in MIL 03346 and its paired stones (Sautter et al., 2006; McCubbin et al., 2009, 2013). Melt patches, however, differ from melt inclusions because they are larger and represent a later capture of the most evolved magma between accumulated phenocrysts (Sautter et al., 2006). Chloro-amphiboles reported in the MIL nakhlites have a magmatic origin, and the mechanisms that have been proposed for their formation require the introduction of Cl into the magmatic system from an external source, because the parent magma did not have enough Cl to stabilize chloro-amphibole. Several scenarios have been suggested to explain the source of chlorine in the system: (i) crustal assimilation (Sautter et al., 2006), (ii) exsolved Cl-rich fluid from the magma (Giesting and Filiberto, 2016), and (iii) late-stage K-metasomatism (McCubbin et al., 2008, 2013). In the discussion that follows, we debate which is the most likely mechanism among these, based on the chemical composition of the newly discovered amphibole in NWA 998.

Chloro-ferro-ferri-barroisite in NWA 998 apatite melt inclusion is the first sodium-calcium amphibole observed in the nakhlites (based on Hawthorne et al., 2012 classification, Table 3.3), instead of calcic, the only type found to date. In fact, the observed zonation in the amphibole (Fig. 3.6c) likely records a compositional gap between Na- and Ca-bearing amphibole, because Ca and K are detected in the core with STEM-EDS, while the rim contains Na and Ca, but lacks K. Therefore, the zonation

indicates that the amphibole started crystallizing as a Ca-rich amphibole and evolved towards Na, Ca-rich compositions. The T site is almost all occupied by Si, with only a small T-site Al amount (Table 3.3). The MnO content is higher than previous reported amphiboles, but this is consistent with apatite hosting the melt inclusion in NWA 998 instead of olivine (McCubbin et al., 2013) or pyroxene (McCubbin et al., 2009; Sautter et al., 2012; McCubbin et al., 2013) in the MIL nakhlites. Manganese is compatible in olivine and pyroxene and therefore, the first olivine or pyroxene crystallizing around the melt inclusion will deplete the melt inclusion in Mn. On the contrary, Mn is incompatible in apatite and will stay in the melt inclusion.

Sautter et al. (2006) investigated the origin of Cl-amphiboles in MIL 03346 and concluded that it could not result from a simple entrapment episode of mesostasis and that at least one additional component was required which contained significant amount of Cl. The authors suggested that a small amount of Cl-rich sediment was trapped within the magma when intruding subsurface sediments, at a stage when the crystal/melt ratio was still low enough to allow convection and flow of the parent magma. This model was consistent with Shearer et al. (2017) work on Chassigny, which concluded that the meteorite shows the interaction with two distinct reservoirs, a heavy-Cl crustal reservoir measured in apatite and a light-Cl mantle reservoir preserved in melt inclusions. Alternatively, McCubbin et al. (2013) suggested that the elevated Cl content of NWA 998 silicate liquid resulted from secondary processes involving an exogenous Cl-rich fluid interacting with the parent magma prior to apatite saturation. Giesting and Filiberto (2016) model involved the presence of an alkali-ferrous chloride fluid that exsolved from the parental magma as it crystallized and underwent unmixing of the chloride component

into a chlor-dominant fluid and a water-dominant fluid. The chloride-dominant fluid was then trapped in some melt inclusions and reacted with the silicate to form potassic-chloro-hastingsite (Giesting and Filiberto, 2016). Therefore, based on the chemistry of the different amphiboles found in Martian meteorites, Giesting and Filiberto (2016) argued that potassic-chloro-hastingsites in the nakhlites record crystallization from a fluid, whereas kaersutites in the chassignites and shergottites record crystallization from a melt.

The Fe^{2+}/Mg ratio is a useful indicator on the ability of the amphibole structure to accommodate Cl. Because magmatic melts evolve from Mg- to Fe-rich, trapped melts in more evolved cumulus phenocrysts (e.g., augites in the MIL nakhlites) will be enriched in Fe compared to less evolved melts. Nonetheless, it is possible that the trapped melt in the apatite of NWA 998, being a late-stage mineral, occurred at a similar time when melts in augites were captured in the MIL nakhlites, as discussed above. The high Cl content of the amphibole in NWA 998 (4.75 wt%) is consistent with a melt that was Cl-enriched compared to the chassignites, but it does not necessarily involve the presence of a fluid (K-metasomatism). The positive correlation observed between Fe, Cl, and K among amphiboles is well explained by the Avoidance Rule (Volfinger et al., 1985), which states that higher the Fe content, higher the ability of amphiboles to incorporate Cl and K into their structure. The K content in the amphibole discovered here is lower (0.224 apfu) than previously reported amphiboles in the nakhlites (0.45-0.71 apfu, Table 3.6), but higher than amphiboles in the chassignite melt inclusions, and the difference could be ascribed simply to the fact that the trapped melt in NWA 998 was enriched in silicate incompatible elements (e.g., K) at the time of apatite crystallization. Therefore, we argue that the introduction of Cl into the magmatic system is not necessarily related to K-

metasomatism. In addition, the concentric structure of the inclusion also indicates that the inclusion crystallized *in situ* from trapped melt, without the presence of a fluid. Hence, our observations are more consistent with crystallization from a melt that was enriched in Cl by crustal sediments.

Table 3.6. Compositions of amphiboles in the chassignites and nakhlites extracted from Giesting and Filiberto (2016). Ordered from top to bottom of the nakhlite pile. Chassignites from Giesting and Filiberto (2014) and Giesting et al. (2015), NWA 090032 from McCubbin et al. (2013). NWA 998 (this work) based on Hawthorne et al. (2012) nomenclature.

Meteorite	Amphibole in MI	K (apfu)	Cl (apfu)	FeO (wt%)	Na wt%	$[A]_{(Na+K)}$	Cl wt%
NWA 5790	chloro-hastingsite	0.45	1.39	28.13	1.74	0.99	4.96
MIL 090032	potassic chloro-hastingsite	0.58	1.72	32.12	1.47	0.93	6.11
MIL 090030						1.01	5.57
MIL 03346+		0.55-0.71	1.46-1.99	30.15-34.20	0.93	0.33-0.93	1.89-7.01
NWA 998	chloro-ferro-ferri-barroisite	0.224	1.20	26.75	2.11	0.902	4.75
Chassignites	Ferri-kaersutite	0.04-0.1	≤0.22 wt%	0.14-0.23	3.02	0.66-0.91	0.09-0.72

In terrestrial settings, chloro-amphiboles are rare and mostly associated with high pressure metamorphism, alkali-iron-chloride metasomatism (crust and upper mantle), skarns, and in other magmatic environments, such as in amphibolite- and granulite-facies and igneous rocks (Dick and Robinson, 1979; Suwa et al., 1987; Morrison, 1991; Zhu et al., 1994; Heinrich, 1994; Kullerud, 1996; Leger et al., 1996; Markl et al., 1998; McCormick and McDonald, 1999; Mazdab, 2003; Xiao et al., 2005; Zhang et al., 2012; Teiber et al., 2014; Chan et al., 2016). Chlorine-rich amphiboles at the Sudbury Structure in Canada are believed to have formed by a meteorite impact (Dietz, 1964; French, 1967; Grieve, 1994; Golightly, 1994; Stöffler et al., 1994). Among the chloro-amphiboles, barroisite is very rare and characteristic of relatively high to ultra-high pressures (Heritsch et al., 1957; Ungaretti et al., 1981; Gibbons and Gyopari, 1986). It is found in volcanic rocks (blueschists facies) formed from deep subduction of oceanic crust along a

continental margin (e.g., Liu et al., 2009), and in eclogites (Binns et al., 1967; Lombardo et al., 2000). Previous studies have demonstrated that with decreasing metamorphic grade, amphiboles exhibit decreases in Mg/(Mg+Fe), Ti, Al, Na and K contents, and commensurate increases in Si and total Fe+Mg+Mn (e.g., Robinson et al., 1982; Graham and Powell, 1984; Holland and Blundy, 1994; Ernst and Liu, 1998). If the amphibole crystallized in the presence of a fluid, it is extremely challenging to explain the variations of the Cl content, because their variations are not directly related to changes in the fluid composition but based on a number of factors, such as the crystal chemistry of the amphibole, the pH of the fluid, the pressure and temperature conditions, and the Fe/Mg ratio of the mineral with which the fluid is reacting (e.g., Zhu and Sverjensky, 1991). Furthermore, Cl-rich amphiboles crystallize over a wide range in T (~350-800ºC) and P (0-8 kbar), suggesting that neither of these variables is a strong factor in controlling the growth or stabilizing these particular minerals (McCormic and McDonald, 1999).

Figure 3.17 illustrates variable Cl contents from Cl-bearing amphiboles in the chassignites and nakhlites from this work and the literature, compared with those from terrestrial (a) submarine metabasite amphiboles, (b) high-grade metamorphic amphiboles, (c) skarn amphiboles, and (d) igneous amphiboles, data compiled by Enami et al. (1992). The overlap between the Cl-rich amphibole from this study and from other nakhlites and chassignites with those from high-grade metamorphic amphiboles is evident. There is a small amount of overlap between Cl-rich amphiboles in the nakhlites and those from submarine metabasites and skarns. The majority of the data for chassignites nor nakhlites do not lie within the field ascribed to igneous amphiboles (Fig. 3.17). The major implication of these observations is that Cl-rich amphiboles in the nakhlites may have

stabilized at lower pressures (and temperatures) due to higher chlorine content (5.5. wt% average) compared to terrestrial amphiboles (most of them less than 1 wt% Cl). This implies that the current temperature estimation of potassic-chloro-hastingsite in the MIL nakhlites and NWA 5790 that are based on terrestrial amphiboles from medium to high-grade alteration of a protolith by alkali and/or iron chloride-rich fluids (>400 ºC, Giesting and Filiberto 2016) may be incorrect and the amphiboles actually crystallized at lower temperatures in the Martian rocks.

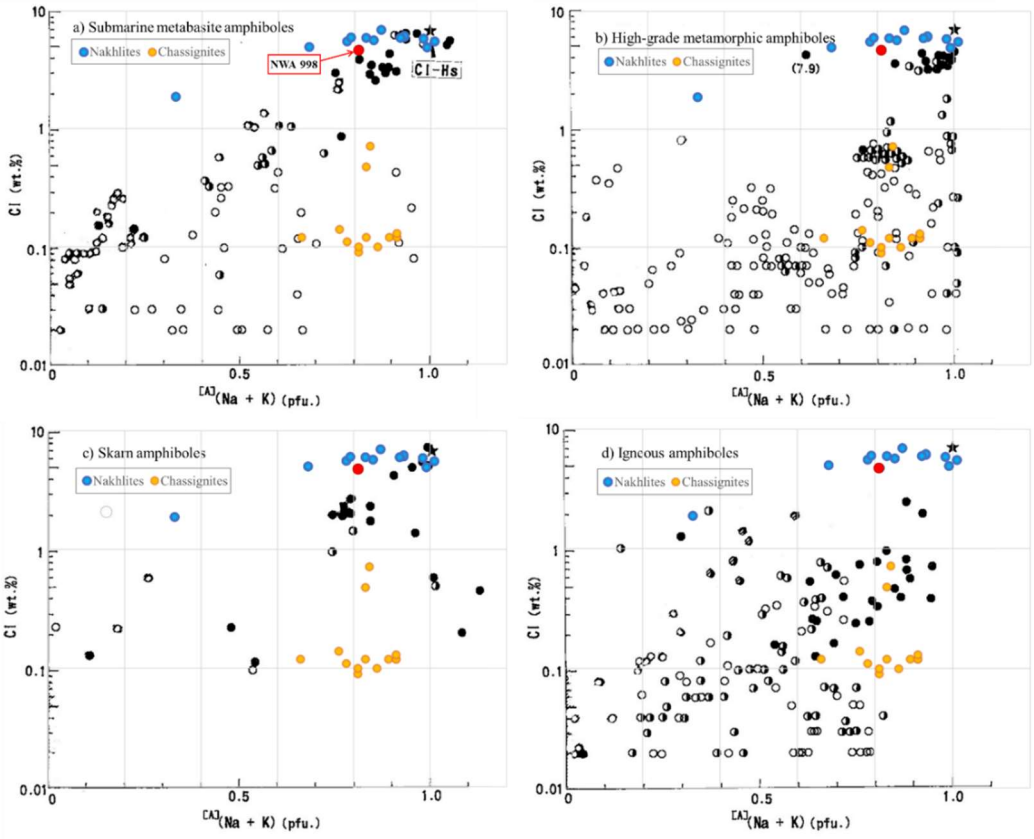

Figure 3.17. Amphibole data (Cl (wt%) as a function of $[A]_{(Na+K)}$ (apfu)) from chassignites (orange) and nakhlites (blue), as compiled by Giesting and Filiberto (2016), compared to information for calcic amphiboles from various geological terrestrial environments (submarine metabasite amphiboles, high-grade metamorphic amphiboles, skarn amphiboles, and igneous amphiboles), as compiled by Enami et al. (1992). Filled black symbols $0.7 \leq X_{Fe}^{2+}$; half black symbols: $0.4 \leq X_{Fe}^{2+} < 0.7$; white symbols: $X_{Fe}^{2+} < 0.4$. The red symbol indicates NWA 998 amphibole data from this work and the star, the composition of idealized chloro-hastingsite $[NaCa_2(Fe^{2+}{}_4Fe^{3+})(Si_6Al_2)O22Cl_2]$.

To summarize, the discovery of chloro-ferro-ferri-barroisite in a melt inclusion in NWA 998 indicates that Cl-rich amphiboles were able to crystallize in all the nakhlites. We do not have any evidence of interaction with a K-rich fluid and the chemistry of amphiboles in the nakhlites can be ascribed to mixing with a crustal component. On a Cl (wt%) versus $[A]_{(Na + K)}$ plot, Martian Cl-rich amphiboles lie on the field for terrestrial high-grade metamorphic amphiboles, implying that high Cl content in the Martian melt stabilized the formation of amphiboles at lower pressures and temperatures than terrestrial values (Figure 3.17). Thus, Martian Cl-rich amphiboles likely crystallized at less than 400ºC.

5. Summary and conclusions

1) We have observed a domain structure at the 5-10 nm scale in apatite in both NWA 998 and Nakhla characterized by high undulosity of the lattice fringes and differences in contrast, which are indicative of elastic strain and small, highly localized misorientations in the crystal. The lack of dislocations, the coherent interfaces, together with understanding the apatite structure suggest that these domains are related to halogen segregation (Cl clusters ordered within the apatite structure) at low temperature (≤600 ºC). The diffuse coherent interfaces between the domains are interpreted as vacancies within the halogen column, which are believed to play an essential role in stabilizing ternary apatites in NWA 998 and Nakhla. These nanostructure domains are a post-magmatic signature but formed during the initial subsolidus cooling. There is no evidence of post-magmatic fluid interactions in the bulk apatite.

2) Nakhla apatites exhibit large variations in Cl/F ratios between and within grains that are only a few microns apart, consistent with crystallization from a magma that

experienced mixing of different materials. Apatite 3 exhibits zonation of elements (the core contains higher F, REEs, Si, and Fe, and the rim is Cl-enriched) that is characteristic of crystallization from a late-stage melt and is inconsistent with the presence of a fluid. The nanostructure of Nakhla apatite is highly heterogeneous: some areas show low strain and low contrast, while other areas show curvature of the lattice fringes in the (010) planes, a feature that is likely related to the different F/Cl ratios mentioned above. Later, post-magmatic surface aqueous fluids interacted with the mesostasis regions but had little or no effect on the primary magmatic apatites.

3) We have discovered the first melt inclusion in extraterrestrial apatite. The melt inclusion contains daughter chloro-apatite and chloro-amphiboles. It is likely that the melt inclusion in NWA 998 apatite and melt inclusions in augite phenocrysts in the MIL nakhlites were captured at similar times. This study confirms that nakhlites record the mixing with a Cl-rich exogenous component that is absent in the chassignites. We discuss processes that can modify the original composition of the trapped melt. For example, the first apatite that crystallized around the melt inclusion (apatite shell) strongly partitioned F over Cl, enriching the melt inclusion in incompatible elements (e.g., Cl), and resulting in an overestimation of the Cl content of the daughter apatite. A late-stage hydrothermal fluid interacted with the host mineral–melt inclusion interface, but there is no evidence that the fluid penetrated in the interior of the inclusion. The lack of fluid signatures in either the host apatite or the melt inclusion rules out a model with a brine-like fluid that percolated into NWA 998.

4) We report the first chloro-amphibole in NWA 998, which is also the first sodium-calcium amphibole in the nakhlites (based on Hawthorne et al., 2012 classification),

identified as chloro-ferro-ferri-barroisite. The fact that evolved melts are enriched in Fe and incompatible elements such as K (e.g., during apatite crystallization in NWA 998 and augite crystallization at the top of the cumulus pile in the MIL nakhlites) can explain the ability of Cl to enter the amphibole structure. Our observations support mixing of sediments rather than K-metasomatism in the mantle source region for the origin of Cl. We show evidence that the higher Cl content in Martian amphiboles (nakhlites have 5x more Cl than terrestrial amphiboles) stabilized the formation of amphiboles at lower pressures and temperatures, thus they formed at less than 400 ºC, based on the current estimate by Giesting and Filiberto (2016).

5) We report epitaxial fluorapatite (>2x more F-rich than the host apatite) as veins (100-200 μm in width) filling opened cleavage planes in NWA 998 F-bearing chlorapatite. The veins record a fluid-mediated replacement of chlorapatite that generated more stable fluorapatite in a closed system. Parent chlorapatite was dissolved, new fluorapatite crystallized in local equilibrium with the fluid, and the fluid became Cl-enriched. The fluid was fairly acidic and the estimated temperature of the hydrothermal system was 300 ºC, based on Cl diffusivities by Li et al. (2020) and the width of the vein. Fluid infiltration occurred after primary magmatic crystallization and could have been triggered by a mild impact.

6) Finally, this work demonstrates that there are fundamental challenges to calculating the amount of water by stoichiometry using the subtraction of OH by assuming F+Cl+OH = 1. This is not a straightforward process, as vacancies are likely to play an important role in the apatite structure that can reduce the miscibility gap of ternary apatites upon cooling. In addition, this work shows that the history of a particular apatite grain is

subjected to numerous effects that can modify their volatile content (e.g., diffusion due to communication between different melts, post-entrapment processes in melt inclusions, etc.). Consequently, there are complications tied to using apatite to calculate melt compositions and taking it a step further, calculating volatile compositions of a source.

Acknowledgments

We would like to thank the Institute of Meteoritics for access to the thin sections of the two nakhlites used in this study. The Wilberforce apatite standard was provided by Zach Sharp. This work was supported and funded by NASA Cosmochemistry Grant NNX15AD28G and NASA Emerging Worlds Grant 80NSSC18K0731 to A. J. Brearley.

References

Abramov, O. and Kring, D. A. 2005. Impact-induced hydrothermal activity on early Mars. *Journal of Geophysical Research: Planets* 110:E12.

Agee, C. B., Wilson, N. V., McCubbin, F. M., Ziegler, K., Polyak, V. J., Sharp, Z. D., ... and Elardo, S. M. 2013. Unique meteorite from early Amazonian Mars: Water-rich basaltic breccia Northwest Africa 7034. *Science* 339:780–785.

Aiuppa, A., Baker, D. R., and Webster, J. D. 2009. Halogens in volcanic systems. *Chemical Geology* 263:1–18.

Ashworth, J. R. and Hutchison, R. 1975. Water in non-carbonaceous stony meteorites. *Nature* 256:714–715.

Barnes, J. J., Thompson, M., McCubbin, F. M., Boyce, J. W., Messenger, S. R., Rahman, Z., ... and Zega, T. 2017. Coordinated microanalysis of the chemical composition, microstructure, and volatile inventory of apatite in high-Ti mare basalts from the moon. *GSA Annual Meeting in Seattle, Washington (USA)*. Paper# 54–3.

Bauer, M. and Klee, W. E. 1993. The monoclinic-hexagonal phase transition in chlorapatite. *European Journal of Mineralogy* 5:307–316.

Beck, P., Barrat, J. A., Gillet, P., Wadhwa, M., Franchi, I. A., Greenwood, R. C., Bohn, M., Cotten, J., van de Moortèle, B. and Reynard, B. 2006. Petrography and geochemistry of the chassignite Northwest Africa 2737 (NWA 2737). *Geochimica et Cosmochimica Acta* 70:2127–2139.

Bellucci, J. J., Whitehouse, M. J., John, T., Nemchin, A. A., Snape, J. F., Bland, P. A., and Benedix, G. K. 2017. Halogen and Cl isotopic systematics in Martian phosphates: Implications for the Cl cycle and surface halogen reservoirs on Mars. *Earth and Planetary Science Letters* 458:192–202.

Binns, R. A. 1967. Barroisite-bearing ecologite from Naustdal, Song og Fjordane, Norway. *Journal of Petrology* 8:349–371.

Birski, Ł., Słaby, E., Chatzitheodoridis, E., Wirth, R., Majzner, K., Kozub-Budzyń, G. A., Sláma, J., Liszewska, K., Kocjan, I., and Zagórska, A. 2019. Apatite from NWA 10153 and NWA 10645—The key to deciphering magmatic and fluid evolution history in nakhlites. *Minerals* 9:695.

Bogard, D. D., and Garrison, D. H. 2008. ^{39}Ar–^{40}Ar age and thermal history of Martian dunite NWA 2737. *Earth and Planetary Science Letters* 273:386–392.

Boyce, J. W., Tomlinson, S. M., McCubbin, F. M., Greenwood, J. P., and Treiman, A. H. 2014. The lunar apatite paradox. *Science* 344:400–402.

Brenan, J. 1993. Kinetics of fluorine, chlorine and hydroxyl exchange in fluorapatite. *Chemical Geology* 110:195–210.

Bridges, J. C. and Grady, M. M. 1999. A halite-siderite-anhydrite-chlorapatite assemblage in Nakhla: Mineralogical evidence for evaporites on Mars. *Meteoritics & Planetary Science* 34:407–415.

Bridges, J. C. and Grady, M. M. 2000. Evaporite mineral assemblages in the nakhlite (martian) meteorites. *Earth and Planetary Science Letters* 176:267–279.

Bridges, J. C. and Schwenzer, S. P. 2012. The nakhlite hydrothermal brine on Mars. *Earth and Planetary Science Letters* 359:117–123.

Bridges, J. C., Catling, D. C., Saxton, J. M., Swindle, T. D., Lyon, I. C., and Grady, M. M. 2001. Alteration assemblages in Martian meteorites: Implications for near-surface processes. *Space Science Reviews* 96:365–392.

Bunch, T. E. and Reid, A. M. 1975. The nakhlites Part I: Petrography and mineral chemistry. *Meteoritics* 10:303–315.

Cartwright, J. A., Gilmour, J. D., and Burgess, R. 2013. Martian fluid and Martian weathering signatures identified in Nakhla, NWA 998 and MIL 03346 by halogen and noble gas analysis. *Geochimica et Cosmochimica Acta* 105:255–293.

Carlson, R. W. and Boyet, M. 2009. Short-lived radionuclides as monitors of early crust–mantle differentiation on the terrestrial planets. *Earth and Planetary Science Letters* 279:147–156.

Chan, A., Jenkins, D. M., and Dyar, M. D. 2016. Partitioning of chlorine between NaCl brines and ferro-pargasite: Implications for the formation of chlorine-rich amphiboles in mafic rocks. *The Canadian Mineralogist* 54:337–351.

Changela, H. G. and Bridges, J. C. 2010. Alteration assemblages in the nakhlites: Variation with depth on Mars. *Meteoritics & Planetary Science* 45:1847–1867.

Channon, M. B., Boyce, J. W., Stolper, E. M., and Eiler, J. M. 2011. Abundances of Cl, F, H, and S in apatites from SNC meteorites. *74th Annual Meeting of the Meteoritical Society*. Abstract #5401.

Channon, M. B. 2013. Oxygen isotopes and volatiles in Martian meteorites. Ph.D. dissertation, California Institute of Technology.

Chen, J. H., and Wasserburg, G. J. 1986. Formation ages and evolution of Shergotty and its parent planet from U-Th-Pb systematics. *Geochimica et Cosmochimica Acta* 50:955–968.

Cottrell, E., Spiegelman, M., and Langmuir, C. H. 2002. Consequences of diffusive reequilibration for the interpretation of melt inclusions. *Geochemistry, Geophysics, Geosystems 3*:1–26.

Danyushevsky, L. V., Della-Pasqua, F. N., and Sokolov, S. 2000. Re-equilibration of melt inclusions trapped by magnesian olivine phenocrysts from subduction-related magmas: petrological implications. *Contributions to Mineralogy and Petrology* 138:68–83.

Day, J., Taylor, L. A., Floss, C., and McSween, H. Y. 2006. Petrology and chemistry of MIL 03346 and its significance in understanding the petrogenesis of nakhlites on Mars. *Meteoritics & Planetary Science* 41:581–606.

Dreibus, G. and Jagoutz, E. 2002. Radiogenic isotopes and bulk composition of Mars. *33rd Lunar and Planetary Science Conference*. Abstract#1040.

Dick, L. A. and Robinson, G. W. 1979. Chlorine-bearing potassian hastingsite from a sphalerite skarn in southern Yukon. *The Canadian Mineralogist* 17:25–26.

Dietz, R. S. 1964. Sudbury structure as an astrobleme. *The Journal of Geology* 72:412–434.

Dreibus, G., and Wanke, H. 1985. Mars, a volatile-rich planet. *Meteoritics* 20:367–381.

Elliott, J. C., Mackie, P. E., and Young, R. A. 1973. Monoclinic hydroxyapatite. *Science* 180:1055–1057.

Enami, M., Liou, J. G., and Bird, D. K. 1992. Cl-bearing amphibole in the Salton Sea geothermal system, California. *The Canadian Mineralogist* 30:1077–1092.

Engvik, A. K., Golla-Schindler, U., Berndt, J., Austrheim, H., and Putnis, A. 2009. Intragranular replacement of chlorapatite by hydroxy-fluor-apatite during metasomatism. *Lithos* 112:236–246.

Ernst, W. G. and Liu, J. 1998. Experimental phase-equilibrium study of Al-and Ti-contents of calcic amphibole in MORB; a semiquantitative thermobarometer. *American Mineralogist* 83:952–969.

Eugster, O. 2003. Cosmic-ray exposure ages of meteorites and lunar rocks and their significance. *Chemie der Erde-Geochemistry* 63:3–30.

Eugster, O., Busemann, H., Lorenzetti, S., and Terribilini, D. 2002. Ejection ages from krypton-81-krypton-83 dating and pre-atmospheric sizes of martian meteorites. *Meteoritics & Planetary Science* 37:1345–1360.

Ferraris, C., White, T. J., Plévert, J., and Wegner, R. 2005. Nanometric modulation in apatite. *Physics and Chemistry of Minerals* 32:485–492.

Floran, R. J., Prinz, M., Hlava, P. F., Keil, K., Nehru, C. E., and Hinthorne, J. R. 1978. The Chassigny meteorite: A cumulate dunite with hydrous amphibole-bearing melt inclusions. *Geochimica et Cosmochimica Acta* 42:1213–1229.

Franz, H. B., Kim, S. T., Farquhar, J., Day, J. M., Economos, R. C., McKeegan, K. D., Schmitt, A. K., Irving, A. J., Hoek, J., and Dottin III, J. 2014. Isotopic links between atmospheric chemistry and the deep sulphur cycle on Mars. *Nature* 508:364–368.

French, B. M. 1967. Sudbury structure, Ontario: Some petrographic evidence for origin by meteorite impact. *Science* 156:1094–1098.

Fritz, J., Artemieva, N., and Greshake, A. 2005. Ejection of Martian meteorites. *Meteoritics & Planetary Science* 40:1393–1411.

Filiberto J. and Treiman A. H. 2009. Martian magmas contained abundant chlorine, but little water. *Geology* 37:1087–1090.

Gaetani, G. A. and Watson, E. B. 2000. Open system behavior of olivine-hosted melt inclusions. *Earth and Planetary Science Letters* 183:27–41.

Gaetani, G. A. and Watson, E. B. 2002. Modeling the major-element evolution of olivine-hosted melt inclusions. *Chemical Geology* 183:25–41.

Graham, C. M. and Powell, R. 1984. A garnet–hornblende geothermometer: calibration, testing, and application to the Pelona Schist, Southern California. *Journal of metamorphic Geology* 2:13–31.

Gibbons, W. and Gyopari, M. 1986. A greenschist protolith for blueschist in Anglesey, UK. In *Blueschists and eclogites*. *Geological Society of America Memoir* 164:217–228.

Giesting, P. A. and Filiberto, J. 2014. Quantitative models linking igneous amphibole composition with magma Cl and OH content. *American Mineralogist* 99:852–865.

Giesting, P. A. and Filiberto, J. 2016. The formation environment of potassic-chloro-hastingsite in the nakhlites MIL 03346 and pairs and NWA 5790: Insights from terrestrial chloro-amphibole. *Meteoritics & Planetary Science* 51:2127–2153.

Gillet, P., Barrat, J. A., Deloule, E., Wadhwa, M., Jambon, A., Sautter, V., ... and Lesourd, M. 2002. Aqueous alteration in the Northwest Africa 817 (NWA 817) Martian meteorite. *Earth and Planetary Science Letters* 203:431–444.

Goldoff, B., Webster, J. D., and Harlov, D. E. 2012. Characterization of fluor-chlorapatites by electron probe microanalysis with a focus on time-dependent intensity variation of halogens. *American Mineralogist* 97:1103–1115.

Golightly, J. P. 1994. The Sudbury Igneous Complex as an impact melt: Evolution and ore genesis: Ontario Geological Survey Special. In *Proceedings of the Sudbury-Noril'sk Symposium* 105–117.

Gooding, J. L., Wentworth, S. J., and Zolensky, M. E. 1991. Aqueous alteration of the Nakhla meteorite. *Meteoritics* 26:135–143.

Goodrich, C. A., Treiman, A. H., Filiberto, J., and Jercinovic, M. J. 2010. The Nakhla parent magma: old problems, new approaches. *41st Lunar and Planetary Science Conference*. Abstract #1387.

Goodrich, C. A., Treiman, A. H., Filiberto, J., Gross, J., and Jercinovic, M. 2013. K_2O-rich trapped melt in olivine in the Nakhla meteorite: Implications for petrogenesis

of nakhlites and evolution of the Martian mantle. *Meteoritics & Planetary Science* 48:2371–2405.

Greenwood, J. P., Blake, R. E., and Coath, C. D. 2003. Ion microprobe measurements of $^{18}O/^{16}O$ ratios of phosphate minerals in the Martian meteorites ALH84001 and Los Angeles. *Geochimica et Cosmochimica Acta* 67:2289–2298.

Grieve, R. A. F. 1994. An impact model of the Sudbury structure: Ontario Geological Survey Special. In *Proceedings of the Sudbury-Noril'sk Symposium. Ministry of Northern Development and Mines, Ontario*. Pp. 119–132.

Guzmics, T., Kodolányi, J., Kovács, I., Szabó, C., Bali, E., and Ntaflos, T. 2008. Primary carbonatite melt inclusions in apatite and in K-feldspar of clinopyroxene-rich mantle xenoliths hosted in lamprophyre dikes (Hungary). *Mineralogy and Petrology* 94:225.

Halliday, A. N., Wänke, H., Birck, J. L., and Clayton, R. N. 2001. The accretion, composition and early differentiation of Mars. *Space Science Reviews* 96:197–230.

Hallis, L. J., Taylor, G. J., Nagashima, K., and Huss, G. R. 2012. Magmatic water in the martian meteorite Nakhla. *Earth and Planetary Science Letters 359*:84–92.

Harvey, R. P. and McSween Jr, H. Y. 1992. Petrogenesis of the nakhlite meteorites: Evidence from cumulate mineral zoning. *Geochimica et Cosmochimica Acta* 56:1655–1663.

Hawthorne, F. C., Oberti, R., Harlow, G. E., Maresch, W. V., Martin, R. F., Schumacher, J. C., and Welch, M. D. 2012. Nomenclature of the amphibole supergroup. *American Mineralogist* 97:2031–2048.

Heinrich, W. 1994. Potassium-fluor-richterite in metacherts from the Bufa del Diente contact-metamorphic aureole, NE-Mexico. *Mineralogy and Petrology* 50:259–270.

Hewins, R. H., Humayun, M., Barrat, J. A., Zanda, B., Lorand, J. P., Pont, S., Assayag, N., Cartigny, P., Yang, S., and Sautter, V. 2020. Northwest Africa 8694, a ferroan chassignite: Bridging the gap between nakhlites and chassignites. *Geochimica et Cosmochimica Acta 282*:201–226.

Heritsch, H., Paulitsch, P., and Walitzi, E. M. 1957. Die Struktur von Karinthin und einer barroisitischen Hornblende. *Tschermaks mineralogische und petrographische Mitteilungen* 6:215–225.

Hess, P. C., Horzempa, P., Rutherford, M. J., and Devine, J. 1990. Phosphate equilibria in lunar basalts. *21st Lunar and Planetary Science Conference*. Pp 105–106.

Hicks, L. J., Bridges, J. C., and Gurman, S. J. 2014. Ferric saponite and serpentine in the nakhlite martian meteorites. *Geochimica et Cosmochimica Acta* 136:194–210.

Holland, H. D. 1972. Granites, solutions, and base metal deposits. *Economic Geology* 67:281–301.

Holland, T. and Blundy, J. 1994. Non-ideal interactions in calcic amphiboles and their bearing on amphibole-plagioclase thermometry. *Contributions to Mineralogy and Petrology* 116:433–447.

Hounslow A. W. and Chao G. Y. 1968. Monoclinic chlorapatite from Ontario. *The Canadian Mineralogist* 10:252–259

Howarth, G. H., Pernet-Fisher, J. F., Bodnar, R. J., and Taylor, L. A. 2015. Evidence for the exsolution of Cl-rich fluids in martian magmas: Apatite petrogenesis in the enriched lherzolitic shergottite Northwest Africa 7755. *Geochimica et Cosmochimica Acta* 166:234–248.

Hu, S., Lin, Y., Zhang, J., Hao, J., Feng, L., Xu, L., ... and Yang, J. 2014. NanoSIMS analyses of apatite and melt inclusions in the GRV 020090 Martian meteorite: Hydrogen isotope evidence for recent past underground hydrothermal activity on Mars. *Geochimica et Cosmochimica Acta* 140:321–333.

Hughes, J. M., Cameron, M., and Crowley, K. D. 1989. Structural variations in natural F, OH, and Cl apatites. *American Mineralogist* 74:870–876.

Hughes, J. M., Cameron, M., and Mariano, A. N. 1991. Rare-earth-element ordering and structural variations in natural rare-earth-bearing apatites. *American Mineralogist* 76:1165–1173.

Hughes, J. M. and Rakovan, J. 2002. The crystal structure of apatite, $Ca_5(PO_4)_3(F,OH,Cl)$. *Reviews in Mineralogy and Geochemistry* 48*:*1–12.

Irving, A. J., Kuehner, S. M., Rumble III, D., Carlson, R. W., Hupé, A. C., and Hupé, G. M. 2002. Petrology and isotopic composition of orthopyroxene-bearing nakhlite NWA 998. *Meteoritics and Planetary Science Supplement* 37:A70.

Jagoutz, E. 1991. Chronology of SNC meteorites. *Space Science Reviews* 56:13–22.

Jolliff, B. L., Haskin, L. A., Colson, R. O., and Wadhwa, M. 1993. Partitioning in REE-saturating minerals: Theory, experiment, and modelling of whitlockite, apatite, and evolution of lunar residual magmas. *Geochimica et Cosmochimica Acta* 57:4069–4094.

Jones, J. H. 1989. Isotopic relationships among the shergottites, the nakhlites and Chassigny. *Proceedings of the 19th Lunar and Planetary Science Conference.* Pp. 465–474.

Kelly, S. R., Rakovan, J., and Hughes, J. M. 2017. Column anion arrangements in chemically zoned ternary chlorapatite and fluorapatite from Kurokura, Japan. *American Mineralogist* 102:720–727.

Kent, A. J. 2008. Melt inclusions in basaltic and related volcanic rocks. *Reviews in Mineralogy and Geochemistry* 69:273–331.

Kilinc, I. A. and Burnham, C. W. 1972. Partitioning of chloride between a silicate melt and coexisting aqueous phase from 2 to 8 kilobars. *Economic Geology* 67:231–235.

Korochantseva, E. V., Schwenzer, S. P., Buikin, A. I., Hopp, J., Ott, U., and Trieloff, M. 2011. 40Ar-39Ar and cosmic-ray exposure ages of nakhlites—Nakhla, Lafayette, Governador Valadares—and Chassigny. *Meteoritics & Planetary Science* 46:1397–1417.

Kress, V. C. and Ghiorso, M. S. 2004. Thermodynamic modeling of post-entrapment crystallization in igneous phases. *Journal of Volcanology and Geothermal Research* 137:247–260.

Kullerud, K. 1996. Chlorine-rich amphiboles: interplay between amphibole composition and an evolving fluid. *European Journal of Mineralogy* 355–370.

Kusebauch, C., John, T., Whitehouse, M. J., Klemme, S., and Putnis, A. 2015. Distribution of halogens between fluid and apatite during fluid-mediated replacement processes. *Geochimica et Cosmochimica Acta* 170:225–246.

Lambert, P. 1987. SNC Meteorites: The metamorphic record. *18th Lunar and Planetary Science Conference*. Pp 529–530.

Lee, M. R., MacLaren, I., Andersson, S. M. L., Kovacs, A., Tomkinson, T., Mark, D. F., and Smith, C. L. 2015. Opal-A in the Nakhla meteorite: A tracer of ephemeral liquid water in the Amazonian crust of Mars. *Meteoritics & planetary science* 50:1362–1377.

Leger, A. 1996. Cl-rich biotite and amphibole from the Black forest, Cornwall, New York. *American Mineralogist* 81:277–289.

Lentz, R. F., Taylor, G. J., and Treiman, A. H. 1999. Formation of a martian pyroxenite: a comparative study of the nakhlite meteorites and Theo's Flow. *Meteoritics & Planetary Science* 34:919–932.

Leshin, L. A., Epstein, S., and Stolper, E. M. 1996. Hydrogen isotope geochemistry of SNC meteorites. *Geochimica et Cosmochimica Acta* 60:2635–2650.

Li, W. and Costa, F. 2020. A thermodynamic model for F-Cl-OH partitioning between silicate melts and apatite including non-ideal mixing with application to constraining melt volatile budgets. *Geochimica et Cosmochimica Acta* 269:203–222.

Li, W., Chakraborty, S., Nagashima, K., and Costa, F. 2020. Multicomponent diffusion of F, Cl and OH in apatite with application to magma ascent rates. *Earth and Planetary Science Letters* 550: 116545.

Lin, Y., Hu, S., Miao, B., Xu, L., Liu, Y., Xie, L., Feng, L., and Yang, J. 2013. Grove Mountains 020090 enriched lherzolitic shergottite: A two-stage formation model. *Meteoritics & Planetary Science 48*:1572–1589.

Liu, Y., Liu, H., Theye, T., and Massonne, H. J. 2009. Evidence for oceanic subduction at the NE Gondwana margin during Permo-Triassic times. *Terra Nova* 21:195–202.

Lombardo, B., Rolfo, F., and Compagnoni, R. 2000. Glaucophane and barroisite eclogites from the Upper Kaghan nappe: implications for the metamorphic history of the NW Himalaya. *Geological Society, London, Special Publications* 170:411–430.

Longhi, J. 1991. Complex magmatic processes on Mars-Inferences from the SNC meteorites. In *Lunar and Planetary Science Conference Proceedings* 21:695–709.

Malavergne, V., Guyot, F., Benzerara, K., and Martinez, I. 2001. Description of new shock-induced phases in the Shergotty, Zagami, Nakhla and Chassigny meteorites. *Meteoritics & Planetary Science* 36:1297–1305.

Markl, G., Ferry, J., and Bucher, K. 1998. Formation of saline brines and salt in the lower crust by hydration reactions in partially retrogressed granulites from the Lofoten Islands, Norway. *American Journal of Science* 298:705–757.

Marti, K. and Mathew, K. J. 2004. Martian mantle signatures in Yamato nakhlites. *Antarctic meteorite research 17*:117.

Martínez, M, Brearley, A. J., and Shearer, C. K. 2020. Reading the Microstructure of Apatite in the Moon and Mars to Constrain the Petrogenetic Evolution of Chassignites and Nakhlites and Assess Their Volatile Sources. *51st Lunar and Planetary Science Conference,* Abstract #1878.

Mathez, E. A. and Webster, J. D. 2005. Partitioning behavior of chlorine and fluorine in the system apatite-silicate melt-fluid. *Geochimica et Cosmochimica Acta* 69:1275–1286.

Mazdab, F. K. 2003. The diversity and occurrence of potassium-dominant amphiboles. *The Canadian Mineralogist* 41:1329–1344.

McConnell, D. 1973. Apatite: Its Crystal Chemistry, Mineralogy and Geologic and Biologic Occurrences. Springer Science & Business Media (Vol. 5).

McCormick, K. A., and McDonald, A. M. 1999. Chlorine-bearing amphiboles from the Fraser Mine, Sudbury, Ontario, Canada; description and crystal chemistry. *The Canadian Mineralogist* 37:1385–1403.

McCubbin, F. M., and Nekvasil, H. 2008. Maskelynite-hosted apatite in the Chassigny meteorite: Insights into late-stage magmatic volatile evolution in martian magmas. *American Mineralogist* 93:676–684.

McCubbin, F. M., Tosca, N. J., Smirnov, A., Nekvasil, H., Steele, A., Fries, M., and Lindsley, D. H. 2009. Hydrothermal jarosite and hematite in a pyroxene-hosted melt inclusion in martian meteorite Miller Range (MIL) 03346: Implications for magmatic-hydrothermal fluids on Mars. *Geochimica et Cosmochimica Acta* 73:4907–4917.

McCubbin, F. M., Elardo, S. M., Shearer Jr, C. K., Smirnov, A., Hauri, E. H., and Draper, D. S. 2013. A petrogenetic model for the comagmatic origin of chassignites and nakhlites: Inferences from chlorine-rich minerals, petrology, and geochemistry. *Meteoritics & Planetary Science* 48*:*819–853.

McCubbin, F. M., Vander Kaaden, K. E., Tartèse, R., Whitson, E. S., Anand, M., Franchi, I. A., Mikhail, S., Ustunisik, G., Hauri, E. H., Wang, J., and Boyce, J. W. 2014. Apatite-melt partitioning in basaltic magmas: The importance of exchange equilibria and the incompatibility of the OH component in halogen-rich apatite. *45th Lunar and Planetary Science Conference*. Abstract #2741.

McCubbin, F. M., Vander Kaaden, K. E., Tartèse, R., Boyce, J. W., Mikhail, S., Whitson, E. S., Bell, A. S., Anand, M., Franchi, I. A., Jianhua, W., and Hauri, E. H. 2015. Experimental investigation of F, Cl, and OH partitioning between apatite and Fe-

rich basaltic melt at 1.0–1.2 GPa and 950–1000 C. *American Mineralogist* 100:1790–1802.

Meurer, W. P. and Boudreau, A. E. 1996. An evaluation of models of apatite compositional variability using apatite from the Middle Banded series of the Stillwater Complex, Montana. *Contributions to Mineralogy and petrology* 125:225–236.

Mikouchi, T. and Miyamoto, M. 2002. Comparative cooling rates of nakhlites as inferred from iron-magnesium and calcium zoning of olivines. *33rd Lunar and Planetary Science Conference*. Abstract #1343.

Mikouchi, T., Koizumi, E., Monkawa, A., Ueda, Y., and Miyamoto, M. 2003. Mineralogical comparison of Y000593 with other nakhlites: implications for relative burial depths of nakhlites. *34th Lunar and Planetary Science Conference*. Abstract #1883.

Mikouchi, T., Miyamoto, M., Koizumi, E., Makishima, J., and McKay, G. 2006. Relative burial depths of nakhlites: an update. *37th Lunar and Planetary Science Conference.* Abstract #1865.

Mikouchi, T., Makishima, J., Kurihara, T., Hoffmann, V. H., and Miyamoto, M. 2012. Relative burial depth of nakhlites revisited. *43rd Lunar and Planetary Science Conference.* Abstract #2363

Morrison, J. 1991. Compositional constraints on the incorporation of Cl into amphiboles. *American Mineralogist* 76:1920–1930.

Murty, S. V. S., Mahajan, R. R., Goswami, J. N., and Sinha, N. 2005. Noble gases and nuclear tracks in the nakhlite MIL 03346. *36th Annual Lunar and Planetary Science Conference*. Abstract #1280.

Muttik, N., McCubbin, F. M., Keller, L. P., Santos, A. R., McCutcheon, W. A., Provencio, P. P., Rahman, Z., Shearer, C. K., Boyce, J. W., and Agee, C. B. 2014. Inventory of H_2O in the ancient Martian regolith from Northwest Africa 7034: The important role of Fe oxides. *Geophysical Research Letters* 41:8235–8244.

Newsom, H. E. 1980. Hydrothermal alteration of impact melt sheets with implications for Mars. *Icarus* 44:207–216.

Nielsen, R. L., Michael, P. J., and Sours-Page, R. 1998. Chemical and physical indicators of compromised melt inclusions. *Geochimica et Cosmochimica Acta* 62:831–839.

Nishiizumi K., Hillegonds D. J., McHargue L. R., and Jull A. J. T. 2004. Exposure and terrestrial histories of new lunar and Martian meteorites. *35th Lunar and Planetary Science Conference*. Abstract #1130.

Nyquist, L. E., Bogard, D. D., Shih, C. Y., Greshake, A., Stöffler, D., and Eugster, O. 2001. Ages and geologic histories of Martian meteorites. In *Chronology and evolution of Mars*. Springer, Dordrecht. Pp. 105–164.

Ott, U. 1988. Noble gases in SNC meteorites: Shergotty, Nakhla, Chassigny. *Geochimica et Cosmochimica Acta* 52:1937–1948.

Park, J., Garrison, D. H., and Bogard, D. D. 2009. ^{39}Ar–^{40}Ar ages of martian nakhlites. *Geochimica et Cosmochimica Acta* 73:2177–2189.

Piccoli, P. M. and Candela, P. A. 2002. Apatite in igneous systems. *Reviews in Mineralogy and Geochemistry* 48:255–292.

Pittarello, L., Ferrière, L., Feignon, J. G., Osinski, G. R., and Koeberl, C. 2020. Preferred orientation distribution of shock-induced planar microstructures in quartz and feldspar. *Meteoritics & Planetary Science* 55:1082–1092.

Pollok, K., Putnis, C. V., and Putnis, A. 2011. Mineral replacement reactions in solid solution-aqueous solution systems: Volume changes, reactions paths and end-points using the example of model salt systems. *American Journal of Science* 311:211–236.

Putnis, A. and Putnis, C. V. 2007. The mechanism of reequilibration of solids in the presence of a fluid phase. *Journal of Solid State Chemistry* 180:1783–1786

Raufaste, C., Jamtveit, B., John, T., Meakin, P., and Dysthe, D. K. 2011. The mechanism of porosity formation during solvent-mediated phase transformations. *Proceedings of the Royal Society A: Mathematical, Physical and Engineering Sciences* 467:1408–1426.

Robinson, P., Doolan, B. L., and Schumacher, J. C. 1982. Phase relations of metamorphic amphiboles; natural occurrence and theory; general review of metamorphic amphibole compositions; composition space of metamorphic amphiboles and its population. *Reviews in Mineralogy and Geochemistry 9*:22–43.

Roedder, E. 1984. Fluid inclusions. In *Reviews in Mineralogy*, edited by Paul H. Ribbe. Vol. 12. Mineralogical Society of America. Pp. 47–48.

Russell, S. S., Zipfel, J., Folco, L., Jones, R., Grady, M. M., McCoy, T., and Grossman, J. N. 2003. The Meteoritical Bulletin, No. 87, 2003 July. *Meteoritics & Planetary Science* 38:A189–A248.

Sautter, V., Jambon, A., and Boudouma, O. 2006. Cl-amphibole in the nakhlite MIL 03346: Evidence for sediment contamination in a Martian meteorite. *Earth and Planetary Science Letters 252*:45–55.

Sautter, V., Toplis, M. J., Lorand, J. P., and Macri, M. 2012. Melt inclusions in augite from the nakhlite meteorites: A reassessment of nakhlite parental melt and implications for petrogenesis. *Meteoritics & Planetary Science* 47:330–344.

Schiano, P. and Bourdon, B. 1999. On the preservation of mantle information in ultramafic nodules: glass inclusions within minerals versus interstitial glasses. *Earth and Planetary Science Letters* 169:173–188.

Sharp, Z., Williams, J., Shearer, C., Agee, C., and McKeegan, K. 2016. The chlorine isotope composition of Martian meteorites 2. Implications for the early solar system and the formation of Mars. *Meteoritics & Planetary Science* 51:2111–2126.

Shearer, C. K., Messenger, S., Sharp, Z. D., Burger, P. V., Nguyen, N., and McCubbin, F. M. 2017. Distinct chlorine isotopic reservoirs on Mars: Implications for character, extent and relative timing of crustal interaction with mantle-derived magmas, evolution of the Martian atmosphere, and the building blocks of an early Mars. *48th Lunar and Planetary Science Conference*. Abstract #1546.

Shearer, C. K., Messenger, S., Sharp, Z. D., Burger, P. V., Nguyen, A. N., and McCubbin, F. M. 2018. Distinct chlorine isotopic reservoirs on Mars. Implications for character, extent and relative timing of crustal interactions with mantle-derived magmas, evolution of the martian atmosphere, and the building blocks of an early Mars. *Geochimica et Cosmochimica Acta* 234:24–36.

Shih, C. Y., Nyquist, L. E., Reese, Y., and Wiesmann, H. 1998. The chronology of the nakhlite, Lafayette: Rb-Sr and Sm-Nd isotopic ages. *29th Lunar and Planetary Science Conference*. Abstract #1145.

Słaby, E., Förster, H. J., Wirth, R., Giera, A., Birski, Ł., and Moszumańska, I. 2017. Validity of the apatite/merrillite relationship in evaluating the water content in the Martian mantle: Implications from shergottite Northwest Africa (NWA) 2975. *Geosciences* 7:99.

Sobolev, A. V. 1996. Melt inclusions in minerals as a source of principle petrological information. *Petrology* 4:209–220.

Sobolev, V. S. and Kostyuk, V. P. 1975. Magmatic crystallization based on a study of melt inclusions. *Fluid Inclusion Research* 9:182–253.

Spandler, C., O'Neill, H. S. C., and Kamenetsky, V. S. 2007. Survival times of anomalous melt inclusions from element diffusion in olivine and chromite. *Nature* 447:303–306.

Stöffler, D., Deutsch, A., Avermann, M., Bischoff, L., Brockmeyer, P., Buhl, D., ... and Miiller-Mohr, V. 1994. The formation of the Sudbury Structure, Canada: Toward a unified impact model. In *Large meteorite impacts and planetary evolution*, edited by B. O. Dressler, R.A.F. Grieve, and V. L. Sharpton. Vol. 293. Pp. 303.

Stockstill, K. R., McSween Jr, H. Y., and Bodnar, R. J. 2005. Melt inclusions in augite of the Nakhla Martian meteorite: Evidence for basaltic parental melt. *Meteoritics & Planetary Science 40*:377–396.

Stormer, J. C. and Carmichael, I. S. E. 1971. Fluorine-hydroxyl exchange in apatite and biotite: A potential igneous geothermometer. *Contributions to Mineralogy and Petrology* 31:121–131.

Stormer, J. C., Pierson, M. L., and Tacker, R. C. 1993. Variation of F and Cl X-ray intensity due to anisotropic diffusion in apatite during electron microprobe analysis. *American Mineralogist 78*:641–648.

Sudarsanan, K. T. and Young, R. A. 1969. Significant precision in crystal structural details. Holly Springs hydroxyapatite. *Acta Crystallographica Section B: Structural Crystallography and Crystal Chemistry* 25:1534–1543.

Suwa, K., Enami, M., Hiraiwa, I., and Yang, T. M. 1987. Zn-Mn ilmenite in the Kuiqi Granite from Fuzhou, Fujian Province, East China. *Mineralogy and Petrology* 36:111–120.

Swindle, T. D., Treiman, A. H., Lindstrom, D. J., Burkland, M. K., Cohen, B. A., Grier, J. A., Li, B., and Olson, E. K. 2000. Noble gases in iddingsite from the Lafayette meteorite: Evidence for liquid water on Mars in the last few hundred million years. *Meteoritics & Planetary Science* 35:107-115.

Swindle, T. D. 2002. Martian noble gases. *Reviews in Mineralogy and Geochemistry* 47:171–190.

Tait, S. 1992. Selective preservation of melt inclusions in igneous phenocrysts. *American Mineralogist* 77:146–155.

Taylor, G. J. 2013. The bulk composition of Mars. *Geochemistry* 73:401–420.

Teiber, H., Marks, M. A., Wenzel, T., Siebel, W., Altherr, R., and Markl, G. 2014. The distribution of halogens (F, Cl, Br) in granitoid rocks. *Chemical Geology* 374:92–109.

Treiman, A. H. 2005. The nakhlite meteorites: Augite-rich igneous rocks from Mars. *Geochemistry* 65:203–270.

Treiman, A. H. and Goodrich, C. A. 2001. A parent magma for the Nakhla martian meteorite: reconciliation of estimates from 1-bar experiments, magmatic inclusions in olivine, and magmatic inclusions in augite. *32nd Lunar and Planetary Science Conference*. Abstract #1107.

Treiman, A. H., Dyar, M. D., McCanta, M., Noble, S. K., and Pieters, C. M. 2007. Martian Dunite NWA 2737: Petrographic constraints on geological history, shock events, and olivine color. *Journal of Geophysical Research: Planets* 112(E4).

Treiman, A. H. and Irving, A. J. 2008. Petrology of martian meteorite Northwest Africa 998. *Meteoritics & Planetary Science* 43:829–854.

Ungaretti, L., Smith, D., and Rossi, G. 1981. Crystal-chemistry by X-ray structure refinement and electron microprobe analysis of a series of sodic-calcic to alkali-amphiboles from the Nybö eclogite pod, Norway. *Bulletin de Minéralogie* 104:400–412.

Ustunisik, G., Nekvasil, H., and Lindsley, D. 2011. Differential degassing of H_2O, Cl, F, and S: Potential effects on lunar apatite. *American Mineralogist* 96:1650–1653.

Usui, T., Alexander, C. M. D., Wang, J., Simon, J. I., and Jones, J. H. 2012. Origin of water and mantle–crust interactions on Mars inferred from hydrogen isotopes and volatile element abundances of olivine-hosted melt inclusions of primitive shergottites. *Earth and Planetary Science Letters* 357:119–129.

Varela, M. E., Kurat, G., and Clocchiatti, R. 2001. Glass-bearing inclusions in Nakhla (SNC meteorite) augite: heterogeneously trapped phases. *Mineralogy and Petrology* 71:155–172.

Volfinger, M., Robert, J. L., Vielzeuf, D., and Neiva, A. M. R. 1985. Structural control of the chlorine content of OH-bearing silicates (micas and amphiboles). *Geochimica et Cosmochimica Acta 49*:37–48.

Wadhwa, M. and Crozaz, G. 1992. REE in minerals in Nakhla and Lafayette: A comparative study of trace element microdistributions. *23rd Lunar and Planetary Science Conference*. Pp. 1483–1484.

Wadhwa, M. and Crozaz, G. 1995. Trace and minor elements in minerals of nakhlites and Chassigny: Clues to their petrogenesis. *Geochimica et Cosmochimica Acta* 59:3629–3645.

Wadhwa, M. and Crozaz, G. 2003. Trace element geochemistry of new nakhlites from the Antarctic and the Saharan Desert: further constraints on nakhlite petrogenesis on Mars. *34th Lunar and Planetary Science Conference*. Abstract #2075.

Wänke, H., and Dreibus, G. 1988. Chemical composition and accretion history of terrestrial planets. *Philosophical Transactions of the Royal Society London A* 325(1587):545–557.

Wänke, H. 1991. Chemistry, accretion, and evolution of Mars. *Space Science Reviews* 56:1–8.

Webster, J. D. and De Vivo, B. 2002. Experimental and modeled solubilities of chlorine in aluminosilicate melts, consequences of magma evolution, and implications for exsolution of hydrous chloride melt at Mt. Somma-Vesuvius. *American Mineralogist* 87:1046–1061.

Webster, J. D. and Piccoli, P. M. 2015. Magmatic apatite: A powerful, yet deceptive, mineral. *Elements* 11:177–182.

White, T., Ferraris, C., Kim, J., and Madhavi, S. 2005. Apatite–an adaptive framework structure. *Reviews in Mineralogy and Geochemistry* 57:307–401.

Williams, J. T., Shearer, C. K., Sharp, Z. D., Burger, P. V., McCubbin, F. M., Santos, A. R., Agee, C. B., and McKeegan, K. D. 2016. The chlorine isotopic composition of Martian meteorites 1: Chlorine isotope composition of Martian mantle and crustal reservoirs and their interactions. *Meteoritics & Planetary Science* 51:2092–2110.

Xiao, Y., Hoefs, J., and Kronz, A. 2005. Compositionally zoned Cl-rich amphiboles from North Dabie Shan, China: Monitor of high-pressure metamorphic fluid/rock interaction processes. *Lithos* 81:279–295.

Yanagisawa, K., Rendon-Angeles, J. C., Ishizawa, N., and Oishi, S. 1999. Topotaxial replacement of chlorapatite by hydroxyapatite during hydrothermal ion exchange. *American Mineralogist* 84:1861–1869.

Young, R. A. 1980. Large effects from small structural differences in apatites. In *Proceedings of the International Congress of Phosphorous Compounds*. Pp. 73-88.

Zhang, C., Holtz, F., Ma, C., Wolff, P. E., and Li, X. 2012. Tracing the evolution and distribution of F and Cl in plutonic systems from volatile-bearing minerals: a case study from the Liujiawa pluton (Dabie orogen, China). *Contributions to Mineralogy and Petrology* 164:859–879.

Zhu, C. and Sverjensky, D. A. 1991. Partitioning of F-Cl-OH between minerals and hydrothermal fluids. *Geochimica et Cosmochimica Acta* 55:1837–1858.

Zhu, C., Xu, H., Ilton, E. S., Veblen, D. R., Henry, D. J., Tivey, M. K., and Thompson, G. 1994. TEM-AEM observations of Cl-rich amphibole and biotite and possible petrologic implications. *American Mineralogist* 79:909–920.

CHAPTER 4

High pressure phase transformations in a shock melt vein in Villalbeto de la Peña L6 ordinary chondrite: Insights into the shock behavior of diopside and estimation of the peak shock conditions

In collaboration with:
Adrian J. Brearley
Josep Ma. Trigo-Rodríguez
Jordi Llorca

Citation:
Martínez, M., Brearley, A. J., Trigo-Rodríguez, J. M., and Llorca, J. (2019) New observations on high-pressure phases in a shock melt vein in the Villalbeto de la Peña meteorite: Insights into the shock behavior of diopside. *Meteoritics & Planetary Science*, **54**, 2845–2863.

Abstract

The petrology and mineralogy of shock melt veins in a highly shocked L6 ordinary chondrite fall, Villalbeto de la Peña, have been investigated in detail using Scanning Electron Microscopy, Transmission Electron Microscopy, Raman Spectroscopy, and Electron Probe Microanalysis. Entrained olivine, enstatite, diopside, and plagioclase are transformed into ringwoodite, low-Ca majorite, high-Ca majorite, and an assemblage of jadeite-lingunite, respectively, in several shock melt veins and pockets. We have focused on the shock behavior of diopside in a particularly large shock melt vein (up to 10 mm long and up to 4 mm wide) in order to provide additional insights into its high-pressure polymorphic phase transformation mechanisms. We report the first evidence of diopside undergoing shock-induced melting, and the second reported occurrence of natural tetragonal majorite formed by solid-state transformation from

diopside. Magnesiowüstite has also been found as veins injected into diopside in the form of nanocrystalline grains that crystallized from a melt and also occurs interstitially between majorite-pyrope grains in the melt-vein matrix. In addition, we have observed compositional zoning in majorite-pyrope grains in the matrix of the shock-melt vein, which has not been described previously in any shocked meteorite. Collectively, all these different lines of evidence are suggestive of a major shock event with high cooling rates. The minimum peak-shock conditions are estimated to have been between 16 to 24 GPa and 2000-2200 ºC, although higher pressure and temperature conditions are also possible.

1. Introduction

Many ordinary chondrites record hypervelocity impacts in asteroidal settings that triggered the occurrence of high-pressure phase transformations (Chen et al., 1996; Sharp et al., 1997; Sharp and DeCarli, 2006; Tomioka and Kimura, 2003; Ohtani et al., 2004; Zhang et al., 2006; Miyahara et al., 2008, 2011; Ozawa et al., 2009; Feng et al., 2011). During these dynamic events, the major mineralogical constituents of ordinary chondrites –olivine, pyroxene, and plagioclase–, undergo a variety of phase transformations that provide insights into high-pressure polymorphic phase transformations, as well as the conditions of shock melt vein formation during asteroidal impacts. These samples provide a unique opportunity to study natural high-pressure phases that are stable in the mantle of the Earth, but are inaccessible for study. For example, several important, natural high-pressure phases have been discovered recently in meteorites, such as bridgmanite (Tschauner et al., 2014), tissintite (Ma et al., 2015), and tetragonal majorite (Tomioka et al. 2016).

The high pressure polymorphs of **olivine** - wadsleyite (β-$(Fe,Mg)Si_2O_4$) and ringwoodite (γ-$(Fe,Mg)Si_2O_4$) -, **pyroxene** - majorite ($MgSiO_3$-garnet) + $CaSiO_3$-perovskite, akimotoite ($MgSiO_3$-ilmenite) + $CaSiO_3$-perovskite, tetragonal majorite + $CaSiO_3$-perovskite, and bridgmanite ($MgSiO_3$-perovskite) + $CaSiO_3$-perovskite -, and **plagioclase** - jadeite ($NaAlSi_2O_6$) or tissintite ($CaAlSi_2O_6$) + silica phase, lingunite ($NaAlSi_2O_8$-hollandite), and $NaAlSiO_4$ (calcium ferrite-type), have been extensively studied in shocked meteorites and in high pressure experimental studies. Hydrostatic, multi-anvil experiments are most commonly used to understand the high-pressure phase equilibria of these polymorphs and their melting relationships (e.g., Agee et al., 1995; Chen et al., 1996; Ohtani et al., 2004; Xie et al., 2006; Akaogi et al., 2010). Asteroidal impacts, however, generate natural conditions of high pressures that last from tens of milliseconds to a few seconds (Sharp and DeCarli, 2006; Gillet et al., 2007), resulting in conditions which may deviate substantially from equilibrium. Therefore, while experiments on the scale of one to several seconds can be reproduced in the laboratory, for extremely fast shock events, some uncertainties still exist.

Even though diopside is found widely in ordinary chondrites (Brearley and Jones, 1998), its abundance is comparatively low and very few occurrences of its high-pressure polymorph Ca-rich majorite have been reported in the literature. Calcium-rich majorite was first reported in the Shergotty Martian meteorite (Malavergne et al., 2001). It has an augitic composition ($En_{46}Fs_{29}Wo_{25}$) and formed by solid-state transformation. Subsequently, Ca-rich majorite has been found in just two ordinary chondrites: Yamato 75100 (H6) (Tomioka and Kimura, 2003), and Tenham (L6) (Xie and Sharp, 2007). In Yamato 75100, the Ca-rich majorite is formed by a dissociation reaction of diopside by a

solid-state mechanism. Tomioka and Kimura (2003) found that the majorite has a different composition from the precursor diopside and hence, they suggested that formation by crystallization from a melt, rather than by solid-state transformation, should also be considered. However, they ruled out this possibility, because the majorite has low Al and Fe contents, despite being in contact with melted plagioclase. The Ca-rich majorite ($En_{65}Fs_9Wo_{26}$) in Yamato 75100 has a granular texture and is associated with a Ca-rich glass ($En_{23}Fs_5Wo_{72}$), whereas in Tenham, Ca-rich majorite ($En_{64}Fs_{10}Wo_{27}$) occurs as a nanometer symplectic intergrowth with amorphous Ca-poor glass (Xie and Sharp, 2007). Electron diffraction data for the Ca-rich majorite are consistent with tetragonal rather than cubic symmetry, but with larger unit cell parameters than Mg-rich majorite, which Xie and Sharp (2007) attributed to the expansion of the unit cell due to the high Ca content.

Chopelas and Serghiou (2002) found that the room temperature Raman spectrum of diopside at 20.2 GPa was nearly identical to that at 1 atm, demonstrating that the transformation of diopside into Ca-rich majorite is strongly temperature dependent, consistent with diopside phase transitions reported by Akaogi et al. (2004). For the Yamato 751000 H6 ordinary chondrite, Tomioka and Kimura (2003) estimated a solidus P-T for the shock melt vein of 18-24 GPa at 1100-1900ºC. In the Sixiangkou L5 ordinary chondrite, diopside in the melt vein did not undergo a phase transformation, but coexists with ringwoodite. This association constrains the stability field of diopside under high P-T conditions and suggests that either the local P-T conditions did not exceed the stability field of diopside, or the rate of phase transformation of diopside is very low and the shock duration was too short to induce the transformation (Zhang et al., 2006). The current

available constraints indicate a shock pressure of 20 GPa, low temperatures (less than ~1500 °C), and a peak shock duration less than several seconds (previously suggested by Chen et al., 2002, 2004, 2006) in order to prevent transformation into Ca-rich majorite. However, Zhang et al. (2006) also suggested that the preservation of diopside during large shock events of several seconds to minutes of duration implies that the transformation rates of diopside have to be very sluggish. These observations demonstrate that there is still significant uncertainty in the high P-T transformation behavior of diopside in shocked ordinary chondrites.

In the present work, we have studied in detail the transformation behavior of diopside as a result of high-pressure shock metamorphism in the Villalbeto de la Peña (hereafter, VP) meteorite, an L6 ordinary chondrite that fell in Spain in 2004 (Llorca et al., 2005). Villalbeto de la Peña is currently classified as a moderately shocked (S4) chondrite with petrologic type L6 (Llorca et al., 2005). This paper focuses on an unusually large shock melt vein (hereafter, SMV) with entrained host rock fragments. The goals of this study are to (i) more fully understand the high-pressure transformation behavior of diopside in the SMV and ii) constrain the peak shock conditions experienced by VP.

2. Analytical methods

A rectangular polished thin section of VP, 37 mm wide and 18 mm long on its maximum dimensions, was used in this study and is in the possession of the Meteorite Collection at the Institute of Space Sciences (ICE-CSIC) in Barcelona (Catalonia). The textural, mineralogical, and petrological characteristics of the VP meteorite were characterized using a variety of different analytical techniques described below.

Petrographic characterization of the sample was performed on the polished thin section by optical microscopy using transmitted and reflected light. A mosaic of the thin section was acquired using a ZEISS Scope petrographic microscope in order to locate the targeted regions correctly and also to provide the petrologic context of regions of interest within the sample. For scanning electron microscopy (SEM), we used a FEI Quanta 650 field emission gun SEM with a backscattered electron detector (BSED) at the *Institut Català de Nanociència i Nanotecnologia* (ICN2). X-ray spectra and X-ray maps were acquired on a FEI Quanta 3D FEG-SEM/FIB using an EDAX Genesis EDS system equipped with an Apollo 40 SDD 40 mm^2 EDS detector at the University of New Mexico. The thin section was carbon coated prior to SEM imaging and X-ray mapping and was analyzed under high-vacuum conditions. Semiquantitative EDS analyses obtained on the FEI Quanta 650 at ICN2 were used for mineral identification. The standards used for EDS analyses were as follows: calcite ($CaCO_3$) for C; silica (SiO_2) for O and Si; albite ($NaAlSi_3O_8$) for Na; MgO for Mg; Al_2O_3 for Al; FeS_2 for S; wollastonite ($CaSiO_3$) for Ca; Mn metal for Mn; and Fe metal for Fe.

A total of four FIB sections were prepared from different Ca-rich high-pressure phases using a FEI Quanta 3D Dualbeam® FEG-SEM/FIB instrument in the Department of Earth and Planetary Sciences, University of New Mexico. Platinum strips, ~2 μm-wide, ~2.5 μm-thick, and up to 20 μm in length, were first deposited across each area of interest to protect the TEM sections from ion beam damage during sample preparation. The sections were extracted from the thin section by the *in-situ* lift-out technique using an Omniprobe 200 micromanipulator and were attached to copper (Cu) Omniprobe TEM

half grids. Ion milling to electron transparency was carried out at an accelerating voltage of 30 kV and a beam current gradually decreasing from 0.5 nA to 50 pA.

Detailed characterization of the microstructures and mineralogy of the FIB sections were conducted using a JEOL 2010F FASTEM FEG scanning transmission electron microscope (STEM), operated at 200 kV. The FIB sections were studied using high-resolution TEM (HR-TEM), high-angle annular dark-field (HAADF) scanning TEM (STEM), and electron diffraction. Digital TEM images were acquired and processed using GATAN Microscopy Suite® (GMS) imaging software. In addition, full spectral X-ray maps were collected in STEM mode using the JEOL 2010F, and quantitative X-ray microanalyses were obtained using an Oxford AZTec X-ray analysis system with a X-Max 80N 80 mm^2 SDD energy dispersive X-ray spectrometer (EDS) detector system. Quantification of EDS spectra was carried out using the Cliff-Lorimer thin film approximation using theoretical k-factors.

Raman spectroscopy provides information about the chemical bonds in solids and, therefore, allows the identification of high-pressure polymorphs (Sharp and deCarli, 2006; Fritz and Greshake, 2009, and references therein). Raman spectra were recorded in backscattering geometry at room temperature, using the 514.5 nm line of an argon-ion laser with a Jobin-Yvon T-64000 Raman spectrometer attached to an Olympus microscope, and equipped with a liquid nitrogen-cooled CCD detector at ICMAB (Barcelona). The instrument has high lateral spatial resolution of about ~ 1μm. To avoid degradation due to heating, the laser power on the sample was kept between 0.6-0.7 mW. The Raman spectrometer provided high resolution spectra in working windows between 100 and 1400 cm^{-1}. The identification of mineral compounds was performed using the

database from the *Handbook of Minerals Raman Spectra* (ENS-Lyon, France) and from The RRUFF Project (Lafuente et al., 2015).

Chemical compositions of minerals were determined using a JEOL JXA-8230 electron microprobe at the Scientific and Technological Center of the University of Barcelona. Quantitative wavelength dispersive X-ray spectrometry (WDS) analyses were conducted using a 20 kV accelerating voltage and 15 nA beam current with a focused electron beam of 1 μm diameter for all phases except for plagioclase, where a 3 to 5 μm beam was used to minimize alkali loss. Wollastonite (SiO_2, CaO), corundum (Al_2O_3), rutile (TiO_2), Cr_2O_3 (Cr_2O_3), albite (Na_2O), periclase (MgO), rhodonite (MnO), Fe_2O_3 (FeO), Co (CoO), Ni (NiO), orthoclase (K_2O), FeS_2 (S), and apatite (P_2O_5) were used as standards. Full ZAF corrections were applied to the data to obtained quantitative analyses.

3. Results

3.1. Petrographic description

Villalbeto de la Peña is currently classified as a L6 ordinary chondrite with shock stage S4 (Llorca et al., 2005). The major constituents of VP in the less-shocked host rock are olivine (Fo_{75}), enstatite ($En_{77}Fs_{22}Wo_1$), diopside ($En_{47}Fs_8Wo_{45}$), plagioclase completely transformed to maskelynite ($Ab_{79}An_{15}Or_6$), metallic iron-nickel, and troilite. Representative mineral analyses are reported in Table 4.1. Minor phases include chromite and phosphates such as chlorapatite and merrillite. Hence, our results are in agreement with Llorca et al. (2005) for olivine and low-Ca pyroxene, but not for maskelynite since we found a higher albite content ($Ab_{69.2}$ vs. $Ab_{79.3}$, Table 4.1). Llorca et al. (2007) assumed that plagioclase was present in the host rock and explained the lack of its Raman

bands in their results by the effect of strong fluorescence at 400-520 cm^{-1} that possibly obscured the most intense feldspar Raman bands at about 500 cm^{-1}. However, in this study, we did not find any residual plagioclase in VP; all the plagioclase we observed has been transformed to maskelynite.

In the studied thin section, most chondrules in the host rock are poorly defined, but some chondrules with barred olivine and porphyritic textures can still be distinguished. Hence, the overall sample has a highly recrystallized texture characteristic of a type 6 chondrite (Llorca et al., 2005). There are two large SMVs and several minor SMVs and melt-pockets within the thin section. The main SMV has an elongated triangular shape (10 mm long x 4 mm wide), it is located at one side of the thin section, and crosscuts the meteorite (Fig. 4.1a). This SMV contains several high-pressure phases that are the result of transformation of entrained clasts in the SMV, such as Ca-poor majorite, Ca-rich majorite, jadeite–lingunite, and ringwoodite (Fig. 4.1b). On the opposite side of the thin section, there is a complex network of veins with different widths that meanders throughout a large area of the host rock and is associated with several minor shock melt pockets. An example of a thin vein, ~5μm size in width, from this SMV network is shown in Figure 4.2a, and consists predominantly of glass with metal-sulfide droplets, associated with rapid quench. At the contact with the shock melt veins and pockets, the host rock shows a pronounced brown staining (Fig. 4.1b), inferred to correspond to recrystallization (Stöffler et al., 1991). Olivine and pyroxene grains contain pervasive mosaicism, and some pyroxenes have a homogeneous distribution of small sulfide inclusions (~1-3 μm). Maskelynite in the host rock is abundant and consistently has a smooth texture without fractures. However, many of maskelynite grains contain

small inclusions (~1μm-size) of metal-troilite, or euhedral chromite with troilite. The chromite grains often show a distinct crystallographic orientation suggesting they may have exsolved from the precursor plagioclase prior to shock transformation to maskelynite. The texture is similar to that described in a plagioclase-chromite inclusion from the Los Martinez L6 chondrite (Brearley et al., 1991).

The large SMV that we have analyzed has a pronounced flow texture defined by the alignment of elongated clasts consisting of high-pressure minerals entrained within the SMV and of metal-troilite blebs in the matrix of the SMV that occur in bands (Figs. 4.1, 4.2b). The SMV consists of two distinct types of domains with distinct textural and mineralogical characteristics that are intermingled parageneses. The first type mostly consists of abundant, large (~50-600 μm), rounded, fractured, and unfractured host rock fragments entrained in the melt vein, crosscut by several fractures (Fig. 4.1b). The second type is a fine-grained melt matrix of idiomorphic majorite-pyrope crystals with eutectic-like metal-troilite grains with interstitial magnesiowüstite in the wider regions (Fig. 4.2c). The two types of domains are distributed randomly within the SMV along the length of the vein. Large chromite grains (~120 μm in size) with exsolution textures are also present within the SMV (Fig. 4.2d).

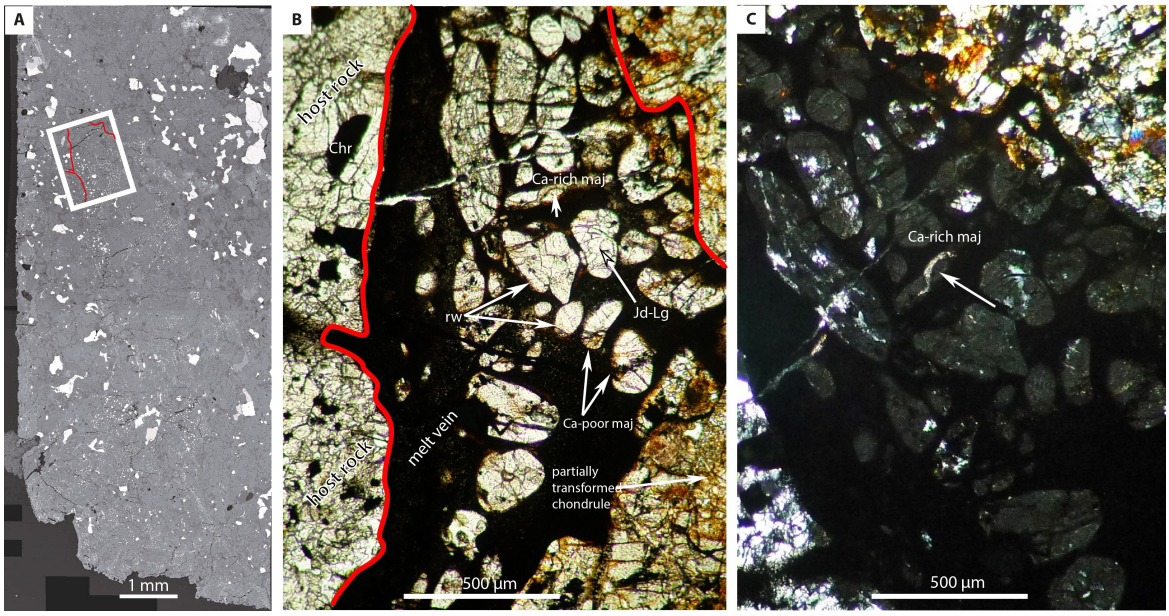

Figure 4.1. Scanning electron microscopy and optical light microscopy mosaics of the studied shock melt vein in Villalbeto de la Peña meteorite. a) Backscattered electron (BSE) mosaic of the studied shock melt vein; b) and c) Transmitted and plane-polarized light images, respectively, of the upper and thinner part of the main SMV in VP where entrained fragments are aligned and completely transformed to their high-pressure polymorphs. Legend: Ca-rich maj = Ca-rich majorite; rw = ringwoodite; Jd-Lg = jadeite-lingunite; Ca-poor maj = Ca-poor majorite; Chr = chromite. The red line delineates the boundary between the host rock with the SMV.

Table 4.1. Electron microprobe analyses of the minerals in the Villalbeto de la Peña host rock, their high-pressure polymorphs in the SMV, and in the chromite-maskelynite intergrowth. Mean L chondrite chromite values from Bunch et al. (1967). HR = host rock; SMV = shock melt vein; Maj= majorite; Jad-ling = jadeite-lingunite assemblage; n= numbers of analyses; av = average compositions of the minerals; σ = standard deviation, n.d. = not detected; #all iron is assumed as ferrous.

	Olivine (HR)		Ringwoodite (HR)		Enstatite (HR)		Ca-poor maj (SMV)		Ca-rich maj (SMV)		Masklynite (HR)		Jad-ling (SMV)		Maj-pyrope (SMV)		Maskelynite (intergrowth)		Merrillite (intergrowth)		Chromite (intergrowth)		Chromite (mean L-chondrite)
n	15		9		11		3		4		4		8		3		3		3		3		
Chemical composition (oxides wt%)																							
	av	σ	av	σ	av	σ	av	σ	av	σ	av	σ	av	σ	av	Σ	av	σ	av	σ	av	σ	av
SiO_2	37.64	0.31	37.55	0.32	54.67	0.55	54.33	0.10	53.22	0.38	65.52	0.36	65.98	0.89	49.04	0.39	65.29	0.40	0.10	0.06	0.05	0.03	n.d.
P_2O_5	0.03	0.03	0.03	0.02	0.01	0.02	0.02	0.02	0.01	0.01	0.02	0.02	0.05	0.03	0.09	0.02	0.01	0.01	43.62	1.79	0.02	0.01	n.d.
TiO_2	0.01	0.01	0.05	0.01	0.18	0.02	0.20	0.03	0.46	0.03	0.07	0.02	0.04	0.03	0.13	0.03	0.04	0.01	0.02	0.02	3.06	0.02	2.81
Al_2O_3	0.01	0.02	0.03	0.06	0.15	0.02	0.15	0.01	0.47	0.02	22.24	0.44	23.04	0.81	2.83	0.34	22.1	0.40	0.03	0.02	5.13	0.08	5.3
Cr_2O_3	0.01	0.02	0.01	0.02	0.10	0.03	0.09	0.02	0.88	0.12	0.00	0.00	0.01	0.02	1.54	0.82	0.25	0.08	0.40	0.07	56.29	0.29	56.1
FeO#	23.02	0.39	23.38	0.62	14.24	0.68	13.95	0.07	5.20	0.14	0.25	0.11	0.39	0.08	11.74	0.87	0.19	0.04	0.50	0.20	30.18	0.07	33
MnO	0.47	0.02	0.36	0.10	0.51	0.02	0.51	0.04	0.26	0.04	0.02	0.03	0.22	0.24	0.47	0.05	n.d.	0.00	0.01	0.01	0.53	0.05	0.74
SO_3	0.01	0.01	0.01	0.01	0.01	0.01	0.02	0.02	0.01	0.01	0.01	0.01	0.00	0.1	0.06	0.04	0.01	0.01	0.02	0.02	0.00	0.00	n.d.
MgO	38.08	0.39	37.73	0.44	28.70	0.01	28.83	0.07	16.50	0.17	0.01	0.01	0.09	0.17	28.14	1.59	0.01	0.01	2.41	2.09	2.97	0.06	1.99
CaO	0.03	0.03	0.06	0.08	0.73	0.13	0.87	0.05	21.63	0.38	2.23	0.01	2.54	0.47	1.92	0.28	2.07	0.07	45.97	5.98	0.05	0.04	n.d.
Na_2O	0.04	0.04	0.05	0.05	0.05	0.06	0.06	0..07	0.59	0.04	6.76	0.42	7.41	1.06	0.64	0.11	6.51	0.18	2.06	1.47	0.01	0.01	n.d.
K_2O	0.00	0.00	0.01	0.00	0.01	0.00	0.01	0.00	0.01	0.01	0.81	0.14	0.59	0.14	0.01	0.00	0.86	0.02	0.06	0.03	0.01	0.01	n.d.
Total	99.35		99.28		99.36		99.04		99.22		97.94		100.37		96.62		97.33		95.19		98.31		
Cation formula																							
Si	0.99		0.99		1.98		1.97		1.97		2.90		2.87				2.91		0.04				
P	n.d.		n.d.		n.d.		n.d.		n.d.		n.d.		n.d.				n.d.		18.87				
Ti	n.d.		n.d.		0.01		0.01		0.01		0.00		0.00				n.d.		0.01				
Al	n.d.		n.d.		0.01		0.01		0.02		1.16		1.18				1.16		0.01				
Cr	n.d.		n.d.		0.01		0.00		0.03		0.00		0.00				0.01		0.12				
Fe	0.51		0.52		0.43		0.42		0.16		0.01		0.01				0.01		0.16				
Mn	0.01		0.01		0.02		0.02		0.01		0.00		0.01				n.d.		n.d.				
Mg	1.50		1.49		1.55		1.56		0.91		0.00		0.01				n.d.		1.35				
Ca	n.d.		n.d.		0.03		0.03		0.86		0.11		0.12				0.10		18.50				
Na	n.d.		n.d.		0.00		0.00		0.04		0.58		0.63				0.56		1.50				
K	n.d.		n.d.		0.00		0.00		0.00		0.05		0.03				0.05		0.03				
Total	3.01		3.01		4.02		4.02		4.01		4.82		4.86				4.81		21.72				
O	4		4		6		6		6		8		8				8		28				
Molecular proportions																							
	Fo75		Fo74		En77		En77		En47		Ab79		Ab81				Ab79						
	Fa25		Fa26		Fs22		Fs21		Fs8		An15		An15				An14						
					Wo1		Wo2		Wo45		Or6		Or4				Or7						

Electron microprobe analyses and Raman spectra show that original low-Ca pyroxene, high-Ca pyroxene, olivine, and plagioclase in the SMV are transformed into their high-pressure polymorphs, low-Ca majorite, high-Ca majorite, ringwoodite, and a mixture of jadeite-lingunite, respectively (Table 4.1, Fig. 4.3). The high-pressure shock transformation products of plagioclase in the host rock, maskelynite, show slightly variable CaO, Na_2O, and FeO contents compared to its high pressure polymorph, lingunite in the SMV, which contains no detectable FeO measured by EPMA.

We also observe a unique texture consisting of veins of troilite that define a complex network in the pyroxene (Fig. 4.2d,e) and is probably the result of shock injection of molten troilite into the pyroxene. Although veins usually have random orientations through the pyroxene, in some regions they follow the pyroxene cleavage. This texture is observed at the wider region of the largest SMV and can occur within large radial fractures in chondrules (~0.7-1 mm in size) that are entrained within the SMV (Fig. 4.2e). A smaller SMV contains a diverse range of shock effects that were not investigated in detail in this study. These include high pressure phases such as Ca-rich majorite grains, blue ringwoodite, tuite, and chromite-maskelynite assemblages (e.g., Fig. 4.3, bottom left). Complex shock textures are also common including dissociation textures in Mg_2SiO_4 clasts showing radial symplectites of a high Z phase and a low Z phase (Fig. 4.2f), many Fe-rich veins crosscutting entrained high-pressure clasts in chondrules, Mg-rich rims on the edge of entrained olivine chondrules (e.g., Fig. 4.2f), and metal-troilite bleb accumulations at the chondrule margins.

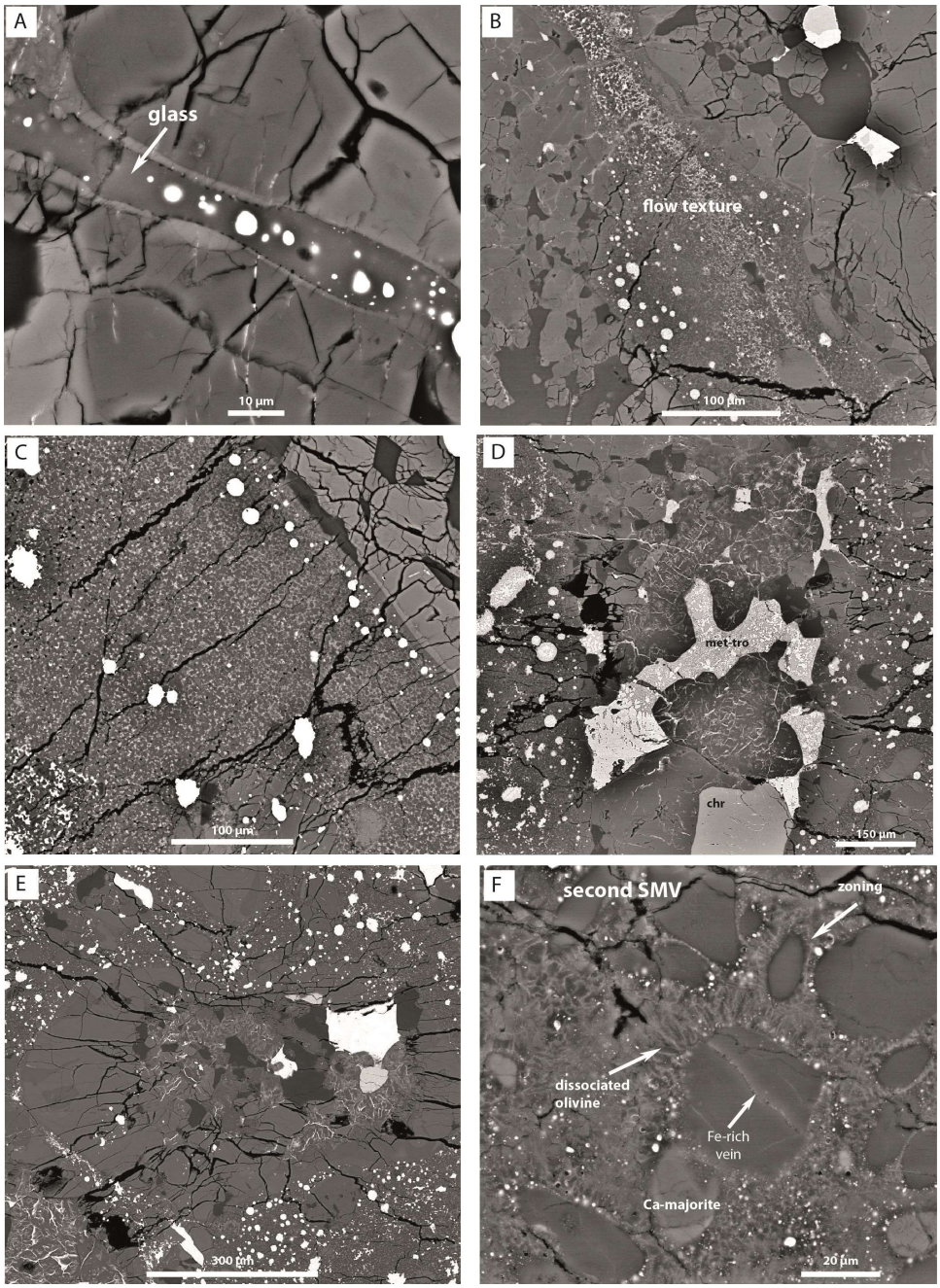

Figure 4.2 BSE images of shock melt veins in Villalbeto de la Peña. a) Very thin vein of glass and metal-troilite. b) Flow texture in a region of the main SMV characterized by elongated clasts oriented in the same direction and a flow textured matrix around them. c) Matrix of a region of the main SMV. Rounded metal-troilite blebs dominate the edges of the vein, and dendritic metal-troilite blebs, the interior. d) Large metal-troilite grains in the SMV associated with large chromites with exsolved troilite. e) Shock texture consisting of troilite filling radial fractures within a large chondrule, probably due to injection of a troilite shock melt. f) Portion of the second SMV with partially dissociated olivine, Ca-rich majorite, compositionally zoned mineral fragments (probably ringwoodite) and metal droplets around them.

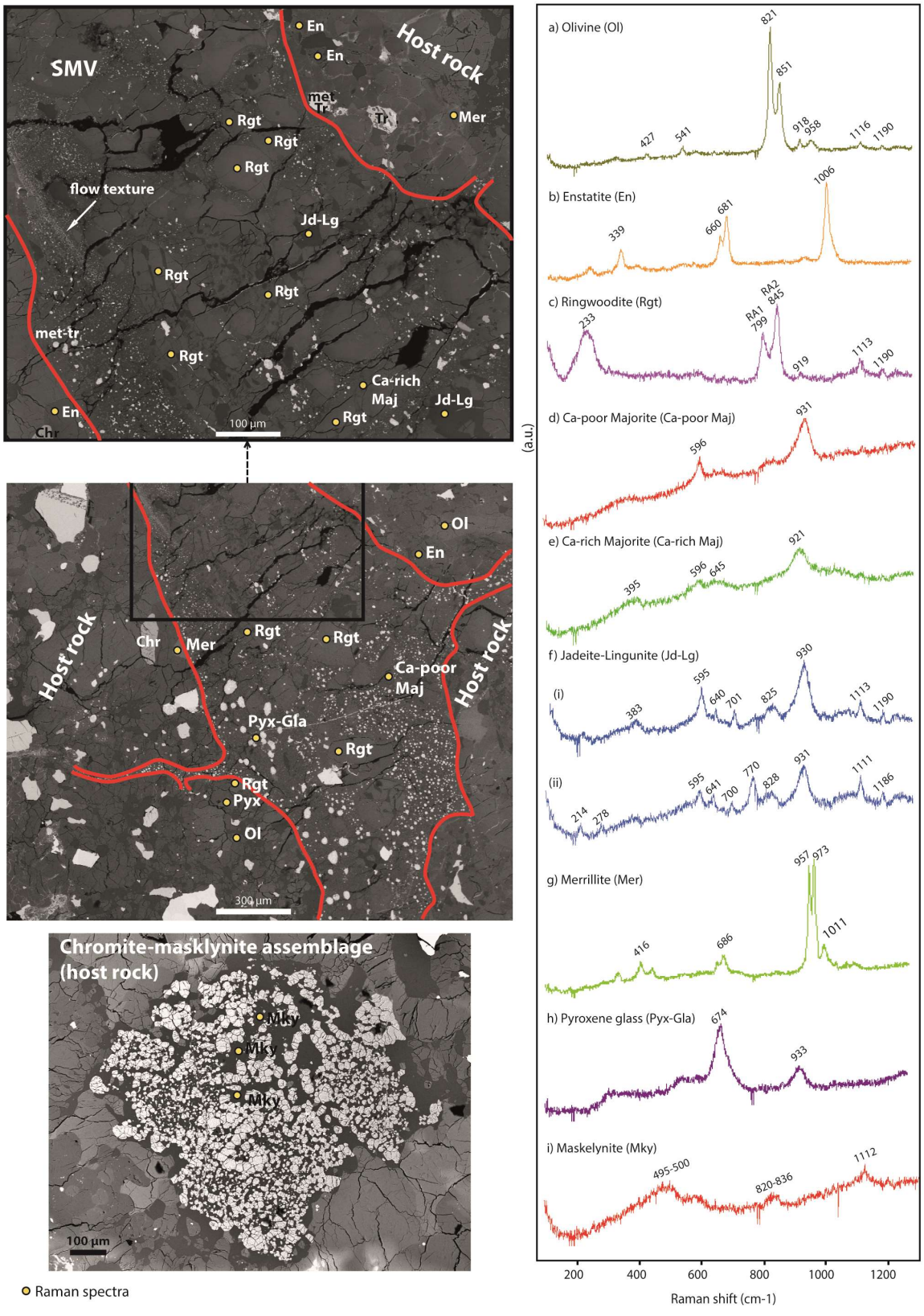
SMV
Host rock
En
En
met
Tr
Tr
Mer
Rgt
Rgt
Rgt
flow texture
Jd-Lg
Rgt
Rgt
met-tr
Rgt
Ca-rich
Maj
Jd-Lg
En
Chr
100 µm
Rgt
Ol
En
Host rock
Chr
Mer
Rgt
Rgt
Ca-poor
Maj
Host rock
Pyx-Gla
Rgt
Rgt
Pyx
Ol
300 µm
Chromite-masklynite assemblage
(host rock)
Mky
Mky
Mky
100 µm
Raman spectra
a) Olivine (Ol)
821
851
427
541
918
958
1116
1190
b) Enstatite (En)
1006
681
339
660
c) Ringwoodite (Rgt)
R42
845
RA1
799
233
1113
1190
919
d) Ca-poor Majorite (Ca-poor Maj)
931
596
e) Ca-rich Majorite (Ca-rich Maj)
921
596
645
395
f) Jadeite-Lingunite (Jd-Lg)
(i)
930
595
640
701
825
1113
1190
383
(ii)
931
595
641
770
828
1111
1186
700
214
278
g) Merrillite (Mer)
957
973
1011
686
416
h) Pyroxene glass (Pyx-Gla)
674
933
i) Maskelynite (Mky)
1112
495-500
820-836
(a.u.)
200
400
600
800
1000
1200
Raman shift (cm-1)

Figure 4.3. *(On previous page)*. Raman spectra in high-pressure phases in the studied SMV and the chromite-maskelynite intergrowth. Top and center on the left: Backscattered electron (BSE) images of the SMV showing the locations of Raman measurements. Bottom on the left: BSE image of a chromite-maskelynite assemblage (~800 μm size) from the host rock with its corresponding Raman measurements. Legend: Ol = olivine; En = enstatite; Rgt = ringwoodite; Jd-lg = jadeite-lingunite; Ca-rich maj = Ca-rich majorite; Ca-poor maj = Ca-poor majorite; Mer = merrillite; Met = FeNi; Tr = troilite; Chr = chromite. Right: Raman spectra of the main minerals found in the thinner part of the SMV.

3.2. Diopside to tetragonal Ca-rich majorite

Calcium-rich majorite grains are produced by high pressure transformation of Ca-rich pyroxene. An unusual anisotropic Ca-rich silicate phase with a composition consistent with diopside ($En_{47}Fs_8Wo_{45}$) (Table 4.1), based on EPMA, was identified in the SMV, associated with ringwoodite. This phase was identified as Ca-rich majorite based on Raman Spectroscopy (Fig. 4.3). The optical anisotropy of these grains, seen by cross-polarized light optical microscopy, suggests that these grains might have tetragonal symmetry ($I4_1/a$), instead of cubic ($Ia\bar{3}d$) (Martínez-Jiménez and Brearley, 2017). SEM imaging suggests that the Ca-rich majorite has a very fine-scale, granular microstructure at the submicron scale, which is too fine-grained to resolve. Therefore, we investigated its structure and chemistry in detail using TEM. Two FIB (designated FIB1 and FIB2) sections were extracted from this Ca-rich majorite grain (Fig. 4.4a).

Transmission electron microscopy shows a complex structure consisting of single crystals of Ca-rich majorite (a few microns in size) embedded within a nanometer-scale symplectic intergrowth of Ca-rich majorite and glass, in which the finger-like crystals and glass have the same sizes (~20 nm width, and up to 1 μm long) (Figs. 4.4c,d and 4.5b,c). The single crystal shows the same symplectic dissociation gradationally occurring at its margins (Fig. 4.4b). Scanning transmission electron microscope X-ray mapping shows

that the Ca-rich majorite in the symplectic intergrowth is Mg-rich and Ca-poor compared with single-crystal Ca-rich majorite and the glass shows the inverse relationship, being Ca-rich. A [111] zone axis SAED pattern (Fig. 4.4e) obtained from the single-crystal Ca-rich majorite in FIB1 shows reflections of the type $\{h0l\}$ (where h,l = odd), and therefore violates the extinction rule for Bragg diffraction for cubic space group $Ia\bar{3}d$. This observation implies that the garnet has tetragonal symmetry instead of cubic, the most common symmetry type found in majorites from meteorites (e.g., Tomioka and Kimura, 2003). Furthermore, the [211] zone axis in Fig. 4.5d shows the diffraction maxima $\{0kl\}$ where (k,l = odd), which is also indicative of tetragonal symmetry. The faint reflections $\{0kl\}$ where (k,l = odd) are forbidden reflections in the cubic structure, but appear in the tetragonal space group $I4_1/a$ due to increased ordering.

The diffraction pattern from the symplectic intergrowth shows a diffuse diffraction ring, which is consistent with the presence of glass (Fig. 4.4f). The presence of glass is also consistent with the Raman spectrum, which shows broader peaks associated with amorphous material in comparison with Ca-poor majorite spectra, which have pronounced and narrower peaks (Fig. 4.3). In the FIB2 section, Ca-rich majorite crystals represent the major part of the section in comparison to the symplectic intergrowth (Fig. 4.5). Ca-rich majorite forms a mosaic of subgrains (~2 μm), with some amorphous material between the crystallites (Fig. 4.5a). The symplectic intergrowth consists of Ca-poor majorite fingers within Ca-rich glass similar to the FIB1 TEM section. The electron diffraction data also show that the Ca-rich majorite crystals in the symplectic intergrowth all have the same crystallographic orientation, albeit with some misorientation, which is apparent in the arcs observed for individual diffraction maxima. Despite this

misorientation, it is apparent that the symplectite crystallites have essentially the same orientation as the single crystal of Ca-rich majorite that they surround.

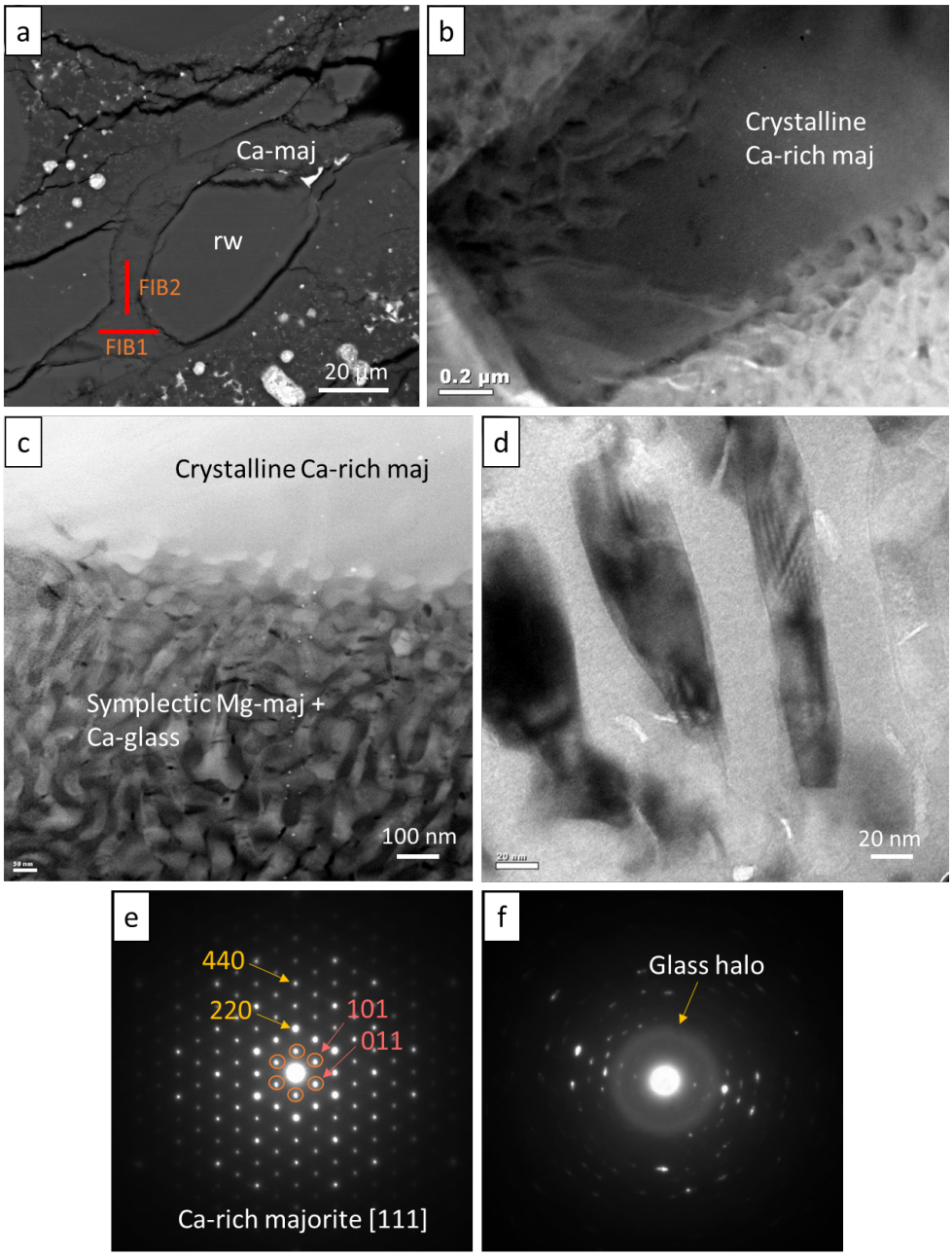

Figure 4.4. SEM and TEM images of the Ca-rich majorite (FIB1) studied in the main SMV. a) BSE image of the Ca-rich majorite (Ca-maj) associated with ringwoodite (rw) in the SMV showing the locations of the two FIB sections extracted from the sample. b) Bright-field TEM image of a crystalline Ca-rich majorite undergoing a symplectic dissociation at its margins. c) Higher magnification image of the symplectic Mg-rich majorite plus Ca-rich glass. *(Caption continues on the following page).*

Figure 4.4. *(Caption continued from the previous page).* d) Bright-field TEM image at higher magnification of the symplectic wormy Ca-poor majorite crystals (dark gray) showing some lattice fringes, and the glass (light gray). e) [111] zone axis diffraction pattern of the single crystal in (b) showing the presence of reflections $\{h0l\}$ where (h,l = odd) (circled in red on the diffraction pattern), which are absent in the cubic structure and therefore indicative of tetragonal symmetry (space group $I4_1/a$). f) Diffraction pattern showing a diffuse ring indicative of an amorphous material. Arcing of the diffraction maxima for the Ca-rich majorite crystals in the symplectite are also present indicative of crystallites that are slightly misoriented, but overall have the same crystallographic orientation as the single crystal of Ca-rich majorite that they surround.

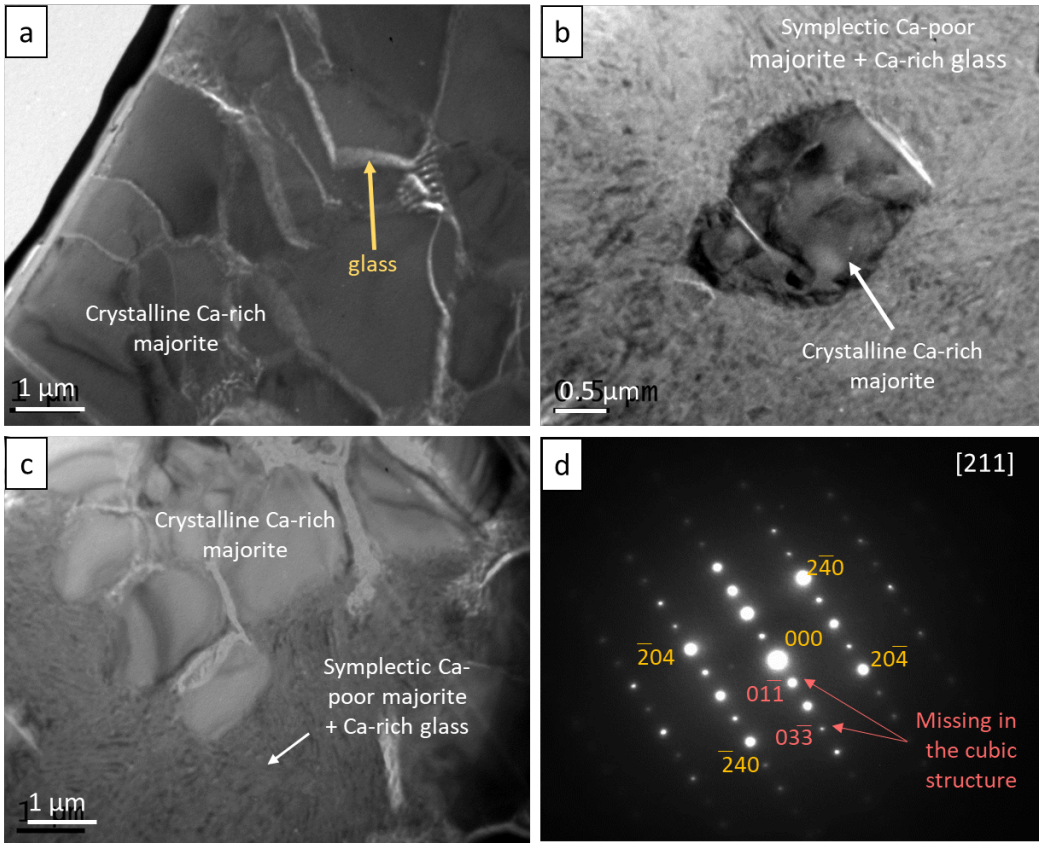

Figure 4.5. Bright-field TEM images of Ca-rich majorite in FIB2 marked in Fig. 4.4a. a) Crystalline Ca-rich majorite consisting of multiple subgrains of ~1-2 µm size with possible glass at the grain boundaries, which could represent the earliest stages of symplectite intergrowth development along the grain boundaries. b) A subrounded single crystal of Ca-rich majorite embedded within a symplectic intergrowth of Ca-poor majorite plus Ca-rich glass. The single crystal consists of several subgrains shown by the strain contrast in it. c) Other crystalline grains embedded in the symplectic Ca-poor majorite plus Ca-rich glass similar to FIB1 (Fig. 4.4). d) Diffraction pattern of the Ca-rich majorite on the [211] zone axis showing the presence of $\{0kl\}$ where (k,l = odd) is indicative of tetragonal symmetry.

3.3. Diopside undergoing direct melting

A third FIB section was extracted within an entrained chondrule fragment located in a wider region of the SMV. The chondrule fragment is 200 μm wide and 500 μm long and is surrounded by melted matrix with abundant metal-troilite blebs and other rounded clasts of ringwoodite, shocked chromite, and chlorapatite. This area within the chondrule fragment displays a complex relationship between the different phases shown in an X-ray map (Si-Al-Ca) in Figure 4.6a. The Ca-rich silicate grain has an irregular shape, contains several fractures, and is embedded in a more homogeneous-looking, isotropic phase with the same apparent composition observed by BSE imaging. It is associated with an assemblage of jadeite-lingunite assemblage (dark gray area in Fig. 4.6b), identified by Raman spectroscopy (Fig. 4.3). The FIB section was removed precisely from the fractured Ca-rich silicate phase across the interface with the surrounding, smooth homogeneous phase. Electron diffraction patterns of this phase show it is amorphous, whereas diffraction patterns from the fractured phase show that it is crystalline diopside, rather than the high-pressure polymorph, majorite. In the TEM, the interface between these two phases is extremely sharp and well-defined and quantitative STEM-EDS data from the crystalline and amorphous phase show that they have identical compositions ($En_{54}Fs_5Wo_{41}$). Thus, we interpret the amorphous Ca-rich phase with a $(CaMg)Si_2O_6$ composition to be glass resulting from high-pressure melting of diopside. Scanning-TEM and dark-field STEM images also reveal a network of veins along fractures that are crystallographically oriented. Compositionally, the veins contain material with high concentrations of FeO (~79 wt%) with minor MgO (~8 wt%) (Fig. 4.6). These veins have been identified as nanocrystalline magnesiowüstite based on their diffraction patterns,

being ring patterns due their small grain sizes (Fig. 4.6d). The EDS analyses from these veins also contain SiO_2 and CaO suggesting that minor diopside or diopside melt probably occurs interstitially to the magnesiowüstite. Magnesiowüstite veins (0.1-0.4 μm width) are crystallographically oriented along the diopside (110) cleavage planes, as well as parallel to the (001) and (111) planes. They show many fractures that generally lie both parallel and normal to the vein boundaries. The veins truncate at the edge of the diopside crystal, but arrays of pores (40 to 400 nm in size) extend into the glass from the truncation of the magnesiowüstite veins (Fig. 4.6c). In addition to the magnesiowüstite veins, pockets of a Ca-rich nanocrystalline phase also occur within the diopside and along the interfaces between the magnesiowüstite and the diopside. This Ca-rich phase has a higher FeO content than the diopside (Fig. 4.6c).

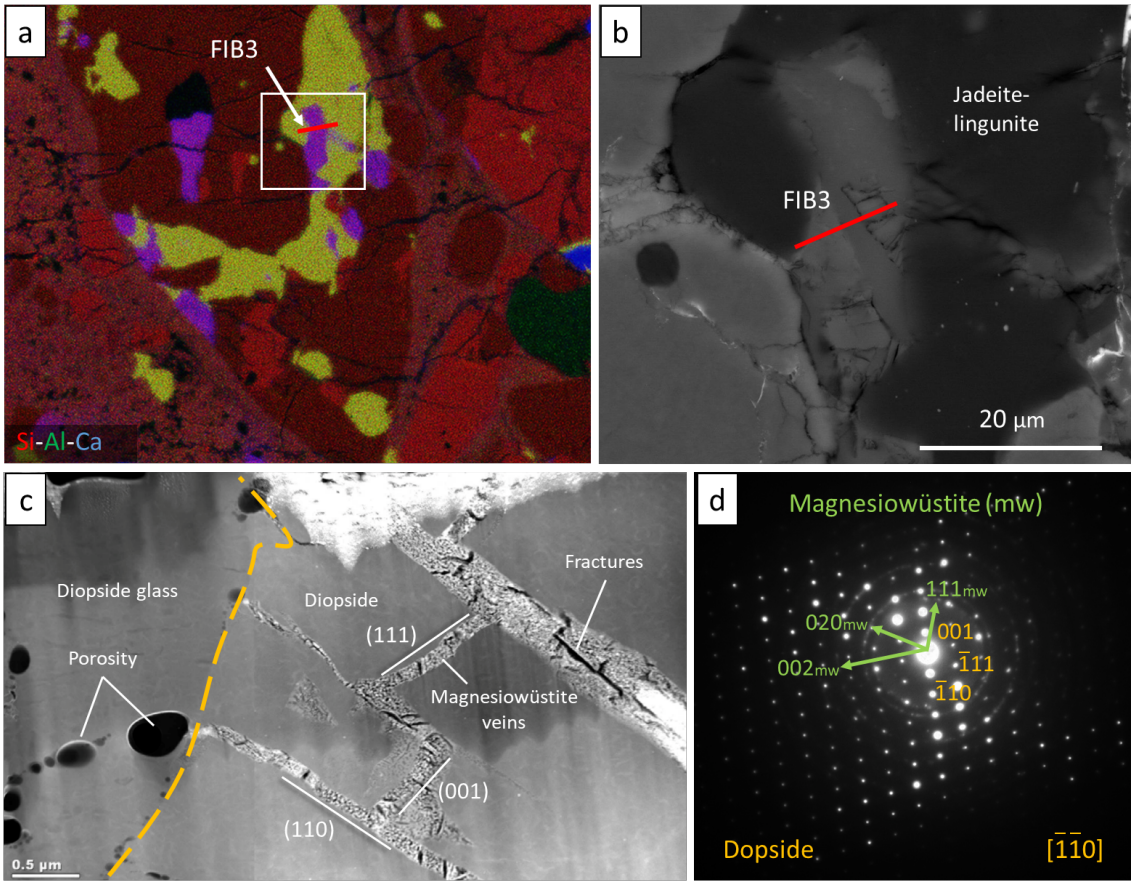

Figure 4.6. SEM and TEM images of diopside and diopside glass in the SMV (FIB3). a) Si-Al-Ca RGB X-ray map of the entrained chondrule fragment in the SMV (Si-Al-Ca). b) BSE image showing the position of the TEM foil extracted by FIB in red. c) HAADF STEM image of the amorphous Ca-rich silicate phase (diopside melt), crystalline diopside, magnesiowüstite veins with abundant fractures, and porosity. d) [TT0] zone axis diffraction pattern from diopside (Di) with an indexed ring pattern from the nanocrystalline magnesiowüstite (Mw).

3.4. Olivine to ringwoodite

Based on Raman Spectroscopy and EPMA, most olivine grains entrained in the SMV are transformed to ringwoodite ($Mg_{1.49}Fe_{0.52}Si_{0.99}O_4$, Table 1). No wadsleyite has been found. Ringwoodite grains are observed with different textures, with smooth monomineralic grains predominating (e.g., Fig. 4.4a). Polycrystalline ringwoodite aggregates are also found (Fig. 4.7a), similar to those seen in the Tenham (Xie and Sharp, 2007; Langenhorst et al., 1995; Chen et al., 1996), Yamato 791384 (Miyahara et al.,

2010), and Sixiangkou (Chen et al., 1996, 2007) chondrites. However, we have also identified oriented lamellae of ringwoodite in olivine grains in the host rock adjacent to the SMV (Fig. 4.7b,c). Backscattered electron images show that lamellae are richer in Fe_2SiO_4 than the surrounding host olivine. The respective widths and lengths of lamellae are ~5 μm x ~60 μm in Figure 4.7b, and less than ~1 μm x ~10 μm in Figure 4.7c. Ringwoodite with a slightly blue coloration in plane polarized transmitted light was also recognized in another melt pocket associated with the second SMV.

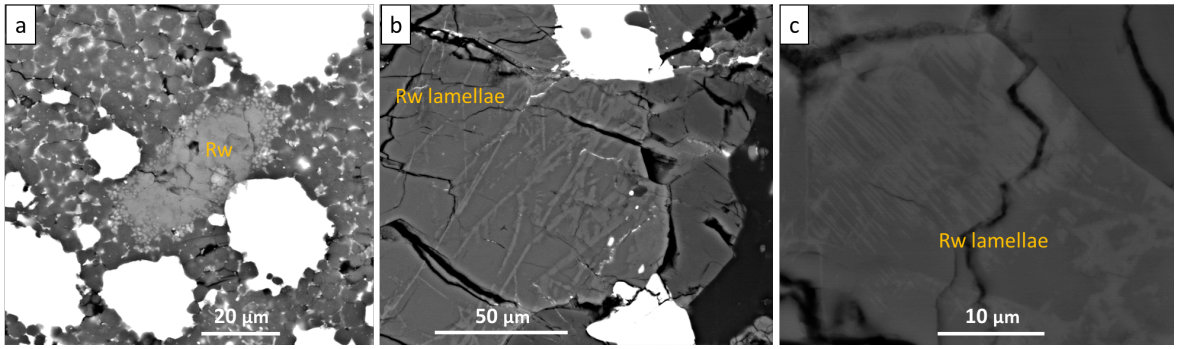

Figure 4.7. BSE images of different ringwoodite textures in VP. a) Olivine fragment in the SMV replaced by polycrystalline ringwoodite. b) Ringwoodite with thick lamellae (50-60 μm) with higher iron content than the host grain. c) Olivine with thin (~1 μm) crystallographically-oriented lamellae of ringwoodite with higher Fe content near the SMV.

3.5. Jadeite-lingunite

The jadeite-lingunite phase, which was identified by Raman spectrometry, EPMA, and TEM, formed subsequent to the breakdown of feldspar, being the high-pressure polymorph of plagioclase. It is a predominant phase in the SMVs of the VP meteorite, commonly occurring within chondrule fragments, interstitial to ringwoodite and majorite. The jadeite-lingunite grains are anhedral in shape with grain sizes of 0.5-1 μm. They are optically isotropic, but some grains show slight anisotropy that may indicate incomplete transformation to the high-pressure phase. Electron microprobe analyses of the jadeite-

lingunite phase show a chemical composition of ($Na_{0.63}Ca_{0.12}K_{0.03}Mg_{0.01}Fe_{0.01}Al_{1.18}Si_{2.87}O_8$) (Table 4.1). We attribute some analytical errors due to the focused electron beam (1 μm) used for the analysis, which likely caused volatile loss in the host rock maskelynite and thereby, can cause compositional differences (Ribbe and Smith, 1966; Spray and Rae, 1995). Thus, higher Na contents in the jadeite-lingunite phase may be related to less volatile loss compared to maskelynite. However, although the composition is close to its parental phase in the host rock, lingunite shows a significant enrichment in Mn (0.22 wt% MnO) that is not apparent in the host rock maskelynite (0.02 wt% MnO, Table 4.1), which may suggest incorporation during melting. The Raman spectra of the jadeite-lingunite phase vary slightly among measurements, with typical peaks at 214, 278, 383, 595, 640, 700, 770, 825, 930, 1113, and 1189 cm^{-1} (Fig. 4.3). Some of the peaks correspond to jadeite (383 and 700 cm^{-1} peaks) and others to lingunite (214, 278, 640, 770, and 825 cm^{-1}). Majorite Raman peaks are also identified (593 and 931 cm^{-1} peaks), probably because the Raman laser beam penetrated into a region of majorite deeper in the sample that is not visible at the surface.

A fourth FIB section was extracted from a Na-, Ca-, Al-rich phase identified as jadeite-lingunite based on the Raman spectra (Fig. 4.3, on the right). A porous vein, ~1 μm wide, crosscuts the coarse crystalline majorite (Fig. 4.8a). Two different minerals were identified within the FIB section: jadeite-lingunite is embedded in majorite, an occurrence that appears to be typical of other jadeite-lingunite grains (Fig. 4.8a). Ca-poor majorite was identified based on EDS analyses and electron diffraction patterns, consisting of equant crystals of sizes around 0.5 μm. Most of the FIB section consists of nanocrystalline lingunite that occurs in two distinct regions with two different grain sizes

(marked as 1 and 2 in Fig. 4.8b), <100 nm, and <10 nm, respectively, separated by a distinct boundary. Fast Fourier Transforms (FFTs) obtained from high-resolution TEM images from the nanocrystallites show that this phase has the hollandite-structure of Na-plagioclase (lingunite) (Fig. 4.8c-e).

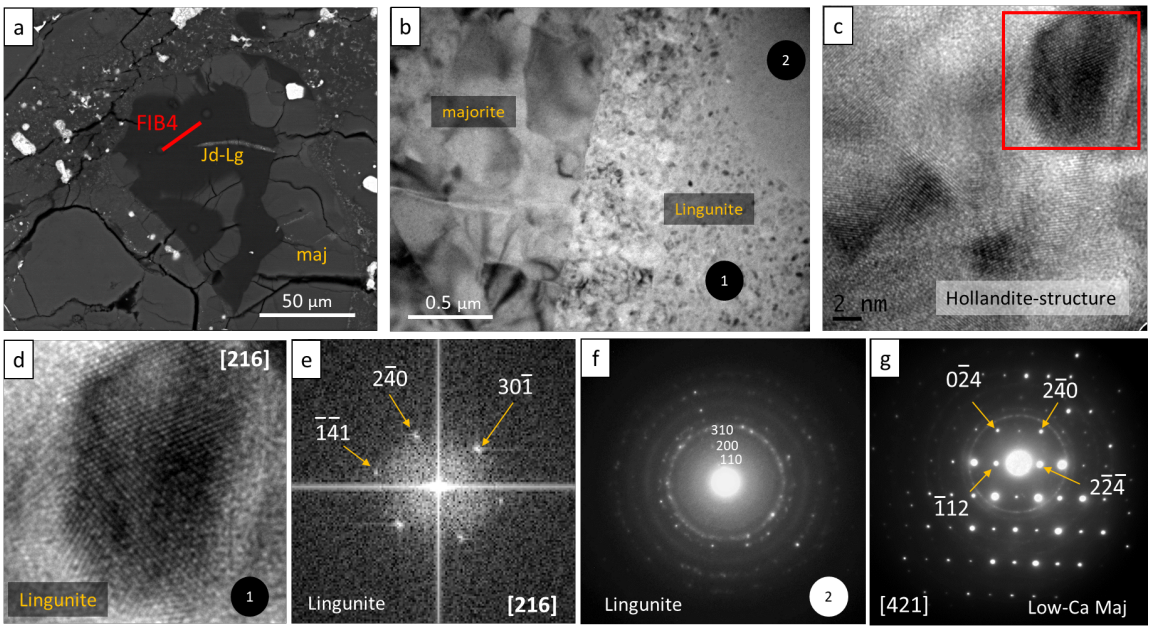

Figure 4.8. TEM images of the lingunite phase (FIB4) in the SMV. a) SEM image of the jadeite-lingunite grain showing the location where the FIB section was extracted (FIB4). b) Bright-field TEM image showing that the interface between majorite and lingunite distinguished is sharp. Lingunite is present in two regions that are distinguished by different grain sizes (separated by a distinct boundary). One region (marked as 1) contains randomly oriented crystallites <100 nm in size, whereas the second region (marked as 2) consists of myriad nanocrystals of lingunite <10 nm in size. c) High-resolution TEM image of the lingunite nanocrystallites from region (1) showing lattice fringes from multiple crystals in random orientations. d) Higher magnification from the red square in (c). e) Corresponding FFT obtained from the crystallites shown in the red box in (c), which can be indexed as the [216] zone axis of lingunite. f) Diffraction ring pattern from lingunite extracted from phase (2). g) [421] zone axis SAED pattern from the single crystal of low-Ca majorite.

3.6. The matrix

The matrix of the SMVs is complex and consists of several different phases. Raman spectra obtained from the matrix show the two characteristic Raman bands at 674

cm^{-1} and 933 cm^{-1} from majorite-pyrope (Fig. 4.3, on the right). However, the 674 cm^{-1} peak could also correspond to $MgSiO_3$ pyroxene glass (Kubicki et al., 1992; Imae and Ikeda, 2010) or vitrified $MgSiO_3$-perovskite (Durben and Wolf, 1992). The matrix in the larger SMV consists of equant and/or euhedral isotropic Ca-rich majorite-$pyrope_{ss}$ with grain sizes of ~3-5 μm (Fig. 4.9, Table 4.1). The majorite-pyrope garnets are rich in Al_2O_3, CaO, Na_2O, and Cr_2O_3. The matrix is dominated by a cellular texture, although other textures such as microporphyritic are also observed in many regions of both SMVs and melt pockets (e.g., Fig. 4.9a,b). Ferropericlase grains <~1μm in size are also found filling interstices between the majorite-pyrope (Fig. 4.9c). The ferropericlase occurs as rounded grains, either isolated or in clusters, similar to those reported by Fritz and Greshake (2009) in the Chassigny meteorite and Chen et al. (1996) in the Sixiangkou L5 ordinary chondrite. The clusters of ferropericlase are embedded within a glassy phase that has lower BSE contrast (Fig. 4.9c). In some areas of the matrix, the interstices between grains are filled with a phase enriched in Fe and S, associated with crystallization from a melt of a mixture of majorite-pyrope and troilite.

Backscattered electron imaging shows that in some areas of the matrix the majorite-pyrope grains show compositional zoning, which is apparent as distinct lower Z rims ~0.5-1 μm thick due to a higher concentration of MgO (Fig. 4.9d). Some grains also have Mg-rich cores (2-3 μm) (Fig. 4.9d); it seems most likely that all the grains have Mg-rich cores, but the centers of the grains are not exposed at the surface of the sample. These observations represent the first reported evidence of zoning in garnet in a matrix of a SMV and suggests crystallization from a melt that occurred too rapidly to allow the grains to equilibrate due to very high cooling rates. Eutectic FeNi-troilite blebs with sizes

ranging from few microns to ~50 μm are commonly found in some regions of the matrix and can be very abundant or even dominate the matrix (Fig. 4.9a). Many metal-troilite blebs are zoned with metal concentrated at the core and troilite at the rims. Metal-troilite spherule textures vary from the edge (rounded) (Fig. 4.9b) to the center of the SMV (dendritic) (Fig. 4.9a).

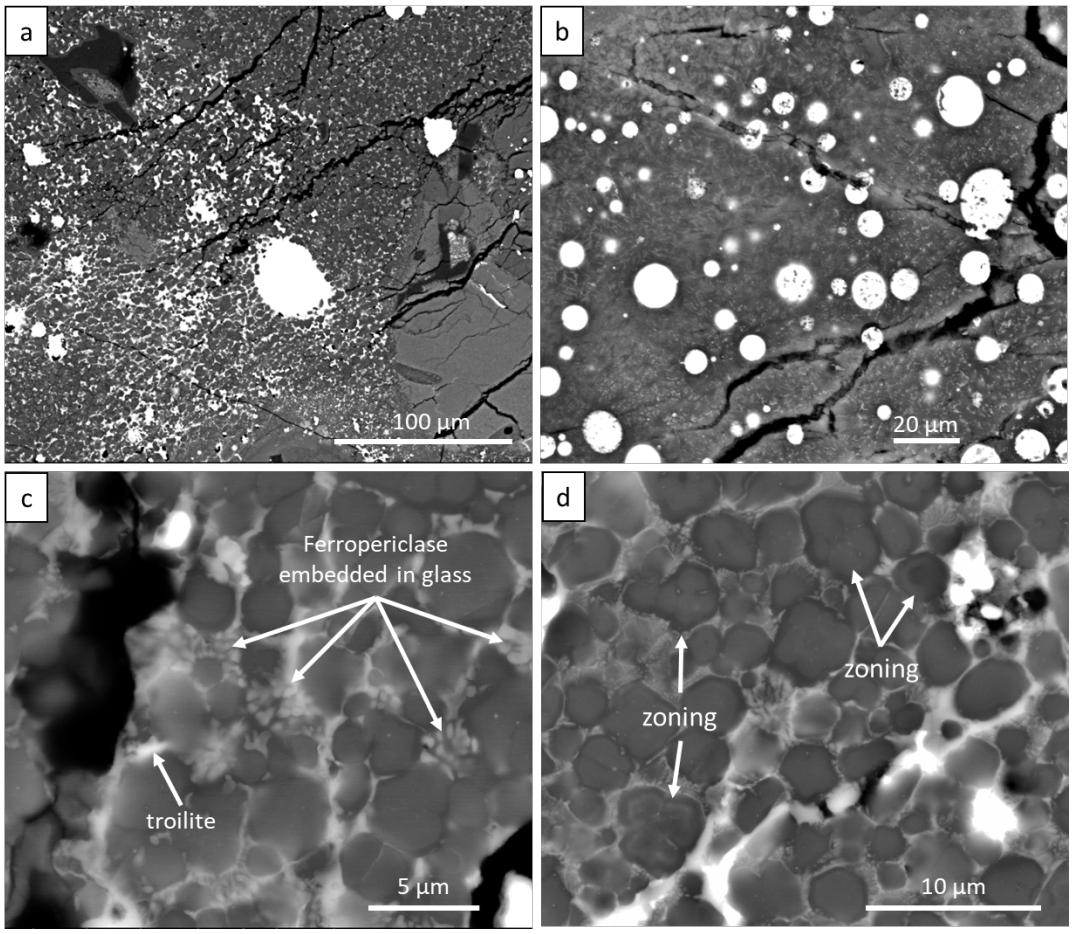

Figure 4.9. BSE images showing the textures of the matrix in the main SMV. A) Example of metal-troilite blebs with dendritic edges that dominate the matrix of a central region of the SMV. b) Example of metal-troilite spherules with rounded shapes in the wider part of the SMV. c) Patches of interstitial ferropericlase grains between the majorite-pyrope grains are embedded in a glassy phase with lower BSE contrast. Troilite occurs along grain boundaries between the majorite-pyrope phase. d) Zoning in the majorite-pyrope solid-solution grains in a region of the matrix with a high abundance of majorite-pyrope grains with interstitial phases. Magnesium is higher at the rims (0.5-1 μm) and most likely in all the cores as well (~2-4 μm), although only some grain cores are exposed at the surface of the sample (shown with arrows in the image).

4. Discussion

Although there have been several studies of shock features in ordinary chondrites, in the present work we report new observations made in the main shock melt vein of the Villalbeto de la Peña L6 chondrite, which provide additional insights into high-pressure phase transformations, in particular the behavior of diopside. Although diopside is ubiquitous in ordinary chondrites, it is much less abundant (between 5.7-8.8%, Dunn et al., 2010) than the major silicate phases, olivine and low-Ca pyroxene. Calcium-rich majorite, its high-pressure polymorph phase mineral, is thus rarely found in ordinary chondrites (Tomioka and Kimura, 2003; Xie et al., 2006), resulting in unclear phase transformation mechanisms and kinetics of diopside. Therefore, the stability of diopside during shock metamorphism has been studied using high-pressure experiments at high temperatures (> 1000ºC) (e.g., Canil, 1994; Gasparik, 1990; Oguri et al., 1997; Irifune et al., 2000; Asahara et al., 2005).

Here, we report the third occurrence of Ca-rich majorite in an ordinary chondrite, but the main contribution of this work is to provide a better understanding of the shock-induced transformations of diopside. We distinguish three different behaviors for diopside depending on the width of the SMV, which indicate different shock conditions: (1) diopside transformed to Ca-rich majorite, (2) single crystals of Ca-rich majorite undergoing a transformation to a symplectic intergrowth of Ca-poor majorite and Ca-rich glass, and (3) diopside undergoing direct melting without transforming to a high-pressure phase.

The first two transformation behaviors of diopside are observed within the same grain studied by TEM, which was taken from the thinner part of the SMV. First, diopside

is transformed to single crystals of Ca-rich majorite through a solid-state phase transformation since its composition is identical to the diopside in the host rock. The Ca-rich majorite has tetragonal symmetry seen by the presence of several reflections in electron diffraction patterns. For example, the (0*kl*) reflections where (*k*,*l* = odd) in the [211] zone axis diffraction pattern appear only in the tetragonal structure. Second, and counter to previous studies by Xie and Sharp (2007), the single crystal is, in turn, dissociated into a symplectic intergrowth of Ca-poor majorite plus Ca-rich glass. The Ca-rich glass is interpreted to be Ca-perovskite that vitrified under decompression, similar to the example seen in the Shergotty Martian meteorite (Tomioka and Kimura, 2003), the first meteorite where Ca-rich majorite was reported (Malavergne et al., 2001). In Shergotty, the majorite and the Ca-rich glass have a granular texture and are complementary in composition to one another. According to high pressure experiments on $CaSiO_3$, a phase with the perovskite structure is stable above ~12 GPa and ~1000°C, but it progressively transforms into glass during decompression (Liu and Ringwood, 1975; Liu, 1987). The two different transformation behaviors that we have found in the same Ca-rich majorite grain are interpreted as a temporal sequence, starting with the solid-state high-pressure transformation of diopside to Ca-rich majorite, and followed by dissociation of the Ca-rich majorite. The majorite in the symplectite has the same crystallographic orientation as the large single crystal that it formed from, suggesting that the dissociation reaction does not necessarily involve nucleation and growth of new majorite crystals, but retains the structural elements of the precursor phase. The dissociation was incomplete, likely due to a fast shock duration and/or large grain sizes.

These grains are also fractureless and smooth seen under the SEM at high magnifications, suggesting no evidence of a fine-grained structure.

Diopside examined by TEM from a wider region of the SMV is found within a large entrained chondrule fragment surrounded by matrix with abundant FeNi-troilite blebs, which shows a completely different behavior. In this case, diopside underwent direct shock-induced melting, because an amorphous phase with the exact same diopside composition surrounds the crystal, interpreted as quenched glass. The magnesiowüstite veins are crystallographically oriented in the diopside, but are absent within the glass phase. Rather, porosity in the glass is continuous from the magnesiowüstite veins (Fig. 4.6c), suggesting that magnesiowüstite, as a melt, was injected into the diopside at the same time diopside was undergoing melting. One possible explanation for the porosity in the glass that is coincident with the termination of the veins is that the magnesiowüstite melt contained a gaseous phase when it was injected into the diopside, which could have helped reduce the viscosity of the melt and hence, allowed it to travel further. The gas escaped into the diopside melt as the magnesiowüstite veins crystallized, but before the diopside melt quenched, i.e., occurred at high temperature. This is consistent with the numerous fractures seen within the magnesiowüstite veins and the presence of porosity in the melt phase (Fig. 4.6c). We interpret this whole scenario as evidence of a very fast, but intense shock event within this particular region of the SMV. Temperature could have been higher than in the thinner region of the SMV according to the phase diagram of diopside, but the Fe content of magnesiowüstite could have decreased the melting point of diopside (Agee et al., 1995). The presence of magnesiowüstite veins in a shocked chondrite has not been described before. The formation of a melt with primarily

magnesiowüstite composition that injects into diopside is interpreted as the residual fractionated product of a melt vein matrix that crystallized majorite-pyrope grains.

In this study, we also found the first evidence of compositional zoning at an extremely fine scale in the majorite-pyrope grains that dominate the matrix of the widest region of the SMV. The Mg-rich cores of the majorite-pyrope grains are consistent with the experimental silicate-melt partitioning data for crystallization of majorite (Drake et al., 1993). As cooling took place, both the majorite-pyrope crystals and the melt became Fe-rich, but the partition coefficient required the melt to be more Fe-enriched than the crystals. We attribute the observed change in Mg/Fe ratio in majorite-pyrope crystals to the crystallization of micron-sized clusters of magnesiowüstite in the interstitial residual melt, which depleted the melt in Fe and, therefore, the Fe content in the majorite-pyrope crystals dropped and became more Mg-rich (Fig. 4.9c,d). The rate of Mg-Fe interdiffusion in majorite-pyrope is much slower than, for example, in olivine (Van Mierlo et al., 2013). Therefore, fast cooling rates are not necessary to preserve the compositional zonation and prevent equilibration. Nevertheless, fast cooling rates within the wider region of the SMV are clearly indicated by (i) the very fine-grained texture of the melt vein and (ii) the presence of quenched diopside glass within a chondrule fragment, as discussed above.

In order to estimate the peak shock conditions at which the main SMV of Villalbeto de la Peña crystallized, we have used the following constraints: (1) the experiments performed by Oguri et al. (1997) on diopside, which show that the assemblage of majorite plus vitrified Ca-rich perovskite is stable at ~18-24 GPa and ~1100º-2100ºC, (2) the tetragonal majorite stability field determined by experiments on

enstatite ($MgSiO_3$) (Gasparik, 1990), and (3) the jadeite-lingunite stability field boundary based on Akaogi (1989). Our estimated P-T conditions for the SMV are shown in Figure 4.10a. From our results, we observe that the thinner part of the SMV (FIB sections 1, 2 and 4) had different peak-shock conditions than the wider part where FIB3 was extracted. The high-pressure transformations of diopside in the thinner part of the vein indicate higher pressures (between 18 and 23 GPa) than the high-pressure effects in diopside in the wider area of the vein, which appears to record lower pressures (P < 18 GPa) (Fig. 4.10a, stippled oval regions). Temperature is less variable or, at least, the observed phase transformations in different regions of the vein could occur at similar temperatures, which is estimated to be around 2000-2200ºC (Fig. 4.10), based on the phase diagram constraints. However, if we assume that these assemblages represent peak shock pressures, we conclude that the maximum shock conditions are heterogeneous in the SMV and that this variability in peak shock pressures may be a function of the SMV width.

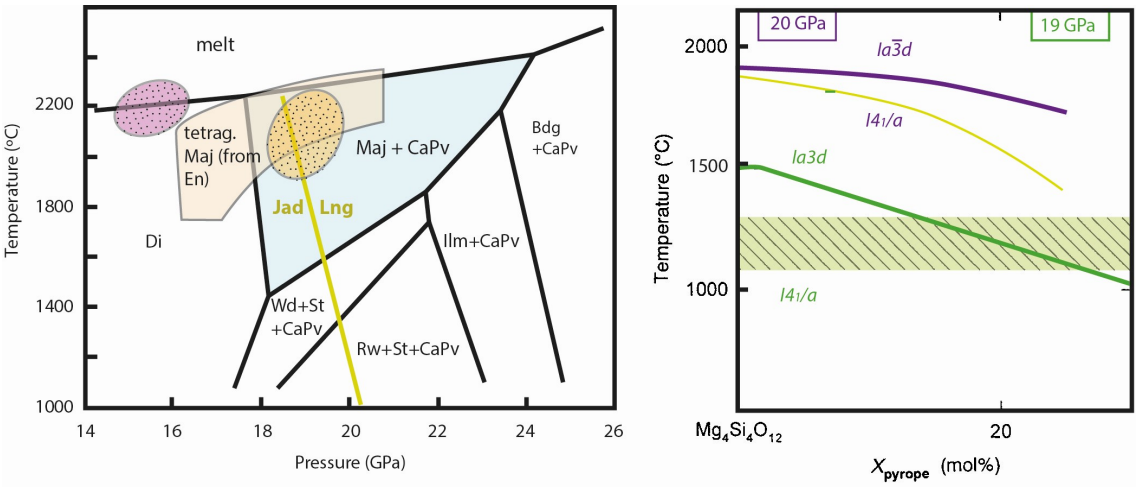

Figure 4.10. Phase diagrams of high-pressure phases present in the SMV of VP. *(Caption continues on the following page).*

Figure 4.10. *(Caption continued from the previous page).* a) Diopside phase equilibria diagram based on the experimental study of Oguri et al. (1997), combined with the stability field of tetragonal majorite dissociated from enstatite ($MgSiO_3$) based on Gasparik (1990), and the jadeite-lingunite phase boundary from Akaogi (1989). The two stippled ovals represent the estimated peak shock conditions for FIB 1, 2 and 4 (purple), and FIB 2 (yellow), which represent the thinner and the wider regions, respectively. Legend: Di = diopside, Wd = wadsleyite, St = stishovite, CaPv = calcium perovskite, Rw = ringwoodite, Ilm = ilmenite, Maj = majorite, En = enstatite, Bdg = bridgmanite, Jad = jadeite, Lgn = lingunite. b) Superimposed isobaric T-X phase diagrams for tetragonal and cubic majorite at 20 GPa (purple) adapted from Tomioka et al. 2002, and at 19 GPa (green), from Heinemann et al. (1997). The dashed area represents the estimated cut-off temperature at which intracrystalline ordering processes are frozen in for a quench rate of ~850°C/sec (the experimental quench rate of Heinemann et al. 1997), which occurs at a pyrope content of 20 mol%.

Another important caveat is that the experimental phase diagrams we have used to estimate the peak shock conditions may not accurately reflect the behavior of a natural system due to compositional differences and faster cooling rates in the meteoritic samples than those performed in experiments. For example, it is known that an increase in FeO in solid solution in a given phase lowers the melting temperature (Agee et al., 1995). In addition, Ca content affects the stability field of majorite since it results in ordering and distortion of the unit cell at high pressures and temperatures. The stability field for tetragonal ($I4_1/a$) and cubic ($Ia\bar{3}d$) symmetry represented in Figure 4.10b is based on the work of Tomioka et al. (2002) and Heinemann et al. (1997) and shows the strong effect of pressure on the thermal stability of tetragonal and cubic majorite garnets. However, these experiments were performed with Ca-poor majorite, whereas the tetragonal majorite we observe in VP is Ca-rich ($En_{47}Fs_8Wo_{45}$). Consequently, the likelihood of cation ordering could be higher as well, because the distortion from cubic to tetragonal majorite is caused by Ca-Mg cation ordering in the dodecahedral sites, and Mg-Si cation ordering in the octahedral sites with decreasing temperatures (Hatch and Ghose, 1989). Therefore, the transformation curves from cubic to tetragonal symmetry as a function of pressure

and temperature represented in Figure 4.10b might be shifted upwards – i.e., tetragonal garnet could be stable at higher temperatures at any specific pressure. Majorite in meteorites is commonly found with cubic symmetry rather than tetragonal, because either the Ca content (responsible for ordering) is not very high, or because the cooling rate is very high and hence, the cubic structure with disordering on the cation sites is quenched at high temperatures (Fig. 4.10b).

Furthermore, based on kinetic data obtained on albite under static conditions (Kubo et al., 2008), and experiments using internally laser-heated Mao-Bell type diamond anvil cells between 15 and 30 GPa (Tutti, 2007), the lingunite phase suggests pressures between ~20.5 to 24 GPa if the duration of the shock event is 1 second or more. However, if the shock event that formed the SMV in the VP meteorite lasted <1 second, then lingunite could crystallize at higher P-T conditions, implying that the peak shock conditions would be higher than we have estimated. The incomplete dissociation of Ca-rich majorite into a symplectic intergrowth of Ca-poor majorite plus Ca-rich glass also supports very fast cooling rates. Although we do not have experimental data to quantify the cooling rate, we conclude that the SMV of VP crystallized at a very fast duration based on TEM observations.

Reclassification of Villalbeto de la Peña meteorite

Based on our estimates of the peak-shock conditions, the presence of large (up to 10 mm-size) shock melt veins, abundant ringwoodite, majorite, and lingunite grains in the shocked melt veins and pockets, and the complete replacement of plagioclase by maskelynite in the host rock, we conclude that Villalbeto de la Peña should be reclassified as a shock stage S6 instead of S4.

5. Conclusions

There are very few descriptions of the effects of shock in diopside in ordinary chondrites, possibly due to relatively low modal abundances of diopside compared to Ca-poor pyroxenes. However, in this study we have gained new insights into the high-pressure shock behavior of diopside that have not been reported previously in the literature. The discovery of shocked transformed diopside in VP may be attributable to the fact that the SMV we have studied is unusually large, and therefore, there is a larger volume of target material that has been affected by shock.

Specifically, we have observed three different types of shock transformation mechanisms for diopside under high pressure and temperature conditions. We have observed the first natural occurrence of the solid-state transformation of diopside into tetragonal Ca-rich majorite in the thinner region of the SMV. The Ca-rich majorite has, in turn, dissociated into a symplectic intergrowth of Ca-poor majorite and Ca-rich glass. In addition, we have observed the first example of diopside undergoing direct melting in a wider region of the SMV.

Majorite-pyrope grains have been previously described in the matrix of SMV in other shocked ordinary chondrites (e.g., Chen et al., 1996; Miyahara et al., 2010), but are compositionally homogeneous. In this study, we report the occurrence of compositionally-zoned majorite-pyrope grains, with Mg-rich cores zoned to more Fe-rich compositions outwards, with Mg-rich overgrowth rims. This phenomenon has not been reported previously in a matrix of a SMV. Although this compositional zoning does not provide a good constraint for the cooling rate of the vein, we conclude that the wider part of the SMV crystallized at higher cooling rates than the thinner part. This conclusion is

based on the direct melting of diopside to form quenched glass in the wider part. The tetragonal symmetry in majorite grains in the thinner part of the SMV could record slower cooling rates, although the high Ca content may influence the rate of cation ordering compared to Ca-poor majorite.

Acknowledgements

JMT acknowledges funding from grants AYA2011-26522 and AYA2015-67175-P. JL is a Serra Húnter Fellow and is grateful to ICREA Academia program and GC 2017 SGR 128. Additional support for MMJ and AJB was provided by NASA Cosmochemistry grant NNX15AD28G to A. J. Brearley (PI). Special acknowledgements to Narcís Mestres (ICMAB-CSIC) for offering his Raman Spectrometer and providing his guidance. Sample preparation (focused ion beam) and transmission electron microscope analysis were carried out in the Electron Microbeam Analysis Facility in the Department of Earth and Planetary Sciences and Institute of Meteoritics, University of New Mexico.

References

Agee C. B., Li J., Shannon M. C., and Circone S. 1995. Pressure-temperature phase diagram for the Allende meteorite. *Journal of Geophysical Research: Solid Earth* 100:17725–17740.

Akaogi M., Ito E., Navrotsky A. 1989. Olivine-modified spinel-spinel transitions in the system Mg_2SiO_4–Fe_2SiO_4: calorimetric measurements, thermochemical calculation, and geophysical application. *Journal of Geophysical Research* 94:15,671–15,685.

Akaogi M., Yano M., Tejima Y., Iijima M., and Kojitani H. 2004. High-pressure transitions of diopside and wollastonite: phase equilibria and thermochemistry of $CaMgSi_2O_6$, $CaSiO_3$ and $CaSi_2O_5$–$CaTiSiO_5$ system. *Physics of the Earth and Planetary Interiors* 143:145–156.

Akaogi M., Haraguchi M., Nakanishi K., Ajiro H., and Kojitani H. 2010. High-pressure phase relations in the system $CaAl_4Si_2O_{11}$–$NaAl_3Si_3O_{11}$ with implication for Na-

rich CAS phase in shocked Martian meteorites. *Earth and Planetary Science Letters* 289:503–508.

Asahara Y., Ohtani E., Kondo T., Kubo T., Miyajima N., Nagase T., Fujino K., Yagi T., and Kikegawa T. 2005. Formation of metastable cubic-perovskite in high-pressure phase transformation of $Ca(Mg,Fe,Al)Si_2O_6$. *American Mineralogist* 90:457–462.

Brearley A. J., Casanova I., Miller M. L., and Keil K. 1991. Mineralogy and possible origin of an unusual Cr-rich inclusion in the Los Martinez (L6) chondrite. *Meteoritics* 26:287–300.

Bunch T. E., Keil K., and Snetsinger K. G. 1967. Chromite composition in relation to chemistry and texture of ordinary chondrites. *Geochimica et Cosmochimica Acta* 31:1569–1582.

Brearley A. J. and Jones R. H. 1998. Chondritic meteorites. In *Planetary Materials*, edited by Papike J. J. Reviews in Mineralogy, vol. 36. Washington, D.C.: Mineralogical Society of America. pp. 3.1–3.398.

Canil D. 1994. Stability of clinopyroxene at pressure-temperature conditions of the transition region. *Physics of Earth and Planetary Interiors* 86:25–34.

Chen M., Sharp T. G., El Goresy A., Wopenka B., and Xie X. 1996. The majorite-pyrope+magnesiowüstite assemblage: Constraints on the history of shock veins in chondrites. *Science* 271:1570–1573.

Chen M., Xie X., Wang D., and Wang S. 2002. Metal-troilite-magnetite assemblage in shock veins of Sixiangkou meteorite. *Geochimica et Cosmochimica Acta* 66:3143–3149.

Chen M., El Goresy A., and Gillet P. 2004. Ringwoodite lamellae in olivine: Clues to olivine-ringwoodite phase transition mechanisms in shocked meteorites and subducting slabs. *Proceedings of the National Academy of Sciences* 101:15033–15037.

Chen M., Li H., El Goresy A., Liu J., and Xie X. 2006. Fracture-related intracrystalline transformation of olivine to ringwoodite in the shocked Sixiangkou meteorite. *Meteoritics & Planetary Science* 41:731–737.

Chen M., Chen J., Xie X., and Xu J. 2007. A microstructural investigation of natural lamellar ringwoodite in olivine of the shocked Sixiangkou chondrite. *Earth and Planetary Science Letters* 264:277–283.

Chopelas A., and Serghiou G. 2002. Spectroscopic evidence for pressure-induced phase transitions in diopside. *Physics and Chemistry of Minerals* 29:403–408.

Drake M. J., McFarlane E. A., Gasparik T., and Rubie D. C. 1993. MG-perovskite/silicate melt and majorite garnet/silicate melt partition coefficients in the SYSTEM CaO-MgO-SiO2 at high temperatures and pressures. *Journal of Geophysical Research: Planets* 98:5427–5431.

Dunn T. L., Cressey G., McSween Jr H. Y., and McCoy, T. J. 2010. Analysis of ordinary chondrites using powder X-ray diffraction: 1. Modal mineral abundances. *Meteoritics & Planetary Science* 45:123–134.

Durben D. J., and Wolf G. H. 1992. High-temperature behavior of metastable $MgSiO_3$ perovskite. *American Mineralogist* 77:890–893.

Feng L., Lin Y., Hu S., Xu L., and Miao B. 2011. Estimating the composition of natural ringwoodite in the heavily shocked Grove Mountains 052049 meteorite from Raman spectra. *American Mineralogist* 96:1480–1489.

Fritz J., and Greshake A. 2009. High-pressure phases in an ultramafic rock from Mars. *Earth and Planetary Science Letters* 288:619–623.

Gasparik T. 1990. Phase relations in the transition zone. *Journal of Geophysical Research* 95:15751–15769.

Gillet P., El Goresy A., Beck P., and Chen M. 2007. High-pressure mineral assemblages in shocked meteorites and shocked terrestrial rocks: mechanisms of phase transformations and constraints to pressure and temperature histories. *Geological Society of America Special Papers* 421:57–82.

Hatch D. M., and Ghose S. 1989. Symmetry analysis of the phase transition and twinning in $MgSiO_3$ garnet: Implications to mantle mineralogy. *American Mineralogist* 74:1221–1224.

Heinemann S., Sharp T. G., Seifert F., and Rubie D. C. 1997. The cubic-tetragonal phase transition in the system majorite ($Mg_4Si_4O_{12}$)–pyrope ($Mg_3Al_2Si_3O_{12}$), and garnet symmetry in the Earth's transition zone. *Physics and Chemistry of Minerals* 24:206–221.

Imae N., and Ikeda Y. 2010. High-pressure polymorphs of magnesian orthopyroxene from a shock vein in the Yamato-000047 lherzolitic shergottite. *Meteoritics & Planetary Science* 45:43–54.

Irifune T., Miyashita M., Inoue T., Ando J., Funakoshi K., and Utsumi W. 2000. High-pressure phase transformation in $CaMgSi_2O_6$ and implications for origin of ultra-deep diamond inclusions. *Geophysical Research Letters* 27:3541–3544.

Kubicki J. D., Hemley R. J., Hofmeister A. M. 1992. Raman and infrared study of pressure-induced structural changes in $MgSiO_3$, $CaMgSi_2O_6$, and $CaSiO_3$ glasses. *American Mineralogist* 77:258–269.

Kubo T., Kimura M., Nishi M., Tominaga A., Kato T., Kikegawa T., Funakoshi K., and Miyahara M. 2008. Formation of jadeite from plagioclase: Constraints on the P-T-t conditions of shocked meteorites. *Meteoritics & Planetary Science* 43:A82.

Lafuente B., Downs R. T.. Yang H., and Stone N. 2015. The power of databases. The RRUFF project. In *Highlights in Mineralogical Crystallography*, edited by Armbruster T., and Danisi R. M., Berlin: W. De Gruyter, pp 1–30.

Langenhorst F., Joreau P., and Doukhan J. C. 1995. Thermal and shock metamorphism of the Tenham chondrite: a TEM examination. *Geochimica et Cosmochimica Acta* 59:1835–1845.

Liu L. 1987. New silicate perovskites. *Geophysical Research Letters* 14:1079–1082.

Liu L., Ringwood A. E. 1975. Synthesis of a perovskite-type polymorph of $CaSiO_3$. *Earth and Planetary Science Letters* 28:209–211.

Llorca J., Trigo-Rodríguez J. M., Ortiz J. L., Docobo J. A., Garcia-Guinea J., Castro-Tirado A. J., Rubin A. E., Eugster O., Edwards W., Laubenstein M., and Casanova I. 2005. The Villalbeto de la Peña meteorite fall. I. Fireball energy, meteorite recovery, strewn field, and petrography. *Meteoritics & Planetary Science* 40:795–804.

Llorca J., Gich M., and Molins E. 2007. The Villalbeto de la Peña meteorite fall. III. Bulk chemistry, porosity, magnetic properties, ^{57}Fe Mössbauer spectroscopy, and Raman spectroscopy. *Meteoritics & Planetary Science* 42:A117–A182.

Ma C., Tchauner O., Beckett J. R., Liu Y., Rossman G. R., Zhuravlev K., Prakapenka V., Dera P., Taylor L. A. 2015. Tissintite, $(Ca,Na,\square)AlSi_2O_6$, a highly defective, shock-induced, high-pressure clinopyroxene in the Tissint martian meteorite. *Earth and Planetary Science Letters* 422:194–205.

Malavergne V., Guyot F., Benzerara K., and Martinez I. 2001. Description of new shock induce phases in the Shergotty, Zagami, Nakhla and Chassigny meteorites. *Meteoritics & Planetary Science* 36:1297–1305.

Martinez-Jimenez M., and Brearley A. J. 2017. Phase Transformation Mechanisms of Ca-Majorite in the Shocked Villalbeto de la Peña Ordinary Chondrite: Clues to Cooling Paths in Shocked Meteorites (abstract #6160). 80th Annual Meeting of the Meteoritical Society. *Meteoritics & Planetary Science* 52.

Miyahara M., Goresy A. E., Ohtani E., Nagase T., Nishijima M., Vashaei Z., Ferroir T., Gillet P., Dubrovinsky L, and Simionovici A. 2008. Evidence for fractional crystallization of wadsleyite and ringwoodite from olivine melts in chondrules entrained in shock-melt veins. *Proceedings of the National Academy of Sciences* 105:8542–8547.

Miyahara M., Ohtani E., Kimura M., El Goresy A., Ozawa S., Nagase T., Nishikima M., and Hiraga K. 2010. Coherent and subsequent incoherent ringwoodite growth in olivine of shocked L6 chondrites. *Earth and Planetary Science Letters* 295:321–327.

Miyahara M., Ohtani E., Ozawa S., Kimura M., El Goresy A., Sakai T., and Ohishi Y. 2011. Natural dissociation of olivine to $(Mg,Fe)SiO_3$ perovskite and magnesiowüstite in a shocked Martian meteorite. *Proceedings of the National Academy of Sciences* 108:5999–6003.

Miyahara M., Ohtani E., El Goresy A., Ozawa S., and Gillet P. 2016. Phase transition processes of olivine in the shocked Martian meteorite Tissint: Clues to origin of ringwoodite-, bridgmanite-and magnesiowüstite-bearing assemblages. *Physics of the Earth and Planetary Interiors* 259:18–28.

Oguri K., Funamori N., Skai F., Kondo T., Uchida T., and Yagi T. 1997. High-pressure and high-temperature phase relations in diopside $CaMgSi_2O_6$. *Physics of the Earth and Planetary Interiors* 104:363–370.

Ohtani E., Kimura Y., Kimura M., Takata T., Kondo T., and Kubo T. 2004. Formation of high-pressure minerals in shocked L6 chondrite Yamato 791384: Constraints on shock conditions and parent body size. *Earth and Planetary Science Letters* 227:505–515.

Ozawa S., Ohtani E., Miyahara M., Suzuki A., Kimura M., and Ito Y. 2009. Transformation textures, mechanisms of formation of high-pressure minerals in shock melt veins of L6 chondrites, and pressure-temperature conditions of the shock events. *Meteoritics & Planetary Science* 44:1771–1786.

Ribbe P. H., and Smith J. V. 1966. X-ray-emission microanalysis of rock-forming minerals: IV. Plagioclase. *The Journal of Geology* 74:217-233.

Sharp T. G., Lingemann C. M., Dupas C., and Stöffler D. 1997. Natural occurrence of $MgSiO_3$-ilmenite and evidence for $MgSiO_3$-perovskite in a shocked L chondrite. *Science* 277:352–355.

Sharp T. G., and DeCarli P. S. 2006. Shock effects in meteorites. In *Meteorites and the Early Solar System II*, edited by Lauretta, D. S. and McSween H. Y. Jr. Tucson, Arizona: University of Arizona Press. pp. 653–677.

Spray J. G., and Rae D. A. 1995. Quantitative electron-microprobe analysis of alkali silicate glasses: A review and user guide. *Canadian Mineralogist* 33:323–332.

Stöffler D., Keil K., and Scott E. R. D. 1991. Shock metamorphism of ordinary chondrites. *Geochimica et Cosmochimica Acta* 55:3845–3867.

Tomioka N., Fujino K., Ito E., Katsura T., Sharp T., and Kato T. 2002. Microstructures and structural phase transition in $(Mg,Fe)SiO_3$ majorite. *European Journal of Mineralogy* 14:7–14.

Tomioka N., and Kimura M. 2003. The breakdown of diopside to Ca-rich majorite and glass in shocked H chondrite. *Earth and Planetary Science Letters* 208:271–278.

Tomioka N., Miyahara M., and Ito M. 2016. Discovery of the natural $MgSiO_3$ tetragonal garnet in a shocked chondritic meteorite. *Science Advances* 2(3), doi: 10.1126/sciadv.1501725.

Tschauner O., Ma C., Beckett J. R., Prescher C., Prakapenka V. B., and Rossman G. R. 2014. Discovery of bridgmanite, the most abundant mineral in Earth, in a shocked meteorite. *Science* 346:1100–1102.

Tutti F. 2007. Formation of end-member $NaAlSi_3O_8$ hollandite-type structure (lingunite) in diamond anvil cell. *Physics of the Earth and Planetary Interiors* 161:143–149.

Van Mierlo W. L., Langenhorst F., Frost D. J., and Rubie D. C. 2013. Stagnation of subducting slabs in the transition zone due to slow diffusion in majoritic garnet. *Nature Geoscience* 6:400.

Xie X., Sharp T. G., and DeCarli P. S. 2006. High-pressure phases in a shock-induced melt vein of the Tenham L6 chondrite: Constraints on shock pressure and duration. *Geochimica et Cosmochimica Acta* 70:504–515.

Xie Z., and Sharp T. G. 2007. Host rock solid-state transformation in a shock-induced melt vein of Tenham L6 chondrite. *Earth and Planetary Science Letters* 254:433–445.

Zhang A., Hsu W., Wang R., and Ding M. 2006. Pyroxene polymorphs in melt veins of the heavily shocked Sixiangkou L6 chondrite. *European Journal of Mineralogy* 18:719–726.

APPENDICES

APPENDIX 1

Individual EPMA analyses in QUE 99177

1. Individual EPMA analyses of pyroxenes from chondrules (SIRs and chondrule interiors) that contain smooth rims.

Table A1.1. Individual EPMA analyses (oxides wt%) of pyroxenes in Ch1, Ch3, Ch8, Ch22, Ch23 (section 19), Ch13, and Ch14 (section 18).

Oxides wt%	Ch1	Ch1	Ch3	Ch3	Ch3	Ch3	Ch3	Ch8	Ch8	Ch8	Ch8
SiO_2	55.30	55.51	50.06	51.62	57.01	52.62	57.41	48.18	44.67	52.24	52.80
TiO_2	0.08	0.23	1.07	0.68	0.09	0.02	0.10	0.36	0.27	0.06	0.06
Al_2O_3	0.49	1.54	6.11	4.47	0.74	0.34	0.75	2.00	2.06	0.37	0.39
Cr_2O_3	1.53	2.43	2.90	2.56	0.96	0.40	0.74	2.46	1.48	0.56	0.59
SO_3	0.25	0.01	n.d.	0.02	0.01	0.57	0.07	0.03	n.d.	0.01	n.d.
FeO	5.76	2.08	2.59	1.90	2.34	27.41	3.10	2.60	17.19	2.50	1.97
MnO	1.20	1.72	1.95	1.72	0.38	0.57	0.21	3.39	1.81	0.15	0.14
MgO	35.34	28.78	16.53	20.29	36.62	12.82	38.67	23.92	14.91	38.37	38.38
CaO	0.70	9.34	18.31	16.57	0.51	0.48	0.43	11.99	9.89	0.27	0.33
Na_2O	0.02	0.03	0.22	0.06	0.01	0.20	0.01	0.08	0.10	0.01	0.01
K_2O	n.d.	n.d.	0.02	n.d.	n.d.	0.02	0.01	n.d.	0.06	0.01	n.d.
NiO	0.06	0.05	0.03	0.01	0.03	0.85	0.06	0.06	0.07	0.03	0.03
Total	100.75	101.72	99.87	99.99	98.71	96.32	101.56	95.10	92.57	94.59	94.69
formula based on 6 oxygens											
Si	1.91	1.92	1.83	1.86	1.97	2.08	1.93	1.84	1.86	1.89	1.90
Ti	n.d.	0.01	0.03	0.02	n.d.	n.d.	n.d.	0.01	0.01	n.d.	n.d.
Al	0.02	0.06	0.26	0.19	0.03	0.02	0.03	0.09	0.10	0.02	0.02
Cr	0.04	0.07	0.08	0.07	0.03	0.01	0.02	0.07	0.05	0.02	0.02
S	0.01	n.d.	n.d.	n.d.	n.d.	0.03	n.d.	n.d.	n.d.	n.d.	n.d.
Fe	0.17	0.06	0.08	0.06	0.07	0.91	0.09	0.08	0.60	0.08	0.06
Mn	0.04	0.05	0.06	0.05	0.01	0.02	0.01	0.11	0.06	n.d.	n.d.
Mg	1.82	1.49	0.90	1.09	1.88	0.76	1.94	1.36	0.93	2.07	2.06
Ca	0.03	0.35	0.72	0.64	0.02	0.02	0.02	0.49	0.44	0.01	0.01
Na	n.d.	n.d.	0.02	n.d.	n.d.	0.02	n.d.	0.01	0.01	n.d.	n.d.
K	n.d.	n.d.	n.d.	n.d.	n.d.	n.d.	n.d.	n.d.	n.d.	n.d.	n.d.
Ni	n.d.	n.d.	n.d.	n.d.	n.d.	0.05	n.d.	n.d.	0.01	n.d.	n.d.
Total	4.05	4.01	3.98	3.99	4.01	3.92	4.04	4.07	4.06	4.09	4.08
En	90	79	53	61	96	45	95	70	47	96	97
Wo	1	18	42	36	1	1	1	25	22	0	1
Fs	8	3	5	3	3	54	4	4	30	4	3

Table A1.1. *(Continued).* Individual EPMA analyses (oxides wt%) of pyroxenes in Chs 1, 3, 8, 22, 23 (section 19), 13, and 14 (section 18).

Oxides wt%	Ch22	Ch22	Ch22	Ch22	Ch22	Ch22	Ch22	Ch22	Ch22	Ch22	Ch22	Ch23
SiO_2	53.01	56.93	55.60	49.26	56.64	55.34	50.23	53.20	55.86	52.49	58.98	57.70
P_2O_5	n.d.	n.d.	0.04	0.05	n.d.	0.03	0.01	0.02	0.04	0.01	n.d.	0.01
TiO_2	0.47	0.11	0.12	0.54	0.17	0.12	0.14	0.44	0.38	0.67	0.18	0.14
Al_2O_3	8.19	0.87	0.86	7.07	1.04	0.85	0.85	3.55	2.22	3.70	0.97	0.82
Cr_2O_3	1.98	0.69	0.70	2.61	0.50	0.69	0.61	1.80	0.97	1.33	0.50	1.82
SO_3	0.14	n.d.	n.d.	n.d.	n.d.	0.05	0.02	0.10	0.12	0.09	0.03	n.d.
FeO	6.74	1.06	1.00	4.87	1.03	1.01	5.24	1.81	8.79	2.40	1.00	2.14
MnO	4.24	0.12	0.14	5.29	0.08	0.11	0.11	1.65	0.62	0.55	0.05	1.07
MgO	8.75	37.16	37.70	11.79	38.73	37.63	32.86	19.96	13.95	19.15	39.79	37.87
CaO	11.80	0.53	0.54	14.96	0.41	0.53	0.41	18.22	14.34	20.35	0.42	0.65
Na_2O	2.49	n.d.	n.d.	0.43	0.02	n.d.	n.d.	0.08	0.06	0.05	n.d.	0.01
K_2O	0.02	n.d.	n.d.	0.01	n.d.	n.d.	0.02	0.01	0.02	n.d.	n.d.	n.d.
NiO	0.10	0.05	0.03	0.07	0.01	0.04	0.13	0.07	0.08	0.10	0.08	0.04
Total	97.93	97.53	96.73	96.94	98.64	96.40	90.64	100.90	97.44	100.88	101.99	102.26
					formula based on 6 oxygens							
Si	1.97	1.97	1.95	1.88	1.94	1.94	1.92	1.90	2.07	1.88	1.95	1.93
Ti	0.01	n.d.	n.d.	0.02	n.d.	n.d.	n.d.	0.01	0.01	0.02	n.d.	n.d.
Al	0.36	0.04	0.04	0.32	0.04	0.04	0.04	0.15	0.10	0.16	0.04	0.03
Cr	0.06	0.02	0.02	0.08	0.01	0.02	0.02	0.05	0.03	0.04	0.01	0.05
S	0.01	n.d.	n.d.	n.d.	n.d.	n.d.	n.d.	0.01	0.01	n.d.	n.d.	n.d.
Fe	0.21	0.03	0.03	0.16	0.03	0.03	0.17	0.05	0.27	0.07	0.03	0.06
Mn	0.13	n.d.	n.d.	0.17	n.d.	n.d.	n.d.	0.05	0.02	0.02	n.d.	0.03
Mg	0.49	1.92	1.97	0.67	1.98	1.97	1.87	1.06	0.77	1.02	1.96	1.89
Ca	0.47	0.02	0.02	0.61	0.02	0.02	0.02	0.70	0.57	0.78	0.01	0.02
Na	0.18	n.d.	n.d.	0.03	n.d.	n.d.	n.d.	0.01	n.d.	n.d.	n.d.	n.d.
K	n.d.	n.d.	n.d.	n.d.	n.d.	n.d.	n.d.	n.d.	n.d.	n.d.	n.d.	n.d.
Ni	0.01	n.d.	n.d.	n.d.	n.d.	n.d.	0.01	n.d.	n.d.	0.01	n.d.	n.d.
Total	3.90	4.00	4.02	3.93	4.03	4.03	4.05	3.99	3.86	4.00	4.02	4.02
En	42	97	98	47	98	98	91	59	48	55	98	96
Wo	40	1	1	43	1	1	1	38	35	42	1	1
Fs	18	2	1	11	1	1	8	3	17	4	1	3

Table A1.1. *(Continued).* Individual EPMA analyses (oxides wt%) of pyroxenes in Chs 1, 3, 8, 22, 23 (section 19), 13, and 14 (section 18).

Oxides wt%	Ch14	Ch14	Ch14	Ch14	Ch14	Ch14	Ch13	Ch13	Ch13	Ch13	Ch13	Ch13
SiO_2	37.37	51.45	49.27	50.47	44.32	41.89	49.92	43.79	44.81	43.33	45.50	43.59
P_2O_5	0.03	n.d.	n.d.	n.d.	0.09	0.11	0.01	0.02	0.02	0.03	0.05	0.03
TiO_2	0.74	0.09	0.09	0.11	0.57	1.44	0.08	0.38	0.23	0.40	0.21	0.25
Al_2O_3	2.87	0.55	1.48	0.48	3.89	5.09	0.43	1.88	1.57	1.84	0.98	7.48
Cr_2O_3	1.62	0.65	0.62	1.68	2.40	4.45	0.64	2.11	1.29	2.00	1.80	1.60
SO_3	n.d.	0.03	n.d.	0.01	n.d.	0.01	0.01	0.03	0.03	0.02	n.d.	0.02
FeO	20.01	1.96	3.28	2.51	1.34	2.26	2.32	5.26	12.81	6.04	5.39	5.87
MnO	1.91	0.04	0.05	0.90	1.14	3.00	0.10	2.29	1.93	2.08	2.46	2.15
MgO	10.81	37.61	31.39	35.39	18.82	15.29	38.17	23.66	20.07	22.02	29.87	22.13
CaO	8.06	0.39	0.38	1.46	19.38	18.77	0.31	9.67	3.83	9.69	3.60	7.17
Na_2O	0.10	n.d.	0.01	n.d.	0.02	0.05	0.01	0.08	0.26	0.12	0.05	0.68
K_2O	0.13	n.d.	0.02	0.01	n.d.	n.d.	n.d.	0.01	0.08	n.d.	n.d.	0.01
NiO	0.14	0.11	0.20	0.05	0.02	0.03	0.03	n.d.	0.78	0.04	0.06	0.05
Total	83.78	92.87	86.79	93.07	92.01	92.41	92.03	89.19	87.71	87.60	89.98	91.02
formula based on 6 oxygens												
Si	1.78	1.89	1.94	1.88	1.77	1.70	1.86	1.80	1.90	1.82	1.82	1.73
Ti	0.03	n.d.	n.d.	n.d.	0.02	0.04	n.d.	0.01	0.01	0.01	0.01	0.01
Al	0.16	0.02	0.07	0.02	0.18	0.24	0.02	0.09	0.08	0.09	0.05	0.35
Cr	0.06	0.02	0.02	0.05	0.08	0.14	0.02	0.07	0.04	0.07	0.06	0.05
S	n.d.	n.d.	n.d.	n.d.	n.d.	n.d.	n.d.	n.d.	n.d.	n.d.	n.d.	n.d.
Fe	0.80	0.06	0.11	0.08	0.04	0.08	0.07	0.18	0.45	0.21	0.18	0.20
Mn	0.08	n.d.	n.d.	0.03	0.04	0.10	n.d.	0.08	0.07	0.07	0.08	0.07
Mg	0.77	2.06	1.85	1.96	1.12	0.93	2.12	1.45	1.27	1.38	1.78	1.31
Ca	0.41	0.02	0.02	0.06	0.83	0.82	0.01	0.43	0.17	0.44	0.15	0.31
Na	0.01	n.d.	n.d.	n.d.	n.d.	n.d.	n.d.	0.01	0.02	0.01	n.d.	0.05
K	0.01	n.d.	n.d.	n.d.	n.d.	n.d.	n.d.	n.d.	n.d.	n.d.	n.d.	n.d.
Ni	0.01	0.01	0.01	n.d.	n.d.	n.d.	n.d.	n.d.	0.05	n.d.	n.d.	n.d.
Total	4.10	4.09	4.02	4.08	4.08	4.06	4.12	4.11	4.07	4.10	4.13	4.09
En	39	96	94	94	56	51	96	70	67	68	84	72
Wo	21	1	1	3	42	45	1	21	9	22	7	17
Fs	40	3	5	4	2	4	3	9	24	10	9	11

n.d. = not detected

2. Individual EPMA analyses of mesostasis regions in chondrules (SIRs and chondrule interiors) that contain smooth rims.

Table A1.2. Individual EPMA analyses (oxides wt%) of mesostasis regions in Ch1.

Oxides wt%	1	2	3	4	5	6	7	8	9	10	11	Mean
SiO_2	60.83	63.64	63.53	60.38	36.82	37.85	40.44	86.41	43.49	68.66	52.82	55.90
P_2O_5	0.01	n.d.	0.01	n.d.	0.28	0.13	0.13	0.03	n.d.	0.05	0.05	0.06
TiO_2	0.08	0.10	0.09	0.08	0.08	0.07	0.06	0.09	0.06	0.55	1.34	0.24
Al_2O_3	19.57	20.49	20.59	17.46	1.19	6.71	4.68	1.19	34.35	9.25	12.09	13.41
Cr_2O_3	0.02	0.03	0.04	0.20	0.19	0.07	0.08	0.05	n.d.	0.03	0.45	0.11
SO_3	n.d.	n.d.	n.d.	n.d.	n.d.	n.d.	n.d.	n.d.	n.d.	n.d.	n.d.	n.d.
FeO	2.32	0.54	0.46	2.15	38.00	35.70	35.27	6.24	0.32	8.41	7.50	12.45
MnO	0.09	0.08	0.08	0.40	0.32	0.24	0.38	0.07	0.01	n.d.	0.19	0.17
MgO	0.52	0.41	0.44	4.23	1.29	4.16	1.61	0.30	0.80	0.89	9.27	2.18
CaO	9.25	9.39	9.31	7.29	0.62	1.24	1.77	0.50	18.95	4.34	13.01	6.88
Na_2O	1.93	2.04	1.95	2.92	0.41	0.54	0.56	0.29	0.10	0.11	0.08	0.99
K_2O	0.02	0.03	0.02	0.03	0.05	0.01	0.06	0.01	0.01	0.02	0.01	0.02
NiO	0.03	0.03	n.d.	0.04	0.93	0.05	0.11	0.11	0.01	0.22	0.25	0.16
Total	94.67	96.77	96.51	95.17	80.19	86.78	85.15	95.31	98.09	92.53	97.06	92.57

n.d. = not detected

Table A1.3. Individual EPMA analyses (oxides wt%) of mesostasis regions in Ch3 (Silica-rich Igneous Rim and chondrule interior).

Oxides wt%	Sp1(SIR)	Sp2(SIR)	Sp3(SIR)	Sp4(SIR)	Sp5(SIR)	Sp6(SIR)	Sp7(SIR)	Sp8(SIR)	Sp9(SIR)	Sp10(SIR)	Sp11(SIR)	Sp12(SIR)	Sp13(SIR)
SiO_2	83.84	76.23	74.04	54.44	63.63	75.59	69.25	67.17	73.17	66.79	62.96	91.20	80.01
P_2O_5	0.03	0.02	0.06	0.07	0.03	0.01	n.d.	0.03	0.02	0.01	n.d.	0.01	0.02
TiO_2	0.09	0.18	0.11	0.09	0.05	0.24	0.18	0.17	0.19	0.38	0.34	0.05	0.15
Al_2O_3	3.76	7.55	5.27	3.36	3.61	15.83	13.22	13.34	7.37	17.50	17.23	1.07	7.26
Cr_2O_3	0.12	0.29	0.04	0.21	0.03	0.02	0.04	0.08	0.39	0.28	0.24	0.01	0.06
SO_3	0.13	0.17	0.41	0.59	0.23	0.04	0.12	0.13	0.09	n.d.	n.d.	n.d.	n.d.
FeO	6.11	6.26	10.80	8.00	10.36	0.84	2.39	3.56	3.53	0.82	2.75	5.16	3.60
MnO	0.29	0.75	0.22	0.68	0.12	0.41	0.72	0.82	1.03	1.08	0.91	0.08	0.34
MgO	1.33	1.74	0.25	3.52	0.70	0.51	0.36	0.69	1.77	1.68	2.07	0.55	0.32
CaO	0.50	1.59	0.26	0.49	0.18	0.52	0.23	0.62	2.32	6.98	7.14	0.10	0.14
Na_2O	0.65	1.01	1.38	1.27	0.92	2.04	0.03	0.04	0.11	3.91	3.75	0.63	3.94
K_2O	0.66	1.68	1.29	0.62	0.45	3.10	1.66	0.53	0.41	0.57	0.66	0.03	1.32
NiO	0.27	0.42	0.67	2.41	0.35	0.03	0.16	0.23	0.18	n.d.	0.24	0.14	0.14
Total	97.78	97.88	94.80	75.75	80.64	99.19	88.36	87.41	90.57	99.99	98.28	99.04	97.31

Oxides wt%	Sp14(SIR)	Mean SIR	Sp1 (Int)	Sp2 (Int)	Sp3 (Int)	Sp4 (Int)	Sp5 (Int)	Sp6 (Int)	Sp7 (Int)	Sp8 (Int)	Sp9 (Int)	Mean Int
SiO_2	58.55	71.21	52.43	61.71	73.77	73.30	72.21	72.41	75.32	70.76	74.51	69.60
P_2O_5	0.03	0.02	n.d.	n.d.	0.06	0.06	0.02	0.05	0.04	0.04	n.d.	0.03
TiO_2	0.13	0.17	0.27	0.28	0.72	0.87	0.54	0.59	0.90	0.53	0.92	0.62
Al_2O_3	1.09	8.39	19.08	20.65	13.34	11.50	13.50	15.00	12.23	12.55	11.71	14.39
Cr_2O_3	1.36	0.23	0.34	0.21	0.07	0.12	0.04	0.08	0.13	0.02	0.16	0.13
SO_3	n.d.	0.14	n.d.	n.d.	0.01	n.d.	n.d.	0.01	0.01	n.d.	0.03	0.01
FeO	3.09	4.81	7.98	1.08	1.17	1.50	2.54	0.93	0.80	4.20	3.02	2.58
MnO	1.19	0.62	0.56	0.39	0.65	0.88	0.64	0.66	0.88	0.37	0.88	0.66
MgO	32.81	3.45	4.08	1.51	0.82	1.33	0.58	0.76	1.45	0.93	1.42	1.43
CaO	2.60	1.69	10.20	10.07	4.67	4.60	4.27	5.81	5.00	5.80	4.24	6.07
Na_2O	0.06	1.41	2.51	2.95	0.73	0.25	1.33	1.19	0.15	1.65	0.79	1.28
K_2O	0.02	0.93	0.23	0.36	1.12	0.96	1.03	0.92	0.87	0.04	1.13	0.74
NiO	0.18	0.39	0.24	0.04	0.04	0.08	0.16	0.03	0.03	0.07	0.13	0.09
Total	101.11	93.44	97.90	99.24	97.17	95.46	96.86	98.43	97.81	96.95	98.92	97.64

n.d. = not detected
Int = chondrule interior

Table A1.4. Individual EPMA analyses (oxides wt%) of mesostasis regions in Ch8 (SIR).

Oxides wt%	Sp1(SIR)	Sp2(SIR)	Sp3(SIR)	Sp4(SIR)	Sp5(SIR)	Sp6(SIR)	Sp7(SIR)	Sp8(SIR)	Sp9(SIR)	Sp10(SIR)	Sp11(SIR)
SiO_2	82.18	69.74	61.87	71.02	71.66	71.85	70.26	69.55	66.55	70.64	72.14
P_2O_5	n.d.	0.05	0.03	n.d.	n.d.	0.02	n.d.	0.01	n.d.	n.d.	0.04
TiO_2	0.17	0.14	0.13	0.33	0.22	0.29	0.33	0.36	0.19	0.30	0.28
Al_2O_3	4.61	9.34	10.08	17.06	15.83	15.03	14.34	15.92	18.07	16.18	15.94
Cr_2O_3	0.42	0.02	0.03	0.31	0.15	0.08	0.51	0.49	0.06	0.18	0.14
SO_3	0.03	0.51	0.08	n.d.	n.d.	n.d.	n.d.	n.d.	0.03	n.d.	0.02
FeO	3.63	9.87	16.73	1.09	1.00	2.48	0.88	0.92	10.12	2.91	1.09
MnO	0.84	0.96	0.24	0.47	0.45	0.65	0.59	0.60	0.14	0.81	0.70
MgO	3.13	0.52	1.11	1.32	1.40	0.62	2.99	2.95	0.83	1.41	1.37
CaO	3.08	0.71	0.38	1.41	1.28	0.30	3.77	3.89	1.17	2.10	1.97
Na_2O	0.58	1.48	5.36	9.40	8.11	9.37	7.64	3.25	2.03	0.28	0.20
K_2O	0.53	1.11	0.20	1.20	1.47	1.25	1.11	0.92	1.99	1.30	1.06
NiO	0.03	0.69	0.03	0.05	0.03	0.30	0.04	0.01	0.37	0.05	0.03
Total	99.25	95.13	96.26	103.65	101.60	102.24	102.46	98.89	101.55	96.17	94.99

(Cont.)	Sp12(SIR)	Sp13(SIR)	Sp14(SIR)	Sp15(SIR)	Sp16(SIR)	Sp17(SIR)	Sp18(SIR)	Sp19(SIR)	Sp20(SIR)	Sp21(SIR)	Mean SIR
SiO_2	72.89	72.85	76.56	64.49	64.75	56.05	66.77	63.49	69.57	66.98	67.51
P_2O_5	n.d.	n.d.	0.01	0.01	0.04	n.d.	n.d.	0.01	0.02	n.d.	n.d.
TiO_2	0.32	0.35	0.32	0.32	0.31	0.53	0.24	0.25	0.29	0.32	0.32
Al_2O_3	17.01	17.16	16.80	18.02	18.07	12.67	16.31	14.45	15.30	13.90	13.36
Cr_2O_3	0.27	0.26	0.05	0.16	0.13	1.23	0.22	0.10	0.17	0.04	0.11
SO_3	0.01	n.d.	n.d.	0.02	n.d.	n.d.	0.02	n.d.	n.d.	n.d.	0.02
FeO	1.04	0.94	1.18	0.91	0.81	1.07	0.81	2.75	0.79	3.13	1.06
MnO	0.74	0.81	0.69	0.48	0.48	1.33	0.35	1.05	0.40	0.60	1.05
MgO	1.87	1.88	0.37	1.08	1.14	6.39	1.29	0.58	1.58	0.35	0.85
CaO	2.82	3.08	2.01	1.35	1.47	9.08	2.06	2.00	1.61	0.26	2.32
Na_2O	0.06	0.10	0.24	0.39	0.45	0.58	0.66	0.52	0.25	1.01	0.39
K_2O	0.77	0.98	0.83	1.19	1.26	0.22	1.07	1.45	1.12	0.85	1.24
NiO	0.03	0.04	0.04	0.04	0.02	0.04	0.04	0.10	n.d.	0.05	0.03
Total	97.83	98.45	99.09	88.45	88.93	89.20	89.84	86.75	91.12	87.49	88.25

Table A1.4. (*Continuation*). Individual EPMA analyses (oxides wt%) of mesostasis regions in Ch8 (interior).

Oxides wt%	Sp1 (Int)	Sp2 (Int)	Sp3 (Int)	Sp4 (Int)	Sp5 (Int)	Mean Int
SiO_2	62.68	57.11	55.70	52.69	48.95	60.17
P_2O_5	0.02	n.d.	n.d.	n.d.	0.02	0.02
TiO_2	0.37	0.15	0.61	0.67	0.43	0.27
Al_2O_3	18.91	25.56	20.89	20.93	21.62	20.08
Cr_2O_3	0.20	0.03	0.47	0.46	0.44	0.07
SO_3	n.d.	n.d.	n.d.	n.d.	n.d.	n.d.
FeO	1.50	0.50	1.02	2.33	4.19	1.01
MnO	0.51	0.22	0.14	0.22	0.25	0.47
MgO	1.59	0.58	4.33	5.58	5.78	0.75
CaO	8.07	10.16	15.24	14.59	13.92	7.38
Na_2O	4.71	4.58	0.64	1.11	0.79	3.19
K_2O	0.56	0.25	n.d.	0.08	0.02	0.47
NiO	0.07	0.06	0.04	0.18	0.40	0.04
Total	99.18	99.20	99.09	98.85	96.80	93.91

n.d. = not detected
Int = chondrule interior

Table A1.5. Individual EPMA analyses (oxides wt%) of mesostasis regions in Ch22 (Silica-rich Igneous Rim and chondrule interior).

Oxides wt%	Sp1 (SIR)	Sp2 (SIR)	Sp3 (SIR)	Sp4 (SIR)	Sp5 (SIR)	Mean SIR	Sp1 (Int)	Sp2 (Int)	Sp3 (Int)	Mean Int
SiO_2	50.87	59.28	49.93	64.13	54.22	3.40	53.12	54.43	52.75	3.71
P_2O_5	0.06	0.01	0.08	0.01	0.02	3.02	0.08	0.10	0.09	2.98
TiO_2	0.07	0.36	0.09	0.04	0.05	13.22	0.04	0.07	0.05	26.92
Al_2O_3	11.01	9.00	24.68	13.25	8.14	55.69	27.84	25.36	27.55	53.43
Cr_2O_3	0.05	1.48	0.02	0.02	0.16	0.20	0.05	0.18	0.06	0.06
SO_3	0.71	0.16	n.d.	0.18	0.50	5.04	0.01	n.d.	0.02	11.35
FeO	20.04	4.47	2.51	10.54	23.05	0.12	0.79	0.35	1.81	0.06
MnO	0.22	2.17	0.13	0.25	0.99	0.35	0.07	0.37	0.09	0.10
MgO	0.90	10.61	1.69	0.60	1.30	0.75	1.57	5.82	1.56	0.18
CaO	0.47	12.47	11.12	0.10	1.02	12.12	11.69	10.96	11.41	0.98
Na_2O	0.47	1.05	4.04	6.75	4.68	0.18	4.30	2.60	4.23	0.10
K_2O	0.44	0.35	0.06	0.09	0.07	0.31	0.08	0.04	0.07	0.01
NiO	0.33	0.15	0.14	0.08	0.22	0.04	0.08	0.02	0.20	0.09
Total	85.65	101.54	94.48	96.05	94.42	94.43	99.72	100.30	99.87	99.96

n.d. = not detected

Int = chondrule interior

Table A1.6 Individual EPMA analyses (oxides wt%) of mesostasis regions in Ch14 (SIR).

Oxides wt%	Sp1 (SIR)	Sp2 (SIR)	Sp3 (SIR)	Sp4 (SIR)	Sp5 (SIR)	Mean SIR
SiO_2	41.54	85.40	84.49	54.53	76.66	68.52
P_2O_5	0.10	n.d.	n.d.	0.02	n.d.	0.02
TiO_2	0.07	0.11	0.06	0.09	0.10	0.08
Al_2O_3	23.77	0.32	2.04	19.63	3.67	9.89
Cr_2O_3	n.d.	0.03	n.d.	0.09	0.01	0.02
SO_3	0.01	n.d.	n.d.	0.02	0.01	0.01
FeO	6.78	0.42	0.74	1.05	1.12	2.02
MnO	0.12	0.03	0.01	0.14	0.01	0.06
MgO	0.91	0.14	0.16	1.20	0.30	0.54
CaO	12.82	0.33	0.99	11.32	1.97	5.49
Na_2O	1.41	0.02	0.08	1.45	0.19	0.63
K_2O	0.10	0.02	0.01	0.05	0.01	0.04
NiO	0.33	0.01	0.01	n.d.	0.04	0.08
Total	87.94	86.84	88.59	89.58	84.07	87.40

n.d. = not detected

3. Individual EPMA analyses of smooth rims around chondrules

Table A1.7. Individual EPMA analyses (oxides wt%) of smooth rims around Ch1 in QUE 99177,19, n=23.

Oxides wt%	Sp1	Sp2	Sp3	Sp4	Sp5	Sp6	Sp7	Sp8	Sp9	Sp10	Sp11	Sp12	Sp13	Sp14
SiO_2	33.96	37.90	35.83	31.55	35.30	34.90	35.83	36.64	29.06	29.33	32.79	27.39	28.01	33.60
P_2O_5	0.21	0.17	0.23	3.08	0.19	0.17	0.16	0.15	0.19	0.19	0.25	0.23	0.21	0.37
TiO_2	0.03	0.03	0.04	0.03	0.05	0.05	0.04	0.04	0.01	0.16	0.04	0.18	0.03	0.05
Al_2O_3	1.96	2.02	1.57	1.33	1.10	1.16	0.84	0.80	0.54	3.11	1.73	6.30	0.86	2.58
Cr_2O_3	0.23	0.09	0.26	0.04	0.18	0.05	0.08	0.05	0.05	0.13	0.19	0.09	0.07	0.41
FeO	38.83	38.29	38.79	33.20	37.34	38.81	39.45	40.35	41.77	40.95	37.66	43.37	42.24	34.57
MgO	7.32	6.22	5.84	4.88	5.33	3.98	4.38	3.78	2.81	2.66	5.84	2.40	2.03	8.44
CaO	1.19	0.21	0.33	4.35	0.36	0.13	0.21	0.14	0.10	0.67	0.30	0.37	0.14	0.61
MnO	0.26	0.29	0.30	0.26	0.33	0.23	0.31	0.27	0.22	0.90	0.29	0.23	0.26	0.52
Na_2O	0.17	0.07	0.08	0.36	0.16	0.18	0.18	0.21	0.07	0.08	0.12	0.23	0.08	0.10
K_2O	0.03	0.02	0.01	0.05	0.07	0.07	0.05	0.07	0.05	0.06	0.05	0.12	0.07	0.02
NiO	0.45	0.39	0.36	0.68	0.72	0.81	0.68	0.55	0.69	0.73	0.70	0.72	0.63	0.63
SO_3	0.45	0.07	0.05	0.03	0.09	0.04	0.09	0.02	0.05	0.06	0.06	0.07	0.02	0.16
Total	85.96	85.77	83.68	79.85	81.21	80.59	82.30	83.06	75.60	79.04	80.02	81.69	74.66	82.05

Oxides wt%	Sp15	Sp16	Sp17	Sp18	Sp19	Sp20	Sp21	Sp22	Sp23	Mean	σ
SiO_2	34.67	35.45	36.38	32.76	37.42	38.01	39.92	29.48	40.50	34.20	3.69
P_2O_5	0.25	0.31	0.27	0.28	0.33	0.20	0.73	0.20	0.29	0.38	0.60
TiO_2	0.03	0.04	0.03	0.03	0.03	0.11	0.17	0.33	0.10	0.07	0.07
Al_2O_3	2.86	3.33	3.02	3.08	3.10	1.41	1.41	9.15	2.98	2.45	1.94
Cr_2O_3	0.10	0.15	0.11	0.16	0.31	2.00	3.51	0.14	1.17	0.42	0.81
FeO	36.28	35.60	38.31	37.26	34.41	29.69	26.42	38.65	30.64	37.08	4.13
MgO	6.95	8.02	5.78	6.74	9.32	8.00	7.79	4.67	9.22	5.76	2.19
CaO	0.14	0.23	0.11	0.13	0.54	2.74	4.47	0.90	2.33	0.90	1.30
MnO	0.28	0.26	0.21	0.23	0.38	0.48	0.80	0.18	0.90	0.37	0.21
Na_2O	0.02	0.13	0.04	0.07	0.13	1.02	1.93	0.19	0.44	0.26	0.42
K_2O	0.02	0.03	0.02	0.03	0.03	0.03	0.02	0.03	0.04	0.04	0.03
NiO	0.53	0.71	0.71	1.05	0.64	0.48	0.74	0.86	0.65	0.70	0.20
SO_3	0.08	0.20	0.24	0.67	0.08	0.04	0.07	0.38	0.16	0.14	0.16
Total	82.21	84.46	85.23	82.49	86.71	84.22	87.98	85.17	89.41	82.75	3.57

Table A1.8. Individual EPMA analyses (oxides wt%) of smooth rims around Ch3 in QUE 99177,19, n=22.

Oxides wt%	Sp1	Sp2	Sp3	Sp4	Sp5	Sp6	Sp7	Sp8	Sp9	Sp10	Sp11	Sp12	Sp13	Sp14
SiO_2	39.92	39.38	38.54	41.08	39.13	39.00	44.71	38.16	40.51	39.37	45.77	37.83	37.68	42.54
P_2O_5	0.08	0.66	0.07	0.26	0.07	0.09	0.07	0.12	0.07	0.19	0.11	0.19	0.17	0.11
TiO_2	n.d.	0.03	0.05	0.04	0.04	0.06	0.12	0.04	0.04	0.03	0.17	0.05	0.03	0.08
Al_2O_3	0.47	1.41	2.21	1.81	1.17	1.63	1.43	0.90	1.73	2.28	1.50	3.75	1.42	1.93
Cr_2O_3	0.04	0.10	0.05	0.10	0.09	0.06	1.26	0.08	0.27	0.05	1.62	0.10	0.03	0.57
FeO	37.63	36.61	35.04	34.15	39.33	38.14	24.42	37.80	32.66	36.14	22.49	36.09	39.08	31.08
MgO	4.79	3.83	5.64	6.29	1.45	3.65	9.45	4.43	6.30	5.77	11.05	3.66	2.62	8.38
CaO	0.13	1.14	0.18	0.60	0.35	0.45	6.74	0.39	0.89	0.40	6.57	0.44	0.23	2.58
MnO	0.47	0.72	0.47	0.58	0.88	0.57	1.13	0.43	0.65	0.50	1.59	0.62	0.65	1.16
Na_2O	0.16	0.16	0.22	0.24	0.07	0.10	0.69	0.35	0.28	0.09	0.89	0.13	0.07	0.19
K_2O	0.10	0.11	0.14	0.14	0.21	0.15	0.09	0.17	0.14	0.21	0.15	0.22	0.15	0.10
NiO	0.24	0.15	0.25	0.26	0.17	0.20	0.23	0.31	0.29	0.26	0.19	0.31	0.32	0.28
SO_3	0.04	0.02	0.15	0.11	0.07	0.08	0.32	0.19	0.06	0.13	0.15	0.41	0.27	0.40
Total	84.08	84.32	83.04	85.67	83.02	84.18	90.67	83.38	83.90	85.42	92.23	83.78	82.72	89.40

Oxides wt%	Sp15	Sp16	Sp17	Sp18	Sp19	Sp20	Sp21	Sp22	Mean	σ
SiO_2	42.32	38.37	38.78	35.74	37.24	35.66	37.04	39.40	39.46	2.57
P_2O_5	0.12	0.70	0.04	1.15	0.03	0.09	1.02	0.03	0.25	0.32
TiO_2	0.09	0.01	0.04	0.06	0.01	0.04	0.03	0.06	0.05	0.04
Al_2O_3	2.06	1.69	0.38	1.82	0.48	1.95	1.50	1.56	1.59	0.72
Cr_2O_3	0.80	0.10	0.05	0.25	0.03	0.02	0.06	0.06	0.26	0.43
FeO	31.06	37.89	38.43	32.29	36.07	38.35	34.88	39.27	34.95	4.52
MgO	6.67	3.56	2.97	6.21	5.15	1.13	6.40	1.61	5.05	2.53
CaO	2.78	1.47	0.14	2.57	0.13	0.17	1.43	0.40	1.37	1.90
MnO	1.07	0.60	0.58	0.74	0.43	0.73	0.55	0.78	0.72	0.29
Na_2O	0.42	0.08	0.07	0.11	0.06	0.02	0.07	0.04	0.21	0.22
K_2O	0.09	0.12	0.23	0.05	0.11	0.09	0.08	0.15	0.14	0.05
NiO	0.29	0.26	0.20	0.22	0.28	0.18	0.30	0.11	0.24	0.06
SO_3	0.06	0.17	0.04	0.03	0.05	0.06	0.03	0.02	0.13	0.12
Total	87.85	85.02	81.96	81.23	80.07	78.49	83.39	83.51	84.42	3.24

Table A1.9. Individual EPMA analyses (oxides wt%) of smooth rims around Ch8 in QUE 99177,19, n=26.

Oxides wt%	Sp1	Sp2	Sp3	Sp4	Sp5	Sp6	Sp7	Sp8	Sp9	Sp10	Sp11	Sp12	Sp13	Sp14
SiO_2	37.90	33.65	35.01	36.58	36.39	32.17	45.51	37.03	33.93	27.58	32.12	35.92	39.81	34.82
P_2O_5	0.03	0.03	n.d.	0.03	0.01	0.05	0.02	0.02	n.d.	0.30	n.d.	0.04	0.08	n.d.
TiO_2	0.17	0.12	0.02	0.08	0.03	0.01	0.12	0.10	0.03	0.04	0.08	0.08	0.08	0.08
Al_2O_3	3.79	4.72	3.55	2.90	2.36	1.96	6.66	1.76	1.81	1.27	3.20	2.19	0.81	2.97
Cr_2O_3	0.57	0.03	0.06	0.08	0.07	0.18	0.04	0.22	0.05	0.24	0.07	0.13	0.18	0.06
FeO	32.41	40.11	38.88	40.31	40.51	35.09	28.81	34.74	41.48	34.66	42.12	39.51	28.11	39.06
MgO	6.05	2.13	3.23	2.42	3.31	4.69	1.08	4.35	2.46	8.89	1.60	1.78	4.73	2.13
CaO	5.16	0.16	0.18	0.30	0.46	0.38	0.28	5.11	0.37	5.00	0.62	1.13	10.53	0.74
MnO	1.07	0.31	0.25	0.34	0.30	0.34	0.41	1.08	0.23	0.23	0.31	0.52	1.91	0.37
Na_2O	0.29	0.07	0.05	0.04	0.34	0.37	0.50	0.35	0.06	1.33	0.53	0.22	1.05	0.55
K_2O	0.19	0.36	0.31	0.23	0.19	0.22	0.38	0.11	0.16	0.11	0.27	0.23	0.07	0.23
NiO	0.01	n.d.	0.04	0.02	0.02	0.13	n.d.	n.d.	0.01	0.17	0.02	n.d.	n.d.	n.d.
SO_3	0.18	0.03	0.02	0.07	0.26	2.42	0.07	0.04	0.29	1.46	0.63	0.08	0.12	0.06
Total	87.83	81.72	81.62	83.37	84.26	78.01	83.88	84.93	80.89	81.27	81.56	81.81	87.49	81.07

Oxides wt%	Sp15	Sp16	Sp17	Sp18	Sp19	Sp20	Sp21	Sp22	Sp23	Sp24	Sp25	Sp26	Mean	σ
SiO_2	24.64	31.90	34.36	35.10	33.35	32.67	34.01	32.56	32.44	33.80	23.07	34.73	33.89	4.37
P_2O_5	0.07	0.01	0.04	n.d.	0.05	0.01	0.01	n.d.	0.03	0.02	0.13	n.d.	0.04	0.06
TiO_2	0.04	0.06	0.04	0.06	n.d.	n.d.	0.01	n.d.	0.01	0.02	n.d.	0.05	0.05	0.04
Al_2O_3	1.12	4.04	2.14	3.12	0.73	1.04	1.03	0.53	1.02	0.42	0.03	1.29	2.17	1.54
Cr_2O_3	0.11	0.13	0.17	0.17	0.01	0.02	0.08	0.04	0.03	0.21	1.34	0.05	0.17	0.26
FeO	48.85	39.22	33.95	34.01	42.16	41.82	40.69	42.50	43.14	41.12	40.23	42.10	38.68	4.69
MgO	3.94	3.03	5.29	4.35	2.32	2.39	2.67	2.80	2.36	3.88	1.49	1.62	3.27	1.72
CaO	4.27	0.57	3.34	5.22	0.17	0.21	1.68	0.13	0.14	1.05	0.17	1.08	1.86	2.56
MnO	0.78	0.31	0.58	0.98	0.22	0.25	0.52	0.21	0.26	0.46	0.17	0.50	0.50	0.39
Na_2O	0.60	0.08	0.25	0.35	0.08	0.06	0.09	0.13	0.18	0.21	0.71	0.20	0.34	0.32
K_2O	0.06	0.33	0.12	0.15	0.15	0.15	0.11	0.08	0.11	0.08	0.08	0.18	0.18	0.09
NiO	0.07	n.d.	0.07	0.01	n.d.	0.03	n.d.	0.02	0.03	0.04	0.55	0.06	0.05	0.11
SO_3	0.28	0.04	0.03	0.13	0.07	0.10	0.09	0.09	0.04	0.38	6.24	0.18	0.52	1.28
Total	84.82	79.71	80.37	83.64	79.31	78.77	80.99	79.10	79.77	81.70	74.21	82.02	81.70	2.91

Table A1.10. Individual EPMA analyses (oxides wt%) of smooth rims around Ch22 in QUE 99177,19, n=30.

Oxides wt%	Sp1	Sp2	Sp3	Sp4	Sp5	Sp6	Sp7	Sp8	Sp9	Sp10	Sp11	Sp12	Sp13	Sp14
SiO_2	40.65	37.08	40.80	41.61	37.83	38.00	38.24	38.67	35.88	35.67	40.67	34.64	39.59	43.72
P_2O_5	0.02	0.07	0.18	0.06	0.03	0.05	0.05	0.09	0.25	0.15	0.11	0.17	0.11	0.11
TiO_2	0.01	0.02	0.03	0.05	0.02	0.03	0.02	0.04	0.04	0.02	0.04	0.07	0.04	0.06
Al_2O_3	0.75	0.63	1.78	2.27	1.50	1.73	1.90	0.67	1.96	1.77	1.45	1.51	1.64	1.61
Cr_2O_3	0.03	0.12	0.17	0.13	0.04	0.09	0.10	0.34	0.31	0.12	0.21	0.49	0.12	0.52
FeO	35.62	40.58	35.70	34.51	36.02	39.97	40.22	37.97	39.20	38.65	35.31	37.47	36.57	31.66
MgO	3.84	1.87	2.46	2.72	5.92	0.92	1.00	3.72	2.76	3.68	3.72	3.35	3.64	4.00
CaO	0.11	0.16	1.62	0.74	0.10	0.13	0.12	0.15	1.43	0.15	1.28	0.74	0.75	2.57
MnO	0.27	0.19	0.68	0.91	0.13	0.27	0.23	0.23	0.73	0.27	1.55	0.35	1.45	1.60
Na_2O	0.06	0.14	0.41	0.88	0.09	0.22	0.20	0.16	0.56	0.14	0.38	0.21	0.24	0.50
K_2O	0.03	0.04	0.05	0.06	0.03	0.08	0.08	0.05	0.06	0.05	0.06	0.06	0.06	0.06
NiO	0.10	0.97	0.65	0.68	0.17	0.17	0.15	0.31	0.92	0.49	0.26	0.70	0.16	0.17
SO_3	0.03	0.11	0.17	0.24	0.05	0.09	0.11	0.13	0.69	0.26	0.21	0.44	0.09	0.09
Total	81.51	81.98	84.68	84.87	81.91	81.74	82.42	82.54	84.80	81.42	85.26	80.19	84.45	86.66

Oxides wt%	Sp15	Sp16	Sp17	Sp18	Sp19	Sp20	Sp21	Sp22	Sp23	Sp24	Sp25	Sp26	Sp27	Sp28
SiO_2	44.16	39.27	47.33	37.41	38.91	40.42	39.55	36.56	36.03	41.84	43.03	43.06	42.13	40.94
P_2O_5	0.05	0.11	0.09	0.04	0.03	0.07	0.14	0.05	0.06	0.09	0.05	n.d.	0.07	0.04
TiO_2	0.01	0.03	0.10	0.02	0.07	0.02	0.01	n.d.	n.d.	0.12	n.d.	0.04	0.05	0.04
Al_2O_3	0.75	0.78	1.51	0.36	0.74	3.02	2.04	0.29	0.25	4.92	0.30	1.76	0.79	0.66
Cr_2O_3	0.07	0.04	0.44	0.24	0.04	0.06	0.06	0.04	0.08	0.68	0.08	0.07	0.08	0.06
FeO	39.15	38.21	26.06	40.22	40.34	36.99	38.15	40.26	41.78	29.56	36.37	37.52	39.92	38.09
MgO	0.97	2.42	6.28	2.22	0.90	1.75	1.68	3.19	2.28	4.00	2.97	0.66	1.30	0.62
CaO	0.39	0.19	5.70	0.21	0.13	0.47	0.57	0.12	0.10	4.16	0.12	0.52	0.35	0.21
MnO	0.22	0.23	2.14	0.18	0.22	0.82	0.61	0.15	0.13	1.19	0.23	0.15	0.09	0.13
Na_2O	0.23	0.35	0.53	0.21	0.18	0.88	0.46	0.22	0.12	0.83	0.08	0.17	0.09	0.19
K_2O	0.09	0.06	0.04	0.08	0.07	0.06	0.07	0.06	0.05	0.06	0.04	0.08	0.05	0.05
NiO	0.36	0.39	0.07	0.57	0.17	0.52	0.41	0.56	0.62	0.66	0.44	0.21	0.30	0.28
SO_3	0.15	0.14	0.03	0.09	0.04	0.12	0.11	0.12	0.08	0.26	0.24	0.10	0.16	0.09
Total	86.59	82.20	90.33	81.84	81.84	85.19	83.86	81.62	81.56	88.35	83.95	84.33	85.36	81.42

Table A1.10. *(Continuation).* Individual EPMA analyses (oxides wt%) of smooth rims around Ch22 in QUE 99177,19, n=30.

Oxides wt%	Sp29	Sp30	Mean	σ
SiO_2	42.75	38.12	39.82	2.93
P_2O_5	0.15	0.11	0.09	0.06
TiO_2	0.10	0.02	0.04	0.03
Al_2O_3	1.61	0.48	1.38	0.96
Cr_2O_3	0.77	0.07	0.19	0.20
FeO	30.14	42.53	37.16	3.75
MgO	6.18	0.85	2.73	1.60
CaO	4.73	0.25	0.94	1.46
MnO	1.41	0.09	0.56	0.57
Na_2O	0.17	0.20	0.30	0.23
K_2O	0.04	0.09	0.06	0.02
NiO	0.72	0.47	0.42	0.25
SO_3	0.25	0.06	0.16	0.13
Total	89.04	83.34	83.84	2.50

Table A1.11. Individual EPMA analyses (oxides wt%) of smooth rims around Ch23 in QUE 99177,19, n=17.

Oxides wt%	Sp1	Sp2	Sp3	Sp4	Sp5	Sp6	Sp7	Sp8	Sp9	Sp10	Sp11	Sp12	Sp13	Sp14
SiO_2	41.37	42.86	40.24	42.37	37.82	42.05	44.27	44.86	38.06	39.11	40.03	38.75	36.00	37.62
P_2O_5	0.01	0.05	0.04	0.04	0.07	0.06	0.09	0.10	0.11	0.13	0.04	0.03	0.21	0.06
TiO_2	0.06	0.05	0.05	0.05	0.03	0.07	0.22	0.10	0.03	0.05	0.06	0.08	0.05	0.01
Al_2O_3	1.80	1.69	2.39	1.25	0.73	1.49	5.56	2.85	0.92	1.99	1.40	2.49	1.54	0.38
Cr_2O_3	0.30	0.16	0.08	0.49	0.24	0.32	0.89	0.20	0.21	0.12	0.46	0.41	0.06	0.10
FeO	32.71	35.06	40.86	34.77	39.78	34.37	24.14	34.90	40.76	40.89	34.57	36.44	39.84	40.55
MgO	7.16	7.37	1.39	6.66	3.54	6.27	5.71	2.48	1.73	3.05	6.02	5.41	3.07	1.94
CaO	0.56	0.27	0.21	1.87	0.57	1.05	4.40	1.13	1.22	0.40	2.16	0.49	0.53	0.35
MnO	0.71	0.68	0.35	1.00	0.60	1.10	1.85	1.38	0.40	0.40	0.98	0.60	0.36	0.44
Na_2O	0.32	0.25	0.17	0.26	0.08	0.14	0.25	0.16	0.23	0.10	0.16	0.34	0.10	0.12
K_2O	0.13	0.14	0.13	0.11	0.06	0.07	0.28	0.17	0.12	0.09	0.11	0.12	0.11	0.11
NiO	0.41	0.37	0.34	0.34	0.74	0.33	0.61	0.49	1.64	0.41	0.30	0.55	0.60	0.39
SO_3	0.03	0.05	0.15	0.06	0.15	0.10	0.38	0.17	0.19	0.46	0.09	0.45	0.27	0.27
Total	85.56	88.99	86.39	89.26	84.41	87.42	88.64	88.99	85.61	87.20	86.38	86.18	82.73	82.34

Oxides wt%	Sp15	Sp16	Sp17	Mean	σ
SiO_2	44.44	40.69	36.22	40.40	2.81
P_2O_5	0.03	0.06	0.11	0.07	0.05
TiO_2	0.14	0.02	0.02	0.06	0.05
Al_2O_3	1.45	0.72	0.90	1.74	1.19
Cr_2O_3	2.38	0.09	0.07	0.39	0.55
FeO	26.66	38.43	42.52	36.31	5.09
MgO	8.12	4.62	1.56	4.48	2.27
CaO	3.62	0.23	0.30	1.14	1.23
MnO	2.10	0.47	0.47	0.82	0.53
Na_2O	0.81	0.17	0.06	0.22	0.17
K_2O	0.08	0.08	0.08	0.12	0.05
NiO	0.28	0.38	0.46	0.51	0.32
SO_3	0.06	0.06	0.32	0.19	0.14
Total	90.17	86.02	83.09	86.43	2.36

Table A1.12. Individual EPMA analyses (oxides wt%) of smooth rims around Ch14 in QUE 99177,18, n=16.

Oxides wt%	Sp1	Sp2	Sp3	Sp4	Sp5	Sp6	Sp7	Sp8	Sp9	Sp10	Sp11	Sp12	Sp13	Sp14
SiO_2	33.04	32.16	32.61	33.10	33.76	33.94	32.49	31.88	33.41	32.91	34.49	33.99	34.35	33.53
P_2O_5	0.04	0.04	n.d.	0.04	0.01	0.02	0.05	n.d.	0.01	0.05	n.d.	0.01	0.04	0.01
TiO_2	0.03	0.04	0.06	0.08	0.01	0.05	0.06	0.04	0.05	0.05	0.10	0.04	0.09	0.06
Al_2O_3	0.71	0.26	0.76	0.95	0.15	0.17	0.84	0.71	0.49	0.32	0.96	1.14	1.03	0.55
Cr_2O_3	0.01	0.02	0.02	0.01	0.01	0.01	0.29	0.05	0.04	0.01	0.07	0.03	0.32	0.04
FeO	41.78	43.69	43.48	41.78	43.69	42.96	40.01	39.50	40.75	41.05	39.40	41.61	33.16	38.10
MgO	1.47	2.21	1.12	2.75	0.99	0.77	6.06	5.86	3.66	2.98	4.13	2.63	11.78	5.68
CaO	0.19	0.46	0.18	0.54	0.25	0.14	0.63	0.44	0.15	0.14	0.38	0.67	1.31	0.20
MnO	0.08	0.07	0.05	0.06	0.04	0.06	0.43	0.17	0.10	0.10	0.11	0.12	0.46	0.07
Na_2O	0.27	0.14	0.18	0.23	0.18	0.28	0.17	0.21	0.12	0.15	0.13	0.23	0.18	0.09
K_2O	0.33	0.25	0.36	0.32	0.39	0.58	0.22	0.25	0.24	0.28	0.27	0.38	0.13	0.18
NiO	n.d.	n.d.	0.01	n.d.	n.d.	n.d.	n.d.	n.d.	0.03	n.d.	n.d.	n.d.	0.20	n.d.
SO_3	n.d.	0.57	0.02	0.34	0.20	0.04	0.58	0.50	0.06	0.05	0.05	0.62	2.03	0.09
Total	77.94	79.91	78.84	80.21	79.68	79.02	81.84	79.62	79.11	78.09	80.08	81.47	85.08	78.60

Oxides wt%	Sp15	Sp16	Mean	σ
SiO_2	34.20	30.56	33.15	1.04
P_2O_5	0.02	n.d.	0.02	0.02
TiO_2	0.06	0.04	0.05	0.02
Al_2O_3	0.77	0.18	0.62	0.33
Cr_2O_3	0.02	0.02	0.06	0.10
FeO	40.80	46.81	41.16	3.00
MgO	3.00	2.12	3.57	2.77
CaO	0.15	0.38	0.39	0.31
MnO	0.11	0.07	0.13	0.13
Na_2O	0.20	0.17	0.18	0.05
K_2O	0.29	0.26	0.30	0.10
NiO	n.d.	0.04	0.02	0.05
SO_3	0.06	0.41	0.35	0.50
Total	79.67	81.06	80.01	1.75

4. Individual EPMA analyses of matrices adjacent to smooth rims around chondrules

Table A1.13. Individual EPMA analyses (oxides wt%) of matrix adjacent to the smooth rim around Ch1 in QUE 99177,19, n=11.

Oxides wt%	Sp1	Sp2	Sp3	Sp4	Sp5	Sp6	Sp7	Sp8	Sp9	Sp10	Sp11	Mean	σ
SiO_2	29.57	34.45	29.81	33.96	35.49	27.22	32.64	33.70	31.03	29.55	28.49	31.45	2.73
P_2O_5	0.47	0.30	0.36	0.21	0.25	0.34	0.21	0.19	0.19	0.52	0.47	0.32	0.12
TiO_2	0.03	0.03	0.07	0.03	0.04	0.03	0.07	0.04	0.05	0.06	0.06	0.05	0.02
Al_2O_3	0.60	0.98	1.23	1.96	0.75	1.15	1.31	1.26	1.04	1.44	1.35	1.19	0.36
Cr_2O_3	0.52	0.42	0.72	0.23	0.27	0.22	0.38	0.20	0.27	0.64	0.34	0.38	0.18
FeO	42.73	36.85	42.05	38.83	30.70	44.39	31.54	37.23	37.17	38.27	40.25	38.18	4.28
MgO	3.86	6.39	7.42	7.32	19.06	6.98	14.57	7.11	11.26	12.03	9.35	9.58	4.35
CaO	1.71	0.90	1.22	1.19	0.40	0.28	0.39	0.31	0.20	0.21	0.18	0.64	0.53
MnO	0.31	0.30	0.50	0.26	0.20	0.20	0.17	0.24	0.20	0.19	0.15	0.25	0.10
Na_2O	0.23	0.27	0.31	0.17	0.13	0.07	0.08	0.25	0.25	0.17	0.16	0.19	0.08
K_2O	0.02	0.01	0.01	0.03	0.01	n.d.	0.02	0.06	0.04	0.03	0.03	0.02	0.02
NiO	2.57	1.36	2.92	1.32	5.53	2.66	7.94	2.75	6.19	7.96	8.01	4.47	2.70
SO_3	0.80	0.70	1.50	0.45	1.99	1.61	1.62	0.93	1.11	1.45	1.32	1.23	0.47
Total	83.43	82.96	88.12	85.96	94.80	85.17	90.92	84.27	89.00	92.52	90.16	87.94	3.91

Table A1.14. Individual EPMA analyses (oxides wt%) of matrix adjacent to the smooth rim around Ch3 in QUE 99177,19, n=8.

Oxides wt%	Sp1	Sp2	Sp3	Sp4	Sp5	Sp6	Sp7	Sp8	Mean	σ
SiO_2	32.07	38.60	37.17	35.79	39.15	32.79	43.29	39.27	37.27	3.68
P_2O_5	0.21	0.10	0.53	1.23	0.18	0.19	0.16	0.16	0.34	0.38
TiO_2	0.08	0.04	0.04	0.04	0.04	0.05	0.08	0.07	0.06	0.02
Al_2O_3	1.76	0.64	0.93	0.78	0.88	1.12	1.69	0.95	1.09	0.41
Cr_2O_3	0.45	0.17	0.27	0.23	0.31	0.32	0.60	1.54	0.49	0.45
FeO	31.67	30.85	31.71	31.60	26.85	27.39	21.17	27.89	28.64	3.65
MgO	13.53	9.42	11.16	9.41	15.26	11.31	23.16	10.09	12.92	4.61
CaO	0.60	0.15	1.10	2.17	0.54	4.74	0.97	2.07	1.54	1.48
MnO	0.27	0.35	0.37	0.37	0.34	0.32	0.63	1.08	0.47	0.27
Na_2O	0.77	0.54	0.64	0.52	0.46	0.56	0.47	0.81	0.60	0.13
K_2O	0.10	0.13	0.13	0.12	0.11	0.10	0.08	0.10	0.11	0.02
NiO	10.46	2.21	2.67	3.11	3.40	3.66	4.77	2.01	4.03	2.74
SO_3	1.79	0.67	1.04	1.91	1.25	0.94	1.15	0.90	1.21	0.43
Total	93.76	83.88	87.77	87.26	88.76	83.49	98.23	86.93	88.76	4.97

Table A1.15. Individual EPMA analyses (oxides wt%) of matrix adjacent to the smooth rim around Ch8 in QUE 99177,19, n=14.

Oxides wt%	Sp1	Sp2	Sp3	Sp4	Sp5	Sp6	Sp7	Sp8	Sp9	Sp10	Sp11	Sp12	Sp13	Sp14	Mean	σ
SiO_2	35.07	33.05	28.08	33.80	30.35	36.69	33.31	25.05	28.33	30.68	30.04	31.26	31.81	32.41	31.42	3.03
P_2O_5	0.01	0.03	n.d.	n.d.	n.d.	0.08	n.d.	0.16	0.06	n.d.	0.10	0.05	0.01	0.13	0.05	0.05
TiO_2	0.04	0.05	0.06	0.07	0.06	n.d.	0.05	0.04	0.06	0.05	0.07	0.07	0.07	0.08	0.06	0.02
Al_2O_3	0.70	1.32	1.43	1.68	2.10	0.64	1.21	1.04	1.36	1.03	1.23	1.25	1.68	1.82	1.32	0.41
Cr_2O_3	0.16	0.39	0.36	0.38	0.32	0.07	0.27	0.24	0.35	0.25	0.31	0.34	0.39	0.47	0.31	0.10
FeO	33.70	28.06	33.70	32.26	33.88	39.43	35.10	39.43	34.97	33.05	33.68	31.96	28.23	28.47	33.28	3.52
MgO	9.19	18.03	11.97	13.20	9.94	4.08	11.13	8.48	10.57	11.96	15.97	17.75	19.43	16.70	12.74	4.35
CaO	0.37	0.71	0.54	0.66	0.48	1.36	0.74	1.25	1.19	0.59	1.11	1.38	0.78	2.25	0.96	0.50
MnO	0.46	0.35	0.26	0.27	0.26	0.34	0.22	0.19	0.21	0.33	0.29	0.31	0.26	0.33	0.29	0.07
Na_2O	0.26	0.45	0.94	0.69	0.62	0.58	0.89	0.65	1.05	0.53	0.82	0.84	0.59	0.60	0.68	0.21
K_2O	0.19	0.14	0.20	0.17	0.17	0.14	0.13	0.08	0.22	0.19	0.13	0.12	0.08	0.13	0.15	0.04
NiO	0.08	0.38	0.63	0.41	0.38	n.d.	0.12	0.10	0.49	0.47	0.57	0.70	0.47	0.52	0.38	0.22
SO_3	0.99	1.11	1.55	1.39	2.60	0.07	1.48	3.20	1.47	2.35	2.72	3.00	1.24	1.98	1.80	0.88
Total	81.23	84.06	79.72	84.99	81.16	83.49	84.65	79.90	80.34	81.49	87.03	89.03	85.06	85.90	83.43	2.87

Table A1.16. Individual EPMA analyses (oxides wt%) of matrix adjacent to the smooth rim around Ch22 in QUE 99177,19, n=27.

Oxides wt%	Sp1	Sp2	Sp3	Sp4	Sp5	Sp6	Sp7	Sp8	Sp9	Sp10	Sp11	Sp12	Sp13	Sp14	Sp15
SiO_2	37.37	39.76	42.13	33.99	35.78	35.69	36.39	35.64	43.35	39.26	45.90	39.35	35.84	35.89	31.02
P_2O_5	0.27	0.26	0.26	0.18	0.99	0.29	0.39	0.41	0.21	0.43	0.32	0.20	0.38	0.27	0.26
TiO_2	0.06	0.06	0.08	0.04	n.d.	0.05	0.07	0.09	0.16	0.07	0.04	0.08	0.05	0.06	0.07
Al_2O_3	1.82	1.93	1.75	1.27	0.06	2.04	2.10	1.74	1.68	1.34	1.57	1.24	1.17	1.24	1.37
Cr_2O_3	0.35	0.39	0.44	0.33	0.13	0.30	0.35	0.60	0.44	0.37	0.29	0.37	0.27	0.29	0.39
FeO	35.06	30.40	24.75	30.45	36.52	33.60	30.84	29.40	24.31	28.40	22.50	27.44	32.45	31.27	32.89
MgO	9.18	8.76	18.91	10.56	1.80	10.24	12.51	15.44	17.02	16.22	17.35	18.24	13.07	14.71	13.49
CaO	0.83	1.93	1.35	0.28	0.20	0.88	1.04	0.59	1.32	1.48	1.25	1.05	0.96	0.91	0.48
MnO	0.33	0.94	0.34	0.18	0.21	0.33	0.36	0.20	0.52	0.34	0.64	0.34	0.23	0.24	0.15
Na_2O	0.35	0.61	0.13	0.13	0.32	0.28	0.39	0.19	0.40	0.20	0.27	0.18	0.12	0.19	0.25
K_2O	0.21	0.04	0.03	0.03	0.05	0.05	0.08	0.02	0.02	0.03	0.04	0.01	0.03	0.05	0.03
NiO	1.95	2.64	3.19	3.52	2.13	2.52	3.19	4.53	3.29	3.28	2.07	5.14	3.33	3.35	7.86
SO_3	1.27	1.26	1.43	1.91	4.13	1.21	1.64	1.51	1.93	1.71	0.85	2.65	1.29	1.35	1.81
Total	89.06	88.97	94.79	82.86	82.32	87.48	89.34	90.35	94.64	93.14	93.10	96.27	89.18	89.82	90.07

Oxides wt%	Sp16	Sp17	Sp18	Sp19	Sp20	Sp21	Sp22	Sp23	Sp24	Sp25	Sp26	Sp27	Mean	σ
SiO_2	36.44	36.29	34.99	30.30	40.24	39.37	39.42	39.81	39.16	40.91	40.11	38.47	37.88	3.44
P_2O_5	0.39	0.22	0.29	0.18	0.26	0.23	0.35	0.25	0.34	0.09	0.22	0.22	0.30	0.16
TiO_2	0.05	0.06	0.04	0.04	0.05	0.05	0.07	0.06	0.06	0.05	0.06	0.04	0.06	0.03
Al_2O_3	1.23	1.22	1.10	1.16	1.19	1.32	1.42	1.41	1.36	1.41	1.37	0.66	1.38	0.41
Cr_2O_3	0.32	0.33	0.26	0.31	0.31	0.33	0.34	0.36	0.32	0.34	0.34	0.16	0.33	0.09
FeO	32.13	30.99	32.43	29.96	31.25	30.35	29.31	29.34	30.42	28.87	29.79	37.87	30.48	3.37
MgO	14.41	15.28	12.98	9.42	15.48	15.79	17.28	17.29	15.84	13.95	12.17	6.86	13.49	3.92
CaO	1.13	0.89	0.88	0.25	1.00	1.00	1.16	1.04	1.10	0.33	0.37	0.60	0.90	0.41
MnO	0.23	0.22	0.22	0.13	0.22	0.21	0.29	0.24	0.25	0.19	0.16	0.24	0.29	0.17
Na_2O	0.15	0.12	0.15	0.22	0.09	0.13	0.23	0.15	0.14	0.12	0.16	0.15	0.22	0.12
K_2O	0.04	0.03	0.04	0.04	0.02	0.03	0.02	0.02	0.02	0.03	0.02	0.05	0.04	0.04
NiO	3.26	3.62	3.08	4.26	3.07	3.27	3.40	3.04	3.08	2.33	2.46	1.90	3.29	1.18
SO_3	1.27	1.51	1.13	1.31	1.20	1.36	1.40	1.24	1.25	1.27	1.09	1.17	1.52	0.63
Total	91.06	90.77	87.58	77.58	94.37	93.44	94.68	94.24	93.35	89.89	88.33	88.40	90.19	4.26

Table A1.17. Individual EPMA analyses (oxides wt%) of matrix adjacent to the smooth rim around Ch23 in QUE 99177,19, n=9.

Oxides wt%	Sp1	Sp2	Sp3	Sp4	Sp5	Sp6	Sp7	Sp8	Sp9	Mean	σ
SiO_2	34.28	32.35	42.10	39.81	38.84	37.47	31.70	36.44	34.43	36.38	3.50
P_2O_5	0.26	0.72	0.31	0.40	0.11	0.06	0.28	0.16	0.18	0.28	0.20
TiO_2	0.03	0.05	0.12	0.06	0.03	0.03	0.08	0.06	0.09	0.06	0.03
Al_2O_3	1.64	0.52	1.48	1.42	0.77	0.61	2.65	1.04	1.98	1.35	0.69
Cr_2O_3	0.67	2.19	1.74	0.42	0.19	0.20	0.43	0.27	0.56	0.74	0.72
FeO	33.64	29.13	28.79	28.86	33.67	34.67	32.96	35.01	27.09	31.53	3.02
MgO	3.95	8.64	8.83	14.59	8.77	8.31	14.60	9.48	18.07	10.58	4.31
CaO	5.02	2.56	3.24	1.53	0.41	0.50	0.57	0.42	0.96	1.69	1.61
MnO	0.50	0.92	1.45	0.42	0.46	0.47	0.26	0.29	0.28	0.56	0.39
Na_2O	0.35	0.54	0.79	0.24	0.23	0.20	0.47	0.28	0.30	0.38	0.19
K_2O	0.10	0.10	0.10	0.06	0.09	0.08	0.10	0.09	0.07	0.09	0.02
NiO	4.99	5.30	1.32	1.88	1.86	2.28	5.96	2.45	8.57	3.85	2.47
SO_3	1.67	4.57	1.05	1.09	0.89	1.10	1.92	1.68	2.17	1.79	1.13
Total	87.10	87.60	91.32	90.78	86.32	85.99	91.98	87.68	94.76	89.28	3.03

Table A1.18. Individual EPMA analyses (oxides wt%) of matrix adjacent to the smooth rim around Ch13 in QUE 99177,18, n=4.

Oxides wt%	Sp1	Sp2	Sp3	Sp4	Mean	σ
SiO_2	28.89	25.76	26.32	27.83	27.20	1.42
P_2O_5	0.06	0.01	0.02	0.01	0.03	0.02
TiO_2	0.05	0.06	0.06	0.05	0.05	n.d.
Al_2O_3	1.39	1.74	1.63	1.14	1.47	0.27
Cr_2O_3	0.28	0.24	0.26	0.30	0.27	0.03
FeO	30.75	37.08	35.03	32.99	33.96	2.72
MgO	15.77	15.07	15.91	12.40	14.79	1.63
CaO	0.26	0.86	0.89	0.28	0.57	0.35
MnO	0.18	0.28	0.31	0.20	0.24	0.06
Na_2O	0.48	0.28	0.31	0.42	0.37	0.09
K_2O	0.11	0.04	0.05	0.09	0.07	0.03
NiO	0.52	0.85	0.77	0.79	0.73	0.15
SO_3	1.72	1.96	2.48	1.21	1.84	0.53
Total	80.46	84.22	84.05	77.70	81.61	3.13

Table A1.19. Individual EPMA analyses (oxides wt%) of matrix adjacent to the smooth rim around Ch14 in QUE 99177,18, n=10.

Oxides wt%	Sp1	Sp2	Sp3	Sp4	Sp5	Sp6	Sp7	Sp8	Sp9	Sp10	Mean	σ
SiO_2	32.69	33.20	33.45	37.57	33.28	39.54	30.44	32.29	31.49	31.50	33.55	2.84
P_2O_5	0.02	0.03	0.02	0.03	n.d.	0.04	0.05	0.01	n.d.	0.04	0.02	0.02
TiO_2	0.05	0.05	0.04	0.06	0.03	0.07	0.14	0.06	0.07	0.05	0.06	0.03
Al_2O_3	0.97	0.99	0.93	1.27	0.68	1.39	2.27	1.21	1.71	1.51	1.29	0.46
Cr_2O_3	0.27	0.26	0.22	0.32	0.21	0.41	0.35	0.33	0.37	0.31	0.31	0.06
FeO	32.67	34.13	35.05	30.72	38.56	26.58	27.01	31.73	32.27	31.86	32.06	3.55
MgO	11.48	9.38	8.90	13.05	10.58	16.50	18.27	14.45	11.11	13.29	12.70	3.04
CaO	0.30	0.21	0.17	1.28	1.09	1.21	1.56	1.23	0.50	0.72	0.83	0.51
MnO	0.17	0.10	0.11	0.42	0.26	0.48	0.16	0.18	0.16	0.17	0.22	0.13
Na_2O	0.32	0.31	0.24	0.21	0.26	0.21	0.18	0.12	0.25	0.32	0.24	0.07
K_2O	0.20	0.23	0.17	0.18	0.21	0.16	0.10	0.13	0.22	0.23	0.18	0.04
NiO	0.14	0.19	0.21	0.13	0.09	0.21	0.31	0.12	0.37	0.58	0.23	0.15
SO_3	1.58	1.46	1.57	1.18	1.53	1.86	2.70	1.96	2.05	2.07	1.80	0.43
Total	80.84	80.54	81.08	86.41	86.79	88.67	83.54	83.81	80.58	82.65	83.49	2.93

5. Individual EPMA analyses of smooth rims high and low Z-contrasts (dark and light areas) around chondrules 1 and 3.

Table A1.20. Individual EPMA analyses (oxides wt%) of BSE dark areas (n=20)

Oxide wt%	Ch1 Sp1	Ch1 Sp2	Ch1 Sp3	Ch1 Sp4	Ch1 Sp5	Ch1 Sp6	Ch1 Sp7	Ch1 Sp8	Ch1 Sp9	Ch1 Sp10	Ch1 Sp11	Ch1 Sp12
SiO_2	33.96	31.55	25.08	38.01	32.79	39.92	33.60	34.67	35.45	40.50	37.42	34.81
P_2O_5	0.21	3.08	0.18	0.20	0.25	0.73	0.37	0.25	0.31	0.29	0.33	0.56
TiO_2	0.03	0.03	0.07	0.11	0.04	0.17	0.05	0.03	0.04	0.10	0.03	0.06
Al_2O_3	1.96	1.33	1.55	1.41	1.73	1.41	2.58	2.86	3.33	2.98	3.10	2.20
Cr_2O_3	0.23	0.04	0.47	2.00	0.19	3.51	0.41	0.10	0.15	1.17	0.31	0.78
SO_3	1.32	0.68	0.43	0.48	0.70	0.74	0.63	0.53	0.71	0.65	0.64	0.68
FeO	38.83	33.20	34.48	29.69	37.66	26.42	34.57	36.28	35.60	30.64	34.41	33.80
MnO	0.26	0.26	0.44	0.48	0.29	0.80	0.52	0.28	0.26	0.90	0.38	0.44
MgO	7.32	4.88	4.21	8.00	5.84	7.79	8.44	6.95	8.02	9.22	9.32	7.27
CaO	1.19	4.35	0.70	2.74	0.30	4.47	0.61	0.14	0.23	2.33	0.54	1.60
Na_2O	0.17	0.36	0.38	1.02	0.12	1.93	0.10	0.02	0.13	0.44	0.13	0.44
K_2O	0.03	0.05	0.05	0.03	0.05	0.02	0.02	0.02	0.03	0.04	0.03	0.03
NiO	0.45	0.03	0.03	0.04	0.06	0.07	0.16	0.08	0.20	0.16	0.08	0.12
Total	85.96	79.85	68.07	84.22	80.02	87.98	82.05	82.21	84.46	89.41	86.71	91.09

Oxides wt%	Ch3 Sp1	Ch3 Sp2	Ch3 Sp3	Ch3 Sp4	Ch3 Sp5	Ch3 Sp6	Ch3 Sp7	Ch3 Sp8	Mean D
SiO_2	39.92	39.00	44.71	40.51	35.74	37.24	0.42	0.07	32.77
P_2O_5	0.08	0.09	0.07	0.07	1.15	0.03	6.67	6.40	1.07
TiO_2	n.d.	0.06	0.12	0.04	0.06	0.01	2.06	1.50	0.23
Al_2O_3	0.47	1.63	1.43	1.73	1.82	0.48	42.32	37.04	5.67
Cr_2O_3	0.04	0.06	1.26	0.27	0.25	0.03	0.09	0.08	0.57
SO_3	0.24	0.20	0.23	0.29	0.22	0.28	2.78	1.43	0.69
FeO	37.63	38.14	24.42	32.66	32.29	36.07	0.09	0.03	30.35
MnO	0.47	0.57	1.13	0.65	0.74	0.43	0.80	0.06	0.51
MgO	4.79	3.65	9.45	6.30	6.21	5.15	1.07	0.55	6.22
CaO	0.13	0.45	6.74	0.89	2.57	0.13	31.06	34.88	4.80
Na_2O	0.16	0.10	0.69	0.28	0.11	0.06	0.06	0.03	0.34
K_2O	0.10	0.15	0.09	0.14	0.05	0.11	0.29	0.30	0.08
NiO	0.04	0.08	0.32	0.06	0.03	0.05	0.12	1.02	0.16
Total	84.08	84.18	90.67	83.90	81.23	80.07	87.85	83.39	83.87

Table A1.21. Individual EPMA analyses (oxides wt%) of BSE light areas (n= 23).

Oxide wt%	Ch1 Sp1	Ch1 Sp2	Ch1 Sp3	Ch1 Sp4	Ch1 Sp5	Ch1 Sp6	Ch1 Sp7	Ch1 Sp8	Ch1 Sp9	Ch1 Sp10	Ch1 Sp11	Ch1 Sp12
SiO_2	37.90	35.83	35.30	34.90	35.83	36.64	29.06	25.14	29.33	27.39	28.01	32.30
P_2O_5	0.17	0.23	0.19	0.17	0.16	0.15	0.19	0.19	0.19	0.23	0.21	0.19
TiO_2	0.03	0.04	0.05	0.05	0.04	0.04	0.01	0.05	0.16	0.18	0.03	0.06
Al_2O_3	2.02	1.57	1.10	1.16	0.84	0.80	0.54	1.18	3.11	6.30	0.86	1.77
Cr_2O_3	0.09	0.26	0.18	0.05	0.08	0.05	0.05	0.05	0.13	0.09	0.07	0.10
SO_3	0.39	0.36	0.72	0.81	0.68	0.55	0.69	0.53	0.73	0.72	0.63	0.62
FeO	38.29	38.79	37.34	38.81	39.45	40.35	41.77	40.92	40.95	43.37	42.24	40.21
MnO	0.29	0.30	0.33	0.23	0.31	0.27	0.22	0.24	0.90	0.23	0.26	0.33
MgO	6.22	5.84	5.33	3.98	4.38	3.78	2.81	1.88	2.66	2.40	2.03	3.75
CaO	0.21	0.33	0.36	0.13	0.21	0.14	0.10	0.14	0.67	0.37	0.14	0.25
Na_2O	0.07	0.08	0.16	0.18	0.18	0.21	0.07	0.10	0.08	0.23	0.08	0.13
K_2O	0.02	0.01	0.07	0.07	0.05	0.07	0.05	0.06	0.06	0.12	0.07	0.06
NiO	0.07	0.05	0.09	0.04	0.09	0.02	0.05	0.03	0.06	0.07	0.02	0.05
Total	85.77	83.68	81.21	80.59	82.30	83.06	75.60	70.51	79.04	81.69	74.66	79.83

Oxides wt%	Ch3 Sp1	Ch3 Sp2	Ch3 Sp3	Ch3 Sp4	Ch3 Sp5	Ch3 Sp6	Ch3 Sp7	Ch3 Sp8	Ch3 Sp9	Ch3 Sp10	Ch3 Sp11	Mean L
SiO_2	39.38	38.54	39.13	38.16	42.54	38.78	35.66	39.40	39.37	37.83	37.68	35.40
P_2O_5	0.66	0.07	0.07	0.12	0.11	0.04	0.09	0.03	0.19	0.19	0.17	0.17
TiO_2	0.03	0.05	0.04	0.04	0.08	0.04	0.04	0.06	0.03	0.05	0.03	0.05
Al_2O_3	1.41	2.21	1.17	0.90	1.93	0.38	1.95	1.56	2.28	3.75	1.42	1.75
Cr_2O_3	0.10	0.05	0.09	0.08	0.57	0.05	0.02	0.06	0.05	0.10	0.03	0.10
SO_3	0.15	0.25	0.17	0.31	0.28	0.20	0.18	0.11	0.26	0.31	0.32	0.43
FeO	36.61	35.04	39.33	37.80	31.08	38.43	38.35	39.27	36.14	36.09	39.08	38.68
MnO	0.72	0.47	0.88	0.43	1.16	0.58	0.73	0.78	0.50	0.62	0.65	0.50
MgO	3.83	5.64	1.45	4.43	8.38	2.97	1.13	1.61	5.77	3.66	2.62	3.76
CaO	1.14	0.18	0.35	0.39	1.47	0.14	0.17	0.40	0.40	0.44	0.23	0.36
Na_2O	0.16	0.22	0.07	0.35	0.19	0.07	0.02	0.04	0.09	0.13	0.07	0.13
K_2O	0.11	0.14	0.21	0.17	0.10	0.23	0.09	0.15	0.21	0.22	0.15	0.11
NiO	0.02	0.15	0.07	0.19	0.40	0.04	0.06	0.02	0.13	0.41	0.27	0.11
Total	84.32	83.04	83.02	83.38	89.40	81.96	78.49	83.51	85.42	83.78	82.72	81.61

APPENDIX 2

Supporting data for Chapter 3

1. Additional BSE images of apatite grains in NWA 998 and Nakhla

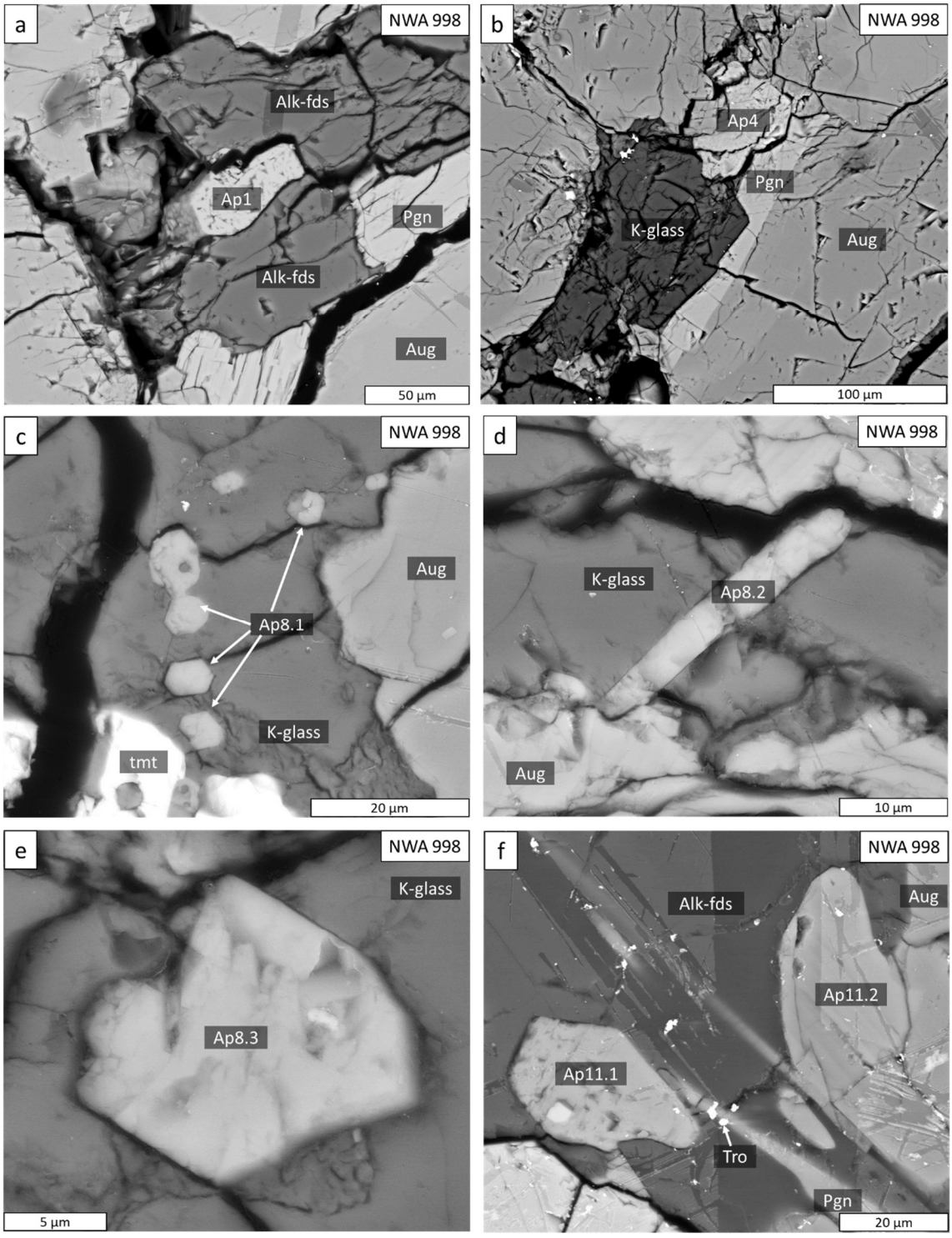

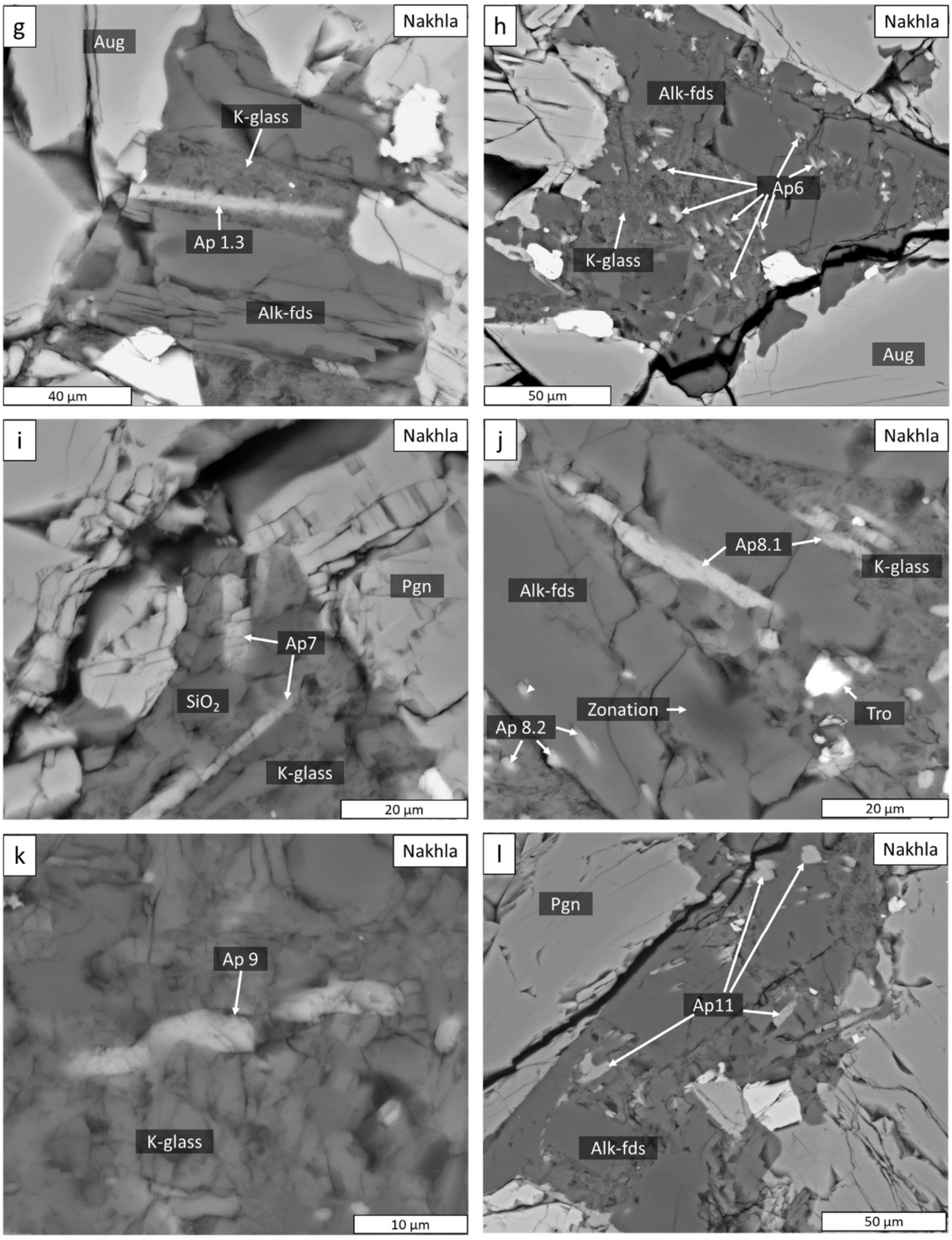
g
Nakhla
Aug
K-glass
Ap 1.3
Alk-fds
40 µm
h
Nakhla
Alk-fds
Ap6
K-glass
Aug
50 µm
i
Nakhla
Pgn
Ap7
SiO_2
K-glass
20 µm
j
Nakhla
Ap8.1
K-glass
Alk-fds
Zonation
Tro
Ap 8.2
20 µm
k
Nakhla
Ap 9
K-glass
10 µm
l
Nakhla
Pgn
Ap11
Alk-fds
50 µm

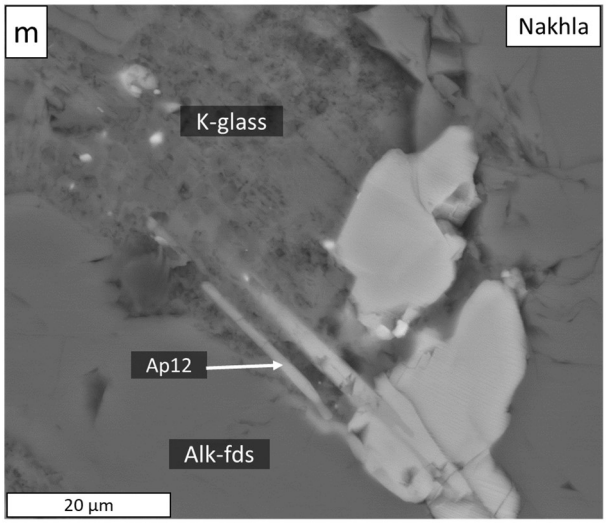

Figure A2.1. *(On present and previous pages).* Additional BSE images of apatites in NWA 998 and Nakhla. Apatite numbers referred in Fig. 3.1 in Chapter 3. NWA 998 (a-f): **a)** Apatite 1 (Ap1): Anhedral cumulus chlorapatite, ~50 µm in size, associated with K-rich glass, pigeonite, augite, and fractures. **b)** Apatite 4 (Ap4): Anhedral cumulus chlorapatite, ~50 µm in size, included in zoned pyroxene and associated with K-rich glass. **c)** Apatite 8.1 (Ap8.1) Several euhedral intercumulus apatites, ~5 µm in size, embedded in K-rich glass and as inclusions in titanomagnetite. **d)** Apatite 8.2 (Ap8.2): Acicular intercumulus apatite, ~30 x 4 µm, long and short dimensions, included in K-rich glass. **e)** Apatite 8.3 (Ap8.3): Subhedral intercumulus apatite, ~15 µm in size, included in K-rich glass. **f)** Apatites 11 (Ap11): Subhedral apatites that are included in both alkali-rich feldspar and pigeonite. Nakhla (g-m): **g)** Apatite 1.3 (Ap1.3): Acicular intercumulus apatite, ~50 x 5 µm in size, included in K-rich glass and alkali-rich feldspar. **h)** Apatite 6 (Ap6): Numerous micron-sized acicular intercumulus apatites cut perpendicular to the *c* axis, included in K-rich glass and alkali-rich feldspar. **i)** Apatite 7 (Ap7): Acicular Cl-rich apatites, ~20 x 5 µm-size, included in K-rich glass and silica. **j)** Apatite 8.1 (Ap8.1): Elongated intercumulus apatites at similar orientations, included in alkali-rich feldspar that shows zonation, K-rich glass, and associated with troilite. **k)** Apatite 9 (Ap9): Acicular chlorapatite, 3 x 25 µm, shortest and longest dimensions, that shows deformation, included in a mixture of K-rich feldspar and alkali-rich feldspar. **l)** Apatite 11 (Ap11): Numerous intercumulus micron-sized apatites at random orientations, included in alkali-rich feldspar. **m)** Apatite 12 (Ap12): Acicular micron-sized apatites cut parallel to the elongated direction, showing that apatites usually decorate the interface between K-rich glass and alkali-rich feldspar. Legend: K-glass = K-rich glass, Alk-fds = alkali-rich feldspar (Na being dominant). tmt = titanomagnetite, tro = troilite, Pgn = pigeonite, Aug = augite.

2. STEM-EDS analyses (oxides wt%) of accessory minerals in FIB3.

Table A2.1. STEM-EDS analyses (oxides wt%) of clay minerals, K-rich feldspar, amorphous silica, and tridymite in Nakhla (FIB3). Clays+ indicate that clay minerals analyses are contaminated by adjacent phases (amorphous silica and/or K-rich feldspar).

Oxides (wt%)	Clays+	Clays+		K-fds	Amor	Tridymite
SiO_2	62.62	64.47		73.84	99.11	100
Al_2O_3	4.62	3.4		19.1	0.89	n.d.
MgO	9.76	10.07		n.d.	n.d.	n.d.
FeO	17.28	17.14		n.d.	n.d.	n.d.
K_2O	4.58	3.67		5.02	n.d.	n.d.
Na_2O	n.d.	n.d.		2.03	n.d.	n.d.
Cl	1.15	1.26		n.d.	n.d.	n.d.
Total	100	100		100	100	100
		Mineral formulae				
Si	8.24	8.4		3.17	0.99	1
Al	0.72	0.52		0.97	0.01	n.d.
Fe	1.9	1.87		n.d.	n.d.	n.d.
Mg	1.91	1.96		n.d.	n.d.	n.d.
K	0.77	0.61		0.27	n.d.	n.d.
Na	n.d.	n.d.		0.17	n.d.	n.d.
Cl	0.26	0.28		n.d.	n.d.	n.d.
O	22	22		8	2	2
Total tetrahedral	8.24	8.4		4.14		
Total octahedral	4.53	4.35	6-fold	0.44		
Total interlayer	1.03	0.89				

n.d. = not detected

Nearly everything is really interesting if you go into it deeply enough.

Richard P. Feynman